Philipps Universität Marburg

Polymer-Coated Inorganic Nanoparticles: Nanotools for Life Science Applications

Dissertation

zur Erlangung des Doktorgrades
der Naturwissenschaften
(Dr. rer. nat.)

Dem
Fachbereich Physik
der Philipps-Universität Marburg
vorgelegt von

Qian Zhang

aus

Shandong, China

Marburg, 2015

Vom Fachbereich Physik der Philipps-Universität (Hochschulkennziffer: 1180) als Disssertation angenommen am 29.09.2015

Erstgutachter: Prof. Dr. Wolfgang. J. Parak

Zweitgutachter: Prof. Dr. Martin Koch

Prüfer: Prof. Dr. Reinhard Noack

Tag der mündlichen Prüfung: 01.10.2015

Die Vorliegende Arbeit wurde am Fachbereich Physik

Der Philipps-Universität Marburg unter Anleitung von

Herrn Prof. Dr. Wolfgang. J. Parak

In der Zeit von September 2011 bis September 2015 angefertigt.

Abstract

This cumulative dissertation focuses on the synthesis, surface modification and characterization of inorganic nanoparticles (NPs), including magnetic, plasmonic and semiconductor NPs. These nano-scale particles have an inorganic core, which is typically stabilized by hydrophobic ligands on the surface. By controlling the reaction conditions during the synthesis, different particle diameters in the range of 4 nm to 30 nm were produced. Moreover, composite nanoparticles, as well as core-shell structures, were synthesized by doping with other materials using one-pot synthesis or seeds-mediated growth methods. With the aim of producing shape-controlled highly monodisperse particles, synthetic methods performed in organic solvents are typically used. Thus, if these particles are to be used in bioapplications, the particles need to be transferred to aqueous phase. Herein, a polymer coating process was successfully applied to different materials by overcoating the NPs with an amphiphilic polymer, which interacts with capping ligands on the core surface; the hydrophilic backbone is used to render the NPs water-soluble. The polymer coating allows for further functionalization with molecules of biological relevance.

This work aimed to produce the polymer-coated nanoparticles, analyze and compare their physico-chemical properties based on different materials, and further, to test their potentialfor different biological applications. Three types of inorganic NPs were studied during this Ph.D: magnetic nanoparticles, plasmonic nanoparticles and titanium dioxide nanoparticles.

Firstly, magnetic nanoparticles (core only or core@shell systems) were produced, whose magnetic anisotropy was optimized by controlling the NP's design. The optimized system presents very high specific power loss (SPL) under alternating magnetic fields. We show theoretically and experimentally that the effective magnetic anisotropy can be tuned by changing Co ferrite ratio with constant size.

Secondly, plasmonic nanoparticles have unique optical properties based on the localized surface plasmon resonance property. Three kinds of plasmonic nanoparticles made of gold, silver and copper were synthesized and polymer coated. By making three equivalent plasmonic materials with the same size, shape and organic coating, we can investigate their relative impaction cell cultures (on going work). Plasmonic NPs are highly useful for various applications, including hyperthermia, catalysis, biosensing, etc.

Thirdly, titanium dioxide nanoparticles have strong UV absorption capability, which make them suitable materials for catalysis. Herein, we obtained highly uniform

aliphatic-coated titanium dioxide NPs, which were successfully transferred into aqueous solution with the polymer coating method. The polymer-coated TiO_2 NPs have promising applications.

Zusammenfassung

Diese kumulative Dissertation beinhaltet die Synthese, Oberflächenmodifizierung und Charakterisierung anorganische Nanopartikel (NPs), wie magnetische, plasmonische und halbleitende NPs. Diese Partikel mit Nanometer Größe haben einen anorganischen Kern, der typischerweise mit hydrophoben Liganden auf der Oberfläche stabilisiert ist. Durch Kontrolle der Reaktionsbedingungen währen der Synthese wurden verschiedene Partikel mit Durchmessern im Bereich von 4 nm bis 30 nm hergestellt. Weiterhin wurden Komposit-Nanopartiekl, wie auch Kern-Schale Strukturen synthetisiert. Dazu wurde Dotierung mit anderen Materialien in Ein-Topf-Synthesen oder Keim-vermittelten Wachstums Methoden verwendet. Um Form-kontrollierte Nanopartikel mit möglichst guter Größenverteilung zu bekommen wurden die Synthesen typischerweise in organischen Lösungsmitteln durchgeführt. Daher müssen die Partikel vor Gebrauch in biologischen Anwendungen in wässrige Lösung transferiert werden. Dazu wurde ein Polymer-Beschichtungs-Verfahren verwendet, in dem die verschiedenen Nanopartikel mit einem amphiphilen Polymer ummantelt wurden, bei dem die hydrophoben Seitengruppen mit den Liganden der Partikeloberfläche wechselwirken und das hydrophile Rückgrat die Partikel wasserlöslich macht. Diese Polymerbeschichtung erlaubt auch weitere Modifizierung mit anderen biologisch relevanten Molekülen.

In dieser Arbeit wurden Polymer-beschichtete Nanopartikel produziert, analysiert, deren physicochemischen Eigenschaften untersucht und deren Potential für biologische Anwendungen getestet. Im Rahmen dieser Dissertation wurden drei verschiedene Typen von anorganischen Nanopartikel hergestellt: magnetische NPs, plasmonische NPs und Titandioxid NPs.

Als Ersten wurden magnetische NPs (nur Kern oder Kern-Hülle Struktur) produziert, deren magnetische Anisotropie durch Kontrolle des NP Designs optimiert wurde. Das optimierte NP System hat sehr hohen spezifischen Leistungsverslust (SPL) unter alternierenden magnetischen Feldern. Es wurde theoretisch und experimentell gezeigt, dass die magnetische Anisotropie durch Variation des Co Ferrit Verhältnisses bei konstanter Größe eingestellt werden kann.

Zweitens wurden plasmonische NPs hergestellt, deren einmalige optische Eigenschaften auf lokalisierten Oberflächenplasmonen basieren. Es wurden drei verschiedene NPs aus Gold, Silber und Kupfer hergestellt und mit Polymer beschichtet. Durch Herstellung von drei verschiedenen plasmonischen Materialien

mit der gleichen Größe, Form und Oberflächenbeschichtung kann spezifische Wechselwirkung der NPs mit Zellen untersucht werden. Plasmonische NPs sind für verschiedene Anwendungen wir Hyperthermie, Katalyse und Biosensorik von Interesse.

Drittens wurden Titandioxid NPs hergestellt, die eine starke Absorption im UV haben, was sie nützlich für Anwendungen in der Katalyse mach. Es wurden organisch beschichtete Titandioxide NPs mit exzellenter Größenverteilung herstellt, welche durch Polymer-Beschichtung in wässrige Lösung transferiert wurden. Auch für diese Partikel gibt es zahlreiche Anwendungen.

Acknowledgements

First of all, I would like to thank Professor Wolfgang J. Parak for offering me the opportunity to work in his group during my Ph.D study, it was an honor for me to study in the Biophotonics group at Philipps-Universität Marburg with the supervision of Wolfgang J. Parak, and I appreciate his continuous support and kind help in all the time of my research.

I'm also grateful to my ex-supervisor, Dr. Nadja C. Bigall, for giving her advices at my first year, and I also want to express my thanks to my supervisors as well as good friends, Dr. Pablo del Pino and Dr. Beatriz Pelaz Garcia, for their constructive discussions and always helping me to fix problems.

I want to thank all the members of the Biophotonics group to let me work in a very pleasant and friendly atmosphere, special thanks to Daniel, Christian, Mikhail, Nadeem, Alberto and Fang for many nice memories during the years in Marburg.

Besides, I want to thank Marta Gallego for measuring the TEM images in CIC biomaGUNE (San Sebastián, Spain), and to Stefanie Kramer and Andreas Rentzos for administrative andtechnical support from during these years.

Further, I want to thank Karsten for helping me with ICP-MS measurements; and many thanks to Daniel for the final edition of my thesis.

Thanks the fellowship support from China Scholarship Council (CSC).

At last, I'm grateful to my parents as well as my whole family for your mental support; I have no words to express my gratitude for your encouragement. Thank to my boyfriend, Xiang, always takes care of me when I was ill and helps me when I was depressed.

Table of Contents

1. Introduction

Over the past two decades, nanotechnology has increasingly gained attention from scientists and in general, from society. Products (*e.g.,*solar cells[1], in-vitro diagnostic reagents[2]) based on or produced by nanotechnology are being developed by the industry and some of these nano-based products are starting to be used in our daily lives. Nowadays, nanoparticles (NPs) have become an essential research tool widely applied in biology and medicine areas.

Compared to bulk materials, nanoscale materials typically present size-dependent physical and chemical properties, such as superparamagnetism[3] (*e.g.*, iron oxide NPs), surface plasmons[4] (*e.g.*,metallic NPs), or UV-blocking ability and photocatalytic properties[5](*e.g.*,titanium dioxide NPs). In addition, current synthetic methods allow to produce a variety of surface-engineered nanomaterials, which are colloidally stable and have high solubility in aqueous solution. NPs can be surface modified with molecules with biological relevance, such as proteins, antibodies, DNA, *etc*[6]. Therefore, NPs have become suitable candidates which enable many promising biology applications in various fields. For instance, superparamagnetic NPs (*e.g.,*Fe_3O_4 NPs) can be applied for magnetic resonance imaging (MRI) based on their magnetic relaxation under magnetic fields[7]; they can also be used for hyperthermia as well as metallic NPs (especially Au NPs)[8]; photocatalysis for organic decomposition can be accomplished by titanium dioxide NPs[9], *etc*.

Due to the highly useful physico-chemical properties of nanomaterials, significant research efforts have been devoted to the fabrication of nanocrystal products. Basically, two kinds of approaches have been developed to manufacture nanometer products, typically referred to as “top-down” and “bottom-up” approaches[10]. “Top-down” approaches refer to physical methods which normally used a bulk piece of metal to break it into nanoscale devices. As a traditional technique, “top-down” approaches are widely used in photolithography, electronics productions and optics, *etc*[11]. “Bottom-up” approaches typically start from metal compounds, which then decompose and generate metal atoms in the presence of surfactants; after nucleation and size growth, nanomaterials are formed by molecular self-assembly. Compared with “top-down” approaches based on costly equipment, “bottom-up” approaches allow for the production of bulk qualities of NPs with a superior control of size and shape.

During the synthesis of nanomaterials by “bottom-up” approaches, several methods can be used, including wet chemical synthesis, hydrothermal methods, reverse micelles,

physical and chemical vapor deposition, *etc*. In a classical synthesis, mechanisms of atomic nucleation and size growth of colloidal nanocrystals was explained by LaMer and Dinegar in 1950[12], *cf.*, Figure 1. Generally, the first step is the generation of metal atoms from metallic precursors. As an energy-consuming period, there is no nuclei produced even if the atoms in solution are saturated (in C_s); in case the concentration of atoms in solution is high enough to the critical value (in C_{min}^{nu}), the atoms start the self-nucleation; less energy is used during this step. Afterwards, some small crystals are formed by several nuclei. Some of them are used as seeds for growing larger crystals. Once enough big particles are created, some smaller crystals will dissolve and deposit onto the bigger particles in order to minimize the surface-to-area ratio, obtaining the most stable state. Finally, NPs with uniform size are obtained. This dissolution and deposition phenomenon is called Ostwald ripening.

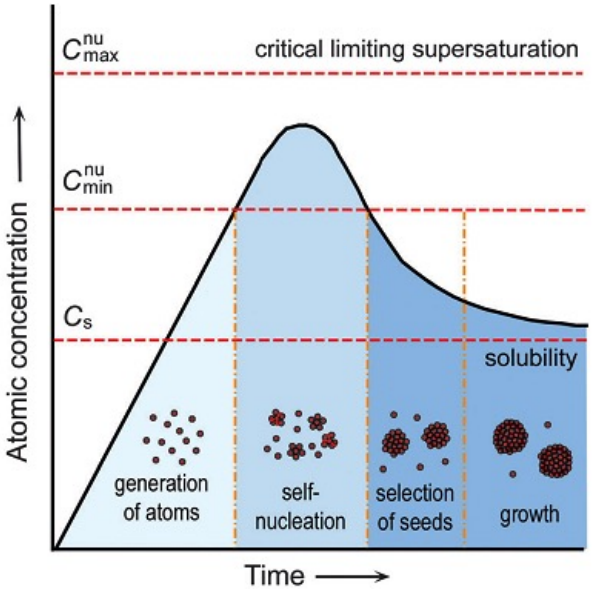

Figure 1. Schematic representation of the LaMer model for nucleation and size growth of NPs based on the atomic concentration and reaction time[13, 14]*. Reproduced from* LaMer and Dinegar[12].

1.1 About my Ph.D thesis

The development of nanobiotechnology is strongly influenced by the development of new (or more robust) nanomaterials. Hence, it is of utmost importance to produce high quality well dispersed nanomaterials with long term stability, which can be safely used for biological and medicinal applications. In this study, it is described how to produce polymer-coated inorganic nanoparticles, and how to use them as nanotools in applications of life science, such as hyperthermia, catalysis and cytotoxicity. In particular,

the synthesis of various inorganic nanoparticles by several procedures, phase transfer and stabilization by polymer coating process, and further functionalization by biomolecules are described. Data about their physico-chemical properties are also presented.

This cumulative work is based on the experiments from publications, in which the author contributed during her Ph.D work. Depending on the different properties of the nanomaterials produced, the present work is separated into three chapters: magnetic NPs, plasmonic NPs and titanium dioxide NPs, in which their biological applications is also illustrated with examples.

In the second chapter, strategies for the synthesis and surface modification of magnetic NPs are introduced, and systems of core-shell ferrite magnetic NPs are designed in order to compare their magnetic behaviors under alternating magnetic fields, and further, to obtain the maximum specific power loss (SPL) for applications in hyperthermia. In the third chapter, we describe the synthesis and polymer coating of different plasmonic NPs, made of Au, Ag or Cu. The characterization of their physico-chemical properties is presented. The bioapplications based on their optical properties are also introduced. In the fourth chapter, synthetic procedures and phase transfer process of titanium dioxide NPs (TiO_2 NPs) are introduced. Their application as photocatalysts is discussed; the mechanism is explained with one example for catalytic applications, *i.e.*, reducing organic pollution. In the fifth chapter, the main results are presented, with focus on the polymer coating as a reliable and robust technique to provide colloidal stability for different applications. Finally, all the publications produced during this PhD work (published, submitted or in preparation) are briefly summarized in the last chapter.

2.Magnetic Nanoparticles

2.1 Introduction

Magnetic NPs have attracted the attention of researchers for many applications in different areas such as magnetic storage media[15] and environmental remediation[16]. Particularly, magnetic NPs have been proven suitable materials for applications in medicine (*e.g.*, targeted drug delivery[17], MRI[18]) and bioapplications (*e.g.*,molecular detection[19]). The interest on these materials is based on their size-dependent magnetic behavior. In general, magnetic materials exhibit magnetism (magnetic moment) originated from the electrons spinning and orbital motion. Under an applied magnetic field, electrons are polarized and aligned in parallel or antiparallel states, which induce the bulk material to present different magnetic responses. Depending on the interaction of electrons, the bulk materials are categorized as ferromagnets, antiferromagnets, ferrimagnets or paramagnets.

Ferromagnets are the most common magnet form, which presents a strong, interacting magnetic moment. In a ferromagnetic material (*e.g.*,bulk materials of Co, Fe and Pt), electrons align parallel with their neighboring ones. Ferromagnets exhibit a large magnetization in the presence of an external magnetic field, and still keep magnetized states after removing the magnetic field. In contrast, electrons in antiferromagnetic materials align antiparallel with each other, and exhibit opposite magnetic moment, with the result of net zero magnetization, such as Fe_2O_3, Cr, and NiO. However, when the electrons align antiparallel with their neighboring ones, but present different magnetic moment values, the materials exhibit net magnetization. These materials are called ferrimagnets, and include Fe_3O_4, $CoFe_2O_4$, *etc*. Magnetic properties of paramagnets appear only in the presence of an external magnetic field. Normally, the magnetic dipoles aligned randomly, which show a net zero magnetic moment state; in case a magnetic field is applied, the magnetic dipoles align immediately to the field direction, with a result of net magnetization.

In general, the magnetic behavior of any magnetic material is strongly dependent on the size, which means that the magnetic response can be tailored for some materials by varying the size[20]. In general, most of the magnetic materials separate into many magnetic domains, also named multidomain (MD) regime. Magnetic dipoles align parallel to the same direction within each domain, while all the domains usually have different aligned direction. By shrinking the size of magnetic materials bellow a critical

radius, which depends on the material and temperature, ferro- and ferrimagnets present one single domain (*i.e.*, SD NPs). Furthermore, SD NPs with sizes bellow a certain material-dependent critical value, for which magnetic reversal can be thermally activated, are typically called superparamagnetic particles (SPM). Because of the small size, SPM particles are single domain, and all the magnetic moments rotate randomly. Therefore, when the temperature is higher than the blocking temperature, SPM particles exhibits net zero magnetic moment in the absence of an external magnetic field, while they exhibit the net statistical magnetization in case a magnetic field applies. Figure 2 shows the magnetic behavior of SD NPs and SPM NPs under an external magnetic field (H), *i.e.*, hysteresis diagram. SD NPs start to generate magnetization above the coercive field (H_c) and reach the saturation magnetization (M_s) in a high magnetic field; after the external magnetic field is switched off, magnetic hysteresis phenomenon occurs, resulting in residual magnetization, called remanent magnetization (M_R). In contrast, there is no coercivity or remanence from SPM particles; that means that an ideal SPM particle has net zero magnetization in the absence of a magnetic field, but reaches to maximum magnetization rapidly at very low applied magnetic field. Notice that for simplicity, we omit the description of hysteresis in MD NPs, which are produced by domain wall displacement[21].

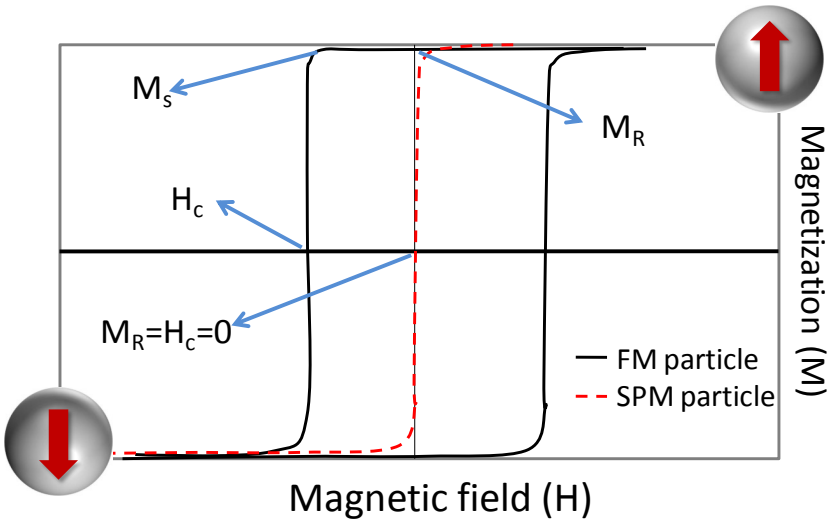

Figure 2. The corresponding relationship between magnetization and magnetic field curve of SD and SPM particles[21].

In addition to act as contrast agents in magnetic resonance imaging (MRI), one of the most promising applications of magnetic NPs relies on their use as "nanoheaters"[22]. Magnetic NPs can generate heat in the presence of an alternating magnetic field (AMF) due to magnetic "friction", This makes them promising materials for hyperthermia,

which can in general terms defined as body temperature increase above normal level to obtain disease treatment, such as cancer treatment. In general, under high enough strength of magnetic field (B_0) with high frequency (f), magnetization of magnetic NPs is continuously reversed, with the result of converting magnetization into heat. This heat capacity is called specific absorption rate (*SAR*), also called specific power loss (*SPL*), which is calculated by equation 1:

$$SPL = C\frac{\Delta T}{\Delta t}\frac{1}{m} \qquad Eq.\ (1)$$

Where C is the specific heat capacity of the medium in which the magnetic NPs are dispersed; ($\Delta T/\Delta t$) is the temperature enhancement overtime and m is the mass of magnetic NPs.

The heating capability of magnetic NPs is directly proportional to the area of the so-called hysteresis loop and the frequency of the AMF (in the magnetization *versus* external magnetic field diagram). In case the external magnetic field is applied in a loop to magnetic NPs, *i.e.*, turned on and then again turned off, then the magnetization will not be brought back to the original starting level. This irreversible phenomenon is called hysteresis and its area depends of several factors including NPs' effective anisotropy, their volume, the temperature, and the frequency and amplitude of the magnetic field. In case of heating applications, these parameters should be optimized to produce hysteresis loops as large as possible. Several authors distinguish between two different heating processes driven by magnetic reversal, which are related to the type of NPs (composition, size and shape). These are hysteresis losses and relaxation losses, which have been typically associated to heating using SD NPs and SPM NPs, respectively. Herein, we follow the criteria of Carrey *et al.*, more correct in our opinion, in which relaxation losses are considered a particular case for SD NPs. The difference between SD and SPM NPs relies in the range of validity of the theories used to model the corresponding heating mechanisms, *i.e.*, the linear response theory (LRT) and Stoner-Wohlfarth model based theories, respectively[23].

Besides hyperthermia magnetic NPs have become suitable platforms for a variety of applications in life science, including drug delivery[24], magnetic resonance imaging (MRI)[25], magnetic separation[26] and biosensing[27], *etc*. We have however chosen to only focus about heating because it was one of the main NP-based applications explored during this Ph.D work.

2.2 Synthesis and surface modification

1) Synthesis of magnetic NPs

Mainly since the early nineties, many scientists have been working on the development of different chemical methods for the synthesis of magnetic NPs, including coprecipitation, microemulsions, thermal decomposition, *etc*[28]. The physicochemical properties of magnetic NPs such as size, shape, monodispersity, surface chemistry, or even their magnetic behavior, are highly depended on the synthetic conditions. The coprecipitation method relies on the mixture of ferrous (Fe^{2+}) and ferric (Fe^{3+}) salts in a basic aqueous solution, which leads to the formation of magnetite NPs (Fe_3O_4 NPs), which then can be transformed into the more stable phase of maghemite NPs (γ-Fe_2O_3 NPs) after oxidation[29]. The coprecipitation technique is widely used because of low cost and ease to produce large quantities. However, the products usually have poor size distribution and the oxidation step is hard to control, which limits this method for certain bioapplications in which size and oxidation state are crucial (*e.g.*, MRI and nanoheating).

Thermal decomposition has become the most widely used method for the synthesis of "high-quality" magnetic NPs for biomedical applications, because the products are more uniform, the size/shape can be easily controlled, and they can be easily coated with organic shells, which expand their colloidal stability to various dispersion media[30]. Under high boiling point (b.p.) organic solvents, the chemical compounds of the metal precursors are decomposed and nucleated again with surfactants as stabilizing ligands. During the nucleation and growth process, various synthesis parameters affect the particle size and quality[31]. For instance, using higher boiling points solvents(*e.g.*,dioctyl ether, b.p.~330°C) typically lead to bigger NPs than using a lower boiling point solvents (*e.g.*,penzyl ether, b.p. ~265°C); the ratio of metal precursors-to-surfactant is also important, *i.e.*, more amount of surfactant will lead to smaller NP sizes; also, longer grain growth time will lead to bigger NPs. In addition, the heating speed can also affect the size distribution. Compared with too fast heating speed, slower heating rate (*e.g.*,3.3 k/min) will typically lead to an uniform particle size during the seed growth process[32].

Considering the wide range of sizes required for different applications (*e.g.,* smaller for MRI or larger for nanoheating), methods have been developed which allow sizes in the range of 4-30 nm to be produced[33]. The synthesis of magnetic NPs can be easily controlled by the one-pot synthesis method[34] or the seeds-mediated growth method. The one-pot method is a way to produce magnetic NPs in one reaction, by which

different sizes can be obtained by changing the synthetic conditions as briefly indicated above. This strategy is normally used to produce small NPs, typically > 9 nm. The seeds-mediated growth method requires smaller NPs as seeds, which by growing more layers leads to bigger NPs. Typically, two or more reaction steps are required to achieve the desired sizes. Depending on the size increment required or amount of seeds used, various sizes can be achieved. Figure 3 shows different sizes of iron oxide NPs, from 4 nm to 28 nm, by one-pot synthesis or seeds-mediated growth methods, which were produced during this Ph.D work for publications of [A6] and [A10].

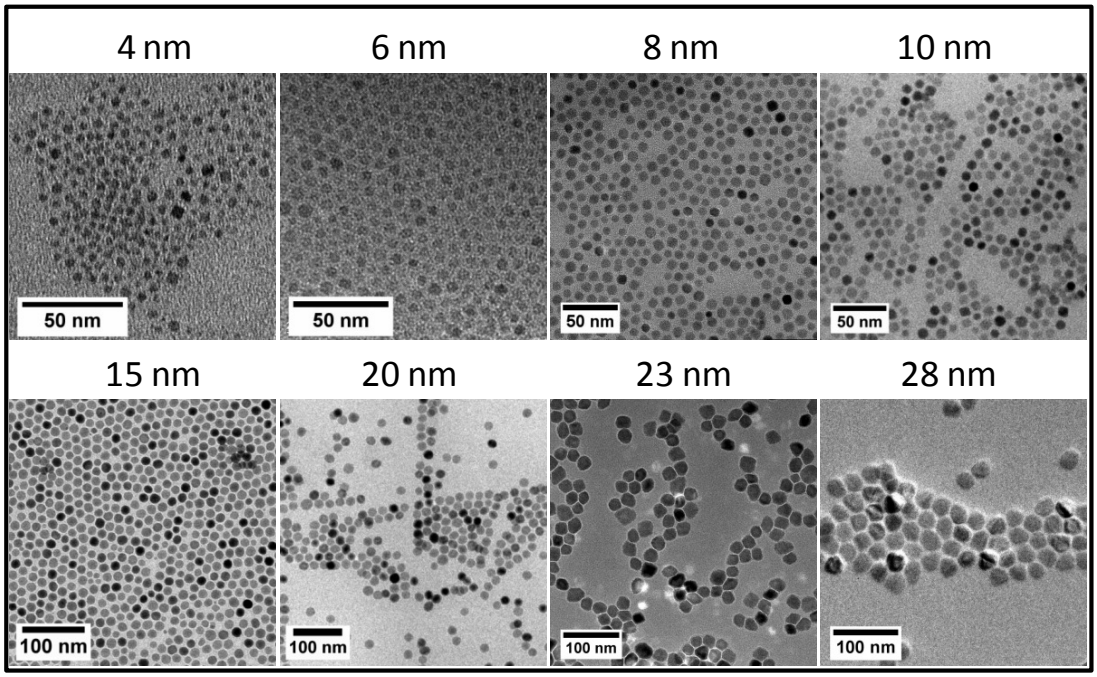

Figure 3. TEM images of different size Fe_3O_4 NPs via seeds-mediated growth or one-pot synthesis methods. The NPs size can be controlled from 4 nm to 28 nm; the scale bars correspond to 50 nm (upper images) and 100 nm (lower images), respectively.

In addition, upon mixing of other metal precursors (*e.g.*, cobalt, manganese, *etc.*) with the iron precursor, using a ratio 1:2 of other metal to Fe, metal doped magnetic NPs can be produced, such as Co-ferrite NPs and Mn-ferrite NPs[35]. Moreover, by using "small" doped metal NPs (*e.g.*, Co-ferrite NPs) as seeds, shells of other doped metal NPs (*e.g.*,Mn-ferrite NPs) can be grown on the surface of the seeds *via* the seed-mediated growth method. In this way, core-shell NPs can be derived with the structure of Co@Mn ferrite NPs. Likewise, the doped metal materials can be exchanged by adding different metals during the seeds synthesis and shell growth procedure (*e.g.*,Mn@Co ferrite NPs), and the thickness of core and shell can be controlled by shrinking the seeds size or limiting the shell growth time (*e.g.*,Mn@Co-TL ferrite NPs, TL=thin layer).The TEM images and synthesis process of them are described in Figure 4 and 5. Therefore, with

the seeds-mediated growth methods, single phase inorganic NPs can be assembled into core-shell composite NPs, which exhibit new physico-chemical properties. Some designed core-shell nanocomposite materials with new properties are described in detail in publication [A12].

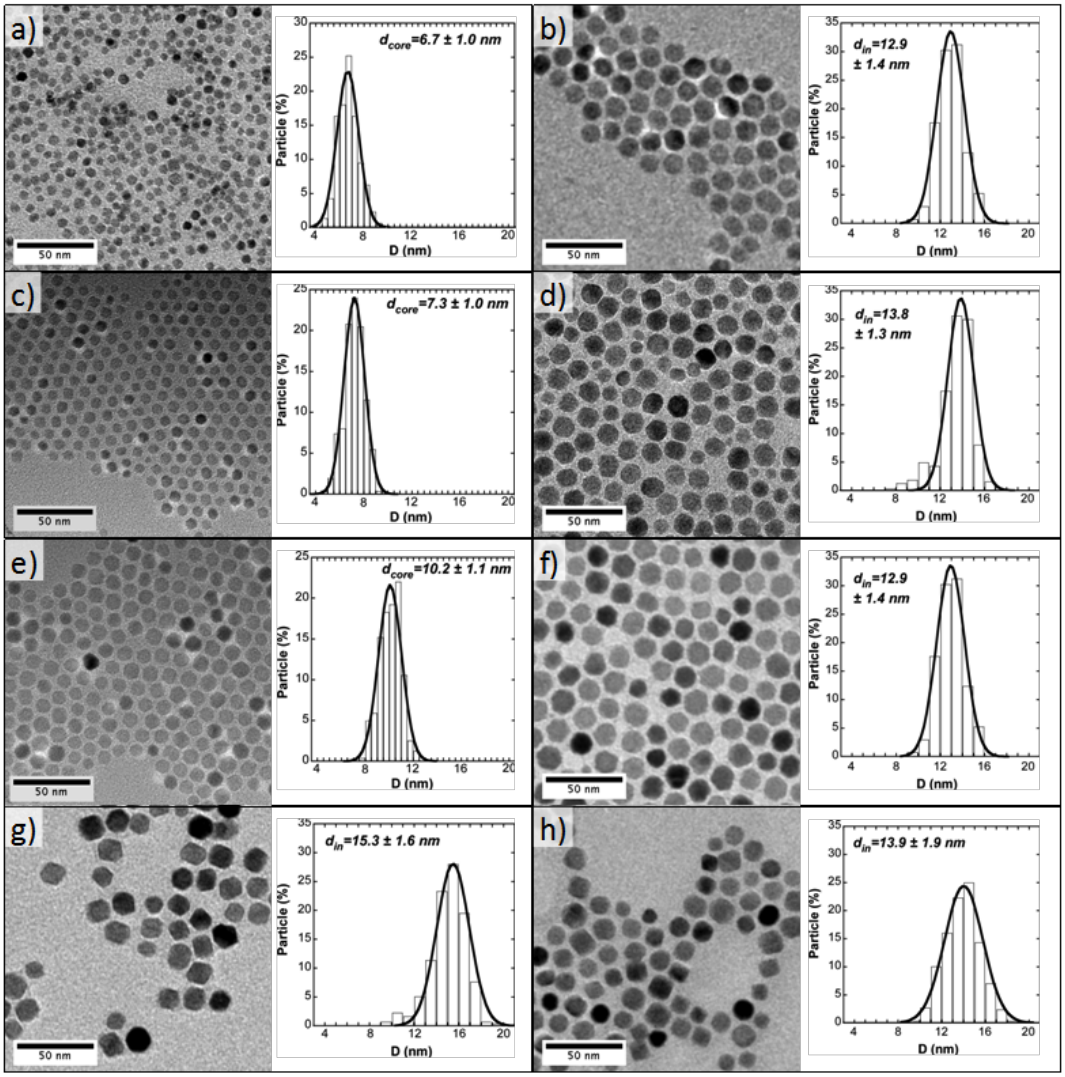

Figure 4. TEM micrographs and corresponding diameter histograms, (from > 300 MNPs, analyzed by Image J): a) Co ferrite seeds of d_{core} = 6.7 ± 1.0 nm; b) Co@Mn NPs of d_{in} = 12.9 ± 1.4 nm; c) Mn ferrite seeds of d_{core} = 7.3 ± 1.0 nm; d) Mn@Co NPs of d_{in} = 13.8 ± 1.3 nm; e) Mn ferrite seeds of d_{core} = 10.2±1.1 nm; f) Mn@Co-TLNPs of d_{in} = 14.3±1.5 nm; g) Co ferrite NPs of d_{in} = 15.3±1.6 nm and h) Mn ferrite NPs of d_{in} = 13.9±1.9 nm.

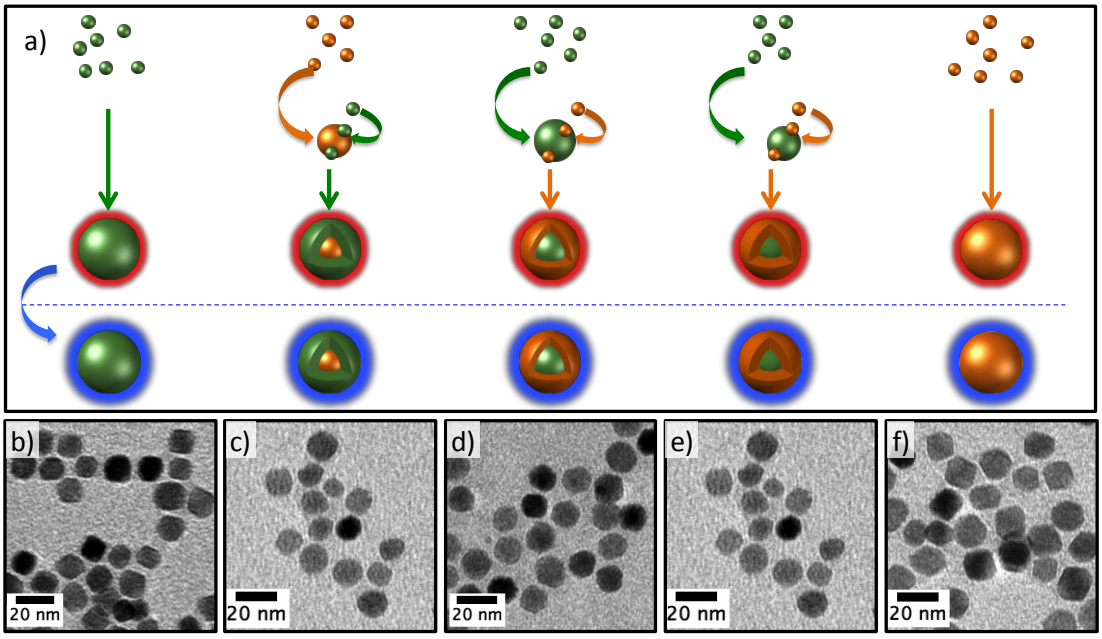

Figure 5. a) Schematic representation of the synthetic method used for the production of metal doped NPs: consistent size (d=14 nm) of single-phase NPs and core-shell NPs were produced via one-pot synthesis process or seeds-mediated growth method (green and orange components refer to Mn-ferrite and Co-ferrite, respectively). Then, the aliphatic chain-capped NPs (red shell) were transferred to aqueous solution by the PMA-coating process (blue shell). b-f) TEM micrographs of NPs: b) Mn ferrite NPs, c) Co@Mn NPs (core size: d=7 nm), d) Mn@Co-TL NPs (core size: d=10 nm), e) Mn@Co NPs (core size: d=7 nm) and f) Co ferrites NPs. The corresponded scale bars are 20 nm.

2) Surface modification of NPs

The magnetic NPs produced by thermal decomposition are typically coated by aliphatic chains and thus, they can only be dispersed in nonpolar solvents. However, all biological applications occur in aqueous media. Therefore, the NPs need to be transferred from nonpolar to polar solvents. There are many possible strategies[36] to make the NPs water-soluble: 1) Exchange the aliphatic capping ligands by hydrophilic ligands (*e.g.*, ligands terminated in highly charged groups[37], hydrophilic polymers, *etc.*). 2) Polymerization of a silica shell by which a hydrophilic glass shell is grown around the NPs[38]. 3) Polymer coating with an amphiphilic polymer[39]. *cf.*, Figure 6. The amphiphilic polymer consists of two parts: the hydrophobic side chains which are intercalated with aliphatic ligands attached to the core, and a hydrophilic backbone which supply enough negative charges for stabilization in aqueous solution. Compared with the first two strategies, polymer coated NPs present high water solubility over longer periods of time.

Hence, all the NPs mentioned in the thesis and publications attached are coated with this amphiphilic polymer which exhibit an excellent stability in *vitro*[40].

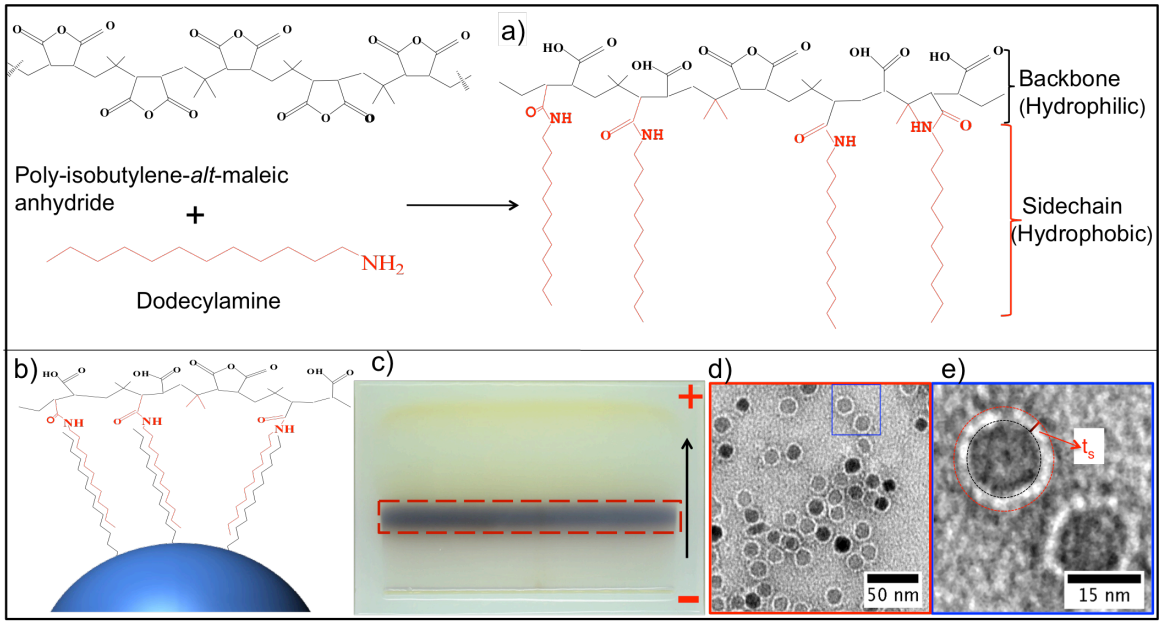

Figure 6. a) Scheme of amphiphilic polymer (PMA) structure which includes a hydrophilic backbone and hydrophobic side chain; b) Scheme of the polymer coated NP in which dodecylamine side chains are intercalated with the surfactants on the NP surface, while the negatively charged backbone can stabilize the particle in aqueous solvent; c) photograph of 2% agarose gel loaded with polymer coated NPs after running for 1h at 100 V in tris-borate EDTA (0.5x TBE buffer) in order to purify the NPs from micelles formed by excess polymer; the black band enclosed in red dotted area are the clean NPs. d-e) Selected negative staining TEM micrograph of magnetic NPs (e.g.,Mn@Co-TL), which showed a homogeneous organic coating around the NPs of 2.7± 0.7 nm.

In addition, polymer coated NPs have sufficient carboxylic groups (-COOH) on the polymer shell, which not only supply negative charges for stabilization, but also they can be reacted with molecules which contain an amino group (-NH_2) to form amide bonds *via* 1-Ethyl-3-(3-dimethylaminopropyl)carbodiimide (EDC) chemistry, *cf.*, Figure 7. Hence, polymer coated NPs can be modified with many aminated biomolecules, such as proteins[41] (*e.g.*,bovineserumalbumin, BSA), antibodies, DNA[42] and/orpoly(ethylene glycol) (PEG)[43], by which multifunctionalization can be achieved, *i.e.*, targeting capabilities (*e.g.*,Ab), fluorescence labels[44] (*e.g.*,amino-modified dyes), improved colloidal stability (*e.g.*,PEG), reduced unspecific protein adsorption[45] (*e.g.*, PEG, carbohydrates), prolonged circulation time *in vivo*[46] (*e.g.*, dendrimers or PEG), *etc.*.

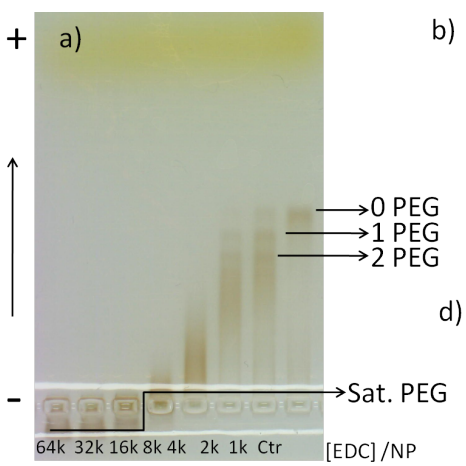

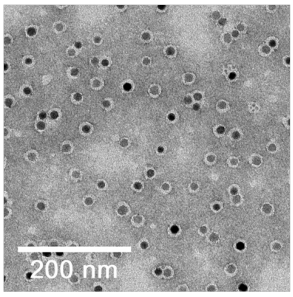

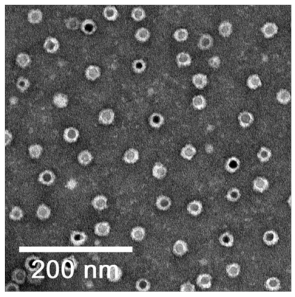

d)

Name (Mn@Co)	NPs in $CHCl_3$	NPs -PMA in H_2O	NPs -PMA +PEG in H_2O	NPs -PMA +BSA in H_2O
d_c (nm)	13.8±1.3	19.2±0.7	24.8±1.9	27.7±2.4
t_s (nm)	0	2.7	2.8	4.25

Figure 7. Surface functionalization of Mn@Co NPs with PEG and BSA. a) Functionalization process of PEG (NH_2-PEG-CH_3, Mw, 10 kDa) with PMA coated Mn@Co NPs via EDC chemistry with a ratio of $64 \cdot 10^3$ (64 k) to $1 \cdot 10^3$ (1 k) EDC molecules per NPs; PEGylated NPs reached saturation when the EDC/NP ratio was above 16 k; b) negative staining TEM micrograph of PEGylated Mn@Co NPs; c) negative staining TEM micrograph of BSA functionalized Mn@Co NPs; d) the diameter (d_c) and thickness (t_s) values of the aliphatic-coated NPs, PMA coated NPs, PEGylated NPs and BSA modified NP were analyzed by Image J by counting > 300 NPs. The scale bars are 200 nm.

2.3 Tailoring magnetic properties by NP´s design

One of the most active research fields concerning magnetic NPs focuses on heating under AMF, that is, how to maximize heat release from magnetic NPs to the environment. In general, the heating capability of magnetic NPs exposed to AMF depends on the NPs properties (size, shape, magnetization, and magnetic anisotropy) and the properties of the AMF (*i.e.*, field strength: *H*and frequency: *f*). Hyperthermia is based on heating tumors of animals or tissues *in vivo*, which limits the applied AMF (*i.e.*,*f*< 1 MHz, *H*< 20 kA/m) because non-specific heating (*i.e.*, regions without NPs) should be avoided. The aforementioned AMF limits are based on experiments with humans[32]. The physicochemical properties of the NPs should also be suitable for *in vivo* experiments since the end target of hyperthermia is cancer treatment in humans. Therefore, the ideal NP agents for this technology should be biocompatible and if possible biodegradable and/or “small” enough to be excreted by the kidneys. Regarding the size, one should also consider that “big” magnetic NPs would tend to agglomerate, which again should be avoided for two reasons: (i) magnetic coupling might decrease the heating efficiency of the NPs and (ii) large agglomerates can produce a stroke.

As explained before, maximizing the hysteresis area will result in more heating, which typically requires materials with optimum size (between 10 to 30 nm), large M_s(as large as possible) and optimum magnetic anisotropy(between $0.5 \cdot 10^4$ and $4.0 \cdot 10^4$ $J \cdot m^{-3}$)[47]. Unfortunately, "classic" magnetic NPs (maghemite, magnetite, or Co/Mn substitute iron oxide) do not comply these requirements. For instance, maghemite typically exhibit low SPL values due to the relatively small value of its M_s (40–60 emu/g), although its magnetic anisotropy lies within the optimal range ($1.6 \cdot 10^4$ $J \cdot m^{-3}$). On the other hand, "soft" magnets such as magnetite or $MnFe_2O_4$ presents high M_s but low anisotropy, whereas "hard" magnets such as $CoFe_2O_4$ presents too large anisotropy. Hence, it is essential to have one kind of magnetic NPs with optimum magnetic anisotropy and large saturation magnetization for generating as much heat as possible. Yet, apparently, the single-phase materials that we can produce do not suit our needs. In this direction, exchange coupling of "hard" and "soft" magnetic phases in a core@shell NP has been proven to effectively "tune" the magnetic anisotropy[47]. In order to develop a guide to maximizing hysteretic loss by matching the design and synthesis of SPM NPs to the desired hyperthermia application, we synthesized three different core@shell ferrite NPs as well as pure Mn and Co-ferrite NPs with same size (d_c~14 nm) whose the TEM micrographs after polymer coating are shown in Figure 8. In detail, we prepared and magnetically characterized, including their AMF heating efficiency, the following samples: $MnFe_2O_4$ NPs, $CoFe_2O_4$@$MnFe_2O_4$ NPs, $MnFe_2O_4$@$CoFe_2O_4$-TL NPs (TL=thin layer), $MnFe_2O_4$@$CoFe_2O_4$ NPs and $CoFe_2O_4$ NPs. The size, composition and magnetic properties of all the samples are summarized in Table 1. The samples are ordered with respect to the Co ferrite volume. The reduced remanence (M_r/M_s) and coercive field ($\mu_0 H_c$) at 5 K increase as the volume of the Co phase.

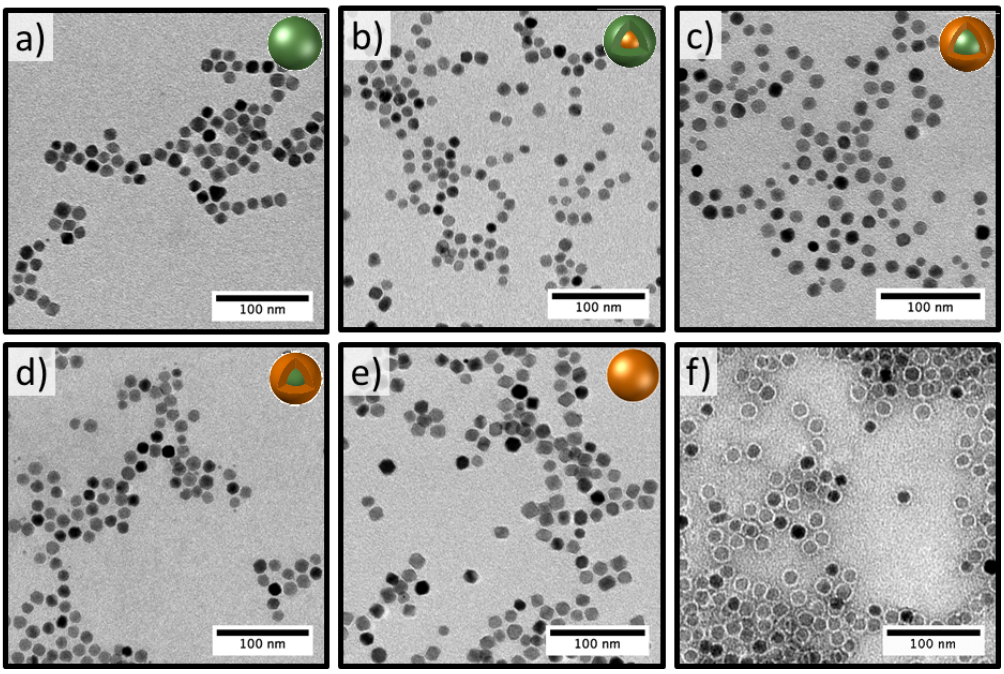

Figure 8.TEM micrographs of PMA-coated MNPs, a-e) Mn, Co@Mn, Mn@Co-TL, Mn@Co and Co ferrites. f) An example of how polymer coated NPs look like under negative staining TEM micrograph which is from Mn@Co-TL NPs.

Table 1. Size, composition and magnetic properties of the samples

Sample	$d_{in}\pm\sigma^{\alpha}$ (nm)	$d_{core}\pm\sigma^{\alpha}$ (nm)	Co^{α} % vol	$M_s(RT)^{\alpha}$ (Am^2/kg)	$M_r/M_s{}^{\alpha}$ (5K)	$\mu_0 H_c{}^{\alpha}$ (5K) (T)
Mn	13.9±1.9	13.9±1.9	0	90.5	0.47	0.026
Co@Mn	12.9±1.4	6.7±1.0	14	87	0.75	0.505
Mn@Co-TL	14.3±1.5	10.2±1.1	63	84	0.80	1.268
Mn@Co	13.8±1.3	7.3±1.0	85	82	0.87	2.20
Co	15.3±1.6	15.3±1.6	100	80	0.88	1.84

$^{\alpha}$Diameter of the inorganic NP (core + shell) and inorganic core (d_{core}); Co ferrite volume fraction in the samples; saturation magnetization (M_s) at RT, reduced remanence (M_r/M_s) at 5°K and coercive field ($\mu_0 H_c$) at 5°K.

In general, we show that by increasing the volume of the Co phase, the samples present an increased effective magnetic anisotropy(details can be found in publication [A6]). From the ZFC/FC measurements, we can see that the peaks of the ZFC curves shift to higher temperatures with increasing of Co content, *cf.*, Figure 9 (left), which indicate higher blocking temperature (T_{bl}). Since the energy barrier (E_B) is proportional to the T_{bl}, and $E_B = K_{eff}V$, the effective magnetic anisotropy (K_{eff}) increases with the Co content, cf., Figure 9 (center). Likewise, the coercive field increases with the Co content, *cf.*, Figure 9 (right).

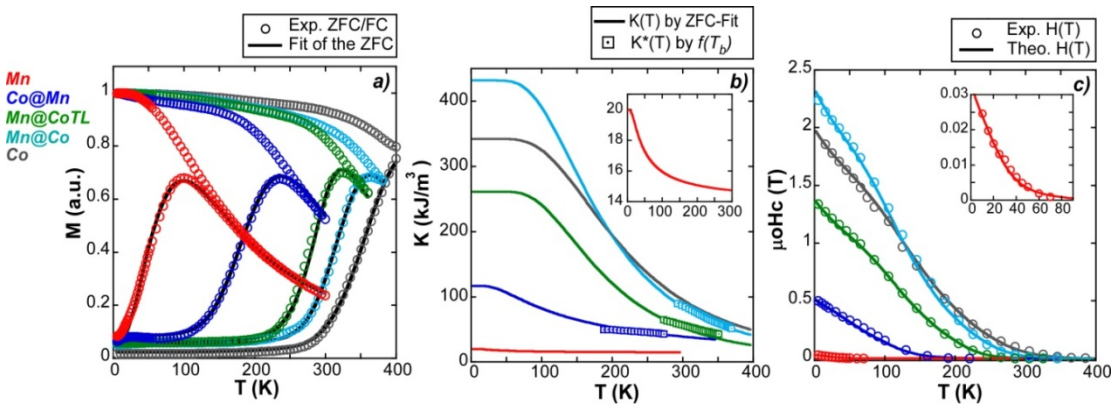

Figure 9. a) ZFC/FC measurements at 1 mT (circular markers) with the fit of the ZFC branch (solid line). b) $K_{eff}(T)$ obtained from the fit of the ZFC (solid line) and K_{eff}(T) from the statistical approach (square markers); the inset gives a closer look of the Mn curve. c) Experimental thermal dependence of the coercive field ($\mu_0 H$) (circular markers) and the theoretical H(T) curves (solid line) using the obtained $K_{eff}(T)$.*

In order to compare the magnetic behaviors of all the five samples, the magnetization in colloidal dispersion and in immobilized state (on a filter paper) were measured, at room temperature (RT, 300 K) or low temperature (5 K). At RT, all the five samples in colloidal dispersion exhibit SPM properties (all the left images in Figure 10, 11 and 12), as well as the fixed samples with low Co content (*i.e.*,Mn NPs and Co@Mn NPs, in Figure 11, left). However, the NPs rich in Co ferrite (*i.e.*, Co NPs, Mn@Co NPs and Mn@Co-TL NPs) present significant hysteresis (e.g., Mn@Co NPs in Figure 10, center, in Figure 12, right).That is because under R.T., the energy barrier E_B of Mn NPs and Co@Mn NPs is much lower than the blocking temperature value ($K_{eff}V \ll k_B$). However, the other three NPs with high Co contents exhibit hysteresis in fixed paper and present ferromagnetic behavior. At low temperature (5 k), all five fixed samples exhibit ferromagnetic behaviors with magnetic hysteresis (Figure 10, right).

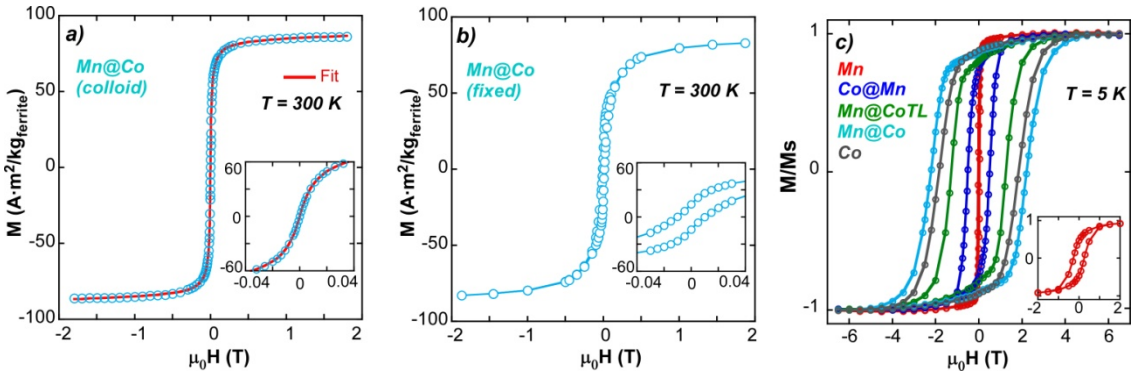

Figure 10. Magnetization (M) versus magnetic field (H) measurements at RT (300 k)and low temperature for colloidal and fixed NPs. a) M(H) curve of Mn@Co in colloidal dispersion with corresponding fit at RT; b) M(H) curve of Mn@Co on filter paper with corresponding fit at RT; c) M(H) curves of all five fixed samples at 5 K.

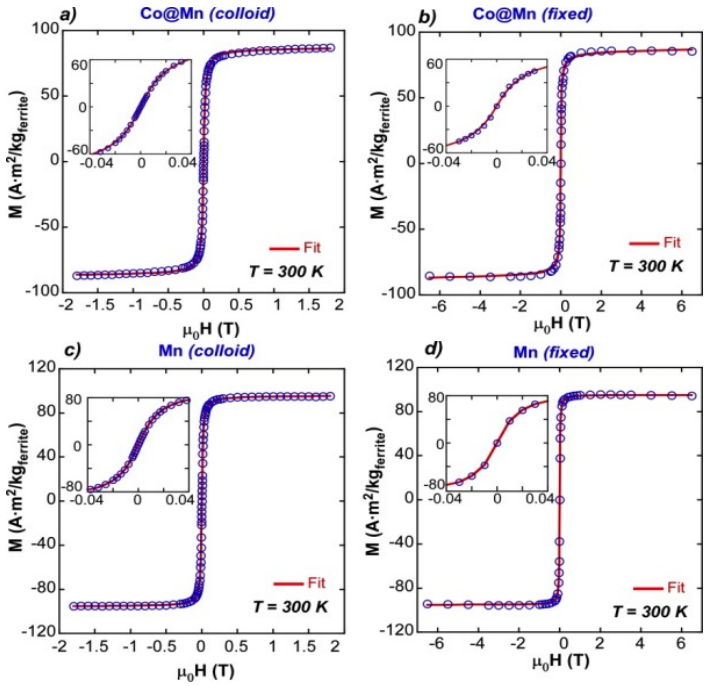

Figure 11. Magnetization (M) versus magnetic field (H) measurements at RT (300 k)for colloidal and fixed NPs. a, b) M(H) curve of Co@Mn with corresponding fit at R.T in colloidal dispersion and filter paper, respectively; c, d) M(H) curve of Mn with corresponding fit at R.T in colloidal dispersion and filter paper, respectively.

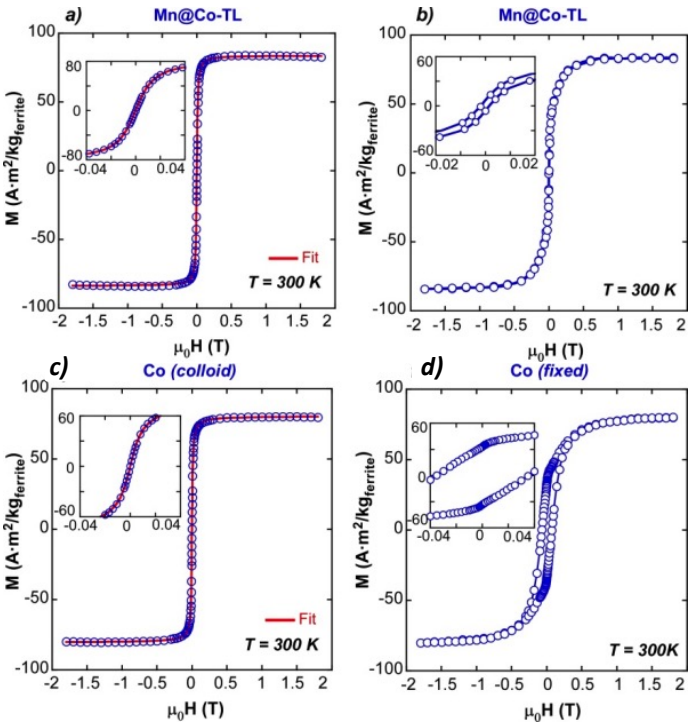

Figure 12. Magnetization (M) versus magnetic field (H) measurements at RT (300 k) for colloidal and fixed NPs. a, b) M(H) curve of Mn@Co-TL with corresponding fit at R.T in colloidal dispersion and filter paper, respectively; c, d) M(H) curve of Co with corresponding fit at R.T in colloidal dispersion and filter paper, respectively.

With the aim of making a theoretical calculation of the SLP of the five samples, we employed the quasi-Linear Response theory (q-LRT), in which non-linear effects are taken into account by using an effective non-linear susceptibility calculated from the Langevin function[48]. The theoretical values, predicts fairly well the experimental values, taken into account the uncertainty of some variables, such as concentration of MNPs, polydispersity, diameter, and calculated effective anisotropies, *cf.*, Figure 13.Regarding to the heat release capability of the five samples studied, the maximum SLP value in aqueous solution, at room temperature and for the AMF used (412.5 kHz and 22.4 kA/m), is achieved with the Co@Mn NPs as expected because of its size and effective magnetic anisotropy (*i.e.*,39 kJ/m^3) lies within the optimum range. Table 2 compares the SLP values obtained from the experiments and from the calculated curves for NPs of *ca*. 14 nm.

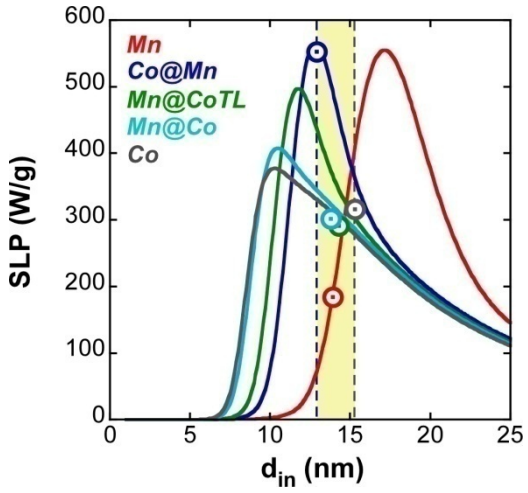

Figure 13.Simulation of SLP value versus diameter of inorganic NPs under AMF with 412.5 kHz and 22.4 kA/m.

Table 2. Experimental *dT/dt* values and SLP values of the samples.

Sample	Structure	Conc (mg/mL)	dT/dt (^{o}C/s)	SLP (W/g) Exp	SLP (W/g) Calc.
Mn		0.00256	0.112±0.001	183.8 ± 1.7	190±60
Co@Mn		0.00221	0.275±0.005	552.6 ± 9.5	560±50
Mn@Co-TL		0.00428	0.297±0.001	291.4 ± 1.0	340±50
Mn@Co		0.00271	0.195±0.01	302 ± 15	320±40
Co		0.00363	0.273±0.008	315.9 ± 9.3	280±30

**dT/dt is the slope of a linear fit at first 5 s of heating; SLP (Exp) is the data measured from the experiment with magnetic field (412.5 kHz, 22.4 kA/m.); SLP (Calc.) is a simulated data.*

2.4 Heating application

Biological applications based on magnetic NPs have been widely explored during the last decades due to their unique magnetic properties, which as shown above can be tailored

by choosing the appropriate NP design, including size, shape, composition and structure. That is, given an application of interest, such as MRI imaging, nanoheating or magnetic separation, the magnetic properties of the colloids can be tuned accordingly. On the other hand, uniform magnetic NPs produced in organic solvents can be transferred to aqueous solution by using suitable organic coating, thereby providing the NPs with high stability, and further surface functionalization with molecules of biological relevance, by which other functions turn accessible such as targeting, antifouling, improved/specific cellular uptake, *etc*. Therefore, magnetic NPs are applied for various fields, including molecular detection and separation in *vitro* (*i.e.*, protein[49], DNA[50] or bacteria[26]), imaging (*i.e.*, MRI in *vivo*), drug delivery for cancer treatment and heating (hyperthermia).

Nowadays, hyperthermia based on magnetic NPs under AMF has become a promising application, which is already successfully used in clinical studies due to the high efficiency for tumor treatment. In general, tumor cells are more sensitive to the temperature increase compared to healthy ones. Cell death of cancers occurs in the range of 40 to 44 °C. Based on this, the heat release from magnetic NPs under an AMF can be applied for tumor treatment. As we know, the Co@Mn ferrite NPs described before have a high SPL value, which can generate more energy for the surrounded environment, thereby providing an ideal model for hyperthermia. A similar core@shell system has been successfully used in mice by Cheon et al[47]. We employed different existing synthetic methods based on the thermal-decomposition of metal precursors. Although for the preparation of the seeds we used methods similar to those reported by Cheon *et al*.[47], our single-phase systems (seeds or *ca.* 14 nm Co or Mn ferrites) appear slightly less monodisperse (σ< 15% *versus* σ< 10%). It might be due to the use of different synthetic details (molar ratios, heating rate, *etc.*), which however we could not find in their reports/patents. The core@shell systems reported by Cheon *et al*[47]. appear slightly more monodisperse than ours. For the preparations of the core@shell systems, we adapted and mixed previous well-established protocols. Although we did not use any new approach or protocol, by adapting/mixing methods we were able to produce core@shell systems with a fairly satisfactory monodispersity ((σ< 11% *versus* σ< 10%). As far as we could find in their papers/patents, the major difference with our methods and the ones reported by Cheon et al. is that they used trioctylamine as solvent, whereas we used benzyl ether, or dioctyl ether (only for the 14 nm Mn ferrite NPs). As capping agents we both used oleic acid/oleylamine. Concerning the metal precursors, we used metal acetylacetonate compounds (we only used $MnCl_2$ in the case of the 15 nm Mn ferrite NPs), whereas they combined $Fe(acac)_3$ and $CoCl_2$,$FeCl_2$ and/or $MnCl_2$. They do not report though molar ratios, volume, heating rates, *etc*. Indeed we were not

able to reproduce their results (maybe due to the lack of synthetic details in the original patent/papers). To our knowledge, no other Lab has reported similar core@shell systems.Moreover, as a big issue about agglomeration for hyperthermia, high stability after polymer coating make ourmagnetic NPs to be more suited for biological applications compared to the basic ligand exchange, such as 2,3-dimercaptosuccinic acid which they used in the paper of Cheon. The magnetic NPs injected to the brain of mice can set up a system under a magnetic field, for wireless magnetothermal deep brain stimulation, in order to study the intact brain circuits as well as treatment of neurological disorders[51]. On the other hand, magnetic hyperthermia can be used *in vitro* as well. For instance, DNA functionalized iron oxide NPs can hybridize with fluorescent labeled DNA, which can used as a molecular local thermal probe to analyze the local temperature on the particle surface in presence of AMF[42].

3 Plasmonic Nanoparticles

3.1 Introduction

Due to their unique optical properties, plasmonic NPs (*e.g.*, gold, silver and copper) were already used in ancient roman times. After a significant mass of study during the last two centuries, since the early nineties, the application of plasmonic NPs has been extended to biology and medicine, including photothermal therapy[52], drug delivery[53], optoacoustic imaging[54], biosensing[55], *etc.*

In general, plasmonic NPs have unique size-dependent optical properties, mainly dependent on their localized surface plasmon resonance (LSPR)[4]. Specifically, in metallic NPs, their free surface electrons can resonantly couple to light, producing their collective oscillation, *i.e.*,surface plasmons. Surface plasmons in metallic NPs can be typically activated by light with wavelengths in the range from *ca.* 400 – 1200 nm. When the electric field of an incoming light source matches the frequency of surface plasmons (*i.e.*, electrons in the conduction band), light is absorbed, obtaining the typical colors of colloidal dispersion of metallic NPs. This color (*i.e.*, the position of the LSPR band) is strongly dependent on the NPs composition (Au, Ag, Cu or alloyed NPs), their size, shape, structure (solid, hollow or core@shell), as well as the surrounding environment (*i.e.*, the dielectric environment). Taking spherical Au NPs with a diameter in the range of 10-100 nm as an example, the LSPR band shifts as AuNPs size is increased, which leads to a color change of the colloidal suspension from red to blue.

In addition, plasmonic NPs have strong capabilities for absorbing and scattering light since they have high extinction coefficients[56]. These are normally several orders of magnitude higher than common fluorophores. Moreover, surface plasmons induce strong localized electromagnetic (EM) fields, which make the NPs very sensitive to the local refractive index[57]. Therefore, the absorption peak shifts and/or broadens as soon as NP's local environment changes, for instance by agglomeration or attachment of molecules to the surface of the NPs.

Metallic NPs also provide excellent electrical and thermal conductivity properties, which are applied to make electrical interconnections; whereas their high surface area is suitable to produce catalytic reactions on the surface, *i.e.*, surface atoms can be used for catalysis[58]. Furthermore, Au or AgNPs have been proven to be particularly suitable for biology and medicine applications. For instance, functionalized colloid AuNPs have been used to detect Human Chorionic Gonadotropin (HCG) for a pregnancy test kit[59]. Also,

because of Ag^+ ions release, AgNPs can be used as broad-spectrum antimicrobial reagents[60].

3.2 Synthesis

Regarding the synthesis of plasmonic NPs, the most widely employed strategy relies on reducing the metal precursors(*e.g.*, $HAuCl_4$[61],$AgNO_3$[58], $CuCl_2$[62], *etc.*) with reducing agents such as sodium citrate[63], ascorbic acid[64], sodium borohydride[43], *etc.* This is followed by a nucleation and a next growth step, either in aqueous or organic solvents, in the presence of ligands responsible of providing colloidal stability to the NPs. Current synthetic methods allow to produce plasmonic NPs with diameters between 4-200 nm with different morphologies, including pseudo-spherical[65], rods, prims, stars[66], cubes, hollow structures[67], *etc.*

The citrate method is among the most popular routes to produce metallic NPs. This method relies on the reduction of metal salts (*e.g.*, $HAuCl_4$, $AgNO_3$) with citrate agents (*e.g.*, sodium citrate, trisodium citrate), to obtain citrate ions stabilized metallic NPs after nucleation and growth. In general, the sizes of NPs can be tuned by adjusting the reaction conditions, such as amount of citrate agents, reaction time, *etc.*; one the other hand, small metallic NPs can be produced as "seeds", which then can be grown to bigger size NPs or even different shaped NPs *via* seed-mediated method by altering the growth direction during the synthesis. This citrate-reduction method is fast, cheap and size-controlled. In order to provide the NPs with long-lasting stability against agglomeration, NPs can be overcoated with some other surfactant molecules, which can be anchored to the NPs' surface by different interactions (*i.e.,* covalent, electrostatic, hydrophobic,*etc.*). As an example, gold form covalent bonds with thiolated molecules, including mercaptosuccinic acid[68], thiol-PEG-MeO[69] and thiolated peptides[70], *etc.*

Moreover, plasmonic NPs originated in aqueous solution (*e.g.,* citrate capped Au NPs or CTAB-coated Au NPs[61]) can be dispersed in organic solvents *via* phase transfer[69]. In a two-phase system, NPs in the aqueous phase can be transferred into organic solvents (*e.g.,*chloroform, dichloromethane, *etc.*) by ligand exchange with hydrophobic surfactants (*e.g.,* dodecylamine[69]).

The other well-known route for synthesis plasmonic NPs is thermal decomposition method in organic solvents. In a classical synthesis process, metal precursors (*e.g.,* $HAuCl_4$, $AgNO_3$[71] or $Cu(acac)_2$[72]) can be decomposed, followed by nucleation and size growth in the presence of ligands (*e.g.,* oleic acid[73], oleylamine). In contrast to the aqueous methods, the production of NPs in organic phase, typically yield highly

monodisperse nanocrystals, and the N_2 flow is essential for any air sensitive material, such as copper. The aqueous methods are on the other hand more versatile for producing a wide variety of sizes and shapes. During the synthesis of CuNPs, the presence of even small amount of oxygen will induce CuNPs to oxidize into CuO or Cu_2O NPs[72, 74]. Thus, the most suitable reaction solvent depends on the purpose or materials.

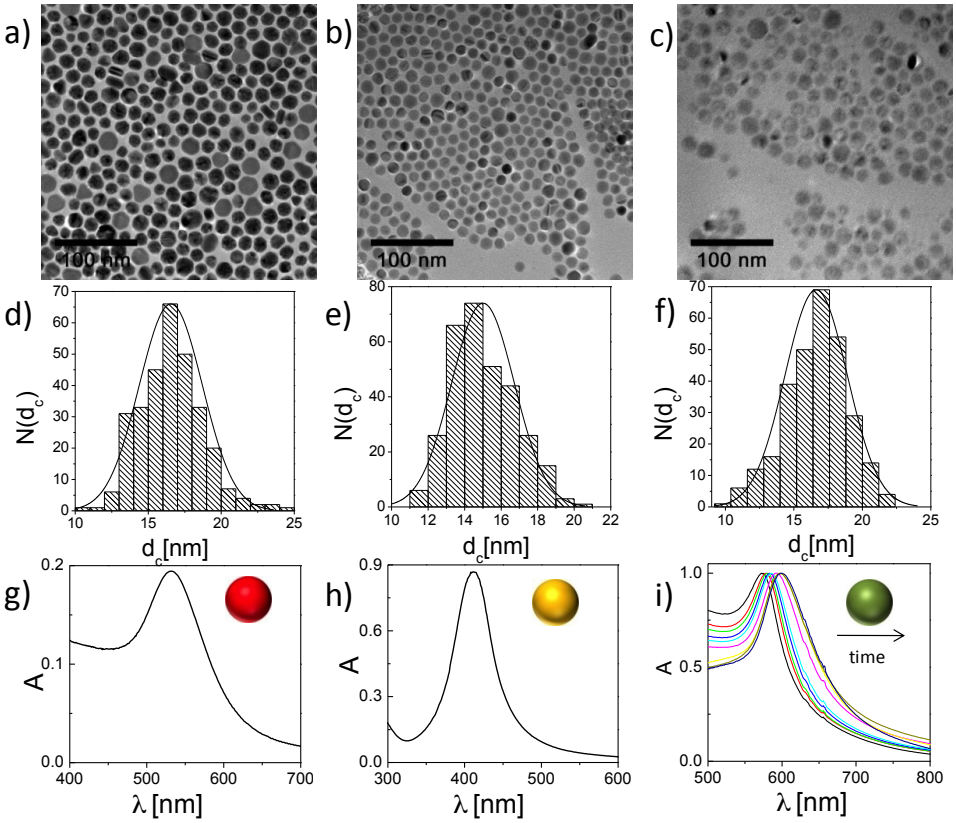

Figure 14. a,d and g) TEM micrographs of AuNPs produced by citrate-reduction procedure with the corresponding diameter histograms; the average size c = 16.5±2.2 nm, and the UV-Vis spectra of plasmonic peak is at 530 nm in $CHCl_3$; b,e and h) TEM micrographs of AgNPs obtained from thermal decomposition method with the corresponding diameter histograms, the average size dc = 15.0±1.7 nm, and the UV-Vis spectra of plasmonic peak is at 412 nm in $CHCl_3$; c,f and i) TEM micrographs of CuNPs obtained from thermal decomposition method with the corresponding diameter histograms, the average size dc = 16.7±2.3 nm, the UV-Vis spectra of plasmonic peak is at 573 nm in $CHCl_3$, and it was red shift slowly due to the air oxidation. The scale bars correspond to 100 nm, and the diameter histograms were measured by software Image J by analyzing > 300 NPs.

3.3 Applications

Several applications can be attributed to plasmonic NPs. These ones can be classified into labeling[54], detection and optical sensing[55] (based on SERS, LSPR spectroscopy, *etc.*), therapy (hyperthermia, drug delivery[53]) and catalysis[58].

Regarding labeling, plasmonic NPs have been used as contrast agents due to their optical properties. *Via* their addition in a region of interest, they provide contrast for the correct visualization of the region since they strongly absorb and scatter light[54].

The optical properties also confer plasmonic NPs the possibility of being used as sensors capable of registering the presence of specific analytes in solution and the subsequently concentration read out. The LSPR frequency of plasmonic NPs can be modified after these analytes bind onto the NPs surface, allowing their detection due to the plasmon resonance change[53]. Several techniques allow the detection of the analytes-NPs binding, *cf.*, particle-based fluorescence sensors are applied for ions quantification in publication [A3]. A widely used assay is based in surface-enhanced Raman scattering (SERS), able to sense either DNA or proteins close to the surface of plasmonic NPs. The incident light is scattered and this phenomena is characteristic of the chemical structure where this occur, obtaining a specific Raman spectrum which can be identified. Plasmonic NPs are able to enhance this natural scattering due to the SPR electrons that increase the electric field in the regions close to the NPs in comparison with the electric field value of the incident light.

Free LSPR electrons of plasmonic NPs undergo excitation when a specific wavelength is applied, leading to an oscillation of these free electrons. Subsequently, these excited free electronsthermally relax and the energy is transferred to the metallic NP, obtaining heating *via* light absorption[75]. The ability of plasmonic NPs to convert light absorption into heat is typically used for photothermal therapy either for *in vitro* or for *in vivo* experiments[76]. Meanwhile, NIR light is the best source for heating in biological systems because its absorption is minimum in typical physiological components (*i.e.,* water, fat, blood, *etc.*[77]). Therefore, the NPs with a LSPR band in NIR wavelength are more suitable candidates for hyperthermia (*e.g.,* Au nanoprisms[54], Au nanorods[78], *etc.*). Since human cells are sensitive to small changes in temperature (few degrees increase can be lethal), the use of plasmonic NPs has a great interest in cancer treatment. By adding plasmonic particles, previously conjugated with a tumor marker sensitive to proteins over expressed on cancer cells, a local treatment in these specific cancer cells can be performed. *Via* an external light source applied on the tumor area, the tumoral cells can

be selectively heated and therefore killed due to the plasmonic NPs capability of transforming light absorption into heat.

Due to their high surface-volume ratio, plasmonic NPs present outstanding catalytic properties when added to organic substrates such as silanes oxidation to silanols[79], epoxides into alkenes[80], *etc.* Plasmonic NPs modified with PEG molecules show an efficient catalytic behavior reducing methylene blue (blue) to leucomethylene blue (colorless) in the presence of $NaBH_4$, *cf.* Figure 15. Details about the (bio)physicochemical characterization of a number of PEGylated Au NPs can be found in publication [A6].

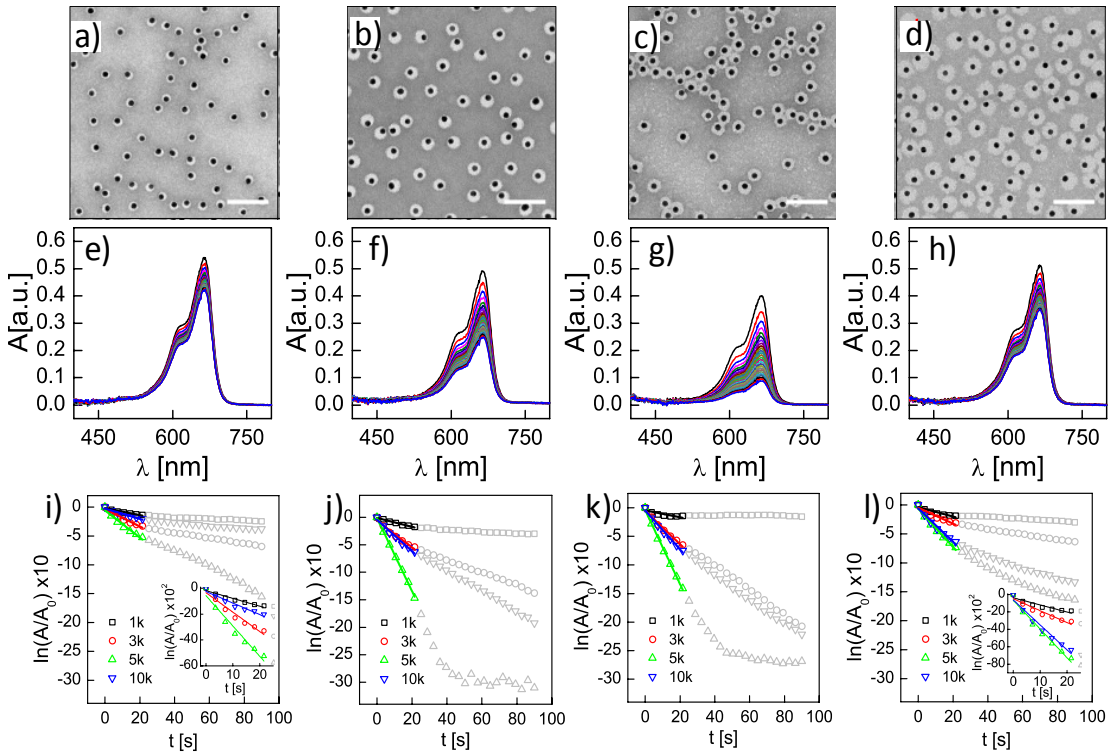

Figure 15. Catalytic measurements of PEGlated AuNPs to reduce methylene blue (MB, blue color) to leucomethylene blue (LMB, colorless) under visible light in the presence of $NaBH_4$ solution at R.T. a-d) negatively staining of TEM images of AuNPs (d_c=13.8 nm) saturated with different molecular weight of PEG (1 kDa, 3 kDa,5 kDa and 10 kDa); e-h) Absorption spectra of catalytic measurements with four PEGlated AuNPs collected over 90 s, each spectra was collected per 3.6 s. i-l) λ_{max} vs. time for four PEGlated AuNPs, data considered for the kinetic fitting are colored (initial 22 s). Inserts show zoom areas of the fitting regions for selected samples, kinetic constant values k [s^{-1}] were calculated by $ln(A/A_0) = -k \cdot t$. i) 6.0 x10^{-3} s^{-1}*, j) 15.0 x10^{-3} s^{-1}, k) 23.4 x 10^{-3} s^{-1}, l) 8.9 x10^{-3} s^{-1}.*

Investigating the interactions of these nanomaterials with biological systems to provide knowledge about the safety assessment is crucial. For that reason, nanotoxicology has emerged as a novel discipline inside nanoscience, which is mainly discussed in publication [A4]. In comparison to AuNPs, both AgNPs and CuNPs are less stable since they can release Ag^{+} and Cu^{2+}respectively over time. Therefore, their cytotoxicity have received close attention, since some experiments have shown that both AgNPs and CuNPs might induce DNA damage, formation of reactive oxygen species (ROS) and cell death[81]. For this reason they can be used for bactericidal and fungicidal applications. In parallel, developmental and structural malformations based on AgNPs can be applied for the study of human diseases and developmental abnormalities.

4. Titanium Dioxide Nanoparticles

4.1 Introduction

Titanium dioxide (TiO_2) is a very common material in nature[82]. There are three common polymorphs: anatase, rutile and brookite. Anatase, the most widely used form in industry, is photocatalytically active. As a low temperature stable form, brookite is usually existent mixed with other polymorphs. Rutile has a high density and it becomes the most stable phase at high temperature or pressure. Under certain conditions, anatase or brookite can turn into rutile[83].

TiO_2 is one kind of white inorganic material, which has been worldwide used in various areas[84, 85]. Due to its poor solubility, brightness and high refractive index, TiO_2 has become a well-known white pigment in industries and among customers, with applications in coating, paper, plastics, printing inks, cosmetics, food colorants, tooth paste as well as medicines[86]. TiO_2 is also very popular component of sunscreens and other cosmetics products, as it can efficiently protect from ultraviolet (UV) light. As an inorganic material from nature, it is much safer than other organic UV blocking chemicals[87].

With high surface/volume ratio, TiO_2 NPs are considered as a suitable semiconductor for photocatalysis under UV light, especially the anatase form, with a wide band gap of 3.2 eV, *cf.*, Figure 16. Under UV-light illumination, the electrons (e^-) on the surface of TiO_2 NPs are excited from valence band to conduction band, leaving behind holes (h^+) in the valence band. The excited electrons (e^-) in the conduction band can reduce oxygen (O_2) to O_2^-,whereas the holes (h^+) have very strong oxidative capability, which can oxidize water or organic compounds to produce OH^* radicals; then OH^* radicals can reduce almost any pollutant[88]. Due to their excellent photocatalysis properties, as well as low cost and high physic-chemical stability, TiO_2 NPs are widely used in wastewater treatment[89], air purification[84, 85], self-cleaning devices and pesticides[90], *etc*.

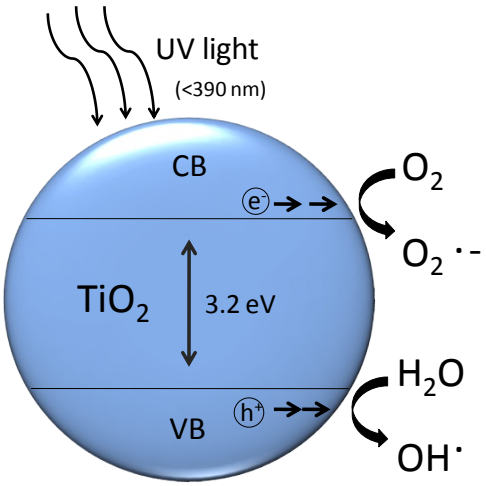

Figure 16. Scheme of photocatalysis mechanism of anataseTiO_2 NPs *under UV light illumination, modified from Pelaez et al*[88].

4.2 Synthesis

Due to their extended use in various areas, scientists have developed different kinds of techniques for the synthesis of TiO_2 NPs, including sol-gel process, chemical precipitation, hydrothermal synthesis, chemical vapor deposition (CVD), physical vapor deposition (DVD), *etc*[5].

As a typical method for producing metal nanomaterials, the sol-gel process has been used to produce TiO_2 NPs from titanium precursors (*e.g.*,titanium (IV) alkoxide) by hydrolysis or polymerization reaction[91]. The sol-gel process is a fast and easy way to get TiO_2 NPs without special equipment, and different sizes and shapes can be obtained by changing the reaction parameters. For instance, Chemseddine *et al.* produced several kinds of TiO_2 NPs by hydrolysis of $Ti(OR)_4$ in a tetramethylammonium hydroxide solution[92].

Hydrothermal synthesis is another commonly used way to obtain TiO_2 NPs under high temperature[93] (*e.g.,*using high boiling point solvent: 1-octadecene) or pressure conditions[92] (*e.g.,*autoclave). As a well-known synthesis method, hydrothermal is becoming more and more popular to synthesize TiO_2 NPs because of the high quality products. Changes in various reaction parameters, such as different titanium precursors or reaction solvents (*e.g.*, aqueous or organic solutions) allow sizes from 5 nm to 300 nm to be produced; different shapes can be accomplished as well, including spherical nanoparticles, nanoplates, nanorods[94], nanowires[95], nanobones, nanotubes[96], *etc.*

Murray *et al* reported a seeded growth technique to produce homogenous TiO_2 NPs in the 10–200 nm size range[93]. During the synthesis, titanium(IV) fluoride (TiF_4) or titanium(IV) chloride ($TiCl_4$) were used as precursors, and different shapes of TiO_2 NPs were synthesized with capping ligands such as oleylamine and oleic acid in presence of high boiling point solvent, such as 1-octadecene and 1-octadecanol, respectively. The highly uniform products can be kept in nonpolar solvent, such as $CHCl_3$ or hexane. As we mentioned above, organic surfactant stabilized NPs need to be transferred to aqueous solution by polymer coating in order to be used for further biological applications. However, as the surfactants on the surface of TiO_2 NPs, OLAM and OLA cannot be effectively anchored to the NP's surface, and eventually, the NPs aggregate during the polymer coating process. Therefore, surface ligand exchange before polymer coating is a key step to keep the NPs more stable in non-polar solutions. Phosphonic ligands (*e.g.,*OPA or TDPA) are suitable surfactants for the TiO_2 NPs, and the ligand exchange procedure can be carried out, followed by several washing steps with methanol[97]. The phosphonic ligand-coated NPs can be effectively polymer coated and transferred to aqueous solution as explained before.

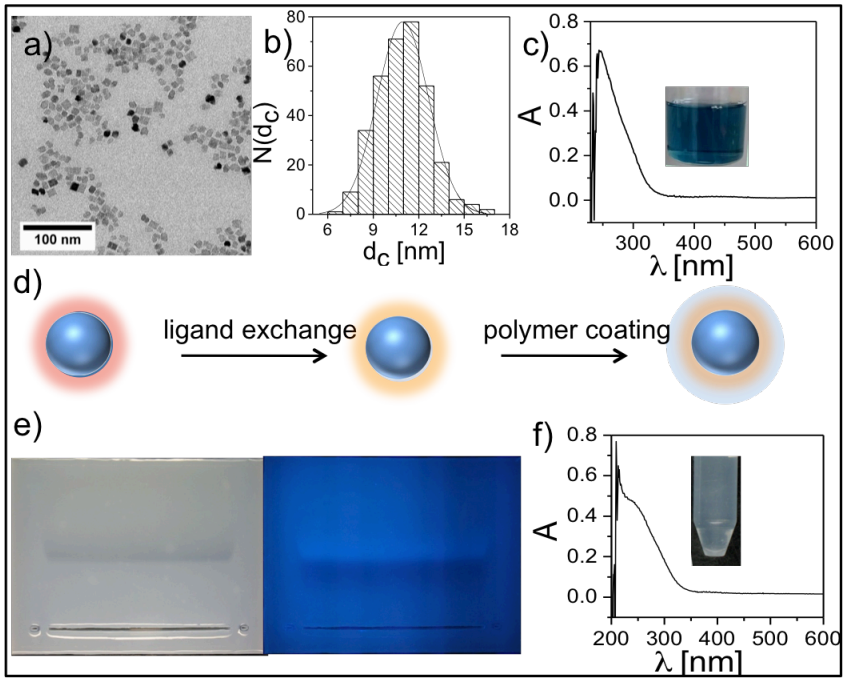

Figure 17. a and b) TEM micrographs of TiO_2 NPs with the corresponding diameter histogram measured by software Image J (> 300 NPs), the average size (d_c) = 11.0±1.7 nm; c) the UV-Vis spectra of absorption peak is at 250 nm in $CHCl_3$ with a blue color solution which due to the oxygen vacancies of fluorine from precursors (e.g.,TiF_4) during the synthesis; d) surface modification process: firstly, ligand exchange of TiO_2 NPs from OLAM and OLA to TDPA in organic solution; secondly, polymer coating procedure to

make the TiO_2 NPs water soluble; e) Visible light (left) and UV light (right) photograph of 2% agarose gel loaded with TiO_2 NPs after polymer coating, the blue fluorescent band is the mixture of micelles and free fluorine which was released during the dissolution process with the treatment of SBB 12 solution, and the dark band behind under UV light photograph was the PMA coated TiO_2 NPs; f) the UV-Vis spectra of absorption peak is at 250 nm in H_2O with a light blue color solution.

4.3 Applications

TiO_2 NPs present strong catalytic activity due to their large surface to volume ratio, and they are commonly applied for photocatalytic applications[9]. Take biodegradation as an example, under UV illumination, TiO_2 NPs can produce electrons and holes which can separately react with O_2 or H_2O to generate $O_2^{\bullet-}$ or $OH^{\bullet}$, and degrade any pollutants. As the typical pollutants in experiments, Methylene blue (MB) and Rhodamine B (Rh.B) can be reduced to colorless Leucomethylene blue (LMB) and colorless Rhodamine B phase, respectively, in presence of TiO_2 NPs with UV light irradiation, *cf.*, Figure18. In previous biodegradation studies, large particle size, with low water-solubility and poor size distribution, has shown limited efficiency of catalysis[98]. Thus, in our experiments, we synthesize uniform size of TiO_2 NPs (d= 11 nm), and perform the polymer coating method, which make the NPs stable in aqueous solution. Thus, to improve the "quality" of the NPs increases the opportunity of pollutants to reach the surface of the NPs, which results on high biodegradation efficiency.

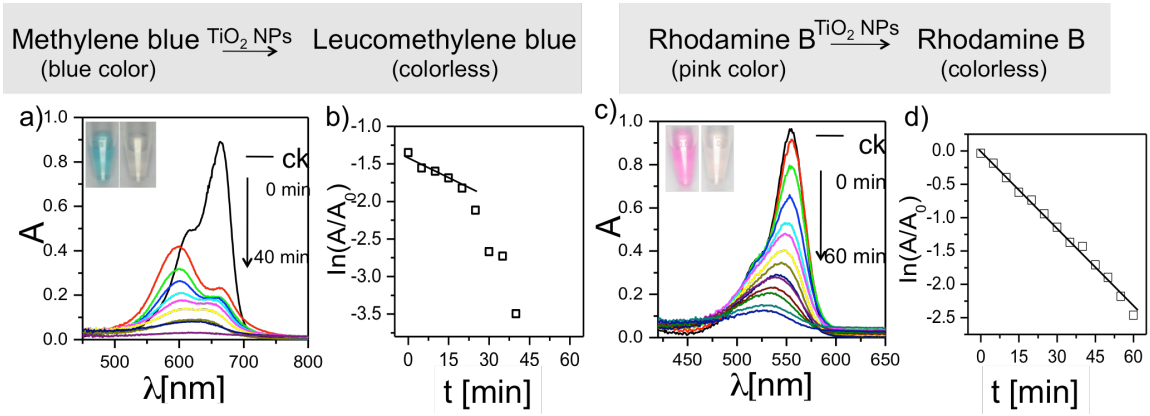

Figure 18. Photocatalytic degradation of pollutants with polymer coated TiO_2 NPs in an aqueous solution under UV light illumination. a) Reduction of blue colored methylene blue (MB) to colorless leucomethylene blue (LMB) by TiO_2 NPs: absorption spectrum of degradation process with adding MB (9.37×10^{-4} M, 400 µL) and TiO_2 NPs (0.5µM, 10 µL), the maximum absorption of MB (λ_{max}= 664 nm) was decreased with time until all the MB

degradated during 40 min UV light illumination. Black line is MB solution with 10 µL H_2O as control, the spectra was collected per 5 min; b) Kinetic constant values k [min^{-1}] of MB photodegradation was calculated by $ln(A/A_0) = -k \cdot t$ during the first 25 min, k=2.7 x10^{-2} min^{-1}, R^2=0.933; c) Reduction of pink colored Rhodamine B (Rh.B) to colorless solution by TiO_2 NPs: absorption spectrum of degradation process with adding Rh.B (1.5× 10^{-4} M, 400 µL) and TiO_2 NPs (0.5 µM, 10 µL), the maximum absorption of Rh.B (λ_{max}= 554 nm) was decreased with time until all the Rh.B degradated during 1 h UV light illumination. Black line is Rh.B solution with 10 µL H_2O as control, the spectra was collected per 5 min; d) Kinetic constant values k [min^{-1}] of Rh.B photodegradation was calculated by $ln(A/A_0) = -k \cdot t$ during 1 h, k=3.86 x10^{-2} min^{-1}, R^2=0.993. All the reactions were protected from light.

However, due to their physico-chemical properties, TiO_2 NPs as photocatalysts are limited to UV light excitation. Thus, how to extend their catalytic properties to the visible light wavelength has become a new challenge. After serious studies in recent years, many strategies are developed to solve this problem: 1) Doping with other elements during the synthesis of TiO_2 NPs; the doping elements can be metal[99] (*e.g.,* Fe, Ti^{3+}or La^{3+}) or nonmetal[100] (*e.g.,*B, C and Br). The doping process can modify the chemical composition of TiO_2, with the result of band gap decrease or intra-band gap state generation, which can induce a bathochromic shift for enhancement of optical response. 2) Surface sensitization of TiO_2 NPs *via* colorful organic/inorganic dyes. The well-known application is dyes-sensitized solar cell[101]; in this type of thin-film photovoltaic cell where the electrons of organic dye are excited with coming sunlight, and release into the TiO_2 NPs, energy can be created and collected on a transparent conduction surface. 3) Composite TiO_2 NPs with other semiconductors particles, including TiO_2-CdS, TiO_2-SnO_2, TiO_2-Fe_2O_3, *etc.*[82,5]. Coupled semiconductors exhibit much higher photocatalytic efficiency by enhancing the charge separation as well as extending energy range. Therefore, after the improvement from the strategies described above, TiO_2 NPs increase their optical activity and extend their applications.

Preliminary Cytotoxicity Study: TiO_2 fine particles with diameters in the microscale are considered as safe materials widely used for cosmetics, foods and medicines. However, the toxicity and environment impact of TiO_2 NPs is still a problematic issue[102]. Since NPs for bioapplications are the main object of this Ph.D work, we made a preliminary cytotoxicity evaluation of TiO_2 NPs in HeLa cells, *cf.*, Figure19.

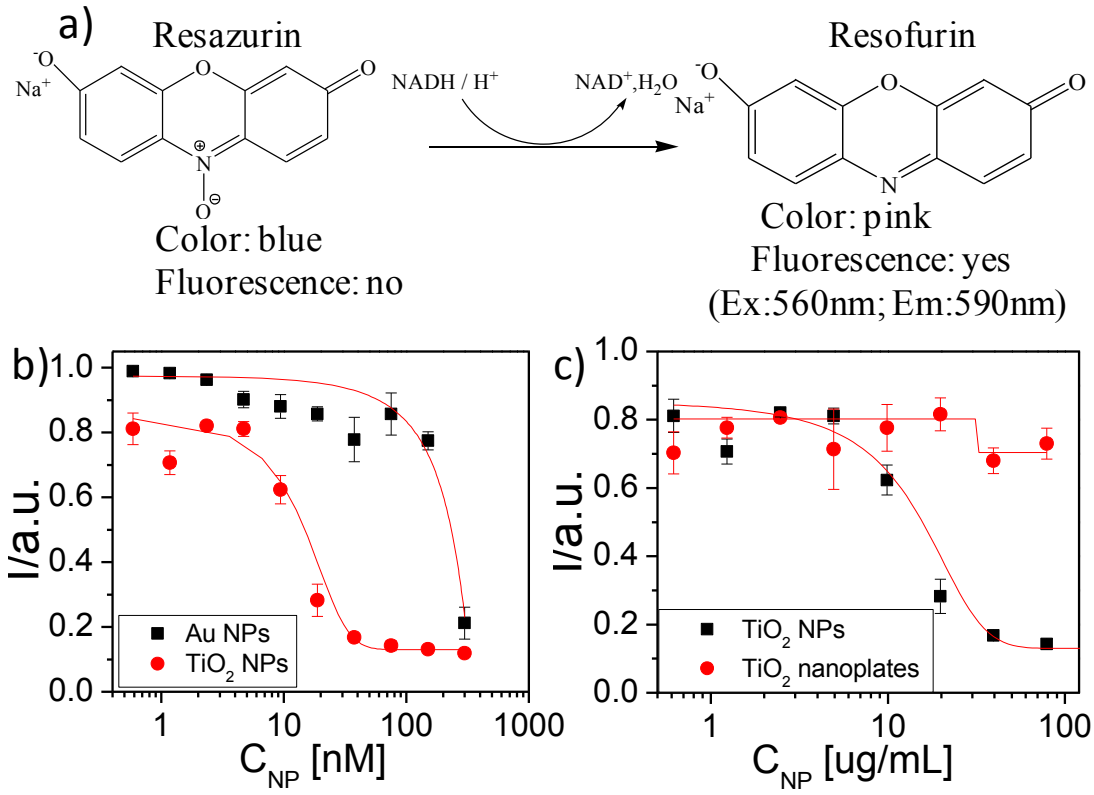

Figure 19. Cytotoxicity measurement of TiO_2 NPs synthesized above based on resazurin viability after incubate with HeLa cells for 24 h. a) mechanism of resazurin (blue color) transferred into resofurin (pink color) with living cell; b) Cytotoxicity comparison of PMA coated AuNPs (d_c=4 nm) and TiO_2 NPs with same molar concentration from 0.6 nM to 300 nM, from the data we can see, TiO_2 NPs are much more toxic than AuNPs; c) Cytotoxicity comparison of bigger PMA coated TiO_2 nanoplates (L= 120 nm, W=10 nm) with TiO_2 NPs with same mass from 0.6 µg/mL to 100 µg/mL, from result we can see, TiO_2 NPs are more toxic with small size.

Compared to PMA coated AuNPs (d_c = 4 nm), which are taken as a NP model typically used for cell uptake, *cf.* publication [A9], TiO_2 NPs present toxic features at lower concentrations (more than one order of magnitude). Moreover small size of TiO_2NPs (*i.e.,* d_c=11 nm) are much toxic than the bigger ones(*i.e.,* L=120 nm, W=10 nm), when they are incubated using equal mass. Similar studies have also proved that, compared to TiO_2 fine particles (diameter from 1 µm to 2.5 µm), nano-sized TiO_2 (diameter<1 µm) are more toxic because TiO_2 NPs have higher surface area with the same mass of TiO_2 fine particles[103]. This is because, due to their high surface-volume ratio, small sized TiO_2 NPs are more reactive to generate oxygen species, which is very toxic for cells by damaging their membrane and then, they induce cell death. In addition, it was reported from *in vivo* experiments that TiO_2 NPs can go into the lung and gastrointestinal tract (GIT), and

afterwards translocate to other organs such as brain, liver and kidneys, and finally, induce the pathological lesions[103]. Schiestl *et.al* reported that, after drinking water contained TiO_2 NPs, mice showed negative health effects, such as genotoxicity, DNA damage and inflammation[104]. To our knowledge, TiO_2 NPs used to date *in vivo* experiments present low stability, which can induce particle agglomeration, with the result of NPs favored accumulation and therefore, damage. In work in progress, we will study the effect of polymer coated TiO_2 NPs in mice, for which we will study different sizes and shapes of highly stable TiO_2 NPs.

5. Conclusion and Outlook

As discussed above, nanoparticles made of various materials and with a wide range of sizes can be synthesized with the aim of different biological applications, which are based on their unique physico-chemical properties. In general, there are several protocols for producing different NPs, and the size of NPs can be easily controlled with varying parameters during the synthesis procedure. With the aim of making NPs as monodisperse as possible, many types of NPs stabilized with aliphatic chains are produced in organic solvents. Yet in order to make them water soluble, which is obviously necessary to work in biological environments, the NPs have to be transferred to aqueous solution without compromising their colloidal stability. One of the common methods used to transfer NPs to an aqueous phase relies on the amphiphilic polymers. During this Ph.D work, this method has been extensively used with success for a variety of NPs, in which the hydrophobic side chains are intercalated with capping ligands on the core. Upon hydrolysis of the anhydride rings of the polymer, a negatively charged hydrophilic backbone composed of carboxylates is produced, which stabilize the NPs in aqueous solution. In addition, due to the carboxylate rich surface, polymer coated NPs can be further functionalized with other biomolecules *via* EDC chemistry, which allows new surface functionalities to be introduced.

Magnetic NPs can release heat under an altering magnetic field, which has been widely applied for magnetic fluid hyperthermia. In order to obtain maximum hysteresis losses (*i.e.*, specific loss power, SLP), three different exchange-coupled core-shell ferrite magnetic NPs, together with two single phase magnetic NPs, were produced with different content ratios of “soft” Mn ferrite and “hard” Co ferrite phases. The experimental data match very well the experimental data (*i.e.*, magnetic characterization and heating properties), concluding that their effective magnetic anisotropy are highly dependent on the Co ferrite content. Moreover, among the five samples studies, Co@Mn MNPs exhibit the highest SLP value, in the order of the best-suited materials reported to date for hyperthermia.

Plasmonic NPs exhibit unique optical properties based on the mechanism of localized surface plasmon resonance, which for instance, has been extensively used with NIR-active plasmonic NPs for photothermal therapy, SERS, colorimetric biosensing, *etc*. In the present work, in order to compare the (bio) properties of three types of plasmonic NPs with the same size, *i.e.*, AuNPs, AgNPs and CuNPs, were synthesized and then, they were coated with the same amphiphilic polymer. In this way, the impact of these NPs of cell cultures (work in progress) can be directly related to the composition of the

inorganic core (*i.e.,*Au, Ag or Cu). In another work, in which different PEGylated Au NPs (4 different inorganic cores, *i.e.*,13, 18.5, 23.5 and 28 nm, were combined with 4 different PEGs, *i.e.*, 1, 3, 5 and 10 kD) were thoroughly (bio)characterized, PEGylated AuNPs showed excellent catalytic activity for reducing methylene blue. Particularly, and AuNPs modified with 5 kDa PEG present the best catalytic ability.

As one kind of semiconductor materials, TiO_2 NPs are welcomed in many industrial areas. TiO_2 NPs exhibit strong UV light absorption and good photocatalytic properties. Uniform TiO_2 NPs were synthesized in organic solvents. The aliphatic-coated NPs were stable in aqueous solution after ligand exchange and polymer coating; the polymer-coated TiO_2NPs present long term stability and high surface volume ratio, which can be used for reducing organic pollutants, such as methylene blue and rhodamine B, under UV light.

In summary, three types of nanomaterials with interesting properties (*i.e.*, optimized nanoheating under AMF, plasmonic or photocatalytic) were produced and coated with a common amphiphilic polymer, which provides the NPs with enhanced colloidal stability in aqueous solution. The use of robust coating methods is very important to disentangle the correlation between the physicochemical properties of NPs and their (bio) performance (*e.g.*, nanoheating, toxicity, catalytic activity, *etc.*). For instance, in order to assess the capability of one type of NP as nanoheater, the NPs should not aggregate (or corrode) in the medium where they are supposed to work (*e.g.*, inside the body), as otherwise, inter-NP coupling effects (or “defective” NPs) can limit their performance. Likewise, agglomeration of NPs can enhance or hide cytotoxic effects, depending of the NP model under study. Thus, the use of a common robust polymer coating on different NP models allows for: (i) producing stable colloids in different media, which is important to preserve the physicochemical properties of the NPs, (ii) correlating physicochemical properties of NPs with toxicity features, and (iii) reliably comparing different NP models.

6. Publications

The described data in the previous chapters is based on my publications during my PhD study from 2011 to 2015, which are listed below. Each publication is briefly summarized; my contributions to these publications are also briefly described. The publications (published, submitted or in preparation) are attached in the Appendix.

6.1 Reviews

[A1] P. del Pino, B. Pelaz, **Q. Zhang**, P. Maffre, G. U. Nienhaus, W. J. Parak. Protein corona formation around nanoparticles – from the past to the future. *Materials Horizons* **2014**, 1, 301–313.

The protein corona, which is typically formed on the surface of nanoparticles, plays a quite important role for bioapplications of colloidal NPs. This paper mainly analyze how existing simple analytical models such as the adopted Hill model may help to extract quantitative data such as equilibrium dissociation and kinetic coefficients. Careful quantitative assessment of equilibrium and kinetic properties would allow for a comparison of protein binding data from the vast array of engineered nanoparticles, so that basic principles could be revealed.

The author contributed to the synthesis and characterization of dispersed and agglomerated gold NPs, as well as to the edition of figures and to literature searching.

[A2]M. Nazarenus, **Q. Zhang**, M. G. Soliman, P. del Pino, B. Pelaz, S. Carregal-Romero, J. Rejman, B. Rothen-Rutishauser, M. J. D. Clift, R. Zellner, G.U Nienhaus, J. B. Delehanty, I. L. Medintz, W. J. Parak. In vitro interaction of colloidal nanoparticles with mammalian cells: What have we learned thus far? *Beilstein Journal of Nanotechnology***2014**, 5, 1477–1490.

In this paper, we discuss the more generally accepted concepts about the interfacing of colloidal nanoparticles with mammalian cells. While details of these complex interactions strongly depend, amongst others, upon the specific properties of the nanoparticles used, the cell type, and their environmental conditions, a number of fundamental principles exist, which are outlined in this review.

The author contributed with TEM images of dispersed and agglomerated gold NPs, as well as to the edition of figures and to literature searching.

[A3]S. Ashraf, C. Carrillo-Carrion, **Q. Zhang**, M.G.Soliman, R. Hartmann, B.Pelaz, P. del Pino, W. J. Parak. Fluorescence-based ion-sensing with colloidal particles. *Current Opinion in Pharmacology***2014**, 18:98–103.

The paper outlines particle-based fluorescence sensors for the quantification of ions. The systems discussed are based on ion-sensitive fluorophores coupled to carrier particles, or on intrinsically fluorescent particles whose fluorescence properties depend on the concentration of the ions. These sensors are particularly well suited for intracellular sensing applications and advances in drug screening. Limitations associated with these sensors are addressed using different strategies

The author contributed to literature searching.

[A4] N. Feliu, B. Pelaz, **Q. Zhang**, P. del Pino, A. Nyström, W. J. Parak. Nanoparticle dosage-anontrivial task of utmost importance for quantitative nanotoxicology. *WIREs Nanomedicine&Nanobiotechnology*. In revision.

This paper summarizes the cytotoxicity of the NPs based on their physico-chemical properties, such as size, shape, surface charge and colloidal stability. In particular, nanotoxicology based on dosage is outlined, and calculation based on the particle concentration for uptake is addressed.

The author contributed to literature searching, as well as to the the particle concentration calculation evaluation.

[A5] S. Ashraf, B. Pelaz, P. del Pino, A. Escudero, W. J. Parak, **Q. Zhang**, C. Carillo. Gold-based nanomaterials for applications in nanomedicine. *Topics in Current Chemistry*. Accepted.

This paper gives an overview about the medical applications of gold nanomaterials based on their unique physico-chemical properties. In this paper, synthesis and functionalization of AuNPs are summarized, and recent medical application from diagnostics to therapeutics are outlined, as well as promising field of theranostic based on gold nano-platforms.

The author contributed to the literature research and corrections, and some part of editing before submission.

6.2 Research papers

[A6]**Q. Zhang***, I. Castellanos-Rubio*, R. Munshi*, I. Orue, B. Pelaz, W. J. Parak, P. del Pino, A. Pralle. Model Driven Optimization of Magnetic Anisotropy of Exchange-coupled Core-Shell Ferrite Nanoparticles for Maximal Hysteretic Loss. *Chemistry of materials.* In revision..

*equal contribution

In this paper, five different of magnetic nanoparticles (core only or core@shell systems) with constant size were produced, whose magnetic anisotropy was optimized by controlling the NP's design. From the study we know, the optimized system presents very high specific power loss (SPL) under alternating magnetic fields. According to the theoretical evaluation and experimental results we found that, the effective magnetic anisotropy can be tuned by changing Co ferrite ratio with constant size.

The author contributed o all the experiments of nanoparticles synthesis, characterization and their data evaluation, as well as to the writing and editing of the manuscript.

[A7] P. del Pino, B. Pelaz, F. Yang, **Q. Zhang**, K. Kantner, N. M. d. Baroja, M. Gallego, M. Möller, B. Manshian, S. Soenen, N. Hampp, W. J. Parak. Physicochemical Properties of PEGylated Gold Nanoparticles: Impact on Cell Fitness. To be submitted to *AngewandteChemie International Edition*.

This paper provides a detailed (bio)physicochemical characterization of a number of PEGylated Au NPs. The impact of these NPs in cell cultures was investigated, revealing that hydrophobicity and charge of selected NPs dictates some negative effects *in vitro*.

The author contributed to the synthesis and characterization (mainly the catalytic measurements, DLS and ICP-MS)of the different samples, as well as to the edition of the figures and part of the writing.

[A8]G. Tan, K. Kantner, **Q. Zhang**, M. G. Soliman, P. del Pino, W. J. Parak, M. A. Onur, D. Valdeperez, J. Rejman, B.Pelaz. Conjugation of polymer-coated gold nanoparticles with antibodies - synthesis and characterization. *Nanomaterials*. Accepted.

This paper mainly give a strategy of functionalizing polymer coated AuNPs with antibodies. The synthesis and characterization of the NPs are outlined, and the effect with two types of cells are studied.

The author contributed to the characterization of AuNPs and some editing part.

[A9]O.T. Marisca, K. Kanter, C. Pfeiffer, **Q. Zhang**, B. Pelaz, N. Leopold, W. J. Parak, J. Rejman. Can the coating make a difference: comparison of the in vitro performance of collagen- and synthetic polymer coated gold nanoparticles. *Nanomaterials*. Accepted.

This paper describes collagen stabilized AuNPs. All the physico-chemical properties of collagen-coated AuNPs are discussed and compared with same size of PMA-coated AuNPs. From the cell uptake and toxicity experiment we can see that the collagen-coated AuNPs have low cytotoxicity and higher uptake levels with the same amount of PMA-coated AuNPs.
The author contributed to the synthesis and characterization of dy647 labeled PMA-coated AuNPs, and data analysis and writing of this part.

[A10]C. Shi, F. Yang, **Q. Zhang**, S. Neitemeier, C. Thum, N. Hampp, C. Culmsee, W. J. Parak, M. Schneider. Morphological change and ablation of cancer cells via interaction of drug-magnetic co-loaded nanoparticles in weak rotating magnetic fields. In preparation.
This paper describesa polymeric nanoparticle (*ca.* 200 nm) based on PLGA, which is loaded with iron oxide NPs and an anticancer drug (also called co-loaded PLGA NPs). Under a rotating magnetic field, iron oxide NPs can enhance the movement of co-loaded PLGA NPs after uptake in cells, which can improve the efficiency of drug delivery. The synthesis of co-loaded PLGA NPs is outlined and the drug delivery process is addressed.

The author contributed to all the part of Fe_3O_4 NPs, including the synthesis, characterization, data analysis and manuscript writing.

[A11]F. Yang, B. Pelaz, X. Yu, R. Riedel, **Q. Zhang**, B. Zhang, P. del Pino, W. J. Parak, N. Hampp. Hybrid bioconjugation based on assembly of functional gold nanoparticles on mutant purple membrane via Ni-NTA and histidine interaction. In preparation.

This paper developed a new functional biosystem based on integration of nanoparticle (NP) and biomembrane. AuNPs can couple with nickel-nitrilotriacetate (Ni^{2+}-NTA) via EDC chemistry, which can be combined with mutated purple membrane (PM) assembly by NTA-Ni^{2+}-histidine interaction. In this paper, the

characterizations of this biosystem are outlined compared with other two uncombined systems, and promising applications are discussed.

The author contributed to the characterizations of AuNPs and new biosystem.

6.3 Book chapter

[A12] B. Pelaz, Q. Zhang, P. del Pino, W. J. Parak. “Metal and Metal Oxide Core-shell Nanocomposites”. 1.09.04. Inorganic core-shell Nanoparticles.

This book chapter outlines common strategies for the synthesis of core-shell composite NPs via seeds-mediated growth methods. Core-shell nanoparticles exhibit new physico-chemical properties which make them more suitable for certain applications.

The author contributed to the synthesis part of core-shell magnetic nanoparticles.

Abbreviations

Ag	silver
$AgNO_3$	Silver nitrate
AMF	Alternating magnetic field
Au	gold
BSA	bovine serum albumin
$CHCl_3$	Chloroform
Cu	Copper
DNA	deoxyribonucleic acid
EDC	N-(3-dimethylaminopropyl)-N'-ethylcarbodiimide
EDTA	ethylenediamintetraacetic acid
FM particle	ferro- or ferri-magnetic particle
$HAuCl_4$	Hydrogen tetrachloroaurate(III) hydrate
HCG	Human Chorionic Gonadotropin
LMB	leucomethylene blue
LSPR	localized surface plasmon resonance
MB	Methylene blue
MRI	magnetic resonance imaging
NP(s)	nanoparticle(s)
OPA	Octylphosphonic acid
PEG	polyethylene glycol
q-LRT	quasi-Linear Response theory
REF	domain wall displacement
Rh.B	Rhodamine B
ROS	reactive oxygen species

SERS	surface-enhanced Raman scattering
SPM particle	superparamagnetic particle
TBE	Tris-borate-EDTA
TDPA	Tetradecylphosphonic acid
$TiCl_4$	titanium(IV) chloride
TiF_4	titanium(IV) fluoride
TiO_2	Titanium dioxide
Tris	tris(hydroxymethyl)aminomethane
UV	ultra violet

References

1. Green, M. A., Thin-film solar cells: review of materials, technologies and commercial status. *J Mater Sci-Mater El* **2007,** *18*, S15-S19.

2. Azzazy, H. M. E.; Mansour, M. M. H., In vitro diagnostic prospects of nanoparticles. *Clin Chim Acta* **2009,** *403* (1-2), 1-8.

3. Knobel, M.; Nunes, W. C.; Socolovsky, L. M.; De Biasi, E.; Vargas, J. M.; Denardin, J. C., Superparamagnetism and other magnetic features in granular materials: A review on ideal and real systems. *J Nanosci Nanotechno* **2008,** *8* (6), 2836-2857.

4. Petryayeva, E.; Krull, U. J., Localized surface plasmon resonance: Nanostructures, bioassays and biosensing-A review. *Anal Chim Acta* **2011,** *706* (1), 8-24.

5. Chen, X.; Mao, S. S., Titanium dioxide nanomaterials: Synthesis, properties, modifications, and applications. *Chemical Reviews* **2007,** *107* (7), 2891-2959.

6. Sperling, R. A.; Parak, W. J., Surface modification, functionalization and bioconjugation of colloidal inorganic nanoparticles. *Philosophical Transactions of the Royal Society A - Mathematical Physical and Engineering Science* **2010,** *368* (1915), 1333-1383.

7. Basly, B.; Felder-Flesch, D.; Perriat, P.; Billotey, C.; Taleb, J.; Pourroy, G.; Begin-Colin, S., Dendronized iron oxide nanoparticles as contrast agents for MRI. *Chem Commun* **2010,** *46* (6), 985-987.

8. del_Pino, P.; Pelaz, B., Hyperthermia Using Inorganic Nanoparticles. In *Nanobiotechnology: Inorganic Nanoparticles vs Organic Nanoparticles: Frontiers of Nanoscience, Vol. 4.*, Fuente, J. M. d. l.; Grazu, V., Eds. Elsevier: Amsterdam, The Netherlands, 2012; pp 309 - 335.

9. Daghrir, R.; Drogui, P.; Robert, D., Modified TiO_2 For Environmental Photocatalytic Applications: A Review. *Ind Eng Chem Res* **2013,** *52* (10), 3581-3599.

10. Wang, Y. L.; Xia, Y. N., Bottom-up and top-down approaches to the synthesis of monodispersed spherical colloids of low melting-point metals. *Nano Letters* **2004,** *4* (10), 2047-2050.

11. Stewart, M. E.; Mack, N. H.; Malyarchuk, V.; Soares, J. A. N. T.; Lee, T. W.; Gray, S. K.; Nuzzo, R. G.; Rogers, J. A., Quantitative multispectral biosensing and 1D imaging using quasi-3D plasmonic crystals. *Proceedings of the National Academy of Sciences of the United States of America* **2006,** *103* (46), 17143-17148.

12. Lamer, V. K.; Dinegar, R. H., Theory, Production and Mechanism of Formation of Monodispersed Hydrosols. *Journal of the American Chemical Society* **1950,** *72* (11), 4847-4854.

13. Murray, C. B.; Kagan, C. R.; Bawendi, M. G., Synthesis and characterization of monodisperse nanocrystals and close-packed nanocrystal assemblies. *Annu Rev Mater Sci* **2000,** *30*, 545-610.

14. Sun, Y. G., Controlled synthesis of colloidal silver nanoparticles in organic solutions: empirical rules for nucleation engineering. *Chemical Society Reviews* **2013,** *42* (7), 2497-2511.

15. Sun, S.; Murray, C. B.; Weller, D.; Folks, L.; Moser, A., Monodisperse FePt Nanoparticles and Ferromagnetic FePt Nanocrystal Superlattices. *Science* **2000,** *287* (March 17), 1989-1992.

16. Chen, L. G.; Wang, T.; Tong, J., Application of derivatized magnetic materials to the separation and the preconcentration of pollutants in water samples. *Trac-Trend Anal Chem* **2011,** *30* (7), 1095-1108.

17. Tartaj, P.; Morales, M.; Veintemillas-Verdaguer, S.; Gonzalez-Carreno, T.; Serna, C., The preparation of magnetic nanoparticles for applications in biomedicine. *J Phys D Appl Phys* **2003,** *36* (13), R182-R197.

18. Rai, P.; Mallidi, S.; Zheng, X.; Rahmanzadeh, R.; Mir, Y.; Elrington, S.; Khurshid, A.; Hasan, T., Development and applications of photo-triggered theranostic agents. *Advanced Drug Delivery Reviews* **2010,** *62* (11), 1094-1124.

19. Colombo, M.; Carregal-Romero, S.; Casula, M. F.; Gutiérrez, L.; Morales, M. P.; Böhm, I. B.; Heverhagen, J. T.; Prosperi, D.; Parak, W. J., Biological Applications of Magnetic Nanoparticles. *Chemical Society Reviews* **2012,** *41*, 4306-4334.

20. Lu, A. H.; Salabas, E. L.; Schuth, F., Magnetic Nanoparticles: Synthesis, Protection, Functionalization, and Application. *Angewandte Chemie, International Edition* **2007,** *46* (8), 1222-1244.

21. Figuerola, A.; Di Corato, R.; Manna, L.; Pellegrino, T., From iron oxide nanoparticles towards advanced iron-based inorganic materials designed for biomedical applications. *Pharmacol Res* **2010,** *62* (2), 126-143.

22. Derfus, A. M.; von Maltzahn, G.; Harris, T. J.; Duza, T.; Vecchio, K. S.; Ruoslahti, E.; Bhatia, S. N., Remotely triggered release from magnetic nanoparticles. *Adv. Mater.* **2007,** *19* (22), 3932-3936.

23. Carrey, J.; Mehdaoui, B.; Respaud, M., Simple models for dynamic hysteresis loop calculations of magnetic single-domain nanoparticles: Application to magnetic hyperthermia optimization (vol 109, 083921, 2011). *Journal of Applied Physics* **2011,** *110* (3).

24. Gupta, A. K.; Gupta, M., Synthesis and surface engineering of iron oxide nanoparticles for biomedical applications. *Biomaterials* **2005,** *26* (18), 3995-4021.

25. Jang, J. T.; Nah, H.; Lee, J. H.; Moon, S. H.; Kim, M. G.; Cheon, J., Critical Enhancements of MRI Contrast and Hyperthermic Effects by Dopant-Controlled Magnetic Nanoparticles. *Angewandte Chemie-International Edition* **2009,** *48* (7), 1234-1238.

26. Kell, A. J.; Stewart, G.; Ryan, S.; Peytavi, R.; Boissinot, M.; Huletsky, A.; Bergeron, M. G.; Simard, B., Vancomycin-modified nanoparticles for efficient targeting and preconcentration of Gram-positive and Gram-negative bacteria. *Acs Nano* **2008,** *2* (9), 1777-1788.

27. Grancharov, S. G.; Zeng, H.; Sun, S. H.; Wang, S. X.; O'Brien, S.; Murray, C. B.; Kirtley, J. R.; Held, G. A., Bio-functionalization of monodisperse magnetic nanoparticles and their use as biomolecular labels in a magnetic tunnel junction based sensor. *J Phys Chem B* **2005,** *109* (26), 13030-13035.

28. Laurent, S.; Forge, D.; Port, M.; Roch, A.; Robic, C.; Vander Elst, L.; Muller, R. N., Magnetic Iron Oxide Nanoparticles: Synthesis, Stabilization, Vectorization, Physicochemical Characterizations, and Biological Applications. *Chemical Reviews* **2008,** *108* (6), 2064-2110.

29. Jolivet, J. P.; Chaneac, C.; Tronc, E., Iron oxide chemistry. From molecular clusters to extended solid networks. *Chem Commun* **2004,** (5), 481-487.

30. Rockenberger, J.; Scher, E. C.; Alivisatos, A. P., A New Nonhydrolytic Single-Precursor Approach to Surfactant-Capped Nanocrystals of Transition Metal Oxides. *J. Am. Chem. Soc.* **1999,** *121* (49), 11595-11596.

31. Sun, S.; Zeng, H., Size-Controlled Synthesis of Magnetite Nanoparticles. *Journal of the American Chemical Society* **2002,** *124* (28), 8204-8205.

32. Chen, R.; Christiansen, M. G.; Anikeeva, P., Maximizing Hysteretic Losses in Magnetic Ferrite Nanoparticles via Model-Driven Synthesis and Materials Optimization. *Acs Nano* **2013,** *7* (10), 8990-9000.

33. Yu, W. W.; Falkner, J. C.; Yavuz, C. T.; Colvin, V. L., Synthesis of monodisperse iron oxide nanocrystals by thermal decomposition of iron carboxylate salts. *Chem Commun* **2004,** (20), 2306-2307.

34. Xie, J.; Peng, S.; Brower, N.; Pourmand, N.; Wang, S. X.; Sun, S. H., One-pot synthesis of monodisperse iron oxide nanoparticles for potential biomedical applications. *Pure Appl Chem* **2006,** *78* (5), 1003-1014.

35. Sun, S.; Zeng, H.; Robinson, D. B.; Raoux, S.; Rice, P. M.; Wang, S. X.; Li, G., Monodisperse MFe_2O_4 (M = Fe, Co, Mn) Nanoparticles. *J. Am. Chem. Soc.* **2004,** *126* (1), 273-279.

36. Pellegrino, T.; Kudera, S.; Liedl, T.; Javier, A. M.; Manna, L.; Parak, W. J., On the Development of Colloidal Nanoparticles towards Multifunctional Structures and their Possible Use for Biological Applications. *Small* **2005,** *1* (1), 48-63.

37. Caballero-Díaz, E.; Pfeiffer, C.; Kastl, L.; Rivera-Gil, P.; Simonet, B.; Valcárcel, M.; Jiménez-Lamana, J.; Laborda, F.; Parak, W. J., The Toxicity of Silver Nanoparticles Depends on Their Uptake by Cells and Thus on Their Surface Chemistry. *Particle and Particle Systems Characterization* **2013,** *30* (12), 1079-1085.

38. Lee, J.; Lee, Y.; Youn, J. K.; Bin Na, H.; Yu, T.; Kim, H.; Lee, S. M.; Koo, Y. M.; Kwak, J. H.; Park, H. G.; Chang, H. N.; Hwang, M.; Park, J. G.; Kim, J.; Hyeon, T., Simple synthesis of functionalized superparamagnetic magnetite/silica core/shell nanoparticles and their application as magnetically separable high-performance biocatalysts. *Small* **2008,** *4* (1), 143-152.

39. Lin, C.-A. J.; Sperling, R. A.; Li, J. K.; Yang, T.-Y.; Li, P.-Y.; Zanella, M.; Chang, W. H.; Parak, W. J., Design of an Amphiphilic Polymer for Nanoparticle Coating and Functionalization. *Small* **2008,** *4* (3), 334-341.

40. Soenen, S. J.; Parak, W. J.; Rejman, J.; Manshian, B., (Intra)Cellular Stability of Inorganic Nanoparticles: Effects on Cytotoxicity, Particle Functionality, and Biomedical Applications. *Chemical Reviews* **2015**.

41. Moros, M.; Pelaz, B.; Lopez-Larrubia, P.; Garcia-Martin, M. L.; Grazu, V.; de la Fuente, J. M., Engineering biofunctional magnetic nanoparticles for biotechnological applications. *Nanoscale* **2010,** *2* (9), 1746-1755.

42. Dias, J. T.; Moros, M.; del Pino, P.; Rivera, S.; Grazú, V.; de la Fuente, J. M., DNA as a Molecular Local Thermal Probe for the Analysis of Magnetic Hyperthermia. *Angewandte Chemie* **2013,** *52* (44), 11526–11529.

43. Sperling, R. A.; Pellegrino, T.; Li, J. K.; Chang, W. H.; Parak, W. J., Electrophoretic Separation of Nanoparticles with a Discrete Number of Functional Groups. *Advanced Functional Materials* **2006,** *16* (7), 943-948.

44. Ashraf, S.; Carrillo-Carrion, C.; Zhang, Q.; Soliman, M. G.; Hartmann, R.; Pelaz, B.; del Pino, P.; Parak, W. J., Fluorescence-based ion-sensing with colloidal particles. *Curr Opin Pharmacol* **2014,** *18*, 98-103.

45. Del Pino, P.; Pelaz, B.; Zhang, Q.; Maffre, P.; Nienhaus, G. U.; Parak, W. J., Protein corona formation around nanoparticles - from the past to the future. *Mater Horizons* **2014,** *1* (3), 301-313.

46. Pelaz, B.; del Pino, P.; Maffre, P.; Hartmann, R.; Gallego, M.; Rivera-Fernández, S.; de la Fuente, J. M.; Nienhaus, G. U.; Parak, W. J., Surface Functionalization of Nanoparticles with Polyethylene Glycol: Effects on Protein Adsorption and Cellular Uptake. *ACS Nano* **2015,** *9* (7), 6996-7008.

47. Lee, J. H.; Jang, J. T.; Choi, J. S.; Moon, S. H.; Noh, S. H.; Kim, J. W.; Kim, J. G.; Kim, I. S.; Park, K. I.; Cheon, J., Exchange-coupled magnetic nanoparticles for efficient heat induction. *Nature Nanotechnology* **2011,** *6* (7), 418-422.

48. Kita, E.; Oda, T.; Kayano, T.; Sato, S.; Minagawa, M.; Yanagihara, H.; Kishimoto, M.; Mitsumata, C.; Hashimoto, S.; Yamada, K.; Ohkohchi, N., Ferromagnetic nanoparticles for magnetic hyperthermia and thermoablation therapy. *J Phys D Appl Phys* **2010,** *43* (47).

49. Mazzucchelli, S.; Colombo, M.; De Palma, C.; Salvade, A.; Verderio, P.; Coghi, M. D.; Clementi, E.; Tortora, P.; Corsi, F.; Prosperi, D., Single-Domain Protein A-Engineered Magnetic Nanoparticles: Toward a Universal Strategy to Site-Specific Labeling of Antibodies for Targeted Detection of Tumor Cells. *Acs Nano* **2010,** *4* (10), 5693-5702.

50. Obata, K.; Tajima, H.; Yohda, M.; Matsunaga, T., Recent developments in laboratory automation using magnetic particles for genome analysis. *Pharmacogenomics* **2002,** *3* (5), 697-708.

51. Chen, R.; Romero, G.; Christiansen, M. G.; Mohr, A.; Anikeeva, P., Wireless magnetothermal deep brain stimulation. *Science* **2015,** *347* (6229), 1477-1480.

52. Huang, X. H.; Jain, P. K.; El-Sayed, I. H.; El-Sayed, M. A., Plasmonic photothermal therapy (PPTT) using gold nanoparticles. *Laser Med Sci* **2008,** *23* (3), 217-228.

53. Muñoz Javier, A.; del Pino, P.; Bedard, M. F.; Skirtach, A. G.; Ho, D.; Sukhorukov, G. B.; Plank, C.; Parak, W. J., Photoactivated Release of Cargo from the Cavity of Polyelectrolyte Capsules to the Cytosol of Cells. *Langmuir* **2008,** *24*, 12517-12520.

54. Bao, C.; Beziere, N.; del Pino, P.; Pelaz, B.; Estrada, G.; Tian, F.; Ntziachristos, V.; de la Fuente, J. M.; Cui, D., Gold Nanoprisms as Optoacoustic Signal Nanoamplifiers for in Vivo Bioimaging of Gastrointestinal Cancers. *Small* **2013,** *9* (1), 68-74.

55. Wang, Z. X.; Levy, R.; Fernig, D. G.; Brust, M., Kinase-catalyzed modification of gold nanoparticles: A new approach to colorimetric kinase activity screening. *Journal of the American Chemical Society* **2006,** *128* (7), 2214-2215.

56. Haiss, W.; Thanh, N. T. K.; Aveyard, J.; Fernig, D. G., Determination of size and concentration of gold nanoparticles from UV-Vis spectra. *Anal Chem* **2007,** *79* (11), 4215-4221.

57. Maier, S. A.; Atwater, H. A., Plasmonics: Localization and guiding of electromagnetic energy in metal/dielectric structures. *Journal of Applied Physics* **2005,** *98* (1).

58. Linic, S.; Christopher, P.; Xin, H. L.; Marimuthu, A., Catalytic and Photocatalytic Transformations on Metal Nanoparticles with Targeted Geometric and Plasmonic Properties. *Accounts of Chemical Research* **2013,** *46* (8), 1890-1899.

59. Idegami, K.; Chikae, M.; Kerman, K.; Nagatani, N.; Yuhi, T.; Endo, T.; Tamiya, D., Gold nanoparticle-based redox signal enhancement for sensitive detection of human chorionic gonadotropin hormone. *Electroanal* **2008,** *20* (1), 14-21.

60. Kim, J. S.; Kuk, E.; Yu, K. N.; Kim, J. H.; Park, S. J.; Lee, H. J.; Kim, S. H.; Park, Y. K.; Park, Y. H.; Hwang, C. Y.; Kim, Y. K.; Lee, Y. S.; Jeong, D. H.; Cho, M. H., Antimicrobial effects of silver nanoparticles. *Nanomedicine-Nanotechnology Biology and Medicine* **2007,** *3* (1), 95-101.

61. Sau, T. K.; Murphy, C. J., Room temperature, high-yield synthesis of multiple shapes of gold nanoparticles in aqueous solution. *Journal of the American Chemical Society* **2004,** *126* (28), 8648-8649.

62. Gou, L. F.; Murphy, C. J., Solution-phase synthesis of Cu_2O nanocubes. *Nano Letters* **2003,** *3* (2), 231-234.

63. Zhang, Q.; Li, N.; Goebl, J.; Lu, Z.; Yin, Y., A Systematic Study of the Synthesis of Silver Nanoplates: Is Citrate a "Magic" Reagent? *Journal of the American Chemical Society* **2011,** *133* (46), 18931-18939.

64. Nikoobakht, B.; El-Sayed, M. A., Preparation and Growth Mechanism of Gold Nanorods (NRs) Using Seed-Mediated Growth Method. *Chem. Mater.* **2003,** *15* (10), 1957-1962.

65. Lee, Y. J.; Schade, N. B.; Sun, L.; Fan, J. A.; Bae, D. R.; Mariscal, M. M.; Lee, G.; Capasso, F.; Sacanna, S.; Manoharan, V. N.; Yi, G. R., Ultrasmooth, Highly Spherical Monocrystalline Gold Particles for Precision Plasmonics. *Acs Nano* **2013,** *7* (12), 11064-11070.

66. Nehl, C. L.; Liao, H. W.; Hafner, J. H., Optical properties of star-shaped gold nanoparticles. *Nano Letters* **2006,** *6* (4), 683-688.

67. Skrabalak, S. E.; Chen, J. Y.; Sun, Y. G.; Lu, X. M.; Au, L.; Cobley, C. M.; Xia, Y. N., Gold Nanocages: Synthesis, Properties, and Applications. *Accounts of Chemical Research* **2008,** *41* (12), 1587-1595.

68. Zhu, T.; Krasimir Vasilev; Maximilian Kreiter; Silvia Mittler; Knoll, W., Surface Modification of Citrate-Reduced Colloidal Gold Nanoparticles with 2-Mercaptosuccinic Acid. *Langmuir* **2003,** *2003* (19), 9518-9525.

69. Soliman MG; Pelaz B; Parak WJ; dP, P., Phase transfer and polymer coating methods toward improving the stability of metallic nanoparticles for biological applications. *Chem Mater* **2015,** *27*, 990-997.

70. Levy, R.; Thanh, N. T. K.; Doty, R. C.; Hussain, I.; Nichols, R. J.; Schiffrin, D. J.; Brust, M.; Fernig, D. G., Rational and Combinatorial Design of Peptide Capping Ligands for Gold Nanoparticles. *J. Am. Chem. Soc.* **2004,** *126* (32), 10076-10084.

71. Peng, S.; McMahon, J. M.; Schatz, G. C.; Gray, S. K.; Sun, Y. G., Reversing the size-dependence of surface plasmon resonances. *Proceedings of the National Academy of Sciences of the United States of America* **2010,** *107* (33), 14530-14534.

72. Uk Son, S.; Kyu Park, I.; Park, J.; Hyeon, T., Synthesis of Cu_2O coated Cu nanoparticles and their successful applications to Ullmann-type amination coupling reactions of aryl chlorides. *Chem Commun* **2004,** (7), 778-779.

73. Yin, M.; Wu, C.-K.; Lou, Y.; Burda, C.; Koberstein, J. T.; Zhu, Y.; O'Brien, S., Copper Oxide Nanocrystals. *Journal Of The American Chemical Society* **2005,** *127* (26), 9506-9511.

74. Shi, M.; Kwon, H. S.; Peng, Z. M.; Elder, A.; Yang, H., Effects of Surface Chemistry on the Generation of Reactive Oxygen Species by Copper Nanoparticles. *Acs Nano* **2012,** *6* (3), 2157-2164.

75. Govorov, A. O.; Zhang, W.; Skeini, T.; Richardson, H.; Lee, J.; Kotov, N. A., Gold nanoparticle ensembles as heaters and actuators: melting and collective plasmon resonances. *Nanoscale Research Letters* **2006,** *1* (1), 84-90.

76. Krpetic, Z.; Nativo, P.; See, V.; Prior, I. A.; Brust, M.; Volk, M., Inflicting Controlled Nonthermal Damage to Subcellular Structures by Laser-Activated Gold Nanoparticles. *Nano Letters* **2010,** *10* (11), 4549-4554.

77. Qin, Z.; Bischof, J. C., Thermophysical and biological responses of gold nanoparticle laser heating. *Chem. Soc. Rev.* **2011**.

78. Huang, X.; El-Sayed, I. H.; Qian, W.; El-Sayed, M. A., Cancer Cell Imaging and Photothermal Therapy in the Near-Infrared Region by Using Gold Nanorods. *Journal of the American Chemical Society* **2006,** *128*, 2115-2120.

79. Mitsudome, T.; Noujima, A.; Mizugaki, T.; Jitsukawa, K.; Kaneda, K., Supported gold nanoparticle catalyst for the selective oxidation of silanes to silanols in water. *Chem Commun* **2009,** (35), 5302-5304.

80. Mitsudome, T.; Noujima, A.; Mikami, Y.; Mizugaki, T.; Jitsukawa, K.; Kaneda, K., Supported Gold and Silver Nanoparticles for Catalytic Deoxygenation of Epoxides into Alkenes. *Angewandte Chemie-International Edition* **2010,** *49* (32), 5545-5548.

81. Ahamed, M.; AlSalhi, M. S.; Siddiqui, M. K. J., Silver nanoparticle applications and human health. *Clin Chim Acta* **2010,** *411* (23-24), 1841-1848.

82. Gupta, S.; Tripathi, M., A review of TiO_2 nanoparticles. *Chinese Sci Bull* **2011,** *56* (16), 1639-1657.

83. Carp, O.; Huisman, C. L.; Reller, A., Photoinduced reactivity of titanium dioxide. *Prog Solid State Ch* **2004,** *32* (1-2), 33-177.

84. Lee, J.; Mahendra, S.; Alvarez, P. J. J., Nanomaterials in the Construction Industry: A Review of Their Applications and Environmental Health and Safety Considerations. *Acs Nano* **2010,** *4* (7), 3580-3590.

85. Anselmann, R.,Nanoparticles and nanolayers in commercial applications. *J Nanopart Res* **2001,** *3* (4), 329-336.

86. Buxbaum, G., *Industrial inorganic pigments*. John Wiley & Sons: 2008.

87. Jacobs, J. F.; Van de Poel, I.; Osseweijer, P., Sunscreens with titanium dioxide (TiO_2) nano-particles: A societal experiment. *Nanoethics* **2010,** *4* (2), 103-113.

88. Pelaez, M.; Nolan, N. T.; Pillai, S. C.; Seery, M. K.; Falaras, P.; Kontos, A. G.; Dunlop, P. S. M.; Hamilton, J. W. J.; Byrne, J. A.; O'Shea, K.; Entezari, M. H.; Dionysiou, D. D., A review on the visible light active titanium dioxide photocatalysts for environmental applications. *Appl Catal B-Environ* **2012,** *125*, 331-349.

89. Han, F.; Kambala, V. S. R.; Srinivasan, M.; Rajarathnam, D.; Naidu, R., Tailored titanium dioxide photocatalysts for the degradation of organic dyes in wastewater treatment: A review. *Appl Catal a-Gen* **2009,** *359* (1-2), 25-40.

90. Li, H. B.; Li, J.; Xu, Q.; Hu, X. Y., Poly(3-hexylthiophene)/TiO_2 Nanoparticle-Functionalized Electrodes for Visible Light and Low Potential Photoelectrochemical Sensing of Organophosphorus Pesticide Chlopyrifos. *Anal Chem* **2011,** *83* (24), 9681-9686.

91. Oskam, G.; Nellore, A.; Penn, R. L.; Searson, P. C., The growth kinetics of TiO_2 nanoparticles from titanium(IV) alkoxide at high water/titanium ratio. *J Phys Chem B* **2003,** *107* (8), 1734-1738.

92. Chemseddine, A.; Moritz, T., Nanostructuring titania: Control over nanocrystal structure, size, shape, and organization. *Eur J Inorg Chem* **1999,** (2), 235-245.

93. Gordon, T. R.; Cargnello, M.; Paik, T.; Mangolini, F.; Weber, R. T.; Fornasiero, P.; Murray, C. B., Nonaqueous Synthesis of TiO_2 Nanocrystals Using TiF4 to Engineer Morphology, Oxygen Vacancy Concentration, and Photocatalytic Activity. *Journal of the American Chemical Society* **2012,** *134* (15), 6751-6761.

94. Seo, J. W.; Jun, Y. W.; Ko, S. J.; Cheon, J., In situ one-pot synthesis of 1-dimensional transition metal oxide nanocrystals. *J Phys Chem B* **2005,** *109* (12), 5389-5391.

95. Wen, B. M.; Liu, C. Y.; Liu, Y., Bamboo-shaped ag-doped TiO_2 nanowires with heterojunctions. *Inorganic Chemistry* **2005,** *44* (19), 6503-6505.

96. Morales, A. G. R.; Guzman, M. O. C.; Arteaga, C. C., A brief review on fabrication and applications of auto-organized TiO_2 nanotube arrays. *Corros Rev* **2011,** *29* (1-2), 105-121.

97. Cozzoli, P. D.; Kornowski, A.; Weller, H., Low-temperature synthesis of soluble and processable organic-capped anatase TiO_2 nanorods. *Journal of the American Chemical Society* **2003,** *125* (47), 14539-14548.

98. Cotto-Maldonado, M. d. C.; Campo, T.; Elizalde, E.; Gómez-Martínez, A.; Morant, C.; Márquez, F., Photocatalytic degradation of Rhodamine-B under 2 UV-visible light irradiation using different 3 nanostructured catalysts 4. **2013**.

99. Liu, B.; Chen, H. M.; Liu, C.; Andrews, S. C.; Hahn, C.; Yang, P. D., Large-Scale Synthesis of Transition-Metal-Doped TiO_2 Nanowires with Controllable Overpotential. *Journal of the American Chemical Society* **2013,** *135* (27), 9995-9998.

100. Chen, X. B.; Burda, C., The electronic origin of the visible-light absorption properties of C-, N- and S-doped TiO_2 nanomaterials. *Journal of the American Chemical Society* **2008,** *130* (15), 5018-+.

101. Lin, J. T.; Chen, P. C.; Yen, Y. S.; Hsu, Y. C.; Chou, H. H.; Yeh, M. C. P., Organic Dyes Containing Furan Moiety for High-Performance Dye-Sensitized Solar Cells. *Org Lett* **2009,** *11* (1), 97-100.

102. Cassee, F. R., Reflections on the scope and the future of Particle and Fibre Toxicology. *Particle and Fibre Toxicology* **2011,** *8*.

103. Shi, H. B.; Magaye, R.; Castranova, V.; Zhao, J. S., Titanium dioxide nanoparticles: a review of current toxicological data. *Particle and Fibre Toxicology* **2013,** *10*.

104. Trouiller, B.; Reliene, R.; Westbrook, A.; Solaimani, P.; Schiestl, R. H., Titanium Dioxide Nanoparticles Induce DNA Damage and Genetic Instability In vivo in Mice. *Cancer Res* **2009,** *69* (22), 8784-8789.

Appendix

Wissenschaftlicher Werdegang

Persönliche Angaben

Vorname: Qian Familienname: Zhang

Geburtsdatum：30. Jan 1987 Geburtsort: Shan Dong / China

Staatsangehörigkeit： Chinese

Ausbildung

09/2011-09/2015 **Doktorarbeit, Physik. Philipps-Universität Marburg**

AG. Biophotonik (Prof. W. J. Parak), Fachbereich Physik.

Thema: Polymer-Coated Inorganic Nanoparticles: Nanotools for Life Science Applications

Betreuer: Prof. Dr.Wolfgang*J*.Parak

09/2008 - 07/2011 ***M.Sc.*** **Biophysik. Sichuan Agricultural University**

Fachbereich Life Science

Thema: Synthesis of AuNPs and AuNCs, and studying their enzymatic properties for modification of Glucose oxidase

09/2004 - 07/2008 ***B.Sc.*** **Biology. Qingdao Agricultural University**

Fachbereich Life Science

Wissenschaftliche Veröffentlichungen

[A1] P. del Pino, B. Pelaz, **Q. Zhang**, P. Maffre, G. U. Nienhaus, W. J. Parak. Protein corona formation around nanoparticles– from the past to the future. *Materials Horizons* **2014**, 1,301–313.

[A2] M. Nazarenus, **Q. Zhang**, M. G. Soliman , P. del Pino, B. Pelaz, S. Carregal-Romero, J. Rejman, B. Rothen-Rutishauser, M. J. D. Clift, R. Zellner, G. U Nienhaus, J. B. Delehanty, I. L. Medintz, W. J. Parak. In vitro interaction of colloidal nanoparticles with mammalian

cells: What have we learned thus far? *Beilstein Journal of Nanotechnology* **2014**,5, 1477–1490.

[A3] S. Ashraf, C. Carrillo-Carrion, **Q. Zhang**, M. G. Soliman, R. Hartmann, B. Pelaz, P. del Pino, W. J. Parak. Fluorescence-based ion-sensing with colloidal particles. *Current Opinion in Pharmacology* **2014**, 18:98–103.

[A4] N. Feliu, B. Pelaz, **Q. Zhang**, P. del Pino, A. Nyström, W. J. Parak. Nanoparticle dosage-a nontrivial task of utmost importance for quantitative nanotoxicology. *WIREs Nanomedicine&Nanobiotechnology*. In the revision.

[A5] S. Ashraf, B. Pelaz, P. del Pino, A. Escudero, W. J. Parak, **Q. Zhang**, C. Carillo. Gold-based nanomaterials for applications in nanomedicine. *Topics in Current Chemistry*. Accept.

[A6] **Q. Zhang***, I. Castellanos-Rubio*, R. Munshi*, I. Orue, B. Pelaz, W. J. Parak, P. del Pino, A. Pralle. Model Driven Optimization of Magnetic Anisotropy of Exchange-coupled Core-Shell Ferrite Nanoparticles for Maximal Hysteretic Loss. *Chemistry of materials.* In revision.

[A7] P. del Pino, B. Pelaz, F. Yang, **Q. Zhang**, K. Kantner, N. M. d. Baroja, M. Gallego, M. Möller, B. Manshian, S. Soenen, N. Hampp, W. J. Parak. Physicochemical Properties of PEGylated Gold Nanoparticles: Impact on Cell Fitness. *AngewandteChemie International Edition.* In the revision.

[A8] G. Tan, K. Kantner, **Q. Zhang**, M. G. Soliman, P. del Pino, W. J. Parak, M. A. Onur, D. Valdeperez, J. Rejman, B. Pelaz. Conjugation of polymer-coated gold nanoparticles with antibodies - synthesis and characterization. *Nanomaterials*. Accepted.

[A9] O.T. Marisca, K. Kanter, C. Pfeiffer, **Q. Zhang**, B. Pelaz, N. Leopold, W. J. Parak, J. Rejman. Can the coating make a difference: comparison of the in vitro performance of collagen- and synthetic polymer coated gold nanoparticles. *Nanomaterials*. Accepted.

[A10] C. Shi, F. Yang, **Q. Zhang**, S. Neitemeier, C. Thum, N. Hampp, C. Culmsee, W. J. Parak and M. Schneider. Increased drug efficiency of multifunctional magnetic particles in rotating magnetic field (RMF). In preparation.

[A11] F. Yang, B. Pelaz, X. Yu, R. Riedel, **Q. Zhang**, B. Zhang, P. del Pino, W. J. Parak, N. Hampp. Hybrid bioconjugation based on assembly of functional gold nanoparticles on mutant purple membrane via Ni-NTA and histidine interaction. In preparation.

Book chapter

[A12] B. Pelaz, Q. Zhang, P. del Pino, W. J. Parak. “Metal and Metal Oxide Core-shell Nanocomposites”. 1.09.04. Inorganic core-shell Nanoparticles.

*Gleichberechtigte Erstautorenschaft

Materials Horizons

REVIEW

View Article Online
View Journal | View Issue

Cite this: *Mater. Horiz.*, 2014, **1**, 301

Protein corona formation around nanoparticles – from the past to the future†

Pablo del Pino,[ad] Beatriz Pelaz,[a] Qian Zhang,[a] Pauline Maffre,[b] G. Ulrich Nienhaus[bc] and Wolfgang J. Parak*[ad]

The protein adsorption layer (*a.k.a.* the "protein corona") that forms on the surface of colloidal nanoparticles plays an important role in their interaction with living matter. Thus, characterization of the protein corona is of utmost importance for understanding how exposure to nanoparticles affects the biological responses of cells and organisms. Although a lot of experimental studies have been reported in this direction, a comprehensive picture is still missing, in particular due to the multitude of different scenarios under which experiments have been performed. In this review an analysis of existing experimental data about the protein corona, and an outline for required future work will be given. In particular we review how existing simple analytical models such as the adopted Hill model may help to extract quantitative data from such experiments such as equilibrium dissociation and kinetic coefficients. Careful quantitative assessment of equilibrium and kinetic properties would allow for a comparison of protein binding data from the vast array of engineered nanoparticles, so that basic principles could be revealed. This review outlines that the field is in dire need of more quantitative studies to further our understanding of protein corona formation and its biological consequences.

Received 21st September 2013
Accepted 14th October 2013

DOI: 10.1039/c3mh00106g

rsc.li/materials-horizons

Published on 14 October 2013. Downloaded on 29/07/2015 15:45:54.

[a]*Fachbereich Physik, Philipps Universität Marburg, Marburg, Germany. E-mail: wolfgang.parak@physik.uni-marburg.de*

[b]*Institute of Applied Physics, Karlsruhe Institute of Technology (KIT), Karlsruhe, Germany*

[c]*Department of Physics, University of Illinois at Urbana-Champaign, Urbana, Illinois, USA*

[d]*CIC Biomagune, San Sebastian, Spain*

† Electronic supplementary information (ESI) available. See DOI: 10.1039/c3mh00106g

Development of new materials demands consistent characterization techniques

The development of new materials always goes hand-in-hand with their characterization. A wide variety of analytical techniques exist that allow materials properties to be assessed in a quantitative fashion. Still, the results often depend on a range of experimental parameters. If these are being varied from experiment to

Pablo del Pino graduated in Physics from Universidad de Sevilla (Spain) in 2002 and obtained his PhD degree from Technische Universität München (Germany) in 2007. After post-doctoral positions at the Ludwig-Maximilians-Universität München (2007–2009, Munich, Germany), and at the Institute of Nanoscience of Aragon (INA) (2009–2013, Zaragoza, Spain), he has recently joined the Bio-functional Nanomaterials Unit at CIC biomaGUNE, San Sebastian, Spain.

Beatriz Pelaz graduated in Chemistry from Valladolid University (Spain) in 2005 and in Biochemistry from Zaragoza University (Spain) in 2011. She obtained her PhD from Zaragoza University (Spain) in 2012, working in the Institute of Nanoscience of Aragon. Then, she joined the group of Prof. Dr Wolgang Parak as postdoctoral researcher. In 2013, she was awarded a postdoctoral fellowship from the Alexander von Humboldt Foundation.

[A1] 1

Published on 14 October 2013. Downloaded on 29/07/2015 15:45:54.

experiment, this may prevent meaningful comparisons of data. Only through reliable, consistent procedures, materials properties can be thoroughly assessed, and further improved in response to feedback from the application side. The interrelation between the physicochemical properties of new materials and their function can then be better understood. Characterization must always include realistic operation conditions. Colloidal nanoparticles (NPs) are an exciting class of "new" materials, which actually go back to ancient times (see the famous Lycurgus cup as an example).[1] However, due to impressive advances in the synthesis of colloids, new waves of applications from diverse disciplines ranging from the life sciences to the energy sciences have been initiated only in the last decades. In life science applications, the initial characterization would involve dispersions of the NPs in simple solvents such as water, or the original solution in which the NPs had been synthesized. However, aiming at *in vitro* and *in vivo* applications of the NPs, they also need to be studied in biological fluids, which typically contain high amounts of ions and proteins.[2] These solution conditions may lead to substantial changes of the physicochemical properties of the NPs as compared to model solutions such as water.

Colloidal nanoparticles have to be characterized in relevant media, especially with respect to colloidal stability and the effect of salt

Many of the original synthesis methods developed in the past yield NPs that are not colloidally stable under conditions present in biological fluids. In particular, inorganic NPs are naturally colloidally instable and prone to agglomeration because they attract each other by van der Waals forces. To stabilize the NPs in a solvent, *i.e.*, to disperse them requires a repulsive force between the NPs. Such an interaction can be introduced by providing the surface of the NPs with charge (which results in repulsion of equally charged NPs)

Qian Zhang obtained her B.S. in Biological Science in 2008 at the Qingdao Agricultural University (China). She received her M.S. in Biophysics in 2011 at Sichuan Agricultural University (China). Since 2011, she has been a PhD student in the group of Prof. Dr Wolfgang Parak at the Philipps-Universität Marburg (Germany).

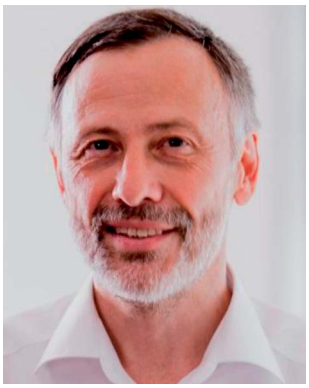

Gerd Ulrich Nienhaus studied Physics and received his PhD degree in Physical Chemistry from the University of Münster, Germany, in 1988. In 1990, he was awarded a Feodor Lynen Fellowship of the Alexander von Humboldt Foundation and joined the Department of Physics of the University of Illinois at Urbana-Champaign, USA, where he became an Assistant Professor (1991), Associate Professor (1996) and Adjunct Professor (1997–present). In 1996, he was appointed as a Chair Professor and Head of the Institute of Biophysics at the University of Ulm, Germany. In 2009, he moved to the Karlsruhe Institute of Technology (KIT), Germany, where he is currently Chair Professor and Head of the Institute of Applied Physics.

Pauline Maffre obtained her French-German double diploma with an engineer's degree in 2010 at the National Engineering School of Physics of Grenoble (Phelma, INPG), Grenoble, France, and a physics diploma in 2010 at the Karlsruhe Institute of Technology (KIT), Karlsruhe, Germany. Since 2011, she has been a doctoral student in biophysics in the Nienhaus group at the Institute of Applied Physics, KIT.

Wolfgang J. Parak obtained his PhD at the LMU München, Germany (1999) in the group of Prof. Dr Hermann Gaub. After a postdoctoral stay at the University of California, Berkeley, CA, USA in the group of Prof. Dr Paul Alivisatos he returned to Munich as an Assistant Professor in 2002. Since 2007, he has been a Full Professor at the Physics Department of the Philipps Universität Marburg, Marburg, Germany. In addition, he was appointed as Head of the Biofunctional Nanomaterials Unit at CIC biomaGUNE, San Sebastian, Spain in 2013. He is also Associate Editor of ACS Nano.

[A1] 2

This journal is © The Royal Society of Chemistry 2014

Published on 14 October 2013. Downloaded on 29/07/2015 15:45:54.

or molecular spacers (which results in steric repulsion as the shields of molecular spacers cannot fully interpenetrate).[3,4] Consider a classical example of NPs, CdSe/ZnS quantum dots (QDs), which are often stabilized by a shell of mercaptopropionic acid (MPA). Yet, the MPA-coated NPs will precipitate over the time course of days to weeks if the concentration of salt, a major constituent of most biological fluids, is increased up to the physiological range (150 mM NaCl). The effect is especially pronounced in the presence of divalent ions such as Ca^{2+}. Loss of colloidal stability results from the adsorption of counterions, which screen the negative surface charge provided by the $-COO^-$ groups of the MPA. Thus, the electrostatic repulsion between the NPs is drastically reduced.[5] In addition, if these NPs are dialyzed against pure water over extended periods of time (days or weeks), they will gradually lose their ligand shell and agglomerate. The bond between the thiol groups (–SH) of MPA and the CdSe/ZnS NPs is subject to photooxidation,[6] which ultimately leads to a loss of the MPA ligands. As long as the NPs are in a solution that contains MPA at a sufficiently high concentration, such as the one in which they have been synthesized or modified, there is a dynamic equilibrium of unbinding and rebinding of MPA. However, if the NPs are dialyzed against water, unbound MPA is irreversibly lost to the dialysis bath. Once a certain fraction of MPA ligands have been lost from the NP surface, charge repulsion is no longer sufficient to ensure colloidal stability. A similar process would occur, if these NPs were to be injected into the blood stream. Simply due to the dilution effect, any accidentally detached MPA ligand would eventually be lost. Thus, while MPA-stabilized QDs display sufficient colloidal stability in model solutions, they are typically not well dispersed in more realistic media for biological applications (though protein adsorption from the media might again assist in their dispersion, as will be discussed below). Nowadays, there are myriads of advanced surface coating methods which ensure colloidal stability of NPs even in the presence of high salt concentrations,[7–15] and the physicochemical principles of the effects of salt are well understood. Nevertheless, this example illustrates vividly that a meaningful analysis of the performance of NPs requires their characterization in environments that can be considered as realistic for a particular application.

Proteins adsorb onto nanoparticle surfaces

Next to salt, proteins are major constituents of biological fluids. It is a well-established fact that proteins generally adsorb onto the surface of materials. Adsorption of proteins from serum-containing media to surfaces can be easily visualized, for example, by atomic force microscopy (AFM). With the sharp tip of an AFM, proteins adsorbed to a plane surface can be scratched away, leading to a protein free hole.[16] Protein adsorption onto surfaces has been investigated vigorously for a long time, in particular, in the biomaterials community, with the aim to develop adsorption-resistant, inert surfaces.[17–20] Indeed, the adsorption of proteins onto biomaterials implanted inside the body, and subsequent protein–protein competition and displacement steps (known as the Vroman effect), is an issue of utmost importance.[21] Also in bioanalytics, adsorption of the proteins to be analysed onto the surfaces of tubing connected to the detection device is a well-known problem. Traditionally, this problem has been circumvented by flushing the device first with bovine serum albumin (BSA), which blocks the binding sites and thus reduces adsorption of the protein to be analysed. From the large body of work on protein adsorption, it is quite obvious that proteins will also adsorb onto the surfaces of colloidal particles.[22–27] For instance, we have observed that the differences in the cellular uptake of colloidal microparticles with different charge were partly suppressed by the presence of serum due to the adsorption of proteins onto the particle surface. At that time, we simply noted that "adsorption of constituents from the medium smears out charge differences".[28] Thus, while the effect was, in principle, known in the nanoparticle community, the role of protein adsorption in modulating the interaction between NPs and cells was not systematically investigated and remained a secondary issue until it was moved centre stage by the pioneering work by Dawson, Linse, and colleagues.[29] In this report, a detailed description on protein adsorption onto NPs, then termed "protein corona", was given, which stimulated a whole field of investigations. Nowadays, there are thousands of manuscripts dedicated to studies of the protein corona. In the meantime, it has been described that the formation of the protein corona depends on the size,[30–33] charge,[32,34,35] and colloidal stability of NPs,[36] as well as on the types of proteins,[37] ambient temperature,[38,39] incubation conditions and time,[37,40–42] *etc.* A lot of details are known for different NPs, however, our knowledge of the protein corona is still not comprehensive.[43] The complexity of this topic requires huge datasets (many different combinations of proteins and NPs) to gain sufficiently broad knowledge. Moreover, many studies in the literature were done on very unique systems, and the results can be hardly extrapolated to others, and are too different from each other to allow for comparison among different reports. Having so far reviewed the "past" of protein corona research, we shall discuss the "future" in the following. We will present our opinion about the still missing knowledge, and we will point to characterization techniques that could help advance the field and also discuss potential pitfalls on the way.

Protein adsorption to nanoparticles as described by classical ligand-binding models developed in biochemistry

From the physicochemical point of view, protein adsorption onto NPs resembles ligand binding, which has been discussed above. Proteins can adsorb and desorb to the surface of NPs, they can displace other proteins, or even parts of the original ligand shell around the NPs. We shall start with modelling a solution of inert NPs in contact with only one protein species P. Let us treat protein adsorption according to the following reaction equation,

$$\mathrm{NP} + n\mathrm{P} \leftrightarrow \mathrm{P}_n\mathrm{NP} \quad (1)$$

Thus, each NP has n binding sites for proteins, so that P_nNP is a NP fully saturated with n proteins. We emphasize that this

[A1] 3

Published on 14 October 2013. Downloaded on 29/07/2015 15:45:54.

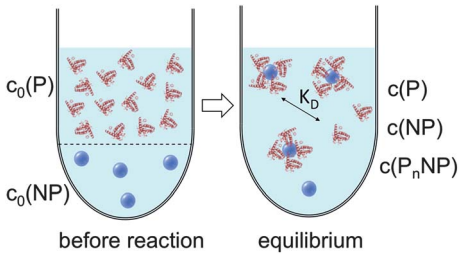

Fig. 1 Prior to the reaction, free proteins with concentration c_0(P), and free NPs with concentration c_0(NP) are separated. After the reaction has progressed to equilibrium, according to the law of mass action, eqn (1) and (2), a fraction of proteins is bound to the NP surface, and another fraction of proteins, with concentration c(P), remains free in solution. In this all-or-none model the NPs are either saturated with proteins, with an NP concentration $c(P_nNP)$, or they remain free of protein, with an NP concentration c(NP).

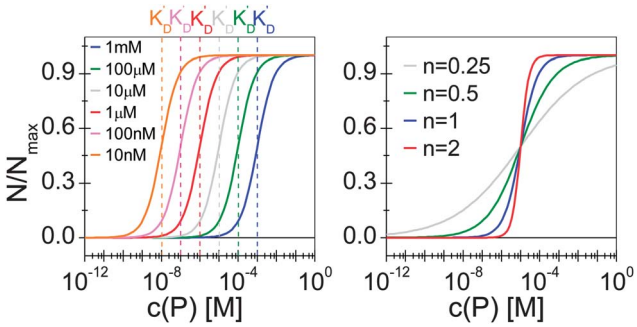

Fig. 2 Fraction of NPs saturated with proteins (N/N_{max}) as a function of the concentration of free protein c(P), calculated with eqn (4) under variation of the concentration at half saturation K'_D, and using the Hill coefficient n. At low protein concentrations, almost all NPs are without proteins ($N \to 0$ for $c(P) \ll K'_D$), whereas at high concentrations, all NPs are saturated with protein ($N \to N_{max}$ for $c(P) \gg K'_D$). (a) $n = 1$, $K'_D = 10$ nM, 100 nM, 1 μM, 10 μM, 100 μM, 1 mM. The concentration at half saturation K'_D describes the midpoint of the transition. (b) $K'_D = 10$ μM, $n = 0.25$, 0.5, 1, 2. The Hill coefficient n describes the steepness of the transition.

"all-or-none" ansatz, which is the basis of the original Hill model for modelling oxygenation of haemoglobin,[44] is overly simplistic because it implies that partially saturated species can be neglected. According to the law of mass action, the partitioning between the different species (free NPs ↔ protein-saturated NPs, free proteins ↔ proteins bound to NPs) in thermal equilibrium is described by the dissociation equilibrium coefficient, K_D, which is given by the ratio of the off- to on-rates for protein binding to the NPs.[45]

$$K_D = \frac{c(\mathrm{NP})c^n(\mathrm{P})}{c(\mathrm{P}_n\mathrm{NP})} = \frac{k_{off}}{k_{on}} \quad (2)$$

here, c(NP), c(P), and $c(P_nNP)$ represent the concentrations of free NPs, unbound proteins, and protein–NP complexes, respectively. In other words, if we mix two solutions, one containing NPs and the other proteins (with initial concentrations of NPs and proteins, c_0(NP) and c_0(P), respectively), and wait until equilibrium is reached, the concentration of free NPs and proteins will finally be c(NP) and c(P), respectively, and protein–NP complexes with concentration $c(P_nNP)$ will be present in the solution, *cf.* Fig. 1. Often, instead of the dissociation coefficient K_D, the concentration at which half of the NPs are saturated with proteins, K'_D, is used.

$$K'_D = {K_D}^{1/n} \quad (3)$$

The Hill model for a single protein species in equilibrium with a nanoparticle surface

According to eqn (1)–(3),[44] the ratio of the number of NPs saturated with proteins (N) to the total number of NPs (N_{max}) is then given by

$$\frac{N}{N_{max}} = \frac{1}{1 + \left(\frac{K'_D}{c(\mathrm{P})}\right)^n} \quad (4)$$

Thus the fraction of NPs which are saturated with proteins (N/N_{max}) depends on the concentration of free proteins c(P) and the concentration at which half of the NPs are saturated (K'_D), *cf.* Fig. 2. Even for haemoglobin, which has four oxygen binding sites, the parameter n, the so-called Hill coefficient, was always found to be lower than four, indicating that the restrictive "all-or-none" ansatz is inappropriate. The Hill coefficient is thus treated as an empirical parameter which describes the steepness of the transition from bare to protein-saturated NPs, *cf.* Fig. 2. The more free protein in solution is required to achieve the midpoint of the protein binding transition, the larger K'_D will be. Mathematical details are described in the ESI.† It is clear that an all-or-none scenario, in which all proteins bind simultaneously to the NPs, is entirely unrealistic. Eqn (4) nevertheless provides a useful model for protein binding to NPs, if the involved parameters are suitably reinterpreted.

Eqn (4) and, thus, the curves shown in Fig. 2 can also be reinterpreted as follows (see the ESI† for more details): in equilibrium, the NPs are loaded on average with N proteins, and N_{max} is the maximum number of proteins which each NP can bind to, *cf.* Fig. 3. In this interpretation, the Hill coefficient describes how proteins bound on a NP influence the adsorption of further proteins from the solution onto the same NP. A Hill coefficient $n > 1$ indicates cooperative binding, *i.e.*, proteins already bound to a NP facilitate the binding of further proteins to the remaining vacant sites. By contrast, $n < 1$ refers to anti-cooperative binding, so that proteins already adsorbed onto the NP lower the tendency for binding additional ones. This is a very realistic scenario because, upon binding, proteins interact with the NP surface and the proteins already bound to that surface.

It is trivial that the concentration of unbound protein remaining free in solution, c(P), is smaller than the initial concentration of added protein c_0(P). Both are related *via* eqn (5), which allows for calculation of c(P) from knowing c_0(P) and the parameters of the saturation curve. The total protein concentration c_0(P) comprises the free proteins c(P), as well as the proteins which are bound to NPs Nc_0(NP), as given by eqn (4):

[A1] 4

This journal is © The Royal Society of Chemistry 2014

Published on 14 October 2013. Downloaded on 29/07/2015 15:45:54.

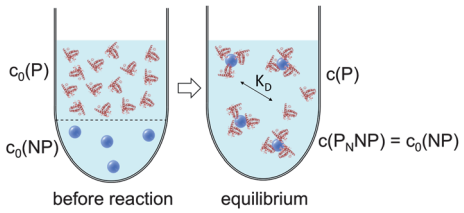

Fig. 3 Before the reaction, free proteins with concentration $c_0(\mathrm{P})$, and free NPs with concentration $c_0(\mathrm{NP})$ are separated. After the reaction has progressed to equilibrium, some proteins are bound to the NP surface (which is in general not yet saturated by proteins), and only a fraction of proteins, with concentration $c(\mathrm{P})$, remain free in solution. Technically all NPs are assumed to have the same number $N \leq N_{\max}$ of proteins bound per NP. However, please note that N in fact represents the average number of proteins per NP. This is a reinterpretation of the same situation as depicted in Fig. 1 (same values for $c_0(\mathrm{P})$, $c_0(\mathrm{NP})$, $c(\mathrm{P})$). As a sufficiently high protein concentration is assumed ($c_0(\mathrm{P}) \gg c_0(\mathrm{NP})$), as otherwise there would be no protein corona, there are no bare NPs without adsorbed proteins.

$$c_0(\mathrm{P}) = c(\mathrm{P}) + \frac{N_{\max}}{1 + \left(\frac{K'_\mathrm{D}}{c(\mathrm{P})}\right)^n} c_0(\mathrm{NP}) \tag{5}$$

Using eqn (5), the fraction of proteins bound to NPs, $\left(\frac{c_0(\mathrm{P}) - c(\mathrm{P})}{c_0(\mathrm{P})}\right)$, can be calculated depending on the initial parameters $c_0(\mathrm{P})$, $c_0(\mathrm{NP})$, *cf.* Fig. 4. Here, $c(\mathrm{P})$ needs to be derived implicitly from eqn (5). For all steps of the calculation, we refer to the ESI.† If $c(\mathrm{P})$ is much greater than K'_D, each NP is saturated with $N_{\max}$ proteins, and the fraction becomes

$$\frac{c_0(\mathrm{P}) - c(\mathrm{P})}{c_0(\mathrm{P})} \rightarrow \frac{N_{\max} c_0(\mathrm{NP})}{c_0(\mathrm{P})} \text{ for } c(\mathrm{P}) \gg K'_\mathrm{D}. \tag{6}$$

In this case, even if more and more protein is added, additional protein cannot be bound to the NP surface, as all NPs are already saturated with $N_{\max}$ proteins. Some examples are displayed in Fig. 4.

With the examples presented in Fig. 4 several effects can be visualized. Fig. 4a illustrates how the fraction of proteins bound depends on the value of K'_D in a case without cooperativity, *i.e.*, where proteins do not influence each other upon binding ($n = 1$). At a total protein concentration $c_0(\mathrm{P})$ much lower than K'_D, most of the binding sites are vacant and each protein has a certain probability to bind to the NPs that only depends on the ratio of the off- to the on-rate coefficients, *i.e.*, K'_D. At low protein concentration, the fraction of proteins bound directly reflects this probability (it corresponds to the range where the fraction is constant). A smaller K'_D corresponds to a higher probability for a protein to stay on the NP surface, *i.e.*, a higher fraction of proteins is bound. If the total protein concentration reaches values around K'_D, significant amounts of proteins are already bound and the probability for one protein to bind to the surface no longer depends on K'_D only, but also on the probability for a binding site to be free. Thus, relatively fewer proteins bind to the NPs and the fraction of bound proteins decreases. Once the NPs are saturated with proteins ($c_0(\mathrm{P}) \gg K'_\mathrm{D}$), no more proteins can bind anymore and the fraction of proteins bound decreases proportionally to the total protein concentration. Fig. 4b illustrates how the fraction of bound proteins depends on the value of $c_0(\mathrm{NP})$ for a case without cooperativity ($n = 1$). At total protein concentrations much smaller than K'_D, the fraction of bound proteins $c_{\mathrm{NP}}(\mathrm{P})$ is again directly proportional to the probability for each protein to bind to the surface of one NP. As K'_D is the same for all three curves, this probability is the same. However, for a higher NP concentration, the absolute number of bound proteins is higher and thus the fraction of bound proteins is higher for high $c_0(\mathrm{NP})$. Thus, under these conditions ($c_0(\mathrm{NP}) \gg c_0(\mathrm{P})$, $K'_\mathrm{D} \gg c_0(\mathrm{P})$, $n \leq 1$) proteins can be sufficiently removed from solution, which might be interesting for purification applications. The fraction of bound proteins starts to decrease when the total protein concentration reaches the range of K'_D. Note that the onset of the decrease shifts to the right in Fig. 4b for high NP concentration because the maximum number of binding sites is higher. Thus, for a fixed total protein concentration, the probability of a binding site to be vacant is also higher. Fig. 4c illustrates the effect of the Hill coefficient n on the fraction of proteins bound. At a total protein concentration smaller than K'_D, cooperativity leads to fewer proteins bound than in a reaction without cooperativity. Indeed, in a reaction with cooperativity, it is easier for several proteins to bind jointly than for each protein to bind individually. At low protein concentrations, the probability of several proteins binding to a single NP is low and, consequently, fewer proteins are bound to the NPs compared to that in the non-cooperative case. This probability increases linearly

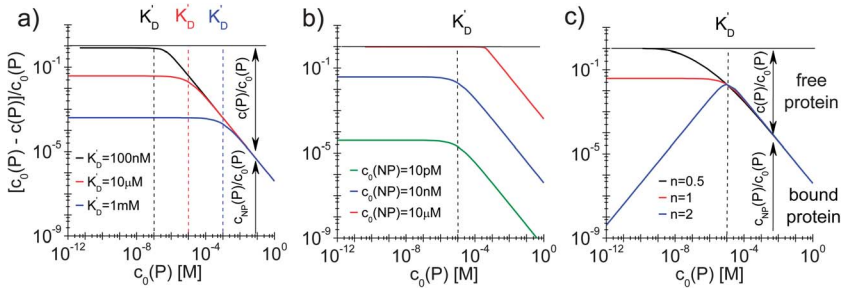

Fig. 4 Fraction of proteins bound to the NPs $(c_0(\mathrm{P}) - c(\mathrm{P}))/(c_0(\mathrm{P}) = c_{\mathrm{NP}}(\mathrm{P})/c_0(\mathrm{P}))$ depending on the total protein concentration $c_0(\mathrm{P})$, according to eqn (5), using $N_{\max} = 40$ as the maximum number of proteins which each NP can bind to. The total concentration of NPs, $c_0(\mathrm{NP})$, the protein concentration at half saturation, K'_D, and the Hill coefficient n are varied. (a) $c_0(\mathrm{NP}) = 10$ nM, $n = 1$, $K'_\mathrm{D} = 100$ nM, 10 μM, 1 mM. (b) $c_0(\mathrm{NP}) = 10$ pM, 10 nM, 10 μM, $n = 1$, $K'_\mathrm{D} = 10$ μM. (c) $c_0(\mathrm{NP}) = 10$ nM, $n = 0.5$, 1, 2, $K'_\mathrm{D} = 10$ μM. The dashed lines indicate the respective protein concentrations at half saturation, K'_D. The arrows in the graphs indicate how the proteins are divided into a fraction of proteins bound to NPs ($c_{\mathrm{NP}}(\mathrm{P})/c_0(\mathrm{P})$) and a fraction of free proteins ($c(\mathrm{P})/c_0(\mathrm{P})$).

[A1] 5

Published on 14 October 2013. Downloaded on 29/07/2015 15:45:54.

(the blue line has a slope of 1 in Fig. 4c) with the free protein concentration. Thus, at a concentration of free proteins smaller than K'_D, cooperativity leads to less overall protein binding onto the NPs. By contrast, if the reaction is anti-cooperative, the probability that a protein binds to a NP is higher if there are no other proteins already bound, *i.e.*, at lower protein concentration. Thus, anti-cooperativity enhances protein binding at low free protein concentration, compared to the non-cooperative case. Naturally, once the NP surface is saturated with proteins ($c_0(P) \gg K'_D$), there is no longer any effect of n, as n is associated only with the binding process and thus has no relevance when all the binding sites are already occupied. Such theoretical considerations/simulations may be useful to choose relevant protein and NP concentration ranges by designing experiments.

The Hill model for two protein species in equilibrium with the nanoparticle surface

We can extend this description to the case in which not only one, but two protein species $P_{(1)}$ and $P_{(2)}$ can bind to the surface of NPs. In analogy to eqn (1) and (2), yet for two protein species, the following equations are considered:

$$\mathrm{NP} + n_{(1)}\mathrm{P}_{(1)} \leftrightarrow \mathrm{P}_{n(1)}\mathrm{NP}\ K_{\mathrm{D}(1)} = \frac{c(\mathrm{NP})c^{n_{(1)}}(\mathrm{P}_{(1)})}{c(\mathrm{P}_{n(1)}\mathrm{NP})};\ K'_{\mathrm{D}(1)} = (K_{\mathrm{D}(1)})^{1/n_{(1)}}$$

$$\mathrm{NP} + n_{(2)}\mathrm{P}_{(2)} \leftrightarrow \mathrm{P}_{n(2)}\mathrm{NP}\ K_{\mathrm{D}(2)} = \frac{c(\mathrm{NP})c^{n_{(2)}}(\mathrm{P}_{(2)})}{c(\mathrm{P}_{n(2)}\mathrm{NP})};\ K'_{\mathrm{D}(2)} = (K_{\mathrm{D}(2)})^{1/n_{(2)}} \quad (7)$$

Let us discuss the case that NPs are saturated with proteins of species $P_{(1)}$, which are then brought into contact with free protein of species $P_{(2)}$. Subsequently, a dynamic exchange between proteins of both species can occur:

$$\mathrm{P}_{n(1)}\mathrm{NP} + n_{(2)}\mathrm{P}_{(2)} \leftrightarrow \mathrm{P}_{n(2)}\mathrm{NP} + n_{(1)}\mathrm{P}_{(1)}$$

$$K_{\mathrm{D}} = \frac{c^{n_{(2)}}(\mathrm{P}_{(2)})c(\mathrm{P}_{n(1)}\mathrm{NP})}{c(\mathrm{P}_{n(2)}\mathrm{NP})c^{n_{(1)}}(\mathrm{P}_{(1)})} = \frac{K_{\mathrm{D}(2)}}{K_{\mathrm{D}(1)}} \quad (8)$$

Likewise, if bare NPs are incubated with both protein species simultaneously, NPs can be covered with proteins $P_{(1)}$ or with proteins $P_{(2)}$:

$$\mathrm{NP} + n_{(1)}\mathrm{P}_{(1)} + n_{(2)}\mathrm{P}_{(2)} \leftrightarrow \mathrm{P}_{n(1)}\mathrm{NP} + \mathrm{P}_{n(2)}\mathrm{NP} \quad (9)$$

In analogy to eqn (4) one can calculate the ratio of NPs saturated with proteins $P_{(1)}$, and $P_{(2)}$ to the total amount of NPs, $N_{(1)}/N_{\max}$, and $N_{(2)}/N_{\max}$, respectively:

$$\frac{N_{(1)}}{N_{\max}} = \frac{1}{1 + \left(\frac{K'_{\mathrm{D}(1)}}{c(\mathrm{P}_{(1)})}\right)^{n_{(1)}}\left(1 + \left(\frac{c(\mathrm{P}_{(2)})}{K'_{\mathrm{D}(2)}}\right)^{n_{(2)}}\right)}$$

$$\frac{N_{(2)}}{N_{\max}} = \frac{1}{1 + \left(\frac{K'_{\mathrm{D}(2)}}{c(\mathrm{P}_{(2)})}\right)^{n_{(2)}}\left(1 + \left(\frac{c(\mathrm{P}_{(1)})}{K'_{\mathrm{D}(1)}}\right)^{n_{(1)}}\right)} \quad (10)$$

In line with the description of only one protein species (*cf.* Fig. 1 and 3), eqn (10) describes how many ($N_{(1)}$ and $N_{(2)}$) of the $N_{\max}$ binding sites per NP are occupied by proteins of species $P_{(1)}$ and $P_{(2)}$, *cf.* Fig. 5. With eqn (10), the protein corona formed by the two protein species can be analysed, *cf.* Fig. 6. The data show that one protein species ($P_{(2)}$) displaces the other one ($P_{(1)}$) if it has a much lower half saturation concentration ($K'_{D(2)} \ll K'_{D(1)}$) or is present at a much higher concentration ($c(P_{(2)}) \gg c(P_{(1)})$). Please note that this "adapted" Hill formalism is appropriate only for describing the binding reaction in the special case $N_{\max(1)} = N_{\max(2)} = N_{\max}$, and that in eqn (10) $N_{(1)} + N_{(2)} \leq N_{\max}$ is supposed. This assumption certainly will not hold true in case two very different protein species (in particular in terms of size) are considered, but it helps understanding the concept of competition of different protein species for the binding sites on the surface of NPs. In this way, concepts like "soft" *versus* "hard" corona[30] could be quantitatively described, as will be discussed in more detail later.

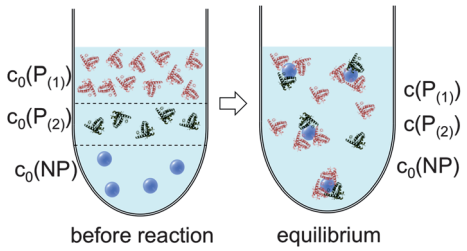

Fig. 5 Before the reaction, free proteins of species $P_{(1)}$ and $P_{(2)}$ with concentrations $c_0(P_{(1)})$ and $c_0(P_{(2)})$, respectively, and free NPs with concentration $c_0(NP)$ are separated. After the reaction has progressed to equilibrium, some proteins are bound to the NP surface (which is in general not yet saturated by proteins), while other proteins, with concentrations $c(P_{(1)})$ and $c(P_{(2)})$, are free in solution. All NPs are assumed to have the same average numbers $N_{(1)}$ and $N_{(2)}$ of proteins bound per NP ($N_{(1)} + N_{(2)} \leq N_{\max}$). It should be clearly pointed out, however, that, actually, there will be a statistical distribution of the number of proteins per NP (which we only represent here by the average number). Thus, $N_{(1)}$ and $N_{(2)}$ have to be viewed as average numbers of proteins bound per NP. There also might be interaction between both protein species, which is not included in our simple model.

Quantification of the number of proteins bound per nanoparticle and the problem of determining nanoparticle concentrations

Having described protein binding to the surface of NPs with concepts originating from protein biochemistry, we can now try to understand their significance for the experimental determination of the protein corona. An essential parameter that characterizes a protein corona is the average number of proteins N that are bound to the surface of a NP under a given experimental condition. Assuming that virtually all NPs have some proteins bound to their surface (other conditions are not of interest, as then there would be no protein corona), two main parameters are required for a complete characterization of the protein corona, that is, the concentration of NPs in the solution ($c_0(NP)$, *cf.* Fig. 3), and the concentration of proteins bound to the NP surface ($c_{NP}(P)$):

$$N = c_{\mathrm{NP}}(\mathrm{P})/c_0(\mathrm{NP}) \quad (11)$$

This journal is © The Royal Society of Chemistry 2014

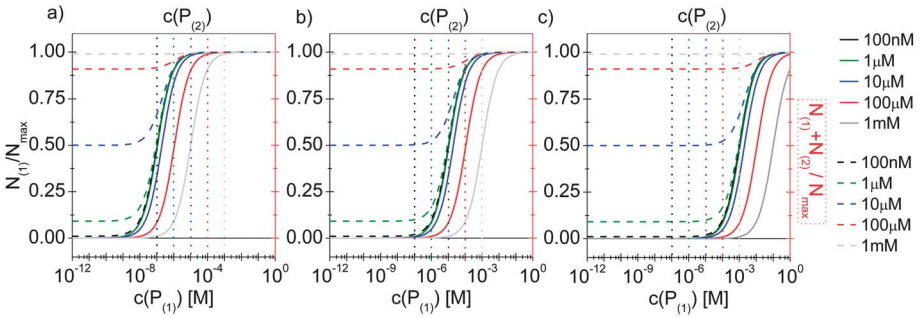

Fig. 6 The fractions $N_{(1)}/N_{max}$ and $N_{(2)}/N_{max}$ of proteins of species $P_{(1)}$ and $P_{(2)}$ per NP, are plotted as a function of the concentration $c(P_{(1)})$ of free protein $P_{(1)}$. $N_{(1)} + N_{(2)} \leq N_{max}$ according to eqn (10). The Hill coefficients of both protein species are assumed to be $n_{(1)} = n_{(2)} = 1$, and the concentration of half saturation of protein species $P_{(2)}$ is $K'_{D(2)} = 10$ μM. Different concentrations for protein species $P_{(2)}$ are used: $c(P_{(2)}) = 100$ nM, 1 μM, 10 μM, 100 μM, 1 mM. Solid and dashed lines represent $N_{(1)}$ and $N_{(1)} + N_{(2)}/N_{max}$ *versus* the concentration $c(P_{(1)})$ of free protein $P_{(1)}$, (black and red axes) respectively. (a) $K'_{D(1)} = 100$ nM. (b) $K'_{D(1)} = 10$ μM, (c) $K'_{D(1)} = 1$ mM. The vertical dashed lines indicate $c(P_{(2)})$.

Published on 14 October 2013. Downloaded on 29/07/2015 15:45:54.

Though this sounds trivial, unfortunately, the complication lies in the experimental details. Already the NP concentration is hard to determine. First of all, NP concentrations can be quantified differently.[2] In our work, we always measure NP concentrations in terms of molarities, *i.e.*, the number of NPs (in [mol]) per volume (in [L]), resulting in the unit M = mol L^{-1}. However, often, NPs are also quantified in terms of mass concentrations in the unit g L^{-1}, or in the overall molar concentration of atoms contained in the NP solution, in mol L^{-1}. Weighing of a dried NP solution can give an estimate for the mass concentration (in g L^{-1}), and the molar concentration of the atoms of dissolved NPs can be determined with element detection techniques such as inductively coupled plasma mass spectrometry (ICP-MS) or atomic absorption spectrometry (AAS), but conversion of these concentration into molar NP concentrations is not straightforward. This is due to the fact that, most often, the molecular mass and the number of atoms per NP, which are the coefficients relating the different concepts of concentration, are not precisely known. We have discussed this problem in a previous review in detail.[2]

A number of correlation techniques exist with which NP concentrations can be determined directly in solution with high precision, including fluorescence correlation spectroscopy (FCS)[46,47] and photothermal absorption correlation spectroscopy (PhACS).[48] However, these techniques are very sensitive to agglomeration and, therefore, only suitable for colloidally very stable NPs. For some types of NPs, concentrations can be determined *via* absorption measurements, in particular, if the NP solution has characteristic absorption peaks. This is, for example, the case for the surface plasmon resonance peak of plasmonic NPs such as Au and Ag, or for the first exciton peak of quantum dots (QDs). In such cases, (more or less precise) estimations for molecular extinction coefficients have been obtained, enabling determination of NP concentrations *via* determination of the absorption of the NP solution.[49–51] However, even if reliable values exist, for example for CdSe NPs, the situation can be complicated if the same NPs are enclosed within an additional shell, *e.g.*, CdSe/ZnS. The shell also changes the optical spectrum of these QDs. In particular, it increases the absorption cross-section and thus the extinction coefficient, which can be observed in the red-shift of the first exciton peak, which indicates an increase in the NP diameter.[52] In our experience, determination of the concentration of NPs can easily involve an error of 50% or more. Thus, it is paramount to precisely describe for each experimental study how the concentration of NPs was determined, for example, by stating the molar extinction coefficients used in the calculation. Only in this way, different studies can be compared, taking into account the big

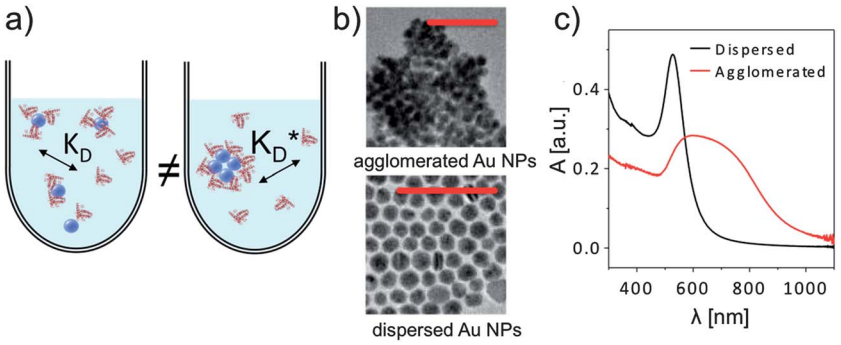

Fig. 7 (a) Formation of the protein corona is sensitive to the dispersion of the NPs in solution, for example *via* steric effects. (b) If dried NPs (in this case gold NPs of *ca.* $d_c = 15$ nm in core diameter) are observed to form agglomerates in TEM imaging (scale bars are 100 nm in both micrographs), they are usually also agglomerated in solution. (c) Agglomeration in solution can be observed with UV/vis absorption spectroscopy, in which the absorption A is plotted *versus* the wavelength λ.

[A1] 7

Published on 14 October 2013. Downloaded on 29/07/2015 15:45:54.

experimental error in determining c_0(NP). In addition, also the NP dispersion plays a crucial role. Most NPs tend to agglomerate, in particular, in the presence of salt.[3] As sketched in Fig. 7, formation of the protein corona around well dispersed NPs is likely to be different compared to a situation in which NPs are highly agglomerated. Thus, experimental studies about the protein corona should always be accompanied by a profound NP characterization, in particular in regard to their colloidal properties. One key parameter in this direction is the hydrodynamic diameter of the NPs (d_h), which can, for example, be determined by dynamic light scattering (DLS)[35] or by FCS.[53,54] In the case that d_h is much bigger than the geometric diameter d_c of the inorganic core of the NPs, as, for example, determined by transmission electron microscopy (TEM), it is likely that the NPs are not well dispersed but agglomerated.[2] Furthermore, absorption spectra are helpful in this direction.[35] Extinction at long wavelength (~1000 nm) is often not due to absorption but scattering of agglomerated NPs, *cf.* Fig. 7, unless it is due to specific features such as plasmon or exciton peaks, as for example in Au nanorods.

Separation of unbound proteins from nanoparticle–protein conjugates

Not only the NP concentration, but also the concentration of proteins attached to the NPs, c_{NP}(P), is difficult to determine precisely. *In situ* techniques such as fluorescence correlation spectroscopy (FCS) or analytical ultracentrifugation exist, which do not require separation of the NPs from the solution (in which, in general, unbound proteins are also present). More often, *ex situ* techniques are employed, in which unbound protein needs to be separated from bound proteins (and NPs). c_{NP}(P) may be determined indirectly *ex situ* by measuring the concentration of unbound proteins c(P) in the supernatant:

$$c_{NP}(P) = c_0(P) - c(P) \quad (12)$$

Alternatively, c_{NP}(P) can also be measured directly *ex situ*. The required separation step can be quite challenging experimentally. For sufficiently large NPs, they can be precipitated by centrifugation, whereby the NPs with attached proteins are precipitated and the unbound proteins remain in the supernatant.[55,56] The supernatant can be separated from the pellet of purified NPs (without excess protein), though, technically it is quite difficult to separate 100% of the supernatant. In particular, all subsequent purification steps (to further remove residual unbound proteins) are associated with complications. Let us assume that the pellet of NPs is redissolved in fresh buffer, precipitated again by centrifugation, followed again by separation of supernatant and NP pellet. Upon removal of free proteins, the equilibrium of eqn (1) and (2) is shifted, and bound proteins will dissociate from the NP surfaces and go into solution. This is relevant for all proteins with mean residence times (inverse k_{off} rates) on the NPs shorter than the duration of the analysis. Consequently, only those proteins that are very strongly (persistently) bound remain on the NPs, and the weakly bound part of the original protein corona is lost. Based on this scenario, Dawson and coworkers have suggested to differentiate between a "hard" and a "soft" corona.[57–60] This is a direct consequence of the law of mass action, in which removal of unbound proteins from the solution is compensated by detachment of part of the originally bound proteins. In the case that the protein corona is formed by multiple species $P_{(i)}$, the species with the highest concentration of half saturation $K'_{D(i)}$ will dissociate first. The distinction between proteins forming the "hard" and "soft" corona thus, to first order, is directly related to the half saturation concentrations $K'_{D(i)}$ of the respective protein species $P_{(i)}$. Detachment of bound proteins upon removal of free unbound protein can be clearly visualized with the examples shown in Fig. 4. If NPs are incubated with a protein solution of initial concentration c_0(P), the curves shown in Fig. 4 predict the concentration of bound proteins c_{NP}(P). Yet, if the free protein is removed, as aforementioned, the total protein concentration is reduced, $c'_0(P) < c_0(P)$, and this involves that proteins dissociate from the NP surface. Now the new value c'_0(P) has to be used in the curves shown in Fig. 4, leading to a new value of bound protein c'_{NP}(P). We can see from Fig. 4, that if $c'_0(P) \gg K'_D$ there will be an increase in the ratio $c'_{NP}(P)/c'_0(P) > c_{NP}(P)/c_0(P)$ (though $c'_{NP}(P) < c_{NP}(P)$, as, in total, proteins have been removed with the supernatant). This means that due to shortage of protein, a higher percentage of the available proteins are bound to the NP surface. Thus, repetitive purification steps change the equilibrium of the protein corona and do not reflect the original situation. Furthermore, with small NPs (≤10 nm), separation of unbound proteins by centrifugation can be complicated (it may require ultracentrifugation)[61] and time-costly due to the very small mass of these NPs. In the case of magnetic NPs, if their magnetic moment is big enough to allow for magnetic precipitation, the NPs can be also trapped in a magnetic field gradient, while unbound proteins can be rinsed away.[39] However, according to eqn (1) and (2), this rinsing step again leads to a partial loss of the original protein corona.

Quantification of unbound proteins to deduce the amount of bound proteins

Taking into account the aforementioned technical challenges involved in the separation of unbound proteins from protein–NP conjugates, we continue here with a discussion of methods to determine the concentration of free protein from the separated supernatant. The fraction of protein $c(P)/c_0(P)$ remaining free in solution can be derived from Fig. 4. These examples highlight the importance of assessing, at least qualitatively, the strength of the interaction between proteins and NPs (*i.e.*, K'_D). Please note that for practical purpose protein concentrations bigger than the NP concentrations ($c_0(NP) \ll c_0(P)$) are desirable, as otherwise no saturated NPs can be obtained. (i) If $c_0(P) \gg K'_D$ (and $c_0(NP) \ll c_0(P)$) most of the proteins will remain free in solution, *i.e.*, all NPs are already saturated with proteins and, thus, all additionally added proteins will remain unbound, *cf.* Fig. 4. Therefore, only a tiny fraction of proteins is removed from the supernatant and attaches to the NP surface, *i.e.* $(c_0(P) - c(P))/c_0(P) = c_{NP}(P)/c_0(P) \rightarrow 0$. The tiny reduction of protein concentration is experimentally very hard to detect, thus prone to error, and absolute

[A1] 8

 This journal is © The Royal Society of Chemistry 2014

Published on 14 October 2013. Downloaded on 29/07/2015 15:45:54.

quantitative values have to be interpreted with utmost care. In addition, if not all supernatant containing unbound protein has been removed (this is likely due to pipetting errors), then this "contaminates" the solution, and the fraction of proteins attached to the NPs will be wrongfully overestimated. However, there are scenarios in which concentration determination needs to be performed under saturation conditions. One major issue for indirect determination of the fraction of bound proteins is the analysis of competitive binding of proteins to NPs, as it is necessary to analyse the difference between the soft and hard corona.[57] In that case, a large excess of protein might be required to displace already bound proteins. (ii) If $c_0(\mathrm{P}) \approx K_\mathrm{D}'$ (and $c_0(\mathrm{NP}) \ll c_0(\mathrm{P})$), the NPs are half saturated with proteins on average, and the amounts of free and attached proteins will be in a similar range, *cf.* Fig. 4. This is the optimum situation in which it is possible to analyse the free proteins as well as the bound proteins. For instance, using ultracentrifugation and chromatography as alternative methods, Lundqvist *et al.* quantified unbound proteins in the presence of silica NPs (ratio NPs : protein = 1 : 1).[26] It is important to point out that in the mentioned work, the estimation of the attached protein is possible because of the working conditions ($c_0(\mathrm{P}) \approx K_\mathrm{D}'$). In fact, if the experiments would have been performed at oversaturation ($c_0(\mathrm{P}) \gg K_\mathrm{D}'$), these methods would not have been reliable.[26] (iii) At low protein concentrations ($c_0(\mathrm{P}) \ll K_\mathrm{D}'$), changes in free protein upon protein binding to NPs can be easily detected in the case of non-cooperative ($n = 1$) and anti-cooperative binding ($n < 1$) because a significant fraction of the available proteins is attached to the surface of the NPs, *cf.* Fig. 4. However, in the case of cooperative binding, almost all proteins are free in solution at very low protein concentrations. Due to the cooperativity of the binding process, significant binding can occur only at higher protein concentrations ($c_0(\mathrm{P}) \approx K_\mathrm{D}'$), *cf.* Fig. 4. Thus, the predictions of Fig. 4 help in choosing the experimental conditions under which changes in protein concentration can be determined best.

Direct quantification of proteins bound to nanoparticles

Notwithstanding that, due to the required washing steps, part of the original protein corona has been lost (*cf.* eqn (1) and (2)), the direct determination of the proteins attached per NP is straightforward. It is not only possible to quantify the amount of attached proteins, but also to specify the species of proteins forming the protein corona. A classical method is enzymatic digestion of the proteins bound to the NP surface, and their subsequent quantification with polyacrylamide gel electrophoresis or with mass spectroscopy.[37,39,58,61] Thereby, the attached proteins are sorted by their molecular weight,[55] which together with protein databases enables identification of the protein species. As will be demonstrated later, for small NPs (≤10 nm), typically less than $N_\mathrm{max} = 100$ proteins are bound per NP, and they are statistically distributed. Contributions of hundreds of proteins to the protein corona around NPs have been identified in several reports. It is obvious that not every NP will have the same protein corona.[37] Due to a statistical distribution of ≥100 existing protein species (in realistic media which, for example, contain serum) bound to ≤100 protein binding sites per NP, the protein corona of each individual NP can be quite different. Consequently, these details cannot be described with our simplified model.

Indirect quantification of proteins bound to nanoparticles by size measurements

The proteins adsorbed to the NPs can also be quantified indirectly *via in situ* size measurements. The more proteins are attached per NP, the greater its hydrodynamic radius r_h will become. Therefore, the amount of bound proteins can be determined *via* size measurements of NPs. Obviously, this is only possible for colloidally stable NPs with a narrow size distribution. Such indirect quantification has the huge conceptual advantage that, typically, measurements can be carried out without having to separate unbound excess proteins, and thus, measurements in real equilibrium are possible. There are several standard methods for quantifying hydrodynamic radii, such as dynamic light scattering (DLS[59]), centrifugation (differential centrifugal sedimentation,[59,62] analytical ultracentrifugation[63]), and fluorescence correlation spectroscopy (FCS[53,64]). DLS is based on the light scattering from the NPs. To separate the light scattered from the free proteins and the NPs by DLS measurements, the NPs have to be significantly larger (≥10 nm) than the proteins. DLS can then allow for convenient observation of the *in situ* formation of the protein corona, enabling determination of hydrodynamic radii of protein–NP complexes. For NPs in the size range of proteins, their scattering can no longer be unequivocally separated from the one of unbound proteins.[35] FCS is a very attractive alternative to DLS, which however requires fluorescence labelling of the NPs.[9] Assuming that fluorescence labelling of the NPs does not interfere with protein corona formation, FCS is only sensitive to the fluorescent protein–NP complexes, provided that the autofluorescence from unbound proteins can be neglected. FCS allows the measurement of hydrodynamic diameters $d_\mathrm{h} = 2r_\mathrm{h}$ of small protein–NP complexes (if one assumes spherical NPs; anisotropic shape in general is complicated to analyse[39]). The measurement of protein corona formation *via* size determination by FCS or DLS is only possible for smaller NPs. Upon protein adsorption, the hydrodynamic radius of the NPs will increase on the order of the linear dimensions of the protein. While adsorption of 5 nm (diameter) protein may easily be detected on a NP with $r_\mathrm{h} = 5$ nm (*i.e.*, a change of 100%), measurement of the size increase of a NP with 100 nm radius (*i.e.* a change of only 5%) upon protein binding will not be feasible.

Quantification of protein adsorption with fluorescence correlation spectroscopy

Following a simple approximation, we can consider the volume of a protein–NP conjugate as the volume of the NP and N times

This journal is © The Royal Society of Chemistry 2014

Published on 14 October 2013. Downloaded on 29/07/2015 15:45:54.

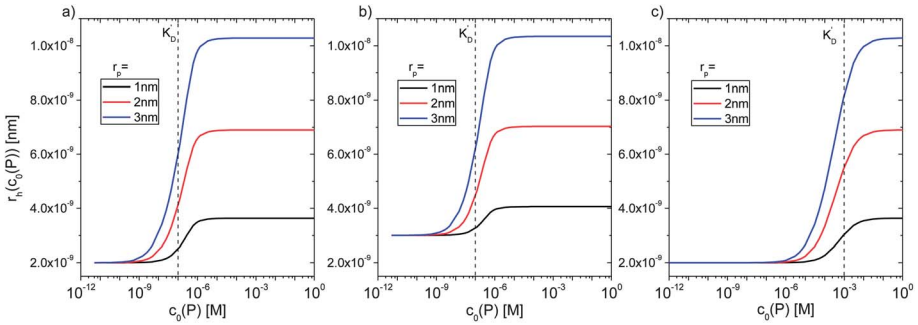

Fig. 8 Hydrodynamic radius r_h of NPs for different protein concentrations c_0(P), as calculated according to eqn (14) with the parameters $N_{max} = 40$, $n = 1$, $c_0(NP) = 10$ nM, $V_P = \frac{4}{3}\pi r_p^3$ where $r_P = 1$, 2, or 3 nm (idealized globular proteins were considered in these examples). (a) $r_{NP} = 2$ nm, $K_D' = 100$ nM, (b) $r_{NP} = 3$ nm, $K_D' = 100$ nM, (c) $r_{NP} = 2$ nm, $K_D' = 1$ mM.

the volume of one protein V_P, given that each NP binds N proteins.[54] The hydrodynamic diameter of this conjugate is then

$$r_h(N) = \sqrt[3]{r_h{}^3(0) + \frac{3}{4\pi} N V_P} \quad (13)$$

where $r_{NP} = r_h(0)$ is the hydrodynamic radius of one plain NP without adsorbed proteins.[54] Using eqn (4) for the number of adsorbed proteins per NP, the hydrodynamic radius of protein–NP complexes can be given as a function of the concentration of free protein c(P):[54]

$$r_h(c(P)) = \sqrt[3]{r_{NP}{}^3 + \frac{3}{4\pi} N_{max} \frac{1}{1 + \left(\frac{K_D'}{c(P)}\right)^n} V_P} \quad (14)$$

However, as for Fig. 4, where the fraction of bound proteins is represented depending on c_0(P), also eqn (14) can be recast in terms of c_0(P), by using eqn (5), which transforms c_0(P) into c(P). This enables an estimation of the NP radius depending on the amount of added protein, *cf.* Fig. 8. FCS (and also DLS) allows measurements of $r_h(c_0(P))$ as a function of the concentration c_0(P) of added protein.[54,65,66] Thus, fitting of these experimental data with eqn (14) yields the hydrodynamic radii of the NPs without protein $r_h(0)$ and saturated with protein $r_h(N_{max})$, respectively. The Hill coefficient n, the concentration of half saturation K_D', and the number of potential binding sites N_{max} of proteins per NP remain then as fit parameters. In this way, quantitative data, in particular, K_D', can be extracted. Table 1 summarizes some experimental data extracted in this way for a variety of different NPs and proteins. One of the most striking results from these data is that, under saturation conditions, the corona consists of a single protein monolayer, at least when using highly defined model NPs and only one protein species.[54,65,66] The data in Table 1 show, for example, how the

Table 1 Protein adsorption quantified by the Hill model as determined for NPs of different materials (FePt, Au, CdSe/ZnS) and surface coatings (PMA = poly(isobutylene-*alt*-maleic anhydride),[68] P(−) = PMAPHOS-*stat*-PLMA,[35] P(+) = PTMAEMA-*stat*-PLMA,[35] PAA = polyacrylic acid) with different proteins (HSA = human serum albumin, apo-Tf = apo-transferrin, apoA-I = apolipoprotein A-I, apoE4 = apolipoprotein E4) at different temperatures T (RT = room temperature). The radius r_c of the (spherical) inorganic cores of the NPs was determined by transmission electron microscopy (TEM). For the FePt NPs reported here,[54,65,66] the r_c data are taken from Lehmann *et al.*[69] In the case of the CdSe/ZnS NPs, according to the provider (Invitrogen), these NPs are not spherical but ellipsoids with 6 nm and 12 nm axes. $r_h(0)$ and $r_h(N_{max})$ are the hydrodynamic radii of NPs without adsorbed proteins and upon saturation of the NP surface with proteins ($\Delta r_h = r_h(N_{max}) - r_h(0)$), respectively, as determined by FCS using the Hill model. The Hill coefficient n controls the steepness of the binding curve, N_{max} is the maximum number of proteins adsorbing onto a single NP, and K_D' represents the concentration of protein molecules at half coverage

NP core	r_c [nm]	NP coating	Protein	T [°C]	$r_h(0)$ [nm]	$r_h(N_{max})$ [nm]	Δr_h [nm]	K_D' [μM]	n	N_{max}	Report
FePt	1.6 ± 0.2	PMA	HSA	RT	5.6 ± 0.2	8.9 ± 0.3	3.3 ± 0.3	5.1 ± 1.3	0.7 ± 0.1	22 ± 4	54
FePt	1.6 ± 0.2	PMA	HSA	RT	6.0 ± 0.1	9.3 ± 0.3	3.3 ± 0.3	9.9 ± 4.7	0.9 ± 0.2	27 ± 3	66
FePt	1.7 ± 0.3	PMA	HSA	13	5.5 ± 0.3	9.2 ± 0.4	3.7 ± 0.5	10 ± 4	0.6 ± 0.1	31 ± 5	39
FePt	1.7 ± 0.3	PMA	HSA	23	6.0 ± 0.1	9.3 ± 0.2	3.3 ± 0.2	6.3 ± 2.2	0.9 ± 0.2	30 ± 3	39
FePt	1.7 ± 0.3	PMA	HSA	43	6.0 ± 0.1	8.8 ± 0.2	2.8 ± 0.2	0.8 ± 0.4	0.7 ± 0.2	23 ± 2	39
FePt	1.6 ± 0.2	PMA	apo-Tf	RT	5.1 ± 0.2	12.1 ± 0.4	7.0 ± 0.4	26 ± 6	1.7 ± 0.2	23 ± 3	65
FePt	1.7 ± 0.3	PMA	apo-Tf	9	5.1 ± 0.2	15.1 ± 0.8	10.0 ± 0.8	13 ± 4	0.6 ± 0.1	47 ± 7	39
FePt	1.7 ± 0.3	PMA	apo-Tf	22	5.0 ± 0.2	14.3 ± 0.7	9.3 ± 0.7	16 ± 6	0.7 ± 0.1	40 ± 6	39
FePt	1.7 ± 0.3	PMA	apo-Tf	43	5.3 ± 0.1	11.0 ± 0.4	5.7 ± 0.4	5 ± 1	0.7 ± 0.1	17 ± 2	39
FePt	1.6 ± 0.2	PMA	apoA-I	RT	6.0 ± 0.1	10.8 ± 1.4	4.8 ± 1.4	140 ± 60	1.0 ± 0.3	52 ± 10	66
FePt	1.6 ± 0.2	PMA	apoE4	RT	6.0 ± 0.1	11.7 ± 0.2	5.7 ± 0.2	0.021 ± 0.003	1.4 ± 0.2	65 ± 3	66
Au	2.3 ± 0.6	P(−)	HSA	RT	7.9 ± 0.2	10.4 ± 0.3	2.5 ± 0.3	1.5 ± 0.8	0.8 ± 0.3	32 ± 4	35
Au	2.3 ± 0.6	P(+)	HSA	RT	5.1 ± 0.1	9.4 ± 0.4	4.3 ± 0.4	1.0 ± 0.3	0.8 ± 0.3	35 ± 3	35
CdSe/ZnS	6 × 12	PAA	HSA	RT	7.9 ± 0.3	11.1 ± 0.4	3.2 ± 0.5	37 ± 12	0.8 ± 0.2	36 ± 8	54

[A1] 10

This journal is © The Royal Society of Chemistry 2014

Published on 14 October 2013. Downloaded on 29/07/2015 15:45:54.

surface chemistry of the NPs influences protein adsorption. It has been observed that proteins can preferentially adsorb to surfaces with different charge density by different facets.[67] Thus, FCS measurements allow for investigation of protein oriented adsorption to NP surfaces.[65]

Future perspectives

As discussed in this review, there is no need to reinvent the wheel in regard to characterization of the protein corona because a body of work from protein biochemistry can be adapted to this problem. Further continuing along this path will lead to more quantitative data, for example, dissociation constants, on- and off-rate coefficients, *etc.* Nowadays, the literature is mainly based on qualitative statements like "the protein corona is what the cell sees".[62] In the future, however, such statements need to be placed in the context of more quantitative data. While the protein corona is of high importance, it is not the only relevant feature of the bio-interface of NPs. Quantitative data will help to compare different systems and to better understand the underlying molecular mechanisms. In our view, the most relevant technical problems that need to be solved to obtain more solid, quantitative data are (i) insufficient NP quality, especially in regard to size distribution and agglomeration, (ii) lack of precise data on NP concentrations, and (iii) purification of protein–NP complexes from unbound protein, without changing the nature of the original protein corona. The last point maybe is the most important one and comprises also an experimental dilemma. As pointed out above, purification (as required for *ex situ* quantification) can change the equilibrium, and part of the original protein corona will dissociate. Whether this occurs or not is mainly determined by the k_{off} rate coefficients. Inverse off-rates (*i.e.*, how fast proteins can dissociate from the NP surface) can be on the minute time scale, and even faster, which is faster than possible purification steps.[54] Thus, meaningful characterization of the protein corona would also involve determination of off-rates (which, together with the equilibrium dissociation coefficients, would also provide the corresponding on-rate coefficients, according to eqn (2)). Improvement regarding (i)–(iii) will help to extend future studies to new fields. Here we have only considered equilibrium conditions, but equilibrium may not always be reached if the kinetics are too slow. In this context, the determination of on- and off-rates will be crucial. We however want to point out that our models as presented here will not provide any details about the actual absorption mechanism, *i.e.* whether proteins are bound by electrostatic or hydrophobic interaction,[32] or whether NPs change the conformation of adsorbed proteins,[33,70] *etc.*

So far, there are two distinct directions in which the analysis of the protein corona has progressed. On the one hand, model systems have been widely investigated in which NPs are incubated with only one protein species, whose behaviour can be analysed quantitatively. These systems are highly simplified, but allow for the quantitative determination of equilibrium and kinetic parameters.[54] On the other hand, because nature is more complex, and hundreds of different types of proteins can adsorb from serum to the surface of NPs, we also require studies that more closely resemble the more realistic biological situation. Methods such as mass spectroscopy allow for a time-dependent analysis of the composition of the protein corona.[37] However, the systems are too complex for allowing the extraction of quantitative parameters of individual protein species. In the future, both directions should be merged, leading to more complex model systems, in which, for example, replacement of one protein species by another one is investigated in detail, such as is in principle treated by eqn (9) and (10). Development of such models will again lead to quantitative investigations. While the literature is full of qualitative description about the protein corona formed around hundreds of different NPs, the future will lie towards a more quantitative analysis, which will lead to a better understanding of the underlying principles and comparability of different studies.

Acknowledgements

This work was funded in part by HFSP (project RGP0052/2012 to WJP). We thank the Deutsche Forschungsgemeinschaft (DFG) for financial support through the Priority Program SPP1313 (to GUN and WJP). QZ is grateful for a fellowship from the Chinese Government and BP for a fellowship from the Alexander von Humboldt Foundation.

References

1 I. Freestone, N. Meeks, M. Sax and C. Higgitt, *Gold Bull.*, 2007, **40**, 270–277.
2 P. Rivera Gil, D. Jimenez de Aberasturi, V. Wulf, B. Pelaz, P. del Pino, Y. Zhao, J. de la Fuente, I. Ruiz de Larramendi, T. Rojo, X.-J. Liang and W. J. Parak, *Acc. Chem. Res.*, 2013, **46**, 743–749.
3 T. Pellegrino, S. Kudera, T. Liedl, A. M. Javier, L. Manna and W. J. Parak, *Small*, 2005, **1**, 48–63.
4 H. Takeuchi, B. Omogo and C. D. Heyes, *Nano Lett.*, 2013, **13**(10), 4746–4752.
5 K. Boldt, O. T. Bruns, N. Gaponik and A. Eychmüller, *J. Phys. Chem. B*, 2006, **110**, 1959–1963.
6 J. Aldana, Y. A. Wang and X. Peng, *J. Am. Chem. Soc.*, 2001, **123**, 8844–8850.
7 D. Gerion, F. Pinaud, S. C. Williams, W. J. Parak, D. Zanchet, S. Weiss and A. P. Alivisatos, *J. Phys. Chem. B*, 2001, **105**, 8861–8871.
8 T. Pellegrino, L. Manna, S. Kudera, T. Liedl, D. Koktysh, A. L. Rogach, S. Keller, J. Rädler, G. Natile and W. J. Parak, *Nano Lett.*, 2004, **4**, 703–707.
9 F. Zhang, E. Lees, F. Amin, P. Rivera Gil, F. Yang, P. Mulvaney and W. J. Parak, *Small*, 2011, **7**, 3113–3127.
10 K. E. Sapsford, W. R. Algar, L. Berti, K. B. Gemmill, B. J. Casey, E. Oh, M. H. Stewart and I. L. Medintz, *Chem. Rev.*, 2013, **113**, 1904–2074.
11 J. B. Delehanty, H. Mattoussi and I. L. Medintz, *Anal. Bioanal. Chem.*, 2009, **393**, 1091–1105.
12 E. E. Lees, T. L. Nguyen, A. H. Clayton and P. Mulvaney, *ACS Nano*, 2009, **3**, 1121–1128.

[A1] 11

Published on 14 October 2013. Downloaded on 29/07/2015 15:45:54.

13 C. Tassa, S. Y. Shaw and R. Weissleder, *Acc. Chem. Res.*, 2011, **44**(10), 842–852.
14 M. S. Nikolic, C. Olsson, A. Salcher, A. Kornowski, A. Rank, R. Schubert, A. Fromsdorf, H. Weller and S. Forster, *Angew. Chem., Int. Ed.*, 2009, **48**, 2752–2754.
15 V. V. Breus, C. D. Heyes, K. Tron and G. U. Nienhaus, *ACS Nano*, 2009, **3**, 2573–2580.
16 J. Domke, S. Dannöhl, W. J. Parak, O. Müller, W. K. Aicher and M. Radmacher, *Colloids Surf., B*, 2000, **19**, 367–379.
17 C. D. Heyes, A. Y. Kobitski, E. V. Amirgoulova and G. U. Nienhaus, *J. Phys. Chem. B*, 2004, **108**, 13387–13394.
18 M. Mrksich and G. M. Whitesides, *Annu. Rev. Biophys. Biomol. Struct.*, 1996, **25**, 55–78.
19 E. Ostuni, R. G. Chapman, R. E. Holmlin, S. Takayama and G. M. Whitesides, *Langmuir*, 2001, **17**, 5605–5620.
20 E. V. Amirgoulova, J. Groll, C. D. Heyes, T. Ameringer, C. Rocker, M. Moller and G. U. Nienhaus, *ChemPhysChem*, 2004, **5**, 552–555.
21 S.-Y. Jung, S.-M. Lim, F. Albertorio, G. Kim, M. C. Gurau, R. D. Yang, M. A. Holden and P. S. Cremer, *J. Am. Chem. Soc.*, 2003, **125**, 12782–12786.
22 R. Gref, M. Lück, P. Quellec, M. Marchand, E. Dellacherie, S. Harnisch, T. Blunk and R. H. Müller, *Colloids Surf., B*, 2000, **18**, 301–313.
23 V. C. F. Mosqueira, P. Legrand, A. Gulik, O. Bourdon, R. Gref, D. Labarre and G. Barratt, *Biomaterials*, 2001, **22**, 2967–2979.
24 Y. Zhang, N. Kohler and M. Q. Zhang, *Biomaterials*, 2002, **23**, 1553–1561.
25 S. M. Moghimi and J. Szebeni, *Prog. Lipid Res.*, 2003, **42**, 463–478.
26 M. Lundqvist, I. Sethson and B.-H. Jonsson, *Langmuir*, 2004, **20**, 10639–10647.
27 K. Anikin, C. Rocker, A. Wittemann, J. Wiedenmann, M. Ballauff and G. U. Nienhaus, *J. Phys. Chem. B*, 2005, **109**, 5418–5420.
28 G. B. Sukhorukov, A. L. Rogach, B. Zebli, T. Liedl, A. G. Skirtach, K. Köhler, A. A. Antipov, N. Gaponik, A. S. Susha, M. Winterhalter and W. J. Parak, *Small*, 2005, **1**, 194–200.
29 T. Cedervall, I. Lynch, S. Lindman, T. Berggård, E. Thulin, H. Nilsson, K. A. Dawson and S. Linse, *Proc. Natl. Acad. Sci. U. S. A.*, 2007, **104**, 2050–2055.
30 M. Lundqvist, J. Stigler, G. Elia, I. Lynch, T. Cedervall and K. A. Dawson, *Proc. Natl. Acad. Sci. U. S. A.*, 2008, **105**, 14265–14270.
31 Z. J. Deng, M. Liang, M. Monteiro, I. Toth and R. F. Minchin, *Nat. Nanotechnol.*, 2011, **6**, 39–44.
32 R. Huang, R. P. Carney, F. Stellacci and B. L. T. Lau, *Nanoscale*, 2013, **5**, 6928–6935.
33 S. Goy-Lopez, J. Juarez, M. Alatorre-Meda, E. Casals, V. F. Puntes, P. Taboada and V. Mosquera, *Langmuir*, 2012, **28**, 9113–9126.
34 N. Feliu, M. V. Walter, M. I. Montanez, A. Kunzmann, A. Hult, A. Nystrom, M. Malkoch and B. Fadeel, *Biomaterials*, 2012, **33**, 1970–1981.
35 D. Hühn, K. Kantner, C. Geidel, S. Brandholt, I. De Cock, S. J. H. Soenen, P. Rivera Gil, J.-M. Montenegro, K. Braeckmans, K. Müllen, G. U. Nienhaus, M. Klapper and W. J. Parak, *ACS Nano*, 2013, **7**, 3253–3263.
36 J. S. Gebauer, M. Malissek, S. Simon, S. K. Knauer, M. Maskos, R. H. Stauber, W. Peukert and L. Treuel, *Langmuir*, 2012, **28**, 9673–9679.
37 S. Tenzer, D. Docter, S. Rosfa, A. Wlodarski, J. Kuharev, A. Rekik, S. K. Knauer, C. Bantz, T. Nawroth, C. Bier, J. Sirirattanapan, W. Mann, L. Treuel, R. Zellner, M. Maskos, H. Schild and R. H. Stauber, *ACS Nano*, 2011, **5**, 7155–7167.
38 A. Lesniak, A. Campbell, M. P. Monopoli, I. Lynch, A. Salvati and K. A. Dawson, *Biomaterials*, 2010, **31**, 9511–9518.
39 M. Mahmoudi, A. M. Abdelmonem, S. Behzadi, J. H. Clement, S. Dutz, M. R. Ejtehadi, R. Hartmann, K. Kantner, U. Linne, P. Maffre, S. Metzler, M. K. Moghadam, C. Pfeiffer, M. Rezaei, P. Ruiz-Lozano, V. Serpooshan, M. A. Shokrgozar, G. U. Nienhaus and W. J. Parak, *ACS Nano*, 2013, **7**, 6555–6562.
40 E. Casals, T. Pfaller, A. Duschl, G. J. Oostingh and V. F. Puntes, *ACS Nano*, 2010, **4**, 3623–3632.
41 E. Casals, T. Pfaller, A. Duschl, G. J. Oostingh and V. F. Puntes, *Small*, 2011, **7**, 3479–3486.
42 S. Tenzer, D. Docter, J. Kuharev, A. Musyanovych, V. Fetz, R. Hecht, F. Schlenk, D. Fischer, K. Kiouptsi, C. Reinhardt, K. Landfester, H. Schild, M. Maskos, S. K. Knauer and R. H. Stauber, *Nat. Nanotechnol.*, 2013, **8**, 772–781.
43 B. Fadeel, N. Feliu, C. Vogt, A. M. Abdelmonem and W. J. Parak, *Wiley Interdiscip. Rev.: Nanomed. Nanobiotechnol.*, 2013, **5**, 111–129.
44 A. V. Hill, *J. Physiol.*, 1910, **40**, i–vii.
45 S. Goutelle, M. Maurin, F. Rougier, X. Barbaut, L. Bourguignon, M. Ducher and P. Maire, *Fundam. Clin. Pharmacol.*, 2008, **22**, 633–648.
46 P. Schwille, J. Bieschke and F. Oehlenschläger, *Biophys. Chem.*, 1997, **66**, 211–228.
47 L. Zemanova, A. Schenk, M. J. Valler, G. U. Nienhaus and R. Heilker, *Drug Discovery Today*, 2003, **8**, 1085–1093.
48 V. Octeau, L. Cognet, L. Duchesne, D. Lasne, N. Schaeffer, D. G. Fernig and B. Lounis, *ACS Nano*, 2009, **3**, 345–350.
49 W. W. Yu, L. Qu, W. Guo and X. Peng, *Chem. Mater.*, 2003, **15**, 2854–2860.
50 A. Striolo, J. Ward, J. M. Prausnitz, W. J. Parak, D. Zanchet, D. Gerion, D. J. Milliron and A. P. Alivisatos, *J. Phys. Chem. B*, 2002, **106**, 5500–5505.
51 W. Haiss, N. T. K. Thanh, J. Aveyard and D. G. Fernig, *Anal. Chem.*, 2007, **79**, 4215–4221.
52 B. O. Dabbousi, J. Rodriguez-Viejo, F. V. Mikulec, J. R. Heine, H. Mattoussi, R. Ober, K. F. Jensen and M. G. Bawendi, *J. Phys. Chem. B*, 1997, **101**, 9463–9475.
53 T. Liedl, S. Keller, F. C. Simmel, J. O. Rädler and W. J. Parak, *Small*, 2005, **1**, 997–1003.
54 C. Röcker, M. Pötzl, F. Zhang, W. J. Parak and G. U. Nienhaus, *Nat. Nanotechnol.*, 2009, **4**, 577–580.
55 M. Schaeffler, M. Semmler-Behnke, H. Sarioglu, S. Takenaka, A. Wenk, C. Schleh, S. M. Hauck, B. D. Johnston and W. G. Kreyling, *Nanotechnology*, 2013, **24**, 265103.

[A1] 12

 This journal is © The Royal Society of Chemistry 2014

56 A. S. Pitek, D. O'Connell, E. Mahon, M. P. Monopoli, F. B. Bombelli and K. A. Dawson, *PLoS One*, 2012, **7**, e40685.
57 S. Milani, F. B. Bombelli, A. S. Pitek, K. A. Dawson and J. Radler, *ACS Nano*, 2012, **6**, 2532–2541.
58 A. Lesniak, F. Fenaroli, M. R. Monopoli, C. Aberg, K. A. Dawson and A. Salvati, *ACS Nano*, 2012, **6**, 5845–5857.
59 M. P. Monopoli, D. Walczyk, A. Campbell, G. Elia, I. Lynch, F. B. Bombelli and K. A. Dawson, *J. Am. Chem. Soc.*, 2011, **133**, 2525–2534.
60 M. Lundqvist, J. Stigler, T. Cedervall, T. Berggard, M. B. Flanagan, I. Lynch, G. Elia and K. Dawson, *ACS Nano*, 2011, **5**, 7503–7509.
61 A. Jedlovszky-Hajdu, F. B. Bombelli, M. P. Monopoli, E. Tombacz and K. A. Dawson, *Langmuir*, 2012, **28**, 14983–14991.
62 D. Walczyk, F. B. Bombelli, M. P. Monopoli, I. Lynch and K. A. Dawson, *J. Am. Chem. Soc.*, 2010, **132**, 5761–5768.
63 E. E. Lees, M. J. Gunzburg, T.-L. Nguyen, G. J. Howlett, J. Rothacker, E. C. Nice, A. H. A. Clayton and P. Mulvaney, *Nano Lett.*, 2008, **8**, 2883–2890.
64 G. U. Nienhaus, P. Maffre and K. Nienhaus, *Methods Enzymol.*, 2013, **519**, 115–137.
65 X. Jiang, S. Weise, M. Hafner, C. Röcker, F. Zhang, W. J. Parak and G. U. Nienhaus, *J. R. Soc., Interface*, 2010, **7**, S5–S13.
66 P. Maffre, K. Nienhaus, F. Amin, W. J. Parak and G. U. Nienhaus, *Beilstein J. Nanotechnol.*, 2011, **2**, 374–383.
67 K. W. Mattison, P. L. Dubin and I. J. Brittain, *J. Phys. Chem. B*, 1998, **102**, 3830–3836.
68 C.-A. J. Lin, R. A. Sperling, J. K. Li, T.-Y. Yang, P.-Y. Li, M. Zanella, W. H. Chang and W. J. Parak, *Small*, 2008, **4**, 334–341.
69 A. D. Lehmann, W. J. Parak, F. Zhang, Z. Ali, C. Röcker, G. U. Nienhaus, P. Gehr and B. Rothen-Rutishauser, *Small*, 2010, **6**, 753–762.
70 S. I. Yoo, M. Yang, J. R. Brender, V. Subramanian, K. Sun, N. E. Joo, S. H. Jeong, A. Ramamoorthy and N. A. Kotov, *Angew. Chem., Int. Ed.*, 2011, **50**, 5110–5115.

Published on 14 October 2013. Downloaded on 29/07/2015 15:45:54.

This journal is © The Royal Society of Chemistry 2014

Electronic Supplementary Material (ESI) for Materials Horizons
This journal is © The Royal Society of Chemistry 2013

Pablo del Pino[a,d], Beatriz Pelaz[a], Qian Zhang[a], Pauline Maffre[b], G. Ulrich Nienhaus[b,c], Wolfgang J. Parak[a,4d*]

[a]Fachbereich Physik, Philipps Universität Marburg, Marburg, Germany
[b] Institute of Applied Physics, Karlsruhe Institute of Technology (KIT), Karlsruhe, Germany
[c] Department of Physics, University of Illinois at Urbana-Champaign, Urbana, Illinois, USA
[d]CIC Biomagune, San Sebastian, Spain
[*]corresponding author: wolfgang.parak@physik.uni-marburg.de

Protein corona formation around nanoparticles - from the past to the future

Supporting Information

Detailed steps to obtain the equations as presented in the main manuscript

According to the law of mass action

$$NP + n \cdot P \leftrightarrow P_nNP \quad (1)$$

the dissociation equilibrium coefficient K_D (or also called the apparent dissociation coefficient) of Equation (1), in which one nanoparticle (NP) reacts with n proteins (P) to form a protein-NP complex (P_nNP), is expressed as

$$K_D = \frac{c(NP) \cdot c^n(P)}{c(P_nNP)} = \frac{k_{off}}{k_{on}} \quad (2)$$

Hereby c(NP), c(P), and $c(P_nNP)$ are the concentrations of free (naked) NPs without attached protein, of unbound protein, and of the protein-NP complex, respectively. k_{on} and k_{off} are the on- and off-rates. Thus, the total amount $c_0(NP)$ of NPs which are in the solution comprises the free NPs and the protein-NP complexes. In the same way the total amount of proteins in solution $c_0(P)$ is given by the free proteins and by the proteins bound to the NPs, whereby each NP binds n proteins to form one protein-NP complex P_nNP:

$$c_0(NP) = c(NP) + c(P_nNP) \quad (3)$$

$$c_0(P) = c(P) + n \cdot c(P_nNP) \quad (4)$$

$c_0(NP)$ and $c_0(P)$ can also be regarded as NP and protein concentrations before the reaction between them started, respectively. c(NP) and c(P) are the concentrations of naked, protein-free NPs and free proteins, respectively, after NPs and proteins have been brought into contact and an

This journal is © The Royal Society of Chemistry 2013

equilibrium according to Equation (1) has been reached. One can now calculate the ratio of the number N of NPs with saturated protein shell (*i.e.* the amount of complexes P_nNP) to the total number N_{max} of NPs:

$$\frac{N}{N_{max}} = \frac{c(P_nNP)}{c_0(NP)} \xrightarrow{\text{Eq.(3)}} \frac{c(P_nNP)}{c(NP)+c(P_nNP)} = \frac{1}{\frac{c(NP)}{c(P_nNP)}+1} = \frac{1}{1+\frac{c(NP)}{c(P_nNP)}} \xrightarrow{\text{Eq.(2)}} \frac{1}{1+\frac{K_D}{c^n(P)}} = \frac{c^n(P)}{c^n(P)+K_D} \quad (5)$$

The Hill parameter n hereby describes the cooperativity. n > 1 indicates cooperative binding, *i.e.*, if NPs are already saturated with proteins, it is easier for the following NPs to become saturated. In other words, it is easier for several NPs to collectively become saturated with proteins than for single NPs to become independently saturated. In contrast, n < 1 refers to anti-cooperative binding, so that protein saturation of some NPs lowers the tendency for other NPs to become saturated with proteins. In the context of this simplified model of the reaction between proteins and NPs introduced with Eq. (5), the interpretation of the Hill coefficient can be subject to discussion, as the coverage state of a NP is not supposed to influence, other than through the law of mass action, the coverage state of another second NP. Despite this argument, Eq. (5) nevertheless provides a useful model for protein binding to NPs, if the involved parameters are suitably reinterpreted, as will be described in the following.

In Equation (5) we so far assumed a scenario in which, in equilibrium, N NPs are saturated with proteins (*i.e.*, these NPs form complexes P_nNP), and (N_{max}-N) NPs are naked (*i.e.*, with no protein attached). Of course, the scenario where NPs can only be naked or saturated does not reflect the reality, where NPs can also be partially covered by proteins. To describe the reaction between NPs and proteins exactly, we should consider the Adair scheme, where each partially covered state of the NPs is considered. However, for a large number of binding sites per NP, this scheme becomes very fast very complicated and we instead choose here to consider a second scenario, in which all NPs have the same (partially) coverage state. In other word, all NPs have an average number of N proteins per NP (*i.e.*, there are no naked, protein-free NPs). In this scenario, N_{max} would be the maximum number of binding sites for proteins *per* NP. In the following, we show that the fraction of saturated NPs N/N_{max} from the first scenario is equivalent to the fraction N/N_{max} in this second scenario. The first scenario considers the ratio x of the number of saturated NPs (*i.e.* N_{max} proteins per NP) to the total number of NPs, $x = N/N_{max}$. The ratio of the number of NPs without protein shell (*i.e.*, 0 proteins per NP) is then given by $(1-x) = (N_{max}-N)/N_{max}$. Thus, the total amount of proteins attached to the NPs is equal to the proteins on the saturated NPs and on the bare NPs: $x \cdot N_{max} + (1-x) \cdot 0 = \frac{N}{N_{max}} \cdot N_{max} + \frac{N_{max}-N}{N_{max}} 0 = N$. In the second scenario all NPs have N proteins attached and there are no "naked" NPs, which leads to the same total number of proteins per total number of NPs as in the first scenario. In the following we will continue our discussion according to the interpretation of the second scenario. Thus, N/N_{max} can be interpreted as the fraction of occupied protein sites on the NP surface.

This journal is © The Royal Society of Chemistry 2013

Equation (5) suggests also reinterpretation of n. In a modern view, n is not the stoichiometric factor, and it can also have fractional numbers (instead of only integer values). According to the Hill model, n is the so-called Hill coefficient. This coefficient n describes the cooperativity of binding ligands (in our case proteins) to their substrate (in our case the surface of NPs). $n > 1$ describes cooperative binding. Adhesion of proteins already present on the NP surface is enhanced if more proteins bind next to them. $n < 1$ refers to anti-cooperative binding. Adhesion of proteins already present on the NP surface is suppressed if more proteins bind next to them. $n = 1$ describes non-cooperative binding. Each protein binds individually to the NP surface and does not recognize the proteins that are already bound there.

Instead of the dissociation constant K_D, often, the concentration at which half of protein coverage is achieved (*i.e.* the protein concentration producing half occupation of the NP surface) K'_D is considered. Let us assume half of the NPs are saturated with proteins at a concentration of free proteins $c_{1/2}(P)$:

$$\frac{1}{2} = \frac{N}{N_{max}} \xrightarrow{Eq.(5)} \frac{c_{1/2}^n(P)}{c_{1/2}^n(P)+K_D} \Rightarrow 2 \cdot c_{1/2}^n(P) = c_{1/2}^n(P) + K_D \Rightarrow c_{1/2}^n(P) = K_D \Rightarrow c_{1/2} = K_D^{1/n} := K'_D \quad (6)$$

Thus, Equation (5) can be rewritten as $\frac{N}{N_{max}} \xrightarrow{Eq.(5,6)} \frac{c^n(P)}{c^n(P)+K'^n_D} = \frac{1}{1+(\frac{K'_D}{c(P)})^n}$. (7)

Now, we consider a situation (according to the interpretation with the second scenario) in which, in equilibrium, N proteins are bound to each NP on average. Thus, all NPs have on average N proteins bound *per* NP:

$$c_0(NP) = c(P_N NP). \quad (8)$$

However, there might also be free proteins (= ligands; c(P)) in solution. Thus the total amount of proteins is

$$c_0(P) = c(P) + N \cdot c(P_N NP) \xrightarrow{Eq.(8)} c(P) + N \cdot c_0(NP) \xrightarrow{Eq.(7)} c(P) + \frac{N_{max}}{1+(\frac{K'_D}{c(P)})^n} c_0(NP) \quad (9)$$

If the concentration of free proteins is much smaller than the concentration of half saturation, according to Equation (9) one gets:

$$c_0(P) \xrightarrow{Eq.(9)} c(P) + \frac{N_{max}}{1+(\frac{K'_D}{c(P)})^n} c_0(NP) \xrightarrow{c(P) << K'_D} c(P) + \frac{N_{max}}{(\frac{K'_D}{c(P)})^n} c_0(NP)$$
$$= c(P) + (\frac{c(P)}{K'_D})^n \cdot N_{max}\, c_0(NP) \quad (10)$$

This journal is © The Royal Society of Chemistry 2013

On the other hand, if the concentration of free proteins is much bigger than the concentration of half saturation, then all NPs are saturated with proteins and additional free proteins remain in solution, see also Figure S1.

$$c_0(P) \xrightarrow{\text{Eq.(9)}} c(P) + \frac{N_{max}}{1+(\frac{K'_D}{c(P)})^n} c_0(NP) \xrightarrow{c(P) >> K'_D} c(P) + \frac{N_{max}}{1+0} c_0(NP) = c(P) + N_{max}\, c_0(NP)$$
$$\xrightarrow{c(P) >> N_{max} \cdot c_0(NP)} c(P) \qquad (11)$$

According to Equation (10), at very low protein concentrations c(P), a significant part of the proteins is bound to the surface of NPs: $c_0(P)\text{-}c(P) \rightarrow (\frac{c(P)}{K'_D})^n \cdot N_{max} \cdot c_0(NP)$. On the other hand, at very high protein concentrations c(P), basically all proteins are free proteins, *cf.* Equation (11), as the absolute amount of proteins which is bound to NPs ($c_0(P)\text{-}c(P) \rightarrow 0$) is small, due to the fact that NPs cannot exist at very high concentrations $c_0(NP)$ well above the mM regime. In other words, since all NPs are already saturated with protein, all of the excess of added protein will remain free, *cf.* Figure S1.

Equation (9) is very useful, as experimentally, $c_0(P)$ is the easily accessible protein concentration, *i.e.*, the concentration of protein which has been added to solution, and not c(P), the concentration of protein which remains free in solution, after an equilibrium according to Equation (1) has been reached. It can be used to calculate the fraction of proteins which is bound to NPs (*i.e.*, the ratio of the amount of bound proteins to the total amount of proteins):

$$\frac{c_0(P) - c(P)}{c_0(P)} \xrightarrow{\text{Eq.(9)}} \frac{N_{max}}{1+(\frac{K'_D}{c(P)})^n} \frac{c_0(NP)}{c_0(P)} \qquad (12)$$

In Equation (9) the total protein concentration $c_0(P)$ is given as a function f depending on the concentration of free protein: $c_0(P) = f(c(P))$. Equation (9), however, also provides an implicit equation which allows for calculating c(P) in dependence on $c_0(P)$ as inverse function f^{-1}: $c(P) = f^{-1}(c_0(P))$. In general, the inverse function can be calculated only numerically (Figure S1 shows that, in order to do this, the c(P) and $c_0(P)$ axes simply need to be switched), but not analytically. However, in some special cases, an analytical solution is also possible (such as for n = 0.5, 1, 2). In the case of n= 1, Equation (9) is simplified to

$$c_0(P) \xrightarrow{\text{Eq.(9)}} c(P) + \frac{N_{max}}{1+(\frac{K'_D}{c(P)})^n} c_0(NP) \xrightarrow{n=1} c(P) + \frac{N_{max}}{1+\frac{K'_D}{c(P)}} c_0(NP) \qquad (13)$$

This journal is © The Royal Society of Chemistry 2013

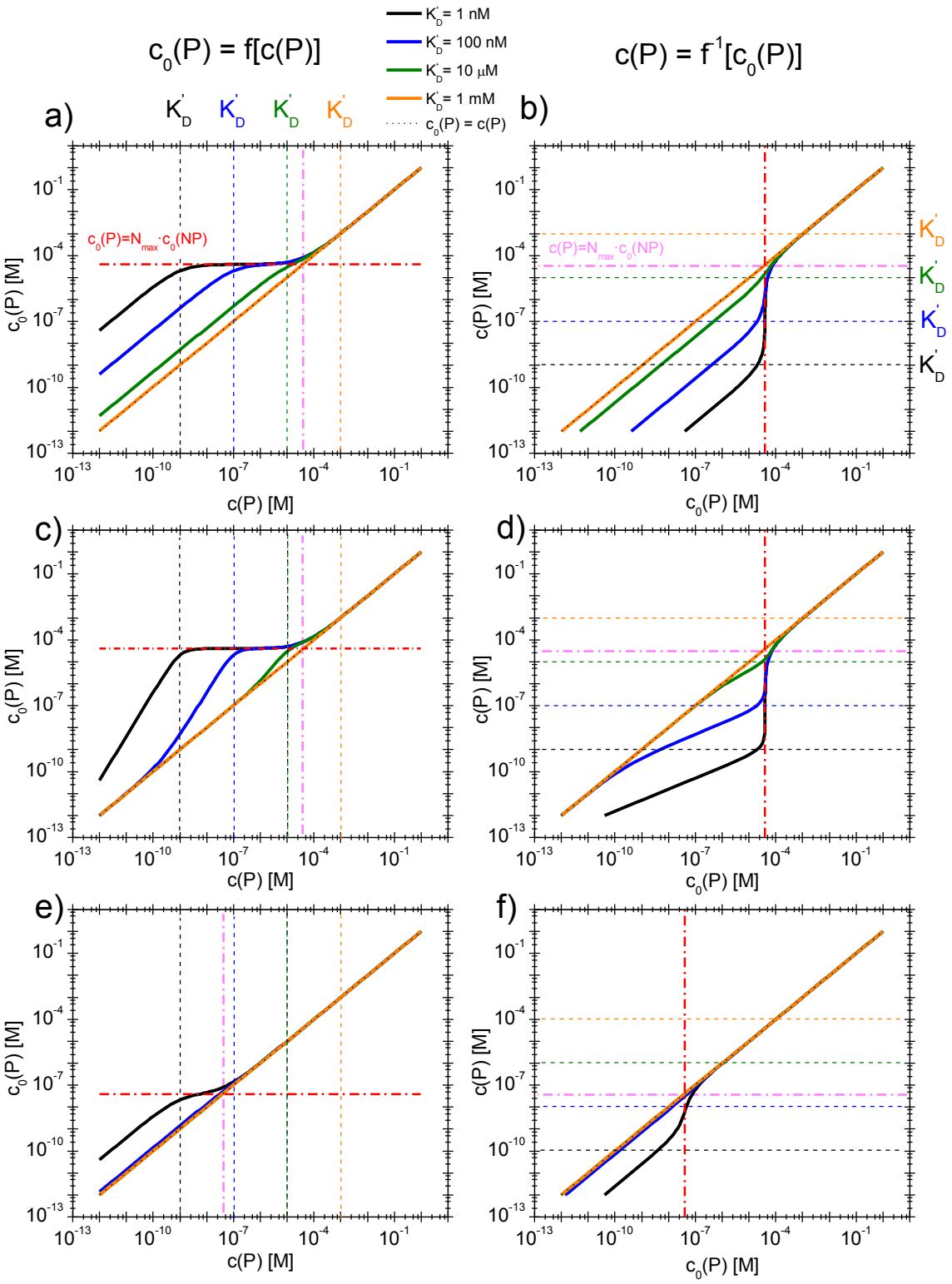

Figure S1. a, c, f) Direct graphical representation of Equation (9) in which $c_0(P)$ is displayed in dependence of c(P). for $K_D' = 1$ nM, 100 nM, 10 µM, and 1 mM with the following additional parameters: a) $N_{max}= 40$, $c_0(NP)= 1$ µM, n=1, c) $N_{max}= 40$, $c_0(NP)= 1$ µM, n=2, and e) $N_{max}= 40$, $c_0(NP)= 1$ nM, n=1. b, d, e) display the corresponding inverse functions, c(P) versus $c_0(P)$, with the same parameters. The dotted/dashed red lines (parallel to the c(P) axes) are guides to the eye and represent $c_0(P)= N_{max}\cdot c_0(NP)$. The dotted/dashed pink lines (parallel to the $c_0(P)$

This journal is © The Royal Society of Chemistry 2013

axes) represents guides to the eyes for $c(P)= N_{max}\cdot c_0(NP)$. The dotted grey lines represent the diagonals $c_0(P)= c(P)$, which can be hardly seen because they are beneath the graphs for $K'_D = 1$ mM.

By restructuring some terms it is possible to express Equation (12) as a quadratic equation:

$$c_0(P) = c(P) + \frac{N_{max}}{1+\frac{K'_D}{c(P)}}\, c_0(NP) \;\Leftrightarrow\; c_0(P) = c(P) + \frac{c(P)\cdot N_{max}}{c(P)+K'_D}\, c_0(NP)$$

$$\Leftrightarrow (c(P) + K'_D)\cdot c_0(P) = (c(P) + K'_D)\cdot c(P) + c(P)\cdot N_{max}\, c_0(NP)$$

$$\Leftrightarrow c(P)^2 + c(P)\cdot [N_{max}\cdot c_0(NP) + K'_D - c_0(P)] - [c_0(P)\cdot K'_D] = 0 \qquad (14)$$

Equation (13) is a quadratic equation of the form $x^2+bx+c=0$ for which the solution is $x = \frac{-b\pm\sqrt{b^2-4c}}{2}$. In the present case, only the "+" is a physically correct solution. Thus, Equation (14) can be solved and therefore, in the case of n = 1, we get the dependence of c(P) on $c_0(P)$ as analytical expression:

$$c(P) = \frac{1}{2}\left[(c_0(P) - N_{max}\cdot c_0(NP) - K'_D) + \sqrt{(N_{max}\cdot c_0(NP) + K'_D - c_0(P))^2 + (4\cdot c_0(P)\cdot K'_D)}\right] \qquad (15)$$

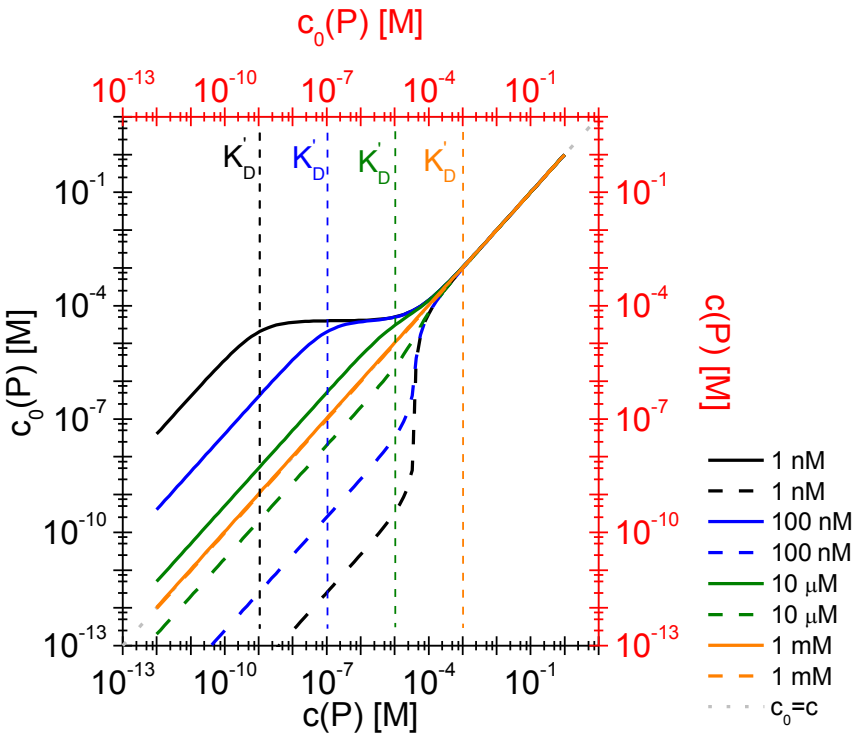

Figure S2. Graphical representation of Equations (13) and (15) for the parameters $N_{max}= 40$, $c_0(NP)= 1$ µM, n=1, and $K'_D = 1$ nM, 100 nM, 10 µM, and 1 mM. The solid lines (with the corresponding black axes) represent $c_0(P)$ versus c(P), and the dashed lines (with the corresponding red axes) represent c(P) versus $c_0(P)$.

This journal is © The Royal Society of Chemistry 2013

For the present example (n = 1), Figure S2 displays Equation (13) and (15) for different K'_D values. The results are the same as in Figure S1, but now obtained analytically and not numerically. However, as already mentioned, in general no analytical solution is possible and thus, c(P) in dependence on c_0(P) has to be numerically derived from the implicit Equation (9).

In the special case n = 1, also Equation (12) can be solved analytically in dependence on c_0(P), by putting Equation (15) into Equation (12). Some results are displayed in Figure S3.

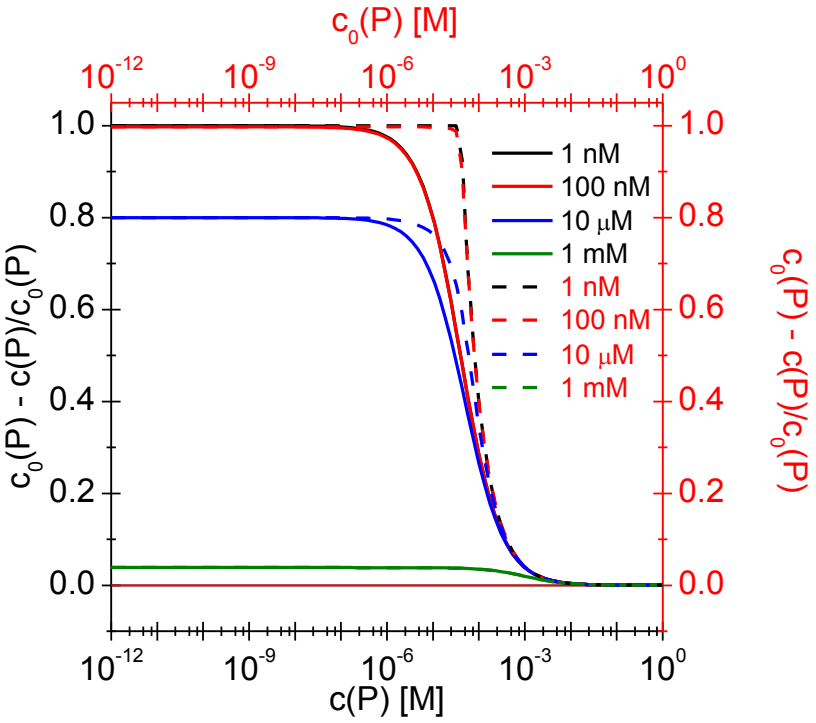

Figure S3. Fraction of the proteins which are bound to the NPs (c_0(P)-c(P))/c_0(P)) in dependence on the free protein concentration c(P) (solid lines, corresponding to the black axes), and in dependence on the total protein concentration c_0(P) (dashed lines, corresponding to the red axes), according to Equations (12) and (15), using the parameters N_{max} = 40, c_0(NP) = 1 µM, n = 1. The protein concentrations at half saturation K'_D were varied: K'_D = 1 nM, 100 nM, 10 µM, and 1 mM.

The same concept as described above can now be applied also for two different types of proteins $P_{(1)}$ and $P_{(2)}$:

$$NP + n_{(1)}\cdot P_{(1)} \leftrightarrow P_{n(1)}NP \qquad K_{D(1)} = \frac{c(NP)\cdot c^{n_{(1)}}(P_{(1)})}{c(P_{n(1)}NP)};\ K'_{D(1)} = (K_{D(1)})^{1/n_{(1)}} \qquad (16)$$

$$NP + n_{(2)}\cdot P_{(2)} \leftrightarrow P_{n(2)}NP \qquad K_{D(2)} = \frac{c(NP)\cdot c^{n_{(2)}}(P_{(2)})}{c(P_{n(2)}NP)};\ K'_{D(2)} = (K_{D(2)})^{1/n_{(2)}}$$

In case NPs which are saturated with protein species $P_{(1)}$ are brought into contact with free protein ligands $P_{(2)}$, an exchange (ligand exchange) can take place:

This journal is © The Royal Society of Chemistry 2013

$$P_{n(1)}NP + n_{(2)}\cdot P_{(2)} \leftrightarrow P_{n(2)}NP + n_{(1)}\cdot P_{(1)} \text{ with } K_D = \frac{c^{n_{(2)}}(P_{(2)})\cdot c(P_{n(1)}NP)}{c(P_{n(2)}NP)\cdot c^{n_{(1)}}(P_{(1)})} = \frac{K_{D(2)}}{K_{D(1)}} \quad (17)$$

If the NPs are incubated with both protein species at the same time, then both of them can bind to the NP surface. For reasons of simplicity, according to the first scenario, we are considering here only NPs with either $P_{(1)}$ or $P_{(2)}$, but not mixtures of both proteins on the same NP, though they certainly exist (as we will later use them in the second scenario):

$$NP + n_{(1)}\cdot P_{(1)} + n_{(2)}\cdot P_{(2)} \leftrightarrow P_{n(1)}NP + P_{n(2)}NP \quad (18)$$

Following the strategy of Equation (5) we can then determine how many NPs will be covered with $P_{(1)}$ and with $P_{(2)}$. Following the first scenario from above, the total amount of NPs is given by free NPs, NPs saturated with protein species $P_{(1)}$, and NPs saturated with protein species $P_{(2)}$:

$$c_0(NP) = c(NP) + c(P_{n(1)}NP) + c(P_{n(2)}NP) \quad (19)$$

Thus, the ratio of number $N_{(1)}$ of NPs with saturated shell of protein $P_{(1)}$ to the total number of NPs N_{max} can be expressed as:

$$\frac{N_{(1)}}{N_{max}} = \frac{c(P_{n(1)}NP)}{c_0(NP)} \xrightarrow{Eq.(19)} \frac{c(P_{n(1)}NP)}{c(P_{n(1)}NP)+c(P_{n(2)}NP)+c(NP)} = \frac{1}{1+\frac{c(P_{n(2)}NP)}{c(P_{n(1)}NP)}+\frac{c(NP)}{c(P_{n(1)}NP)}}$$
$$= \frac{1}{1+\frac{c(P_{n(2)}NP)}{c(P_{n(1)}NP)}\cdot\frac{c(NP)}{c(NP)}+\frac{c(NP)}{c(P_{n(1)}NP)}} = \frac{1}{1+\frac{K_{D(1)}}{c^{n_{(1)}}(P_{(1)})}\cdot\frac{c^{n_{(2)}}(P_{(2)})}{K_{D(2)}}+\frac{K_{D(1)}}{c^{n_{(1)}}(P_{(1)})}}$$
$$= \frac{1}{1+\frac{K_{D(1)}}{c^{n_{(1)}}(P_{(1)})}\cdot\left(1+\frac{c^{n_{(2)}}(P_{(2)})}{K_{D(2)}}\right)} \xrightarrow{Eq.(16)} \frac{1}{1+\left(\frac{K_{D\prime(1)}}{c(P_{(1)})}\right)^{n_{(1)}}\cdot\left(1+\left(\frac{c(P_{(2)})}{K_{D\prime(2)}}\right)^{n_{(2)}}\right)} \quad (20)$$

Equation (20) can also be interpreted according to the second scenario in which, in average, each NP has its N_{max} available binding sites covered with $N_{(1)}$ proteins of species $P_{(1)}$ and $N_{(2)}$ proteins of species $P_{(2)}$. Knowing how many proteins are bound per NP on average, one can calculate the hydrodynamic radius r_h of one protein-NP complex. In case N proteins are adsorbed per NP, the volume V(N) of the NP with the protein corona is

$$V(N) = V_{NP} + N\cdot V_P. \quad (21)$$

Hereby, V_P is the volume of one protein (which can be estimated from protein databases) and

$$V_{NP} = V(0) = \frac{4\pi}{3} r_h{}^3(0) \quad (22)$$

This journal is © The Royal Society of Chemistry 2013

is the volume of one NP without attached proteins (*i.e.*, without proteins in solution). Thus, the hydrodynamic radius $r_h(N)$ of one NP with N adsorbed proteins is

$$r_h(N) = \sqrt[3]{\frac{3}{4\pi}V(N)} = \sqrt[3]{\frac{3}{4\pi}(V_{NP} + N \cdot V_P)} = \sqrt[3]{r^3(0) + \frac{3}{4\pi}N \cdot V_P} \qquad (23)$$

with $r_{NP} = r_h(0)$ being the hydrodynamic radius of one plain NP without adsorbed proteins. Using Equation (7), this becomes

$$r_h(c(P)) = \sqrt[3]{r_{NP}^3 + \frac{3}{4\pi} \cdot N_{max} \cdot \frac{1}{1+(\frac{K_D'}{c(P)})^n} \cdot V_P}\ , \qquad (24)$$

where c(P) is the concentration of free protein, which however can be expressed in terms of the added concentration of protein $c_0(P)$, which is the concentration experimentally accessible. Thus, in order to calculate $r_h(c_0(P))$ in Equation (24), c(P) has to be expressed in terms of $c_0(P)$ *via* the implicit Equation (9). Only in some special cases (such as n = 1), an analytical solution can be directly given by inserting Equation (15) in Equation (24), *cf.* Figure S4.

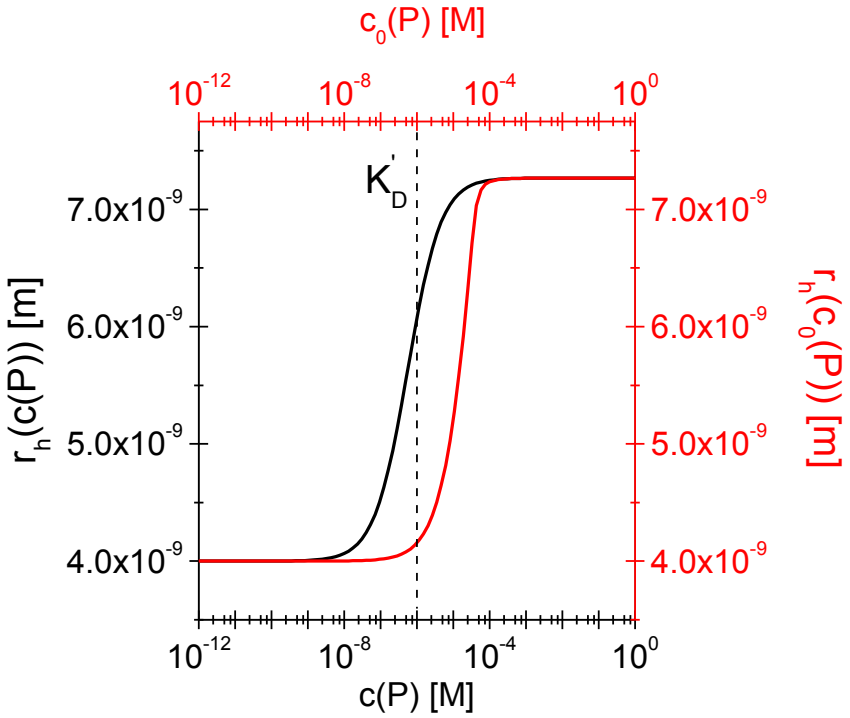

Figure S4. Hydrodynamic radius r_h of NPs in terms of c(P) (black line), and $c_0(P)$ (red line), according to Equation (24) with the parameters N_{max} = 40, n = 1, $c_0(NP)$ = 1 μM, r_{NP} = 4 nm, $V_P = \frac{4}{3}\pi r_p^3$ with r_P = 2 nm (idealized globular proteins were considered in this example) and K'_D = 1 μM.

[A1] 22

BEILSTEIN JOURNAL OF NANOTECHNOLOGY

In vitro interaction of colloidal nanoparticles with mammalian cells: What have we learned thus far?

Moritz Nazarenus[1], Qian Zhang[1], Mahmoud G. Soliman[1], Pablo del Pino[2], Beatriz Pelaz[1], Susana Carregal-Romero[1], Joanna Rejman[1], Barbara Rothen-Rutishauser[3], Martin J. D. Clift[3], Reinhard Zellner[4], G. Ulrich Nienhaus[5,6], James B. Delehanty[7], Igor L. Medintz[7] and Wolfgang J. Parak[*1,2]

Review

Open Access

Beilstein J. Nanotechnol. **2014,** *5,* 1477–1490.
doi:10.3762/bjnano.5.161

Received: 21 March 2014
Accepted: 12 August 2014
Published: 09 September 2014

This article is part of the Thematic Series "Biological responses to NPs".

Guest Editor: R. Zellner

© 2014 Nazarenus et al; licensee Beilstein-Institut.
License and terms: see end of document.

Address:
[1]Fachbereich Physik, Philipps-Universität Marburg, Renthof 7, 35037 Marburg, Germany, [2]CIC Biomagune, Paseo Miramón 182, 20009 San Sebastian, Spain, [3]BioNanomaterials, Adolphe Merkle Institute, University of Fribourg, Route de L'ancienne Papeterie CP 209, Marly 1, 1723, Fribourg, Switzerland, [4]Institute of Physical Chemistry, University of Duisburg-Essen, Universitätsstraße 5, 45141 Essen, Germany, [5]Institute of Applied Physics and Institute of Toxicology and Genetics, Karlsruhe Institute of Technology (KIT), Wolfgang-Gaede-Straße 1, 76131 Karlsruhe, Germany, [6]Department of Physics, University of Illinois at Urbana-Champaign, 1110 West Green Street, Urbana, IL 61801, USA and [7]Center for Bio/Molecular Science & Engineering, Code 6900, U.S. Naval Research Laboratory, 4555 Overlook Avenue Southwest, Washington D.C., 20375, USA

Email:
Wolfgang J. Parak[*] - wolfgang.parak@physik.uni-marburg.de

* Corresponding author

Keywords:
colloidal stability; intracellular particle distribution; nanoparticles; protein corona; toxicity of nanoparticles

Abstract

The interfacing of colloidal nanoparticles with mammalian cells is now well into its second decade. In this review our goal is to highlight the more generally accepted concepts that we have gleaned from nearly twenty years of research. While details of these complex interactions strongly depend, amongst others, upon the specific properties of the nanoparticles used, the cell type, and their environmental conditions, a number of fundamental principles exist, which are outlined in this review.

Introduction

There is a multitude of reports about the interaction of colloidal nanoparticles (NPs) with mammalian cells [1], as this topic is important for analyzing intended (e.g., medical applications [2-4]) and non-intended (e.g., contamination [5-7]) exposure of NPs to humans. However, there is a great number of available NPs made of many different materials [8-10] with a wide range

of different functionalities, cf. Figure 1. For a classification of NPs according to their composition, functionality, and fields of application we refer to a recent review [11]. To complicate the situation, most NPs do not consist of only one substance, but typically are hybrid materials, involving surface coatings and other modifications [12], cf. Figure 2 [13]. Even a homogeneous NP formed out of only one material will turn effectively into a hybrid NP, when it is brought into contact with any biological system (e.g., biological media) because of an organic coating that will form on the surface of the NPs [14]. This all illustrates that virtually no two types of NPs are the same and their inherent structure, properties, and constituent materials will contribute to the way in which they are taken up by cells. For example, a 20 nm diameter polymeric dendrimer may be very flexible, whereas a 20 nm metal NP may not, which leads to different interaction with cells. Furthermore, all of these different NPs can be exposed to different cells (e.g., macrophages, endothelia, and tumor cells) under different exposure scenarios (in vitro and in vivo), which as a consequence culminates in a large, but diverse body of work reported in the literature [15-17]. Due to this overwhelming amount of data, it is not easy to obtain a comprehensive overview. Many studies focus on the details of particular systems, but those can dramatically vary from case to case, and even conflicting trends are reported [17]. In addition, results will depend on the cellular test model used. In order to simplify the discussion, this review focuses on in vitro interaction of NPs with adherent, mammalian, immortalized cell lines. This avoids for example the problem of having to discuss how NPs reach and penetrate tissue, which makes in vivo scenarios more complicated than in vitro test systems. Despite these issues, it is still possible to discern some general trends, as described within this review. However, a limitation to having general trends equates to being permissive of some specific details, though common agreements reported here are clearly not trivial. It also automatically involves the possibility that studies exist, which under particular experimental conditions claim the opposite to the general statements. The most important of these trends will be discussed. In this regard, the current review will focus on physicochemically defined NPs, i.e., solutions of monodisperse NPs with a defined ligand shell attached, and without residual "left-over" impurities of the NP synthesis [13,18].

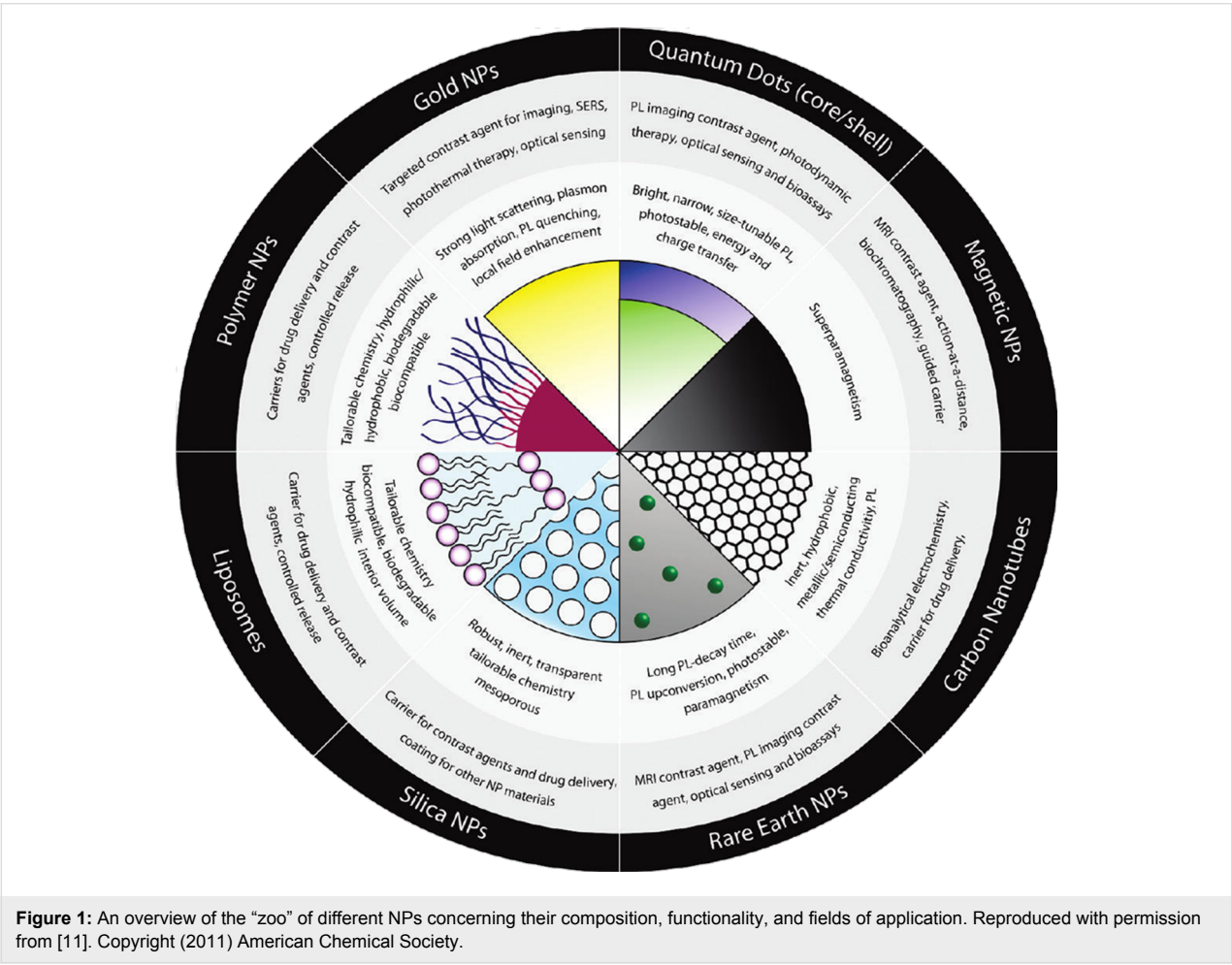

Figure 1: An overview of the "zoo" of different NPs concerning their composition, functionality, and fields of application. Reproduced with permission from [11]. Copyright (2011) American Chemical Society.

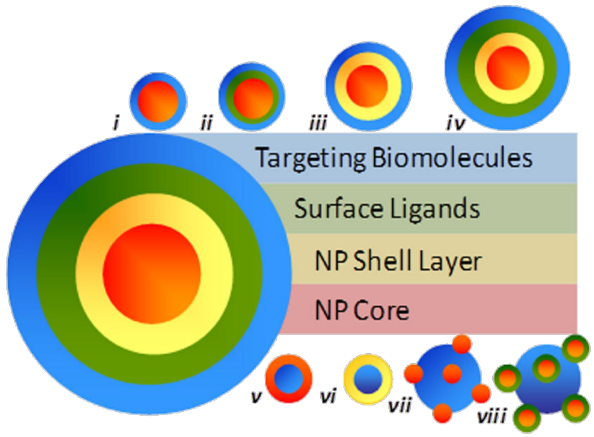

Figure 2: Hybrid nature of typical NPs, comprising different structural compartments. Reproduced with permission from [13]. Copyright (2013) American Chemical Society.

Review

How do particles enter cells and where do they go?

Virtually all cell lines internalize NPs, which are dispersed in the growth medium [19]. Uptake of different NPs by different cell lines, however, can vary significantly in biological kinetics [20-22] (this is also true for larger microparticles [23]). This is particularly important to keep in mind for specific (i.e., targeted) NP uptake, in which NPs modified by ligands (such as folic acid), which bind to appropriate receptors on the cell surface (such as folate receptors [24]), are specifically internalized [25]. Ligand-mediated uptake (which depends also on the ligand "valence", i.e., the number of ligands per NP, their density, and their orientation [26]) is faster and more efficient than non-specific (i.e., not receptor-mediated) uptake [27,28], although also plain or non-targeted NPs will be incorporated by cells. Thus, an important parameter to compare amongst studies, in which specific uptake is reported, is the time scale used within the experimental approach. While after short times of exposure huge differences in the amount of incorporated NPs can exist (e.g., between ligand-modified and plain NPs), those differences typically become less significant after longer exposure times [29], e.g., by the presence of the protein corona [30], as will be discussed later in more detail. Thus, statements which claim that only specifically modified NPs, but not non-modified NPs are taken up by cells, have to be regarded highly critically and put into the correct context of the reported time-scale. In fact, differences in uptake are not digital (i.e., "yes" or "no"), but rather are based on different kinetics. However, non-adhesive cell lines, i.e., cell suspensions, can be different and examples in which no significant internalization of NPs happened are reported [31]. Coming back to adhesive cell-lines, the first step in NP internalization obviously is the contact of the NP with the cell plasma membrane. This is a concentration-dependent process, which for high NP concentrations no longer scales linearly with concentration (i.e., saturation effects may occur). The first association of a non-targeted NP with a cell surface is usually electrostatic. Positively charged NPs are, for example, believed to interact with surface-displayed heparan sulfate proteoglycans [32,33]. As a rule of thumb, NPs which strongly interact with the cell plasma membrane, be it by ligand–receptor-mediated or by charge-mediated adhesion, are also internalized more efficiently [34]. Non-fouling polyethylene glycol (PEG)-modified NPs, for example, stick less to the cell plasma membrane and are, therefore, incorporated by cells less efficiently than other NPs [35-37] (this is also true in vivo as manifested by enhanced retention times [38]). It is clear that, while there are a number of portals through which NPs can gain entry into the cell, they all have as the common denominator the cell plasma membrane. Thus, the NP either must translocate (diffuse) directly across the cell plasma membrane entering the cytosol, or it must be internalized via any of the several routes of cellular endocytosis. While some evidence exists to support the direct membrane translocation of a select number of NP materials (typically partly hydrophobic and very small, as discussed later) the overwhelming evidence to date supports endocytosis as the common route of NP uptake. Thus, once NPs are associated to the outer cell plasma membrane they are typically internalized by endocytosis [39,40]. While a variety of different endocytotic pathways exist, which can be quite different in detail (to appreciate the complexity of endocytosis, we refer the reader to the review by Iversen et al. [41], cf. Figure 3), all of them have in common that the NPs are surrounded by membrane. Pinching-off of the membrane-surrounded NPs from the cell plasma membrane leaves the NPs incorporated into intracellular vesicles. These vesicles undergo a cascade of intracellular trafficking steps passing the NPs to more and more acidic vesicles [42,43], which also comprise enzymes specialized in digesting nutrition (and thus also parts of the NPs are digested in the lysosome [44,45]). In other words, after incorporation, the majority of NPs is not "free" in the cytosol, but inside intracellular vesicles (cf. Figure 4). Inside those intracellular vesicles the NPs are in an environment (acidic pH, enzymes) completely different from that in the cytosol (cf. Figure 5). Endocytosis and the endosomal escape dilemma have to be taken into account in particular concerning the delivery applications of NPs, in which the goal is to deliver something to the cytosol. Getting stuck inside intracellular vesicles is redundant to the purpose of these applications. However, in contrast to endocytosis as described so far, studies exist in which it is claimed that NPs can directly translocate through the cell membrane, thus indicating alternative pathways for NPs to penetrate the cell plasma membrane [46,47]. Besides other possible mechanisms, passive diffusion through (transient)

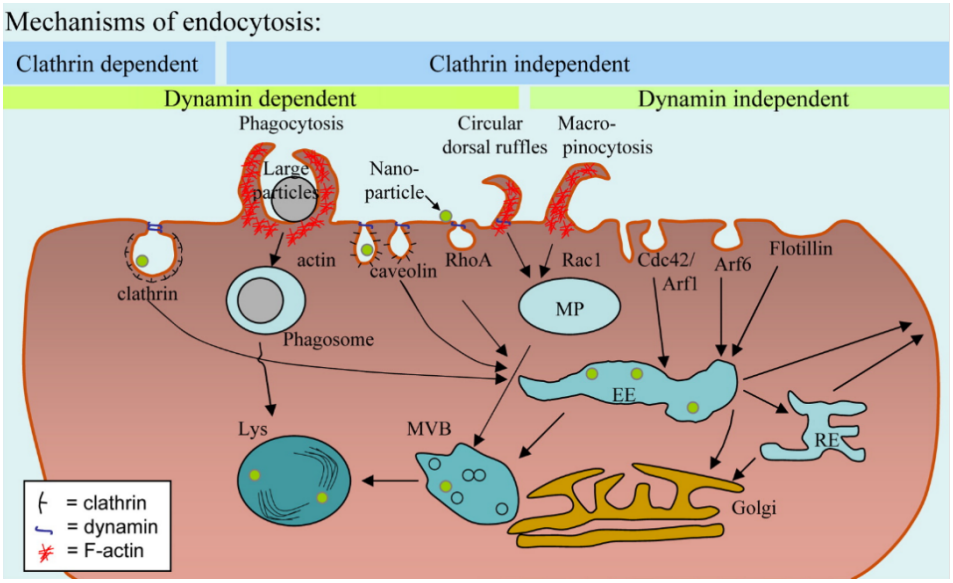

Figure 3: Scheme depicting the different mechanisms of cellular endocytosis. Reproduced with permission from [41]. Copyright (2011) Elsevier.

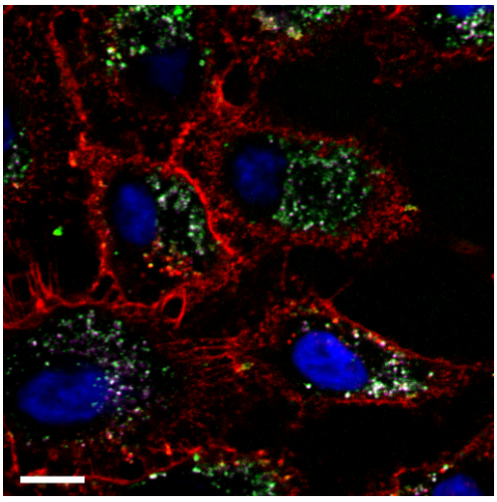

Figure 4: Fluorescence microscopy image showing the granular structure of internalized NPs inside A549 lung cancer cells (two types of iron oxide NPs with different surface chemistry, labelled with different fluorophores (green and magenta)) after 24 h of incubation at a concentration of 1 µg/mL, which are located in individual vesicles. Nuclei are stained with DAPI (blue) and the cell membrane with Wheat Germ Agglutinin (red). Note that due to limited lateral resolution of optical microscopy the spots most likely do not correspond to individual NPs, but to several NPs, which are entrapped inside intracellular vesicles. The scale bar represents 5 µm. Adopted with permission from [65] und Creative Commons Attribution 4.0 International Public License.

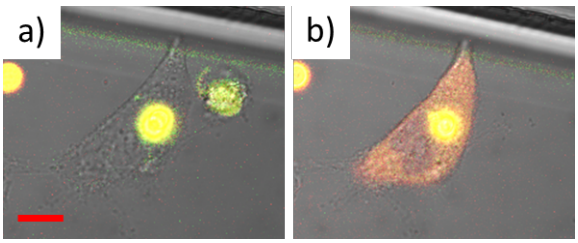

Figure 5: a) A microparticle has been internalized by an A549 lung cancer cell into an intracellular vesicle (here the lysosome [165]) and is thus clearly localized. The microparticle is filled with a pH-sensitive fluorophore (SNARF, from Invitrogen, now LifeTech) linked to dextran and the acidic pH of the lysosome is reported by the yellow fluorescence. b) After release of the pH-sensitive fluorophore linked to dextran to the cytosol (by photothermal heating), the fluorophore–dextran conjugates are freely dispersed, without any visible granular structure. Due to the neutral pH in the cytosol the fluorescence of the fluorophore–dextran conjugates has changed to red. The scale bar corresponds to 10 µm. Adopted with permission from [166]. Copyright (2012) Elsevier.

membrane pores and passive uptake by van der Waals or steric interactions (subsumed as adhesive interactions) have been suggested [48]. Still, it is always important to interpret such studies critically [49]. Most of the time studies involve an analysis of intracellular NP distributions, i.e., they rely on images showing NPs distributed in the cytosol. Additionally, these studies often rely on the observation that cellular NP entry still occurs below physiological temperatures (e.g., 4 °C), at which endocytosis and the active transport machinery are abrogated. However, without probing also for vesicular membranes around the NPs it is complicated to claim that the NPs in fact have passed the cell plasma membrane as "naked" NPs, without having ever been inside any intracellular vesicle. Clearly, there are a lot of indications (e.g., simulations) that NPs can enter cells through transient pore formation, in particular very small NPs [50,51]. Still, in many publications experiments do not

unequivocally demonstrate this pathway, though it surely exists. One possibility of experimental modification would involve, for example, pH-sensitive fluorophores (such as SNARF [52,53]) attached to the surface of the NPs, which can distinguish between the neutral cytosol and highly acidic intracellular vesicles [54]. In a similar direction the reductive capacity of glutathione (the cytosolic concentration of which is between 5 and 10 mM) may be used to displace a fluorescence resonance energy transfer (FRET) acceptor on the surface of the NP as confirmation of a successful NP localization to the cytosol [55]. Such experiments are in particular important for distinguishing between direct translocation to the cytosol versus endocytotic uptake followed by endosomal release. In fact, while there is clear experimental proof that NPs can be transported to the cytosol, the most straightforward pathway is uptake through endocytosis followed by release from the intracellular vesicles to the cytosol [56-58] (and not the diffusion through (transient) membrane pores). Endosomal release is, for example, a scenario which has been unraveled in detail for NPs coated with certain cell penetrating peptides (CPPs) [59-62]. Thus, while NPs can be free in the cytosol, this clearly does not automatically involve that they are membrane-permeable and not endocytosed. As pointed out above, observations based on merely measuring intracellular NP distributions are not sufficient for making profound statements about the uptake pathway. On the other hand it is safe to say that different intracellular locations for NPs exist. NPs have been reported in different intracellular organelles such as mitochondria, the nucleus, and free in the cytosol [63,64]. Most of the time such intracellular distributions are analyzed with transmission electron microscopy (TEM), in which also the structure of the intracellular organelles can be resolved (cf. Figure 6), or with fluorescence microscopy, in which the intracellular organelles have been co-stained with a fluorescent marker [65-67]. However, these data have to be interpreted carefully. In particular, such data should always include a quantitative distribution analysis, which is highly time-consuming. Even plain NPs without any particular surface capping can be found free in the cytosol [68], however, only to a very low extent. Thus, images in which NPs are shown in some particular intracellular organelles are only of limited value if the fraction of NPs that resides in these organelles is not quantified. Quantification, however, is not as trivial as it seems, and there is a need for better quantitative techniques for the future. While TEM offers the lateral resolution to visualize individual NPs, typically only a limited amount of cell sections (i.e., thin slices cut from cells) can be observed and thus for an absolute quantification, which is highly time-consuming, stereological tools need to be employed [68,69]. Also in case of TEM studies knowledge and understanding of cells under TEM conditions is essential. Fluorescence, on the other hand, can be recorded quantitatively by assuming that the emission intensity is proportional to the number of NPs. However, fluorescence can be partly quenched in certain organelles (for example at low pH), and it is impossible to resolve individual NPs due to the limited lateral resolution of optical microscopy [70]. In addition, as mentioned before, NPs can be partly degraded after having been internalized [71,72] and thus, in case fluorescently labeled NPs are used, it is required to prove that the fluorescence (or any other) label is still attached to the NPs inside the cells. Otherwise the recorded intracellular distribution of fluorescence may originate from detached labels and thus would not reflect the distribution of the NPs [73]. Summarizing available data suggests that, while translocation from intracellular compartments to the cytosol and from there to other cellular organelles is possible, translocation efficiencies still are moderate at best. In addition, NPs free in the cytosol may later end up again in intracellular vesicles through auto-phagocytosis [74]. Thus, for many applications, such as intracellular sensing or drug delivery, translocation of NPs to the cytosol after spontaneous endocytotic uptake remains a major challenge. External stimuli may be helpful in this direction [75]. In order to close this section it is also important to think about what happens after endocytotic uptake. It is, for instance, often overlooked that there is an eventual loss of the total NP load per cell as a result of mitotic division, NP exocytosis, and NP transcytosis [76]. This is largely due to the fact that in most experimental systems the primary issues addressed are uptake efficiency of the NPs and subsequent intracellular fate. These parameters are typically asked over the time course required for NP internalization and subcellular localization, and are not tracked over long time courses. It is generally accepted that NPs are partitioned during cell division,

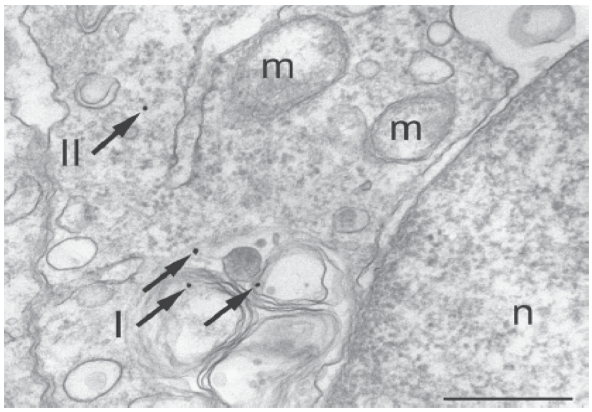

Figure 6: Intracellular compartments after internalization of PEG-coated gold NPs as visualized with TEM. The NPs (which are individually resolved due to the high lateral resolution of TEM) are located within a lysosome (arrows I) and in the cytosol (arrow II). *m* and *n* demark the nucleus and mitochondria, respectively. The scale bar corresponds to 500 nm. Adopted from with permission from [68]. Copyright 2010 Wiley-VCH Verlag GmbH & Co. KGaA, Weinheim.

in which they are passed to the daughter cells [76,77]. Such dilution effect of NP labels is in particular important for studies involving NPs as long-term tracers. Here, the relevant question arises whether upon cell division NPs are passed 50/50 to each daughter cell. Summers et al. have done both a theoretical [78] and experimental assessment [79] showing that, while partitioning of endosomes to daughter cells is symmetric, the number of NPs per endosome is a distribution and therefore NP partitioning to daughter cells is asymmetric. Thus, after several division cycles the NP distribution will not necessarily be representative for the fate of the original "mother" cells anymore. NPs also can be excreted to the extracellular medium, which represents an additional source of NP dilution effects. While endocytosis of NPs has been investigated heavily there are only a limited number of reports investigating exocytosis of NPs [80-82]. Excretion of NPs in exosomes (i.e., membrane surrounded vesicles), however, clearly affects the long-term cellular loading with NPs. In addition, for some particular cells, transcytosis has also been reported, i.e., that NPs are passed from one cell to another one [83].

What are the critical parameters involved in in vitro nanoparticle internalization?

As mentioned before, virtually all NPs are spontaneously internalized by adherent cells, mainly cell lines, that are usually grown on a certain support and covered with cell culture medium under static conditions. In this case, NPs in the medium can directly access cells, and issues like tissue penetration, which need to be considered in in vivo experiments, can be neglected. The kinetics of internalization can depend strongly on the physicochemical properties of the NPs, the type of cells, and other parameters. Cellular uptake studies of NPs require as much characterization of the NP materials as currently possible. Concerning the NPs, this is, unfortunately, hampered by our incapability to synthesize "defined" NPs. For quantitative studies NPs and their bioconjugates should be as monodisperse as possible with regard to all relevant parameters, such as charge and size, well-defined and well-characterized. Moreover, in the case of bioconjugates, the biological molecule, be it protein or drug, should be attached to the NP with control over orientation [84,85], density, affinity, and number or ratio per NP [85]. Although these goals are extremely hard to achieve, the more they can be fulfilled, the less heterogeneity is present in the NP material and the easier the results (i.e., the correlation between the properties of the NPs and the observed interaction of NPs with cells) can be interpreted [13,18,86]. With limitations, a correlation of the spontaneous endocytotic uptake of NPs to the physicochemical properties of the NPs can be found. One, however, has to be aware that many physicochemical properties of NPs, such as size, shape, charge, and colloidal stability are highly entangled [14]. The physicochemical properties are not intrinsically associated with the NPs, but result from the interaction of the NPs with the surrounding particular medium [87]. The colloidal stability is presumably the most influential parameter. NPs with low colloidal stability will agglomerate and thus, originally "small" NPs will transform into agglomerates, resulting in large particles presented to the cells (cf. Figure 7). However, "colloidal stability" is not a defined physicochemical entity such as size, but needs to be put in context with the measurement protocol, such as the tendency to agglomerate. Any correlation to the size of the NPs without any previous demonstration of colloidal stability in the incubation medium has to be seen very critically. Loss of colloidal stability during incubation also complicates dosimetry. If NPs are quantified in numbers, is an agglomerate of NPs considered to be one particle or the number of NPs in the agglomerate [14]? Agglomeration can have direct consequences on cellular uptake [62]. If the cell cultures are turned upside-down, i.e., the cells are hanging in the culture medium, NP agglomerates that have precipitated at the bottom would not reach the cells and thus the effective NP concentration would be dramatically reduced [88]. In contrast, in conventional geometry, in which the culture medium is on top of the cells, a reduced colloidal stability leads to the precipitation of NP agglomerates onto the cells and, thus, to enhanced uptake, which can influence the cell viability negatively [89]. Such different exposure scenarios are highly relevant for the prediction of NP interactions, for instance, in the human body or in ecotoxicology. Some NPs have been mistaken to elicit limited to no adverse effects upon zebrafish assays, as they had precipitated to the bottom, and thus, the fish had not been directly exposed to them. After correct solubilization, however, the same NPs turned out to be highly detrimental to zebrafish health [90]. Colloidal stability does not only interfere with size but also with other parameters such as shape. An agglomerated bundle of sharp NPs may no longer be "sharp". Thus, colloidal stability is the paramount parameter to consider for all correlations between the NP–cell interactions and the physicochemical properties of the NPs.

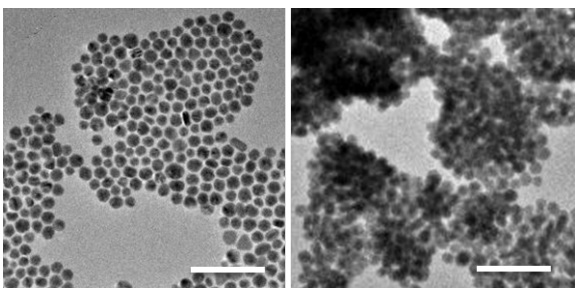

Figure 7: TEM images of a) dispersed and b) agglomerated Au NPs. The scale bars correspond to 100 nm. Adopted with permission from [30]. Copyright 2014 Royal Society of Chemistry.

Reports, in which no characterization of colloidal properties has been performed, therefore have to be regarded very critically. Unfortunately, many NPs are not colloidally stable in cell culture media [91]. The reason is that many NPs are stabilized by charge (in contrast to stabilization through steric repulsion). Salt (in particular NaCl, which always is present at high concentration) in the media screens the NP charge and thus can cause agglomeration [92]. Consequently, data which demonstrate that NPs are colloidally stable in water do not provide any proof that the same NPs also will be stable in cell culture media. Besides salt, proteins are another key compound of (serum-containing) cell media. As discussed later in more detail, proteins adsorb to the surface of NPs, forming the so-called protein corona [93,94], which in fact can increase or reduce colloidal stability [95,96]. Thus, characterization of colloidal stability and other physicochemical properties of NPs needs to be carried out under the same conditions under which later on cells are incubated with the NPs (i.e., in the respective cell culture media [86,97,98]). Obviously, NPs also should be appropriately purified [99], as otherwise effects from impurities rather than from the NPs themselves cannot be excluded. Unfortunately, for unstable NPs (e.g., for NPs to which the organic surface capping is only loosely attached) purification can trigger a loss of colloidal stability and thus agglomeration [14]. As lack of colloidal stability can overrule the other parameters, the following discussion about dependencies of other parameters is done assuming colloidally stable NPs. Uptake of NPs into the cells clearly depends on the size of the NPS. In general, smaller NPs are incorporated by cells faster than bigger ones, though there is some kind of size limit, i.e., the trend does not continue down to ultrasmall NPs [40,100]. As mentioned, upon endocytosis NPs are first wrapped by cellular membrane. Due to intrinsic stiffness and other parameters for membrane bending the radii of curvature cannot become infinitely small, and thus, there is an optimal NP size [101,102]. Excluding ultra-small NPs (smaller than 2–3 nm), smaller NP (smaller than 20–25 nm) are internalized readily in endosomes with most rapid kinetics [103]. Larger NPs (smaller than 60–70 nm) are internalized with lower kinetics to the extent that they are largely associated to the cell membrane over the time courses that see an intake of smaller NPS [62]. This has also been shown in fixed, permeabilized cells (to eliminate cell uptake machinery and pathways) to directly assess the size restrictions of plasma and intracellular membrane barriers on NP passage [104]. In contrast, ultrasmall NPs may be small enough to become membrane-permeable and thus bypass endocytotic uptake. Size-dependent uptake has also been reported for in vivo scenarios [105]. However, in particular for statements concerning size-dependent internalization, the experimental size determination of NP is important. Unfortunately, this is not a straightforward task, as different techniques measure different types of sizes. TEM only provides the geometric size of the NP core which has sufficient contrast, but organic surface cappings are typically not included [14]. In solution there is adsorption of counter ions to the NP surface [106,107] and organic surface coatings can swell, which results in hydrodynamic diameters larger than the core diameters as determined with TEM. There are several techniques for determining the hydrodynamic diameters of NPs [108], of which dynamic light scattering (DLS) might be the most common approach. All techniques have their limitations, and it is always helpful to know the measuring principle they are based on. DLS, for example, is based on calculating autocorrelation functions of the light-scattering signal of the solution. In order to obtain quantitative values, these autocorrelation data need to be fitted with a model, which is, for example, often done by assuming free diffusion of three NP species of different size. Thus, the results are based on the model (which is hidden as "black-box" in the software). To give an example, in case three species are assumed one always will obtain three peaks in the size distribution spectra, even though the sample may contain more different NP species. From the model, diffusion coefficients are yielded as fit parameters, which can be converted to hydrodynamic diameters by the Stokes–Einstein relation. As NPs of larger size also scatter light much more than smaller NPs, the results for DLS-derived size distributions also are quite different depending on whether number or intensity distributions are reported. Thus, simply taking the mean hydrodynamic diameter as displayed by commercial set-ups is prone to errors [109]. Calibration standards of NPs of known size are always a good help to benchmark size measurements and it is highly beneficial to apply several techniques in parallel [108-110]. By applying existing techniques correctly, the hydrodynamic diameters of NPs can be determined with remarkable accuracy, in particular if relative size changes are determined. Detection can be sensitive enough to resolve size-changes due to the attachment of individual macromolecules to the NPs [84,85,111,112]. Besides size, also shape has been proven to modulate the NP uptake of cells. In general, elongated, sharp NPs (i.e., NPs with a prolate spheroid shape) enter cells better than flatter NPs (i.e., NPs with an oblate spheroid shape). This however does no longer hold for very long fibers with high aspect ratios [100]. Flattening of NPs has been used, for example, to reduce NP uptake by cells in a way that flat NPs just adhere to the plasma cell membrane like a “backpack”, without being internalized, in contrast to spherical NPs that are readily incorporated [113,114]. Concerning a third parameter, charged NPs usually are internalized more efficiently than neutral ones, presumably due to enhanced charge-mediated adhesion to the outer cell membrane. Note that the charge pattern of the plasma cell membrane is patchy, and thus, while the overall net charge of cells is negative, there are plenty of positively charged domains. However, due to the overall

negative net charge, positively charged NPs are typically incorporated more efficiently by cells than negatively charged ones [65,97,115-119]. Indeed, the current consensus is that positive charges on NPs, such as those provided by the TAT peptide or surface functionalization, interact initially with the negatively charged heparan sulfate proteoglycan groups on the exterior of the cells. This allows them to then be present on the plasma cell membrane as endocytosis starts. Thus, while details may be very complex, clearly some tendencies for which physicochemical parameters enhance the spontaneous endocytosis of NPs can be given. In general, small, elongated, and positively charged NPs are incorporated preferentially to big, flat, and uncharged NPs. Dependency on other physicochemical parameters such as stiffness [120] has not been investigated extensively yet.

The role of the protein corona

In serum-containing media or inside cells all different types of biologically relevant molecules adsorb to the surface of NPs. i) Ions such as H^+, Na^+, K^+ or Ca^{2+} in the case of negatively charged NPs, or Cl^- in the case of positively charged NPs adsorb to the NPs. As a consequence of counter ion adsorption the local ion concentration around the NPs surface is different from the bulk [54,87,106,107]. ii) Also nucleic acids, such as mRNA or siRNA, which are negatively charged due to their phosphate groups attach to positively charged NPs [121,122]. iii) Lipids present in membranes or second-messenger lipids wrap around NPs driven by hydrophilic/hydrophobic interaction and often result in formation of micelles [123,124]. iv) Thiols, present in glutathione or reduced proteins bind to the surface of noble metal NPs, in particular to Au NPs [125,126]. v) Proteins, in general, tend to adsorb to surfaces, which is also true on the nanometer scale. Adsorption of albumin is, for example, an integral part of opsonization [127,128]. The proteins adsorbed to the surface of NPs are typically termed protein corona [93,94]. The protein corona has a significant impact on how NPs interact with cells and thus will be discussed in the following in more detail. NPs can, in principle, be synthesized in water without any organic surface coating, for example by laser ablation [129-131]. However, also to NPs just stabilized by their surface charge (which can be directly on the inorganic surface) proteins will adsorb in serum-containing cell media and in this way can provide additional colloidal stability [129]. Therefore, there are no "naked" NPs in serum-containing cell culture media and inorganic NP cores are always surrounded by an organic coating [14]. Adsorbed proteins can significantly alter the surface properties of NPs and are of key importance in defining the biological identity of NPs [132,133]. The corona formed around NPs is what the cell will “see” primarily, though certainly also the original properties of the underlying NPs determine interactions with the cells [97]. In general, adsorbed proteins "smear out" differences in the surface chemistry between different NPs. Thus, typically two different types of NPs show more pronounced differences in their interaction with cells in case exposure is done in serum-free media (i.e., without proteins) rather than in serum-containing media [97]. The effect of ligands immobilized on the surface of NPs designated for ligand–receptor-mediated uptake is diminished by the protein corona, which partly overcoats the ligands [134]. However, due to the fact that specific targeting still is possible [84], enough ligands still are biologically active. For highly defined NPs, such as nearly monodisperse NPs overcoated with a shell of an amphiphilic polymer [135], the corona formed by special model proteins can be surprisingly well organized. By using fluorescence correlation spectroscopy (FCS), Röcker et al. investigated the adsorption of human serum albumin onto FePt NPs and found clear evidence that the proteins formed a monolayer on the surface of the NP [136]. Additional FCS studies by using other important serum proteins invariably confirmed the formation of monolayer. The thickness of the monolayer could be related to the molecular dimensions of the adsorbed protein determined by X-ray diffraction. All proteins studied were found to adsorb in a specific orientation determined by local charge distributions on the protein surface [20,137,138]. However, adsorption of proteins to the surface of NPs is not only driven by the basic physicochemical properties of the NP such as size, shape, surface charge, but also by other parameters such as the incubation temperature [139]. While model systems involving only one type of NPs and one type of protein help to analytically quantify protein adsorption, such as by determining binding constants [30,136], the biological reality is more complex. Serum-containing cell culture media comprise hundreds of different proteins. To make it worse to analyze, protein adsorption is also a dynamic process. Thus, proteins which are initially bound to the NP surface can later be replaced by others [140,141], which also is referred to as the Vroman effect [142]. It has been shown, for example, that surfactant lipids bound on multiwall carbon nanotubes are replaced with blood plasma proteins after a subsequent incubation [143]. Mass spectrometry is an invaluable tool for quantifying the amounts of different adsorbed protein species [140,141]. The dynamic exchange of proteins, induced by their different adsorption kinetics and affinities to the NP surface is reflected in the discrimination between "soft" and "hard" corona [144,145]. The initial, soft corona is formed by the most abundant proteins, which are then replaced by the high-affinity proteins to yield the hard corona. It has been suggested that differences for different protein species can be characterized by their dissociation constants [30]. In a simple model the dissociation constant tells which protein concentration is required to saturate half of the NP surface with proteins under equilibrium conditions [30]. With simple treatments such as the Hill Model

[146] one may characterize the protein corona around NPs with only a few parameters, which would be a great help in comparing results obtained with different systems, thus allowing for a more comprehensive understanding. While the protein corona around NPs has been heavily investigated these data ultimately are only relevant for the first interaction of NPs with cells. After spontaneous endocytosis NPs are inside intracellular vesicles. This imposes a completely different environment than that of the extracellular medium, in particular low pH, presence of endo-/lysosomal enzymes, and different reducing agents [147]. Thus, after NP uptake the protein corona around NPs may change significantly. The original proteins can be displaced by other intracellular proteins, and even more severe, part of the original protein corona may be digested enzymatically [44,45,148,149]. Changes of the protein corona in turn may also alter the physicochemical properties (such as colloidal stability) of the NPs [96]. In this manner, for a full understanding of NP interaction with cells along the pathway of NP uptake the physicochemical characterization of NPs should also be done intracellularly, which, however, is complicated. This opens up a window for future research efforts.

Toxic effects of NPs

NPs clearly can trigger toxic effects in cells such as cytotoxicity, oxidative stress, (pro-)inflammation, and genotoxicity [150-152]. While again the detailed mechanisms are very complex and by far not understood in a comprehensive way, yet again there are certain characteristic features [153]. Toxic effects can result from the NPs themselves (e.g., by their catalytic surface or by their organic coating, such as in the case of cetyltrimethylammonium bromide (CTAB), a surfactant commonly used to synthesize gold nanorods) or by ions released from the NPs [154,155]. Ion release from certain materials such as Ag, ZnO, or CdSe is in particular triggered by the highly acidic pH in endo-/lysosomal compartments [156]. In both cases adverse biological effects are typically correlated with the production of reactive oxygen species (ROS) [157,158]. Also membrane damage plays a decisive role. In case of dissolvable NPs, the extent to which toxicity originates from the NPs themselves and to which extent from released ions is still subject to an intense scientific debate. Unfortunately, it is experimentally complicated to separate both effects. Even if before exposure all free ions were removed from the NP solution, inside cells new ions would be released. Thus, it is virtually impossible to have cells exposed exclusively to NPs without free ions [87]. One may argue that on the other hand cells could be exposed just to the free ions. While this is true, exposure to free ions will result in different intracellular ion distributions than the one obtained by ions which have been released from the NPs intracellularly, which again complicates direct comparison. Physicochemical properties can be, in some way, correlated with NP toxicity. In other words, reporting toxicity without accompanying in-depth NP characterization is not very useful concerning a detailed understanding of the mechanism. Surface coatings and impurities in the NPs can play an important role. Thus, also the coatings alone, as well as potential impurities need to be investigated towards potential toxic effect in control experiments. If only the physicochemical properties of "pure" NPs are considered, NPs with low colloidal stability have bigger effective sizes, thus are internalized to a larger extent, and thus typically have a greater adverse biological impact [154]. In order to account for concentration effects, it is advisable to correlate toxicity with particle internalization by using adequate methods. Enhanced uptake is one major reason (amongst others) why positively charged NPs (which are incorporated to a higher extent) elicit an increased adverse cellular effect compared to negatively charged ones [97,117,118]. This opens a dilemma. While in general, positive charge is better for enhanced uptake, too much positive charge becomes so toxic that it outweighs the added benefit of enhanced uptake. Thus, for delivery applications an optimum between both effects has to be found. This opens up another important point about the biological impact of NPs that merits discussion. There is a big difference between the use of NPs for cellular labeling or biosensing studies in research, as opposed to any therapeutic (in vivo) utility, and the two should never be thought of together or directly compared. It was, for example, recently shown that semiconductor quantum dot NPs (QDs) were unable to elicit a more negative biological effect when used for cellular labeling than a panel of dyes commonly used for the same intrinsic purposes [159]. Along with this, often transformed and immortalized cell lines are used in biological research, meaning that they are essentially cancerous. Thus, what appears to be adverse biological impact in these experiments has to be qualified with this context in mind. For cellular labeling, perhaps, there is the need for a particular experiment that should drive the issue of toxicity. If the use is specifically for in vitro labeling, tracking or sensing, there are multiple studies that have shown that over the time course required to perform such studies, the impact on cellular viability/proliferation at appropriate NP concentrations is minimal and is often comparable to or even less impactful than the use of traditional materials designed for the same purpose [159]. In this case "chronic toxicity" does not play a role, as the experiment is terminated before such an effect may occur. In contrast, for in vivo delivery one has to consider that NPs will remain in the organism over extended periods of time [160], and thus, benefits of treatment have to be weighted with long-term toxic effects [161]. Consequently, toxicity of NPs always has to be seen in the context of the applications the NPs are used for, but furthermore, the potential accidental exposure beyond the application has to be considered and its risk has to be assessed. In the

context of this review we have focused on in vitro studies. The advantage of such studies is the easy screening capability and the possibility to monitor in detail biomolecular pathways and changes in gene expression as a measure of a possible biologically adverse response. In case NP toxicity is investigated in a comprehensive study, however, involvement of in vivo experiments is crucial.

Conclusion

Due to their interesting functional properties, numerous applications of NPs exist, e.g., plasmonic NPs [2,75], magnetic NPs [162,163] or fluorescent NPs [164]. For optimizing NP properties for biological applications, an understanding of their interaction with mammalian cells needs to be gained. However, the interaction of NPs with cells is complex due to the many different types of NPs, cells, and exposure scenarios being used within the field. Still, one may make an attempt to reduce details to very general statements, in order to highlight some essential elements, which was the motivation for this review.

Endocytosis is the common route of NP uptake. NPs which strongly interact with the cell plasma membrane are also internalized more efficiently. Hereby differences in uptake are not digital (i.e., "yes" or "no"), but rather are based on different concentration-dependent kinetics. After internalization NPs inside intracellular vesicles are in an environment (acidic pH, enzymes) completely different from that in the cytosol and the extracellular space, which can modify their properties. The translocation of the NPs from these vesicles to the cytosol is a current challenge, which is referred to as endosomal escape dilemma. Uptake studies best should involve a quantitative distribution analysis. While endocytotic uptake of NPs has been extensively investigated, the eventual loss of internalized NPs as a result of mitotic division, NP exocytosis, or NP transcytosis on the other hand has not been comprehensively studied yet. Cellular uptake studies of NPs require as much characterization of the NP material as currently possible. However, many physicochemical properties of NPs such as size, shape, charge, and colloidal stability are highly entangled, which complicates analysis. Analysis of physicochemical properties should be always performed in the incubation medium in which the uptake of NPs by cells is studied. The incubation medium can for example modify the colloidal stability of the NPs. Colloidal stability does not only interfere with size but also with other parameters such as shape. In general, small, elongated, and positively charged NPs are incorporated preferentially to big, flat, and uncharged NPs.

Acknowledgements

This work and a large fraction of quoted work by WJP were supported by the German Research Foundation (DFG, SPP 1313, Project PA794/4-2) and this review represents the final report of this project. The authors are grateful to Dr. Torsten Hotopp from the DFG for managing and guiding the SPP 1313 funding initiative. BP acknowledges a fellowship from the Alexander von Humboldt Foundation. QZ acknowledges a fellowship from the Chinese Scholarship Council (CSC). MGS acknowledges a fellowship from the Youssef Jameel Foundation. JBD and ILM acknowledge the NRL NSI and DTRA for support. GUN acknowledges the DFG for support (DFG grants NI291/7 and NI291/8).

References

1. Verderio, P.; Avvakumova, S.; Alessio, G.; Bellini, M.; Colombo, M.; Galbiati, E.; Mazzucchelli, S.; Avila, J. P.; Santini, B.; Prosperi, D. *Adv. Healthcare Mater.* **2014,** *3,* 957–976. doi:10.1002/adhm.201300602
2. Sperling, R. A.; Rivera Gil, P.; Zhang, F.; Zanella, M.; Parak, W. J. *Chem. Soc. Rev.* **2008,** *37,* 1896–1908. doi:10.1039/b712170a
3. Rivera Gil, P.; Parak, W. J. *ACS Nano* **2008,** *2,* 2200–2205. doi:10.1021/nn800716j
4. Peteiro-Cartelle, J.; Rodríguez-Pedreira, M.; Zhang, F.; Rivera Gil, P.; del Mercato, L. L.; Parak, W. J. *Nanomedicine* **2009,** *4,* 967–979. doi:10.2217/nnm.09.84
5. Bar-Ilan, O.; Chuang, C. C.; Schwahn, D. J.; Yang, S.; Joshi, S.; Pedersen, J. A.; Hamers, R. J.; Peterson, R. E.; Heideman, W. *Environ. Sci. Technol.* **2013,** *47,* 4726–4733. doi:10.1021/es304514r
6. Borm, P. J. A.; Robbins, D.; Haubold, S.; Kuhlbusch, T.; Fissan, H.; Donaldson, K.; Schins, R.; Stone, V.; Kreyling, W.; Lademann, J.; Krutmann, J.; Warheit, D.; Oberdorster, E. *Part. Fibre Toxicol.* **2006,** *3,* No. 11. doi:10.1186/1743-8977-3-11
7. Lewinski, N.; Colvin, V.; Drezek, R. *Small* **2008,** *4,* 26–49. doi:10.1002/smll.200700595
8. Parak, W. J. *Science* **2011,** *334,* 1359–1360. doi:10.1126/science.1215080
9. Lin, C.-A. J.; Yang, T.-Y.; Lee, C.-H.; Huang, S. H.; Sperling, R. A.; Zanella, M.; Li, J. K.; Shen, J.-L.; Wang, H.-H.; Yeh, H.-I.; Parak, W. J.; Chang, W. H. *ACS Nano* **2009,** *3,* 395–401. doi:10.1021/nn800632j
10. Pandey, A.; Roy, M. K.; Pandey, A.; Zanella, M.; Sperling, R. A.; Parak, W. J.; Samaddar, A. B.; Verma, H. C. *IEEE Trans. NanoBiosci.* **2009,** *8,* 43–50. doi:10.1109/TNB.2009.2017316
11. Algar, W. R.; Prasuhn, D. E.; Stewart, M. H.; Jennings, T. L.; Blanco-Canosa, J. B.; Dawson, P. E.; Medintz, I. L. *Bioconjugate Chem.* **2011,** *22,* 825–858. doi:10.1021/bc200065z
12. Sperling, R. A.; Parak, W. J. *Philos. Trans. R. Soc. London, Ser. A* **2010,** *368,* 1333–1383. doi:10.1098/rsta.2009.0273
13. Sapsford, K. E.; Algar, W. R.; Berti, L.; Gemmill, K. B.; Casey, B. J.; Oh, E.; Stewart, M. H.; Medintz, I. L. *Chem. Rev.* **2013,** *113,* 1904–2074. doi:10.1021/cr300143v
14. Rivera Gil, P.; Jimenez de Aberasturi, D.; Wulf, V.; Pelaz, B.; Del Pino, P.; Zhao, Y.; De La Fuente, J. M.; Ruiz De Larramendi, I.; Rojo, T.; Liang, X.-J.; Parak, W. J. *Acc. Chem. Res.* **2013,** *46,* 743–749. doi:10.1021/ar300039j
15. Auffan, M.; Rose, J.; Bottero, J.-Y.; Lowry, G. V.; Jolivet, J.-P.; Wiesner, M. R. *Nat. Nanotechnol.* **2009,** *4,* 634–641. doi:10.1038/nnano.2009.242
16. Sardar, R.; Funston, A. M.; Mulvaney, P.; Murray, R. W. *Langmuir* **2009,** *25,* 13840–13851. doi:10.1021/la9019475

17. Goesmann, H.; Feldmann, C. *Angew. Chem., Int. Ed.* **2010,** *49,* 1362–1395. doi:10.1002/anie.200903053
18. Medintz, I. *Nat. Mater.* **2006,** *5,* 842. doi:10.1038/nmat1776
19. Treuel, L.; Jiang, X.; Nienhaus, G. U. *J. R. Soc., Interface* **2012,** *10,* 20120939. doi:10.1098/rsif.2012.0939
20. Jiang, X.; Weise, S.; Hafner, M.; Röcker, C.; Zhang, F.; Parak, W. J.; Nienhaus, G. U. *J. R. Soc., Interface* **2010,** *7* (Suppl. 1), S5–S13. doi:10.1098/rsif.2009.0272.focus
21. Doiron, A. L.; Clark, B.; Rinker, K. D. *Biotechnol. Bioeng.* **2011,** *108,* 2988–2998. doi:10.1002/bit.23253
22. Li, Y.; Yue, T.; Yang, K.; Zhang, X. *Biomaterials* **2012,** *33,* 4965–4973. doi:10.1016/j.biomaterials.2012.03.044
23. Muñoz Javier, A.; Kreft, O.; Semmling, M.; Kempter, S.; Skirtach, A. G.; Bruns, O. T.; del Pino, P.; Bedard, M. F.; Rädler, J.; Käs, J.; Plank, C.; Sukhorukov, G. B.; Parak, W. J. *Adv. Mater.* **2008,** *20,* 4281–4287. doi:10.1002/adma.200703190
24. Antony, A. C. *Annu. Rev. Nutr.* **1996,** *16,* 501–521. doi:10.1146/annurev.nu.16.070196.002441
25. Ding, H.-m.; Ma, Y.-q. *Biomaterials* **2012,** *33,* 5798–5802. doi:10.1016/j.biomaterials.2012.04.055
26. Avvakumova, S.; Colombo, M.; Tortora, P.; Prosperi, D. *Trends Biotechnol.* **2014,** *32,* 11–20. doi:10.1016/j.tibtech.2013.09.006
27. Ahrens, E. T.; Feili-Hariri, M.; Xu, H.; Genove, G.; Morel, P. A. *Magn. Reson. Med.* **2003,** *49,* 1006–1013. doi:10.1002/mrm.10465
28. Tassa, C.; Duffner, J. L.; Lewis, T. A.; Weissleder, R.; Schreiber, S. L.; Koehler, A. N.; Shaw, S. Y. *Bioconjugate Chem.* **2010,** *21,* 14–19. doi:10.1021/bc900438a
29. Muñoz Javier, A.; Kreft, O.; Piera Alberola, A.; Kirchner, C.; Zebli, B.; Susha, A. S.; Horn, E.; Kempter, S.; Skirtach, A. G.; Rogach, A. L.; Rädler, J.; Sukhorukov, G. B.; Benoit, M.; Parak, W. J. *Small* **2006,** *2,* 394–400. doi:10.1002/smll.200500282
30. del Pino, P.; Pelaz, B.; Zhang, Q.; Maffre, P.; Nienhaus, G. U.; Parak, W. J. *Mater. Horiz.* **2014,** *1,* 301–313. doi:10.1039/C3MH00106G
31. Lin, J.; Yu, Y.; Li, B.; Huang, H.; Lin, S.; Li, C.; Su, Y.; Feng, S.; Chen, G.; Li, Y.; Huang, Z.; Zeng, H.; Chen, R. *Laser Phys. Lett.* **2012,** *9,* 240–246. doi:10.1002/lapl.201110125
32. Orr, G.; Panther, D. J.; Cassens, K. J.; Phillips, J. L.; Tarasevich, B. J.; Pounds, J. G. *Toxicol. Appl. Pharmacol.* **2009,** *236,* 210–220. doi:10.1016/j.taap.2009.01.022
33. Zhang, H.; Xia, T.; Meng, H.; Xue, M.; George, S.; Ji, Z.; Wang, X.; Liu, R.; Wang, M.; France, B.; Rallo, R.; Damoiseaux, R.; Cohen, Y.; Bradley, K. A.; Zink, J. I.; Nel, A. E. *ACS Nano* **2011,** *5,* 2756–2769. doi:10.1021/nn200328m
34. Verma, A.; Stellacci, F. *Small* **2010,** *6,* 12–21. doi:10.1002/smll.200901158
35. Xiao, Y.; Forry, S. P.; Gao, X.; Holbrook, R. D.; Telford, W. G.; Tona, A. *J. Nanobiotechnol.* **2010,** *8,* No. 13. doi:10.1186/1477-3155-8-13
36. Clift, M. J. D.; Rothen-Rutishauser, B.; Brown, D. M.; Duffin, R.; Donaldson, K.; Proudfoot, L.; Guy, K.; Stone, V. *Toxicol. Appl. Pharmacol.* **2008,** *232,* 418–427. doi:10.1016/j.taap.2008.06.009
37. Soenen, S. J.; Manshian, B. B.; Abdelmonem, A. M.; Montenegro, J.-M.; Tan, S.; Balcaen, L.; Vanhaecke, F.; Brisson, A. R.; Parak, W. J.; De Smedt, S. C.; Braeckmans, K. *Part. Part. Syst. Charact.* **2014,** *31,* 794–800. doi:10.1002/ppsc.201300357
38. Lipka, M.; Semmler-Behnke, M.; Sperling, R. A.; Wenk, A.; Takenaka, S.; Schleh, C.; Kissel, T.; Parak, W. J.; Kreyling, W. G. *Biomaterials* **2010,** *31,* 6574–6581. doi:10.1016/j.biomaterials.2010.05.009
39. Gratton, S. E. A.; Ropp, P. A.; Pohlhaus, P. D.; Luft, J. C.; Madden, V. J.; Napier, M. E.; DeSimone, J. M. *Proc. Natl. Acad. Sci. U. S. A.* **2008,** *105,* 11613–11618. doi:10.1073/pnas.0801763105
40. Chithrani, B. D.; Chan, W. C. W. *Nano Lett.* **2007,** *7,* 1542–1550. doi:10.1021/nl070363y
41. Iversen, T.-G.; Skotland, T.; Sandvig, K. *Nano Today* **2011,** *6,* 176–185. doi:10.1016/j.nantod.2011.02.003
42. Grant, B. D.; Donaldson, J. G. *Nat. Rev. Mol. Cell Biol.* **2009,** *10,* 597–608. doi:10.1038/nrm2755
43. Saftig, P.; Klumperman, J. *Nat. Rev. Mol. Cell Biol.* **2009,** *10,* 623–635. doi:10.1038/nrm2745
44. Rivera-Gil, P.; De Koker, S.; De Geest, B. G.; Parak, W. J. *Nano Lett.* **2009,** *9,* 4398–4402. doi:10.1021/nl902697j
45. Chanana, M.; Rivera Gil, P.; Correa-Duarte, M. A.; Liz-Marzán, L. M.; Parak, W. J. *Angew. Chem., Int. Ed.* **2013,** *52,* 4179–4183. doi:10.1002/anie.201208019
46. Geiser, M.; Rothen-Rutishauser, B.; Kapp, N.; Schürch, S.; Kreyling, W.; Schulz, H.; Semmler, M.; Im Hof, V.; Heyder, J.; Gehr, P. *Environ. Health Perspect.* **2005,** *113,* 1555–1560. doi:10.1289/ehp.8006
47. Rothen-Rutishauser, B. M.; Schürch, S.; Haenni, B.; Kapp, N.; Gehr, P. *Environ. Sci. Technol.* **2006,** *40,* 4353–4359. doi:10.1021/es0522635
48. Rothen-Rutishauser, B.; Blank, F.; Mühlfeld, C.; Gehr, P. *Nanoparticle-Cell Membrane Interactions,* 2nd ed.; Informa Healthcare: New York, USA, 2009; pp 226–242.
49. Luccardini, C.; Yakovlev, A.; Gaillard, S.; van't Hoff, M.; Alberola, A. P.; Mallet, J.-M.; Parak, W. J.; Feltz, A.; Oheim, M. *J. Biomed. Biotechnol.* **2007,** No. 68963. doi:10.1155/2007/68963
50. Lin, J.; Alexander-Katz, A. *ACS Nano* **2013,** *7,* 10799–10808. doi:10.1021/nn4040553
51. Wang, T.; Bai, J.; Jiang, X.; Nienhaus, G. U. *ACS Nano* **2012,** *6,* 1251–1259. doi:10.1021/nn203892h
52. Semmling, M.; Kreft, O.; Muñoz Javier, A.; Sukhorukov, G. B.; Käs, J.; Parak, W. J. *Small* **2008,** *4,* 1763–1768. doi:10.1002/smll.200800596
53. Rivera Gil, P.; Nazarenus, M.; Ashraf, S.; Parak, W. J. *Small* **2012,** *8,* 943–948. doi:10.1002/smll.201101780
54. Zhang, F.; Lees, E.; Amin, F.; Rivera Gil, P.; Yang, F.; Mulvaney, P.; Parak, W. J. *Small* **2011,** *7,* 3113–3127. doi:10.1002/smll.201100608
55. Mitra, R. N.; Doshi, M.; Zhang, X.; Tyus, J. C.; Bengtsson, N.; Fletcher, S.; Page, B. D. G.; Turkson, J.; Gesquiere, A. J.; Gunning, P. T.; Walter, G. A.; Santra, S. *Biomaterials* **2012,** *33,* 1500–1508. doi:10.1016/j.biomaterials.2011.10.068
56. Panyam, J.; Zhou, W.-Z.; Prabha, S.; Sahoo, S. K.; Labhasetwar, V. *FASEB J.* **2002,** *16,* 1217–1226. doi:10.1096/fj.02-0088com
57. Fan, Y.; Li, C.; Cao, H.; Li, F.; Chen, D. *Biomaterials* **2012,** *33,* 4220–4228. doi:10.1016/j.biomaterials.2012.02.038
58. Bayles, A. R.; Chahal, H. S.; Chahal, D. S.; Goldbeck, C. P.; Cohen, B. E.; Helms, B. A. *Nano Lett.* **2012,** *10,* 4086–4092. doi:10.1021/nl102172j

59. Boeneman, K.; Delehanty, J. B.; Blanco-Canosa, J. B.; Susumu, K.; Stewart, M. H.; Oh, E.; Huston, A. L.; Dawson, G.; Ingale, S.; Walters, R.; Domowicz, M.; Deschamps, J. R.; Algar, W. R.; DiMaggio, S.; Manono, J.; Spillmann, C. M.; Thompson, D.; Jennings, T. L.; Dawson, P. E.; Medintz, I. L. *ACS Nano* **2013,** *7,* 3778–3796. doi:10.1021/nn400702r
60. Delehanty, J. B.; Bradburne, C. E.; Boeneman, K.; Susumu, K.; Farrell, D.; Mei, B. C.; Blanco-Canosa, J. B.; Dawson, G.; Dawson, P. E.; Mattoussi, H.; Medintz, I. L. *Integr. Biol.* **2010,** *2,* 265–277. doi:10.1039/c0ib00002g
61. Medintz, I. L.; Pons, T.; Delehanty, J. B.; Susumu, K.; Brunel, F. M.; Dawson, P. E.; Mattoussi, H. *Bioconjugate Chem.* **2008,** *19,* 1785–1795. doi:10.1021/bc800089r
62. Oh, E.; Delehanty, J. B.; Sapsford, K. E.; Susumu, K.; Goswami, R.; Blanco-Canosa, J. B.; Dawson, P. E.; Granek, J.; Shoff, M.; Zhang, Q.; Goering, P. L.; Huston, A.; Medintz, I. L. *ACS Nano* **2011,** *5,* 6434–6448. doi:10.1021/nn201624c
63. Nativo, P.; Prior, I. A.; Brust, M. *ACS Nano* **2008,** *2,* 1639–1644. doi:10.1021/nn800330a
64. Yang, L.; Shang, L.; Nienhaus, G. U. *Nanoscale* **2013,** *5,* 1537–1543. doi:10.1039/c2nr33147k
65. Schweiger, C.; Hartmann, R.; Zhang, F.; Parak, W. J.; Kissel, T. H.; Rivera Gil, P. *J. Nanobiotechnol.* **2012,** *10,* No. 28. doi:10.1186/1477-3155-10-28
66. Delehanty, J. B.; Blanco-Canosa, J. B.; Bradburne, C. E.; Susumu, K.; Stewart, M. H.; Prasuhn, D. E.; Dawson, P. E.; Medintz, I. L. *Chem. Commun.* **2013,** *49,* 7878–7880. doi:10.1039/c3cc42781a
67. Lehmann, A. D.; Parak, W. J.; Zhang, F.; Ali, Z.; Röcker, C.; Nienhaus, G. U.; Gehr, P.; Rothen-Rutishauser, B. *Small* **2010,** *6,* 753–762. doi:10.1002/smll.200901770
68. Brandenberger, C.; Mühlfeld, C.; Ali, Z.; Lenz, A.-G.; Schmid, O.; Parak, W. J.; Gehr, P.; Rothen-Rutishauser, B. *Small* **2010,** *6,* 1669–1678. doi:10.1002/smll.201000528
69. Mühlfeld, C.; Mayhew, T. M.; Gehr, P.; Rothen-Rutishauser, B. *J. Aerosol Med.* **2007,** *20,* 395–407. doi:10.1089/jam.2007.0624
70. Rothen-Rutishauser, B.; Kuhn, D. A.; Ali, Z.; Gasser, M.; Amin, F.; Parak, W. J.; Vanhecke, D.; Fink, A.; Gehr, P.; Brandenberger, C. *Nanomedicine* **2014,** *9,* 607–621. doi:10.2217/nnm.13.24
71. Canton, I.; Battaglia, G. *Chem. Soc. Rev.* **2012,** *41,* 2718–2739. doi:10.1039/c2cs15309b
72. Studer, A. M.; Limbach, L. K.; Van Duc, L.; Krumeich, F.; Athanassiou, E. K.; Gerber, L. C.; Moch, H.; Stark, W. J. *Toxicol. Lett.* **2010,** *197,* 169–174. doi:10.1016/j.toxlet.2010.05.012
73. Ducongé, F.; Pons, T.; Pestourie, C.; Hérin, L.; Thézé, B.; Gombert, K.; Mahler, B.; Hinnen, F.; Kühnast, B.; Dollé, F.; Dubertret, B.; Tavitian, B. *Bioconjugate Chem.* **2008,** *19,* 1921–1926. doi:10.1021/bc800179j
74. Zhao, Y.; Howe, J. L. C.; Yu, Z.; Leong, D. T.; Chu, J. J. H.; Loo, J. S. C.; Ng, K. W. *Small* **2013,** *9,* 387–392. doi:10.1002/smll.201201363
75. Muñoz Javier, A.; del Pino, P.; Bedard, M. F.; Ho, D.; Skirtach, A. G.; Sukhorukov, G. B.; Plank, C.; Parak, W. J. *Langmuir* **2008,** *24,* 12517–12520. doi:10.1021/la802448z
76. Symens, N.; Soenen, S. J.; Rejman, J.; Braeckmans, K.; De Smedt, S. C.; Remaut, K. *Adv. Drug Delivery Rev.* **2012,** *64,* 78–94. doi:10.1016/j.addr.2011.11.012
77. Parak, W. J.; Boudreau, R.; Le Gros, M.; Gerion, D.; Zanchet, D.; Micheel, C. M.; Williams, S. C.; Alivisatos, A. P.; Larabell, C. A. *Adv. Mater.* **2002,** *14,* 882–885. doi:10.1002/1521-4095(20020618)14:12<882::AID-ADMA882>3.0.CO;2-Y
78. Summers, H. D.; Rees, P.; Holton, M. D.; Brown, M. R.; Chappell, S. C.; Smith, P. J.; Errington, R. J. *Nat. Nanotechnol.* **2011,** *6,* 170–174. doi:10.1038/nnano.2010.277
79. Summers, H. D.; Brown, M. R.; Holton, M. D.; Tonkin, J. A.; Hondow, N.; Brown, A. P.; Brydson, R.; Rees, P. *ACS Nano* **2013,** *7,* 6129–6137. doi:10.1021/nn4019619
80. Pi, Q. M.; Zhang, W. J.; Zhou, G. D.; Liu, W.; Cao, Y. *BMC Biotechnol.* **2010,** *10,* No. 36. doi:10.1186/1472-6750-10-36
81. Ruan, G.; Agrawal, A.; Marcus, A. I.; Nie, S. *J. Am. Chem. Soc.* **2007,** *129,* 14759–14766. doi:10.1021/ja074936k
82. Bartczak, D.; Nitti, S.; Millar, T. M.; Kanaras, A. G. *Nanoscale* **2012,** *4,* 4470–4472. doi:10.1039/c2nr31064c
83. Blank, F.; Wehrli, M.; Lehmann, A.; Baum, O.; Gehr, P.; von Garnier, C.; Rothen-Rutishauser, B. M. *Immunobiology* **2011,** *216,* 86–95. doi:10.1016/j.imbio.2010.02.006
84. Colombo, M.; Mazzucchelli, S.; Montenegro, J. M.; Galbiati, E.; Corsi, F.; Parak, W. J.; Prosperi, D. *Small* **2012,** *8,* 1492–1497. doi:10.1002/smll.201102284
85. Montenegro, J.-M.; Grazu, V.; Sukhanova, A.; Agarwal, S.; de la Fuente, J. M.; Nabiev, I.; Greiner, A.; Parak, W. J. *Adv. Drug Delivery Rev.* **2013,** *65,* 677–688. doi:10.1016/j.addr.2012.12.003
86. Sapsford, K. E.; Tyner, K. M.; Dair, B. J.; Deschamps, J. R.; Medintz, I. L. *Anal. Chem.* **2011,** *83,* 4453–4488. doi:10.1021/ac200853a
87. Carrillo-Carrión, C.; Nazarenus, M.; Sánchez Paradinas, S.; Carregal-Romero, S.; Almendral, M. J.; Fuentes, M.; Pelaz, B.; del Pino, P.; Hussain, I.; Clift, M. J. D.; Rothen-Rutishauser, B.; Liang, X.-J.; Parak, W. J. *Curr. Opin. Chem. Eng.* **2014,** *4,* 88–96. doi:10.1016/j.coche.2013.11.006
88. Cho, E. C.; Zhang, Q.; Xia, Y. *Nat. Nanotechnol.* **2011,** *6,* 385–391. doi:10.1038/nnano.2011.58
89. Kirchner, C.; Liedl, T.; Kudera, S.; Pellegrino, T.; Muñoz Javier, A.; Gaub, H. E.; Stölzle, S.; Fertig, N.; Parak, W. J. *Nano Lett.* **2005,** *5,* 331–338. doi:10.1021/nl047996m
90. Kim, K.-T.; Truong, L.; Wehmas, L.; Tanguay, R. L. *Nanotechnology* **2013,** *24,* 115101. doi:10.1088/0957-4484/24/11/115101
91. Izak-Nau, E.; Voetz, M.; Eiden, S.; Duschl, A.; Puntes, V. F. *Part. Fibre Toxicol.* **2013,** *10,* No. 56. doi:10.1186/1743-8977-10-56
92. Pellegrino, T.; Kudera, S.; Liedl, T.; MuñozJavier, A.; Manna, L.; Parak, W. J. *Small* **2005,** *1,* 48–63. doi:10.1002/smll.200400071
93. Cedervall, T.; Lynch, I.; Lindman, S.; Berggård, T.; Thulin, E.; Nilsson, H.; Dawson, K. A.; Linse, S. *Proc. Natl. Acad. Sci. U. S. A.* **2007,** *104,* 2050–2055. doi:10.1073/pnas.0608582104
94. Lynch, I.; Cedervall, T.; Lundqvist, M.; Cabaleiro-Lago, C.; Linse, S.; Dawson, K. A. *Adv. Colloid Interface Sci.* **2007,** *134–135,* 167–174. doi:10.1016/j.cis.2007.04.021
95. Orts-Gil, G.; Natte, K.; Thiermann, R.; Girod, M.; Rades, S.; Kalbe, H.; Thünemann, A. F.; Maskos, M.; Österle, W. *Colloids Surf., B* **2013,** *108,* 110–119. doi:10.1016/j.colsurfb.2013.02.027
96. Gebauer, J. S.; Malissek, M.; Simon, S.; Knauer, S. K.; Maskos, M.; Stauber, R. H.; Peukert, W.; Treuel, L. *Langmuir* **2012,** *28,* 9673–9679. doi:10.1021/la301104a

97. Hühn, D.; Kantner, K.; Geidel, C.; Brandholt, S.; De Cock, I.; Soenen, S. J. H.; Rivera Gil, P.; Montenegro, J.-M.; Braeckmans, K.; Müllen, K.; Nienhaus, G. U.; Klapper, M.; Parak, W. J. *ACS Nano* **2013,** *7,* 3253–3263. doi:10.1021/nn3059295
98. Maiorano, G.; Sabella, S.; Sorce, B.; Brunetti, V.; Malvindi, M. A.; Cingolani, R.; Pompa, P. P. *ACS Nano* **2010,** *4,* 7481–7491. doi:10.1021/nn101557e
99. Kinnear, C.; Dietsch, H.; Clift, M. J. D.; Endes, C.; Rothen-Rutishauser, B.; Petri-Fink, A. *Angew. Chem., Int. Ed.* **2013,** *52,* 1934–1938. doi:10.1002/anie.201208568
100. Chithrani, B. D.; Ghazan, A. A.; Chan, W. C. W. *Nano Lett.* **2006,** *6,* 662–668. doi:10.1021/nl052396o
101. Tzlil, S.; Deserno, M.; Gelbart, W. M.; Ben-Shaul, A. *Biophys. J.* **2004,** *86,* 2037–2048. doi:10.1016/S0006-3495(04)74265-4
102. Deserno, M.; Bickel, T. *Europhys. Lett.* **2003,** *62,* 767–773. doi:10.1209/epl/i2003-00438-4
103. Zhang, S.; Li, J.; Lykotrafitis, G.; Bao, G.; Suresh, S. *Adv. Mater.* **2009,** *21,* 419–424. doi:10.1002/adma.200801393
104. Williams, Y.; Sukhanova, A.; Nowostawska, M.; Davies, A. M.; Mitchell, S.; Oleinikov, V.; Gun'ko, Y.; Nabiev, I.; Kelleher, D.; Volkov, Y. *Small* **2009,** *5,* 2581–2588. doi:10.1002/smll.200900744
105. Kreyling, W. G.; Hirn, S.; Möller, W.; Schleh, C.; Wenk, A.; Celik, G.; Lipka, J.; Schäffler, M.; Haberl, N.; Johnston, B. D.; Sperling, R.; Schmid, G.; Simon, U.; Parak, W. J.; Semmler-Behnke, M. *ACS Nano* **2014,** *8,* 222–233. doi:10.1021/nn403256v
106. Zhang, F.; Ali, Z.; Amin, F.; Feltz, A.; Oheim, M.; Parak, W. J. *ChemPhysChem* **2010,** *11,* 730–735. doi:10.1002/cphc.200900849
107. Riedinger, A.; Zhang, F.; Dommershausen, F.; Röcker, C.; Brandholt, S.; Nienhaus, G. U.; Koert, U.; Parak, W. J. *Small* **2010,** *6,* 2590–2597. doi:10.1002/smll.201000868
108. Sperling, R. A.; Liedl, T.; Duhr, S.; Kudera, S.; Zanella, M.; Lin, C.-A. J.; Chang, W. H.; Braun, D.; Parak, W. J. *J. Phys. Chem. C* **2007,** *111,* 11552–11559. doi:10.1021/jp070999d
109. Hagendorfer, H.; Kaegi, R.; Parlinska, M.; Sinnet, B.; Ludwig, C.; Ulrich, A. *Anal. Chem.* **2012,** *84,* 2678–2685. doi:10.1021/ac202641d
110. Hole, P.; Sillence, K.; Hannell, C.; Maguire, C. M.; Roesslein, M.; Suarez, G.; Capracotta, S.; Magdolenova, Z.; Horev-Azaria, L.; Dybowska, A.; Cooke, L.; Haase, A.; Contal, S.; Manø, S.; Vennemann, A.; Sauvain, J.-J.; Staunton, K. C.; Anguissola, S.; Luch, A.; Dusinska, M.; Korenstein, R.; Gutleb, A. C.; Wiemann, M.; Prina-Mello, A.; Riediker, M.; Wick, P. *J. Nanopart. Res.* **2013,** *15,* No. 2101. doi:10.1007/s11051-013-2101-8
111. Pellegrino, T.; Sperling, R. A.; Alivisatos, A. P.; Parak, W. J. *J. Biomed. Biotechnol.* **2007,** 26796. doi:10.1155/2007/26796
112. Sperling, R. A.; Pellegrino, T.; Li, J. K.; Chang, W. H.; Parak, W. J. *Adv. Funct. Mater.* **2006,** *16,* 943–948. doi:10.1002/adfm.200500589
113. Swiston, A. J.; Gilbert, J. B.; Irvine, D. J.; Cohen, R. E.; Rubner, M. F. *Biomacromolecules* **2010,** *11,* 1826–1832. doi:10.1021/bm100305h
114. Stoehr, L. C.; Gonzalez, E.; Stampfl, A.; Casals, E.; Duschl, A.; Puntes, V.; Oostingh, G. J. *Part. Fibre Toxicol.* **2011,** *8,* No. 36. doi:10.1186/1743-8977-8-36
115. Jiang, X.; Dausend, J.; Hafner, M.; Musyanovych, A.; Röcker, C.; Landfester, K.; Mailänder, V.; Nienhaus, G. U. *Biomacromolecules* **2010,** *11,* 748–753. doi:10.1021/bm901348z
116. Jiang, X.; Musyanovych, A.; Röcker, C.; Landfester, K.; Mailänder, V.; Nienhaus, G. U. *Nanoscale* **2011,** *3,* 2028–2035. doi:10.1039/c0nr00944j
117. Yang, S.-H.; Heo, D.; Park, J.; Na, S.; Suh, J.-S.; Haam, S.; Park, S. W.; Huh, Y.-M.; Yang, J. *Nanotechnology* **2012,** *23,* 505702. doi:10.1088/0957-4484/23/50/505702
118. Kim, S. T.; Saha, K.; Kim, C.; Rotello, V. M. *Acc. Chem. Res.* **2013,** *46,* 681–691. doi:10.1021/ar3000647
119. Albanese, A.; Tang, P. S.; Chan, W. C. W. *The Effect of Nanoparticle Size, Shape, and Surface Chemistry on Biological Systems;* Annual Review Of Biomedical Engineering, Vol. 14; Annual Reviews: Palo Alto, USA, 2012; pp 1–16.
120. Bédard, M. F.; Munoz-Javier, A.; Mueller, R.; del Pino, P.; Fery, A.; Parak, W. J.; Skirtach, A. G.; Sukhorukov, G. B. *Soft Matter* **2009,** *5,* 148–155. doi:10.1039/b812553h
121. Xia, T.; Kovochich, M.; Liong, M.; Meng, H.; Kabehie, S.; George, S.; Zink, J. I.; Nel, A. E. *ACS Nano* **2009,** *3,* 3273–3286. doi:10.1021/nn900918w
122. Su, X.; Fricke, J.; Kavanagh, D. G.; Irvine, D. J. *Mol. Pharmaceutics* **2011,** *8,* 774–787. doi:10.1021/mp100390w
123. Yue, T.; Wang, X.; Huang, F.; Zhang, X. *Nanoscale* **2013,** *5,* 9888–9896. doi:10.1039/c3nr02683c
124. Irvine, D. J. *Nat. Mater.* **2011,** *10,* 342–343. doi:10.1038/nmat3014
125. Larsson, J. A.; Nolan, M.; Greer, J. C. *J. Phys. Chem. B* **2002,** *106,* 5931–5937. doi:10.1021/jp014483k
126. Demers, L. M.; Mirkin, C. A.; Mucic, R. C.; Reynolds, R. A., III; Letsinger, R. L.; Elghanian, R.; Viswanadham, G. *Anal. Chem.* **2000,** *72,* 5535–5541. doi:10.1021/ac0006627
127. Moghimi, S. M.; Hunter, A. C.; Andresen, T. L. *Annu. Rev. Pharmacol. Toxicol.* **2012,** *52,* 481–503. doi:10.1146/annurev-pharmtox-010611-134623
128. Karmali, P. P.; Simberg, D. *Expert Opin. Drug Delivery* **2011,** *8,* 343–357. doi:10.1517/17425247.2011.554818
129. Rehbock, C.; Merk, V.; Gamrad, L.; Streubel, R.; Barcikowski, S. *Phys. Chem. Chem. Phys.* **2013,** *15,* 3057–3067. doi:10.1039/c2cp42641b
130. Menéndez-Manjón, A.; Wagener, P.; Barcikowski, S. *J. Phys. Chem. C* **2011,** *115,* 5108–5114. doi:10.1021/jp109370q
131. Barcikowski, S.; Mafune, F. *J. Phys. Chem. C* **2011,** *115,* 4985. doi:10.1021/jp111036a
132. Fadeel, B.; Feliu, N.; Vogt, C.; Abdelmonem, A. M.; Parak, W. J. *Wiley Interdiscip. Rev.: Nanomed. Nanobiotechnol.* **2013,** *5,* 111–129. doi:10.1002/wnan.1206
133. Kittler, S.; Greulich, C.; Gebauer, J. S.; Diendorf, J.; Treuel, L.; Ruiz, L.; Gonzalez-Calbet, J. M.; Vallet-Regi, M.; Zellner, R.; Köller, M.; Epple, M. *J. Mater. Chem.* **2010,** *20,* 512–518. doi:10.1039/b914875b
134. Monopoli, M. P.; Åberg, C.; Salvati, A.; Dawson, K. A. *Nat. Nanotechnol.* **2012,** *7,* 779–786. doi:10.1038/nnano.2012.207
135. Yakovlev, A. V.; Zhang, F.; Zulqurnain, A.; Azhar-Zahoor, A.; Luccardini, C.; Gaillard, S.; Mallet, J.-M.; Tauc, P.; Brochon, J.-C.; Parak, W. J.; Feltz, A.; Oheim, M. *Langmuir* **2009,** *25,* 3232–3239. doi:10.1021/la8038347
136. Röcker, C.; Pötzl, M.; Zhang, F.; Parak, W. J.; Nienhaus, G. U. *Nat. Nanotechnol.* **2009,** *4,* 577–580. doi:10.1038/nnano.2009.195
137. Maffre, P.; Nienhaus, K.; Amin, F.; Parak, W. J.; Nienhaus, G. U. *Beilstein J. Nanotechnol.* **2011,** *2,* 374–383. doi:10.3762/bjnano.2.43
138. Treuel, L.; Brandholt, S.; Maffre, P.; Wiegele, S.; Shang, L.; Nienhaus, G. U. *ACS Nano* **2014,** *8,* 503–513. doi:10.1021/nn405019v
139. Mahmoudi, M.; Abdelmonem, A. M.; Behzadi, S.; Clement, J. H.; Dutz, S.; Ejtehadi, M. R.; Hartmann, R.; Kantner, K.; Linne, U.; Maffre, P.; Metzler, S.; Moghadam, M. K.; Pfeiffer, C.; Rezaei, M.; Ruiz-Lozano, P.; Serpooshan, V.; Shokrgozar, M. A.; Nienhaus, G. U.; Parak, W. J. *ACS Nano* **2013,** *7,* 6555–6562. doi:10.1021/nn305337c

140. Tenzer, S.; Docter, D.; Rosfa, S.; Wlodarski, A.; Kuharev, J.; Rekik, A.; Knauer, S. K.; Bantz, C.; Nawroth, T.; Bier, C.; Sirirattanapan, J.; Mann, W.; Treuel, L.; Zellner, R.; Maskos, M.; Schild, H.; Stauber, R. H. *ACS Nano* **2011,** *5,* 7155–7167. doi:10.1021/nn201950e
141. Tenzer, S.; Docter, D.; Kuharev, J.; Musyanovych, A.; Fetz, V.; Hecht, R.; Schlenk, F.; Fischer, D.; Kiouptsi, K.; Reinhardt, C.; Landfester, K.; Schild, H.; Maskos, M.; Knauer, S. K.; Stauber, R. H. *Nat. Nanotechnol.* **2013,** *8,* 772–781. doi:10.1038/nnano.2013.181
142. Vroman, L. *Nature* **1962,** *196,* 476–477. doi:10.1038/196476a0
143. Gasser, M.; Rothen-Rutishauser, B.; Krug, H. F.; Gehr, P.; Nelle, M.; Yan, B.; Wick, P. *J. Nanobiotechnol.* **2010,** *8,* No. 31. doi:10.1186/1477-3155-8-31
144. Milani, S.; Bombelli, F. B.; Pitek, A. S.; Dawson, K. A.; Rädler, J. *ACS Nano* **2012,** *6,* 2532–2541. doi:10.1021/nn204951s
145. Liu, W.; Rose, J.; Plantevin, S.; Auffan, M.; Bottero, J.-Y.; Vidaud, C. *Nanoscale* **2013,** *5,* 1658–1668. doi:10.1039/c2nr33611a
146. Hill, A. V. *J. Physiol.* **1910,** *40,* iv–vii.
147. Sasmal, P. K.; Carregal-Romero, S.; Han, A. A.; Streu, C. N.; Lin, Z.; Namikawa, K.; Elliott, S. L.; Köster, R. W.; Parak, W. J.; Meggers, E. *ChemBioChem* **2012,** *13,* 1116–1120. doi:10.1002/cbic.201100719
148. Wang, F.; Yu, L.; Monopoli, M. P.; Sandin, P.; Mahon, E.; Salvati, A.; Dawson, K. A. *Nanomedicine* **2013,** *9,* 1159–1168. doi:10.1016/j.nano.2013.04.010
149. Lunov, O.; Syrovets, T.; Röcker, C.; Tron, K.; Nienhaus, G. U.; Rasche, V.; Mailänder, V.; Landfester, K.; Simmet, T. *Biomaterials* **2010,** *31,* 9015–9022. doi:10.1016/j.biomaterials.2010.08.003
150. Oberdörster, G.; Oberdörster, E.; Oberdörster, J. *Environ. Health Perspect.* **2005,** *113,* 823–839. doi:10.1289/ehp.7339
151. Oberdörster, G.; Stone, V.; Donaldson, K. *Nanotoxicology* **2007,** *1,* 2–25. doi:10.1080/17435390701314761
152. Maynard, A. D.; Aitken, R. J.; Butz, T.; Colvin, V.; Donaldson, K.; Oberdörster, G.; Philbert, M. A.; Ryan, J.; Seaton, A.; Stone, V.; Tinkle, S. S.; Tran, L.; Walker, N. J.; Warheit, D. B. *Nature* **2006,** *444,* 267–269. doi:10.1038/444267a
153. Clift, M. J. D.; Gehr, P.; Rothen-Rutishauser, B. *Arch. Toxicol.* **2011,** *85,* 723–731. doi:10.1007/s00204-010-0560-6
154. Caballero-Díaz, E.; Pfeiffer, C.; Kastl, L.; Rivera-Gil, P.; Simonet, B.; Valcárcel, M.; Jiménez-Lamana, J.; Laborda, F.; Parak, W. J. *Part. Part. Syst. Charact.* **2013,** *30,* 1079–1085. doi:10.1002/ppsc.201300215
155. Karlsson, H. L.; Cronholm, P.; Gustafsson, J.; Möller, L. *Chem. Res. Toxicol.* **2008,** *21,* 1726–1732. doi:10.1021/tx800064j
156. Kittler, S.; Greulich, C.; Diendorf, J.; Köller, M.; Epple, M. *Chem. Mater.* **2010,** *22,* 4548–4554. doi:10.1021/cm100023p
157. Hussain, S. M.; Hess, K. L.; Gearhart, J. M.; Geiss, K. T.; Schlager, J. J. *Toxicol. in Vitro* **2005,** *19,* 975–983. doi:10.1016/j.tiv.2005.06.034
158. AshaRani, P. V.; Low Kah Mun, G.; Hande, M. P.; Valiyaveettil, S. *ACS Nano* **2009,** *3,* 279–290. doi:10.1021/nn800596w
159. Bradburne, C. E.; Delehanty, J. B.; Boeneman Gemmill, K.; Mei, B. C.; Mattoussi, H.; Susumu, K.; Blanco-Canosa, J. B.; Dawson, P. E.; Medintz, I. L. *Bioconjugate Chem.* **2013,** *24,* 1570–1583. doi:10.1021/bc4001917
160. Ballou, B.; Lagerholm, B. C.; Ernst, L. A.; Bruchez, M. P.; Waggoner, A. S. *Bioconjugate Chem.* **2004,** *15,* 79–86. doi:10.1021/bc034153y
161. Liu, J.; Erogbogbo, F.; Yong, K.-T.; Ye, L.; Liu, J.; Hu, R.; Chen, H.; Hu, Y.; Yang, Y.; Yang, J.; Roy, I.; Karker, N. A.; Swihart, M. T.; Prasad, P. N. *ACS Nano* **2013,** *7,* 7303–7310. doi:10.1021/nn4029234
162. Morales, M. P.; Bédard, M. F.; Roca, A. G.; de la Presa, P.; Hernando, A.; Zhang, F.; Zanella, M.; Zahoor, A. A.; Sukhorukov, G. B.; del Mercato, L. L.; Parak, W. J. *J. Mater. Chem.* **2009,** *19,* 6381–6386. doi:10.1039/b906455a
163. Colombo, M.; Carregal-Romero, S.; Casula, M. F.; Gutiérrez, L.; Morales, M. P.; Böhm, I. B.; Heverhagen, J. T.; Prosperi, D.; Parak, W. J. *Chem. Soc. Rev.* **2012,** *41,* 4306–4334. doi:10.1039/c2cs15337h
164. Niebling, T.; Zhang, F.; Ali, Z.; Parak, W. J.; Heimbrodt, W. *J. Appl. Phys.* **2009,** *106,* 104701. doi:10.1063/1.3253762
165. Kastl, L.; Sasse, D.; Wulf, V.; Hartmann, R.; Mircheski, J.; Ranke, C.; Carregal-Romero, S.; Martínez-López, J. A.; Fernández-Chacón, R.; Parak, W. J.; Elsasser, H.-P.; Rivera Gil, P. *ACS Nano* **2013,** *7,* 6605–6618. doi:10.1021/nn306032k
166. Carregal-Romero, S.; Ochs, M.; Rivera Gil, P.; Ganas, C.; Pavlov, A. M.; Sukhorukov, G. B.; Parak, W. J. *J. Controlled Release* **2012,** *159,* 120–127. doi:10.1016/j.jconrel.2011.12.013

License and Terms

This is an Open Access article under the terms of the Creative Commons Attribution License (http://creativecommons.org/licenses/by/2.0), which permits unrestricted use, distribution, and reproduction in any medium, provided the original work is properly cited.

The license is subject to the *Beilstein Journal of Nanotechnology* terms and conditions: (http://www.beilstein-journals.org/bjnano)

The definitive version of this article is the electronic one which can be found at: doi:10.3762/bjnano.5.161

Available online at www.sciencedirect.com

ScienceDirect

Current Opinion in Pharmacology

Fluorescence-based ion-sensing with colloidal particles

Sumaira Ashraf[1], Carolina Carrillo-Carrion[1], Qian Zhang[1], Mahmoud G Soliman[1], Raimo Hartmann[1], Beatriz Pelaz[1], Pablo del Pino[2] and Wolfgang J Parak[1,2]

Particle-based fluorescence sensors for the quantification of specific ions can be made by coupling ion-sensitive fluorophores to carrier particles, or by using intrinsically fluorescent particles whose fluorescence properties depend on the concentration of the ions. Despite the advantages of such particle-based sensors for the quantitative detection of ions, such as the possibility to tune the surface chemistry and thus entry portal of the sensor particles to cells, they have also some associated problems. Problems involve for example crosstalk of the ion-sensitive fluorescence read-out with pH, or spectral overlap of the emission spectra of different fluorescent particles in multiplexing formats. Here the benefits of using particle-based fluorescence sensors, their limitations and strategies to overcome these limitations will be described and exemplified with selected examples.

Addresses
[1] Fachbereich Physik, Philipps Universität Marburg, Marburg, Germany
[2] CIC BiomaGUNE, San Sebastian, Spain

Corresponding author: Parak, Wolfgang J (wolfgang.parak@physik.uni-marburg.de)

Current Opinion in Pharmacology 2014, **18**:98–103

This review comes from a themed issue on **New technologies**

Edited by **Gleb B Sukhorukov**

For a complete overview see the Issue and the Editorial

Available online 30th September 2014

http://dx.doi.org/10.1016/j.coph.2014.09.011

1471-4892/© 2014 Elsevier Ltd. All right reserved.

Introduction

Ions play an important role in cells, such as Na^+, K^+, Cl^-, and Ca^{2+} for electric signaling. Irregularities in ion distributions can be associated with medical diseases, such as reduction of Cl^--channels in the case of cystic fibrosis [1,2]. Observation of ion concentrations in cells thus can be relevant in medical diagnosis. Besides *in vivo* diagnosis also cellular *in vitro* models are of interest. Here response in ion concentrations upon pharmacological treatment may help to screen different pharmaceutical agents concerning their biological activity [3••]. For such *in vitro* models particle-based ion sensors with fluorescence-read-out are a helpful tool.

Potential of particles-based ion-sensitive fluorescence sensors

Particle-based fluorescence sensing of specific ions is an interesting methodology as it offers important technical features [4–7,8•,9,10]: firstly, fluorescence-based detection is a very convenient method in the field of sensing in life science applications because of its high sensitivity, simplicity, and diversity of fluorescent materials available. In contrast to electronic detection fluorescence can also be recorded conveniently from the interior of cells, making this technique suitable in particular for *in vitro* sensing. Secondly, besides acting as mere carrier for ion-sensitive organic fluorophores, there is an increasing number of intrinsically fluorescent particles, such as quantum dots, carbon dots, lanthanide nanoparticles, or metal nanoclusters. These particles can exhibit different fluorescence properties than classical organic fluorophores (i.e. (depending on the particle material) continuous absorption spectra, longer fluorescence lifetimes, reduced photobleaching, etc.), and are thus complementary to organic fluorescence dyes [11]. The size of the particles hereby can reach from the nanometer to the micrometer range. Thirdly, particle-based sensors always involve the particle as carrier, which allows for addition of other compounds, such as other fluorophores (e.g. for fluorescence resonance energy transfer, FRET) [12], ligands for colloidal stability or for targeting, or therapeutic compounds [13,14], and thus permits an exceptional tailoring in the design of these systems. In case magnetic nanoparticles are used as carriers the same system could act magnetically guided as drug delivery carrier, which simultaneously monitors the delivered drug [15]. Also polyelectrolyte capsules are a very universal system toward the integration of many different functional units into one particle [16], in addition to the actual ion-sensitive fluorophores [17]. Fourthly, working with a particle-based system offers the possibility of having a universal interaction with cells, as the interaction of particles with the cell environment is predominantly governed by the physico-chemical properties of the particle surface, and thus can be made similar for particles responsive to different ions [18]. Cellular uptake and intracellular distribution is thus predominantly determined by the particle carrier. Different ion-sensitive fluorophores on the other hand typically have very different chemical structure and thus may interact in a different way (i.e. being cell-permeable, incorporated by endocytotic pathways, no cellular entry). Finally, it is important to point out that particle-based sensors detect

ion concentrations at their surface, which can be quite different from bulk concentrations [19]. This however can be turned into an advantage as presence of the particle surface helps tuning the working-point by adjusting the surface chemistry [20]. While these points illustrate the huge potential of such sensors, unfortunately there are also problems associated with particle-based fluorescence sensing, which will be highlighted in the following sections, together with some potential solutions to address them.

Crosstalk with pH

The crosstalk of ion-sensitive fluorophores with pH is a major problem, that is fluorescence readout does not only response to changes in concentrations of the ion species which are to be quantified, but also to changes in pH. This is very critical and difficult to solve in the case of intracellular sensing applications, in case particle sensors are administered via cellular internalization. Spontaneous internalization of particles predominantly is via endocytotic pathways, and thus involves massive changes in pH, in which the particles are translocated from neutral to slightly alkaline extracellular medium to highly acidic intracellular vesicles [3••,21]. Thus, in case of a particulate ion-sensitive fluorophore, which does not only respond to its target ion, but also to pH, it is not straightforward to interpret changes in fluorescence readout, as they may reflect changes in target ion concentration or in pH. An illustration of this problem is shown in Figure 1, where quantum dots (QDs) bar-coded polyelectrolyte

Figure 1

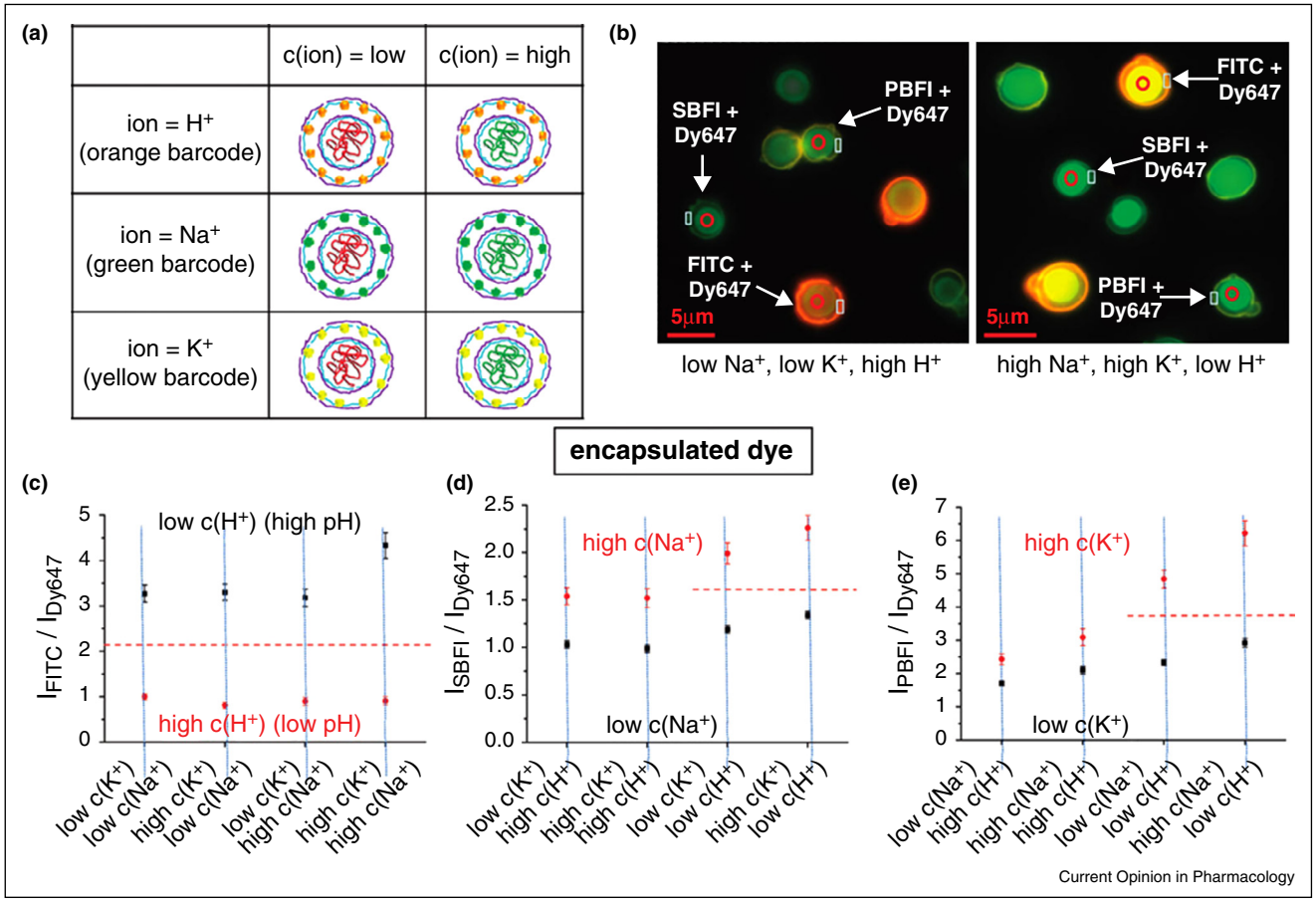

QDs barcoded polyelectrolyte capsules with ion-sensitive fluorophores embedded in their cavity were used for multiplexed measurements of several ions simultaneously. **(a)** Different sensor fluorophores such as FITC (fluorescein 5(6)-isothiocyanate; sensitive toward pH), SBFI (sodium-binding benzofuran isophthalate in the form of tetra-ammonium salt; sensitive toward Na^+), and PBFI (potassium binding bezofuran isophthalate in the form of tetra-ammonium salt; sensitive toward K^+) and a reference fluorophore Dy647 (Dy647 as N-hydroxysuccinimidyl-ester; Dy647 is not sensitive to the cellular environment) conjugated with dextran were loaded inside the cavities of these porous capsules. To distinguish the different capsule species barcodes made by mixtures of QDs with different color were embedded inside the outer shell of these capsules. **(b)** Fluorescence microscopic images of a mixture of all the capsules at low and high concentrations of sodium, potassium and protons are shown from left to right. Changes in fluorescence could be observed upon changes in ion concentrations. **(c–e)** The pH sensitive capsules were able to sense low and high pH even in the presence of other ions. On the other hand, the Na^+ and K^+ sensors were not able to sense their respective ions at all pH values. Due to crosstalk with pH it was not possible to determine Na^+ and K^+ concentrations at low pH, and in this way these capsules would not have been able to distinguish Na^+ and K^+ in highly acidic lysosomes.Adapted from Ref [8•].

capsules with different ion-sensitive fluorophores embedded in their cavity were used for multiplexed measurements of several ions [8•]. While this system has been demonstrated being able to detect Na^+ and K^+ ions simultaneously, this was only possible at controlled pH. In this way this sensor system could not be used for reporting local Na^+ and K^+ concentrations upon the internalization pathway of the particles, upon which severe changes in pH are involved. This problem could be resolved by integrating a pH sensor, which then would be based on a calibration curve to deconvolute pH effects.

Uncertainty in fluorescence intensity-based detection

According to the signal-output mode, particle-based fluorescent probes can work in different sensing mechanisms, in which upon presence of the target ions intensity, wavelength, lifetime, and polarization of fluorescence is changed. To date, most of the proposed particle-based fluorescent sensors are based on fluorescence-intensity changes. Unfortunately they suffer from uncertainties in the calibration of the responses, particularly when these systems are applied as intracellular probes (i.e. fluctuations in intracellular particle densities), which can produce misleading readouts. One solution to partially overcome this problem is by means of ratiometric approaches [6,22–25], which only require relative determination of fluorescence intensities to a reference, instead of absolute intensity measurements. As mentioned, particles allow for easy incorporation of reference fluorophores [20]. Alternatively fluorescence wavelength-shift and lifetime detection are recently used approaches to overcome this limitation. However, there are relatively few ion-sensitive fluorophores involving wavelength-shift modes available. One demonstrated example involves an alteration in the band-gap energy of QDs upon the presence of target ions, causing shift of the emission wavelength [26]. Fluorescence lifetime-based sensing approaches are more universal. The combination of time-resolved fluorescence with QDs is of particular interest due to the longer fluorescence lifetime of QDs (typically five to hundreds of nanoseconds) as compared to that of most organic fluorophores and cell autofluorescence. The potential of these systems for quantifying ions, such as Cl^- or H^+ in bulk solutions mimicking the intracellular environment has recently been demonstrated [27,28,29••]. A novel step in this direction is the use of fluorescence lifetime imaging microscopy (FLIM) for sensing purposes, which is based on using the fluorescence lifetime of QD probes collected from FLIM images as analytical signal for determining the concentration of the target ions. The example illustrated in Figure 2 clearly shows the great potential of FLIM for intracellular imaging and sensing [29••].

Spectral overlap in multiplexing formats

Nowadays there is an increasing demand for multiparameter chemical and biological sensing. However, unfortunately the emission spectra of many ion-sensitive fluorophores show overlap, and thus the number of fluorophores that can be spectrally resolved and independently detected in parallel is limited [30,31]. To solve this major problem of spectral crosstalk the use of particle-based fluorescence systems plays an important role. There are several ways of discrimination between different fluorescence signals: spectral resolution (i.e. fluorescence signals of different wavelength), spatial resolution (i.e. fluorescence originating from different locations), and temporal resolution (i.e. fluorescence with different lifetimes) [30]. In this direction, two very promising strategies of realizing multiplexing without spectral overlap problems are the use of temporal resolution (distinguishing the emission of different fluorophores with time-dependent fluorescence spectroscopy), the interaction of different fluorophores in FRET, or the combination of both strategies. While organic fluorophores have similar lifetimes of a few ns, QDs have much longer fluorescence lifetimes, reaching even ms by doping. By using QDs as donor and several (ion-sensitive) fluorophores as acceptors, successful FRET systems based on lifetime measurements have been developed [32–34,35•]. The combination of QDs (as donors and/or acceptors) with organic dyes (as acceptors) and lanthanide complexes (as donors) allows for the use of different FRET pathways and spectral candidates for the design of time-resolved fluorescence multiplexing formats due to their long photoluminescence lifetimes (ms) [36,37•]. This advantage has been used for time-resolved immunoassays based on FRET from luminescent terbium complexes (LTC) to different quantum dots or five different organic fluorophores [38,39], allowing the simultaneous determination of several tumor markers from a single sample. These examples show how the problem of spectral overlap, which has blocked the advance in multiplexing platforms during years, can be solved via FRET and fluorescence lifetime based spectrotemporal approaches.

Intracellular delivery

Delivery of particle sensors to specific intracellular locations is not trivial, and in fact one of the biggest challenges nowadays. Endocytosis is the classical natural entry of particles into cells [21], consequently leading to a localization of the particles inside acidic intracellular vesicles (endosomes and lysosomes) [40]. Delivery routes to different cellular regions such as the cytosol, mitochondria, and the nucleus can be divided in two main groups, physical and biochemical strategies. Physical strategies include microinjection, electroporation, and photothermal heating [41], which allow (optionally in the context with receptor-specific ligands on their surface) for the delivery of the particles to intracellular targets. In contrast, biochemical strategies involve specific surface ligands of the particles. In this way particles are released from the intracellular vesicles after

Figure 2

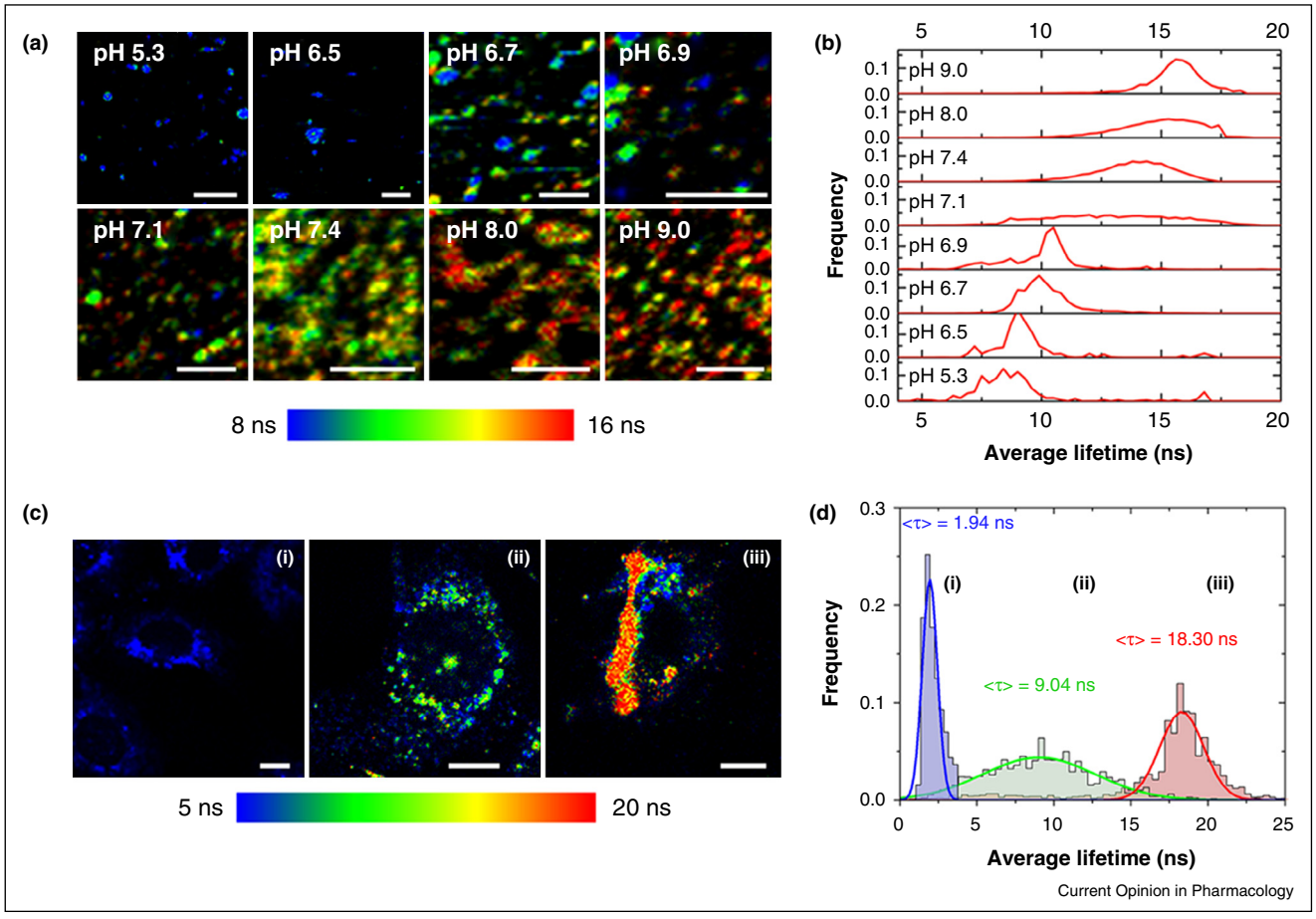

Example for the use of FLIM in combination with pH-sensitive CdSe/ZnS QDs for sensing of intracellular pH. **(a)** FLIM images of QDs suspended in solutions mimicking the intracellular environment at different pH values. The scale bars (white lines) represent 10 μm. **(b)** Fluorescence lifetime histograms collected from the images in (a). **(c)** FLIM images of MC3T3-E1 cells before (i) and after incubation with QDs (ii and iii). Image (i) shows the autofluorescence of the cells. MC3T3-E1 cells were incubated with nigericin and buffers mimicking the extracellular medium at pH 4.87 (ii) and 8.14 (iii). The scale bars (white lines) represent 10 μm. **(d)** Fluorescence lifetime histograms collected from the images in (c).
Adapted from Ref [29••].

endocytosis to the cytolsol ('endosomal escape') [42,43]. Several functionalizations of the particle surface with specific ligands are used in this direction, such as cell penetrating peptides (CCPs) [44], transferrin [45], nuclear-localization sequence (NLS) peptides [46], endoplasmic reticulum (ER) signal peptides [47], triphenylphosphonium derivates (TPP) [48], and polyethyleneimine (PEI) [49]. It even has been suggested that under certain conditions very small particles can directly traverse the cell membrane (i.e. by transient poration) [50] and thus bypass the endocytotic uptake. However, the details of such mechanisms are still under scientific discussion and controversial results can be found in the literature. In spite of all the studies carried out in this topic, there are not yet reliable general methods for delivering particles into the cytosol, and even less for sub-cellular organelles [51]. Thus, successful delivery strategies still must be determined for each particle-based system on a case-by-case basis.

Calibration

The performance of most of the reported sensing systems for intracellular applications are based on the interpolation of the intracellular readouts using corresponding extracellular calibration plots [27,28]. It is well-known that the intracellular environment can alter the behavior of the response of the sensor, as consequence for example of the fact of 'protein corona' formation [52]. Even working with solutions mimicking the intracellular environment, one never can be sure that the scenario is exactly the same as inside the cells. Therefore a proper way to face this problem may be by carrying out a calibration inside cells, in order to introduce all the factors of uncertainty in the calibration model. In addition one has to take

into account that particles can be also partially disintegrated inside cells (e.g. by proteolytic enzymes), which obviously may impact fluorescence readout [53].

Outlook

Particle-based ion-sensitive fluorescence sensing is an interesting methodology, in particular for the development of *in vitro* assays. Due to the particular nature these sensors (in case they are big enough) can be easily localized and could be introduced as artificial 'cellular organelles', allowing for spatially resolved online monitoring of intracellular ion concentrations. In particular the possibility of measuring the changes in intracellular ion concentration upon exposure of cells to specific pharmaceutical agents would offer a convenient way to measure dose-response curve and pharmacokinetics on the level of individual cells [54]. Thus, these platforms could provide significant advances in drug screening, also in the direction of 'personalized medicine', in which cellular response to treatment can be detected.

Conflict of interest statement

The authors do not have any conflicting interests.

Acknowledgements

This project was funded by LOEWE (project SynChemBio to WJP). SA, CCC, and BP are grateful to the Alexander von Humboldt Foundation for a postdoctoral fellowship. QZ and MGS are grateful to the Chinese Scholarship Council (CSC) and the Yousef Jameel Scholarship Fund, respectively, for a fellowship working toward their PhD thesis.

References and recommended reading

Papers of particular interest, published within the period of review, have been highlighted as:

- • of special interest
- •• of outstanding interest

1. Linsdell P: **Cystic fibrosis transmembrane conductance regulator chloride channel blockers: pharmacological, biophysical and physiological relevance**. *World J Biol Chem* 2014, **5**:26-39.

2. Matsui H, Grubb BR, Tarran R, Randell SH, Gatzy JT, Davis CW, Boucher RC: **Evidence for periciliary liquid layer depletion, not abnormal ion composition, in the pathogenesis of cystic fibrosis airways disease**. *Cell* 1998, **95**:1005-1015.

3. •• Rivera Gil P, Nazarenus M, Ashraf S, Parak WJ: **pH sensitive capsules as intracellular optical reporters for monitoring lysosomal pH changes upon stimulation**. *Small* 2012, **8**: 943-948.

An example on how response to pharmaceutical treatment can be monitored *in vitro* based on fluorescent ion-sensitive particles.

4. Lee YEK, Smith R, Kopelman R: **Nanoparticle PEBBLE sensors in live cells and in vivo**. *Annu Rev Anal Chem* 2009, **2**:57-76.

5. Kreft O, Muñoz Javier A, Sukhorukov GB, Parak WJ: **Polymer microcapsules as mobile local pH-sensors**. *J Mater Chem* 2007, **17**:4471-4476.

6. Si D, Epstein T, Lee Y-EK, Kopelman R: **Nanoparticle PEBBLE sensors for quantitative nanomolar imaging of intracellular free calcium ions**. *Anal Chem* 2012, **84**:978-986.

7. Carregal-Romero S, Montenegro J-M, Parak WJ, Rivera Gil P: **Subcellular carrier-based optical ion-selective nanosensors**. *Front Pharmacol* 2012, **3**:70-76.

8. • del Mercato LL, Abbasi AZ, Ochs M, Parak WJ: **Multiplexed sensing of ions with barcoded polyelectrolyte capsules**. *ACS Nano* 2011, **5**:9668-9674.

An example for multiplexed measurements using spatial instead of spectral discrimination of different fluorescent particles.

9. Rana S, Singla AK, Bajaj A, Elci SG, Miranda OR, Mout R, Yan B, Jirik FR, Rotello VM: **Array-based sensing of metastatic cells and tissues using nanoparticle-fluorescent protein conjugates**. *ACS Nano* 2012, **6**:8233-8240.

10. Dennis AM, Rhee WJ, Sotto D, Dublin SN, Bao G: **Quantum dot-fluorescent protein FRET probes for sensing intracellular pH**. *ACS Nano* 2012, **6**:2917-2924.

11. Hötzer B, Medintz IL, Hildebrandt N: **Fluorescence in nanobiotechnology: sophisticated fluorophores for novel applications**. *Small* 2012, **8**:2297-2326.

12. Jin Z, Hildebrandt N: **Semiconductor quantum dots for *in vitro* diagnostics and cellular imaging**. *Trends Biotechnol* 2012, **30**:394-403.

13. del Mercato LL, Ferraro MM, Baldassarre F, Mancarella S, Greco V, Rinaldi R, Leporatti S: **Biological applications of LbL multilayer capsules: from drug delivery to sensing**. *Adv Colloid Interface Sci* 2014, **207**:139-154.

14. Xiong R, Soenen SJ, Braeckmans K, Skirtach AG: **Towards theranostic multicompartment microcapsules: in-situ diagnostics and laser-induced treatment**. *Theranostics* 2013, **3**:141-151.

15. Mitra RN, Doshi M, Zhang X, Tyus JC, Bengtsson N, Fletcher S, Page BD, Turkson J, Gesquiere AJ, Gunning PT *et al.*: **An activatable multimodal/multifunctional nanoprobe for direct imaging of intracellular drug delivery**. *Biomaterials* 2012, **33**:1500-1508.

16. Sukhorukov GB, Rogach AL, Garstka M, Springer S, Parak WJ, Muñoz-Javier A, Oliver Kreft, Skirtach AG, Susha AS, Ramaye Y *et al.*: **Multifunctionalized polymer microcapsules: novel tools for biological and pharmacological applications**. *Small* 2007, **3**:944-955.

17. Reibetanz U, Halozan D, Brumen M, Donath E: **Flow cytometry of HEK 293T cells interacting with polyelectrolyte multilayer capsules containing fluorescein-labeled poly(acrylic acid) as a pH sensor**. *Biomacromolecules* 2007, **8**:1928-1933.

18. Sapsford KE, Algar WR, Berti L, Gemmill KB, Casey BJ, Oh E, Stewart MH, Medintz IL: **Functionalizing nanoparticles with biological molecules: developing chemistries that facilitate nanotechnology**. *Chem Rev* 2013, **113**:1904-2074.

19. Zhang F, Ali Z, Amin F, Feltz A, Oheim M, Parak WJ: **Ion and pH sensing with colloidal nanoparticles: influence of surface charge on sensing and colloidal properties**. *ChemPhysChem* 2010, **11**:730-735.

20. Zhang F, Lees E, Amin F, Rivera Gil P, Yang F, Mulvaney P, Parak WJ: **Polymer-coated nanoparticles: a universal tool for biolabelling experiments**. *Small* 2011, **7**:3113-3127.

21. Kastl L, Sasse D, Wulf V, Hartmann R, Mircheski J, Ranke C, Carregal-Romero S, Martínez-López JA, Fernández-Chacón R, Parak WJ *et al.*: **Multiple internalization pathways of polyelectrolyte multilayer capsules into mammalian cells**. *ACS Nano* 2013, **7**:6605-6618.

22. del Mercato LL, Abbasi AZ, Parak WJ: **Synthesis and characterization of ratiometric ion-sensitive polyelectrolyte capsules**. *Small* 2011, **7**:351-363.

23. Chen T, Hu Y, Cen Y, Chu X, Lu Y: **A dual-emission fluorescent nanocomplex of gold-cluster-decorated silica particles for live cell imaging of highly reactive oxygen species**. *J Am Chem Soc* 2013, **135**:11595-11602.

24. Zong C, Ai K, Zhang G, Li H, Lu L: **Dual-emission fluorescent silica nanoparticle-based probe for ultrasensitive detection of Cu^{2+}**. *Anal Chem* 2011, **83**:3126-3132.

25. Ju E, Liu Z, Du Y, Tao Y, Ren J, Qu X: **Heterogeneous assembled nanocomplexes for ratiometric detection of highly reactive**

oxygen species *in vitro* and *in vivo*. *ACS Nano* 2014, **8**: 6014-6023.

26. Gui M, Bao L, Xia Y, Wei C, Zhang S, Zhu C: **Indication of intracellular physiological pH changes by L-cysteine-coated CdTe quantum dots with an acute alteration in emission color**. *Biosens Bioelectron* 2011, **30**:324-327.

27. Ruedas-Rama MJ, Orte A, Hall EAH, Alvarez-Pez JM, Talavera EM: **A chloride ion nanosensor for time-resolved fluorimetry and fluorescence lifetime imaging**. *Analyst* 2012, **137**:1500-1508.

28. Ruedas-Rama MJ, Orte A, Hall EAH, Alvarez-Pez JM, Talavera EM: **Quantum dot photoluminescence lifetime-based pH nanosensor**. *Chem Commun* 2011, **47**:2898-2900.

29. •• Orte A, Alvarez-Pez JM, Ruedas-Rama MJ: **Fluorescence lifetime imaging microscopy for the detection of intracellular pH with quantum dot nanosensors**. *ACS Nano* 2013, **7**:6387-6395.

An excellent example in which detection of fluorophores by their lifetimes is demonstrated *in vivo*.

30. Abbasi AZ, Amin F, Niebling T, Friede S, Ochs M, Carregal-Romero S, Martos JMM, Rivera Gil P, Heimbrodt W, Parak WJ: **How colloidal nanoparticles could facilitate multiplexed measurements of different analytes with analyte-sensitive organic fluorophores**. *ACS Nano* 2011, **5**:21-25.

31. Wan X, Yao S, Liu H, Yao Y: **Selective fluorescence sensing of Hg^{2+} and Zn^{2+} ions through dual independent channels based on the site-specific functionalization of mesoporous silica nanoparticles**. *J Mater Chem A* 2013, **1**:10505-10512.

32. Kaiser U, Aberasturi DJd, Malinowski R, Amin F, Parak WJ, Heimbrodt W: **Multiplexed measurements by time resolved spectroscopy using colloidal CdSe/ZnS quantum dots**. *Appl Phys Lett* 2014, **104**:041901-041904.

33. Algar WR, Ancona MG, Malanoski AP, Susumu K, Medintz IL: **Assembly of a concentric Förster resonance energy transfer relay on a quantum dot scaffold: characterization and application to multiplexed protease sensing**. *ACS Nano* 2012, **6**:11044-11058.

34. Algar WR, Wegner D, Huston AL, Blanco-Canosa JB, Stewart MH, Armstrong A, Dawson PE, Hildebrandt N, Medintz IL: **Quantum dots as simultaneous acceptors and donors in time-gated forster resonance energy transfer relays: characterization and biosensing**. *J Am Chem Soc* 2012, **134**:1876-1891.

35. • Algar WR, Kim H, Medintz IL, Hildebrandt N: **Emerging non-traditional Förster resonance energy transfer configurations with semiconductor quantum dots: investigations and applications**. *Coord Chem Rev* 2014, **263**:65-85.

An example for spectro-temporal multiplexing based on simultaneous FRET from LTC-to-QD (QD acceptor) and QD-to-dye (QD donor).

36. Hildebrandt N, Wegner KD, Algar WR: **Luminescent terbium complexes: superior Förster resonance energy transfer donors for flexible and sensitive multiplexed biosensing**. *Coord Chem Rev* 2014, **273**:125-138.

37. • Geißler D, Charbonnière LJ, Ziessel RF, Butlin NG, Löhmannsröben H-G, Hildebrandt N: **Quantum dot biosensors for ultrasensitive multiplexed diagnostics**. *Angew Chem Int Ed* 2010, **49**:1396-1401.

An example for FRET-based multiplexing, in which five different QDs are used as acceptor with one LTC donor.

38. Wegner KD, Jin Z, Lindén S, Jennings TL, Hildebrandt N: **Quantum-dot-based Förster resonance energy transfer immunoassay for sensitive clinical diagnostics of low-volume serum samples**. *ACS Nano* 2013, **7**:7411-7419.

39. Geißler D, Stufler S, Löhmannsröben H-G, Hildebrandt N: **Six-color time-resolved Förster resonance energy transfer for ultrasensitive multiplexed biosensing**. *J Am Chem Soc* 2012, **135**:1102-1109.

40. Wang X, Boschetti C, Ruedas-Rama MJ, Tunnacliffe A, Hall EAH: **Ratiometric pH-dot ANSors**. *Analyst* 2010, **135**:1585-1591.

41. Carregal-Romero S, Ochs M, Rivera Gil P, Ganas C, Pavlov AM, Sukhorukov GB, Parak WJ: **NIR-light triggered delivery of macromolecules into the cytosol**. *J Control Release* 2012, **159**:120-127.

42. Verma A, Uzun O, Hu YH, Hu Y, Han HS, Watson N, Chen SL, Irvine DJ, Stellacci F: **Surface-structure-regulated cell-membrane penetration by monolayer-protected nanoparticles**. *Nat Mater* 2008, **7**:588-595.

43. Guo S, Huang L: **Nanoparticles escaping RES and endosome: challenges for siRNA delivery for cancer therapy**. *J Nanomater* 2011, **2011**:11-22.

44. Liu BR, Huang Y-W, Chiang H-J, Lee H-J: **Cell-penetrating peptide-functionized quantum dots for intracellular delivery**. *J Nanosci Nanotechnol* 2010, **10**:7897-7905.

45. Wang J, Tian S, Petros RA, Napier ME, DeSimone JM: **The complex role of multivalency in nanoparticles targeting the transferrin receptor for cancer therapies**. *J Am Chem Soc* 2010, **132**:11306-11313.

46. Chen FQ, Gerion D: **Fluorescent CdSe/ZnS nanocrystal-peptide conjugates for long-term, nontoxic imaging and nuclear targeting in living cells**. *Nano Lett* 2004, **4**:1827-1832.

47. Mukai Y, Yoshinaga T, Yoshikawa M, Matsuo K, Yoshikawa T, Matsuo K, Niki K, Yoshioka Y, Okada N, Nakagawa S: **Induction of endoplasmic reticulum-endosome fusion for antigen cross-presentation induced by poly (γ-glutamic acid) nanoparticles**. *J Immunol* 2011, **187**:6249-6255.

48. Biswas S, Dodwadkar NS, Piroyan A, Torchilin VP: **Surface conjugation of triphenylphosphonium to target poly (amidoamine) dendrimers to mitochondria**. *Biomaterials* 2012, **33**:4773-4782.

49. Shim MS, Kwon YJ: **Controlled cytoplasmic and nuclear localization of plasmid DNA and siRNA by differentially tailored polyethylenimine**. *J Control Release* 2009, **133**:206-213.

50. Patil ML, Zhang M, Taratula O, Garbuzenko OB, He H, Minko T: **Internally cationic polyamidoamine PAMAM-OH dendrimers for siRNA delivery: effect of the degree of quaternization and cancer targeting**. *Biomacromolecules* 2009, **10**:258-266.

51. Huang JG, Leshuk T, Gu FX: **Emerging nanomaterials for targeting subcellular organelles**. *Nano Today* 2011, **6**:478-492.

52. del Pino P, Pelaz B, Zhang Q, Maffre P, Nienhaus GU, Parak WJ: **Protein corona formation around nanoparticles — from the past to the future**. *Mater Horiz* 2014, **1**:301-313.

53. Chanana M, Rivera Gil P, Correa-Duarte MA, Parak WJ, Liz-Marzán LM: **Physicochemical properties of protein-coated gold nanoparticles in biological fluids and cells before and after proteolytic digestion**. *Angew Chem Int Ed* 2013, **52**:4179-4183.

54. Zhang Y, Chan HF, Leong KW: **Advanced materials and processing for drug delivery: the past and the future**. *Adv Drug Deliv Rev* 2013, **65**:104-120.

Neus Feliu[1], Beatriz Pelaz[2], Qian Zhang[2], Pablo del Pino[3], Andreas Nyström[4], Wolfgang J. Parak[2,3*]

[1]Department of Clinical Science, Intervention and Technology, Karolinska Institute, Sweden
[2]Fachbereich Physik, Philipps Universität Marburg, Germany
[3]CIC Biomagune, San Sebastian, Spain
[4]Institute of Environmental Medicine, Karolinska Institute, Sweden
[*]corresponding author: wolfgang.parak@physik.uni-marburg.de

Nanoparticle dosage - a nontrivial task of utmost importance for quantitative nanotoxicology

Abstract

For a detailed and correct understanding of effects of colloidal nanoparticles exposed to organisms, a correlation of such effects to the physicochemical properties of the nanoparticles is a necessity. Such correlation is complex by the fact that many physicochemical parameters such as size, shape, surface charge, and colloidal stability are interlinked, and nontrivial to experimentally determine. This review aims to give an overview regarding such correlations. Particular focus will be given on the role of determining nanoparticle concentrations, which is the basis for most quantitative toxicity evaluations. A comparison of mass *versus* particle number concentrations is given, and their respective differences are highlighted.

Introduction

Colloidal nanoparticles (NPs) offer a great potential for a wide range of medical applications. However, there is the concern that human exposure to NPs could lead to significant adverse biological outcomes, both for human health and the general environment.[1, 2] Based on these concerns nanotoxicology is emerging as a scientific discipline attempting to investigate the interactions of engineered nanomaterials, *e.g.* NPs, with biological systems at the nanoscale level in order to provide knowledge about the safety assessment of nanomaterials.[3] Some general directions have been outlined by Oberdörster *et al.*, who identified essential factors in the area of nanotoxicology that need to be addressed for accurate safety assessment and the continued development of future nanotechnologies.[4] This includes dose metrics, exposure routes, and biodistribution of nanomaterials. Oberdörster *et al.* emphasized the importance of utilizing NPs with well-defined physicochemical properties for being able to address these questions, as they also critically assessed

For Peer Review

the significance of standards *in vitro* viability tests. There is a need of nanotoxicology studies that provide hard data to design appropriate quantitative risks assessments of nanomaterials. As will be discussed in this review these issues still remain highly relevant nowadays.

Nanoparticles interact with the human body

In order to evaluate the benefits of using nanomaterials in medical applications one needs to consider the possible exposure risk and understand the inherent biodistribution of the material. NPs can cross biological barriers and enter and distribute within cells *via* different pathways.[5] For this reason, they are considered to be a primary vehicle for passively and actively targeted therapies. In the body one can find i) cellular barriers, including cell membranes, endosomes, lysosomes, as well as intracellular trafficking, and ii) physiological barriers including blood, liver, spleen, kidneys, the immune system, and the barriers that prevent extravasation of foreign substances from the blood. There is a concern for the risk of NPs to translocate to organs and tissues and to cross different barriers [3]. Understanding the barriers imposed by a biological system is critical for the design of new materials for biomedical application.[6] Based on these concerns the study of the interaction of NPs with relevant biological systems is a critical factor in the safe and sustainable development of nanotechnology for biomedical applications.[7]

Once inside the body NPs will be recognized by the immune system. This will further effect biodistribution of the NPs. It has been demonstrated that upon recognition by the immune system NPs may be distributed in the body *via* the lymphatic system, where further immunological reactions can occur. The primary focus of the immune systems is the protection of the organism against foreign materials, which naturally also includes NPs. Exposure of NPs may induce immunotoxicity, resulting in harmful effects to the immune system. Notably, macrophages are key players in the innate immune response, as these cells are capable of phagocytosing micro- and nano-particles. The recognition of the NPs by the immune cells may play an important role. Based on the intrinsic properties of the NPs, nano-immuno interactions may be controlled.[8] Thus, for the design of safer NPs it is important to investigate these nano-immuno interactions. This is especially true for NPs that are intended for systemic administration, as it is well known that NPs in the blood are rapidly cleared by cells of the reticuloendothelial system into the liver and spleen.[9] In fact, the rapid clearance of circulating particles during systemic delivery is a major challenge for diagnostic particle-based contrast agents and drug delivery systems in nanomedicine. The faster the clearance, the lower the chance the NPs will enter their designated target site and for drug delivery applications sufficient therapeutic concentrations will be hard to reach. NP parameters such as size, shape, elasticity, surface chemistry, and shape are of

For Peer Review

particular interest since the effect of the delivery vehicles in the biological systems depends directly on these properties.[10] Jones *et al*. recently showed, that the rate of NP clearance depends on the global status of the immune system.[11] Notably, for such investigations the use of *in vitro* tests involving primary cells (and not cell lines) is of particular relevance, as these model systems are much closer to the *in vivo* situation.[12]

While many direct toxic effects of NPs to cells are known,[13, 14] such as induction of reactive oxygen species (ROS),[15] it is important to point out that nanomaterials could lead also to indirect "secondary" effects. Sood and co-workers demonstrated that NPs can cause indirect DNA damage *in vitro* across trophoblast and corneal barriers, and cause cytokine and chemokine release.[16] This indirect effect depends on the thickness of the cellular barrier through a pathway that involves gap junctions. Serag *et al.* demonstrated that the traffic of single wall carbon nanotubes (SWCNTs) into different subcellular structures can be facilitated or inhibited by attaching a specific functional ligands and by controlling the medium components.[17] For these reasons evaluations of NP safety should consider both direct and indirect effects, in order to avoid any potential risk to targets on the distal side of cellular barriers.[18]

Most nanotoxicology studies are based on understanding of the acute response to exposure of nanomaterials. To give an example, Mahler and co-workers showed that oral exposure of polystyrene NPs affects the absorption of iron. By using an *in vitro* model of the intestinal epithelium as well as an *in vivo* chicken intestinal loop model, they demonstrated that acute exposure can disturb iron transport.[19] However, the impact of chronic exposure (at low but relevant doses) of NPs on human health is also an important factor that should be taken in consideration and that is largely unknown. Similarly, it has been shown that acute exposure of NPs to zebrafish embryos can be used as a model to predict potential long term effects. Troung *et al.* exposed embryos to Au NPs with different surface coatings.[20] They showed that depending on the coating, acute exposure during embryonic development could result in larval behavioral abnormalities that persisted into adulthood. Thinking about possible long-term effects, complete removal of the NPs from the body is of utmost importance. As a general rule of thumb, the longer the NPs reside in the body, the higher the probability of long-term effects. Beside certain physicochemical parameters such as small size, also degradability of the NPs plays an important role in NP excretion. Therefore, the evolution of the degradability of nanomaterials is an important parameter to consider in their toxicity assessment as well as in the future design of improved nanomaterials. As stated, adverse effects may occur when NPs are accumulated or cannot be biodegraded. While degradation breaks down the NPs to smaller parts, which in general would assist with excretion from the body, it is also important to make sure that the degradation products are non-toxic. In accordance, Kagan *et al.*

For Peer Review

showed that single-wall carbon nanotubes could undergo biodegradation *in vitro via* the action of human myeloperoxidase (hMPO), an enzyme present in neutrophils and to a lesser degree in macrophages.[21] Importantly, the enzymatic degradation of nanotubes diminishes the potential of these nanomaterials to induce pro-inflammatory effects, as demonstrated *in vivo.*

Despite ongoing research for many years, most of the literature describes snapshot scenarios of toxicity effects. In order to gain a comprehensive understanding about toxicology of NPs these snapshots still have to be linked together, considering *in vitro versus in vivo* scenarios, direct *versus* secondary effects, as acute *versus* chronic exposure. Taking into account the complexity of biological exposure scenarios and their model test systems, also the NPs introduce additional complexity. In an ideal situation one would have NPs with precisely defined physicochemical properties. NP libraries in which only one parameter is varied, whereas all the other properties remain constant, would then allow for correlation of the biological effects to certain physicochemical parameters of the NPs.[22-24] While from the synthetic point of view controlled NP libraries are complicated or in some cases even impossible to achieve, the fundamental problem still remains that many physicochemical parameters are interlinked, and thus can not be controlled independently.[25] This makes definition of basic physicochemical parameters complicated. Even the most straightforward property, the "size" of a NP is not straightforward to be defined, and moreover to be experimentally determined. Still, some general tendencies on how physicochemical parameter influence toxicity can be given.[26]

Some tendencies on how toxicity varies with the physicochemical properties of nanoparticles

Size represents an important parameter to be considered from a toxicology point of view. When the size of NPs decreases, their surface area-to-volume ratio increases, which determines the number of surface groups present on the material and its reactivity.[27] Size clearly influences *in vivo* uptake, biodistribution, trafficking, and excretion of NPs. For instance, Choi *et al.* synthesized a series of near-infrared (NIR) fluorescent NPs to determine how their physicochemical properties affect their biodistribution, clearance, and their translocation.[28] Their result showed that NPs with hydrodynamic diameter less than 34 nm with non-cationic surface charge translocate rapidly from lungs to regional lymph nodes in rats following intratracheal instillation. In the same direction Au NPs have been shown to better cross the air-blood barrier (ABB), the smaller they are. Translocation efficiency depended inversely with particle size.[29] Also Schleh *et al*. showed that size and surface charge of gold NPs govern absorption across intestinal barriers and accumulation in secondary organs after oral administration

For Peer Review

in a healthy rat model[30] by using different sizes of gold NPs with different surface charges (positive (*i.e.* cationic NPs) and negative (*i.e.* anionic NPs)). In another example NPs with a hydrodynamic diameter of < 6 nm were able to traffic from the lungs to lymph nodes and to the bloodstream, and consequently cleared/excreted by the kidneys.[28] In general, for smaller nanomaterials a higher toxic response is observed.[31] The same trend is true for *in vitro* models. There are detailed *in vitro* studies which demonstrate that endocytosis (in its different forms[32]) of NPs is highly size-dependent. While for ultra-small NPs, below a few nm there are some exceptions, smaller NPs are typically more efficiently endocytosed than bigger ones.[33, 34] In the same direction Zhu *et al.* described size-dependent cellular uptake efficiency of silica NPs in HeLa cells.[35] It has been suggested that for higher intracellular doses of NPs a higher toxic response is observed,[23] *i.e.* the toxic effect scales with the number of incorporated NPs. In a recent study, Gliga *et al.* showed size-dependent cytotoxicity of Ag NPs in human lung epithelial cells.[36] After endocytosis, NPs are typically located inside endosomes/lysosomes, which are rich in proteolytic enzymes and impose a highly acidic environment for the NPs. This can lead to degradation of toxic products, such as metal ions in the case of metal containing NPs (*e.g.* Ag,[37, 38] ZnO,[13, 39-42], or CdSe[43-45]). Even without the release of toxic ions size-dependent impairments of lysosomal function and integrity have been observed.[46]

Whereas the above mentioned example outline the clear importance of NP size as a key parameter in NP toxicity, in many studies it is not very clear to what "size" refers. Leaving away trivial aspects such as confusion between radius and diameter, it is not obvious how size can be precisely defined and in particular also measured. This starts with complex shaped NPs,[47] such as nanorods or nanostars.[48] While in the case of rod-shape NPs one can define two sizes, one along the short and one along the long axis, for more highly complex topologies it is not immediately apparent how size can be determined. In the case of nanostars, will it be the inner spherical diameter or the outer diameter involving the spikes? Even in case of spherical NPs "size" is not a trivial parameter. No solution of NPs (apart maybe from magic clusters [49-52] or extremely well defined polymeric dendrimers) contains NPs of precisely the same size. There always will be a distribution of sizes. In this way only mean values of sizes can be given. However, experimental techniques for determining sizes can be effected by size distribution. In case the size of spherical NPs is distributed according to a Gaussian curve centered around a mean value, analysis of transmission electron microscopy (TEM) images would directly resemble this Gaussian shaped size distribution centered around the mean value. In case of dynamic light scattering (DLS) on the other hand a higher mean value would be obtained. The scattering intensity strongly depends on the NP size, and thus bigger NPs lead to more scattering signal, which would shift the determined mean value to a higher value than the one determined *via* TEM. Though different weighting of the size distributions can be corrected, this only can

For Peer Review

be done based on assumptions and models. Having started the discussion of different experimental methods to determine size one has to be also aware that most measurements lead to different types of "size", even for spherical NPs.[53] In case of crystalline NPs size one can refer to the diameter of the crystalline domain, which in case of multi-domain NPs would be smaller than the geometrical diameter of the NP. The geometrical diameter of NPs can be directly visualized by different microscopy techniques. In case of TEM only the parts of the NPs which provide contrast can be seen. For inorganic NPs with organic shell typically only the inorganic core provides contrast and this the determined diameter refers to this core. Such hybrid character complicates also concentration determination, as will be outlined later in the review. In case of atomic force microscopy (AFM) interaction with the tip of the AFM and the NP surface may distort size measurements,[54] as may indentation of the tip into very soft NPs in case of contact mode measurements, as well as flattening of soft NPs on the surface. While TEM typically needs to be carried out in vacuum, and thus the NPs are dried, in biological applications the NPs are dispersed in a medium. This involves adsorption of counter ions,[55] proteins,[56] lipids, *etc*. A typical way to determine sizes in solution is based on measuring diffusion constants D, from which the hydrodynamic diameter d_h of the NPs can be determined from the Stokes-Einstein relation $d_h \propto 1/D$. Diffusion constants can be determined from example with DLS or fluorescence correlation spectroscopy (FCS),[57] though for determination model assumptions are required. Adsorbed molecules such as proteins will add to the determined hydrodynamic diameter,[58] which is in general larger than the geometrical NP diameter. Also agglomeration, which depends on the medium in which the NPs are dispersed, leads to apparent "larger" hydrodynamic diameters. Due to all those complications the way how "size" has been determined must be described in detail in any toxicity studies of NPs.

There are also many reports in literature describing the effect of NP shape, and how this physicochemical parameter can influence NP uptake and toxicity.[59] As well as size the shape of an NP affects its uptake [60] and biodistribution.[61] Awargal *el al.* evaluated the influence of shape and size of different polyethylene glycol diacrylate based hydrogel NPs.[62] They found that uptake depended on the geometry of the NP and the cell model used. Based on the *in vitro* results, they hypothesized that intracellular uptake of NPs depends on three main factors, the sedimentation effect, directed by the weight of the NPs, the forces between the NP surface and cell membranes, and the cell membrane strain energy necessary for membrane deformation around the NP. The last factor is clearly highly shape-dependent. However, the authors admit that *in vivo* evaluation is required to evaluate the *in vivo* relevance of their study.[62] Another established example is carbon nanotubes, which are thought to exert toxicity due to their "needle-like" shape, which allows them to penetrate cell membranes. This may be relevant at least for multi-walled carbon nanotubes.[63] In addition, differences in shape may

For Peer Review

affect NP clearance as well, as demonstrated by Barua *et al.* in a recent *in vitro* study, which spherical, disk and rod-shaped polystyrene and poly(lactic-co-glycolic acid) (PGLA) nano- and microparticles were evaluated for uptake and intracellular distribution in human cancer cell lines.[64, 65] In general the uptake of spiky objects by cells in enhanced, as are the cytotoxic effects.[26, 59, 66]

Concerning surface charge, in general positively charged materials give a stronger cytotoxic response compared to negatively charged and in particular to neutral NPs.[26] This may be correlated with their enhanced cellular uptake, which follows the same trend.[67-69] Indeed, positive NPs cause larger disruption of the plasma membrane integrity.[70] Cationic poly(amidoamine) (PAMAM) dendrimers have been associated with higher cytotoxic and different cellular responses than non-anionic ones.[71, 72] The cationic response of PAMAMs appears to be generation dependent, which is associated to a different number of amino groups on their surface.[73, 74] Controlling and balancing the density of cationic groups on the surface of the nanomaterials can be used to minimize toxicity, which would be beneficial for specific biomedical applications.[75] In general, neutral or negatively charged NPs show prolonged blood circulation time and higher enhanced permeation and retention (EPR)[76]) than positively charged NPs, that are more toxic and induce larger inflammatory reaction than anionic or neutral NPs.[77] From the experimental point of view surface charge is hard to determine. The sign and magnitude of charge can be derived from zeta-potential measurements. However, one needs to be aware that the zeta-potential is not the surface potential of a NP (which is directly related *via* the Poisson-Boltzmann distribution to surface charge).[78] Surface charge is also a medium-dependent property.[79]

Colloidal stability is a key physicochemical parameter, which determines the dispersion stability of the NPs. It is an important physicochemical characteristic, which directly affects toxicity.[80] Most important, many other physicochemical properties are interlinked with colloidal stability.[25] In the case that NPs are agglomerated, their apparent size becomes bigger. Agglomerated NPs with high aspect ratio may also form a more or less spherical object. Colloidal stability, or the state of agglomeration, which depends on the medium in which the NPs are dispersed, thus always needs to be experimentally determined.[38, 68] Okuda-Shimazaki *et al.* demonstrated the importance of the agglomeration state and revealed that larger agglomerates of TiO_2 NPs (596 nm) were more cytotoxic than smaller agglomerates (166 nm) upon exposure to THP1 cells.[81] In this particular example, the findings suggested that the surface characteristics were more important for cytotoxic effects than the size. This is in good agreement with other studies.[38] Wick *et al.* also illustrated the role of agglomeration on the cytotoxic effect of nanomaterials by using carbon nanotubes as a model NPs.[82] Balasubramanian *et al.* showed the role of the primary size of NPs on the biodistribution by exposing rats to airborne Au NP agglomerates of primary size of

For Peer Review

7 and 29 nm. They showed that the smaller agglomerates of Au NPs were distributed to more organs than the larger ones.[83] In summary, if the colloidal stability of NPs in the relevant medium has not been determined, it is complicated to investigate trends related to other physicochemical parameters such as size, shape, and surface charge, as those are highly interlinked with colloidal stability.[25]

Size, shape, surface charge, and colloidal stability are just some physicochemical properties of NPs, to which their toxicity can be related. However, there are many more such as the band gap of semiconductor/insulator NPs[84, 85] or the mechanical stiffness of the NPs,[86, 87] and even more which have not been investigated in detail yet. Again, the predominant problem for all those studies is that most of the times changes in one physicochemical parameter involve also changes in other parameters. Still, while not having led to an entirely comprehensive image, it is safe to say that qualitative correlation of the toxic effect observed from NPs to selected physicochemical properties has made big progress. While one needs to be additionally aware that physicochemical properties of NPs change after they have been incorporated by cells[21, 88] and thus toxicity should be correlated to the physicochemical properties before and after uptake, there is yet another experimental obstacle to be considered on the road to reach quantitative correlation. In case of quantitative correlations a safe and correct metric for the determination of NP doses is critical.

Appropriate metrics for nanoparticle concentrations

For quantitative analysis of toxic effects of NPs a dose-response curve are needed, as obviously all toxic effects in some way will depend on the NP dose to which a cell / organism has been exposed. In the case of mere descriptive analysis, for example in the case of many complex industrial samples based on composite materials or in the case of "nano"-waste due to wear-off, the best metric for NP dose is mass concentration C_{NP}, *i.e.* the mass of NPs dissolved per volume of medium in mg/mL. In order to determine the concentration, an amount of the solution with defined volume V is taken, the liquid is evaporated, and the mass m of the remaining dried NPs is determined, leading to the NP concentration C_{NP} = m/V. However with this method some problems are associated. First, concentration determination should be only made of a part of the sample which is later discarded, as the colloidal properties of NPs after a drying and redispersion cycle may change. Secondly, in the mass m of the dried NP power also all impurities in the solution contribute, be it proteins or salts from the medium, as well as residual precursors from the NP synthesis. The "real" NP concentration C_{NP} thus often will be smaller than the experimentally determined one. With such metrics the response of NP solution with the same mass concentration C_{NP} can be compared. However, for observing insights into the way how changes in one physicochemical parameter affect toxicity this metrics in general is not the most

For Peer Review

appropriate one. In the case of comparing defined series of tailored model NPs, number concentrations c_{NP} in mol/L, *i.e.* the molar amount of NPs per volume are better to be used. In order to visualize this trivial-sounding statement, a realistic model calculation is helpful. In this model, the effect of PEGylation of Au NPs, *i.e.* modification of the Au surface with polyethylene glycol with specific thiol-linkage, on the toxicity of Au NPs is investigated.[25] For this purpose dose-response curve of Au NPs with and without PEG are required. Corresponding experimental investigations can be found in the literature.[89-92] The NP geometry is sketched in Figure 1.

The problem using mass concentrations C_{NP} is, that upon different surface modifications the molecular weight M_{NP} of the different NPs may dramatically change. In this case we consider Au NPs with a diameter of the Au core of d_c = 5 nm, for which the volume $V_{NP(c)}$ and the surface area $A_{NP(c)}$ of one gold core is as follows:

$$V_{NP(c)} = (4\pi/3)\cdot(d_c/2)^3 \approx 65 \text{ nm}^3 \text{ and } A_{NP(c)} = 4\pi\cdot(d_c/2)^2 \approx 79 \text{ nm}^2$$

Using the density of bulk gold ρ_{Au} = 19.32 g/cm^3 the mass of one singe Au core $m_{NP(c)}$ is calculated to be:

$$m_{NP(c)} = \rho_{Au}\cdot V_{NP(c)} \approx 1.3\cdot10^{-18} \text{ g}$$

Thus, by using Avogadro's number $N_A = 6.02\cdot10^{23}$ mol^{-1} the molar mass $M_{NP(c)}$ of one Au core is:

$$M_{NP(c)} = m_{NP(c)}\cdot N_A \approx 7.6\cdot10^5 \text{ g/mol}$$

Utilizing the molar mass of one gold atom M_{Au} = 196.97 g/mol, in this model one Au core consists of $N_{Au/NP}$ gold atoms:

$$N_{Au/NP} = M_{NP(c)}/M_{Au} \approx 3900$$

In the case of PEGylated Au NPs the resulting molecular mass of one NP M_{NP} will increase by the contribution $M_{NP(PEG)}$ of the PEG shell. If we assume PEG with the molar mass of M_{PEG} = 10 kDa[53, 93] the saturated PEG shell around the Au core will add 6.6 nm to the radius, based on calculations of the radius of gyration of PEG [94]. Thus, the NP has a geometric size of $d_{cs} = d_c + 2\cdot6.6$ nm ≈ 18 nm. Therefore, PEGylation does not only change surface chemistry, but also size of the NP, which again demonstrates that most physicochemical properties are highly interlinked. In case of an assumed surface coverage of PEG on the NPs of s_{PEG} = 1 PEG *per* nm^2,[95] the number $N_{PEG/NP}$ of PEG molecules bound to the surface of one NP can be approximated to:

$$N_{PEG/NP} = s_{PEG}\cdot A_{NP(c)} \approx 79$$

For Peer Review

Using Avogadro's number the mass $m_{NP(PEG)}$ of the PEG shell around one NP and the molar mass of the PEG shell $M_{NP(PEG)}$ then are:

$$m_{NP(PEG)} = (N_{PEG/NP}/N_A)\cdot M_{PEG} \approx 1.3\cdot10^{-18}\ \text{g and } M_{NP(PEG)} = m_{NP(PEG)}\cdot N_A \approx 7.8\cdot10^{5}\ \text{g/mol}$$

The total mass of one Au NP m_{NP} and the molar mass of Au NPs M_{NP} thus is:

$$m_{NP} = m_{NP(c)} + m_{NP(PEG)} \approx 2.6\cdot10^{-18}\ \text{g and } M_{NP} = M_{NP(c)} + M_{NP(PEG)} \approx 15\cdot10^{5}\ \text{g/mol}$$

Note, that the mass of the PEG shell $m_{NP(PEG)} \approx 1.3\cdot10^{-18}$ g has the same order of magnitude as the mass of the Au core $m_{NP(c)} \approx 1.3\cdot10^{-18}$ g. In this example the PEG shell doubles the molecular mass of the NPs. Thus, mass concentrations are no good metrics in this case. A solution with the same mass of PEGylated NPs would only contain half of the number of NPs as a solution with the same mass of non-PEGylated NPs. The number concentration c_{NP}, as determined by the number of NPs (divided by Avogadro's number) *per* volume of solution provides a much better metric, as in this case the solutions with the same number of NPs in solution are compared.

In principle, all number concentrations c_{NP} can be converted in mass concentrations C_{NP}, in case the molecular weight of the NP is known. Unfortunately, in particular in the case of inorganic NPs, which besides their inorganic core comprise an organic surface coating, molecular masses of the entire NPs are not known.

In some special cases, as for Au NPs[96, 97] or CdSe NPs,[98, 99] tables of molecular extinction coefficients exist, and thus number concentration can be derived from the absorption spectrum of NP solution. In cases this is not possible, the most practical way for determining NP number concentration is *via* elemental analysis. In the case of the NPs shown in Figure 1, by determining the mean core diameter d_c, for example *via* TEM images, the number of Au atoms per Au core has been determined to $N_{Au/NP} \approx 3900$. Note, that due to the size distribution this number always must be seen an estimate. The concentration of Au atoms c_{Au} in a solution of Au NPs can be determined, after dissolution of the Au NPs to Au ions, by elemental analysis, as for example by inductively coupled plasma mass spectrometry (ICP-MS). NP concentrations can thus be provided in three different ways, as number concentration of atoms from the dissolved NPs c_{Au}, as number concentration of NPs c_{NP}, and as mass concentration of NPs C_{NP}. Concentrations can be converted. However, in case the molecular mass of the entire NP M_{NP} is not known, the molecular mass of only the NP core $M_{NP(c)}$ needs to be used as approximation, which can lead to significant errors, as indicated in the above shown example:

$$c_{NP} = N_{Au/NP}\cdot c_{Au} \text{ and } C_{NP} = M_{NP}\cdot c_{NP}$$

For Peer Review

In the best case, doses should be provided in all three metrics,[38] which would allow for optimal comparison with other studies.

Conclusions

While big progress has been made, toxic effects of NPs are not yet fully understood in a comprehensive manner. Though much of this is due to biological complexity, there are also problems associated to the materials' side. Correlation to physicochemical properties is hampered by a lack of NP series in which exclusively only one parameter is varied, whereas all others are kept constant. Besides experimental challenges this is also due to strong interlink of several physicochemical properties. In addition there is the remarkable problem of metrics. As many studies quantitative NP doses with different metrics, an absolute comparison is complicated. Thus, in order to reach a comprehensive picture, still basics, such as the problem of unequivocally determining NP doses, need to be solved.[78]

Acknowledgements

This work was supported by the German Research Foundation (DFG GRK 1782 to WJP). BP acknowledges a Postdoctoral fellowship from the Alexander von Humboldt Foundation. QZ acknowledges a PhD fellowship from Chinese Scholarship Council (CSC). NF acknowledges the support of Professor Paolo Macchiarini and all his research group at Advanced Center for Translational Regenerative Medicine, Karolinska Institutet, Sweden. Parts of the introduction are adopted from the PhD thesis of NF and we would like to acknowledge Prof Dr Bengt Fadeel (ATS) for the important contribution to the writing of this thesis and the associated funding for the projects.

References

1. Duncan R, Gaspar R. Nanomedicine(s) under the microscope. *Mol Pharm* 2011, 8:2101-2141.
2. Xia T, Li N, Nel AE. Potential Health Impact of Nanoparticles. *Ann Rev Publ Health* 2009, 30:137-150.
3. Nystrom AM, Fadeel B. Safety assessment of nanomaterials: Implications for nanomedicine. *J Controlled Release* 2012, 161:403-408.
4. Oberdorster G. Safety assessment for nanotechnology and nanomedicine: concepts of nanotoxicology. *J Inter Med* 2010, 267:89-105.
5. Jiang W, Kim BYS, Rutka JT, Chan WCW. Nanoparticle-mediated cellular response is size-dependent. *Nat Nano*tecnol 2008, 3:145.

For Peer Review

6. Kievit FM, Zhang M. Cancer nanotheranostics: improving imaging and therapy by targeted delivery across biological barriers. *Adv Mater* 2011, 23:H217-247.
7. Feliu N, Fadeel B. Nanotoxicology: no small matter. *Nanoscale* 2010.
8. Wang XJ, Reece SP, Brown JM. Immunotoxicological impact of engineered nanomaterial exposure: mechanisms of immune cell modulation. *Toxicol Mech Methods* 2013, 23:168-177.
9. Dobrovolskaia MA, McNeil SE. Immunological properties of engineered nanomaterials. *Nat Nano* 2007, 2:469.
10. Perry JL, Herlihy KP, Napier ME, Desimone JM. PRINT: A Novel Platform Toward Shape and Size Specific Nanoparticle Theranostics. *Acc Chem Res* 2011, 44:990-998.
11. Jones SW, Roberts RA, Robbins GR, Perry JL, Kai MP, Chen K, Bo T, Napier ME, Ting JPY, DeSimone JM, et al. Nanoparticle clearance is governed by Th1/Th2 immunity and strain background. *J Clin Invest* 2013, 123:3061-3073.
12. Kunzmann A, Andersson B, Thurnherr T, Krug H, Scheynius A, Fadeel B. Toxicology of engineered nanomaterials: Focus on biocompatibility, biodistribution and biodegradation. *BBA-General Subjects* 2011, 1810:361-373.
13. Xia T, Kovochich M, Liong M, Madler L, Gilbert B, Shi H, Yeh JI, Zink JI, Nel AE. Comparison of the mechanism of toxicity of zinc oxide and cerium oxide nanoparticles based on dissolution and oxidative stress properties. *ACS Nano* 2008, 2:2121-2134.
14. Meng H, Xia T, George S, Nel AE. A Predictive Toxicological Paradigm for the Safety Assessment of Nanomaterials. *ACS Nano* 2009, 3:1620-1627.
15. Piao MJ, Kang KA, Lee IK, Kim HS, Kim S, Choi JY, Choi J, Hyun JW. Silver nanoparticles induce oxidative cell damage in human liver cells through inhibition of reduced glutathione and induction of mitochondria-involved apoptosis. *Toxicol Lett* 2011, 201:92-100.
16. Sood A, Salih S, Roh D, Lacharme-Lora L, Parry M, Hardiman B, Keehan R, Grummer R, Winterhager E, Gokhale PJ, et al. Signalling of DNA damage and cytokines across cell barriers exposed to nanoparticles depends on barrier thickness. *Nat Nanotechnol* 2011, 6:824-833.
17. Serag MF, Kaji N, Venturelli E, Okamoto Y, Terasaka K, Tokeshi M, Mizukami H, Braeckmans K, Bianco A, Baba Y. Functional Platform for Controlled Subcellular Distribution of Carbon Nanotubes. *ACS Nano* 2011, 5:9264-9270.
18. Bhabra G, Sood A, Fisher B, Cartwright L, Saunders M, Evans WH, Surprenant A, Lopez-Castejon G, Mann S, Davis SA, et al. Nanoparticles can cause DNA damage across a cellular barrier. *Nat Nanotechnol* 2009, 4:876-883.
19. Mahler GJ, Esch MB, Tako E, Southard TL, Archer SD, Glahn RP, Shuler ML. Oral exposure to polystyrene nanoparticles affects iron absorption. *Nat Nanotechnol* 2012, 7:264-U1500.
20. Truong L, Saili KS, Miller JM, Hutchison JE, Tanguay RL. Persistent adult zebrafish behavioral deficits results from acute embryonic exposure to gold nanoparticles. *Comp Biochem Physio C Toxicol Pharmacol* 2012, 155:269-274.
21. Kagan VE, Konduru NV, Feng WH, Allen BL, Conroy J, Volkov Y, Vlasova II, Belikova NA, Yanamala N, Kapralov A, et al. Carbon nanotubes degraded by neutrophil myeloperoxidase induce less pulmonary inflammation. *Nat Nanotechnol* 2010, 5:354-359.
22. Rivera Gil P, Oberdorster G, Elder A, Puntes VF, Parak WJ. Correlating Physico-Chemical with Toxicological Properties of Nanoparticles: The Present and the Future. *ACS Nano* 2010, 4:5527-5531.
23. Fadeel B, Feliu N, Vogt C, Abdelmonem AM, Parak WJ. Bridge over troubled waters: understanding the synthetic and biological identities of engineered nanomaterials. *WIREs Nanomedicine and Nanobiotechnology* 2013, 5:111-129.

For Peer Review

24. Zhu MT, Nie GJ, Meng H, Xia T, Nel A, Zhao YL. Physicochemical Properties Determine Nanomaterial Cellular Uptake, Transport, and Fate. *Acc Chem Res* 2013, 46:622-631.
25. Rivera Gil P, Jimenez de Aberasturi D, Wulf V, Pelaz B, del Pino P, Zhao Y, de la Fuente J, Ruiz de Larramendi I, Rojo T, Liang X-J, et al. The Challenge to Relate the Physicochemical Properties of Colloidal Nanoparticles to Their Cytotoxicity. *Acc Chem Res* 2013, 46:743-749.
26. Nazarenus M, Zhang Q, Soliman MG, del Pino P, Pelaz B, Carregal_Romero S, Rejman J, Rothen-Ruthishauser B, Clift MJD, Zellner R, et al. In vitro Interaction of Colloidal Nanoparticles with Mammalian Cells: What Have We Learned Thus Far? *Beilstein J Nanotech* 2014, 5:1477-1490.
27. Oberdoerster G, Oberdoerster E, Oberdoerster J. Nanotoxicology: An emerging discipline evolving from studies of ultrafine particles. *Environ Health Perspect* 2005, 113:823-839.
28. Choi HS, Ashitate Y, Lee JH, Kim SH, Matsui A, Insin N, Bawendi MG, Semmler-Behnke M, Frangioni JV, Tsuda A. Rapid translocation of nanoparticles from the lung airspaces to the body. *Nat Biotechnol* 2010, 28:1300-1303.
29. Kreyling WG, Hirn S, Müller W, Schleh C, Wenk A, Celik G, Lipka J, Schäffler M, Haberl N, Johnston BD, et al. Air-Blood Barrier Translocation of Tracheally Instilled Gold Nanoparticles Inversely Depends on Particle Size. *ACS Nano* 2014, 8:222-233.
30. Schleh C, Semmler-Behnke M, Lipka J, Wenk A, Hirn S, Schaeffler M, Schmid G, Simon U, Kreyling WG. Size and surface charge of gold nanoparticles determine absorption across intestinal barriers and accumulation in secondary target organs after oral administration. *Nanotoxicology* 2012, 6:36-46.
31. Nel A, Xia T, Madler L, Li N. Toxic potential of materials at the nanolevel. *Science* 2006, 311:622-627.
32. Sahay G, Alakhova DY, Kabanov AV. Endocytosis of nanomedicines. *J Controlled Release* 2010, 145:182-195.
33. Chithrani BD, Chan WCW. Elucidating the mechanism of cellular uptake and removal of protein-coated gold nanoparticles of different sizes and shapes. *Nano Lett* 2007, 7:1542-1550.
34. Chithrani BD, Ghazan AA, Chan CW. Determining the Size and the Shape dependence of gold nanoparticle uptake into mammalian cells. *Nano Lett* 2006, 6:662-668.
35. Zhu J, Liao L, Zhu LN, Zhang P, Guo K, Kong JL, Ji C, Liu BH. Size-dependent cellular uptake efficiency, mechanism, and cytotoxicity of silica nanoparticles toward HeLa cells. *Talanta* 2013, 107:408-415.
36. Gliga AR, Skoglund S, Wallinder IO, Fadeel B, Karlsson HL. Size-dependent cytotoxicity of silver nanoparticles in human lung cells: the role of cellular uptake, agglomeration and Ag release. *Part Fibre Toxicol* 2014, 11.
37. Kittler S, Greulich C, Diendorf J, Koller M, Epple M. Toxicity of Silver Nanoparticles Increases during Storage Because of Slow Dissolution under Release of Silver Ions. *Chem Mater* 2010, 22:4548-4554.
38. Caballero-Díaz E, Pfeiffer C, Kastl L, Rivera-Gil P, Simonet B, Valcárcel M, Jiménez-Lamana J, Laborda F, Parak WJ. The Toxicity of Silver Nanoparticles Depends on Their Uptake by Cells and Thus on Their Surface Chemistry. *Part Part Syst Char* 2013, 30:1079-1085.
39. Chang YN, Zhang MY, Xia L, Zhang J, Xing GM. The Toxic Effects and Mechanisms of CuO and ZnO Nanoparticles. *Materials* 2012, 5:2850-2871.
40. Xia T, Zhao Y, Sager T, George S, Pokhrel S, Li N, Schoenfeld D, Meng H, Lin S, Wang X, et al. Decreased dissolution of ZnO by iron doping yields nanoparticles with reduced toxicity in the rodent lung and zebrafish embryos. *ACS Nano* 2011, 5:1223-1235.

For Peer Review

41. Cho WS, Duffin R, Howie SEM, Scotton CJ, Wallace WAH, MacNee W, Bradley M, Megson IL, Donaldson K. Progressive severe lung injury by zinc oxide nanoparticles; the role of Zn2+ dissolution inside lysosomes. *Part Fibre Toxicol* 2011, 8.
42. Muller KH, Kulkarni J, Motskin M, Goode A, Winship P, Skepper JN, Ryan MP, Porter AE. pH-Dependent Toxicity of High Aspect Ratio ZnO Nanowires in Macrophages Due to Intracellular Dissolution. *ACS Nano* 2010, 4:6767-6779.
43. Derfus AM, Chan WCW, Bhatia SN. Probing the Cytotoxicity of Semiconductor Quantum Dots. *Nano Lett* 2004, 4:11-18.
44. Kirchner C, T. L, Kudera S, Pellegrino T, Muñoz Javier A, Gaub HE, Stölzle S, Fertig N, Parak WJ. Cytotoxicity of Colloidal CdSe and CdSe/ZnS Nanoparticles. *Nano Lett* 2005, 5:331-338.
45. Soenen SJ, Montenegro J-M, Abdelmonem AM, Manshian BB, Doak SH, Parak WJ, Smedt SCD, K. Braeckmans. The effect of nanoparticle degradation on poly(methacrylic acid)-coated quantum dot toxicity: The importance of particle functionality assessment in toxicology. *Acta Biomater* 2014, 10.
46. Fröhlich E, Meindl C, Roblegg E, Ebner B, Absenger M, Pieber TR. Action of polystyrene nanoparticles of different sizes on lysosomal function and integrity. *Part Fibre Toxicol* 2012, 9:1-13.
47. Parak WJ. Complex Colloidal Assembly. *Science* 2011, 334:1359-1360.
48. Barbosa S, Agrawal A, Rodriguez-Lorenzo L, Pastoriza-Santos I, Alvarez-Puebla RA, Kornowski A, Weller H, Liz-Marzan LM. Tuning Size and Sensing Properties in Colloidal Gold Nanostars. *Langmuir* 2010, 26:14943-14950.
49. Schmid G. The Relevance of Shape and Size of Au_{55} Clusters. *Chem Soc Rev* 2008, 37:1909-1930.
50. Vossmeyer T, Reck G, Katsikas L, Haupt ETK, Schulz B, Weller H. A "Double-Diamond Superlattice" Built Up of Cd17S4(SCH2CH2OH)26 Clusters. *Science* 1995, 267:1476-.
51. Zanella M, Abbasi AZ, Schaper AK, Parak WJ. Discontinuous Growth of II-VI Semiconductor Nanocrystals from Different Materials. *J Phys Chem C* 2010, 114:6205-6215.
52. Jadzinsky PD, Calero G, Ackerson CJ, Bushnell DA, Kornberg RD. Structure of a thiol monolayer-protected gold nanoparticle at 1.1 A resolution. *Science* 2007, 318:430-433.
53. Sperling RA, Liedl T, Duhr S, Kudera S, Zanella M, Lin C-AJ, Chang WH, Braun D, Parak WJ. Size Determination of (Bio-) Conjugated Water-Soluble Colloidal Nanoparticles: A Comparison of Different Techniques. *J Phys Chem C* 2007, 111:11552-11559.
54. Ebenstein Y, Nahum E, Banin U. Tapping Mode Atomic Force Microscopy for Nanoparticle Sizing: Tip-Sample Interaction Effects. *Nano Lett* 2002, 2:945-950.
55. Pfeiffer C, Rehbock C, Hühn D, Carrillo-Carrion C, Aberasturi DJd, Merk V, Barcikowski S, Parak WJ. Interaction of colloidal nanoparticles with their local environment: the (ionic) nanoenvironment around nanoparticles is different from bulk and determines the physico-chemical properties of the nanoparticles. *J R Soc Interface* 2014, 11:20130931.
56. Cedervall T, Lynch I, Foy M, Berggad T, Donnelly S, Cagney G, Linse S, Dawson K. Detailed identification of plasma proteins adsorbed on copolymer nanoparticles. *Angew Chem Int Ed* 2007, 46:5754-5756.
57. Liedl T, Keller S, Simmel FC, Rädler JO, Parak WJ. Fluorescent Nanocrystals as Colloidal Probes in Complex Fluids Measured by Fluorescence Correlation Spectroscopy. *Small* 2005, 1:997-1003.
58. Röcker C, Pötzl M, Zhang F, Parak WJ, Nienhaus GU. A Quantitative Fluorescence Study of Protein Monolayer Formation on Colloidal Nanoparticles. *Nat Nanotechnol* 2009, 4:577-580.

For Peer Review

59. Stoehr LC, Gonzalez E, Stampfl A, Casals E, Duschl A, Puntes V, Oostingh GJ. Shape matters: effects of silver nanospheres and wires on human alveolar epithelial cells. *Part Fibre Toxicol* 2011, 8:3-15.
60. Herd H, Daum N, Jones AT, Huwer H, Ghandehari H, Lehr C-M. Nanoparticle Geometry and Surface Orientation Influence Mode of Cellular Uptake. *ACS Nano* 2013, 7:1961-1973.
61. Alexis F, Pridgen E, Molnar LK, Farokhzad OC. Factors affecting the clearance and biodistribution of polymeric nanoparticles. *Mol Pharm* 2008, 5:505-515.
62. Agarwal R, Singh V, Jurney P, Shi L, Sreenivasan S, Roy K. Mammalian cells preferentially internalize hydrogel nanodiscs over nanorods and use shape-specific uptake mechanisms. *Proc Natl Acad Sci U S A* 2013, 110:17247-17252.
63. Nagai H, Okazaki Y, Chew SH, Misawa N, Yamashita Y, Akatsuka S, Ishihara T, Yamashita K, Yoshikawa Y, Yasui H, et al. Diameter and rigidity of multiwalled carbon nanotubes are critical factors in mesothelial injury and carcinogenesis. *Proc Natl Acad Sci U S A* 2011, 108:E1330-E1338.
64. Yoo JW, Doshi N, Mitragotri S. Endocytosis and Intracellular Distribution of PLGA Particles in Endothelial Cells: Effect of Particle Geometry. *Macromol Rapid Commun* 2010, 31:142-148.
65. Barua S, Yoo JW, Kolhar P, Wakankar A, Gokarn YR, Mitragotri S. Particle shape enhances specificity of antibody-displaying nanoparticles. *Proc Natl Acad Sci U S A* 2013, 110:3270-3275.
66. Fox ME, Szoka FC, Fréchet JMJ. Soluble Polymer Carriers for the Treatment of Cancer: The Importance of Molecular Architecture. *Acc Chem Res* 2009, 42:1141-1151.
67. Muñoz Javier A, Kreft O, Piera Alberola A, Kirchner C, Zebli B, Susha AS, Horn E, Kempter S, Skirtach AG, Rogach AL, et al. Combined Atomic Force Microscopy and Optical Microscopy Measurements as a Method to Investigate Particle Uptake by Cells. *Small* 2006, 2:394-400.
68. Hühn D, Kantner K, Geidel C, Brandholt S, De Cock I, Soenen SJH, Rivera Gil P, Montenegro J-M, Braeckmans K, Müllen K, et al. Polymer-Coated Nanoparticles Interacting with Proteins and Cells: Focusing on the Sign of the Net Charge. *ACS Nano* 2013, 7:3253-3263.
69. Schweiger C, Hartmann R, Zhang F, Parak WJ, Kissel T, Rivera Gil P. Quantification of the Internalization Patterns of Superparamagnetic Iron Oxide Nanoparticles with Opposite Charge. *J. Nanobiotechnol.* 2012, 10:28.
70. Frohlich E. The role of surface charge in cellular uptake and cytotoxicity of medical nanoparticles. *Int J Nanomedicine* 2012, 7:5577-5591.
71. Albertazzi L, Gherardini L, Brondi M, Sulis Sato S, Bifone A, Pizzorusso T, Ratto GM, Bardi G. In Vivo Distribution and Toxicity of PAMAM Dendrimers in the Central Nervous System Depend on Their Surface Chemistry. *Mol Pharm* 2012, 10:249-260.
72. Feliu N, Kohonen P, Ji J, Zhang Y, Karlsson HL, Palmberg L, Nyström A, Fadeel B. Next-Generation Sequencing Reveals Low-Dose Effects of Cationic Dendrimers in Primary Human Bronchial Epithelial Cells. *ACS Nano* 2014.
73. Dobrovolskaia MA, Patri AK, Simak J, Hall JB, Semberova J, Lacerda SHDP, McNeil SE. Nanoparticle Size and Surface Charge Determine Effects of PAMAM Dendrimers on Human Platelets in Vitro. *Mol Pharm* 2012, 9:382-393.
74. Mukherjee SP, Lyng FM, Garcia A, Davoren M, Byrne HJ. Mechanistic studies of in vitro cytotoxicity of poly(amidoamine) dendrimers in mammalian cells. *Toxicol Appl Pharmacol* 2010, 248:259-268.
75. Xia T, Kovochich M, Liong M, Meng H, Kabehie S, George S, Zink JI, Nel AE. Polyethyleneimine Coating Enhances the Cellular Uptake of Mesoporous Silica Nanoparticles and Allows Safe Delivery of siRNA and DNA Constructs. *ACS Nano* 2009, -3:3273 - 3286.

For Peer Review

76. Wong C, Stylianopoulos T, Cui JA, Martin J, Chauhan VP, Jiang W, Popovic Z, Jain RK, Bawendi MG, Fukumura D. Multistage nanoparticle delivery system for deep penetration into tumor tissue. *Proc Natl Acad Sci U S A* 2011, 108:2426-2431.
77. Richards D, Ivanisevic A. Inorganic material coatings and their effect on cytotoxicity. *Chem Soc Rev* 2012, 41:2052-2060.
78. Tay CY, Setyawati MI, Xie J, W. J. Parak , Leong DT. Back to Basics: Exploiting the Innate Physico-chemical Characteristics of Nanomaterials for Biomedical Applications. *Adv Funct Mater* 2014, 24:5936 – 5955.
79. Charron G, Hühn D, Perrier A, Cordier L, Pickett CJ, Nann T, Parak WJ. On the Use of pH Titration to Quantitatively Characterize Colloidal Nanoparticles. *Langmuir* 2012, 28:15141-15149.
80. Albanese A, Chan WC. Effect of gold nanoparticle aggregation on cell uptake and toxicity. *ACS Nano* 2011, 5:5478-5489.
81. Okuda-Shimazaki J, Takaku S, Kanehira K, Sonezaki S, Taniguchi A. Effects of Titanium Dioxide Nanoparticle Aggregate Size on Gene Expression. *Int J Mol Sci* 2010, 11:2383-2392.
82. Wick P, Manser P, Limbach LK, Dettlaff-Weglikowska U, Krumeich F, Roth S, Stark WJ, Bruinink A. The degree and kind of agglomeration affect carbon nanotube cytotoxicity. *Toxicol Lett* 2007, 168:121-131.
83. Balasubramanian SK, Poh KW, Ong CN, Kreyling WG, Ong WY, Yu LE. The effect of primary particle size on biodistribution of inhaled gold nano-agglomerates. *Biomaterials* 2013, 34:5439-5452.
84. Lin S, Zhao Y, Xia T, Meng H, Ji Z, Liu R, George S, Xiong S, Wang X, Zhang H, et al. High content screening in zebrafish speeds up hazard ranking of transition metal oxide nanoparticles. *ACS Nano* 2011, 5:7284-7295.
85. George S, Pokhrel S, Ji ZX, Henderson BL, Xia T, Li LJ, Zink JI, Nel AE, Madler L. Role of Fe Doping in Tuning the Band Gap of TiO2 for the Photo-Oxidation-Induced Cytotoxicity Paradigm. *J Am Chem Soc* 2011, 133:11270-11278.
86. Bedard MF, Munoz-Javier A, Mueller R, del Pino P, Fery A, Parak WJ, Skirtach AG, Sukhorukov GB. On the mechanical stability of polymeric microcontainers functionalized with nanoparticles. *Soft Matter* 2009, 5:148-155.
87. Hartmann R, Weidenbach M, Neubauer M, Fery A, Parak WJ. Stiffness-dependent in vitro uptake and lysosomal acidification of colloidal particles. *Angew Chem Int Ed.*
88. Chanana M, Rivera Gil P, Correa-Duarte MA, Parak WJ, Liz-Marzán LM. Physicochemical properties of protein-coated gold nanoparticles in biological fluids and cells before and after proteolytic digestion. *Angew Chem Int Ed* 2013, 52:4179-4183.
89. Brandenberger C, Mühlfeld C, Ali Z, Lenz A-G, Schmid O, Parak WJ, Gehr P, Rothen-Rutishauser B. Quantitative Evaluation of Cellular Uptake and Trafficking of Plain and Polyethylene Glycol-Coated Gold Nanoparticles. *Small* 2010, 6:1669-1678
90. Lipka M, Semmler-Behnke M, Sperling RA, Wenk A, Takenaka S, Schleh C, Kissel T, Parak WJ, Kreyling WG. Biodistribution of PEG-modified gold nanoparticles following intratracheal instillation and intravenous injection. *Biomaterials* 2010, 31:6574-6581.
91. Soenen SJ, Manshian B, Montenegro JM, Amin F, Meermann B, Thiron T, Cornelissen M, Vanhaecke F, Shareen D, Parak WJ, et al. Cytotoxic Effects of Gold Nanoparticles: A Multiparametric Study. *ACS Nano* 2012, 6:5767-5783.
92. Soenen SJ, Manshian BB, Abdelmonem AM, Montenegro J-M, Tan S, Balcaen L, Vanhaecke F, Brisson AR, Parak WJ, Smedt SCD, et al. The Cellular Interactions of PEGylated Gold Nanoparticles: Effect of PEGylation on Cellular Uptake and Cytotoxicity. *Part Part Syst Char* 2014, 31:794-800.

For Peer Review

93. Riedinger A, Zhang F, Dommershausen F, Röcker C, Brandholt S, Nienhaus GU, Koert U, Parak WJ. Ratiometric Optical Sensing of Chloride Ions with Organic Fluorophore - Gold Nanoparticle Hybrids: A Systematic Study of Distance Dependency and the Influence of Surface Charge. *Small* 2010, 6:2590-2597.
94. Fee CJ, Alstine JMV. Prediction of the Viscosity Radius and the Size Exclusion Chromatography Behavior of PEGylated Proteins. *Bioconjugate Chem* 2004, 15:1304-1313.
95. Xia XH, Yang MX, Wang YC, Zheng YQ, Li QG, Chen JY, Xia YN. Quantifying the Coverage Density of Poly(ethylene glycol) Chains on the Surface of Gold Nanostructures. *ACS Nano* 2012, 6:512-522.
96. Liu XO, Atwater M, Wang JH, Huo Q. Extinction Coefficient of Gold Nanoparticles with Different Sizes and Different Capping Ligands. *Colloids Surf, B* 2007, 58:3-7.
97. Haiss W, Thanh NTK, Aveyard J, Fernig DG. Determination of Size and Concentration of Gold Nanoparticles from UV-Vis Spectra. *Anal Chem* 2007, 79:4215-4221.
98. Yu WW, Qu L, Guo W, Peng X. Experimental Determination of the Extinction Coefficient of CdTe, CdSe, and CdS Nanocrystals. *Chem Mater* 2003, 15:2854-2860.
99. Striolo A, Ward J, Prausnitz JM, Parak WJ, Zanchet D, Gerion D, Milliron DJ, Alivisatos AP. Molecular Weight, Osmotic Second Virial Coefficient, and Extinction Coefficient of colloidal CdSe Nanocrystals. *J Phys Chem B* 2002, 106:5500-5505.

For Peer Review

Gold-based nanomaterials for applications in nanomedicine

Sumaira Ashraf[1*], Beatriz Pelaz[1], Pablo del Pino[2], Mónica Carril[2,3], Alberto Escudero[1,4], Wolfgang J. Parak[1,2], Mahmoud Gamal, Mohamed Soliman[1], Qian Zhang[1], Carolina Carrillo-Carrion[1*]

[1] Fachbereich Physik, Philipps Universität Marburg, 35037 Marburg, Germany
[2] CIC biomaGUNE, San Sebastian, Spain
[3] Ikerbasque, Basque Foundation for Science, 48011 Bilbao, Spain
[4] Instituto de Ciencia de Materiales de Sevilla. CSIC-University of Seville, 41092 Seville, Spain

[*]corresponding authors:
ashraf@staff.uni-marburg.de, carolina.carrillocarrion@physik.uni-marburg.de

Abstract

In this review, an overview about the current state-of-the-art of gold-based nanomaterials (Au NPs) in medical applications is given. The unique properties of Au NPs, such as their tunable size, shape, and surface characteristics, optical properties, biocompatibility, low cytotoxicity, high stability, and multifunctionality potential among others, make them highly attractive in many aspects of medicine. First, the preparation methods for various Au NPs including functionalization strategies for selective targeting are summarized. Second, recent progresses on their application, ranging from the diagnostics to therapeutics are highlighted. Finally, the rapidly growing and promising field of gold-based theranostic nano-platforms is discussed. Considering the great body of existing information and the high speed of its renewal, we chose in this review to generalize the data that have been accumulated during the past few years for the most promising directions in the use of Au NPs in current medical research.

Keywords: gold nanoparticles, nanomedicine, diagnostics, therapeutics, theranostics.

1. Introduction

In recent years, there has been an unprecedented expansion in the field of nanomedicine, which involves the development of novel nanoparticles (NPs) envisaged for the diagnosis and treatment of several diseases, especially in cancer. NPs possess extraordinary capabilities to detect, image, and potentially treat diseases at the cellular and molecular levels [1-7]. While micelle-based NPs (such as formulations loaded with doxorubicin, paclitaxel, or cisplatin) [8] are most advanced towards use in clinical practice, also inorganic NPs offer great potential. Among various inorganic NPs, Au NPs are important examples in the field of nanomedicine, thanks to their chemical, physical, and optical properties [9-13]. Their unique physical and chemical properties, such as inertia, biocompatibility, low levels of cytotoxicity, stability against oxidation and degradation *in vivo,* and ease of conjugation to biomolecules, provide significant benefits in comparison with other NPs from a medico-biological point of view. The

optical properties of Au NPs are determined by the so-called localized surface plasmon resonance band (LSPR) [14], which is associated with a collective excitation of conduction electrons. Depending on the size, shape, structure and the NPs environment, the LSPR can be localized in a wide region from the visible to the infrared. Implementation of different surface chemistries enables them to have high stability, high carrier capacity, ability to incorporate both hydrophilic and hydrophobic substances, and compatibility with different administration routes. Due to the nano-size, Au NPs have good tumor retention capabilities because they can penetrate the leaky tumor vasculature. These properties make Au NPs interesting materials towards sensing, detection, imaging, targeted delivery of drugs and genes, photo-induced therapies, enhanced radiotherapy and so on. Furthermore, the multifunctionality potential of Au NPs provides an ideal platform for developing the theranostic modalities combining therapeutic, targeting and imaging functions while possessing synergistic effects of multi-therapies. Figure 1 shows a simplified scheme of different areas of research where Au NPs are involved in the development towards nanomedicine. The evolution of research has progressed from the synthesis and functionalization towards applications. The evolution started with simple and unimodal applications towards more complex multimodal applications (*e.g.* multimodal imaging, dual-mode therapies, etc.). The latest development is focused on theranostics nanoplatforms, which can diagnose, deliver targeted therapy and monitor response to therapy. Although the natural evolution is from the bottom to the top (as drawn in the scheme), in parallel *(i.e.* in transversal mode), studies of toxicity and bio-distribution are key aspects to guarantee the success of their applications. These studies as well as results of the application performances have a direct feedback in synthesis and functionalization for improvements. These inputs are the reason why new strategies of synthesis are continuously an active area of research.

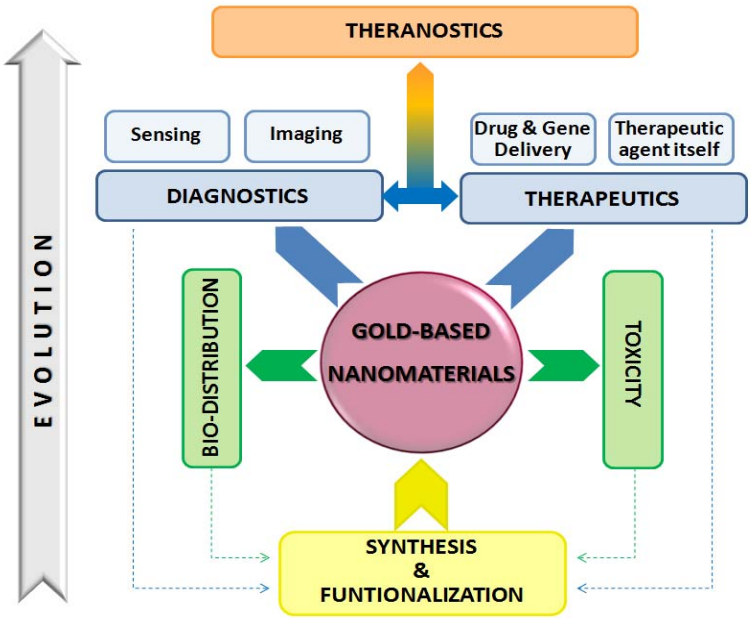

Figure 1. *Scheme showing different areas of research of* Au NPs*, involved in the development of their applications in nanomedicine.*

The following sections describe some recent advances in the different areas of research using Au NPs, mainly focusing on their potential for medical applications, as well as the hurdles to be overcome to translate them into clinical trials. Bio-distribution and toxicity have been extensively reviewed and discussed in a number of recent publications [15-18], thus we will discuss it shortly in the conclusions section. As the topic of this review involves huge amounts of information with a high speed of renewal, we will focus on major ideas and some of the most recent and promising studies performed during the past few years.

2. Synthesis and functionalization of Au NPs

2.1. Synthesis

Before the advent of nanoscience, Au NPs were already attracting interest due to their optical properties. There are many historical examples in which Au NPs were applied even without knowing it (*e.g.* Lycurgus cup, or the church glass windows). In the last decades, the control in the synthesis of Au NPs has evolved greatly. Nowadays it is possible to produce Au NPs with different sizes and shapes in a highly controlled manner. In the last decades, already many reviews and book chapters have been published about the state of the art of the Au NPs synthesis [13, 19-22]. Thus, here we aim to provide an overview of some of the most recent achievements about the synthesis of Au NPs using wet chemistry (though also other routes such as laser ablation exist [23]).

Most wet-chemistry based Au NPs are synthesized in aqueous media, but there are some important examples to produce hydrophobically-capped Au NPs (*e.g.* Brust-Schriffin method) [24]. These NPs are typically spherical with a size less than 10 nm. It is well known, that most of the applications of Au NPs in nanomedicine are based on their optical properties, *i.e.* LSPR [25]. The desire for tuning of the LSPR has been a driving force to develop synthesis strategies allowing for Au NPs with different sizes and shapes. While controlled synthesis of Au NPs is known since the days of Michael Faraday, the origin of the most synthetic strategies to produce water soluble spherical Au NPs are based on the Turkevich method [26]. This method has been continuously improved to produce better samples (*e.g.* with narrow size distribution and more homogeneous NPs). This optimized methodology also allows growing the Au NPs having sizes up to 200 nm [27]. Yet arguably the most interesting Au NPs for bio-applications are anisotropic Au NPs that exhibit their LSPR in the biological window. This biological window comprises the spectral region of 700 - 1100 nm, in which the body tissue components absorb less light. This range therefore is the desired region to locate the LSPR of Au NPs intended to be used for bio-applications (*e.g.* photothermal therapy (PTT) [28, 29], or optoacoustic imaging (OAI) [30]). The recent controls over the shape during the synthesis of Au NPs make it possible to tune the position of the LSPR by changing parameters such as the shape (*e.g.* rods, prisms, etc.) [28, 31], or the structure of the NPs (*e.g.* hollow versus homogeneous) [32]. To induce the growth of anisotropic NPs it is necessary to provoke either a kinetically controlled growth of the NPs or to induce the blocking of some growing facets [33]. The sphere is the most stable shape in terms of energy. If the NPs synthesis is performed under thermodynamically controlled conditions, the obtained NPs will be spherical. In general, to obtain non-spherical NPs the synthetic conditions have to be tuned to induce kinetically controlled NPs growth. This can be performed using surfactants that will block some growing facets (e.g.

cetyltrimetylammonium bromide (CTAB) or polymers) [34], using halides (*e.g.* Br^-, I^-) [35] or weak and mild reductants (*e.g.* $Na_2S_2O_3$) [28].

To date Au nanorods remain the most broadly used anisotropic NPs. These NPs with rod-shape were described almost at the same time by the groups of El-Sayed [36, 37] and Murphy [28]. Since then, the synthesis of these NPs has been deeply explored. In general, the synthesis of Au nanorods is performed by using the growth seeding process. Firstly small spherical Au NPs are synthesized and then are added to the growing solution rich in CTAB to induce rod-shaped growth. Due to the cytotoxicity of CTAB [38], recently Murray *et al.* have developed a modified Au nanorods synthesis method in which the required CTAB concentration is reduced to the half (from 0.1 M from El-Sayed and Murphy to 0.05 M) [31, 39]. This synthesis is based on the use of aromatic additives.

Other important type of anisotropic NPs are the Au nanoshells developed by Halas *et al.* [40]. These structures are built using a silica core in which gold is grown. Their LSPR can be modulated by controlling the relationship between the core size and the thickness of the gold shell. By changing the shape of the core, other similar structures have been also described such as "nanorice" [41]. Halas *et al.* also described a synthesis for "nanomatryushkas", which are multilayered spheres. The simplest "nanomatryushka" contains a core of a gold sphere of ca. 40 nm coated with a SiO_2 shell and a second shell of Au [42]. Several bilayers of SiO_2 and Au can be deposited to obtain more complex "nanomatryushkas".

Au nanoprisms also have been described. The synthesis of triangular nanoprisms often can be achieved only with a low yield [43], and by using toxic surfactants (*e.g.* CTAB or CTAC (cetyltrimethylammonium chloride))[44]. Recently a synthesis route eliminating the use of toxic surfactants has been reported, which allows for tuning the LSPR position by controlling the amount of reductant. This synthesis is based on the reduction of a gold salt by thiosulfate (Figure 2a) [28].

Au nanostars as well exhibit their LSPR in the biological window. Many different synthetic procedures to produce Au nanostars have been reported. For generating Au nanostars, typically the seed-growing method is used. For instance, Liz-Marzán *et al.* published a method in which gold salt was reduced to metallic gold on the top of 15 nm Au NPs stabilized with poly(vinylpyrrolidone) (PVP) in the presence of dimethylformamide and PVP [45].

Finally, Au nanocages, originally developed by the group of Y. Xia, have been applied extensively with different purposes in nanomedicine [46, 47]. These cages are prepared by using a sacrificial silver nanocube, which then is oxidized to promote the reduction of gold through a galvanic replacement process. Similar approaches have been described using silver nanospheres [48] and silver nanoprisms [49].

Aiming to use green chemistry and less toxic reagents, the production of Au NPs using natural extracts from microorganisms (*e.g.* micro alga [50] or fungi [51]) or plants has been also explored [50, 52] . Nevertheless, the yield and quality of these Au NPs is still far below the quality of the previously described approaches.

Au-based hybrid materials have been developed too, trying to combine the great optical properties of gold with the properties of another material. Several examples of core-shell structures of Au containing iron oxide [53-55] or semiconductors cores [54] or Au cores coated

with silver (bimetallic NPs [56]) can be found in literature. More recently, Au has been combined with more novel materials like nanodiamonds [57] or graphene [58, 59].

2.2. Functionalization

After synthesis and before their use in bio-applications, NPs must be provided with stable coatings which should warrant high colloidal stability. Thus, robust organic coatings ensure that the NPs' properties remain intact in biological media [60]. Indeed the NP surface will determine their biological fate [61]. In addition, any kind of by-product related with the synthesis, including excess of reagents or cytotoxic surfactants should be ideally washed off, in order to remove potential toxic effects due to these impurities. To achieve coatings qualifying for these requirements the NPs' surfaces need to be engineered. One of the biggest advantages of the use of Au is its high reactivity with thiol groups [62]. This reactivity allows for stabilizing the NPs with ligands containing a thiol reactive group. Ligand exchange by which original surfactants are replaced by new ones is the most common stabilizing procedure for Au NPs. Ligand exchange can be used to water transfer hydrophobically-capped NPs (*e.g.* NPs capped with alkanethiol chains) [63], and to replace toxic surfactants (*e.g.* CTAB) used to produce anisotropic NPs like Au nanorods [64, 65].

Typically, polyethylene glycol (PEG) chains which provide the NPs with a colloidal high stability in biological media and long *in vivo* retention times [19, 66] are the most widely used stabilizers for Au NPs. Nowadays, there are many companies which offer an sheer endless number of hetero-functional PEG chains. Using bi-functional PEG allows for future chemical modifications for the attachment of molecules (*e.g.* dyes, carbohydrates, antibodies, peptides, etc.) and/or to provide charge to the NPs (Figure 2a) [28, 67, 68]. Not only PEG is used to stabilize Au NPs, but also other ligands such as dihydrolipoic acid [69], proteins (*e.g.* bovine serum albumin) [70], or polymers are used regularly to enhance the NPs' stability in complexes media. Polymers used for this purpose include for example polyelectrolytes [71], PVP [72] or amphiphilic polymers [73].

The use of amphiphilic polymers to stabilize NPs and to promote their transfer from organic solvents to aqueous solutions is based on polymer coating of the NPs. This approach can be used for virtually any kind of NPs containing aliphatic chains on the surface (*e.g.* oleic acid, oleylamine, etc.) [73, 74]. The advantages of this technique are plentiful: *i)* coated NPs exhibit a high colloidal stability against media with high salt concentrations and/or proteins, *ii)* NPs coated with the same polymer will have the same surface chemistry, *iii)* these polymers can be made with reactive groups in their hydrophilic domain (*e.g.* carboxylic acids), which then can be further modified with biologically relevant molecules. The main limitation of this technique is that it can be only applied for NPs soluble in organic solvents. Yet most of the anisotropic Au NPs are synthesized in water. Recently an extension of this method based on phase transfer of the water-soluble Au NPs to organic solvents has been reported. This method has been demonstrated for spherical Au NPs (with size up to 15 nm) and Au nanorods (Figure 2b) [75].

Once Au NPs are sufficiently colloidally stable in biological media, as a function of their surface chemistry, different chemical modifications can be performed. Bioconjugate chemistry protocols developed for modifying proteins, peptides and/or surfaces can be adapted to NPs [76, 77]. Concerning bio-conjugation we refer to some recent reviews [11, 78-80]. In summary,

currently the synthesis and functionalization of Au NPs has become very versatile. This allows scientists to develop the best customized systems for each application.

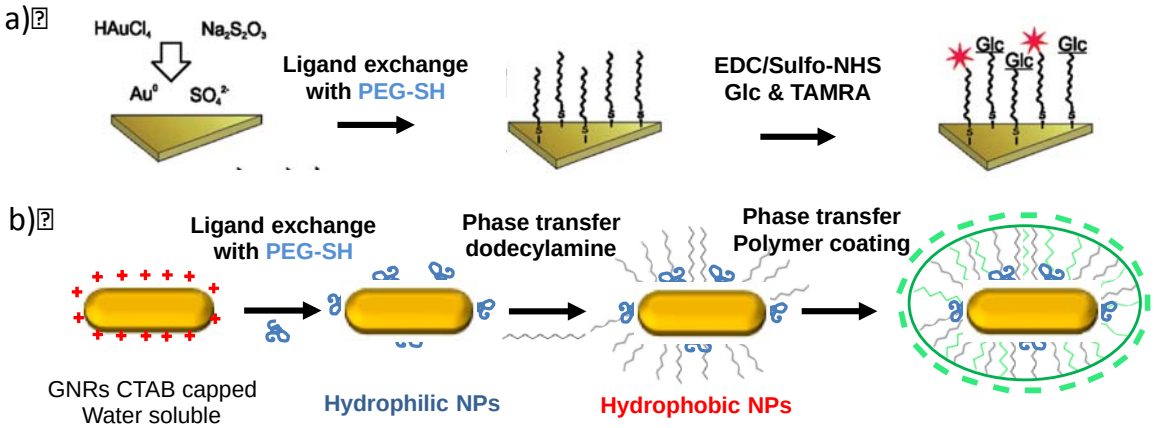

Figure 2. Schemes for the synthesis and functionalization of Au NPs: *a)* synthesis of Au nanoprisms, PEGylation and linkage of glucose (Glc) and tetramethylrhodamine (TAMRA) using carbodiimide (EDC) chemistry [28], and *b)* strategy of phase transfer to coat Au nanorods (GNRs) with amphiphilic polymers [75].

3. Use of Au NPs towards diagnostics

3.1. Detection and sensing

Different analytical assays involving Au NPs are widely used as sensors, ranging from the detection of ions and elements to more complex molecules, including those of biomedical interest, such as oligonucleotides, proteins, antibodies, and even bacteria and other microorganisms. The methods of designing sensing biomarkers that could be associated with the early stage diagnosis of different diseases are nowadays attracting special interest. The current challenges consist of designing sensing devices that are able to recognize more specifically different types of analytes, discriminating molecules with similar characteristics, including the use of sensor arrays, which often combine several analytical approaches. Advances in enhancing the sensitivity and reducing the time of analysis are also currently demanded. The physical and analytical basis of sensing with Au NPs can be summarized in different main areas [81]. They include measurements based on colorimetry and plasmon resonance, fluorescence, electrochemistry, and more recently, surface enhanced Raman spectroscopy (SERS) [82].

Colorimetric assays are based on a visible change of colour of functionalised Au NPs suspensions when interacting with the appropriate analyte [83-86]. Colorimetric analyses are normally fast and can be even often evaluated with the naked eye. As explained before Au NPs exhibit plasmonic properties. The position and intensity of this LSPR band depend not only on the metal type, NPs size, shape, structure, composition and the dielectric constant of the surrounding medium [87], but also on the aggregation of the NPs [88]. Colorimetric assays are based on this effect, since analytes that produce a change in the aggregation state of Au NPs will give rise to a change in the LSPR absorption band of the NPs dispersion [89]. Such effect is

not only used to sense cations and anions [89-92], but has been also applied to sense molecules of biomedical interest. For example, DNA has been detected by Au NPs wrapped with long genomic single- and double-stranded DNA (ssDNA and dsDNA) molecules [93]. Also proteins such as melamine and human carbonic anhydrase II have been sensed by cyanuric acid derivative grafted Au NPs [94], and polypeptide-functionalized Au NPs [95], respectively. More complex molecules such as folate receptors (FRs), consisting of cysteine-rich cell-surface glycoproteins that can bind folate (FA), can be sensed by FA-modified ssDNA functionalised Au NPs. In the presence of FRs, ssDNA terminally tethered to FA is protected from degradation by exonucleases, and an aggregation of the Au NPs takes place through the formation of cross-linked NPs networks, resulting in a colour change of the solution from red to blue [96]. Polyethyleneimine (PEI)-stabilized Au NPs have been used for highly selective and sensitive colorimetric sensing of heparin [97]. Abnormal concentration values of human chorionic gonadotropin (hCG) can be associated with ectopic pregnancy. The concentration of this biomarker can be determined using Au NPs in the presence of positively charged hCG-specific peptides. In this case, hCG inhibits the peptide-induced aggregation of the Au NPs, giving rise to a simple, rapid and sensitive colorimetric assay [98]. A rapid and low-cost colorimetric analysis of bacteria in drinking water has been designed by using β-galactosidase conjugated Au NPs with a colorimetric substrate (chlorophenol red-β-D-galactopyranoside (CPRG)) deposited on a paper-based test strip [99]. The aggregations of antibody-conjugated oval-shaped Au NPs that selectively target specific sites on the surface of pathogens have been used to sense Salmonella [100]. While colorimetric assays based on Au NPs are based on the large shift of the LSPR band depending on NPs aggregation, a small LSPR peak shift can also be produced when an appropriate analyte binds to the surface-bound receptors of plasmonic NPs, due to a change in the refractive index [101]. In contrast to agglomeration-based protocols this shift in the LSPR frequency is not enough to be detected by the naked eye, but can be observed by absorption measurements. Au NPs deposited on several substrates have been used to detect in this way analytes such as DNA [102], human IgG (Immunoglobulin G) [103], and insulin [104]. Recent advances in the detection of microRNAs (miRNAs) by Au nanoprisms without the need for labels [105], and in the sensing of trace oligonucleotides biomarkers [106] have also been reported. Au NPs deposited on the metal sensing surface increase the sensitivity of planar surface plasmon resonance sensors, provided by the high dielectric constants of Au NPs and the electromagnetic coupling with the metal film [107]. This approach has been used for the sensing of different proteins [108] and oligonucleotides [108, 109].

Fluorescence assessments involving Au NPs are widely centred on fluorescence quenching-based methods. Au NPs show an important quenching effect on fluorophores close to their surface due to their extraordinary high molar extinction coefficients and broad energy bandwidths [83, 110]. Specific interactions with the sensing molecules have been used to detect many different molecules of biomedical interest. Some assays are based on the appearance of fluorescence when the target molecules interact with the Au NPs based-sensors. For example, the quenching of a fluorophore attached to a Au NP through an oligonucleotide chain disappears in the presence of DNA [111], when the fluorophore gets detached from the NPs due to displacement by the DNA strand. Similar strategies have been used to sense proteins [112], and bacteria [113], using Au NPs conjugated with fluorescent

polymers. Au NPs functionalised with enzymes have been also used to sense proteins, with an enhanced sensitivity through enzymatic catalysis [114].

Fluorescence quenching assays involving Au NPs are not only restricted to the detection of single analytes. More complicated sensing techniques, focused on the study of the interaction of different analytes have also been reported. For example, dsDNA-conjugated Au NPs (dsDNA-Au NPs) and water-soluble conjugated polyelectrolytes (CPEs) are used as complementary sensing elements to construct hybrid sensors for detecting protein–DNA interactions [115]. The use of sets of sensors showing different patterns of responses in an array can provide fingerprints that allow for classification and identification of different target molecules [116]. Such approach is used with DNA–Au NPs conjugates, in which a combination of colorimetric and fluorescence assessments enables better selectivity to distinguish different proteins [117]. Similar combination of colorimetric and fluorometric approaches has been reported for a sensor array consisting of two types of novel blue-emitting collagen protected Au nanoclusters and macerozyme R-10 protected Au nanoclusters with lower synthetic demands, which has been recently used to sense eight different proteins [118].

The modulation of quenching of fluorescent semiconductor quantum dots (QDs) close to Au NPs in the presence of molecules which inhibit the interaction between QDs- and Au NPs-conjugated biomolecules has been used to sense molecules of biomedical interest such as avidin [119]. Normal, cancerous and metastatic human breast cells have been distinguished by comparing the fluorescence of different cationic Au NPs functionalized with poly(para-phenyleneethynylene) (PPE), which show different affinities for normal and tumour cells [120].

The conductivity, roughening of the conductive sensing interface and the catalytic properties of Au NPs have been harnessed for the huge amount of analytical assays based on electrochemical measurements that involve Au and other metal-based NPs [121]. Different immunosensors based on Au NPs have been recently reported to detect cancer biomarkers [122, 123]. Au NPs deposited on electrode surfaces are known to enhance the electrochemical detection of different analytes, due to their ability to decrease the over potentials of many electroanalytical reactions, while maintaining the reversibility of redox reactions [124, 125]. This approach has been used to detect several drugs such as isoniazid [126], and hCG [127]. Au nanorods have also been used as sensing interface in pencil graphite electrodes for the electrochemical sensing of deferiprone, an anti-HIV drug, resulting in an amplification of the electrochemical sensing signal [128].

Antibody-functionalised Au NPs, showing target specificity and affinity towards different biomarkers [129], have been used to sense salmonella by differential pulse voltammetry (DPV) [130]. Cancer circulating cells have been sensed by combining the specific labelling through antibody-modified Au NPs and the sensitivity of the Au NPs-electro-catalyzed hydrogen evolution reaction (HER) detection technique [131]. The reaction of cell surface proteins with specific antibodies conjugated to Au NPs, as well as the catalytic properties of the Au NPs on hydrogen formation from hydrogen ions can be used to quantify the NPs internalized by cancer cells [132, 133].

Raman scattering permits the detection and analysis of many molecules, by giving a unique spectroscopic signature that potentially identifies the species [134]. The Raman scattering signal can be substantially enhanced by the presence of plasmonic NPs, resulting in SERS

[135, 136]. This effect is highly influenced by the size, shape, orientation and aggregation of the NPs [108]. In fact, Au NPs with different morphologies have been used for SERS-based detection [137-139]. Label-free and Raman-dye labelled assays are two different existing SERS-based detection methods. Label-free assays follow vibrational information about the analytes themselves, whereas the dye-labelled methods detect analytes indirectly by monitoring the SERS signal of a Raman label that is attached to the metallic SERS substrate [140]. Different SERS assays for sensing DNA [141, 142] and proteins [143, 144] using Au NPs can be found in literature. Recently, an extended bi-dimensional array of Au concave nanocubes supported on a polydimethylsiloxane (PDMS) film has been proposed for the SERS sensing of proteins which show low intensity Raman signals [145]. The assembly of spherical Au NPs on a highly anisotropic silica-coated substrate has been recently reported for the detection of prostate specific antigen by SERS [146]. Recently, the selectively quenching of the SERS signals from the dye molecules adsorbed onto star-shaped Au NPs not internalized by cells has been used to identify intracellular distributions of Au NPs [147].

3.2. Imaging

For the treatment of many diseases and non-invasive evaluation/detection of intra-cellular and/or intra-subcellular compartments, molecular imaging based on functional nanomaterials is of paramount importance [148, 149]. For molecular imaging, different types of NPs are currently in use. Examples comprise polymer-based NPs [150-152], dendrimer-based NPs [153, 154], lipid-based NPs [155, 156], magnetic NPs [157-160], QDs [161-163], carbon nanotubes (CNTs) [164, 165], silica NPs [166-168], and Au NPs [169-172], etc. Among all above mentioned NPs, Au NPs possess extraordinary potential for imaging at the cellular and even molecular level. Various Au NPs are currently in use in molecular imaging, based on their different size, shape and physical properties. Examples involve spherical Au NPs [171, 172], nanorods [173-175], nanobipyramids [19], nanoshells [176], nanocages [177-179], core/shell NPs [171, 180], nanostars [181-183], and nanocubes [149], etc.

Au NPs have unique characteristics which enable their use as contrast agents in bio-medical imaging [184, 185]. In this field, they are being used as probes in dark field confocal imaging (DFCI), one and two photon fluorescence imaging (OTPFI), optoacoustic imaging (OI), computed tomography (CT), photothermal optical coherence tomography (POCT), positron emission tomography (PET), and imaging based on surface enhanced Raman scattering (SERS) [175, 184]. Different imaging modalities of the Au NPs can be combined, which can provide complementary information. In the following a description of using Au NPs as contrast agents for the different imaging techniques is given.

DFCI provides contrast enhancement in unstained biological samples but its main limitation is that it provides low light levels in images. Thus, for better visualization the biological samples should be strongly illuminated, which however can damage the samples. The imaging contrast of dark field microscopy can be enhanced by utilizing the high scattering properties of Au NPs [186]. For cellular detection, mostly the light scattering properties of Au NPs are utilized for straightforward image analysis. Light scattered from Au NPs is detected by using high resolution objective lenses of dark field confocal (DFC) microscopes in the form of bright spots, though the size of Au NPs is in general smaller than the diffraction limit of DFC. Recently, by using Au nanoshells it was possible to observe the binding and antibody mediated specific

targeting of cancer cells in *in vitro* experiments, using dark field scattering properties of the NPs [187]. Similarly, for cancer cells localization, targeting and real time tracking of Au nanorods induced DNA damage in cancer cells was visualized using DFCI [188]. Scattering properties of Au NPs are also being utilized for better imaging of breast cancer cells [189]. But despite of the high scattering cross sections of Au NPs for enhancing the contrast in DFCI, their use is only limited for *in vitro* experiments [184].

Photoluminescent properties of sub-nanometer Au nanoclusters made them attractive candidates in OTPFI based on their brightness, non-blinking behavior, and stable emission [190, 191]. The luminescence of Au nanoclusters in the near infrared (NIR) window is used for fluorescence imaging and they have greater photostability than QDs [191]. Not only nanoclusters but also other Au NPs, such as nanoshells and nanostars, can be used in one photon fluorescence imaging (OPFI), after conjugation of the Au NPs with NIR active fluorophores such as indocyanine green or Cy5 [192]. After conjugation with these fluorophores, these structures help in emission enhancement of these dyes for better fluorescence imaging. Presence of a metal surface close to fluorophores does not always quench fluorescence, but can also provide fluorescence enhancement, in particular for very close distances. In OPFI, Au NPs functionalized with fluorophores, offer a suitable platform for *in vitro* and *in vivo* cancer imaging and diagnostics [193, 194]. When Au NPs are excited with femtosecond pulsed lasers whose resonance frequency matches with the LSPR band of the Au NPs, two photon absorption occurs which results in two photon luminescence from the Au NPs [182, 193, 195]. For monitoring *in vivo* biological events, TPLI (two photon luminescence imaging) provides sufficient penetration depth and high 3 dimensional (3D) spatial resolution. The signal intensity of TPL (two photon luminescence) can be enhanced 3 times in magnitude by utilizing the high luminescent properties of Au nanorods and nanocages without photo-bleaching or blinking which is observed in many fluorophores used in this technique [196]. The contrast of Au nanostars conjugated with wheat germ agglutinin in TPL based imaging can be utilized for imaging their uptake [182]. Similarly, other Au NP structures, such as nanorods, nanocages, and nanoshells are also being used as contrast agents in TPL with a resolution at the single NP level inside blood vessels. In this way *in vivo* tracking of Au NPs and fluorescence lifetime imaging for visualizing dynamical processes in cell media is possible [197, 198]. After one and two photon luminescence based imaging, now Au nano-cages are being utilized also in three photon luminescence (TPL), based on their large multi-photon absorption capabilities. TPL using Au nanocages can be used for *in vivo* detection with diminished background signals and reduced photothermal toxicity [199]. Further studies are still required for using Au NPs in TPL for a better understanding of their role in this imaging technique.

The penetration depth of OI based imaging, which typically is carried out with NIR pulsed sources, is similar to ultrasound based imaging, *i.e.* several centimeters in biological tissues (typically less than 5 cm). This is better compared to simple optical imaging, in which depth resolution is only on the millimeter scale. The photothermal properties of Au NPs provide high contrast in OI [30]. Upon photo-excitation, the non-radiative decay of Au NPs converts light energy into heat, which causes a sharp rise of temperature in the local environment of the NPs, resulting in thermal and acoustic response enhancement in those tissues which contain the photoexcited NPs. The increased thermal response of Au NPs enhances the pressure waves

propagating through the surrounding tissues and results in improving the temporal and spatial resolution of tomographic images [200].

In clinical detection of several diseases CT has receiving increasing attention due to high spatial and density resolution. For imaging biological systems using CT, usually contrast agents are required (which can enhance the density of the imaging area) for improving the accuracy in diagnosis. Iodine based small molecules such as “Omnipaque” are normally used in clinics, but are associated with certain drawbacks such as short imaging time, non-specificity and renal toxicity. For overcoming these drawbacks nowadays Au NPs based suitable contrast agents are being developed. In CT, due to high atomic number of Au, Au NPs are providing higher spatial and density resolution as compared to iodine based contrast agents such as “Omnipaque”. In CT based imaging, Au NPs attenuates X-rays much more efficiently as compared to “Omnipaque” resulting in contrast enhancement by several orders of magnitude [201, 202]. Moreover, by suitable tuning the size and functionalization of the Au NPs besides improving CT imaging, it is also possible to achieve target specificity, long circulation time and reduced renal toxicity [203].

Optical coherence tomography (OCT) can image cellular and sub-cellular structures 100 times better than CT and magnetic resonance imaging (MRI) and provides 10-25 times better spatial resolution as compared to ultrasound based images [204]. OCT is non-invasive technique, resembling with ultrasound based imaging, but in this technique instead of sound, reflections of NIR light are used for imaging. NIR active contrast agents *e.g.* Au nanorods can significantly improve OCT based imaging due to their large differences in absorption-scattering profiles. Au nanoshells and nanocages, due to their high scattering properties can also provide enhanced optical contrast and brightness in OCT for improving the imaging of cancerous cells [205]. In this technique tissues are illuminated with low coherent light and matching the coherence between incident and reflected beams of light helps in the detection of back reflected light. This back scattered light thus helps in imaging. Since OCT is much more sensitive towards detection of scattering from the tissues than absorption, therefore, the scattered light helps in studying the morphology of tissues [205]. In OCT Au NPs are being used as exogenous contrast agents based on their ability of producing distinctive backscattered light which is detectable in highly scattering tissues hence helping in studying the morphology of tissues [206]. Though OCT is a powerful 3 D diagnostic tool in real time imaging, its resolution is low due to intense scattering from some optical dense tissues under investigation. To overcome this limitation nowadays POCT (photothermal-OCT) imaging techniques using the photothermal properties of Au NPs are being developed [207]. In POCT, when light resonant with the plasmon energy of Au NPs strikes, Au NPs are excited and light is converted into heat and surface temperature of tissues is enhanced. The increase in surface temperature results in changing the local refractive index of medium which is then optically detected by POCT. Due to active detection of photothermal heating, POCT can identify and separate absorbing targets from scattering background, hence helps in high resolution imaging as compared to OCT [208].

In early stage diagnosis of cancer, PET with its highly sensitive nuclear imaging modality is extensively utilized in clinical studies using small doses of radioactive materials. But these radioactive materials, especially small radioactive molecules, usually have short circulatory life time in *in vivo* studies. Au NPs *e.g.* nanocages, nanoshells and spherical NPs after radiolabelling can remain inside the blood stream for longer periods of time. Hence they facilitate long term

bio-imaging [209]. In PET radioisotopes undergo positron emission decay or positive beta decay and positrons are emitted. These emitted positrons traverse a short distance inside tissues, loose kinetic energy and interact with electrons. This union with electrons results in their annihilation and production of gamma photons in the form of light which is used for making images [209]. Sometimes PET is coupled with Cerenkov luminescence (CL) based imaging for better visualization and cross checking the imaging results. CL based imaging is a molecular imaging technique based on Cerenkov radiation, which can be originated from the decay of alpha, beta or positron emitting radionuclides [179]. Recently, radiolabeled precursor of gold salt ($H^{198}AuCl_4$) was used for the synthesis of radioactive Au nanocages which gave CL. The CL originating from the decay of radionuclides helps in real time CL based imaging and monitoring of tumors over extended periods of time. CL of radionuclides can be increased by using high refractive index materials like gold in conjugation with higher energy radionuclides. Thus CL imaging based on Au NPs can effectively bridge the gap between nuclear and optical imaging [179]. CL based imaging can use radionuclides for diagnosis of diseases, which are routinely used for PET based imaging. CL based imaging improves PET based imaging in terms of resolution. CL imaging signal can be modulated by using smart imaging agents such as NPs hence better insight in tumor biology can be obtained [210]. Since the last decade there are numerous studies for enhancing the efficacy of SERS based molecular imaging using Au NPs conjugated with Raman active moieties. Au NPs enhance the Raman scattering of vicinal molecules by means of chemical and electromagnetic enhancements. Au NPs enable identification of single molecules spectroscopically at room temperature, by amplifying (ca. 10^{15}-fold) the Raman scattering signals of adsorbed species. The LSPR of Au NPs enhances Raman signals in SERS based imaging, which helps in better detection of tumor margins during surgical removal of tumors [211]. The use of Au NPs provides photo-stability, improved contrast, and higher spectral specificity in SERS based imaging [184].

Among all enlisted imaging techniques, no single modality can be considered as ideal and sufficient for getting all requisite information for a particular question. Nowadays, multimodal imaging probes based on Au NPs are being designed which possess integrated or complementary functions. For example, SERS based imaging is highly sensitive and multiplexed imaging is possible with this technique, but it has poor penetration depth. On the other hand, OI has better penetration depth and high spatial resolution, but its sensitivity is limited. For multiplexed imaging, Au nanorods based SERS/ OI can be used for early stage detection of cancer. Similarly Au NPs having triple modality are being used for MRI/SERS/OI based imaging [212]. For disease (particularly cancer) intervention, Au NPs based multifunctional/multimodal imaging platforms have enough potential for the development of future contrast agents useful for nanomedicine. One can envision the potential applications of Au NPs for multiplexed detection and imaging of cancer and other such types of diseases by proper tailoring of their functionalization, size, shape, composition and hybridization with other materials [184].

4. Use of Au NPs towards therapeutics

The properties of Au NPs can be exploited in therapy in two directions, as passive carriers for delivery, in which the therapeutic effect arise from active molecules bound to the carrier, or as active therapeutic agents, where the therapeutic effect directly originates from the Au NPs. First intents of Au NPs for therapeutic applications were done using them as delivery vehicles

for drugs and genes, owing that NPs in the size range of 2–100 nm can interact with biological systems at the molecular level, and can allow for targeted delivery and passage through biological barriers. Later on, also investigations showing that Au NPs can be intrinsically therapeutic became available. This is due to the fact that Au NPs can actively mediate molecular processes to regulate cell functions. In this section we summarize the potential of Au NPs in therapy, providing examples of currently investigated strategies.

4.1. Au NPs as passive carriers in delivery systems

Au NPs are widespread in the field of delivery of different kinds of therapeutic molecules. They are very attractive as nanocarriers due to their colloidal stability, ease of preparation, and their on-demand tunable size and surface modification possibilities. In addition, they are essentially bio-inert, non-toxic and lack immunogenicity. All these features in combination with their ability to naturally enter cells by endocytic pathways make them good vehicles for a plethora of biomolecules and drugs to be delivered inside cells [13, 213]. Normally, the cargoes are loaded onto the Au NPs' surface either by non-covalent binding (*via* ionic or hydrophobic interactions) or by direct binding on the Au surface by thiolated linkers. Once inside the cells, the cargo may slowly detach from the surface of the Au NPs or its release may be triggered by internal stimuli such as pH [214] or cytosolic glutathione [215], which is able to reduce disulfide bonds, releasing molecules linked to the NPs surface *via* that kind of linkage. Furthermore, Au NPs are well known for their optical properties which are not only useful in the field of imaging and biosensing, but also serve to selectively detach molecules from the NPs surface while irradiating with light. Upon irradiation of plasmonic Au NPs at their LSPR frequency with a continuous wave laser, they absorb energy and reduce the attraction between the Au surface and non-covalently linked molecules, which eventually produces desorption of the cargo. On the contrary, high energy pulse irradiation provokes the reshaping of the nanocarriers and the rupture of Au-S bonds releasing more strongly linked cargoes. Interestingly, light irradiation of plasmonic nanomaterials allows for spatio-temporal controlled release of drugs and biomolecules because the delivery only takes place during irradiation of the NPs and stops when the laser is off [216-218]. Most commonly used Au NPs for delivery applications are nanospheres, and nanorods.

Au NPs have been used since decades for the purpose of gene delivery, traditionally developed for the transfection of plants using gene guns [219]. Nowadays Au NPs are also used in gene therapy as non-viral carriers for delivering nucleic acids inside the cells [220]. Gene therapy may include the delivery of DNA inside cells to induce certain protein expression, or the introduction of miRNA able to interfere with the correct translation of messenger RNA inside the cells, avoiding protein production and silencing a particular gene responsible for a cellular malfunction. Gene therapy is increasingly important, particularly in the field of cancer treatment. However delivery of naked nucleic acids is hampered by their fast degradability inside the body and their polyanionic nature that inhibits the cellular uptake. There are many reports in literature that have demonstrated, that adsorption of nucleic acids onto positively charged Au NPs drastically reduced their degradability and helps their internalization into cells. This could be achieved for example by coating Au NPs with positively charged lysine amino acids [221] or with positively charged polymers [222-225]. However, in order to make sure that the genetic material reaches the nucleus, more sophisticated constructions may be required.

Such constructions may involve the use of PEI, a poly-cationic polymer able to escape endosomes due to "proton sponge" effect causing membrane disruption [226], although it has been shown to be cytotoxic after certain dose threshold. Hence, several authors have coated Au NPs with PEI to trap DNA or RNA, taking advantage of the endosomal escaping capacity of PEI, while substantially reducing its cytotoxicity [227-232]. Chen *et al.* have recently described a smart three-layered nano-carrier, based on the layer-by-layer (LBL) deposition of PEI/chitosan-aconitic anhydride (CS-Aco)/ PEI/ shRNA (short/small hairpin RNA) onto Au NPs. CS-Aco was introduced as a pH-triggered charge-reversible compound which hydrolyzed into positively charged CS once inside the lysosomes, causing the disassembly of the nano-carrier layers. The as-released Au-PEI NPs facilitated lysosomal membrane disruption and hence the successful delivery of shRNA-PEI into the cytoplasm [214]. Although PEI is particularly attractive for nucleic acids delivery, similar results have been achieved by other poly-cationic polymers adsorbed onto Au NPs [220, 233]. For instance, Lee and co-workers fabricated siRNA loaded Au NPs using the LBL approach with alternating positively charged poly-L-lysine (PLL) and negatively charged siRNA. They successfully coated the Au NPs with 4 layers of PLL and three layers of siRNA, that were slowly released inside the cells by protease degradation of PLL and displayed gene silencing capability [234]. As already pointed out before, another way of delivering DNA or RNA avoiding normal cell internalization pathways is adsorption onto naked Au NPs or projectiles and direct bombardment inside the cells using gene guns. This strategy is frequently used in plants, but nowadays it has also been explored for mammalian tissues as well [235, 236].

Drug delivery is also an important field in which Au NPs are utilized. This field is of particular interest in the case of cancer treatment in order to avoid systemic toxicity during chemotherapy and to facilitate the delivery of hydrophobic drugs [237]. Indeed, the group of Rotello showed how to entrap two different hydrophobic drugs (tamoxifen and β–lapachone) in hydrophobic pockets created within alkanethiol monolayers surrounding Au NPs and their effective delivery [238]. Some other strategies involve the chemical modifications of drugs to covalently link them onto NPs, which could in some cases compromise the drug performance. Gibson *et al.* covalently functionalized Au NPs with approximately 70 molecules of anticancer drug paclitaxel per NP, but they did not report about the delivery and biological activity of the drug [239]. Nonetheless, most studies are based on systems to deliver doxorubicin (DOX) [240, 241], which is known for its properties for treating cancer, but also for its toxicity and side effects. The group of Li has recently reported high loading of PEGylated hollow Au nanospheres with DOX (up to 63% in weight) and their delivery after NIR light irradiation [242]. Apart from drugs, Au NPs have also been used as carriers for vaccines by decorating their surfaces with appropriate ligands (selected antigens and T-helper peptides) which were able to elicit an immunogenic response [243].

Interestingly, Au NPs have been used not only as carriers, but also as smart container openers. Plasmonic Au NPs were embedded in between polyelectrolyte layers in LBL constructed capsules carrying a therapeutic cargo within the capsule cavity. In a similar fashion as explained before, irradiation of light onto those NPs led to the spatio-temporal controlled disassembly of the polymeric capsules producing the immediate cargo release [244-248].

Nowadays, all these delivery systems are evolving into more sophisticated constructions, which take advantage of the optical properties of Au NPs for combined drug therapy with PTA and imaging [249], also in combination with other materials such as carbon [250, 251]. For instance, some recent reports along this dimension describe the wrapping of Au NPs or nano-rods with hydrophilic graphene oxide nano-sheets as carriers for gene therapy and improved PTA therapy [252-254].

4.2. Au NPs as active therapeutic agents

When Au NPs act as therapeutic agents *per se*, several therapies can be distinguished depending on the NPs properties exploited. In the following we illustrate the wide range of potential therapies using Au NPs with some selected recent examples.

One of the most promising groups of therapeutic strategies using Au NPs are light-based therapies. Those utilize the application of light to irradiate photosensible materials, whereby this light-activation is directly responsible for the desired therapeutic effects (*i.e.* destroying tumor cells). This group of light-based therapies includes photothermal therapy (PTT), photodynamic therapy (PDT) and photoimmunotherapy (PIT) [255, 256]. While PDT and PIT use a photosensitizer (*i.e.* light-activated drugs) for the release of reactive oxygen species (ROS) and the activation of immune responses, PTT is based on the use of photosensible materials (*e.g.* Au NPs) to generate local heat after being irradiated with electromagnetic radiation. The main difference between PIT and PDT is that in PIT, monoclonal antibodies are associated to photosensitizers to improve the selective binding to the target tissues [255]. PTT has lately received more interest because it does not require oxygen to interact with the target cells or tissues and is able to use longer wavelength light, which is less energetic and therefore less harmful to other cells and tissues. PTT using Au NPs, also called plasmonic photothermal therapy (PPTT), exploits the unique LSPR properties of Au NPs. When an energy source such as electromagnetic radiation is applied, conversion to heat energy efficiently occurs in Au NPs owing to electron excitation and subsequent non-radiative relaxation through electron−phonon and phonon−phonon coupling. This generated thermal energy can induce temperature increases of more than 20 °C (*i.e.* hyperthermia), which can thereby induce tumor tissue ablation [255, 256].

There are several advantages of using Au NPs for PTT: *i)* Au NPs have high absorption cross sections, and thus only minimal irradiation energy is required, *ii)* The conversion of light into heat is very fast (about 1 ps), *iii)* Au NPs are biocompatible, and *iv)* the ability of tuning the LSPR absorption (changing the size and shape of Au NPs) to absorb light in the visible up to the NIR region. Although visible light is successful in destroying cells labeled with spherical Au NPs, the NIR region is especially crucial in order to penetrate deep into tissues, with minimal attenuation by water and hemoglobin. The light can penetrate up to 10 cm in soft tissues in the ‘‘biological window’’ (650–900 nm), a region ideal for the LSPR absorption of Au nanoshells, nanorods, nanoprisms, and nanocages [28, 257]. When comparing the different NP structures in terms of their applications in PTT, Au nanorods exhibit the best efficient NIR photothermal heat conversion. Although nanoshells have a larger absorption cross-section owing to their larger size, and as a result they produced more heat, the nanorod shape has been shown two times more efficient in converting light radiation into thermal energy

(photothermal efficiency) [258]. El-Sayed *et al.* determined the most effective Au nanorods size for PTT heat generation [259]. In this context, 28 × 8 nm Au nanorods were found to be the most effective, both in theoretical calculations and in *in vitro* experiments with human oral squamous cell carcinoma. Au nanorods in this dimension were the best compromise between the total light absorbed and the fraction of which is converted into heat. Additionally, nanorods in this size led to an intense electromagnetic field that extends far enough from the NPs surface to allow for field coupling between NPs aggregates, resulting in enhanced experimental photothermal heating in solution. For example, Lin *et al.* [260] synthesized PEG-coated Au nanorods that showed enhanced PTT when used in the soft tissues of a genetically engineered mouse model (GEMM) of sarcoma. This model recapitulates the human disease more accurately in terms of structure and biology than subcutaneous xenograft models. This study represented a nice demonstration of a therapeutic, NPs-mediated thermal ablation protocol in a GEMM. Untargeted PEG-Au nanorods accumulated in the sarcomas at levels comparable to those in subcutaneous xenografts, providing evidence that passive targeting is indeed sufficient for PEG-Au nanorods to accumulate in a physiologic tumor microenvironment. Significant delays in tumor growth with no progression in some instances demonstrated the success of this method. A similar approach was used by Chen *et al.* [261], where PEG Au nanocages could be passively delivered and accumulated into animal tumors, causing irreversible damage to tumor cells after exposing to NIR laser. Interestingly, PEG- Au nanocages were found not only on the surface, but also in the core of the tumor.

There are increasing efforts to enhance therapeutic treatments by combining therapy methods that show synergistic effects as in the case of PTT and PTD. For example, Choi *et al.* have reported a method which combines both, phototherapies using Au nanorods-photosensitizer complexes and two different light sources to excite the photosensitizers and photothermal NPs separately due to their absorption mismatch [262]. In this work, the negatively charged photosensitizer Al(III) phthalocyanine chloride tetrasulfonic acid (AlPcS4) was attached onto the positively charged surface of Au nanorods by electrostatic interaction, and the photodynamic effect of the AlPcS4 photosensitizer was temporarily suppressed after complex formation with Au nanorods. In the intracellular environment the photosensitizer was released and it finally could be optically activated for phototherapeutic effect. Two different light sources were used to separately excite Au rods (810 nm laser) and AlPcS4 photosensitizer (675 nm laser). Tumor growth was suppressed by 95% with PTT/PDT dual therapy, while the suppression was only 79 % with PDT alone.

These examples successfully demonstrate the potential of NIR-active Au NPs for use in light-based therapies. The current challenge in these phototherapies is to increase the level of selectivity to act on tumor tissues with minimum damage on the surrounding healthy tissue. Furthermore, a better control over bio-distribution and clearance are critical issues to be addressed.

Au NPs are also used for enhanced X-ray radiotherapy. A challenge of X-ray radiation therapy in general is that high dose X-ray at therapeutic conditions damage normal cells. Au NPs, upon X-ray irradiation, can act as dose enhancers and/or generate radicals that damage cancer cells and induce cell apoptosis. There are two main features of Au NPs which make them very good candidates for acting as X-ray radiosensitizers. First, Au has high number of protons (Z=79) and

neutrons, as compared with the previous elements evaluated for dose enhancing with iodine (*Z*=53) and gadolinium (*Z*=64). This translates in an increased photoelectric cross-section. Second, the size of Au NPs is critical for escaping the tumor vasculature using the enhanced permeability and retention (EPR) phenomena. Thus, Au NPs have been proposed as potential radiosensitizers for X-rays mediated cancer therapy, allowing for a reduction in X-ray dose with improved therapeutic results [263-266]. Recently, Yang *et al.* have demonstrated the potential effects of radiation-induced killing of melanoma cells as mediated by amphiphilic Au NPs embedded within the walls of lipid nanocapsules. Interestingly, the membrane-penetrating properties of these amphiphilic Au NPs allowed for significant enhancement of the radiotherapy efficiency, which opens a path for improving the efficacy of frontline radiotherapy treatments [264]. An additional way to improve the radio-therapeutic enhancement effects has been reported by using Au NPs with glucose (Glc) and PEG as ligands (PEG-Glc-Au NPs) [265]. The enormous reduction in the tumor size after 47 days of treatment was also due to the role of PEG and Glc in the improvement of uptake and bio-distribution, which led to a concentration of PEG-Glc-Au NPs in tumor tissue 20 times higher than in healthy cells 48 h after injection. Alternatively, the potential of Au NPs to aggregate within tumors can also be exploited in this direction [266]. 15 nm Au NPs have been designed to aggregate and remain largely in the tumor, after direct intra-tumoral infusion, thus changing from NIR-transparent to NIR-absorbent, enabling tumor-specific heating upon NIR illumination. Aggregation within tumors seems to be induced by the lower pH of the tumor milieu and endosomes/lysosomes or other mechanisms, such as by labile ligand bonds and lysosomal enzymes. This aggregation effect, and subsequent heating by NIR followed by X-ray treatment, was able to reduce the X-ray dose needed for tumor control by a factor > 3. Due to the limited penetration of NIR, certain superficial or accessible tumors (*e.g.* a subset of head, neck, and melanoma) would be immediate candidates to evaluate the potential of this strategy. These examples illustrate the huge potential of Au NPs to enhance radiotherapy treatments, providing useful insights for further clinical studies.

It is important to note that the mechanism by which Au NPs can lead to dose enhancements in radiation therapy differs when comparing photon and proton radiations for NPs excitation. The dose enhancement using protons can be up to 14% and is independent of proton energy, in contrast to photon excitation where the dose enhancement is highly dependent on the photon energy used. A theoretical Monte Carlo simulation study [267] concluded that the potential of Au NPs to enhance radiation therapy depends on the type of radiation source, and proton therapy can be enhanced significantly only if the Au NPs are in close proximity to target tissues.

Radioactive Au NPs are being used to make radiation therapy more effective. The radioactive properties of ^{198}Au (β_{max} = 0.96 MeV; half-life of 2.7 days) make it an ideal candidate for use in radio-therapeutic applications [268]. A major challenge in cancer therapy has been delivery and retention, as it is needed to increase the therapeutic payload for getting an effective tumor treatment. In this regard, NPs containing radioactive isotopes are able to concentrate within the tumor and provide an opportunity to tune the radioactive therapeutic dose delivered to tumor cells. Furthermore, ^{198}Au NPs have extraordinary tumor retention capabilities because of their natural affinity to leaky tumor vasculature. In this area relevant

advances have been achieved [268-270]. Khan *et al.* developed a method for the encapsulation of radioactive Au within a dendrimeric composite and demonstrated that radioactive Au NPs could deliver therapeutic doses to tumors [269]. More recently, gum arabic glycoprotein (GA)-functionalized Au NPs, which consisting of beta-emitting ^{198}Au, were used for reducing the sizes of inoperable prostate tumors [268, 270]. Interestingly, the optimum hydrophobicity of the GA matrix allowed for effective penetration across tumor membranes. The therapeutic efficacy of GA-^{198}Au NPs was demonstrated in prostate tumor–bearing severely compromised immunodeficient (SCID) mice models, reaching an unprecedented 82%, 3 weeks after single-dose intratumoral administration of GA-^{198}Au NPs (408 μCi). The findings of significant therapeutic efficacy, good *in vivo* tolerance, and non-toxic features make these NPs potentially ideal candidates for future human applications.

Radiofrequency (RF) fields can be used to induce Au NPs mediated thermal ablation in a similar manner to that of photothermal and radio-sensitization therapies. The efficiency of RF-based therapy is significantly enhanced by using Au NPs, which are accumulated in the tumor area, and then absorb main RF radiation power to heat cancer cells and thus cause their selective destruction. In particular, an intense source of RF radiation with frequency of 13.6 MHz and the power of 600 W induced the heating of suspensions of Au NPs with a heating rate of ~20 K/sec, which resulted in a considerable cell necrosis [271]. The NP heating mechanism in a RF field is a very complex phenomenon. Glazer *et al.* have demonstrated that Au NPs heat primarily via Joule heating [271, 272]. Briefly, the Au NPs are hypothesized to function as tiny resistors, where free electrons on the surface have restricted movements. Therefore the friction created at the individual NP level releases heat into the surrounding aqueous solution [273].

The potential use of Au NPs coupled to RF waves was evaluated for the treatment of human hepatocellular and pancreatic cancer cells [274]. Direct injection of citrate-Au NPs into the tumor allowed for focusing the RF waves (13.56 MHz RF field) for selective heating of cancer cells. The resulting induced heat was lethal to these cancer cells bearing Au NPs *in vitro*. It was also demonstrated that the Au NPs had no intrinsic cytotoxicity or anti-proliferative effects in the two human cancer cell lines studied. In another example, Curley *et al.* designed a method using Au NPs functionalized with the epidermal growth factor receptor (EGFR) inhibitor cetuximab in Panc-1 (pancreatic adenocarcinoma) and Difi (colorectal adenocarcinoma) cells that express high levels of EGFR [275]. This method proved to be cytotoxic to nearly 100 percent of the pancreatic and colorectal cells, but hardly any of the cells from the control group were damaged. The advantages of this therapy are that shortwave (MHz range) RF energy is nonionizing, penetrates deeply into biological tissues with no adverse side effects, and heats Au NPs efficiently. Thus, this technique may represent an effective treatment for numerous human malignant diseases using noninvasive RF hyperthermia.

The finding that Au NPs are able to inhibit angiogenesis (*i.e.* the formation of new vessels in organs or tissues) has also opened a new path to control the growth and spread of cancerous tissues via angiogenesis therapy. One method to inhibit angiogenesis *in vivo* is to block the function of pro-angiogenic heparin-binding growth factors (HB-GFs) such as vascular endothelial growth factor 165 (VEGF165), and basic fibroblast growth factor (bFGF), etc. Mukherjee *et al.* demonstrated that Au NPs inhibit VEGF165 induced proliferation of

endothelial cells in a dose dependent manner [276]. This inhibition effect was tested *in vivo* using a nude mouse ear model, showing that after a week of daily intraperitoneal injections, the ascites volume had reduced in the NPs treated mice compared to the non-treated tumor bearing mice. More recently, detailed studies of the antiangiogenic properties of Au NPs concluded that Au NPs not only inhibit VEGF165-induced HUVEC (Human Umbilical Vein Endothelial Cells) proliferation, but also repress endothelial cell migration and tube formation [277]. Using Au NPs of different sizes and surface charges, it was demonstrated that a naked Au NPs surface is required and that the core size plays an important role to inhibit the function of heparin binding growth factors (HB-GFs) and subsequent intracellular signaling events. Furthermore, the inhibitory effect of Au NPs was due to the change in HB-GFs conformation/configuration (denaturation) by the NPs, whereas the conformations of non-HB-GFs remained unaffected [278]. The antiangiogenic properties of Au NPs have also been exploited for the treatment of chronic inflammatory diseases such as rheumatoid arthritis. Intra-articular delivery of Au NPs has demonstrated to be an effective treatment strategy for collagen-induced arthritis [279].

5. Use of Au NPs towards theranostics

Recent research has paved the way for multimodal 'theranostic' (*i.e.* a combination of therapy and diagnosis) nano-carriers designed for carrying out simultaneous detection/diagnosis and treatment of the disease following administration [184, 280-282]. Au NPs are appealing for developing theranostic NPs thanks to their unique characteristics that enable their use as contrast agents, as therapeutic entities, and as scaffolds to adhere functional molecules, therapeutic cargoes (*e.g.* drugs/genes), and targeting ligands [184, 281]. Several examples of Au-based theranostic NPs are illustrated in Figure 3, which are explained below.

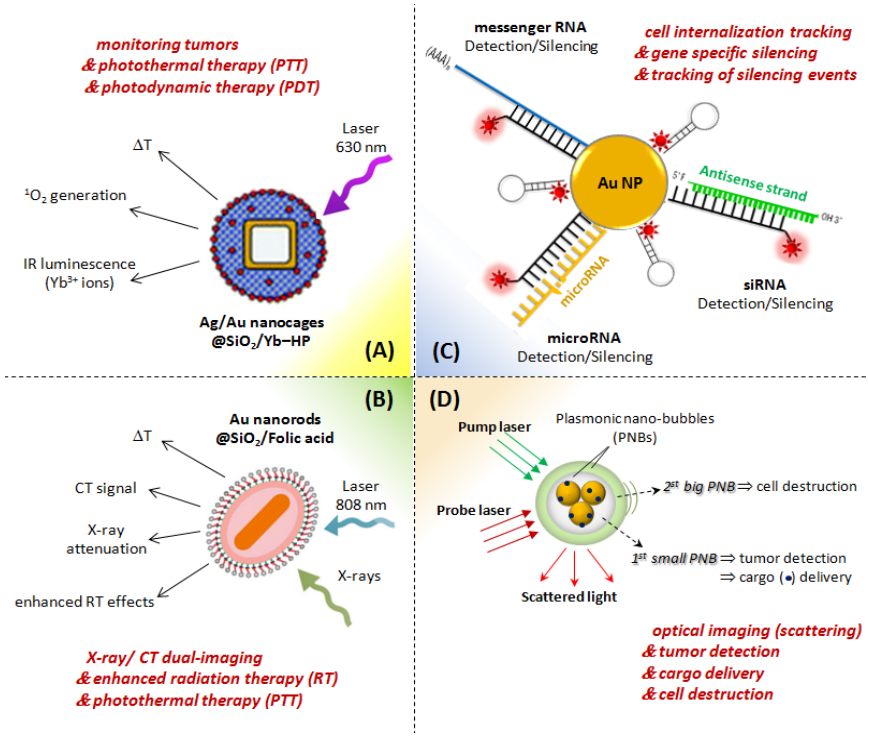

Figure 3. Simplified examples of diverse Au-based theranostic NPs. (A) Silver/gold (Ag/Au) nanocages surrounded by a silica shell containing the NIR photosensitizer Yb–2,4-dimethoxyhematoporphyrin (Yb–HP) for monitoring tumors *via* IR luminescence and simultaneous dual-therapy PTT/PDT [283]; (B) Au nanorods conjugated with folic acid for selective targeting, cancer cells X-ray/CT dual-imaging and treatment *via* enhanced-RT or PTT [284]; (C) Au NPs functionalized with a fluorophore labeled hairpin-DNA for simultaneous gene specific silencing and intracellular tracking of the silencing events [285]; (D) Use of Au NPs, either alone or with linked cargo molecules, for generating plasmonic nano-bubbles (PNBs) which allow tumor detection *via* light scattering, cargo delivery *via* creation of transient holes on the cell membrane and final cell destruction *via* mechanical impact [286].

Au-based theranostic NPs that utilize light-based techniques for monitoring and treating diseases are of special interest as they allow for spatially and temporally controllable drug release, localized therapy and minimally invasive treatment modalities that reduce patients discomfort [282]. An interesting photo-triggered theranostic system has been developed by Khlebtsov *et al*. [283], consisting of a silver/gold (Ag/Au) nanocages core surrounded by a silica shell containing the NIR photosensitizer Yb–2,4-dimethoxyhematoporphyrin (Yb–HP) for monitoring tumors as well as simultaneous dual therapy *i.e.* PTT/PDT (Figure 3A). A significant higher death rate of HeLa cervical cancer cells was observed *in vitro* when they were incubated with the composite NPs and irradiated by 630-nm light, owing to PTT by the Ag/Au NPs as well as PDT using the presence of Yb-HP. Furthermore, the IR luminescence of Yb-HP (900–1060 nm, originating from Yb^{3+} ions, and located in the tissue transparency window) could be used for diagnostic purposes and to control the accumulation and bio-distribution of the composite NPs in tumors. Another example of a theranostic NPs for simultaneous X-rays/ CT dual-imaging and dual-mode enhanced radiation therapy (RT) and PTT was reported by Huan *et al.* [284]. Folic acid-conjugated and silica-modified Au nanorods were synthesized and showed highly selective targeting, excellent X-ray/CT imaging ability and enhanced RT and PTT effects (Figure 3B). These multifunctional NPs could specifically bind to folate receptors on the surface of MGC803 gastric cancer cells and were imaged *in vivo* using both X-ray and CT imaging followed by treatment via RT or PTT. Alternatively, activatable theranostic NPs were developed by using Au@Ag/Au NPs assembled with activatable aptamer probes, which provided high-contrast image-guided site-specific PTT therapy [287]. The Au@Ag/Au NPs simultaneously serve as an optical heater and a fluorescence quencher. The activatable aptamer probes comprised a thiolated aptamer and a fluorophore-labeled complementary DNA. Thus, the activatable theranostic NPs with quenched fluorescence in the free state could undergo signal activation through target binding-induced conformational change of the activatable aptamer probes in specific tumor tissues, and then achieve on-demand treatment under image-guided irradiation. By using S6 aptamer as model, *in vitro* and *in vivo* studies of A549 lung cancer cells verified that these NPs greatly improved imaging contrast and specific destruction. This strategy might be explored as a versatile platform for simultaneous detection and treatment of multiple kinds of cancer cells with the use of specific aptamers for varying cancer targets.

Conde *et al.* [285], developed recently an interesting Au-based theranostic system capable of intersecting all RNA pathways: from gene specific downregulation to silencing the silencers, *i.e.* siRNA and miRNA pathways (Figure 3C). The system consists of Au NPs functionalized with a

fluorophore labeled hairpin-DNA, which allows to directly downregulate a specific gene and also to silence single gene expression, exogenous siRNA and endogenous miRNAs, while simultaneously tracking cell internalization and identifying the cells where silence is occurring (*i.e.* the fluorescence signal is directly proportional to the level of silencing). The usefulness of this approach was applied for silencing an endogenous miRNA (miR-21) commonly upregulated in cancer, such as in colorectal carcinoma cells (HCT-116).The photothermal properties of Au NPs can also be used to generate transient vapor nano-bubbles in order to produce a tunable nanoscale theranostic agent, described as PNBs [286]. These PNBs are generated when the Au NPs are locally overheated with short laser pulses, due to the evaporation of a very thin volume of the surrounding medium, which in turn creates a vapor nano-bubble that expands and collapses within nanoseconds. The bubble scatters the light, thus acting as an optical probe which allows for tumor detection and the fast expansion of the PBN produces a localized mechanical impact which damages cell membranes resulting in cell death, and therefore acting as a therapeutic agent. This novel theranostic system has been successfully applied as an *in vivo* tunable theranostic cellular agent in zebrafish hosting prostate cancer xenografts, presenting higher therapeutic selectivity when compared with Au NPs alone [288]. Au NPs conjugated with anti- EGFR antibody C225 could actively target EGFR-positive A549 lung carcinoma cells. Following cellular uptake, single human prostate cancer cells could be detected and ablated under optical guidance *in vivo* by tunable PNBs in a single theranostic procedure. By varying the energy of the laser pulse, the PNBs size could be dynamically tuned in a theranostic sequence of two PNBs: an initial small PNB detected a cancer cell through optical scattering, followed by a second bigger PNB, which mechanically ablated this cell without damaging the surrounding tissues, while its optical scattering confirmed the destruction of the cells. This innovative and promising theranostic strategy concept of a 'cell theranostics' approach that unites diagnosis, therapy and confirmation (guidance) of the results of therapy in one single process at cellular level, principally can help to improve both, the rapidity and precision of treatment [288]. Recently, the same group has used this concept for both, localized delivery of molecular cargo as well as mechanical destruction of cells by generation of a transient PNB around the Au NPs with a single incident laser pulse. Small PNBs can create a transient hole on the cell membrane to 'inject' molecular cargo without damage to the cells. Large PNBs on the other hand can cause mechanical destruction of the cells of interest [289] (Figure 3D).

Based on these examples it is apparent that theranostic Au NPs have opened the doors to novel and advanced treatment strategies that combine therapeutics with diagnostics, aiming to monitor the response to treatment and increase drug efficacy and safety, which would be a key part of personalized medicine.

6. Applications of Au NPs in clinical trials

Some of the above mentioned medical applications using Au NPs are already in the stage of pre- or clinical trials.

The diagnostics company "Nanosphere" has developed the so-called Nanosphere's Verigene® System, which utilizes advanced automation and Au NPs to enable rapid direct detection of nucleic acids and high-sensitivity protein detection on the same platform. This technology has

already received food-and-drug-administration (FDA) approval in the United States. It is based on Au NPs of 13-20 nm diameter functionalized with either a defined number of oligonucleotides (*i.e.*, short pieces of DNA or RNA) or a defined number of antibodies that are specific to a particular protein of interest.

One therapy using Au NPs which has reached clinical trials is CYT-6091, 27-nm citrate-coated Au NPs conjugated with thiolated-PEG and tumor necrosis factor-α (TNF-α) (Aurimmune; CytImmune Sciences). The NPs have the dual effect of increasing tumor targeting and tumor toxicity in comparison with the use of TNF-α alone [290]. In this trial the side effects and best dose of CYT-6091 in treating patients with advanced solid tumors by intravenous administration have been studied [291]. Future clinical studies will focus on combining CYT-6091 with approved chemotherapies for the systemic treatment of non-resectable cancers.

Using the same CYT-6091 NPs, another clinical trial has been carried out to evaluate the tissue distribution and the selective tumor trafficking of CYT-6091 in patients with primary and metastatic cancers [292]. Patients, stratified according to cancer type, received CYT-6091 and then underwent standard-care surgery. Tumor and normal tissues were removed during surgery for analysis of antitumor effects and tissue distribution of CYT-6091 by electron microscopy.

Au nanoshells (AuroShells®, Nanospectra Biosciences), which consist of a silica core of 120 nm diameter with a 15 nm gold shell, were used in clinical trials to treat head and neck cancers using PPTT. This therapy, called AuroLase® Therapy, consisted of an injection of Au nano-shell NPs into the patient's bloodstream. After 12-24 hours (enough time for the NPs to accumulate inside the tumor) a 808-nm IR laser was used to heat the NPs and destroy tumor cells [293]. These NPs are currently under clinical trials in patients with primary and/or metastatic lung cancer where there is airway obstruction. In this study patients are given a systemic infusion of NPs and a subsequently escalating dose of laser radiation delivered by an optical fiber via bronchoscopy.

In the treatment of atherosclerotic lesions, two delivery techniques for NPs and PPTT are under clinical trials (NANOM FIM) [294]. Patients underwent either nano-intervention with the delivery of silica-Au NPs in a mini-surgery implanted bioengineered on-artery patch, or nano-intervention with the delivery of silica-Au iron-bearing NPs with targeted micro-bubbles or stem cells by means of magnetic navigation system versus stent implantation. The primary results showed a similar degree of regression of total atheroma volume after 12 months for both approaches of delivery.

Another technique being tested in pre-clinical trials works on validating polyvalent Au NPs functionalized with RNAi (RNA interference) as anti-glioma therapeutics [295]. This nano-RNAi platform will be used to target signature lesions of glioblastoma, which play important role in driving glioma pathogenesis, mediating therapeutic resistance and instigating neurologically debilitating necrogenesis. RNAi-Au NPs are being validated on multiple levels, using glioma stem cell cultures, derived xenografts, and genetically engineered glioma mouse models.

Despite of these examples, the full clinical impact of Au NPs based therapies is not known yet. There is clearly a need to translate already developed applications to clinical trials in a timely but safe manner.

7. Concluding remarks and future outlook

We have discussed novel strategies for the synthesis and functionalization of Au NPs in order to evaluate their potential use in nanomedicine. In addition, their detection and sensing properties were explored for diagnosing some diseases. Au NPs either alone or in hybrid form can also improve the performance of practically used imaging techniques. Moreover, Au NPs-based gene and drug therapies are superior in terms of specificity, selectivity and cytotoxicity as compared to the same methods without Au NPs. In terms of efficiency, the performance of various therapeutic systems can be enhanced by conjugating them with Au NPs. Additionally, Au composite NPs have recently been evaluated for their theranostic potential both *in vitro* and *in vivo*. Nowadays, the main focus is the transition of Au NPs from laboratories to the clinics. Though the initial theranostic efficacy of Au NPs shows promising results, there are still many challenges which need to be addressed before their use in clinical practice. Challenges involve the first long term retention, cytotoxicity, and ultimate renal clearance of the NPs. Second, detection and sensing of analytes in complex biological fluids (such as urine, blood, etc.) are still complicated to achieve. Third, non-invasive clinical trials at the molecular level need to be better explored. Forth, the development of personalized medicines for the treatment of individual patients according to their genetic profiles is so far merely a vision described in scientific papers. Last but not least, vaccinations based on Au NPs for humans and/or animals against biologically active factors or diseases still remain a dream to be fulfilled. Adressing these and other such types of challenges may help to shift in future Au NPs-based nanomedicines furthermore into clinics.

Acknowledgments

This work was supported by the European Commission (project Futurenanoneeds to WJP). SA, BP and CCC acknowledge the Alexander von Humboldt Foundation for a PostDoc fellowship. QZ acknowledges CSC for funding. MGMS acknowledges to the Youssef Jameel Foundation for a PhD fellowship. AE acknowledges Junta de Andalucia for a Talentia Postdoc Fellowship, co-financed by the European Union's Seventh Framework Programme, grant agreement no 267226. MC acknowledges a Research Fellow Grant from Ikerbasque, Basque Foundation for Science.

References

1. Patra CR, Bhattacharya R, Mukhopadhyay D, Mukherjee P (2010) Adv. Drug Deliv. Rev. 62:346.
2. Jain KK (2008) Nanomedicine 17:89.
3. Chakraborty M, Jain S, Rani V (2011) Appl. Biochem. Biotechnol. 165:1178.
4. Shi J, Votruba AR, Farokhzad OC, Langer R (2010) Nano Lett. 10:3223.
5. Parveen S, Misra R, Sahoo SK (2012) Nanomed. Nanotech. Biol. Med. 8:147.
6. Hauert S, Bhatia SN (2014) Trends Biotechnol. 32:448.
7. Steichen SD, Caldorera-Moore M, Peppas NA (2013) Eur. J. Pharm. Sci. 48:416.

8. Nishiyama N, Okazaki S, Cabral H, Miyamoto M, Kato Y, Sugiyama Y, Nishio K, Matsumura Y, Kataoka K (2003) Cancer Res. 63:8977.
9. Cai W, Gao T, Hong H, Sun J (2008) Nanotechnol. Sci. Appl. 1:17.
10. Arvizo R, Bhattacharya R, Mukherjee P (2010) Expert Opin. Drug 7:753.
11. Giljohann DA, Seferos DS, Daniel WL, Massich MD, Patel PC, Mirkin CA (2010) Angew. Chem. Int. Ed. 49:3280.
12. Dykman L, Khlebtsov N (2012) Chem. Soc. Rev. 41:2256.
13. Sperling RA, Rivera_Gil P, Zhang F, Zanella M, Parak WJ (2008) Chem. Soc. Rev. 37:1896.
14. Myroshnychenko V, Rodriguez-Fernandez J, Pastoriza-Santos I, Funston AM, Novo C, Mulvaney P, Liz-Marzan LM, Abajo FJGd (2008) Chem. Soc. Rev. 37:1792.
15. Khlebtsov N, Dykman L (2011) Chem. Soc. Rev. 40:1647.
16. Fraga S, Brandão A, Soares ME, Morais T, Duarte JA, Pereira L, Soares L, Neves C, Pereira E, de Lourdes Bastos M (2014) Nanomed. Nanotech. Biol. Med. 10:1757.
17. Simpson CA, Salleng KJ, Cliffel DE, Feldheim DL (2013) Nanomed. Nanotech. Biol. Med. 9:257.
18. Bednarski M, Dudek M, Knutelska J, Nowiński L, Sapa J, Zygmunt M, Nowak G, Luty-Błocho M, Wojnicki M, Fitzner K (2014) Pharmacol. Rep. 67:405.
19. Dreaden EC, Alkilany AM, Huang X, Murphy CJ, El-Sayed MA (2012) Chem. Soc. Rev. 41:2740.
20. Pelaz B, del Pino P (2012) Front. Nanosci. 4:3.
21. Bao C, Conde J, Polo E, del Pino P, Moros M, Baptista PV, Grazu V, Cui D, de la Fuente JM (2014) Nanomedicine 9:2353.
22. Li N, Zhao P, Astruc D (2014) Angew. Chem. Int. Ed. 53:1756.
23. Petersen S, Barcikowski S (2009) J. Phys. Chem. C 113:19830.
24. Brust M, Walker M, Bethell D, Schiffrin DJ, Whyman R (1994) J Chem Soc, Chem Commun. 1994:801.
25. Liz-Marzán LM (2004) Mater. Today 7:26.
26. Turkevich J, Stevenson PC, Hillier J (1951) Discuss. Farad. Soc. 11:55.
27. Bastús NG, Comenge J, Puntes V (2011) Langmuir 27:11098.
28. Pelaz B, Grazu V, Ibarra A, Magen C, del Pino P, de la Fuente JM (2012) Langmuir 28:8965.
29. Perez-Hernandez M, del Pino P, Mitchell SG, Moros M, Stepien G, Pelaz B, Parak WJ, Galvez EM, Pardo J, De La Fuente JM (2014) ACS Nano 9:52.
30. Bao C, Beziere N, del Pino P, Pelaz B, Estrada G, Tian F, Ntziachristos V, de la Fuente JM, Cui D (2013) Small 9:68.
31. Ye X, Zheng C, Chen J, Gao Y, Murray CB (2013) Nano Lett. 13:765.
32. Skrabalak SE, Chen J, Sun Y, Lu X, Au L, Cobley CM, Xia Y (2008) Acc. Chem. Res. 41:1587.
33. Personick ML, Mirkin CA (2013) J. Am. Chem. Soc. 135:18238.
34. Perez-Juste J, Pastoriza-Santos I, Liz-Marzan LM, Mulvaney P (2005) Coordin. Chem. Rev. 249:1870.
35. DuChene JS, Niu W, Abendroth JM, Sun Q, Zhao W, Huo F, Wei WD (2012) Chem. Mater. 25:1392.
36. Nikoobakht B, El-Sayed MA (2003) Chem. Mater. 15:1957.

37. Jana NR, Gearheart L, Murphy CJ (2001) J. Phys. Chem. B 105:4065.
38. Alkilany AM, Nagaria PK, Hexel CR, Shaw TJ, Murphy CJ, Wyatt MD (2009) Small 5:701.
39. Ye X, Jin L, Caglayan H, Chen J, Xing G, Zheng C, Doan-Nguyen V, Kang Y, Engheta N, Kagan CR (2012) ACS Nano 6:2804.
40. Pham T, Jackson JB, Halas NJ, Lee TR (2002) Langmuir 18:4915.
41. Wang H, Brandl DW, Le F, Nordlander P, Halas NJ (2006) Nano Lett. 6:827.
42. Bardhan R, Mukherjee S, Mirin NA, Levit SD, Nordlander P, Halas NJ (2009) J. Phys. Chem. C 114:7378.
43. Ha TH, Koo H-J, Chung BH (2007) The Journal of Physical Chemistry C 111:1123.
44. Chen L, Ji F, Xu Y, He L, Mi Y, Bao F, Sun B, Zhang X, Zhang Q (2014) Nano lett. 14:7201.
45. Kumar PS, Pastoriza-Santos I, Rodriguez-Gonzalez B, de Abajo FJG, Liz-Marzan LM (2008) Nanotechnology 19:015606.
46. Chen J, Wiley B, Li ZY, Campbell D, Saeki F, Cang H, Au L, Lee J, Li X, Xia Y (2005) Adv. Mater. 17:2255.
47. Cobley CM, Chen J, Cho EC, Wang LV, Xia Y (2011) Chem. Soc. Rev. 40:44.
48. Goodman AM, Cao Y, Urban C, Neumann O, Ayala-Orozco C, Knight MW, Joshi A, Nordlander P, Halas NJ (2014) ACS Nano 8:3222.
49. Aherne D, Charles DE, Brennan-Fournet ME, Kelly JM, Gun'ko YK (2009) Langmuir 25:10165.
50. Luangpipat T, Beattie IR, Chisti Y, Haverkamp RG (2011) J. Nanopart. Res. 13:6439.
51. Gericke M, Pinches A (2006) Hydrometallurgy 83:132.
52. Mittal AK, Chisti Y, Banerjee UC (2013) Biotechnol. Adv. 31:346.
53. Levin CS, Hofmann C, Ali TA, Kelly AT, Morosan E, Nordlander P, Whitmire KH, Halas NJ (2009) ACS Nano 3:1379.
54. Bardhan R, Grady NK, Ali T, Halas NJ (2010) ACS Nano 4:6169.
55. Salado J, Insausti M, Lezama L, de Muro IG, Moros M, Pelaz B, Grazu V, de la Fuente J, Rojo T (2012) Nanotechnology 23:315102.
56. Cardinal MF, Rodriguez-Gonzalez B, Alvarez-Puebla RA, Perez-Juste J, Liz-Marzan LM (2010) J. Phys. Chem. C 114:10417.
57. Cheng L-C, Chen HM, Lai T-C, Chan Y-C, Liu R-S, Sung JC, Hsiao M, Chen C-H, Her L-J, Tsai DP (2013) Nanoscale 5:3931.
58. Tan C, Huang X, Zhang H (2013) Mater. Today 16:29.
59. Moon H, Kumar D, Kim H, Sim C, Chang J-H, Kim J-M, Kim H, Lim D-K (2015) ACS Nano 9:2711.
60. Rivera-Gil P, Jimenez De Aberasturi D, Wulf V, Pelaz B, Del Pino P, Zhao Y, De La Fuente JM, Ruiz De Larramendi I, Rojo T, Liang X-J (2012) Acc. Chem. Res. 46:743.
61. Pelaz B, Charron G, Pfeiffer C, Zhao Y, de la Fuente JM, Liang X-J, Parak WJ, del Pino P (2013) Small 9:1573.
62. Love JC, Estroff LA, Kriebel JK, Nuzzo RG, Whitesides GM (2005) Chem. Rev. 105:1103.
63. Yang J, Lee JY, Ying JY (2011) Chem. Soc. Rev. 40:1672.
64. Indrasekara A, Wadams RC, Fabris L (2014) Part. Part. Syst. Char. 31:819.
65. Kinnear C, Dietsch H, Clift MJ, Endes C, Rothen-Rutishauser B, Petri-Fink A (2013) Angew. Chem. 125:1988.
66. Flynn NT, Tran TNT, Cima MJ, Langer R (2003) Langmuir 19:10909.
67. Pino P, áde la Fuente JM (2013) Chem. Commun. 49:3676.

68. Puertas S, Batalla P, Moros M, Polo E, del Pino P, Guisan JM, Grazu V, de la Fuente JsM (2011) ACS Nano 5:4521.
69. Roux S, Garcia B, Bridot J-L, Salomé M, Marquette C, Lemelle L, Gillet P, Blum L, Perriat P, Tillement O (2005) Langmuir 21:2526.
70. Brewer SH, Glomm WR, Johnson MC, Knag MK, Franzen S (2005) Langmuir 21:9303.
71. Mayya KS, Schoeler B, Caruso F (2003) Adv. Funct. Mater. 13:183.
72. Mahl D, Greulich C, Meyer-Zaika W, Köller M, Epple M (2010) J. Mater. Chem. 20:6176.
73. Lin C-AJ, Sperling RA, Li JK, Yang T-Y, Li P-Y, Zanella M, Chang WH, Parak WJ (2008) Small 4:334.
74. Pellegrino T, Kudera S, Liedl T, Muñoz Javier A, Manna L, Parak WJ (2005) Small 1:48.
75. Soliman MG, Pelaz B, Parak WJ, P dP (2015) Chem. Mater. 27:990.
76. Fuentes M, Mateo C, Guisán J, Fernández-Lafuente R (2005) Biosens. Bioelectron. 20:1380.
77. Tang W, Becker ML (2014) Chem. Soc. Rev. 43:7013.
78. Sperling RA, Parak WJ (2010) Phil. Trans. R. Soc. A 368:1333.
79. Montenegro J-M, Grazu V, Sukhanova A, Agarwal S, Jesus M, Nabiev I, Greiner A, Parak WJ (2013) Adv. Drug Deliv. Rev. 65:677.
80. Avvakumova S, Colombo M, Tortora P, Prosperi D (2014) Trends Biotechnol. 32:11.
81. Jimenez de Aberasturi D, Montenegro J-M, Ruiz de Larramendi I, Rojo Tf, Klar TA, Alvarez-Puebla R, Liz-Marzán LM, Parak WJ (2012) Chem. Mater. 24:738.
82. Saha K, Agasti SS, Kim C, Li X, Rotello VM (2012) Chem. Rev. 112:2739.
83. Sapsford KE, Berti L, Medintz IL (2006) Angew. Chem. Int. Ed. 45:4562.
84. Leuvering J, Thal P, Waart Mv, Schuurs A (1980) Fresen. J. Anal. Chem. 301:132.
85. Leuvering JH, Thal PJ, Van der Waart M, Schuurs AH (1981) J. Immunol. Methods 45:183.
86. Elghanian R, Storhoff JJ, Mucic RC, Letsinger RL, Mirkin CA (1997) Science 277:1078.
87. Mie G (1976) Ann. Phys. 25:377.
88. Srivastava S, Frankamp BL, Rotello VM (2005) Chem. Mater. 17:487.
89. Lin S-Y, Liu S-W, Lin C-M, Chen C-h (2002) Anal. Chem. 74:330.
90. Reynolds AJ, Haines AH, Russell DA (2006) Langmuir 22:1156.
91. Watanabe S, Seguchi H, Yoshida K, Kifune K, Tadaki T, Shiozaki H (2005) Tetrahedron Lett. 46:8827.
92. Daniel WL, Han MS, Lee J-S, Mirkin CA (2009) J. Am. Chem. Soc. 131:6362.
93. Deng H, Zhang X, Kumar A, Zou G, Zhang X, Liang X-J (2012) Chem. commun. 49:51.
94. Ai K, Liu Y, Lu L (2009) J. Am. Chem. Soc. 131:9496.
95. Aili D, Selegård R, Baltzer L, Enander K, Liedberg B (2009) Small 5:2445.
96. Zhu Y, Wang G, Sha L, Qiu Y, Jiang H, Zhang X (2015) Analyst 140:1260.
97. Wen S, Zheng F, Shen M, Shi X (2013) Colloid. Surface A 419:80.
98. Chang C-C, Chen C-Y, Chen C-P, Lin C-W (2015) Anal. Methods 7:29.
99. Creran B, Li X, Duncan B, Kim CS, Moyano DF, Rotello VM (2014) ACS Appl. Mater. Inter. 6:19525.
100. Wang S, Singh AK, Senapati D, Neely A, Yu H, Ray PC (2010) Chem. Eur. J. 16:5600.
101. Malinsky MD, Kelly KL, Schatz GC, Duyne RPV (2001) J. Am. Chem. Soc. 123:1471.
102. Moon S, Kim DJ, Kim K, Kim D, Lee H, Lee K, Haam S (2010) Appl. Opt. 49:484.

103. Wang J, Wang L, Sun Y, Zhu X, Cao Y, Wang X, Zhang H, Song D (2010) Colloids Surf., B 75:520.
104. Frasconi M, Tortolini C, Botre F, Mazzei F (2010) Anal. Chem. 82:7335.
105. Joshi GK, Deitz-McElyea S, Johnson M, Mali S, Korc M, Sardar R (2014) Nano Lett. 14:6955.
106. Hu Y, Zhang L, Ying Z, Wang B, Wang Y, Fan Q, huang W, Wang L (2015) ACS Appl. Mater. Inter. 7:2459.
107. Wang J (2005) Small 1:1036.
108. Mitchell JS, Lowe TE (2009) Biosens. Bioelectron. 24:2177.
109. He L, Musick MD, Nicewarner SR, Salinas FG, Benkovic SJ, Natan MJ, Keating CD (2000) J. Am. Chem. Soc. 122:9071.
110. Jain PK, El-Sayed IH, El-Sayed MA (2007) Nano Today 2:18.
111. Dubertret B, Calame M, Libchaber AJ (2001) Nat. Biotechnol. 19:365.
112. You C-C, Miranda OR, Gider B, Ghosh PS, Kim I-B, Erdogan B, Krovi SA, Bunz UH, Rotello VM (2007) Nat. Nanotechnol. 2:318.
113. Phillips RL, Miranda OR, You CC, Rotello VM, Bunz UH (2008) Angew. Chem. Int. Ed. 47:2590.
114. Miranda OR, Chen H-T, You C-C, Mortenson DE, Yang X-C, Bunz UH, Rotello VM (2010) J. Am. Chem. Soc. 132:5285.
115. Lukman S, Aung KMM, Liu J, Liu B, Su X (2013) ACS Appl. Mater. Inter. 5:12725.
116. Albert KJ, Lewis NS, Schauer CL, Sotzing GA, Stitzel SE, Vaid TP, Walt DR (2000) Chem. Rev. 100:2595.
117. Sun W, Lu Y, Mao J, Chang N, Yang J, Liu Y (2015) Anal. Chem. 87:3354.
118. Xu S, Lu X, Yao C, Huang F, Jiang H, Hua W, Na N, Liu H, Ouyang J (2014) Anal. Chem. 86:11634.
119. Oh E, Hong M-Y, Lee D, Nam S-H, Yoon HC, Kim H-S (2005) J. Am. Chem. Soc. 127:3270.
120. Bajaj A, Miranda OR, Kim I-B, Phillips RL, Jerry DJ, Bunz UH, Rotello VM (2009) Proc. Natl. Acad. Sci. 106:10912.
121. Katz E, Willner I, Wang J (2004) Electroanal. 16:19.
122. Munge BS, Coffey AL, Doucette JM, Somba BK, Malhotra R, Patel V, Gutkind JS, Rusling JF (2011) Angew. Chem. 123:8061.
123. Jensen GC, Krause CE, Sotzing GA, Rusling JF (2011) Phys. Chem. Chem. Phys. 13:4888.
124. Li Y, Schluesener HJ, Xu S (2010) Gold Bull. 43:29.
125. Chen A, Chatterjee S (2013) Chem. Soc. Rev. 42:5425.
126. Jena BK, Raj CR (2010) Talanta 80:1653.
127. Chai R, Yuan R, Chai Y, Ou C, Cao S, Li X (2008) Talanta 74:1330.
128. Narang J, Malhotra N, Singh G, Pundir C (2015) Biosens. Bioelectron. 66:332.
129. Omidfar K, Khorsand F, Azizi MD (2013) Biosens. Bioelectron. 43:336.
130. Afonso AS, Pérez-López B, Faria RC, Mattoso LH, Hernández-Herrero M, Roig-Sagués AX, Maltez-da Costa M, Merkoçi A (2013) Biosens. Bioelectron. 40:121.
131. Maltez-da Costa M, de la Escosura-Muñiz A, Nogués C, Barrios L, Ibáñez E, Merkoçi A (2012) Nano Lett. 12:4164.
132. de la Escosura-Muñiz A, Sánchez-Espinel C, Díaz-Freitas Bn, González-Fernández Af, Maltez-da Costa M, Merkoçi A (2009) Anal. Chem. 81:10268.

133. Maltez-da Costa M, de la Escosura-Muñiz A, Nogués C, Barrios L, Ibáñez E, Merkoçi A (2012) Small 8:3605.
134. Kneipp K, Kneipp H, Itzkan I, Dasari RR, Feld MS (1999) Chem. Rev. 99:2957.
135. Willets KA (2009) Anal. Bioanal. Chem. 394:85.
136. Cialla D, März A, Böhme R, Theil F, Weber K, Schmitt M, Popp J (2012) Anal. Bioanal. Chem. 403:27.
137. La Porta A, Grzelczak M, Liz-Marzán LM (2014) ChemistryOpen 3:146.
138. Scarabelli L, Coronado-Puchau M, Giner-Casares JJ, Langer J, Liz-Marzán LM (2014) ACS Nano 8:5833.
139. Quaresma P, Osório I, Dória G, Carvalho PA, Pereira A, Langer J, Araújo JP, Pastoriza-Santos I, Liz-Marzán LM, Franco R (2014) R. Soc. Chem. Adv. 4:3659.
140. Hughes J, Izake EL, Lott WB, Ayoko GA, Sillence M (2014) Talanta 130:20.
141. Thuy NT, Yokogawa R, Yoshimura Y, Fujimoto K, Koyano M, Maenosono S (2010) Analyst 135:595.
142. Harpster MH, Zhang H, Sankara-Warrier AK, Ray BH, Ward TR, Kollmar JP, Carron KT, Mecham JO, Corcoran RC, Wilson WC (2009) Biosens. Bioelectron. 25:674.
143. Wang Y, Lee K, Irudayaraj J (2010) Chem. commun. 46:613.
144. Da P, Li W, Lin X, Wang Y, Tang J, Zheng G (2014) Anal. Chem. 86:6633.
145. Matteini P, de Angelis M, Ulivi L, Centi S, Pini R (2015) Nanoscale 7:3474.
146. Panikkanvalappil SR, El-Sayed MA (2014) J. Phys. Chem. B 118:14085.
147. Xie H-n, Lin Y, Mazo M, Chiappini C, Sánchez-Iglesias A, Liz-Marzán LM, Stevens MM (2014) Nanoscale 6:12403.
148. Liu G, Swierczewska M, Lee S, Chen X (2010) Nano Today 5:524.
149. Doane TL, Burda C (2012) Chem. Soc. Rev. 41:2885.
150. Sun X, Zhang N (2010) Mini. Rev. Med. Chem. 10:108.
151. Koo H, Jin G-w, Kang H, Lee Y, Nam K, Bai CZ, Park J-S (2010) Biomaterials 31:988.
152. Danhier F, Ansorena E, Silva JM, Coco R, Le Breton A, Préat V (2012) J. Control. Release 161:505.
153. Menjoge AR, Kannan RM, Tomalia DA (2010) Drug Discov. Today 15:171.
154. Zhang L, Gu FX, Chan JM, Wang AZ, Langer RS, Farokhzad OC (2008) Clin. Pharmacol. Ther. 83:761.
155. Mulder WJ, Strijkers GJ, van Tilborg GA, Griffioen AW, Nicolay K (2006) NMR Biomed. 19:142.
156. Puri A, Loomis K, Smith B, Lee J-H, Yavlovich A, Heldman E, Blumenthal R (2009) Crit. Rev. Ther. Drug 26:523.
157. Talelli M, Rijcken CJ, Lammers T, Seevinck PR, Storm G, van Nostrum CF, Hennink WE (2009) Langmuir 25:2060.
158. Gupta AK, Naregalkar RR, Vaidya VD, Gupta M (2007) Future Med. 2:23.
159. Figuerola A, Di Corato R, Manna L, Pellegrino T (2010) Pharmacol. Res. 62:126.
160. Singh SP (2011) J. Biomed. Nanotechnol. 7:95.
161. Wang Y, Chen L (2011) Nanomed. Nanotech. Biol. Med. 7:385.
162. Smith AM, Duan H, Mohs AM, Nie S (2008) Adv. Drug Deliv. Rev. 60:1226.
163. Bentolila LA, Ebenstein Y, Weiss S (2009) J. Nucl. Med. 50:493.
164. Kostarelos K, Bianco A, Prato M (2009) Nat. Nanotechnol. 4:627.
165. Son SJ, Bai X, Lee S (2007) Drug Discov. Today 12:657.

166. Jokerst JV, Lobovkina T, Zare RN, Gambhir SS (2011) Nanomedicine 6:715.
167. Lee D-E, Koo H, Sun I-C, Ryu JH, Kim K, Kwon IC (2012) Chem. Soc. Rev. 41:2656.
168. Tasciotti E, Liu XW, Bhavane R, Plant K, Leonard AD, Price BK, Cheng MMC, Decuzzi P, Tour JM, Robertson F, Ferrari M (2008) Nat. Nanotechnol. 3:151.
169. Huang X, Jain PK, El-Sayed IH, El-Sayed MA (2007) Nanomedicine 2:681.
170. Qian X, Peng X-H, Ansari DO, Yin-Goen Q, Chen GZ, Shin DM, Yang L, Young AN, Wang MD, Nie S (2008) Nat. Biotechnol. 26:83.
171. Boisselier E, Astruc D (2009) Chem. Soc. Rev. 38:1759.
172. Murphy CJ, Gole AM, Stone JW, Sisco PN, Alkilany AM, Goldsmith EC, Baxter SC (2008) Acc. Chem. Res. 41:1721.
173. Huff TB, Tong L, Zhao Y, Hansen MN, Cheng JX, Wei A (2007) Nanomedicine 2:125.
174. Tong L, Wei Q, Wei A, Cheng JX (2009) Photochem. Photobiol. 85:21.
175. Ye S, Marston G, McLaughlan JR, Sigle DO, Ingram N, Freear S, Baumberg JJ, Bushby RJ, Markham AF, Critchley K (2015) Adv.Funct. Mater. doi: 10.1002/adfm.201404358:1-11.
176. Bardhan R, Lal S, Joshi A, Halas NJ (2011) Acc. Chem. Res. 44:936.
177. Xia X, Xia Y (2014) Front. Phys. 9:378.
178. Moon GD, Choi S-W, Cai X, Li W, Cho EC, Jeong U, Wang LV, Xia Y (2011) J. Am. Chem. Soc. 133:4762.
179. Wang Y, Liu Y, Luehmann H, Xia X, Wan D, Cutler C, Xia Y (2013) Nano Lett. 13:581.
180. Salgueiriño-Maceira V, Correa-Duarte MA (2007) Adv. Mater. 19:4131.
181. Yuan H, Fales AM, Vo-Dinh T (2012) J. Am. Chem. Soc. 134:11358.
182. Yuan H, Khoury CG, Hwang H, Wilson CM, Grant GA, Vo-Dinh T (2012) Nanotechnology 23:075102.
183. Yuan H, Khoury CG, Wilson CM, Grant GA, Bennett AJ, Vo-Dinh T (2012) Nanomed. Nanotechnol. Biol. Med. 8:1355.
184. Webb JA, Bardhan R (2014) Nanoscale 6:2502.
185. Latterini L, Tarpani L (2014) Bio Bioinspir. Nanomater. 7:173.
186. Wang Z (2013) Sci. China Phys. Mech. Astron. 56:506.
187. Melancon MP, Lu W, Yang Z, Zhang R, Cheng Z, Elliot AM, Stafford J, Olson T, Zhang JZ, Li C (2008) Mol. Cancer Ther. 7:1730.
188. Kang B, Mackey MA, El-Sayed MA (2010) J. Am. Chem. Soc. 132:1517.
189. Rosman C, Pierrat S, Henkel A, Tarantola M, Schneider D, Sunnick E, Janshoff A, Sönnichsen C (2012) Small 8:3683.
190. Wu Z, Jin R (2010) Nano Lett. 10:2568.
191. Wu X, He X, Wang K, Xie C, Zhou B, Qing Z (2010) Nanoscale 2:2244.
192. Dam DHM, Lee JH, Sisco PN, Co DT, Zhang M, Wasielewski MR, Odom TW (2012) ACS Nano 6:3318.
193. Zhu J, Yong K-T, Roy I, Hu R, Ding H, Zhao L, Swihart MT, He GS, Cui Y, Prasad PN (2010) Nanotechnology 21:285106.
194. Hong G, Tabakman SM, Welsher K, Chen Z, Robinson JT, Wang H, Zhang B, Dai H (2011) Angew. Chem. Int. Ed. 50:4644.
195. Li J-L, Gu M (2010) Biomaterials 31:9492.
196. Durr NJ, Larson T, Smith DK, Korgel BA, Sokolov K, Ben-Yakar A (2007) Nano Lett. 7:941.
197. Gao L, Vadakkan TJ, Nammalvar V (2011) Nanotechnology 22:365102.

198. Au L, Zhang Q, Cobley CM, Gidding M, Schwartz AG, Chen J, Xia Y (2009) ACS Nano 4:35.
199. Tong L, Cobley CM, Chen J, Xia Y, Cheng J-X (2010) Angew. Chem. Int. Ed. 49:3485.
200. Wang LV, Hu S (2012) Science 335:1458.
201. Hainfeld JF, Slatkin DN, Focella TM, Smilowitz HM (2006) Br. J. Radiol. 79:248.
202. Ahn S, Jung SY, Lee SJ (2013) Molecules 18:5858.
203. Peng C, Qin J, Zhou B, Chen Q, Shen M, Zhu M, Lu X, Shi X (2013) Polym. Chem. 4:4412.
204. Fujimoto JG (2003) Nat. Biotechnol. 21:1361.
205. Zagaynova E, Shirmanova M, Kirillin MY, Khlebtsov B, Orlova A, Balalaeva I, Sirotkina M, Bugrova M, Agrba P, Kamensky V (2008) Phys. Med. Biol. 53:4995.
206. Ntziachristos V (2010) Nat. Methods 7:603.
207. Sebastián V, Lee S-K, Zhou C, Kraus MF, Fujimoto JG, Jensen KF (2012) Chem. Commun. 48:6654.
208. Boyer D, Tamarat P, Maali A, Lounis B, Orrit M (2002) Science 297:1160.
209. Karmani L, Labar D, Valembois V, Bouchat V, Nagaswaran PG, Bol A, Gillart J, Levêque P, Bouzin C, Bonifazi D (2013) Contrast Media Mol. Imaging 8:402.
210. Das S, Grimm J, Thorek DL (2014) Emerg. Appl. Mol. Imaging Oncol. 124:213.
211. Singhal S, Nie S, Wang MD (2010) Annu. Rev. Med. 61:359.
212. Li J, Gupta S, Li C (2013) Quant. Imaging Med. Surg. 3:284.
213. Ghosh P, Han G, De M, Kim CK, Rotello VM (2008) Adv. Drug Deliv. Rev. 60:1307.
214. Chen Z, Zhang L, He Y, Shen Y, Li Y (2014) Small 11:952.
215. Kong WH, Bae KH, Hong CA, Lee Y, Hahn SK, Park TG (2011) Bioconjugate Chem. 22:1962.
216. Bansal A, Zhang Y (2014) Acc. Chem. Res. 47:3052.
217. Braun GB, Pallaoro A, Wu G, Missirlis D, Zasadzinski JA, Tirrell M, Reich NO (2009) ACS Nano 3:2007.
218. Huschka R, Zuloaga J, Knight MW, Brown LV, Nordlander P, Halas NJ (2011) J. Am. Chem. Soc. 133:12247.
219. Yang N, Burkholder J, Roberts B, Martinell B, McCabe D (1990) Proc. Natl. Acad. Sci. 87:9568.
220. Park J, Kim WJ (2012) J. Drug Target. 20:648.
221. Ghosh PS, Kim C-K, Han G, Forbes NS, Rotello VM (2008) ACS Nano 2:2213.
222. YoungáChoi S, YeongáLee S (2011) J. Mater. Chem. 21:13853.
223. Yan X, Blacklock J, Li J, Möhwald H (2011) ACS Nano 6:111.
224. Ramos J, Rege K (2013) Mol. Pharm. 10:4107.
225. Ramos J, Rege K (2012) Biotechnol. Bioeng. 109:1336.
226. Wagner E (2011) Acc. Chem. Res. 45:1005.
227. Hu C, Peng Q, Chen F, Zhong Z, Zhuo R (2010) Bioconjugate Chem. 21:836.
228. Elbakry A, Zaky A, Liebl R, Rachel R, Goepferich A, Breunig M (2009) Nano Lett. 9:2059.
229. Song W-J, Du J-Z, Sun T-M, Zhang P-Z, Wang J (2010) Small 6:239.
230. Guo S, Huang Y, Jiang Q, Sun Y, Deng L, Liang Z, Du Q, Xing J, Zhao Y, Wang PC (2010) ACS Nano 4:5505.
231. Wang F, Shen Y, Zhang W, Li M, Wang Y, Zhou D, Guo S (2014) J. Control. Release 196:37.
232. Lee M-Y, Park S-J, Park K, Kim KS, Lee H, Hahn SK (2011) ACS Nano 5:6138.

233. Bonoiu AC, Bergey EJ, Ding H, Hu R, Kumar R, Yong K-T, Prasad PN, Mahajan S, Picchione KE, Bhattacharjee A (2011) Nanomedicine 6:617.
234. Lee SK, Han MS, Asokan S, Tung CH (2011) Small 7:364.
235. Uchida M, Li XW, Mertens P, Alpar HO (2009) Biochim. Biophys. Acta 1790:754.
236. Martin-Ortigosa S, Wang K (2014) Transgenic Res. 23:743.
237. Zhu Y, Liao L (2015) J. Nanosci. Nanotechnol. 15:4753.
238. Kim CK, Ghosh P, Pagliuca C, Zhu ZJ, Menichetti S, Rotello VM (2009) J. Am. Chem. Soc. 131:1360.
239. Gibson JD, Khanal BP, Zubarev ER (2007) J. Am. Chem. Soc. 129:11653.
240. Mohammad F, Yusof NA (2014) J. Colloid Interface Sci. 434:89.
241. You J, Zhang R, Zhang G, Zhong M, Liu Y, Van Pelt CS, Liang D, Wei W, Sood AK, Li C (2012) J. Control. Release 158:319.
242. You J, Zhang G, Li C (2010) ACS Nano 4:1033.
243. Hartwell BL, Antunez L, Sullivan BP, Thati S, Sestak JO, Berkland C (2015) J. Pharm. Sci. 104:346.
244. Skirtach AG, Javier AM, Kreft O, Köhler K, Alberola AP, Möhwald H, Parak WJ, Sukhorukov GB (2006) Angew. Chem. Int. Ed. 45:4612.
245. del_Mercato LL, Rivera-Gil P, Abbasi AZ, Ochs M, Ganas C, Zins I, Sönnichsen C, Parak WJ (2010) Nanoscale 2:458.
246. Carregal-Romero S, Ochs M, Parak WJ (2012) Nanophotonics 1:171.
247. Muñoz_Javier A, Pino Pd, Bedard M, Skirtach AG, Ho D, Sukhorukov G, Plank C, Parak WJ (2009) Langmuir 24:12517.
248. De_Geest BG, De Koker S, Sukhorukov GB, Kreft O, Parak WJ, Skirtach AG, Demeester J, De Smedt SC, Hennink WE (2009) Soft Matter 5:282.
249. Choi KY, Liu G, Lee S, Chen X (2012) Nanoscale 4:330.
250. Wang C, Li J, Amatore C, Chen Y, Jiang H, Wang X-M (2011) Angew. Chem. Int. Ed. 50:11644.
251. Modugno G, Ménard-Moyon C, Prato M, Bianco A (2015) Br. J. Pharmacol. 172:975.
252. Xu C, Yang D, Mei L, Lu B, Chen L, Li Q, Zhu H, Wang T (2013) ACS Appl. Mater. Interfaces 5:2715.
253. Xu C, Yang D, Mei L, Li Q, Zhu H, Wang T (2013) ACS Appl. Mater. Interfaces 5:12911.
254. Ma X, Qu Q, Zhao Y, Luo Z, Zhao Y, Ng KW, Zhao Y (2013) J. Mater. Chem. B 1:6495.
255. J Sanchez-Barcelo E, D Mediavilla M (2014) Recent Pat. Endocr. Metab. Immune Drug Discov. 8:1.
256. Menon JU, Jadeja P, Tambe P, Vu K, Yuan B, Nguyen KT (2013) Theranostics 3:152.
257. Huang X, Jain P, El-Sayed I, El-Sayed M (2008) Lasers Med. Sci. 23:217.
258. Pattani VP, Tunnell JW (2012) Lasers Surg. Med. 44:675.
259. Mackey MA, Ali MR, Austin LA, Near RD, El-Sayed MA (2014) J. Phys. Chem. B 118:1319.
260. Lin KY, Bagley AF, Zhang AY, Karl DL, Yoon SS, Bhatia SN (2010) Nano Life 1:277.
261. Chen J, Glaus C, Laforest R, Zhang Q, Yang M, Gidding M, Welch MJ, Xia Y (2010) Small 6:811.
262. Jang B, Park J-Y, Tung C-H, Kim I-H, Choi Y (2011) ACS Nano 5:1086.
263. Kong T, Zeng J, Wang X, Yang X, Yang J, McQuarrie S, McEwan A, Roa W, Chen J, Xing JZ (2008) Small 4:1537.

264. Yang Y-S, Carney RP, Stellacci F, Irvine DJ (2014) ACS Nano 8:8992.
265. Geng F, Xing JZ, Chen J, Yang R, Hao Y, Song K, Kong B (2014) J. Biomed. Nanotechnol. 10:1205.
266. Hainfeld JF, Lin L, Slatkin DN, Dilmanian FA, Vadas TM, Smilowitz HM (2014) Nanomed. Nanotech. Biol. Med. 10:1609-1617.
267. Lin Y, McMahon SJ, Scarpelli M, Paganetti H, Schuemann J (2014) Phys. Med. Biol. 59:7675.
268. Chanda N, Kan P, Watkinson LD, Shukla R, Zambre A, Carmack TL, Engelbrecht H, Lever JR, Katti K, Fent GM (2010) Nanomed. Nanotech. Biol. Med. 6:201.
269. Khan MK, Minc LD, Nigavekar SS, Kariapper MS, Nair BM, Schipper M, Cook AC, Lesniak WG, Balogh LP (2008) Nanomed. Nanotech. Biol. Med. 4:57.
270. Kannan R, Zambre A, Chanda N, Kulkarni R, Shukla R, Katti K, Upendran A, Cutler C, Boote E, Katti KV (2012) Wiley Interdiscip. Rev. Nanomed. Nanobiotechnol. 4:42.
271. Moran CH, Wainerdi SM, Cherukuri TK, Kittrell C, Wiley BJ, Nicholas NW, Curley SA, Kanzius JS, Cherukuri P (2009) Nano Res. 2:400.
272. Glazer ES, Curley SA (2010) Cancer 116:3285.
273. Glazer ES, Curley SA (2011) Ther. Deliv. 2:1325.
274. Gannon CJ, Patra CR, Bhattacharya R, Mukherjee P, Curley SA (2008) J Nanobiotechnology 6:1.
275. Curley SA, Cherukuri P, Briggs K, Patra CR, Upton M, Dolson E, Mukherjee P (2007) J. Exp. Ther. Oncol. 7:313.
276. Mukherjee P, Bhattacharya R, Wang P, Wang L, Basu S, Nagy JA, Atala A, Mukhopadhyay D, Soker S (2005) Clin. Cancer Res. 11:3530.
277. Pan Y, Wu Q, Qin L, Cai J, Du B (2014) BioMed Res. Int. 2014:1.
278. Arvizo RR, Rana S, Miranda OR, Bhattacharya R, Rotello VM, Mukherjee P (2011) Nanomed. Nanotech. Biol. Med. 7:580.
279. Tsai C-Y, Shiau A-L, Chen S-Y, Chen Y-H, Cheng P-C, Chang M-Y, Chen D-H, Chou C-H, Wang C-R, Wu C-L (2007) Arthritis Rheum. 56:544.
280. Muthu MS, Leong DT, Mei L, Feng S-S (2014) Theranostics 4:660.
281. Akhter S, Ahmad MZ, Ahmad FJ, Storm G, Kok RJ (2012) Expert Opin. Drug Deliv. 9:1225.
282. Rai P, Mallidi S, Zheng X, Rahmanzadeh R, Mir Y, Elrington S, Khurshid A, Hasan T (2010) Adv. Drug Deliv. Rev. 62:1094.
283. Khlebtsov B, Panfilova E, Khanadeev V, Bibikova O, Terentyuk G, Ivanov A, Rumyantseva V, Shilov I, Ryabova A, Loshchenov V (2011) ACS Nano 5:7077.
284. Huang P, Bao L, Zhang C, Lin J, Luo T, Yang D, He M, Li Z, Gao G, Gao B (2011) Biomaterials 32:9796.
285. Conde J, Rosa J, Jesús M, Baptista PV (2013) Biomaterials 34:2516.
286. Lukianova-Hleb EY, Oginsky AO, Samaniego AP, Shenefelt DL, Wagner DS, Hafner JH, Farach-Carson MC, Lapotko DO (2011) Theranostics 1:3.
287. Shi H, Ye X, He X, Wang K, Cui W, He D, Li D, Jia X (2014) Nanoscale 6:8754.
288. Wagner DS, Delk NA, Lukianova-Hleb EY, Hafner JH, Farach-Carson MC, Lapotko DO (2010) Biomaterials 31:7567.
289. Lukianova-Hleb EY, Mutonga MB, Lapotko DO (2012) ACS Nano 6:10973.
290. S L (2006-to date) ClinicalTrials.gov. doi:NCT00356980.

291. Libutti S, Paciotti G, Myer L, Haynes R, Gannon W, Walker M, Seidel G, Byrnes A, Yuldasheva N, Tamarkin L (2009) ASCO Annual Meeting Proceedings 27:3586.
292. A RS (2007- to date) ClinicalTrials.gov. doi:NCT00436410.
293. B S (2009- do date) ClinicalTrials.gov. doi:NCT00848042.
294. G G (2012-to date) ClinicalTrials.gov. doi:NCT01679470.
295. H SA. doi:http://www.nu-ccne.org/Research_project4.htm.

Model Driven Optimization of Magnetic Anisotropy of Exchange-coupled Core-Shell Ferrite Nanoparticles for Maximal Hysteretic Loss

Qian Zhang[1‡], Idoia Castellanos-Rubio[2‡], Rahul Munshi[2‡], Iñaki Orue[3], Beatriz Pelaz[1], Wolfgang J. Parak[1,4], Pablo del Pino[4], and Arnd Pralle[2]**

[1]Department of Physics, Philipps University Marburg, Marburg, Germany
[2]Department of Physics, University at Buffalo, Buffalo, NY 14260, USA
[3]SGIker Medidas Magneticas, F. Ciencia y Tecnologia, Sarriena s/n, 48940 Leioa, Spain
[4]CIC biomaGUNE, Paseo Miramón nº 182, 20009 San Sebastian, Spain

KEYWORDS

core-shell nanoparticles, exchange-coupled nanoparticles, Cobalt ferrite, seeded-growth method, magnetic anisotropy, magnetic single domain, superparamagnetism, magnetic hyperthermia

ABSTRACT

This study provides a guide to maximizing hysteretic loss by matching the design and synthesis of superparamagnetic nanoparticles to the desired hyperthermia application. The maximal heat release from magnetic nanoparticles to the environment depends on intrinsic properties of magnetic nanoparticles (e.g. size, magnetization, and magnetic anisotropy), and extrinsic properties of the applied fields (e.g. frequency, field strength). Often, the biomedical hyperthermia application limits flexibility in setting of many parameters (e.g. nanoparticle size and mobility, field strength and frequency). We show that core-shell nanoparticles combining a soft (Mn ferrite) and a hard (Co ferrite) magnetic material form a system in which the effective magnetic anisotropy can be easily tuned independently of the nanoparticle size. A theoretical framework to include the crystal anisotropy contribution of the Co ferrite phase to the nanoparticles total anisotropy is developed. The experimental results confirm that this framework predicts the hysteretic heating loss correctly when including non-linear effects in an effective susceptibility. Hence, we provide a guide on how to characterize the magnetic anisotropy of core-shell magnetic nanoparticles, model the expected heat loss and therefore, synthesize tuned nanoparticles for a particular biomedical application.

TEXT.

Current research on magnetic nanoparticles (MNP) is motivated by biomedical applications utilizing their heat generation capacity in alternating magnetic fields to induce tumor necrosis, remotely release drugs, or stimulate cellular signaling or gene transcription[1–3]. These applications require the design and synthesis of MNPs with maximal heat loss, while limiting some experimental parameters. In an attempt to

minimize damage to tissue without MNP (*i.e.*, by eddy current), the magnetic field frequency is typically kept below 1 MHz, and the field strength below 20 kA/m[4]. To allow the MNPs to diffuse freely between cells, their hydrodynamic diameter after biocompatible coating should be below 30 nm, limiting their magnetic core to less than 20 nm. This leaves the MNP's saturation magnetization (M_s) and the effective magnetic anisotropy to maximize the specific loss power (SLP), also known as specific absorption rate (SAR)[5].

Core-shell MNPs designed to merge the advantageous magnetic properties of soft and hard magnetic materials[6] have shown excellent SLP values and promise tunability of the magnetic anisotropy. Among them, manganese and cobalt substituted ferrites meet the physical requirements to build up exchange-coupled magnetic single domains where the magnetic properties must be averaged over the entire particle volume [7,8]. Customizing this anisotropy to maximize the SLP requires a reliable and predictive theoretical framework. Hence, we develop a theory on how to integrate the magnetic properties of the bulk Mn- and Co-ferrites in one core-shell MNP, and demonstrate its validity on a set of MNPs with diameters around 14 nm. This set includes pure Mn- and Co-ferrite MNPs and three core-shell assemblies: one with Co-ferrite core and Mn-ferrite shell (denoted as Co@Mn) and two with Mn-ferrite and Co-ferrite shell of varying thicknesses (Mn@Co and Mn@Co-TL /Thin Layer).

Core-shell ferrites were synthesized by adapting seed-growth methods based on thermal decomposition of metal precursors (Fe, Co and/or Mn)[9], similarly to Lee et al. [2] (details in SI-1). The MNPs were transferred to the aqueous phase by coating with an amphiphilic polymer (dodecyl-*grafted*-poly-(isobutylene-*alt*-maleic-anhydride /PMA), which confers colloidal stability in high ionic strength media [10], and provides carboxylic groups for further functionalization with other macromolecules. The diameter of the resulting inorganic MNPs (d_{in}) shows good monodispersity (~10%) (Table 1, Figure S1). Their hydrodynamic diameter (d_h) measured by dynamic light scattering increased due to the polymer coating by 2.7 ± 0.7 nm (Table S2), consistent with the shell thickness (d_s) observed by negative staining (Figure 1f).

The magnetization versus field measurements of the MNPs rich in Co ferrite (pure Co, Mn@Co and Mn@Co-TL) show significant hysteresis at room temperature (RT) in fixed, dried samples (Figures2b, S3 and S4). However, the same measurements obtained directly in colloidal suspensionshow no hysteresis (inset Figure 2a) asthenthe Co ferrite rich NPs are free to orient themselvestoa slowly varying external magnetic field.Thus, the magnetic response is almost perfectly superparamagnetic behavior, becauseonly the magnetostaticterm ($-\vec{m}\cdot\vec{B}$, where$\vec{m}$ is the total magnetic moment)contributesto the total energy at thermal equilibrium. This means thatthese M(H) curves in colloidal suspension are also described by a Langevin function and provide an easy way to estimate aneffective magnetic size(see S.I.), which is also obviously true for the other intrinsically superparamagnetic samples (Mn and Co@Mn). The average magnetic diameter obtained this way are between 13 and 15 nm (d_{MvsH} in Table 2, see S.I.)). The good agreement with the physical size of the inorganic part (d_{in}) proves that core and shell act as an exchange couple MNP.Moreover, the saturation magnetization (M_s) values obtained in powder samples are consistent with the average volume fraction of both pure ferrites, and therefore with the formation of core-shell particles (Table 1, see S.I.).

The magnetic anisotropy in nanoscale materials composed of single magnetic domains is typically determined from the thermal dependence of the magnetization[11,12]. In the simplest approximation, the

activation temperature (T_{bl}, blocking temperature) of the superparamagnetic state (SPM) becomes proportional to the energy barrier E_B between equivalent easy directions:

$$T_{bl} = E_B / ln(\tau_m/\tau_0) k_B \qquad (1)$$

where $k_B$is the Boltzmann constant and $\tau_0$is the inverse of the so-called frequency of jump attempts, usually between 10^{-9} and 10^{-11} s, assuming an Arrhenius-type time relaxation where τ_m represents the time window of the experiment. The effective magnetic anisotropy, K_{eff}, is defined by $E_B = K_{eff}V$, with V being the particle volume. Equation (1) allows estimating the effective anisotropy by measuring the magnetization versus temperature after cooling the sample in zero field (zero field cooling (ZFC)). At temperatures close to the maximum of the ZFC, the term $ln(\tau_m/\tau_0)$ is typically approximated to 25 (assuming $\tau_m = 100\ s$ and $\tau_0 = 10^{-9}\ s$). However, at any other temperature some extrapolation and additional modeling concerning the thermal dependence of the anisotropy are needed[13,14]. The effective magnetic anisotropy of MNPs, K_{eff}, is affected by the shape of the MNP and by the magneto-crystalline anisotropy (K_C) of its material, including surface effects.

Often, there exists only one easy direction, either because the crystal has one axis with high symmetry, or because the shape anisotropy (proportional to $\mu_0 M_S^2$) dominates the system as MNP are rarely perfectly spherical and the magneto-crystalline anisotropy (K_C) is small [1516]. In those cases the anisotropy is called uniaxial ($K_{eff} = K_u$). Examples are magnetite and soft magnetic materials, such as pure Mn-ferrite. However, in Co-ferrite the magneto-crystalline anisotropy (K_C) is expected to be cubic and very large, and K_{eff} becomes $K_C/4$[17]. As observed in the Figure 3c, hysteresis loops at 5K of Co rich core-shell MNPs show indeed quite large coercive fields (>1.5 T) and remnant magnetizations above $0.8M_s$ (see Table 1), pointing to a predominantly magneto-crystalline cubic character in the Co richest MNPs[18]

The challenge in modeling the magnetic properties and the SLP of Co-/Mn-ferrite is how to account for the Co's phase contribution to the total anisotropy. We show here that in a core-shell geometry, contrary to mixed Co-/Mn-ferrite MNPs [19], the contribution of both phases can be weighted by volume to combine an effective anisotropy with minor corrections for interface effects between the two phases, and how a temperature description of K_{eff} allows prediction of SLP data.

In inverse spinel ferrites, Co^{2+}cations at octahedral sites contribute strongly to the cubic magneto-crystalline anisotropy because their ground state retains some orbital degeneracy and is embedded in a crystal field of reduced symmetry[20]. The theoretical basis of the anisotropy in Co containing ferrites dates back to the 1950s explaining many bulk material observations [21,22]. In short, the expression for $K_C(T)$ calculated by Tachiki [23] depends on three free parameters that measure the strength of the exchange field (molecular field) ($2\mu_0\mu_B H_e$), the L-S coupling ($\alpha\lambda$) and a crystal field perturbation (a), which accounts for the reduced symmetry originated by the presence of different cations in the octahedral sites. This perturbation (a), that reduces the anisotropy according to the ratio:$\sim \alpha\lambda/a$, is stronger when Co^{2+} is immersed in chemically mixed ferrites [24]. Ultimately the model for the cubic anisotropy constant in pure Co-ferrite is a thermally activated process of the form:

$$K_C(\alpha\lambda, a, T) = \mathcal{F}(\alpha\lambda, a, T) - \mathcal{G}(\alpha\lambda, a, T) e^{-2\mu_0\mu_B H_e/k_B T} \qquad (2)$$

where $\mathcal{F}$ and $\mathcal{G}$ are explicit functions of the L-S coupling, crystal field splitting and temperature (details in S.I) and K_C goes to zero in the limit $T = \infty$. For Co ferrite rich samples we propose to weight contributions proportional to the phases' volume: $K_{eff}(T) = (\%Co) \times K_C/4$, where K_C is given by equation 2 with, for simplicity, only one type of neighbor configuration, due to Co^{2+} and Fe^{3+}, included. Under this approach, all the effects of the crystal field, including surfaces/boundaries effects, are implicitly included in an effective crystal field parameter, a. Other contributions to the anisotropy due to Mn^{+2}, Fe^{+3} and shape are neglected.

Testing the quantitative validity of this approach in MNPs is greatly facilitated if the theoretical $K_{eff}(T)$ can be implemented in a simple framework as the non-interacting single domain theory[25]. Then, the magnetization versus temperature (ZFC) can be fitted to an explicit function of temperature composed of two terms, corresponding to the thermally activated (first) and blocked MNPs (second) as follows:

$$M_{ZFC}(T) = \int_0^{V_c(K_{eff},T)} M_s L\left(\frac{MVH}{k_B T}\right) f(V)dV + \int_{V_c(K_{eff},T)}^{\infty} M_s \frac{MH}{3K_{u,c}} f(V)dV \qquad (3)$$

where, $L(x)$ is the Langevin function, and M and M_s represent respectively the domain and the saturation magnetizations and $f(V, \sigma_V)$ is the size distribution of the MNPs. Possible interparticle interactions are not taken into account because the average interparticle distance is large in the dilute aqueous colloidal suspensions used for the measurements (>50 nm). This assumption is supported by the insensitivity of ZFC/FC to the strength of the applied field (1 or 10 mT) (Figure S5) [26,27].

The peak ZFC magnetization of the core-shell and pure Mn and Co ferrite MNPs (Figure 3a) shift to higher temperatures and sharpen with increasing Co-ferrite content. The superimposed black lines in Figure 3a represent fits using equation (3), whose outputs are the function $K_{eff}(T)$, mean diameter (d_{ZFC}) and standard deviation (σ_{ZFC}).; the latter are found to be consistent with TEM analysis in all cases (Table2). For Co ferrite-rich MNPs (Mn@Co-TL, Mn@Co and pure Co) with $\mu_0 M_S^2 \ll K_C(0)$, the fits use the Tachiki model (equation 2), extracting direct physical conclusions. The L-S coupling is similar in the three samples ($\alpha\lambda \sim 13\ meV$), which is expected as it is affected by the local symmetry around the Co^{+2}cations. The strengths of interactions described in equation (2), ($\mu_B H_e, \alpha\lambda, a$), are found to be similar in the two core-shell Co richest samples Mn@Co-TL and Mn@Co, being that the resulting $K_{eff}(T)$ is fully consistent with the known core/shell volume fraction (60 and 85 % respectively). This discards the existence of significant mixing of Mn and Co phases[19] and fits perfectly in the core-shell model, where the magnetic anisotropies are additive effect, mostly proportional to the Co ferrite volume fraction. $K_C(0\ K)$ in pure Co ferrite MNPs is measured as 1360 kJ/m^3, 30% lower than that of bulk material (1960 kJ/m^3, [21]), while the resulting exchange or molecular field ($\mu_B H_e \sim 50meV$) is comparable to that reported for bulk Co ferrite. In Mn@Co-TL and Mn@Co, this is significantly smaller ($\sim 30\ meV$), reflecting a weaker the exchange interaction, which is a expected in Mn ferrite containing MNPs, due to the low Curie temperature of this material [28].

The Mn@Co and Mn@Co-TL core-shell MNPs show changes of the effective crystal field perturbation (a) relative to pure Co MNPs, which are likely caused by boundary/surface effects considering that both shell interfaces are contributing. As a consequence the anisotropy at 0 K increases ($K_c \approx 1600\ kJ/m^3$ in Mn@Co) and drops faster with temperature than in pure Co ferrite (Figure 3b).

In pure Mn-ferrite MNPs the shape anisotropy is expected to dominate over $K_C(0\,K)$, $\mu_0 M_S^2/K_C(0) \approx 1.5$ ($K_C(0) \approx 22kJ/m^3$ taking from [29]). For Co@Mn uniaxial and cubic anisotropies have to be considered because $\mu_0 M_S^2/K_C(0) \approx 0.15$ if $K_C(0)$ is estimated from the average over relative volumes of Mn and Co. The Tachiki model (equation (2)) cannot be applied to these two systems and a more phenomenological approach has been used instead, similar to that proposed in bulk magnetite[30]. In this, the effective anisotropy decreases with temperature following a pure activation process in the form:$K_{eff}(T) = K_0 - K_1 e^{-Q/k_B T}$, where Q represents the activation energy. Best fits yield $K_{eff}(T) = 22 - 7.5e^{-3/k_B T}$ in the Mn sample and $K_{eff}(T) = 117 - 117e^{-10.5/k_B T}$ in Co@Mn. It means that in the latter the reduction of the anisotropy between 0 and 300 K is less than in the other core-shell ferrites ($\sim$66% versus 75%) and $K_{eff}(T)$ tends also to zero at high T, as in equation (2).

We also validated the modeling of the anisotropy by comparing the size distribution deduced from TEM ($f'(V)$) with that contained in the ZFC/FC (blocking temperature distribution, $f(T_{bl})$). As explained by Yoon and Krishnan[31], the percentage of thermal activated MNPs at a certain temperature, obtained from $f(T_{bl})$, must equal the percentage to those whose size is below a certain critical volume, V_c, calculated from $f'(V)$. This determines numerically a critical volume function $V_c = V_c(T)$ that when inserted in equation (1), allows for the calculation of the effective anisotropy, say $K^*_{eff}(T)$. This approach is especially useful if the anisotropy reduction effect is strong, as in the three core-shell systems. As observed in Figure 3b, this estimation leads to K^*_{eff} values (shown as squared markers), almost overlapping with the functions $K_{eff}(T)$ obtained from the fits of the ZFC branch (see S.I.)

The analysis of the coercive field is a useful opportunity to examine the validity of the magnetic anisotropy modelling. In the non-interacting Stoner-Wohlfarth theories, both properties are directly related: $\mu_0 H_C(0K) = c\left(2K_{eff}(0K)/M_S\right)$, where M_S is the saturation magnetization and the pre-factor c depends on the type of anisotropy: it is equal to 0.48 for uniaxial and 1.3 for cubic anisotropy (or $0.32 \times K_C = 0.32 \times (4K_{eff})$)[32–34]. When the thermal energy comes into play, determination of the coercive field for $T \neq 0$ in a real poly-dispersed assembly of MNPs is challenging because it cannot be calculated as a simple superposition of the individual contributions. Following the approach of Nunes et al. [35], the problem can be addressed in a simplified form as a two phase system, where the relative fractions of SPM and blocked MNPs change with temperature. If the demagnetization curve is approximated by a straight line [36], the resultant coercive field is:

$$H_C(T) = H_{Cbl}(T)\left[M_r(T)/(\chi_{sp}(T)H_{Cbl}(T) + M_r(T))\right] \qquad (4)$$

which is mainly determined by the coercive field of the blocked phase $H_{Cbl}(T)$, being $\chi_{sp}(T)$ the SPM susceptibility that vanishes at low temperatures and $M_r(T)$ the remnant magnetization. The difficulty is further reduced by assuming that the thermal relaxation of magnetization causes the coercive field to decrease as $[1 - (T/\langle T_{bl}\rangle_T)^e]$. The exponent e is widely fixed to 0.5 in the literature but several calculations suggest instead that it tends to 0.75-0.8 in monodisperse uniaxial randomly distributed MNPs [18,37]. In this way, H_{Cbl} can be written as:

$$H_{Cbl}(T) = c\frac{2K_{eff}(T)}{\mu_0 M}\left[1 - \left(\frac{T}{\langle T_b\rangle_T}\right)^e\right] \qquad (5)$$

The thermal dependence of the coercive field is presented in Figure 3c (circular markers) where solid lines correspond to the calculation by equations (4) and (5) by using the functions $K_{eff}(T)$ of Figure 3b and leaving c and e as free parameters. The whole picture shows a good agreement to the experiment with $c = 1.4$ and $e = 0.85$ for the Co ferrite rich samples (Co, Mn@Co-TL and Mn@Co), with $c = 1.2$ and $e = 0.85$ for Co@Mn and $c = 0.48$ and $e = 0.75$ for Mn ferrite. The value of c in the first group matches very well to the theoretical value of 1.32 for randomly oriented single domains with cubic anisotropy, while it is equal to the uniaxial case (0.48) in Mn ferrite. The coercive field of Co@Mn lies between pure uniaxial and cubic behaviors, as happens with the remnant magnetization.

The previous analysis was motivated by the need for a theoretical framework to predict the performance of these core-shell MNPs as heat generators. The experimental determination of the SLP has been carried out in colloidal samples (PMA-coated MNPs) in aqueous suspension (see S.I), where the power dissipation arises from the interaction of magnetization with both the lattice (internal) and the surrounding liquid molecules (external). The prevalent dissipation mechanism can be determined by estimating the characteristic relaxation times of pure internal processes (referred as Neel relaxation, given by $\tau_N \approx \tau_0 e^{K_{eff}V/k_BT}$) and external (Brown relaxation, given by $\tau_B \approx \pi\eta d_h^3/2k_BT$; where η is the viscosity). The available set of values (K_{eff}, d_{in}, d_h) in the five samples indicates that in the hard Co-ferrite MNPs (samples Mn@Co-TL, Mn@Co and Co) the Brown mechanism dominates: $\tau_N/\tau_B > 10^3$. It is just the opposite in the Mn sample ($\tau_N/\tau_B \approx 2 \times 10^{-3}$), while Co@Mn is between both limits ($\tau_N/\tau_B \approx 1$).The contribution of the Brownian dissipation was tested experimentally by attaching proteins to the surface of Mn and Mn@Co samples to increase the hydrodynamic diameter d_h. After the addition of albumin, the SLP of the Mn sample remains almost unchanged (from 184 W/g to 196 W/g); on the contrary, the SLP of the Mn@Co sample is reduced from 302 W/g to 78 W/g.

With the aim of making an easy estimation of the power absorption, the non-linear response effects can be included in an effective non-linear susceptibility calculated from the Langevin function [38], an approach widely used [2] and proven to give correct estimations [39], considering the uncertainty of some variables, such as concentration of MNPs, polydispersity, diameter, and calculated effective anisotropies. The comparison of experimental and theoretical SLP indicates that this quasi-linear approach predicts accurately the heat induction capacity. Figure 4 presents the calculated SLP functions of mean diameter, obtained by fixing the effective anisotropies (at RT) to those calculated in the previous section for each sample and assuming a constant dispersity (taken from TEM data). The experimental SLP values corresponding to each sample are marked with circles (184 W/g for Mn, 553 W/g for Co@Mn, 290 W/g for Mn@Co-TL, 302 for Mn@Co and 280 W/g for Co). This representation provides an overview of which size approaches the best theoretical SLP, and shows how the magnetic anisotropy can be finely tuned to maximize the SLP at room temperature by adjusting the content of Co while keeping the size constant. The Co@Mn sample (15% of Co ferrite in the core) approaches the optimal anisotropy and size under the excitation used (412.5 kHz and 22.4 kA/m).

In summary, we present here a model predicting the magnetic anisotropy of core-shell particles composed of Co ferrite in a whole range of temperatures quantitatively, which allows to correct prediction of their SLP. This model relies on theories well established in bulk materials, and we have experimentally tested its power in predicting the thermal dependence of basic magnetic properties, such as the susceptibility and coercive field of randomly oriented single domains of small size dispersivity. We conclude that the

anisotropy of these exchange-coupled core-shell MNPs is mostly determined by the relative fraction of Co ferrite, whose increase determines a gradual transition to systems with cubic magnetic anisotropy. The correct prediction of the magnetic properties of these MNPs enables designing core-shell MNPs with optimized heat generation for a particular complex biomedical application.

FIGURES

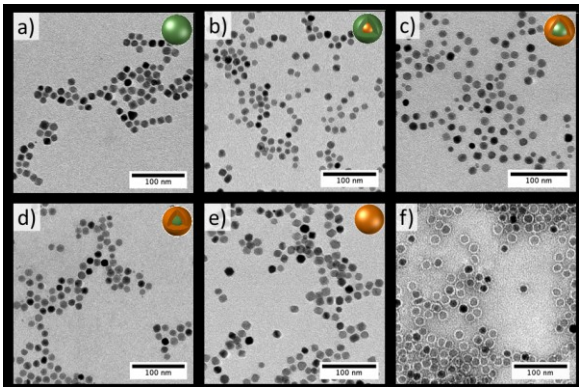

Figure 1.a-e) TEM micrographs of PMA-coated MNPs, *i.e.*, Mn, Co@Mn, Mn@Co-TL, Mn@Co and Co ferrites. **f**) Negative staining TEM micrograph of Mn@Co-TL, which shows a homogeneous coating around the MNPs of *ca.* 3 nm.

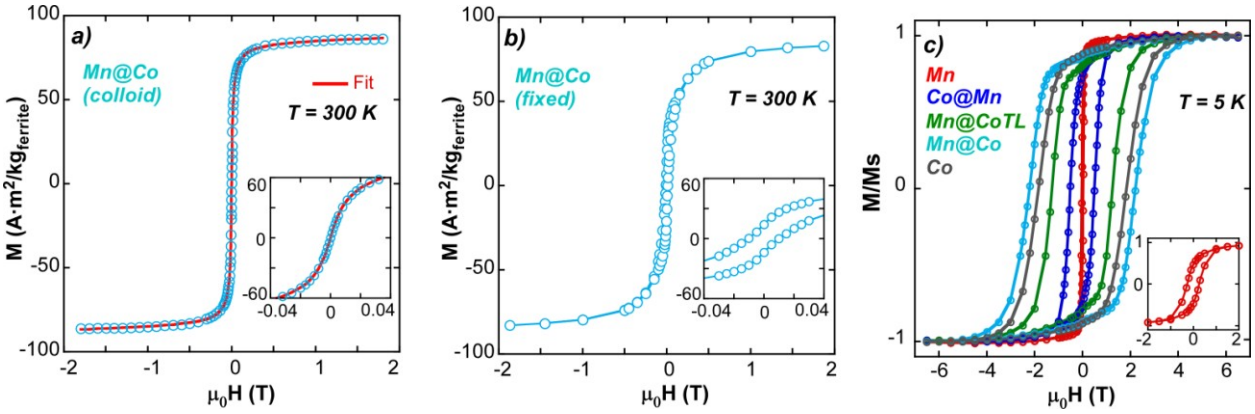

Figure 2. Magnetization versus field measurements at low temperature and RT and for immobilized and freely rotating MNPs.**a)**M(H) curveof Mn@Co at RT and colloidal sample and the corresponding Fit **b)** M(H) curve at RT ofMn@Cocolloidal sample deposited on filter paper (fixed NPs). **c)** M(H) curves at 5K of the 5 samples (fixed NPs)

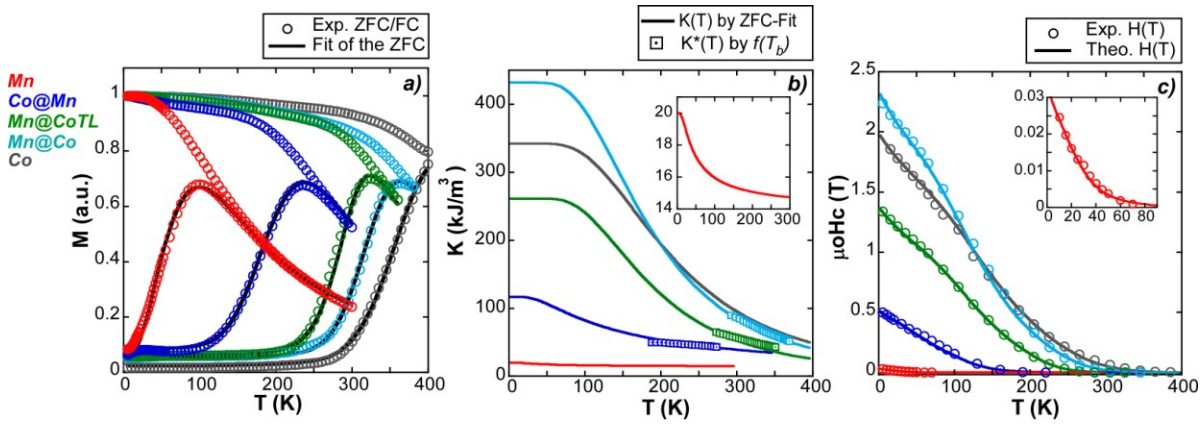

Figure 3. a) Experimental ZFC/FC measurements at 1 mT (circular markers) with the fit of the ZFC branch (solid line). b) $K_{eff}(T)$obtained from the fit of the ZFC (solid line) and K_{eff}*(T) from the statistical approach (square markers); the inset gives a closer look of the Mn curve. c) Experimental thermal dependence of coercive field (μ_0H) (circular markers) and theoretical H(T) function (solid line) calculated by equation (5) and using the obtained$K_{eff}(T)$.

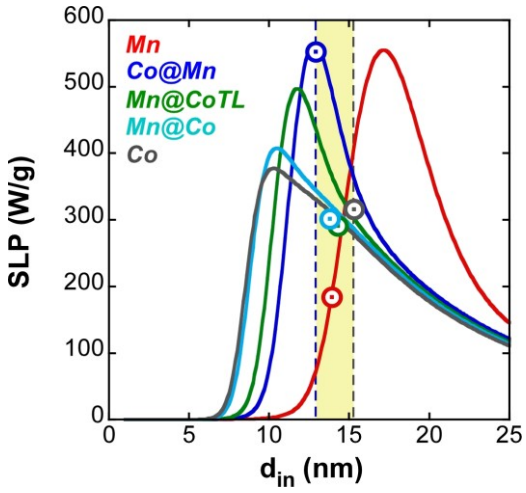

Figure 4. Simulation of SLP versus d_{in} by the quasi-linear approach (solid lines), using the experimental values of M_s, d_{in}, σ, d_h (d_{in}+d_s)and previously determined K_{eff}at RT have been used. The experimental SLP values are superimposed for comparison (circular markers, the size of the markers represents the estimated errors, magnetic field of 412.5 kHz and 22.4 kA/m).

Table 1. Size, composition, and magnetic properties of the core-shell samples

Sample	$d_{in} \pm \sigma$ [α] (nm)	$d_{core} \pm \sigma$ [α] (nm)	Co [α] % vol	M_s(RT) [α] (Am^2/kg)	M_r/M_s [α] (5K)	$\mu_0 H_c$ [α] (5K) (T)
Mn	13.9±1.9	13.9±1.9	0	90.5	0.47	0.026
Co@Mn	12.9±1.4	6.7±1.0	14	87	0.75	0.505
Mn@Co-TL	14.3±1.5	10.2±1.1	63	84	0.80	1.268
Mn@Co	13.8±1.3	7.3±1.0	85	82	0.87	2.20
Co	15.3±1.6	15.3±1.6	100	80	0.88	1.84

[α] Diameter of the inorganic MNP (core + shell) and of the inorganic core (d_{core}); Co ferrite volume fraction in the core-shell structure, saturation magnetization (M_s) at RT, reduced remanence (M_r/M_s) at 5°K and coercive field ($\mu_0 H_c$) at 5°K.

Table 2. Magnetic variables from the magnetization versus magnetic field curves (MvsH) and ZFC branch

Sample	$d_{MvsH} \pm \sigma_{MvsH}$ [α] (nm)	$d_{ZFC} \pm \sigma_{ZFC}$ [α] (nm)	K_0 [α] (kJ/m^3)	K_1 [α] (kJ/m^3)	Q [α] (meV)	K_{eff_RT} [α] (kJ/m^3)	$SLP_{cal.}$ [α] (W/g)	SLP_{exp} [α] (W/g)
Mn	13.4±1.7	13.7±2.2	20	6	3.4	**15**	190±60	184±2
Co@Mn	12.3±1.5	12.8±1.5	117	117	10.5	**39**	560±50	553±10
			$2\mu_0\mu_B H_e$ (meV)	$\alpha\lambda$ (meV)	a (meV)	K_{eff_RT} (kJ/m^3)		
Mn@Co-TL	14.4±1.4	14.1±1.6	30	12.8	17.6	**53**	340±50	291±1
Mn@Co	13.5±4.3	13.8±1.6	30	13.0	17.1	**85**	320±40	302±15
Co	15.6±3.4	15.0±1.9	50	13.1	21.0	**95**	280±30	316±9

[α] d_{MvsH} and σ_{MvsH}(in colloidal samples at RT).d_{ZFC}, $\sigma_{ZFC}$and K_{eff}at RT for the 5 samples; K_0, K_1 and activation energy (Q) for Mn and Co@Mn samples; and the strength of the exchange field ($2\mu_0\mu_B H_e$), the L-S coupling ($\alpha\lambda$) and the crystal field perturbation (a) for Mn@Co-TL, Mn@Co and Co samples;calculated SPL values from Figure 4 for the corresponding d_{in} of each sample (uncertanties are estimated from the experimental error of d_{in}, σ, d_h, M_s, and fixed to 3% for K_{eff}); experimental SPL together with its experimental error.

ASSOCIATED CONTENT

Supporting Information.

Nanoparticle synthesis and polymer coating protocols; TEM, DSL and ICP-MS analysis; Magnetization measurement protocols and results; and specific Loss Power measurement protocols and results, This material is available free of charge via the Internet at http://pubs.acs.org.

AUTHOR INFORMATION

Corresponding Author

*E-mail: apralle@buffalo.edu.

*E-mail: pdelpino@cicbiomagune.es.

Author Contributions

‡These contributed equally.

Notes

The authors declare nocompeting financial interest.

ACKNOWLEDGMENT

This work was supported by HSFP project RGP0052/2012 (to WJP and AP) and NIH (R01MH094730 to AP). QZ, BP, and ICR acknowledge fellowships for Chinese Scholarship Council, the Alexander von Humboldt Foundation, and the Basque Government, respectively.

ABBREVIATIONS

MNP,magnetic nanoparticle; SLP,specific loss power; ZFC; zero-field cooling; PMA, poly (isobutylene-alt-maleic anhydride; K, anisotropy; M, magnetization.

REFERENCES

(1) Huang, H.; Delikanli, S.; Zeng, H.; Ferkey, D. M.; Pralle, A. *Nat. Nanotechnol.***2010**, *5* (8), 602–606.

(2) Lee, J.-H.; Jang, J.-T.; Choi, J.-S.; Moon, S. H.; Noh, S.-H.; Kim, J.-W.; Kim, J.-G.; Kim, I.-S.; Park, K. I.; Cheon, J. *Nat. Nanotechnol.***2011**, *6* (7), 418–422.

(3) Dias, J. T.; Moros, M.; Del Pino, P.; Rivera, S.; Grazú, V.; de la Fuente, J. M. *Angew. Chemie***2013**, *52* (44), 11526–11529.

(4) Hergt, R.; Dutz, S. *J. Magn. Magn. Mater.***2007**, *311* (1), 187–192.

(5) Chen, R.; Christiansen, M. G.; Anikeeva, P. *ACS Nano***2013**, *7*, 8990–9000.

(6) Skoropata, E.; Desautels, R. D.; Chi, C.-C.; Ouyang, H.; Freeland, J. W.; van Lierop, J. *Phys. Rev. B***2014**, *89* (2), 024410.

(7) Skomski, R.; Coey, J. *Phys. Rev. B***1993**, *48* (21), 15812–15816.

(8) Zeng, H.; Sun, S.; Li, J.; Wang, Z. L.; Liu, J. P. *Appl. Phys. Lett.***2004**, *85* (5), 792.

(9) Sun, S.; Zeng, H. *J. Am. Chem. Soc.***2002**, No. 31, 8204–8205.
(10) Lin, C.-A. J.; Sperling, R. A.; Li, J. K.; Yang, T.-Y.; Li, P.-Y.; Zanella, M.; Chang, W. H.; Parak, W. J. *Small***2008**, *4* (3), 334–341.
(11) M, K.; Nunes, W. C.; Socolovky, L. M.; De Biasi, E.; Vargas, J. M.; Denardin, J. C. *J. Nanosci. Nanotechnol.***2008**, *8*, 2836–2857.
(12) Usov, N. A. *J. Appl. Phys.***2011**, *109* (2), 023913.
(13) Van VlecK, J. H. *Phys. Rev.***1937**, *52*, 1178–1198.
(14) Zener, C. *Phys. Rev.***1954**, *96* (1950), 1335–1337.
(15) Correia, M. J.; Figueiredo, W.; Schwarzacher, W. *Phys. Lett. A***2014**, *378* (45), 3366–3371.
(16) Usov, N. A.; Barandiarán, J. M. *J. Appl. Phys.***2012**, *112* (5), 053915.
(17) Gittleman, J. I.; Abeles, B.; Bozowski, S. *Phys. Rev. B***1974**, *9* (9), 3891–3897.
(18) García-Otero, J.; Porto, M.; Rivas, J.; Bunde, a. *J. Appl. Phys.***1999**, *85* (4), 2287.
(19) Song, Q.; Zhang, Z. J. *J. Am. Chem. Soc.***2012**, *134*, 10182–10190.
(20) Slonczewski, J. C. *Phys. Rev.***1958**, *110* (6), 1341–1348.
(21) Shenker, H. *Phys. Rev.***1957**, *107* (5), 1246–1249.
(22) Slonczewski, J. C. *Phys. Rev.***1961**, *122* (5), 1367–1372.
(23) Tachiki, M. *Prog. Theor. Phys.***1960**, *23* (6), 1055–1072.
(24) Melikhov, Y.; Snyder, J. E.; Jiles, D. C.; Ring, A. P.; Paulsen, J. A.; Lo, C. C. H.; Dennis, K. W. *J. Appl. Phys.***2006**, *99* (8), 08R102.
(25) Stoner, E. C.; Wohlfarth, E. P. *Philos. Trans. R. Soc. A Math. Phys. Eng. Sci.***1948**, *240* (826), 599–642.
(26) Dormann, J. L.; Fiorani, D.; Tronc, E. *Adv. Chem. Phys.***1997**, *98*, 283–494.
(27) Pauly, M.; Pichon, B. P.; Panissod, P.; Fleutot, S.; Rodriguez, P.; Drillon, M.; Begin-Colin, S. *J. Mater. Chem.***2012**, *22* (13), 6343.
(28) Harrison, S. E.; Kriessman, C. J.; Pollack, S. R. *Phys. Rev.***1958**, *110*, 844–849.
(29) Dillon, J. F.; Geschwind, S.; Jaccarino, V. *Lett. to Ed.***1955**, 750–752.
(30) Abe, K.; Miyamoto, Y.; Chikazumi, S. *J. Phys. Soc. Japan***1976**, *41* (6).
(31) Yoon, S.; Krishnan, K. M. *J. Appl. Phys.***2011**, *109* (7), 07B534.
(32) Walker, M.; Mayo, P. I.; O´Grady, K.; Charles, S. W.; Chantrell, R. W. *J. Phys. Condens. Matter***1993**, *5*, 2793–2808.
(33) Walker, M.; Mayo, P. I.; O´Grady, K.; Charles, S. W.; Chantrell, R. W. *J. Phys. Condens. Matter***1993**, *5*, 2779–2792.
(34) Usov, N. A.; Peschany, S. E. *J. Magn. Magn. Mater.***1997**, *174* (3), 247–260.
(35) Nunes, W.; Folly, W.; Sinnecker, J.; Novak, M. *Phys. Rev. B***2004**, *70* (1), 014419.
(36) Kneller, E. F.; Luborsky, F. E. *J. Appl. Phys.***1963**, *34* (3), 656–658.
(37) Carrey, J.; Mehdaoui, B.; Respaud, M. *J. Appl. Phys.***2011**, *109* (8), 083921.
(38) Rosensweig, R. E. *J. Magn. Magn. Mater.***2002**, *252*, 370–374.
(39) Castellanos-Rubio, I.; Insausti, M.; Garaio, E.; Gil de Muro, I.; Plazaola, F.; Rojo, T.; Lezama, L. *Nanoscale***2014**, *6*, 7542–7552.

Supporting Information for "Model Driven Optimization of Magnetic Anisotropy of Exchange-coupled Core-Shell Ferrite Nanoparticles for Maximal Hysteretic Loss"

1. Nanoparticles Synthesis and Characterization

Seeds, core-shell and single-phase magnetic nanoparticles (MNPs) were produced by thermal decomposition of metal precursors (*i.e.*, iron(III) acetylacetonate, cobalt(II) acetylacetonate, manganese(II) acetylacetonate or manganese(II) chloride) in the presence of 1,2-hexadecanediol, oleic acid and oleylamine, in high boiling point organic solvents (benzyl ether or dioctyl ether), following largely protocols for single-phase MNPs[12] or core-shell ferrite MNPs[3]. In order to produce colloids with the desired sizes and structure (single-phase or core-shell), we combined and adapted existing methods, except for the production of Mn ferrite MNPs with d ~ 14 nm, which followed [2].

1.1. Synthesis of of core-shell MNPs

Co@Mn MNPs. MonodisperseCo ferrite seeds (d_{in} ~ 7 nm)were synthesized combining previously addressed concepts and details [12].Underan inert atmosphere, iron(III) acetylacetonate ($Fe(acac)_3$, 2 mmol, Strem, #262300), cobalt(II) acetylacetonate ($Co(acac)_2$, 1 mmol, Sigma Aldrich, #227129) and 1,2-hexadecanediol (10 mmol, Sigma Aldrich, #213748) were mixed in a 100 ml flask in the presence of 6 mmol of oleic acid (OLA, Sigma Aldrich, #O1008), 6 mmol of oleylamine (OLAM, Sigma Aldrich, #O7805),and 20 ml of benzyl ether(Sigma Aldrich, #108014). The mixture was degassed for 30 min under vacuum at 100 °C. Under nitrogen flow, the temperature was increased up to 200 °C at a heating rate of 3.3 K/min, left for 2 h at 200 ºC, and then the temperature was again increased at 3.3 K/min and the reaction was heated to reflux (~300 °C) for 1 h. The reaction was stopped by removing the heating mantle, and the black-colored mixture was cooled to room temperature (RT). Upon the addition of 40 ml of ethanol (96 %, Carl Roth, #64-17-5), a black material was precipitated by centrifugation (2888 rcf, 10

min), *i.e.*, the hydrocarbon chain-coated Co ferrite NPs. The supernatant was removed, and the black precipitate was dissolved in 20 mltoluene (Carl Roth, #9558.2)with 0.05 ml of OLA and 0.05 ml of OLAM. The solution was centrifuged (2888 rcf, 10 min) to remove aggregates (*i.e.* the precipitate was discarded). The sample was washed by adding 40 ml of ethanol, centrifuged (2888 rcf, 10 min) to remove the solvent. Lastly, the precipitate was redispersed in 20 ml of chloroform ($CHCl_3$, Carl Roth, #Y015.2), and characterized by transmission electron microscopy (TEM, Jeol 1400 plus) (Figure S1).

Monodisperse Co@Mn MNPs were synthesized by growing a shell of Mn ferrite onto the previously described Co ferrite seeds. As for the preparation of the seeds, the synthetic protocol used for the preparation of the Co@Mn MNPs was adapted from previous work regarding the seed-growth synthetic methods for the preparation of single-phase MFe_2O_3 (M = Fe, Mn, Co) MNPs [412]. In detail, $Fe(acac)_3$ (2 mmol), $Mn(acac)_2$(1 mmol), 1,2-hexadecanediol (10 mmol) and 40 mg of Co ferrite seeds (dispersed in 4 ml of $CHCl_3$) were mixed in a 100 ml flask in the presence of 2 mmol of OLA, 2 of mmolOLAM and 20 m of benzyl ether. Under vacuum, the reaction mixture was firstly heated to 100 °C and kept at this temperature for 30 min to remove the $CHCl_3$. Under nitrogen, with a heating rate of 3.3 K/min, the temperature was increased to 200 °C, kept at this temperature for 1 h, and then heated to reflux (~300 °C) for 30 min. The reaction was stopped by removing the heating mantle and the black-colored mixture was cooled down to RT. The cleaning step was equivalent to the process described previously. Figure S1-b shows TEM of the resultantNPs (*ca.* 13.1 nm in diameter).

Mn@Co MNPs. Mn ferrite seeds (6.9 nm) were synthesized as Co ferrite seeds above, but replacing the 1 mmol of $Co(acac)_2$ by1 mmol of $Mn(acac)_2$ (Figure S1-c). To grow the Mn@Co MNPs, 40 mg Mn ferrite seeds dispersed in 4 ml of $CHCl_3$ were mixed with 2mmol of $Fe(acac)_3$, 1 mmol of $Co(acac)_2$,10 mmol of 1,2-hexadecanediol, 2 mmol of OLA, 2 mmol of OLAM, and 20 ml of benzyl ether. The further reaction protocol was the same as for Co@Mn (Figure S1-d).

Mn@Co-TL /Thin Layer MNPs. In this case, the size of the Mn ferrite core was increased from 7 to 10 nm, and the thickness of the Co ferrite shell was decreased to reach the same MNP size (*ca.* 14 nm) as the previous core shell systems. 10 nm Mn ferrite seeds were synthesized by adding $Fe(acac)_3$(2mmol), $Mn(acac)_2$(1 mmol), 1,2-hexadecanediol(10 mmol), OLA(6 mmol), OLAM (6 mmol) and 10 ml benzyl ether. The further reaction protocol was the same as above (resulting MNP Figure S1-e).

The shell growth was initiated by the addition of 40 mg of 10 nm Mn ferrite seeds (dispersed in 4 ml $CHCl_3$) to the mixture of $Fe(acac)_3$(2mmol), $Co(acac)_2$(1 mmol), 1,2-hexadecanediol(10 mmol), OLA(2 mmol), OLAM (2 mmol), and 20 ml of benzyl ether. The further reaction protocol was the same as for Co@Mn (Figure S1-f).

1.2. One-pot synthesis of 14nm Co ferrite MNPs and 14nm Mn ferrite MNPs

The one-pot synthesis of Co ferrite MNPs was accomplished using the following procedure: 2 mmol of $Fe(acac)_3$, 1 mmolof $Co(acac)_2$, 6 mmol of oleic acid, and 6 mmol of oleylamine were added into a 100 ml three-necked flask, as well as 10 mmol of 1,2-hexadecanediol and 17 ml of benzyl ether. After degassing at 100 °C for 30 min, the mixture was slowly heated up to 200 °C for 2 h under aN_2flow.Then, the temperature was increased to 300 °C for 1 h. The reaction was stopped by removing the heating mantel, and the black solution was precipitated with ethanol and dissolved in chloroform (Figure S1-g).

Mn ferrite MNPs were synthesized as previously described[2]. Specifically, 2 mmol $Fe(acac)_3$, 1 mmol $MnCl_2$ were mixed with 6.31 mmol OLA, 12.16 mmol of OLAM and 2 ml of dioctyl ether. The mixture

was firstly heated to 100 °C for 30 min under vacuum, using a flow of N_2 as protection, then heated to 200 °C at a heating rate of 3.3 K/min and kept at this temperature for 2 h. With the same heating speed, the temperature of the solution was increased to reflux (330°C) and kept there for 1 h (Figure S1-h).

As a summary of the synthetic section, we like to point out that there are several synthetic parameters such as the molar ratio of the reactants, the boiling point of the solvents, the heating rate, reaction times, *etc.*, which can be tuned to achieve the desired size of the MNPs (obviously within some limits) produced by thermal decomposition of metal (Fe, Mn, Co) precursors (Table S1). For instance, the use of solvents with higher boiling points(*e.g.*, dioctyl ether)can be use to produce bigger MNPs than the ones produced in a lower boiling point solvent (*e.g.*, benzyl ether)[5]. Longer reaction times generate in general bigger MNPs.

Table S1. Summary of the synthetic parameters used to produce different ferrite MNPs.

Sample / Reactants	Mn ferrite	Co@Mn	Mn@Co-*TL*	Mn@Co	Co ferrite
Seeds	no seeds	Co ferrite (7 nm)	Mn ferrite (10 nm)	Mn ferrite (7 nm)	no seeds
Precursor	$MnCl_2$	$Mn(acac)_2$	$Co(acac)_2$	$Co(acac)_2$	$Co(acac)_2$
OLA/OLAM	6.31 mmol / 12.16 mmol	2 mmol / 2 mmol	2 mmol / 2 mmol	2 mmol / 2 mmol	6 mmol / 6 mmol
Solvent	Dioctyl ether (2 ml)	Benzyl ether (20 ml)	Benzyl ether (20 ml)	Benzyl ether (20 ml)	Benzyl ether (17 ml)
Temperature	330 °C (1 h)	300 °C (0.5 h)	300 °C (0.5 h)	300 °C(0.5 h)	300 °C (1 h)

1.3. Coating of nanoparticles using amphiphilic polymer PMA

The amphiphilic polymer was synthesized from poly (isobutylene-alt-maleic anhydride) (PMA, Mw ~6,000 g/mol, Sigma Aldrich, #531278, 39 monomers per polymer chain) and dodecylamine (DoCA, Sigma Aldrich, #D222208) following published methods[6]. The reaction product was completely dried and redissolved in anhydrous chloroform at a concentration of 0.5 M monomers (= 20 mmol / 40 ml).The polymer coating was carried out as described elsewhere[6].The amphiphilic polymer and the "hydrophobic" core shell MNPs were mixed in a round bottom flask at a ratio $R_{p/Area}$=300, where $R_{p/Area}$ corresponds to the polymer added per nanoparticle surface unit area (nm^2). After mixing well, the solvent was slowly evaporated with a rotavap until the sample was completely dried. The residual solid film in the flask was redissolved in SBB12 buffer (sodium borate buffer, 50 mM, pH 12) under vigorous stirring until the solution turned clear. The sample was filtrated (0.22 µm, Carl Roth, # P815.1), concentrated by centrifugal filtration (Vivaspin20, MWCO 100 kDa, Sartorius, #VS2042), and transferred into MilliQ water.

1.4. Purification of MNPs with agarose gel electrophoresis

Gel electrophoresis in an agarose gel (2% w/w) electrophoresis (100 V, 200 mA and 60 min) was used to inspect the monodispersity of the sample and to separate polymer-coated MNPs from empty polymer micelles following published procedures[6]. The black bands in the gels, which contain the purified sample, were cut out and placed into Dialysis tubing (50 kDa molecular weight cut-off, MWCO, Sectrum Labs)

with 0.5x TBE buffer. Samples were run in the electrophoresis tank (100 V, 200 mA) for 15 min, extracted from the dialysis membranes, filtered with syringe filters 0.22 µm, and concentrated with 100 kDa MWCO filters by centrifugation.

1.5. Size distribution measurements using transmission electron microscopy (TEM)

The size of the inorganic part (d_{in}) of the MNPs was determined by TEM before and after the PMA coating. Figure S1 shows TEM micrographs and size distribution of the MNPs before the PMA coating.

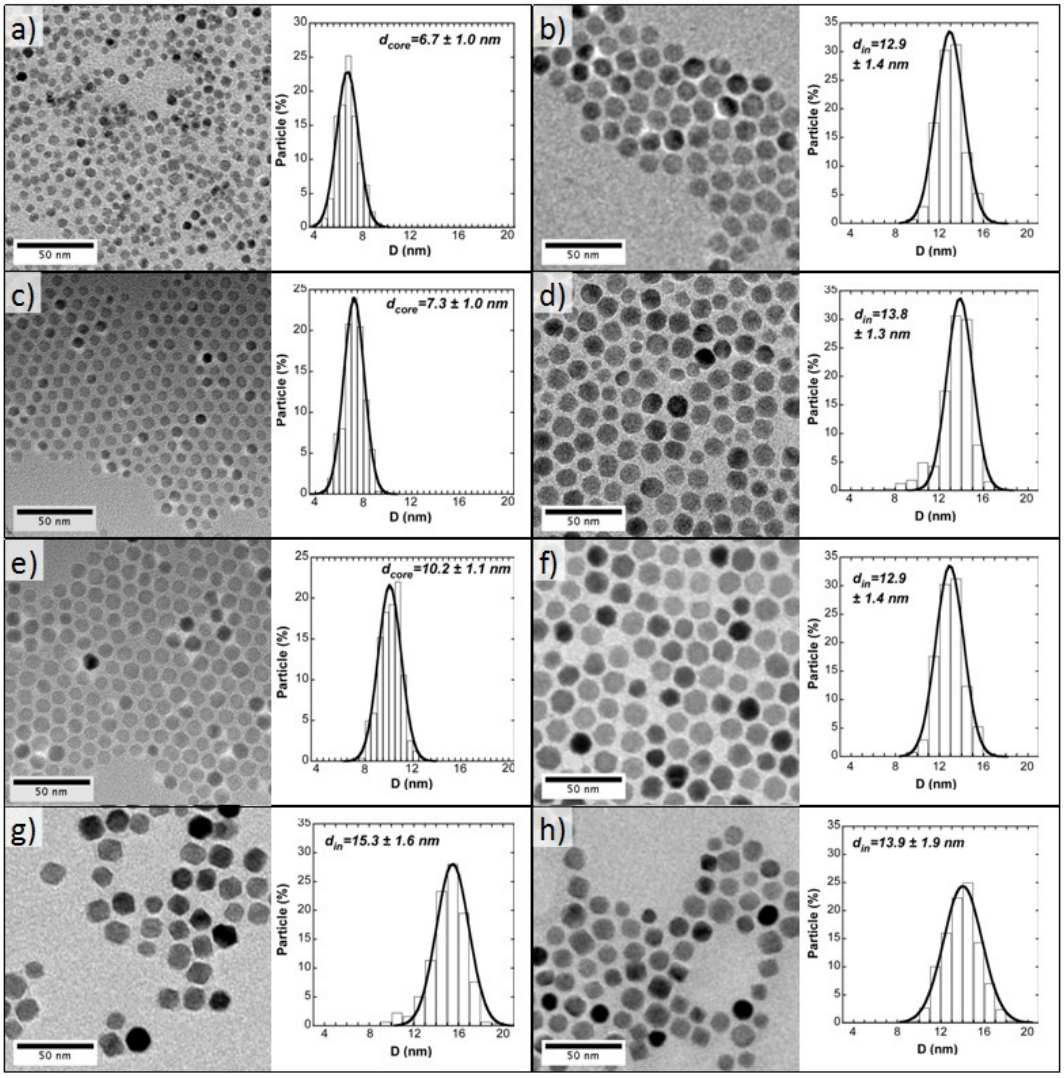

Figure S1. TEM micrographs and corresponding diameter histograms, (from > 300 MNPs, analyzed by Image J): **a)** Co ferrite seeds of d_{core} = 6.7 ± 1.0 nm; **b)**Co@Mn NPs of d_{in} = 12.9 ± 1.4 nm; **c)** Mn ferrite seeds of d_{core} = 7.3 ± 1.0 nm; **d)**Mn@CoNPs of d_{in} = 13.8 ± 1.3 nm; **e)** Mn ferrite seeds of d_{core} = 10.2±1.1 nm; **f)**Mn@Co-TLNPs of d_{in} = 14.3±1.5 nm; **g)** Co ferrite NPs of d_{in} = 15.3±1.6 nm and **h)** Mn ferrite NPs of d_{in} = 13.9±1.9 nm.

In order to estimate the thickness of the PMA shell we performed TME with Uranyl acetate negative staining on Mn@Co-TL (Figure 1). Samples were prepared on carbon film 400 copper mesh grids purchased from Electron Microscopy Sciences (Hatfield, USA), which were treated with glow-discharge under air plasma for 20 s (2.0·10-1 atm and 35 mA). Negatively charged carbon grids were used within 5

min after treatment to ensure hydrophilicity. The on-grid negative staining was performed using a slightly modified single-droplet negative-staining procedure. 1.5 µl sample droplet followed by three 2.5 µl droplets of 0.25% weight/volume (w/v) uranyl acetate aqueous solution were place on a clean Parafilm piece. The treated grid was incubated on the sample droplet for 1 min and then on the staining droplets for 3 s, 3 s, and 1 min respectively. After each incubation step the excess fluid was nearly fully removed by touching the grid edge with Whatman filter paper and finally fully dried for 20 min at $2.0 \cdot 10^{-1}$ atm. Sample images were acquired in a JEM-1230 transmission electron microscope equipped with a LaB6 cathode running at 120kV and an ORIOUS SC1000 4008×2672 pixels CCD camera (Gatan UK, Abingdon Oxon, UK). The average thickness of the PMA shell (l_S) on the Mn@Co-TL was 2.5 – 3 nm.

1.6. Dynamic light scattering (DLS) and ζ- potential

DLS and ζ-potential of the as synthesized MNPs (*i.e.*, coated with aliphatic chains) and PMA-coated hydrophilic NPs were analyzed using a Zetasizer Nano-ZS, Malvern Instruments. A summary of the obtained hydrodynamic diameters and ζ-potentials is shown in Table S2.

Table S2. Summary of the samples values

Sample List	N(d_h) in $CHCl_3$ [nm]	N(d_h) in H_2O [nm]	N(ζ)[mV]
Mn	12.8 ± 0.02	16.8 ± 0.9	-32.4± 1.6
Co@Mn	12.5 ± 0.3	19.5 ± 0.4	-31.9 ± 1.4
Mn@Co-TL	12.9 ± 0.5	17.8± 0.9	-31.8± 1.3
Mn@Co	12.7 ± 0.5	17.1 ± 0.58	-30.7 ± 1.5
Co	13.1 ± 0.8	19.8± 2.1	-30.5 ± 0.6

1.7. ICP-MS analysis

The composition of the MNPs was analyzed by induction coupled plasma mass spectrometry (ICP-MS, Agilent 7500 Series). Following standard procedures, the contents of Fe, Co and Mn ions were obtained. ForCo@Mn MNPs as example, the Fe content determined was 902 ± 33.1 ppb (parts per billion); the Co content was 28 ± 1.1 ppb and the Mn content was 139 ± 6.2 ppb. The oxygen content is not directly measured but inferred from the ratio of Fe/O in the Co/Mn-ferrite core shell structure[3]: $C_o = 2 \cdot C_{Fe} \cdot (M_O/M_{Fe}) = 514 \pm 18.9$ ppb. So 1 ml of Co@Mn MNP stock solution contained: $C_{Fe} = 0.9 \pm 0.03$ mg, $C_{Co} = 0.027 \pm 0.001$ mg, $C_{Mn} = 0.14 \pm 0.006$ mg, and $C_o = 2 \cdot C_{Fe} \cdot (M_O/M_{Fe}) = 0.52 \pm 0.02$ mg.

Table S3. Composition of 1 mg MNP sample as determined by ICP-MS.

Name	$C_{(Fe)}$ (mg)	$C_{(Co)}$ (mg)	$C_{(Mn)}$ (mg)	$C_{(O)}$ (mg)
Mn	0.61	0	0.04	0.35
Co@Mn	0.57	0.02	0.09	0.32
Mn@Co-TL	0.55	0.11	0.03	0.31
Mn@Co	0.54	0.14	0.02	0.30
Co	0.54	0.16	0	0.30

2. Magnetization measurements

2.1. Instruments

Magnetic characterization has been performed directly in colloidal suspensions (M vs H measurements at RT) and in samples obtained by drying the colloidal dispersion on semi-permeable filter paper (M vs H and M vs T measurements). Hysteresis loops at 5 K and 300 K to a maximum field of 6.5 T and the measurements of magnetization versus temperature (at 1 mT and 10 mT in the temperature range of 5-300 K) have been carried out using a Quantum Design MPMS-7 SQUID magnetometer. Hysteresis loops at RT in colloidal samples were performed in a custom built VSM magnetometer up to a maximum field of 1.8 T with high low field resolution.

2.2. Non-Interacting Super-Paramagnetic model: fit of M versus H measurements

The magnetization M of a MNP system as a function of external field H and temperature T is

$$M = \frac{NM_0 v}{V}\,(coth\,x - 1/x) = M_s\,L(x) \qquad x = M_0 v \mu_0 H/k_B T, \tag{1}$$

where N is the number of particles, v the volume of a particle, V the volume of the system, M_0 the *bulk* saturation magnetization, and $L(x)$ the Langevin function[7,8]. The MNP's sizes in real samples are Gauss distributed around the mean hydrodynamic diameter D_h, and hence, the total magnetization of the system is not Nv, but to an integral over the measured size distribution $\int_0^{max} v \cdot f(D_h \pm \sigma)dD$:

$$M = M_s \int_0^{max} L\left(\frac{M_s v \mu_0 H}{k_B T}\right) f(D)dD \tag{2}$$

Saturation magnetization, $[M_s] = A \cdot m^2/kg$, is considered as a variable independent of the MNP or domain magnetization, $[M\,] = kA/m^3$, (different units are used for clarity). Both variables should be linked by the inorganic content of the sample and density. Often, domain magnetization M is fixed a priori to the theoretical value, with the fit then providing a value for the mean size and dispersity of the magnetic core. The fit of these measurements at RT provides the mean size and the standard deviation of the MNP system. The initial susceptibility $\chi_0 = M/H$of the MNP sample can be calculated by adding the contribution of each size in the distribution of MNPs:

$$\chi_0 = \frac{\mu_0 M_S M}{3k_B T} \int_0^{\infty} V f(D)dD \tag{3}$$

It is quite usual to have small errors from the mathematical approach that is in fact unrealistic from the point of view of the physical understanding. In this particular case the non-linear minimization routine makes use of the LM (Levenberg-Marquardt) algorithm and the uncertainties are estimated by performing the square root of the diagonal elements of the covariance matrix multiplied by the MSE (Mean Square Error) or residue.

2.3. Determination of Anisotropy Constant

Fit of ZFC/FC measurements

A simple non-interacting model has been used for the fit, in which the population of MNPs (given by a size distribution $f(D)$) is sharply divided in two groups at each temperature, depending on their particular

size: the fraction in an ideal superparamagnetic state that corresponds to MNPs below a certain critical volume and those, above such limit, whose super spin remains blocked:

$$M_{ZFC}(T) = \int_0^{V_c} M_s L\left(\frac{MV\mu_0 H}{k_B T}\right) f(V)dV + \int_{V_c}^{\infty} M_s \frac{M\mu_0 H}{3K_{u,c}} f(V)dV \qquad (4)$$

In the first term, we make use of the low energy barrier approximation where the energy barrier (defined as $K_{eff}V$, being V the particle volume) is much smaller than the thermal energy ($k_B T$ where k_B is the Boltzmann Constant) and so can be omitted. Accordingly, the response of the magnetization to changes of magnetic field or temperature (H or T) follows a Langevin function, where M is the particle magnetization (A/m in S.I.) and M_s is the experimental saturation magnetization (including non-magnetic mass contribution, in general). Both the experimental magnetization and the particle magnetization are allowed to decrease with temperature following a spin wave-like behavior[9] (Bloch type law) as:

$$M(T) = M(0)e^{-BT^{3/2}} \qquad (5)$$

where the so-called Bloch constant (B) has been obtained from the magnetization measurements as a function of temperature under the maximum field of 7T, being between 2 and 4×10^{-5} in all cases.

The second term component results from the initial susceptibility of a randomly oriented magnetic domains either with uniaxial (K_u) or with cubic anisotropy (K_c), provided that $K_c > 0$, as described elsewhere[10]. Note that K_c is the first cubic anisotropy and is equal to $4K_{eff}$ if $K_c > 0$ as in magnetite or Co ferrite. The threshold between the two populations (it is limiting both integrals) is given by a critical diameter or volume (D_C/V_C) such that:

$$V_c(T) = \frac{25k_B T}{K_{eff}(T)} \qquad (6)$$

In this model, the position and shape of the ZFC maximum depends on the anisotropy through this critical volume that depends explicitly on temperature and also implicitly, through the function $K_{eff}(T)$ which is given by different models as stated in the manuscript, depending on the relative content of Co ferrite.

The expression calculated by Tachiki[11], Sloncweski[12] and others for the anisotropy energy density of Co^{2+} takes the form of a thermal activated process as:

$$K_C = \mathcal{F}(\alpha\lambda, a, T) - \mathcal{G}(\alpha\lambda, a, T)e^{-2\mu_0\mu_B H_e/k_B T} \qquad (7)$$

where $(2\mu_0\mu_B H_e)$ measure the strength of the exchange field, $(\alpha\lambda)$ the L-S coupling and (a) the crystal field perturbation. $\mathcal{F}$ and $\mathcal{G}$ are explicit functions of the L-S coupling, the crystal field splitting and the temperature

given by:

$$\mathcal{F}(\alpha\lambda, a, T) = \frac{9}{32}\frac{(\alpha\lambda)^4}{g^3}\left(tanh(g/k_B T) - g/k_B T\, sech^3(g/k_B T)\right) \quad (7.1)$$

and

$$\mathcal{G}(\alpha\lambda,a,T)=\frac{9}{32}\frac{(\alpha\lambda)^4}{g^3}\frac{cos(g'/k_BT)}{cos(g'/k_BT)}\Bigg[tanh(g/k_BT)-\frac{1}{81}\frac{g^3}{g'^3}tanh(g'/k_BT)$$
$$-g/k_BT\Bigg\{\left(1-\frac{1}{81}\frac{g^3}{g'^3}\right)$$
$$-2tanh(g/k_BT)\left(tanh(g/k_BT)-\frac{1}{9}\frac{g}{g'}tanh(g'/k_BT)\right)\Bigg\}\Bigg] \quad (7.2)$$

where

$$g=\sqrt{\frac{3}{4}(\alpha\lambda)^2+a^2} \quad (7.3)$$

and

$$g'=\sqrt{\frac{1}{12}(\alpha\lambda)^2+a^2} \quad (7.4)$$

2.4. M vs H data at 5K

Figure S2 shows hysteresis loops at 5 K of 5 samples in water dispersion and fixed (*i.e.*, deposited in a filter paper), respectively. Measurements have been normalized to 1 to easily compare the coercive fields.

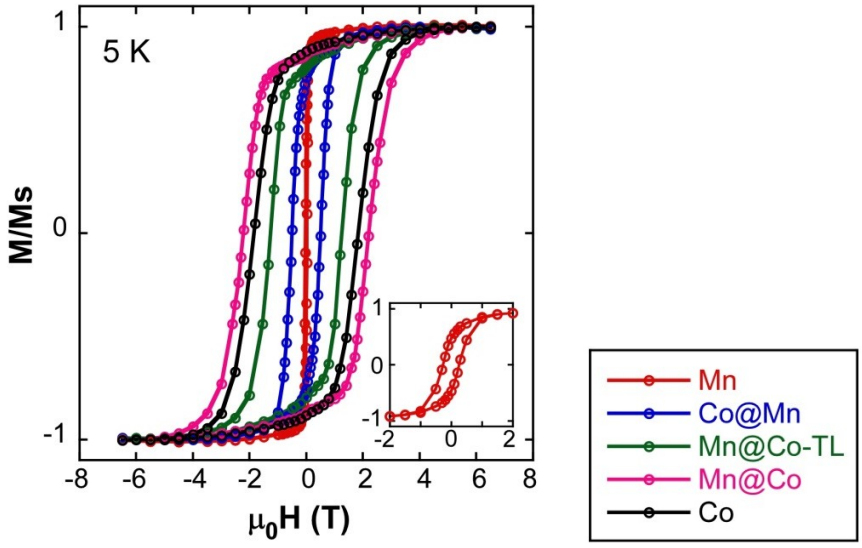

Figure S2. M vs H measurements at 5° K of the samples deposited on filter paper from aqueous dispersions (fixed NPs).

2.5. M vs H Fit and χ_0 calculation

In this case two kind of measurement at RT were carried out: **a)** directly in colloidal dispersion and **b)** in immobilized MNPs (in a filter paper). The aim of these measurements is twofold: firstly, to analyze how the initial susceptibility changes in different media and secondly, to observe empirically the effect of the removal of the Brownian contribution.

In the fits the saturation magnetization, M_s, has been fixed to the experimental value (Am^2/kg) and correspondingly the domain magnetization M (kA/m) for coherency. From Equation 3 it is obvious that the initial susceptibility is correlated with the apparent magnetic diameter d_{MvsH}.

The change of the initial susceptibility when comparing measurements in a liquid and in immobilized MNPs is thought to be a sign of the relevance of the Brownian mechanism in Co@Mn sample (Figure S3a-b). The explanation for the increase of χ_0 in liquid could be either the partial rotation of the easy axis towards the field or a significant decrease of the dipolar interactions due to the random brownian motion. Anyway, it seems that this effect happens just when the Brownian relaxation starts to be significant and so it is a direct evidence of its real weight.

In the Mn sample $K_{eff}V \ll k_B$, so it is not expected to see a change in the initial susceptibility between the sample measured in liquid and in paper. In these conditions the Neel mechanism is the only relevant relaxation process and therefore, no differences are expected in measurement in colloids and in fixed particles (Figure S3c-d).

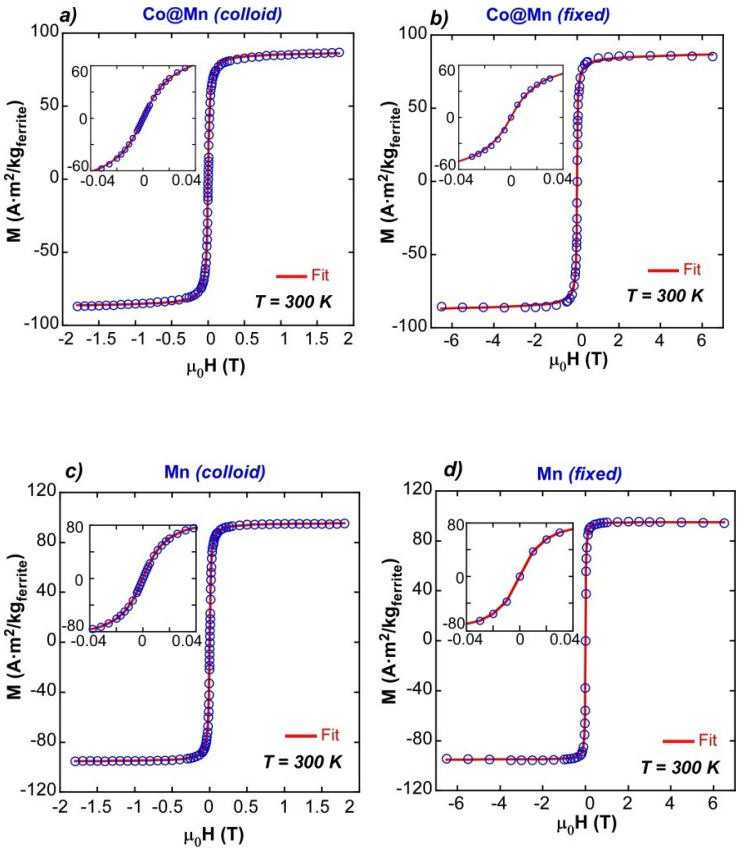

Parameter	Value (a)	Value (b)
M_s (Am^2/kg)	87 (fixed)	87 (fixed)
D (nm)	12.30±0.01	10.93±0.07
σ (nm)	1.50±0.04	3.7±0.1
χ_0 (m^3/kg)	$3.94 \cdot 10^{-3}$	$3.52 \cdot 10^{-3}$
H_c (mT)	**<0.05**	**<0.05**
Mr/Ms	**<0.001**	**<0.001**

Parameter	Value (c)	Value (d)
M_s (Am^2/kg)	90.5(fixed)	90.5(fixed)
D (nm)	13.39±0.01	13.08±0.05
σ (nm)	1.74±0.04	2.7±0.1
χ_0 (m^3/kg)	$5.44 \cdot 10^{-3}$	$5.44 \cdot 10^{-3}$
H_c (mT)	**<0.05**	**<0.05**
Mr/Ms	**<0.001**	**<0.001**

Figure S3. (a) M(H) and Fit of Co@Mn in colloidal sample and **(b)** in fixed NPs; **(c)** M(H) and Fit of Mn in colloidal sample and **(d)** in fixed NPs. The table contains the corresponding parameters of the fits at RT (D and σ) and calculated mass susceptibility.

On the other hand, in the Mn@Co-TL, Mn@Co and in Co samples (Figures S4), the MNPs do not present hysteresis above the detection limit (50 μT). In these samples when the Brownian mechanism comes into play and the MNPs show a SPM-like behavior at room temperature**.** On the contrary, when the MNPs are

fixed in a filter paper they present hysteresis at RT, that is to say, ferromagnetic behavior. This is because at 300 K a significant percentage of MNPs are in the blocking regime.

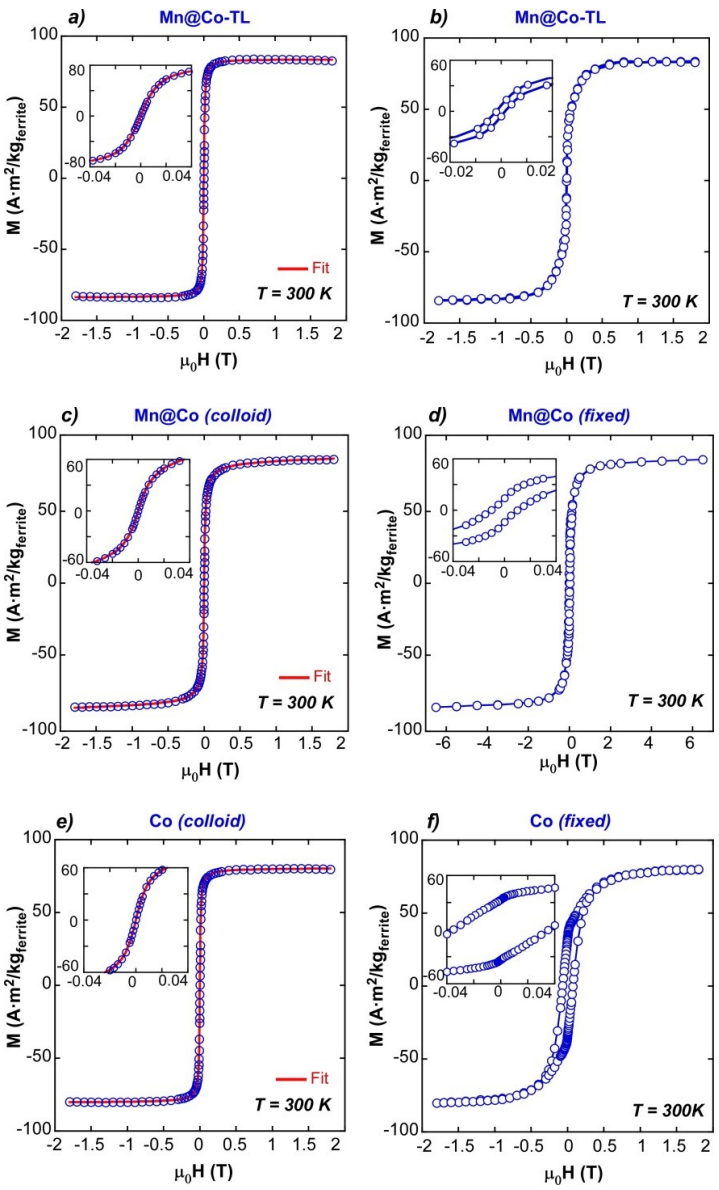

Parameter	Value (a)	Value (b)
M_s (Am^2/kg)	84 (fixed)	84
D (nm)	14.42±0.02	---
σ (nm)	1.42±0.08	---
χ_0 (m^3/kg)	$5.97 \cdot 10^{-3}$	---
H_c (mT)	**<0.05**	**1.7**
Mr/Ms	**<0.001**	**0.075**

Parameter	Value (c)	Value (d)
M_s (Am^2/kg)	82 (fixed)	82
D (nm)	13.54±0.02	---
σ (nm)	4.27±0.03	---
χ_0 (m^3/kg)	$6.02 \cdot 10^{-3}$	---
H_c (mT)	**<0.5**	**10.2**
Mr/Ms	**<0.001**	**0.169**

Parameter	Value (e)	Value (f)
Ms (emu/g)	80(fixed)	80
D (nm):	15.6±0.02	---
σ (nm):	3.42±0.05	---
χ_0 (m3/kg):	$7.81 \cdot 10^{-3}$	---
H_c (Oe)	**<0.5**	**70.4**
Mr/Ms	**<0.001**	**0.417**

Figure S4.**(a)** M(H) and Fit of Mn@Co-TL in colloidal sample and **(b)** M(H) in fixed NPs; **(c)** M(H) and Fit of Mn@Co in colloidal sample and **(d)** M(H) in fixed NPs; **(e)** M(H) and Fit of Co in colloidal sample and **(f)** M(H) in fixed NPs. The table contains the corresponding parameters of the fits at RT (D and σ) and calculated mass susceptibility.

2.6. ZFC/FC measurementsat different magnetic fields (1 mT and 10 mT)

Figure S5 shows ZFC/FC measurements of (a) Co@Mn ,(b) Mn@Co-TL and (c) Mn@Co samples in in water dispersion deposited in the filter paper at two different magnetic fields (1 and 10 mT). There is not

any significant shift in the maximum of the ZFC at different fields in the core-shell systems; so it suggests a minor influence of dipolar interaction among the MNPs.

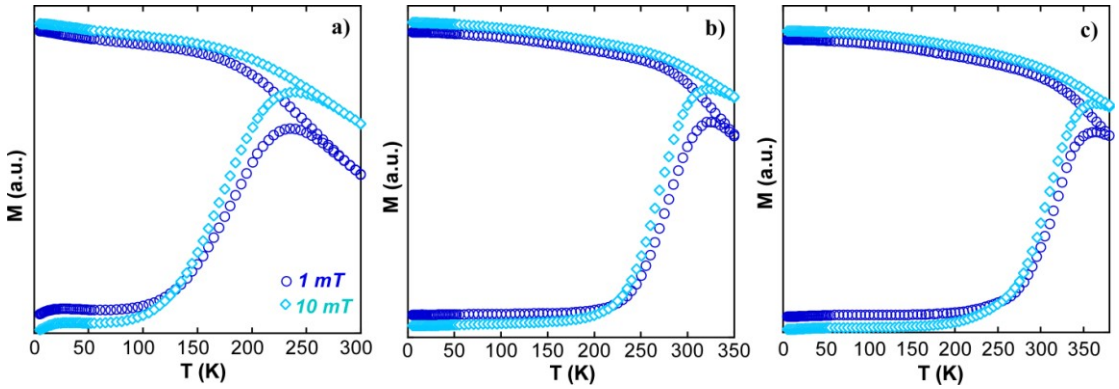

Figure S5. ZFC/FC curves at 1 mT and 10 mT fields: **(a)** Co@Mn , **(b)** Mn@Co-TL and **(c)** Mn@Co.

3. ***Specific Loss Power (SLP)***

3.1. Experimental equipment and measurement of SLP

The radio frequency magnetic field is generated in a custom build, six turn helical, water-cooled coil driven by a power supply from MSI Automation Inc. (Wichita, Kansas). The sample temperature is measured using a fiber optic temperature sensor (T1S-03-WNO-B05) and analogue to digital converter (ReFlex) from Neoptix (Quebec, Canada). The sample holder used was a doubled walled cylindrical glass bottle, sealed with a plastic cap.

The SLP was measured in water-based suspensions of each MNP sample (200 μl), placed inside the sample holder inside the coil. Before applying the field, the samples were allowed to equilibrate to ambient temperature. Annular air gaps between the glass walls of the sample holder and between the sample holder and the coil ensured minimal heat transfer between the sample and its environment. The samples were subjected to magnetic field for 15 s, while the temperature rise was simultaneously recorded. The magnetic flux density along the sample column (1 cm) was (22.4 kA/m) at 412.5 kHz for all the samples.

Temperature versus time data was recorded at 5 Hz. The *dT/dt* values were obtained from the slope of a linear fit to the data for the first 5 seconds of heating. SLP was calculated by using Equation 8:

$$SLP = \frac{C_{water} \cdot \rho_{water}}{\rho_{np}} \frac{dT}{dt} \qquad (8)$$

where, C is the specific heat of water (4.2 J/g^{o}C), ρ is the density of water (1 g/cm^{3}) and ρ_{np} is the density of inorganic part of the MNPs in g/cm^{3}. The experimental SLP data is summarized in table S4 together with the values obtained from the simulation.

Table S4 Experimental *dT/dt* values and SLP values of the samples.

Sample	Structure	Conc (mg/ml)	dT/dt (°C/s)	SLP (W/g) Exp	SLP (W/g) Calc.
Mn		0.00256	0.112±0.001	183.8 ± 1.7	190±60
Co@Mn		0.00221	0.275±0.005	552.6 ± 9.5	560±50
Mn@Co-TL		0.00428	0.297±0.001	291.4 ± 1.0	340±50
Mn@Co		0.00271	0.195 ± 0.01	302 ± 15	320±40
Co		0.00363	0.273±0.008	315.9 ± 9.3	280±30

3.2.2. Theoretical model: Basis of the simulation of SLP by Linear Response Theory (LRT) and quasi-Linear Response Theory (q-LRT)

The expected SLP for sample of MNPs with a specific mean diameter of the inorganic part d_{in} and size dispersity σ_{in} is calculated by convoluting the SLP function,$P_{SPM}(d)$, with a distribution function accounting for size distribution, $f(d_{in}, \sigma_{in})$:

$$SLP(d,\sigma) = \int_0^{\boldsymbol{d}_{max}} P_{SPM}(d) f(d,\sigma) d\mathbf{d} \qquad (9)$$

SLP or absorption power P_{SPM} is given in the linear approximation by[13]:

$$P_{SPM} = \mu_0 \pi f \chi'' H^2 \qquad (10)$$

where χ'' is the imaginary part of complex susceptibility, and χ_0 the DC initial susceptibility[14]:

$$\chi''(\omega) = \chi_0 \frac{\omega\tau_{eff}}{1+(\omega\tau_{eff})^2} \chi_0 = \frac{\mu_0 M_S^2 V}{3k_B T} \qquad (11)$$

being τ_{eff}, the effective relaxation time, resulting from the superposition of Neel relaxation (τ_N) and Brownian relaxation (τ_B), considered as independent processes[15].

$$\frac{1}{\tau_{eff}} = \frac{1}{\tau_N} + \frac{1}{\tau_B} \qquad (12)$$

Neel relaxation time can be calculated by[16]:

$$\tau_N = \frac{\tau_0}{2}\left(\frac{\pi k_B T}{KV}\right)^{1/2} e^{KV/k_B T} \qquad (13)$$

where τ_0 is the inverse of the so-called frequency of jump attempts, usually between 10^{-9} and 10^{-11} s. V is the MNP volume, K the effective anisotropy constant and k_B is the Boltzmann constant.
The Brownian relaxation time is given by:

$$\tau_B = \frac{4\pi\eta r_h^3}{k_B T} \qquad (14)$$

Where η is the viscosity of the solvent, and r_h the hydrodynamic radius.
It is important to underline that the previous model can be corrected for a quasi-Linear Response by using

a modified susceptibility, the so-called chord susceptibility[17] given by:

$$\chi_{\text{chord}} = \frac{M_S L(\xi)}{H_{max}} \qquad (15)$$

Note that in this framework, the non-linearity is included in this susceptibility that becomes dependent on the amplitude of the AC excitation.

References:

(1) Sun, S.; Zeng, H.; Robinson, D. B.; Raoux, S.; Rice, P. M.; Wang, S. X.; Li, G. *J. Am. Chem. Soc.***2004**, *126*, 126–132.

(2) Chen, R.; Christiansen, M. G.; Anikeeva, P. *ACS Nano***2013**, *7* (10), 8990–9000.

(3) Lee, J.-H.; Jang, J.-T.; Choi, J.-S.; Moon, S. H.; Noh, S.-H.; Kim, J.-W.; Kim, J.-G.; Kim, I.-S.; Park, K. I.; Cheon, J. *Nat. Nanotechnol.***2011**, *6* (7), 418–422.

(4) Sun, S.; Zeng, H. *J. Am. Chem. Soc.***2002**, No. 31, 8204–8205.

(5) Xie, J.; Peng, S.; Brower, N.; Pourmand, N.; Wang, S. X.; Sun, S. *Pure Appl. Chem.***2006**, *78* (5), 1003–1014.

(6) Lin, C.-A. J.; Sperling, R. A.; Li, J. K.; Yang, T.-Y.; Li, P.-Y.; Zanella, M.; Chang, W. H.; Parak, W. J. *Small***2008**, *4* (3), 334–341.

(7) Kaiser, R. *J. Appl. Phys.***1970**, *41* (3), 1064.

(8) Weaver, J. B.; Rauwerdink, A. M.; Hansen, E. W. *Med. Phys.***2009**, *36* (5), 1822–1829.

(9) Aquino, R.; Depeyrot, J.; Sousa, M. H.; Tourinho, F. a.; Dubois, E.; Perzynski, R. *Phys. Rev. B***2005**, *72* (18), 184435.

(10) Chikazumi, S. *Physics of ferromagnetism*; Oxford University Press, 2009.

(11) Tachiki, M. *Prog. Theor. Phys.***1960**, *23* (6), 1055–1072.

(12) Slonczewski, J. C. *Phys. Rev.***1958**, *110* (6), 1341–1348.

(13) Kita, E.; Oda, T.; Kayano, T.; Sato, S.; Minagawa, M.; Yanagihara, H.; Kishimoto, M.; Mitsumata, C.; Hashimoto, S.; Yamada, K.; Ohkohchi, N. *J. Phys. D. Appl. Phys.***2010**, *43* (47), 474011.

(14) Coral, D. F.; Mendoza Zélis, P.; de Sousa, M. E.; Muraca, D.; Lassalle, V.; Nicolás, P.; Ferreira, M. L.; Fernández van Raap, M. B. *J. Appl. Phys.***2014**, *115* (4), 043907.

(15) Hergt, R.; Dutz, S.; Müller, R.; Zeisberger, M. *J. Phys. Condens. Matter***2006**, *18* (38), S2919–S2934.

(16) Brown, W. F. *Phys. Rev.***1963**, *130* (5), 1677–1686.

(17) Rosensweig, R. E. *J. Magn. Magn. Mater.***2002**, *252*, 370–374.

Physico-chemical Properties of PEGylated Gold Nanoparticles: Impact on Cell Fitness

Pablo del Pino,*[a] Beatriz Pelaz,[b] Fang Yang,[c] Qian Zhang,[b] Karsten Kantner,[b] Raimo Hartmann,[b] Natalia Martinez de Baroja,[a] Marta Gallego,[a] Marco Möller,[a] Bella Manshian,[d] Stefaan Soenen,[d] Norbert Hampp,[d] and Wolfgang J. Parak*[a,b]

Abstract: The physico-chemical properties of various series of PEGylated gold nanoparticles, varying in the molecular weight of the PEG, size of inorganic core, hydrodynamic size and net charge, are exhaustively described, including stiffness, hydrophobicity and catalytic activity. For a series of PEGylated gold nanoparticles only two parameters, net charge and hydrophobicity were varied, whereas other parameters such as hydrodynamic size, stiffness and catalytic activity were kept constant. The impact on cell fitness of this series of nanoparticles was evaluated, revealing that less negatively charged, more hydrophilic nanoparticles were more effectively uptaken by cells and further, they had a negative impact on membrane health, autophagy and cell area.

Gold nanoparticles (in the following referred to as Au NPs) are among the most widely studied materials is the context of bionanotechnology. The interesting optical properties of Au NPs makes them well-suited materials for myrriad applications in life science, including photothermal therapy, optoacoustic imaging, biosensing, etc. Moreover, Au NPs are considered among the safest nanomaterials, mainly because of the inertness of gold (the most noble metal), which confers Au NPs with good stability against corrosion in physiological media. Indeed, Au NPs are already being applied in clinical trials as photothermal agents.

PEGylation of NPs, i.e., surface modification of NPs with polyethylene glycol (PEG), is among the most widely applied surface modification applied to NPs aimed for biological applications. The extended use of PEGylation relies on two main features: (i) PEGylation improves the colloidal stability of NPs in media of physiological relevance and (ii) PEGylation reduces the unspecific adsorption of proteins.

[a] Dr. P. del Pino, M. Gallego, M. Möller, Dr. N. Martínez de Baroja, Prof. W. J. Parak.
CIC biomaGUNE
San Sebastián, Spain
E-mail: pdelpino@cicbiomagune.es, wolfgang.parak@physik.uni-marburg.de
[b] Dr. B. Pelaz, Q. Zhang, K. Kantner, R. Hartmann, Prof. W. J. Parak
Fachbereich Physik
Philipps Universität Marburg
Marburg, Germany
[c] Dr. B. Manshian, Dr. S. Soenen
Radiology Department
KULeuven Campus Gasthuisberg
Leuven, Belgium
[d] F. Yang, Prof. N. Hampp
Fachbereich Chemie
Philipps Universität Marburg
Marburg, Germany

Supporting information for this article is given via a link at the end of the document.

Herein, differently sized citrate-capped Au NPs (ca. 14, 18, 23 and 28 nm) were PEGylated with four different HS-PEG-COOH polymers with increasing molecular weight (ca. 1, 3, 5 and 10 kDa). This gives a total of 16 samples (each core combined with each PEG), which can vary with respect to each other in size of the inorganic core (d_c), the thickness of the PEG shell (1/2 Δd_S) and the size of the core-shell system (d_{CS}), as well as in the hydrodynamic size, cf., Figure 1.

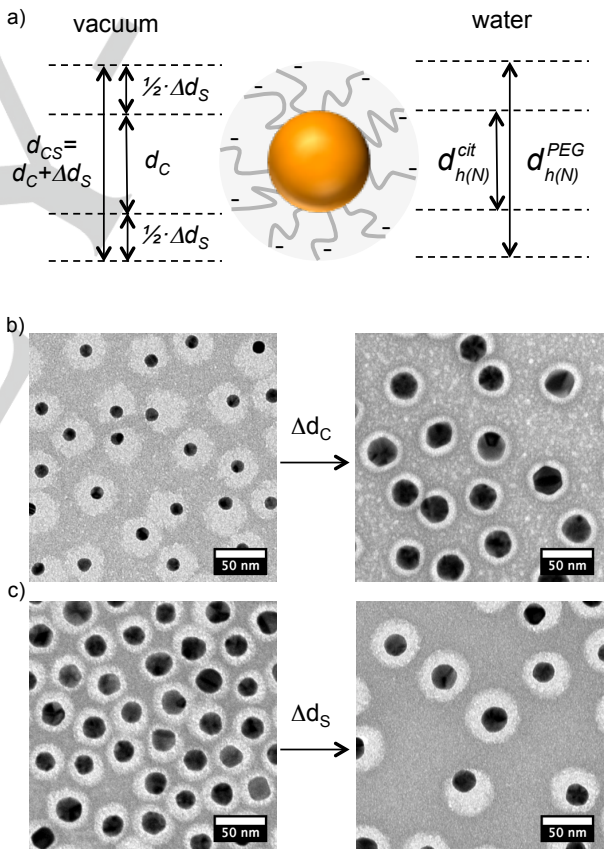

Figure 1. a) Scheme of PEGylated Au NPs, showing different properties in vacuum and in solution. b) Negative stained TEM micrographs of two types of PEGylated NPs are shown, in which d_C increases (from ca. 14 nm to 28 nm) while d_{CS} is kept constant ca. 37 nm. c) Negative stained TEM micrographs of two types of PEGylated NPs are shown, in which d_{CS} increases (from ca. 37 nm to 50 nm) while d_C is kept constant ca. 23 nm.

The physico-chemical properties of these 16 samples, including size (by TEM, negative staining TEM and DLS), dynamic interfacial tension (i.e., hydrophobicity), stiffness and catalytic activity towards the reduction of methylene blue, were

characterized; cf., details can be found in the supporting information.

In order to compare the properties of the different samples, we introduce the following dimensionless parameters: R_{PEG}^{TEM}, which refers to the contribution of PEG to the resulting size as determined by TEM (vacuum), i.e., R_{PEG}^{TEM} equals 0 or 1 if the whole size (d_{CS}) comes from the Au core or the PEG shell, respectively; α, which refers to the contribution of d_C to d_{CS} for one particular size (Δd_{CS} = 0), i.e., α equals 0 or 1 if d_{CS} comes from the PEG shell or the Au core, respectively, cf., Figure 2.

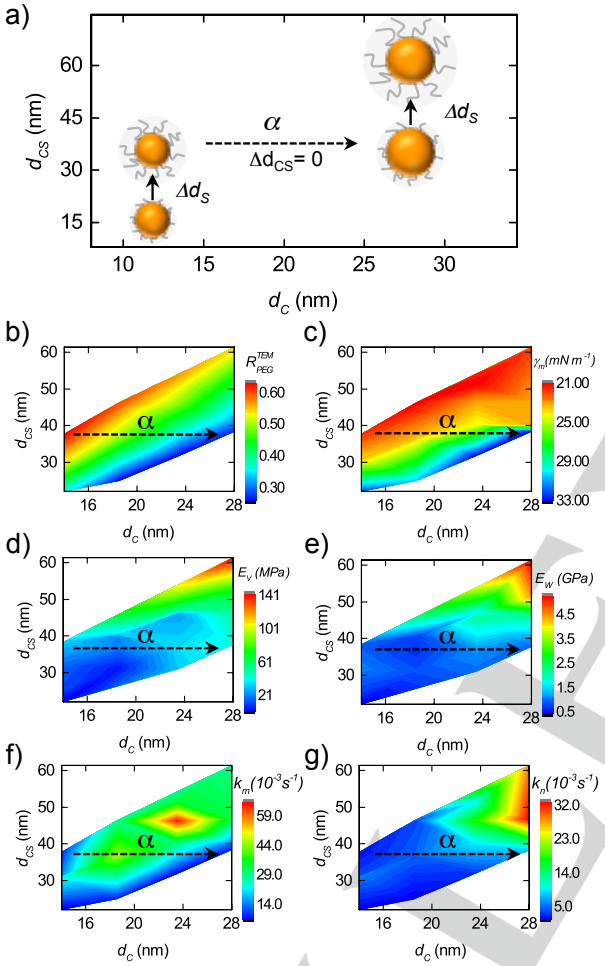

Figure 2. a) Diagram that schematically shows different variables related to the size of the PEGylated Au NPs, i.e., d_C, d_{CS}, Δd_S and α. b-g) Heamaps d_{CS} versus d_C.in which the colour code refers to R_{PEG}^{TEM}, dynamic interfacial tension (γ_m), stiffness in vacuum (E_V), stiffness in water (E_W), catalytic activity at equal mass of gold (k_m) and catalytic activity at equal number of NPs (k_n), respectively.

In Figure 2, for d_{CS} equals at ca. 37 nm, the dotted arrow represent equally sized PEGylated NPs (also by DLS, cf., supporting information) in which *dc* increases (as α does). We can see that for this specific d_{CS}, the hydrophobicity (which is inversely proportional to γ_m) is the only parameter which significantly varies, i.e., it decreases with α. Surprisingly, the stiffness is not significantly affected in the vacuum or water, although the composition of the PEGylated NPs (R_{PEG}^{TEM}) along this arrow varies significantly. In detail, along this dotted arrow four specific samples are represented: 14 nm Au NPs combined with 10 kDa PEGs (in the following referred to as Au1), 18.5 nm Au NPs combined with 5 kDa PEGs (in the following referred to as Au2), 23.5 nm Au NPs combined with 3 kDa PEGs (in the following referred to as Au3) and 28 nm Au NPs combined with 1 kDa PEGs (in the following referred to as Au4). The series of these NPs present ca. size (ca. 37 nm by negative staining TEM or DLS), a similar ζ-potential value (around -40 mV, cf. Figure 3c, left panel), similar stiffness or catalytic activity, yet, their hydrophobicity varies: the higher the molecular weight of the PEG, the higher the relative hydrophobicity is. Thus, we chose to further modify the surface of these colloids for analyzing their impact on cell fitness. That is, the PEGylated samples previously discussed, *i.e.*, Au1, Au2, Au3 and Au4, were functionalized with a NIR dye (dyomics dy647P1, amino derivative, in the following referred to as Dye) and a quaternary ammonium group (positive in all of the pH range, 2-aminoethyl trimethylammonium chloride hydrochloride, in the following referred to as N+). To do so, we used EDC (1-Ethyl-3-(3-dimethylaminopropyl)carbodiimide) chemistry to covalently bind these molecules to the end terminal carboxylic groups of the PEGs.

In order to produce two equivalent series of NPs with different net charge, the "bare" PEGylated NPs (Au1, Au2, Au3 and Au4) were modified only with the Dye, yielding fluorescence labeled NPs (in the following referred to as Au1-, Au2-, Au3- and Au4-) equivalent to the "bare" NPs, yet with a less negative net charge (ζ-potential values are around -30 mV, cf., Figure 3c, central panel). Likewise, the fluorescence labeled PEGylated NPs were further modified with N+, yielding an equivalent series of fluorescence labelled "positive" NPs (in the following referred to as Au1+, Au2+, Au3+ and Au4+). By modifying the NPs with the N+ groups, their ζ-potential values dropped at around -20 mV, cf. Figure 3c, right panel. In summary, we prepared two series of fluorescence labelled PEGylated NPs (in each series the NPs are equivalent expect for the hydrophobicity which decreases with α), which vary with respect to the net charge, i.e., "negative" for the series with the Dye and carboxylic groups, or "positive" in which also N+ groups are attached.

The two series of NPs (8 samples) were incubated with two cell lines, being murine C17.2 neural progenitor cells and primary human umbilical vein endothelial cells (HUVECs). Then, different parameters related to cell fitness were acquired using high-content imaging, where for every condition, several hundreds of images were taken and automated analysis was performed, resulting in minimal 3000 cells per condition that were analyzed. The following parameters related to cell fitness were analysed, cf., supporting information: autophagy (in the following referred to as LC3), cell area (in the following referred to as A), endosome size (in the following referred to as SE), membrane damage (in the following referred to as MD), mitochondrial health (in the following referred to as MH), reactive oxidative species (in the following referred to as ROS), cell skewness (in the following referred to as SK), viability (in the following referred to as V) and focal adhesion (in the following referred to as FA). For cellular exposure studies, cells were incubated with the NPs at equal mass of gold (62.5, 125 or 250

μg/ml) or equal number of NPs (1.25, 2.5 or 5 nM). The data reveal that when NPs are given at equal number of NPs, Au3+ and Au4+ (i.e., “positive”, more hydrophobic NPs) have a negative effect on membrane health, autophagy and cell area, whereas the other parameters remain relatively unaffected compared to the control cells, cf., Figure 3d. In contrast, when cells are incubated with NPs at equal mass of gold, Au1+ and Au2+ ((i.e., “positive”, less hydrophobic NPs) negatively affect also other parameters such as viability and mitochondrial damage, cf. supporting information.

The uptake of the “negative” and “positive” NPs were also investigated by ICP-MS, cf. supporting information. Uptake results closely follow the trend observed in the cell fitness analysis. That is, cells were affected when more NPs were internalized.

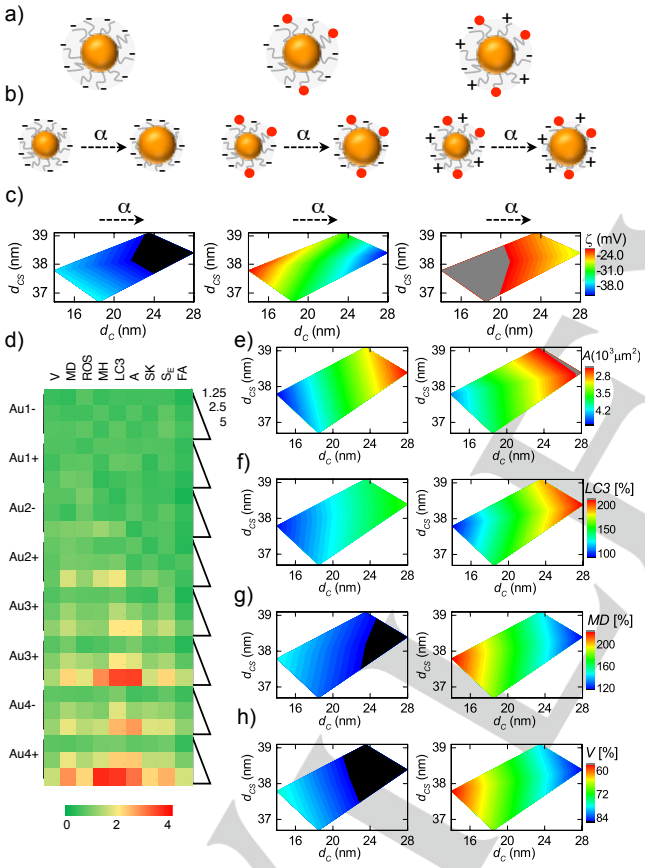

Figure 3. a) Schematic representation of the models used: “bare” (left) and fluorescence “negative” (middle) or “positive” (right) PEGylated NPs. b) For each model with the same dCS, equivalent colloids were prepared by varying *α*. c) ζ-potential heatmaps. d) Heatmap for various parameters related to cell fitness, for the NPs given at equal number to HUVEC cells. e, f) Cell area and autophagy heatmaps for “negative” (left) and “positive” (right) NPs when HUVEC cells were incubated at 5 nM. g, h) Mitochondrial damage and viability heatmaps when cells were incubated at μg/mL.

Experimental Section

Experimental Details can be found in the supporting information: synthesis and characterization of the Au cores, synthesis of PEGylated Au NPs, negative staining of PEGylated NPs, characterization of NP’s dynamic interfacial tension, AFM measurements (stiffness), catalytic properties, functionalization of PEGylated NPs and cell studies.

CONCLUSIONS: to be done.

SUPPORTING INFORMATION

Physicochemical Properties of PEGylated Gold Nanoparticles: Impact on Cell Fitness

Pablo del Pino, Beatriz Pelaz, Fang Yang, Qian Zhang, Karsten Kantner, Raimo Hartmann, Natalia Martinez de Baroja, Marta Gallego, Marco Möller, Bella Manshian, Stefaan Soenen, Norbert Hampp, and Wolfgang J. Parak

Table of Contents:		Page

I) Synthesis of citrate-capped gold nanoparticles (NPs), *i.e.*, Au cores

Five batches of Au NPs of increasing sizes (*i.e.*, inorganic diameters – d_C) were produced using a modified protocol of the seeded growth method reported by Bastus *et al.*,[1] *cf.* Figure S.II-1. The synthesis starts with the production of NPs with diameter of *ca.* 9 nm (~ 6.3 nM), in the following referred to as seeds. Next, seeds were grown to produce NPs with diameter of *ca.* 14 nm (~ 3.8 nM, Au1). Then, Au1, Au2 and Au3 were grown to produce NPs with diameter of *ca.* 19 nm (~ 2.5 nM, Au2), *ca.* 23 nm (~ 1.3 nM, Au3) and *ca.* 27 nm (~ 0.8 nM, Au4), respectively. The NP's size (d_C) was characterized by transmission electron microscopy (TEM, JEOL JEM-1400PLUS) to check the size distribution and their monodispersity, *cf.* Figure S.II-2, -3, -4, -5, -6. Synthetic details for the production of seeds, Au1, Au2, Au3 and Au4 are given in the following:

Synthesis of Seeds: A solution of 2.0 mM sodium citrate (Sigma Aldrich, #W302600) in ultrapure water (150 mL) was heated with a heating mantle in a 250 mL three-necked round-bottomed flask under vigorous stirring. A condenser was utilized to prevent the evaporation of the solvent. 20 min after boiling had started 1 mL of $HAuCl_4$ (25 mM, Strem Chemicals, #16903-35-8) was injected. The color of the solution changed from yellow to bluish gray and then to soft pink in 10 min.

Synthesis of Au1: Immediately after the synthesis of the seeds and in the same reaction vessel, the reaction was cooled until the temperature of the solution reached 90 °C. Then, 1 mL of a $HAuCl_4$ solution (25 mM) was injected. After 30 min, the reaction was finished. This process was repeated twice to yield Au1, *i.e.*, two injections of $HAuCl_4$ into the seeds solution.

Synthesis of Au2: After that, the sample was diluted by extracting 55 mL of sample (Au1, ~ 3.8 nM) and adding 53 mL of ultrapure water and 2 mL of 60 mM sodium citrate. This solution was then used as a seed solution, and the growth process was repeated again, which requires 3 sequential injections of 1 mL of a $HAuCl_4$ solution (25 mM) into Au1, separated by 30 min time intervals at 90 °C, to produce Au2.

Synthesis of Au3: After that, the sample Au2 was diluted by extracting 55 mL of sample (Au2, ~ 2.5 nM) and adding 53 mL of ultrapure water and 2 mL of 60 mM sodium citrate. This solution was then used as a seed solution, and the process was repeated again, which requires 3 sequential injections of 1 mL of a HAuCl4 solution (25 mM), separated by 30 min time intervals at 90 °C, to produce Au3.

Synthesis of Au4: After that, the sample Au3 was diluted by extracting 55 mL of sample (Au3, ~ 1.3 nM) and adding 53 mL of ultrapure water and 2 mL of 60 mM sodium citrate. This solution was then used as a seed solution, and the process was repeated again, which requires 3 sequential injections of 1 mL of a HAuCl4 solution (25 mM), separated by 30 min time intervals at 90°C, to produce Au4 (~ 0.8 nM).

II) Characterization of NPs

Figure S.II-1 shows a photograph of colloidal solutions of NPs as prepared (A), and the corresponding UV-Vis spectra (B). Notice that for comparison, spectra are shown normalized to 1 OD (OD: optical density) at 450 nm. The localized surface plasmon band (LSPR) is blue-shifted as the size of the NPs increases (from seeds to Au4), which also influences the maximum scattering intensity (I_{MAX}), *i.e.* the greater the size of the NPs, the greater the scattering intensity, *cf*. Table S.II-1.

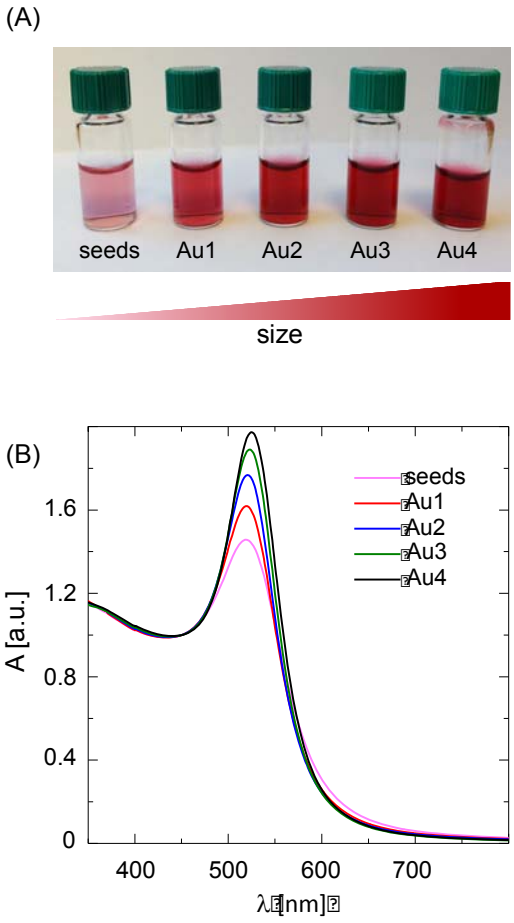

Figure S.I-1. (A) Photograph of colloidal solutions of Au NPs as synthesized. (B) Normalized absorbance at 450 nm for citrate capped NPs after different growth steps. The localized surface plasmon resonance (LSPR) peaked at 518, 519, 521, 523 and 525 nm after 4 growth steps.

The size distribution and mean diameter of NP's inorganic core (d_C) was determined by analyzing > 300 NPs in TEM micrographs with the free software ImageJ. Samples were prepared by deposition of a drop (3 µL) of NP solution on top of a copper grid coated with a layer of carbon. The NPs were characterized by TEM (JEOL JEM-1400PLUS) to check the size distribution and their monodispersity. In the Figures S2 to S6 selected TEM images and the corresponding histograms for the core diameters d_C of all the NPs are presented.

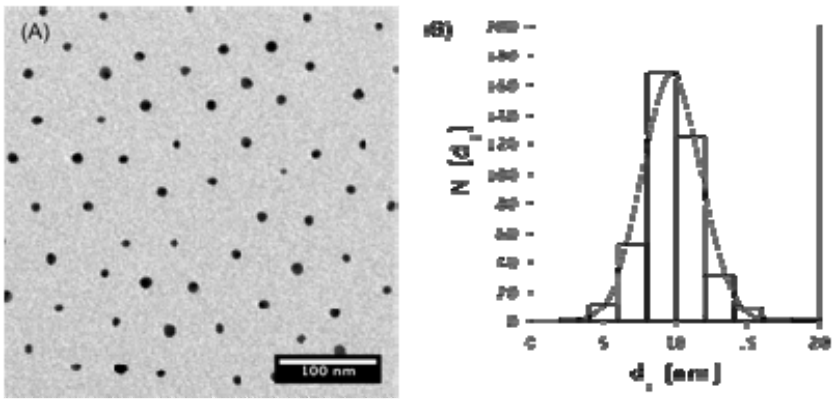

Figure S.II-2. A) TEM image of citrate capped Au seeds. B) Histogram of the size distribution of the Au cores with diameter d_C = 9.7 ± 1.9 nm. N (d_C) refers to the total counts and the scale bar corresponds to 100 nm.

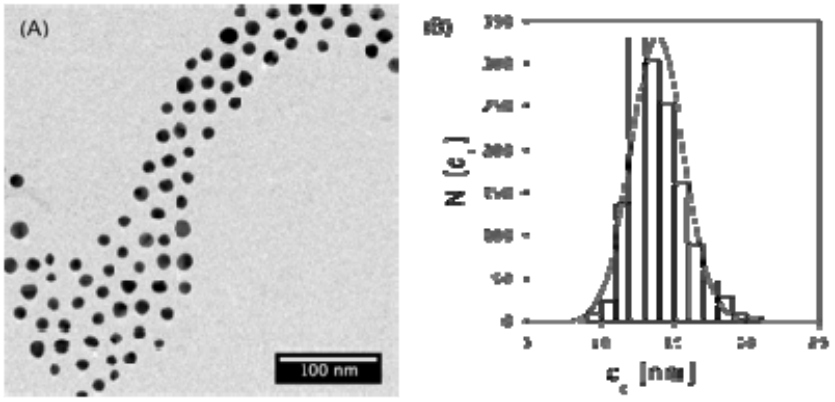

Figure S.II-3. A) TEM image of Au1. B) Histogram of the size distribution of the Au1 cores with diameter d_C = 13.8 ± 1.7 nm. N (d_C) refers to the total counts and the scale bar corresponds to 100 nm.

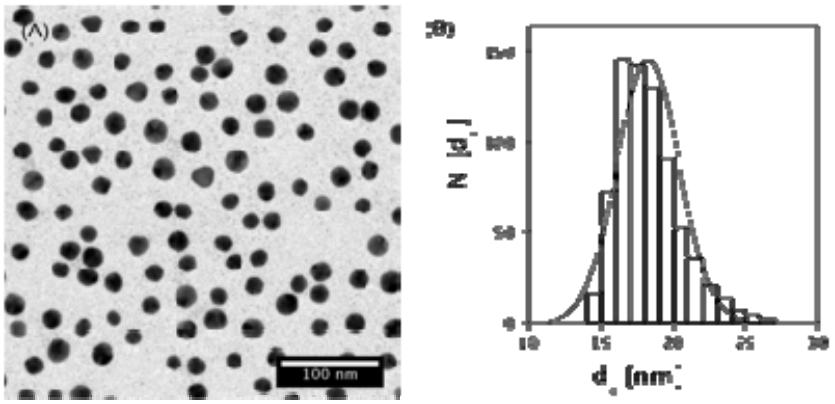

Figure S.II-4. A) TEM image of Au2. B) Histogram of the size distribution of the Au2 cores with diameter d_C = 18.5 ± 2.1 nm. N (d_C) refers to the total counts and the scale bar corresponds to 100 nm.

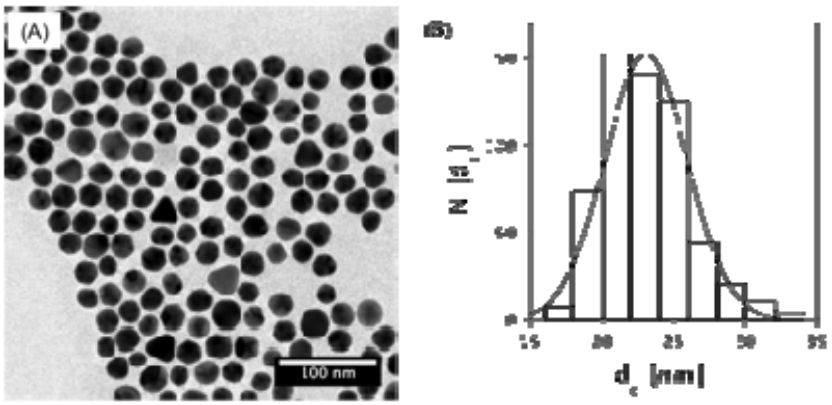

Figure S.II-5. A) TEM image of Au3. B) Histogram of the size distribution of the Au3 cores with diameter d_C = 23.5 ± 2.5 nm. N (d_C) refers to the total counts and the scale bar corresponds to 100 nm.

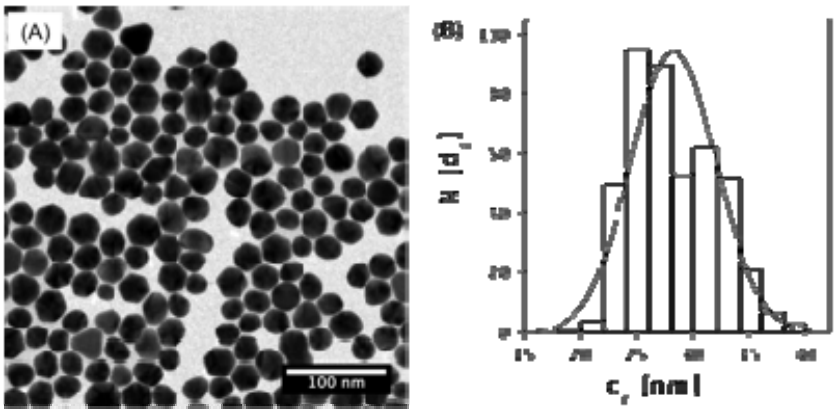

Figure S.II-6. A) TEM image of Au4. B) Histogram of the size distribution of the Au3 cores with diameter d_C = 28.0 ± 3.5 nm. N (d_C) refers to the total counts and the scale bar corresponds to 100 nm.

The concentration of the NPs was determined *via* UV/Vis spectroscopy (Cary 5000 Varian spectrometer) using the Beer-Lambert Law and the molar extinction coefficient (ε_{450})[2], and the absorbance values measured at 450 nm, *cf.* Table S.II-1. A Malvern Zetasizer was used to measure the hydrodynamic diameter d_h (with dynamic light scattering, DLS). All the samples were equilibrated for 5 min at 25 °C to ensure that the changes belong to the Brownian motion and not to any thermal conversion. The NPs were measured at 173° backscatter settings, and using a 633 nm laser. The hydrodynamic diameter d_h [nm] is a good indicator to assess the monodispersity and colloidal stability of the NPs.

Table S.II-1. Diameter of the NP's core as determined by TEM (d_C), data from the UV-Vis spectra (λ_{LSPR} and I_{MAX}), NP's concentration values (C_{NP}, as determined by Haiss *et al.* [2]), mean hydrodynamic diameter (d_h) in number ($d_{h(N)}$), and polydispersity index (PDI).

Sample	d_C [nm]	λ_{LSPR} [nm]	I_{MAX} [a.u.]	ε_{450} [$M^{-1}\cdot cm^{-1}$]	C_{NP} [nM]	$d_{h(N)}$ [nm]	PDI
seeds	9.7 ± 1.9	518	1.5	$5.6\cdot10^{7}$	6.3	–	–
Au1	13.8 ± 1.7	519	1.61	$1.8\cdot10^{8}$	3.8	16.6 ± 0.3	0.4
Au2	18.5 ± 2.1	521	1.76	$4.0\cdot10^{8}$	2.5	19.4 ± 0.3	0.3
Au3	23.5 ± 2.5	523	1.88	$8.8\cdot10^{8}$	1.3	26.4 ± 0.2	0.2
Au4	27.8 ± 3.5	525	1.98	$1.4\cdot10^{9}$	0.8	30.4 ± 0.4	0.2

III) PEGylation of NPs

The goal of this section is to produce PEGylated Au NPs with about the same hydrodynamic size by DLS. We used Au1, Au2, Au3 and Au4 (increasing core size) with PEGs of 10, 5, 3 and 1 kDa (decreasing molecular weight $\rightarrow$ size), respectively. The selected heterofunctional chains bear a thiol group in one end, which binds to the NPs, and a carboxyl group in the other. All of the different polyethylene glycol polymers (PEG) were obtained from Rapp-Polymere.

III.1) Saturation experiments: in order to estimate how many thiolated chains of PEG can be anchored onto citrate-capped NPs, increasing ratios of PEG per NP were added, *i.e.* 50, 500, 1000, 3000 and 5000 PEGs per NP (see Table S.II-1 for the concentration of the stocks). In a typical experiment, selected amounts of PEGs were added to a solution of 15 mL of citrate-capped NPs, to which after 2 minutes of stirring, NaOH was added to increase the pH value to 8-9 (aiming to increase the reactivity of the thiol group of the PEG). Samples were stirred overnight, and then, samples were precipitated by centrifugation (three steps). Therefore, excess of PEG and other chemicals can be washed out. Also, poorly PEGylated NPs (non saturated with PEG) would typically irreversibly agglomerate after adding NaOH and/or during centrifugation, which can be clearly seen in the UV-Vis spectra of the washed samples, *cf.* Figure S.III-1.

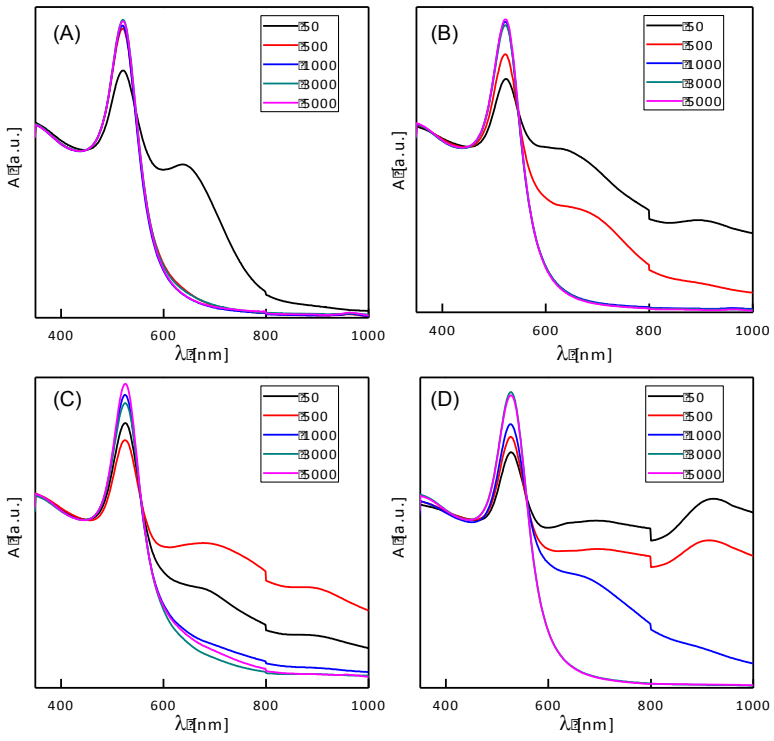

Figure S.III-1. Normalized UV-Vis spectra of PEGylated Au NPs after three washing steps by centrifugation (12100 x g). A) Au1@PEG; B) Au2@PEG; C) Au3@PEG; D) Au4@PEG.

The saturation steps clearly show that 50 and 500 chains per NPs are insufficient to produce stable colloids after precipitation, whereas 3000 and 5000 chains seems to produce stable colloids with equivalent optical features, *cf.* Figure S.III-1.The different NPs were run in a 2% agarose gel at 5 V cm^{-1} for 1 h in Tris-Borate-EDTA buffer (TBE 0.5x), aiming to see differences

in their electrophoretic mobility which could be related to saturation by PEG chains. Please notice that PEG chains employed in this work are heterofunctional molecules with a thiol group in one end (to bind to gold) and a carboxylic group in the other end which will be used for coupling other molecules and provide the colloids with negative charge. The gel indicated that 5000 chains confer colloidal stability to the respective NPs; furthermore NPs are *ca.* saturated with 5000 PEG per NP, *cf.* Figure S.III-2A. Figure S.III-2B shows that Au NPs with less than 1000 PEGs per NP were agglomerated, which can be clearly seen in the loading wells of the gel.

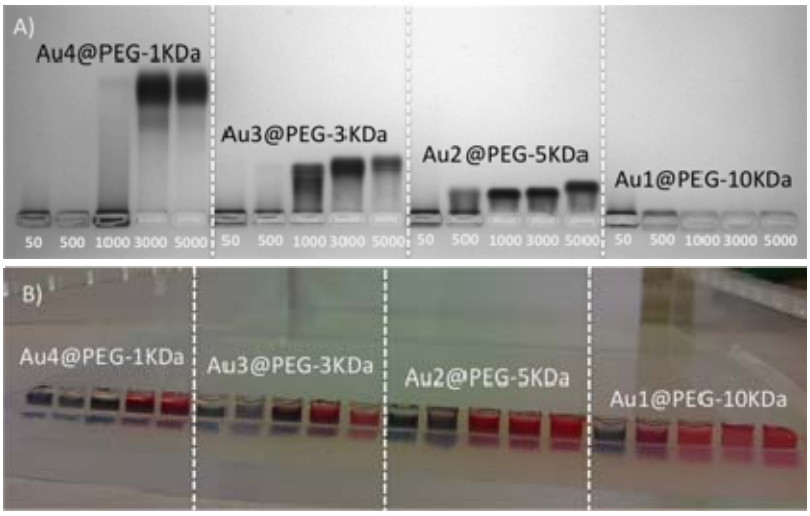

Figure S.III-2. A) Gel of PEGylated Au NPs with increasing PEGs per NP. B) Colors of the samples in the loading wells. Agarose 2%; 5 V cm^{-1}; 90 min.

These samples were analyzed by DLS, with the following results, as shown in Figure S.III-3 and Table S.III-1 (raw data).

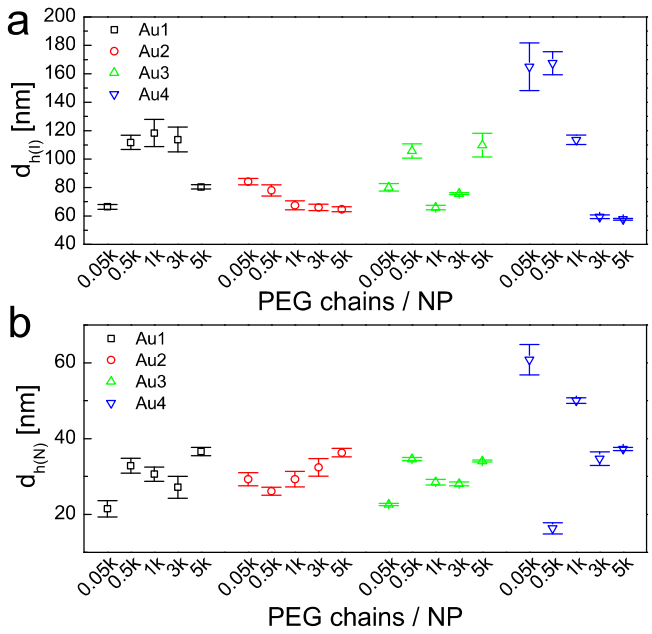

Figure S.III-3. (A) Intensity and (B) number mean values of the hydrodynamic diameters ($d_{h(I)}$ and $d_{h(N)}$), respectively) for Au1 (black squares), Au2 (red circles), Au3 (green triangles) and Au4 (blue inverted triangles), with increasing PEG chains per NP.

PEG saturation of Au1, Au2, Au3 and Au4 with -10kDa, -5kDa, -3kDa and PEG-1kDa, respectively, resulted in the formation of PEGylated NPs with *ca.* the same hydrodynamic diameter (*i.e.*, 35 nm), yet with different size of Au cores (d_C from *ca.* 14 to 28 nm).

Table S.III-1. Mean hydrodynamic diameter d_h [nm] in number ($d_{h(N)}$) and intensity ($d_{h(I)}$), and polydispersity index (PDI) for all of the PEGylated NPs. Notice that for low saturation (typically 50 and 500 chains per NP) the given d_h represent the main DLS peak.

sample	Ratio PEG:NP	$d_{h(I)}$ [nm]	$d_{h(N)}$ [nm]	PDI
Au1@PEG-10k	50	66 ± 2	22 ± 2	0.59
	500	112 ± 5	33 ± 2	0.34
	1000	118 ± 10	31 ± 2	0.33
	3000	114 ± 9	27 ± 3	0.36
	5000	80 ± 1	**37** ± 1	0.22
Au2@PEG-5k	50	84 ± 2	29 ± 2	0.51
	500	78 ± 4	26 ± 1	0.46
	1000	68 ± 3	29 ± 2	0.25
	3000	66 ± 2	32 ± 2	0.21
	5000	65 ± 2	**36** ± 1	0.12
Au3@PEG-3k	50	80 ± 3	23 ± 1	0.55
	500	106 ± 5	35 ± 1	0.53
	1000	65 ± 2	29 ± 1	0.46
	3000	76 ± 1	28 ± 1	0.44
	5000	110 ± 8	**34** ± 1	0.51
Au4@PEG-1k	50	165 ± 17	61 ± 4	0.46
	500	168 ± 8	16 ± 1	0.49
	1000	114 ± 3	50 ± 1	0.41
	3000	59 ± 1	35 ± 2	0.13
	5000	58 ± 1	**37** ± 1	0.10

III.2. PEGylation experiments using different PEGs for the same core: Having in mind the saturation's experiments, in which by using 5000 PEGs per NP all the NPs show *ca.* the same d_h, in the following all the PEGylation experiments were performed by using 10^4 PEGs per NP, thereby assuring full saturation of the PEG shell, and *ca.* the same d_h. We combined each inorganic core, *i.e.* Au1-Au4, with all the different PEGs, *i.e.* 1k, 3k, 5k, 10k Da. Figure S.III-4 shows a gel in which the different electrophoretic mobilities for all the different combinations are apparent. Figure S.III-5 shows the corresponding UV-Vis spectra, in which different PEGs do not affect the optical properties of the PEGylated NPs.

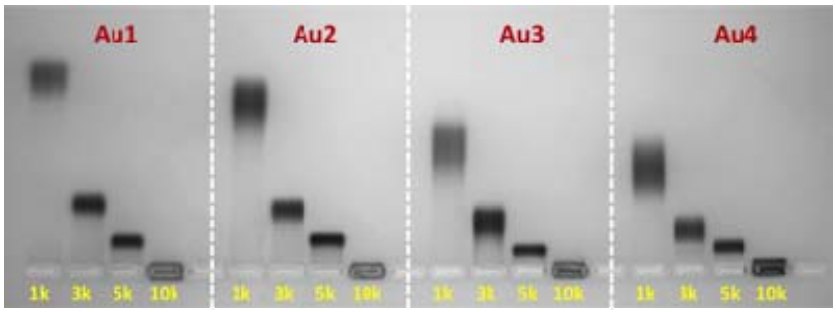

Figure S.III-4. Motion path in gel electrophoresis of Au NPs with different PEGs through a 2% agarose gel to which an electric field of 5 V cm^{-1} had been applied for 90 min.

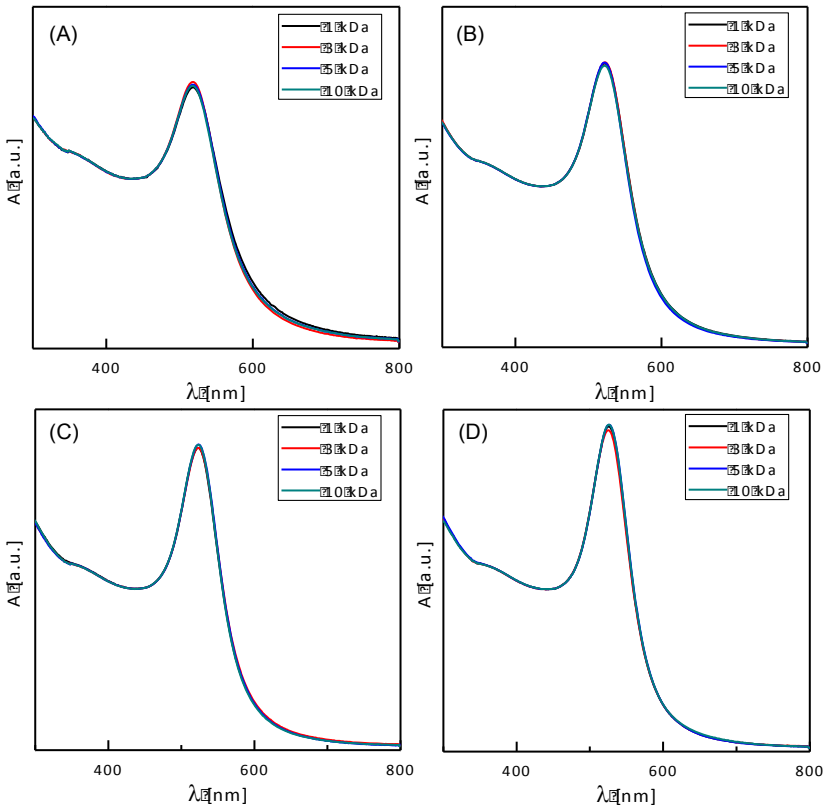

Figure S.III-5. Normalized UV-Vis spectra of (A) Au1, (B) Au2, (C) Au3, and (D) Au4 with different PEGs. Samples were washed three times by centrifugation to wash out excess of PEGs.

III.3. Experimental determination of concentration of PEGylated NPs: As previously mentioned, the extinction coefficients of samples listed in Table S.II-1 were calculated using the tables from Haiss et al.,[2] and confirmed by ICP-MS, *cf.* Figure S.III-6. The concentration determination for the PEGylated Au NPs was accomplished using inductively coupled plasma mass spectrometry (ICP-MS, Agilent 7700 Series) in comparison with UV-vis tables from Haiss *et al*. ICP-MS measures the atomic gold concentration in solution. First 5 µL of the particle suspension was transferred from the transport tubes (5 mL, VWR, #216-0153) into 6 mL perfluoroalkoxy alkane tubes (PFA) prefilled with freshly prepared 395 µL aqua regia, consisting of 1 part HNO_3 (67 wt%, ultra pure, Fisher Chemical, #7697372) and 3 parts HCl (35 wt%, ultra pure, Fisher Chemicals, #7647010) and mixed for at least 4 hours under constant agitation. During this period the gold core as well as the polymer shell was digested and broken down to small basic components. In the second step 4.6 mL of 2 % HCl solution as low matrix was introduced to each digested sample to prevent the acid from digesting the machinery as well as to provide an ion stable environment with constant background conditions for the samples. The overall dilution factor for these types of sample is therefore 1000 times. Measurements were one using 3 repetitions per sample, 100 sweeps and a peak pattern of 3 peaks. The diluted samples were introduced to the ICP-MS through an integrated autosampler coupled to a peltier cooling spray chamber where the sample was nebulized and taken up by the argon gas flow at a speed of ½ m/s. The concentration determination was performed using a calibration curve consisting of 9 measurement points (2500 to 0 µg/L) of freshly prepared, consecutive gold concentrations derived from a gold standard solution from Agilent (1000 mg/L). Results are always the mean of all three measurements and are presented in parts per billion (ppb = µg/L).

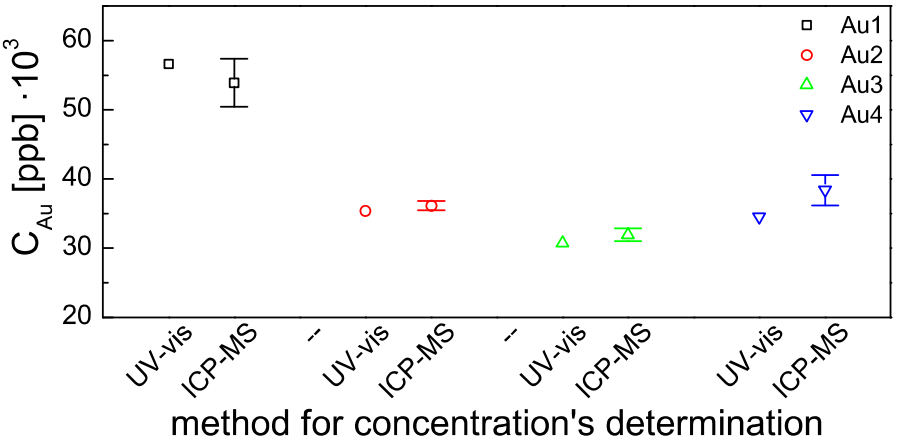

Figure S.III-6. Comparison of Au concentration (C_{Au}) in samples Au1-Au4 as determined by tables from Haiss *et al*.[2] and as determined by ICP-MS.

IV) Negative staining of the PEGylated NPs

In order to estimate the thickness of the PEG shell ($1/2\Delta d_S$) on NPs (*i.e.*, PEGylation on Au cores), the NP samples were analyzed by negative staining TEM. Ideally this technique allows to resolve the true solvent-excluded surface and shape of the core-shell system, which remains after samples have been dried for TEM imaging.[3] All of the combinations of Au cores (Au1 – Au4) and PEGs (PEG-1k – PEG-10k) were analyzed by negative staining (a total of 16 samples). Uranyl acetate was used as negative stain, which allows the formation of a uniform, consistent, and high contrast staining, *cf.* Figure S.IV-1 – SIV-4.

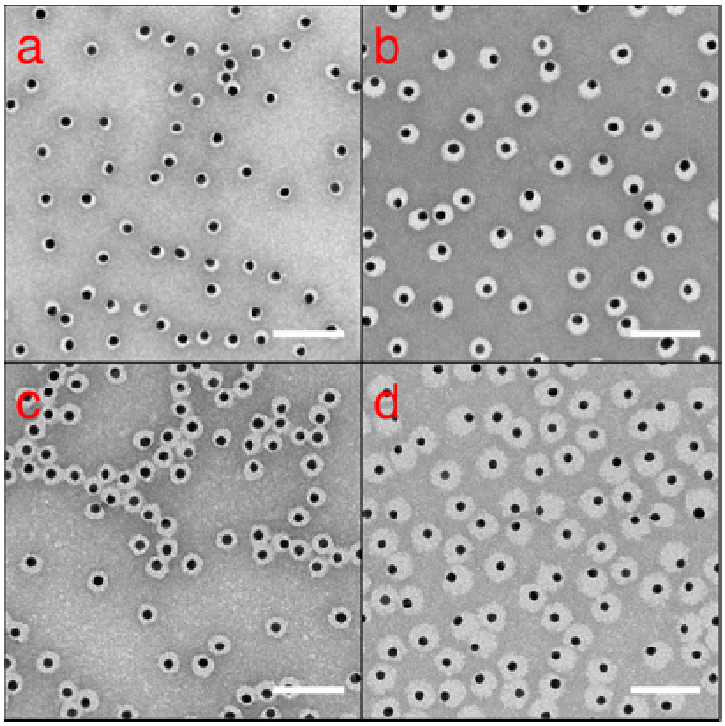

Figure S.IV-1. Selected negative staining TEM micrographs for PEGylated Au1 cores. a) Au1@PEG-1k; b) Au1@PEG-3k; c) Au1@PEG-5k; d) Au1@PEG-10k. Scale bar is 100 nm.

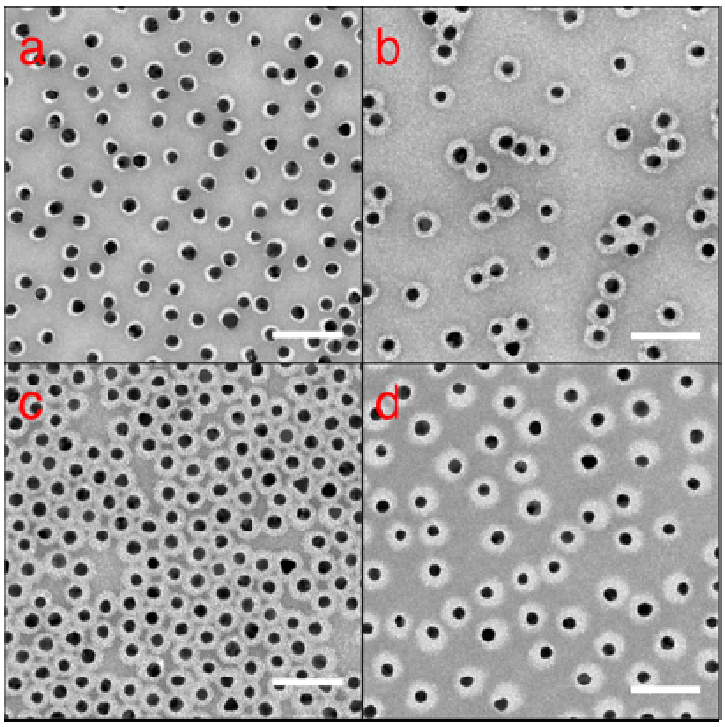

Figure S.IV-2. Selected negative staining TEM micrographs for PEGylated Au2 cores. a) Au2@PEG-1k; b) Au2@PEG-3k; c) Au2@PEG-5k; d) Au2@PEG-10k. Scale bar is 100 nm.

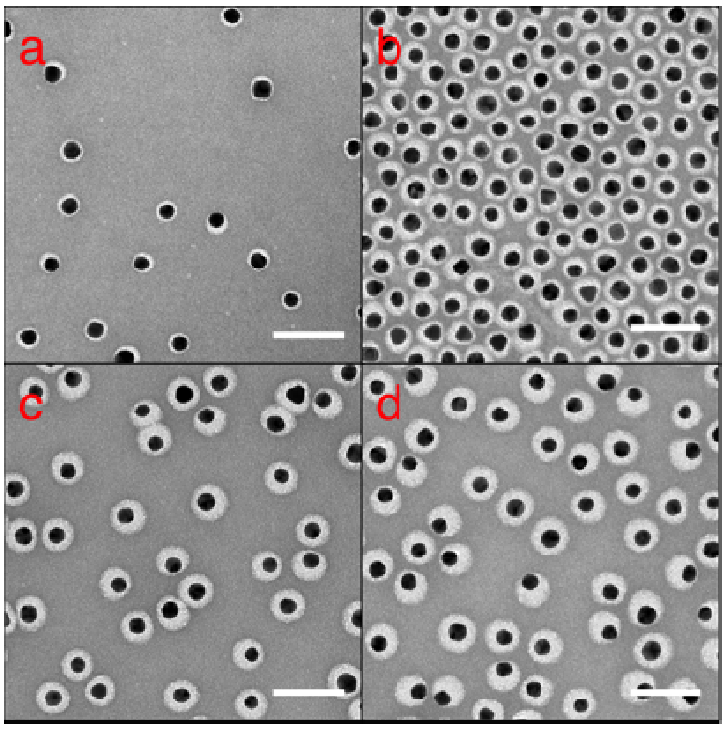

Figure S.IV-3. Selected negative staining TEM micrographs for PEGylated Au3 cores. a) Au3@PEG-1k; b) Au3@PEG-3k; c) Au3@PEG-5k; d) Au3@PEG-10k. Scale bar is 100 nm.

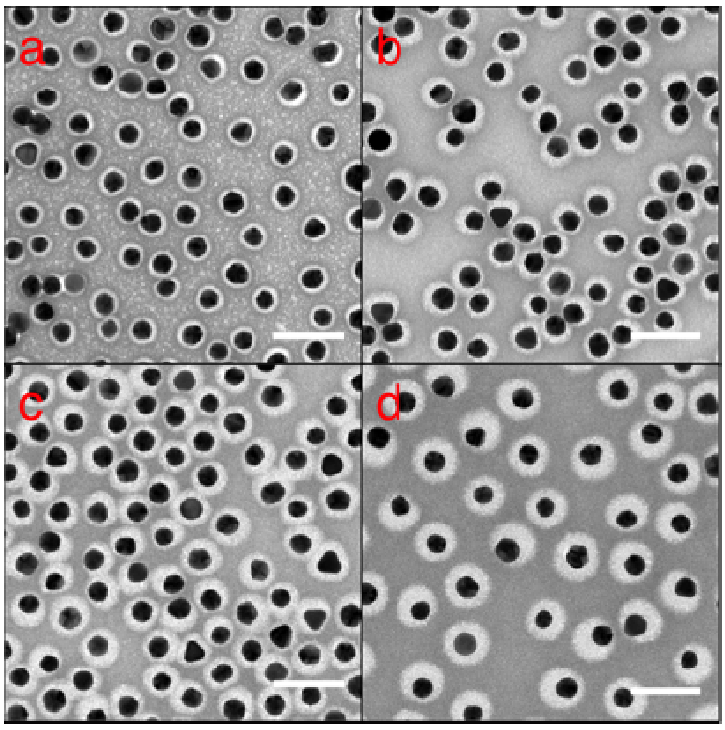

Figure S.IV-4. Selected negative staining TEM micrographs for PEGylated Au4 cores. a) Au4@PEG-1k; b) Au4@PEG-3k; c) Au4@PEG-5k; d) Au4@PEG-10k. Scale bar is 100 nm.

Negative staining sample preparation: samples were prepared on carbon film 400 copper mesh grids purchased from Electron Microscopy Sciences (Hatfield, USA). The specimen grids were exposed to glow-discharge treatment under air plasma for 20 s (2.0·10-1 atm and 35 mA) using a MED 020 modular high vacuum coating system (BAL-TEC AG, Balzers, Fuerstentum Liechtenstein). Negatively charged carbon grids were used within 5 min after treatment to ensure hydrophilicity. The on-grid negative staining was performed using a slightly modified single-droplet negative-staining procedure. 1.5 µL sample droplet of concentration ranging from 6 to 15 nM followed by three 2.5 µL droplets of 0.25% weight/volume (w/v) uranyl acetate aqueous solution were place on a clean Parafilm piece. The treated grid was incubated on the sample droplet for 1 min and then on the staining droplets for 3 s, 3 s, and 1 min respectively. After each incubation step the excess fluid was nearly fully removed by touching the grid edge with Whatman filter paper and finally fully dried for 20 min at $2.0 \cdot 10^{-1}$ atm.[3] Sample images were acquired in a JEM-1230 transmission electron microscope equipped with a LaB6 cathode running at 120kV and an ORIOUS SC1000 4008×2672 pixels CCD camera (Gatan UK, Abingdon Oxon, UK).

The image analysis of several negative staining TEM micrographs (>1000 NPs) for each of the 16 samples provides a quantitative characterization of the diameter of the core-shell system (i.e. Au core plus the PEG shell – d_{CS}). For morphological characterization of the NPs and their corresponding shells, TEM images, such as shown in Figure S.IV-5 – SIV-8, were segmented using Matlab (Mathworks) and Cellprofiler [4]. Firstly, NP cores were identified and characterized regarding size and shape. Secondly, for determination of the thickness ($1/2\Delta d_S$) and the shape of the corresponding polymer shells, the area of the NP core objects was extended based on the negative shell staining without including regions of background. For image enhancement

unsharp masking and morphological image processing was applied. Obtained objects (core + shell) comprising several touching nanoparticles were identified based on their circularity and subsequent declumping was performed using Cellprofiler.

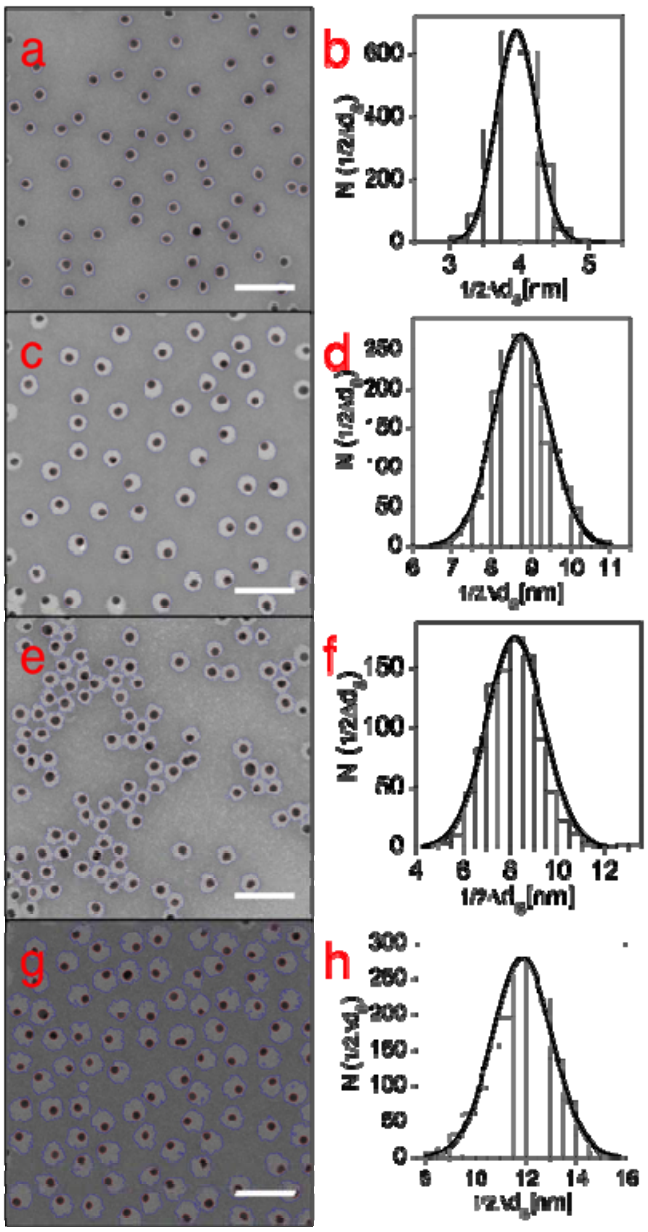

Figure S.IV-5. Selected segmented images for PEGylated Au1 cores. a) Au1@PEG-1k; c) Au1@PEG-3k; e) Au1@PEG-5k; g) Au1@PEG-10k. Panels c, d, f and h represent the corresponding $1/2\Delta d_S$ histograms. The red and blue outlines delimit the Au cores and the PEG shell, respectively. Scale bar is 100 nm.

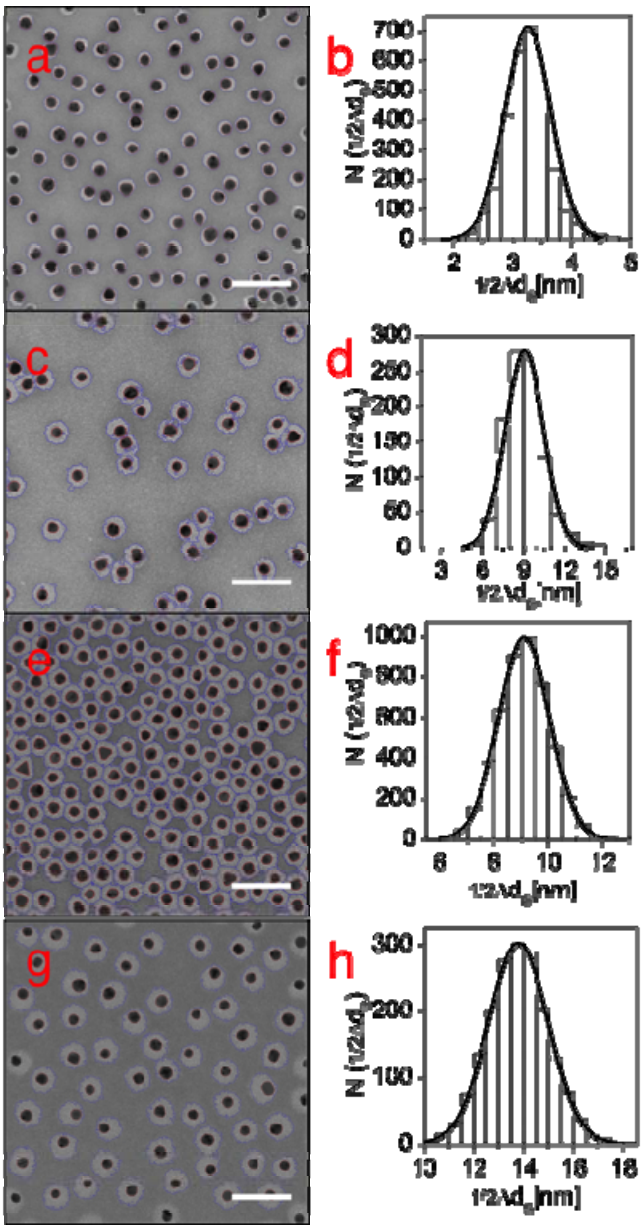

Figure S.IV-6. Selected segmented images for PEGylated Au2 cores. a) Au2@PEG-1k; c) Au2@PEG-3k; e) Au2@PEG-5k; g) Au2@PEG-10k. Panels c, d, f and h represent the corresponding $1/2\Delta d_S$ histograms. The red and blue outlines delimit the Au cores and the PEG shell, respectively. Scale bar is 100 nm.

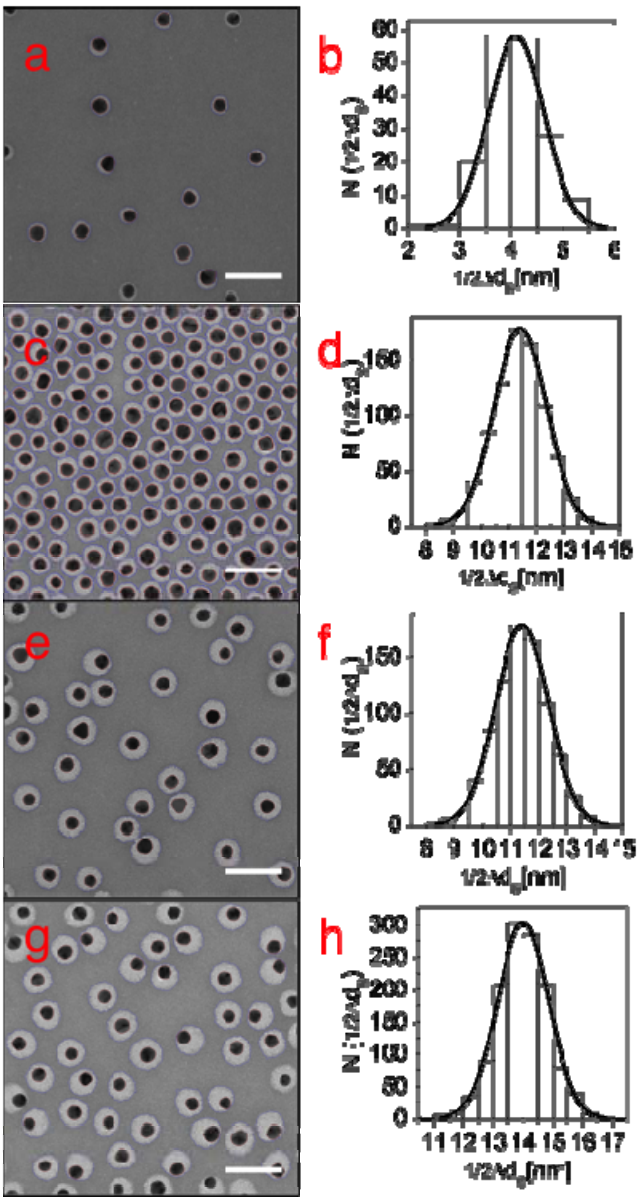

Figure S.IV-7. Selected segmented images for PEGylated Au3 cores. a) Au3@PEG-1k; c) Au3@PEG-3k; e) Au3@PEG-5k; g) Au3@PEG-10k. Panels c, d, f and h represent the corresponding $1/2\Delta d_S$ histograms. The red and blue outlines delimit the Au cores and the PEG shell, respectively. Scale bar is 100 nm.

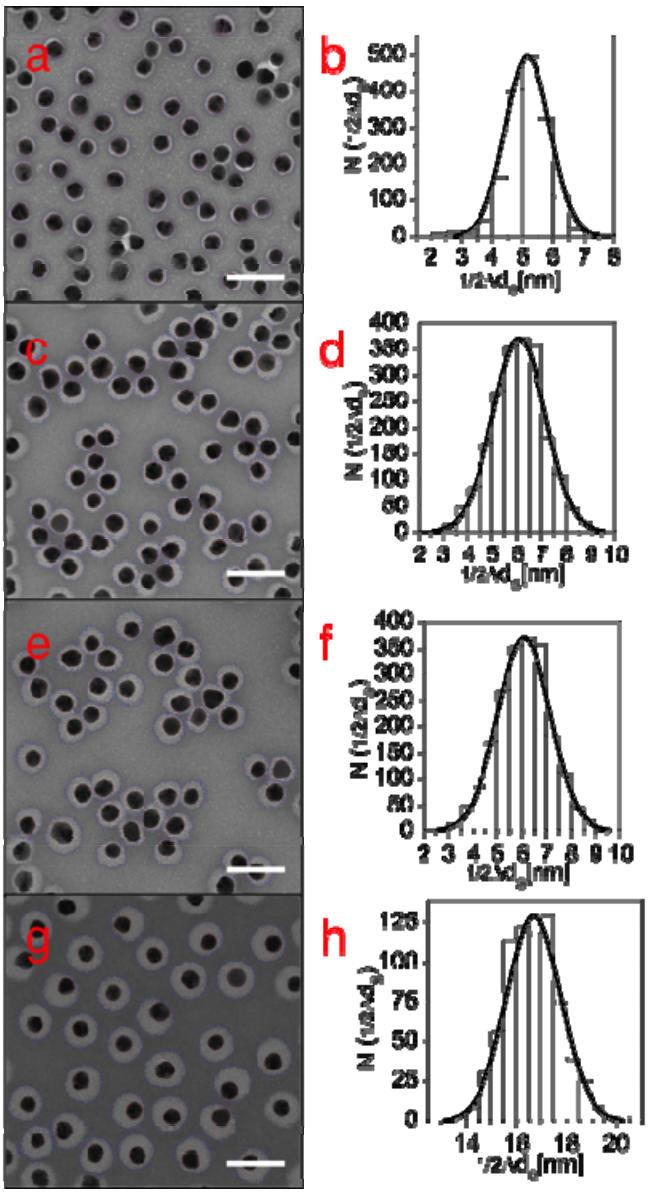

Figure S.IV-8. Selected segmented images for PEGylated Au4 cores. a) Au4@PEG-1k; c) Au4@PEG-3k; e) Au4@PEG-5k; g) Au4@PEG-10k. Panels c, d, f and h represent the corresponding $1/2\Delta d_S$ histograms. The red and blue outlines delimit the Au cores and the PEG shell, respectively. Scale bar is 100 nm.

Figure S.VI-9 summarizes and compares the increment of size which we obtained by negative staining TEM analysis.

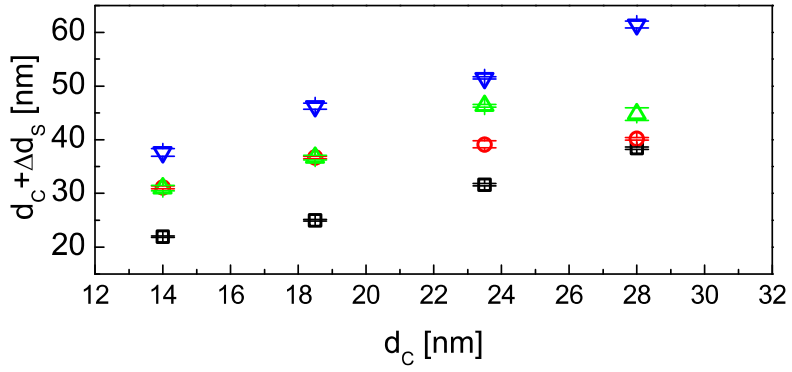

Figure S.IV-9. Comparison of the sizes determined by negative staining analysis of the 16 samples (4 cores: Au1 /14 nm, Au2 /18.5, Au3 /23.5 and Au4 /28 nm; 4 PEGs with increasing molecular weight: 1 kDa / black squares, 3 kDa /red circles, 5 kDa /green triangles, and 10 kDa /inverted blue triangles).

Likewise, hydrodynamic diameters results obtained by DLS of the cores (citrate capped Au NPs) and the 16 PEGylated samples can be represented similarly as in Figure S.IV-9, *cf.* Figure S.IV-10.

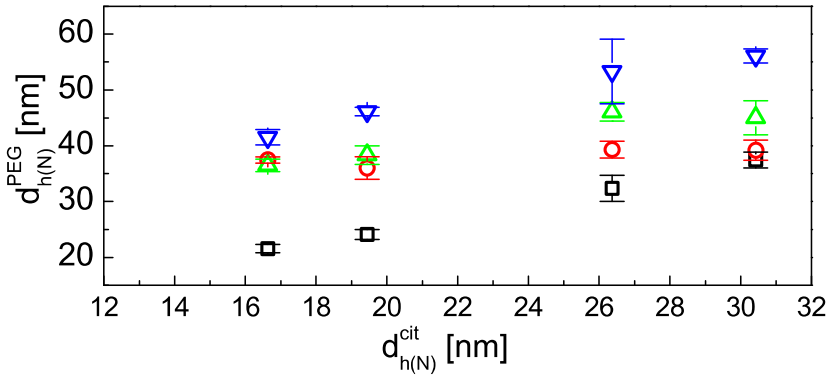

Figure S.IV-10. Comparison of the sizes (hydrodynamic diameter /$d_{h(N)}$) determined by DLS of the 16 samples (4 citrate capped cores: Au1 /16.6 nm, Au2 /19,4, Au3 /26,4 and Au4 /30,4 nm; 4 PEGs with increasing molecular weight: 1 kDa / black squares, 3 kDa /red circles, 5 kDa /green triangles, and 10 kDa /inverted blue triangles).

In the following we introduce two dimensionless parameters, *i.e.*, R^{TEM}_{PEG} and R^{DLS}_{PEG}, which represent the contribution of PEG to the resulting size as determined by TEM (vacuum) and DLS (solution); R^{TEM}_{PEG} or R^{DLS}_{PEG} equals 0 or 1 if the whole size comes from the Au core or the PEG shell, respectively. Notice that although TEM are DLS are experimental techniques which in principle should provide different numbers due to hydration of the samples in solution (DLS), the thickness of the PEG shells is similar for each sample, both in vacuum and in solution. Indeed, this observation indicates that the PEG chains are very efficiently packed onto the Au NPs. The explicit equations used to calculate these parameters are:

$$R_{PEG}^{TEM} = \frac{\Delta d_S}{d_C + \Delta d_S} \quad \text{(Equation S.IV-1)}$$

$$R_{PEG}^{DLS} = \frac{d_{h(N)}^{PEG} - d_{h(N)}^{cit}}{d_{h(N)}^{PEG}} \quad \text{(Equation S.IV-2)}$$

Table S.IV-x. Thickness of the PEG shell as determined by negative staining TEM analysis ($½\Delta d_S$) in vacuum, and DLS ($½(d_{h(N)}^{PEG} - d_{h(N)}^{cit})$) in solution. The dimensionless parameters R_{PEG}^{TEM} and R_{PEG}^{DLS} represent the contribution of PEG to the resulting size as determined by TEM and DLS, respectively.

Sample	$½\Delta d_S$ [nm]	R_{PEG}^{TEM}	$½(d_{h(N)}^{PEG} - d_{h(N)}^{cit})$ [nm]	R_{PEG}^{DLS}
Au1@PEG-1k	4.0 ± 0.1	0.36	2.5 ± 0.8	0.23
Au1@PEG-3k	8.6 ± 0.3	0.55	10.4 ± 0.5	0.56
Au1@PEG-5k	8.5 ± 0.5	0.55	9.9 ± 1.1	0.54
Au1@PEG-10k	11.9 ± 0.7	0.63	12.4 ± 1.4	0.60
Au2@PEG-1k	3.2 ± 0.1	0.26	2.3 ± 0.9	0.19
Au2@PEG-3k	9.1 ± 0.2	0.50	8.3 ± 2.0	0.46
Au2@PEG-5k	9.1 ± 0.4	0.50	9.4 ± 1.7	0.49
Au2@PEG-10k	13.9 ± 0.5	0.60	13.4 ± 0.8	0.58
Au3@PEG-1k	4.1 ± 0.2	0.26	3.0 ± 2.3	0.19
Au3@PEG-3k	7.8 ± 0.6	0.40	6.5 ± 1.5	0.33
Au3@PEG-5k	11.4 ± 0.2	0.49	9.9 ± 1.7	0.43
Au3@PEG-10k	14.0 ± 0.2	0.54	13.5 ± 5.8	0.51
Au4@PEG-1k	5.2 ± 0.2	0.27	3.5 ± 1.4	0.19
Au4@PEG-3k	6.1 ± 0.2	0.30	4.4 ± 1.8	0.22
Au4@PEG-5k	8.4 ± 1.1	0.37	7.3 ± 3.1	0.32
Au4@PEG-10k	16.7 ± 0.6	0.54	12.8 ± 1.3	0.46

Figure S.IV-11 summarizes and compares the mean $1/2\Delta d_S$ for the sixteen samples studied by image analysis. Clearly, $1/2\Delta d_S$ values increase as the molecular weight of the PEGs increase for each type of Au core, *cf*. panel a. In principle, for each molecular weight of the PEG, $1/2\Delta d_S$ remains very similar *cf.* panel b, which points out that increasing the radius of curvature (i.e., increasing the d_C) does not significantly influence the polymer's thickness ($1/2\Delta d_S$). Additionally, Figure S.IV-12 shows a heatmap for $1/2\Delta d_S$ in which we can observe how $1/2\Delta d_S$ increases with R_{PEG}^{TEM}.

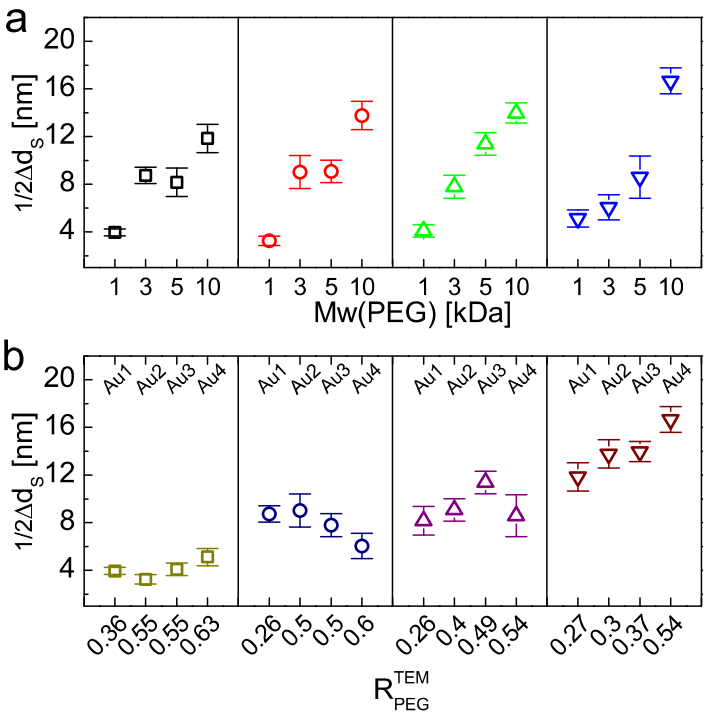

Figure S.IV-11. Comparison of the mean PEG shell thickness $1/2\Delta d_S$ of the PEGylated samples, as determined by negative staining TEM analysis. a) Influence of increasing molecular weight (M_W) of PEG for the same Au core, *i.e.*, Au1 (black squares), Au2 (red circles), Au3 (green triangles) and A4 (blue inverted triangles). b) Influence of increasing the diameter of the inorganic core (d_C) for the same PEG coating, PEG-1k (olive squares), PEG-3k (dark blue circles), PEG-5k (magenta triangles) and PEG-10k (brown inverted triangles).

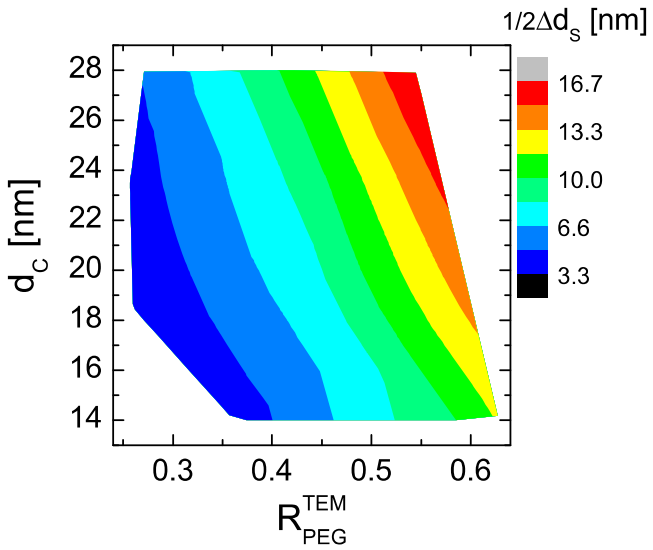

Figure S.IV-12. $1/2\Delta d_S$ heatmap in a diagram d_C versus R_{PEG}^{TEM}.

V) Characterization of NP's dynamic interfacial tension (IFT)

The dynamic interfacial tension was determined by pendant drop tensiometry at the toluene-water interface using a Drop Shape Analysis System (DSA100, Krüss, Germany). A Hamilton syringe plugged to a stainless steel needle (diameter 1.85 mm) immersed in the toluene phase was used to produce a 50 μL sample droplet at 200 μL min^{-1} dosing rate. The sample concentration varied with the Au core used, being 3.0 nM for A1, 1.3 nM for Au2, 0.66 nM for Au3 and 0.41 nM for Au4. The series measurement of the droplet profile upon time was recorded using an ultra fast camera (Krüss). The interfacial tension (γ) was estimated using the analysis software package DSA3 (Krüss) fitting the droplet profile with the Young-Laplace equation:

$$\gamma_t = \frac{\Delta\rho \cdot g \cdot d_e}{H} \qquad \text{(Equation S.V-1)}$$

where $\Delta\rho$ is the density difference between the liquid drop and its surrounding medium, g is the gravitational acceleration, d_e is the largest horizontal diameter of the drop, and H is a function of S_n $(= d_n/d_e)$, in which d_n is the horizontal diameter at a distance equal to d_e (n/10) from the bottom of the drop. All experiments were performed at room temperature.

Figure S.V-1 presents the dynamic surface tension (γ_t) plots for all of the combinations of Au cores (Au1 – Au4) and PEGs (PEG-1k – PEG-10k) (a total of 16 samples), where the interfacial tension decreases with time, approaching an equilibrium value. In the early stage, the interfacial tension drops because of instantaneous self-assembly of the NPs at the interface. Once the droplet is mostly covered by NPs, the decrease in interfacial tension reaches a dynamic equilibrium where the rate of adsorption of NPs at the interface equals the rate of desorption. It can be observed that the experimental meso-equilibrium γ (γ_m) value decreases equivalently for all of the different cores. The variation in interfacial tension with different PEGs (PEG-1k to PEG-10k) can be explained by the effect of their polymer length on the assembly at the toluene−water interface. For any type of Au core (Au1-Au4), PEGylation with PEG-10k results in the maximum reduction in the equilibrium γ_m values, followed by PEG-5k, PEG-3k and PEG-1k. Therefore, although the amphiphilic behavior of PEG is known, the length of the PEG ($1/2\Delta d_S$) determines the hydrophilic behavior of the PEGylated NPs, that is, increasing the $1/2\Delta d_S$ results in a increment of the NP's hydrophobicity. The kinetic behavior of the surface tension of the NP stabilized water-in-toluene emulsions was obtained using γ_t versus time plots fitted to the empirical Hua and Rosen equation,[5] *cf.* Equation S.V-2.

$$\gamma_t = \gamma_m + \frac{\gamma_0 - \gamma_m}{1 + (t/t^*)^n} \qquad \text{(Equation S.V-2)}$$

where γ_t is the surface tension at any time t, γ_0 is the surface tension of the pure solvent (water in toluene), γ_m is the surface tension at mesoequilibrium, t* is the half-time in reaching γ_m, and n is a dimensionless exponent. Assuming that the value of γ_0 is held constant (*ca.* 36 nN/m, the value of the pure buffer surface tension), there are three adjustable parameters: γ_m, t*, and n. These parameters were estimated by computer fitting (with the software origin) of the measured dynamic surface tension data.

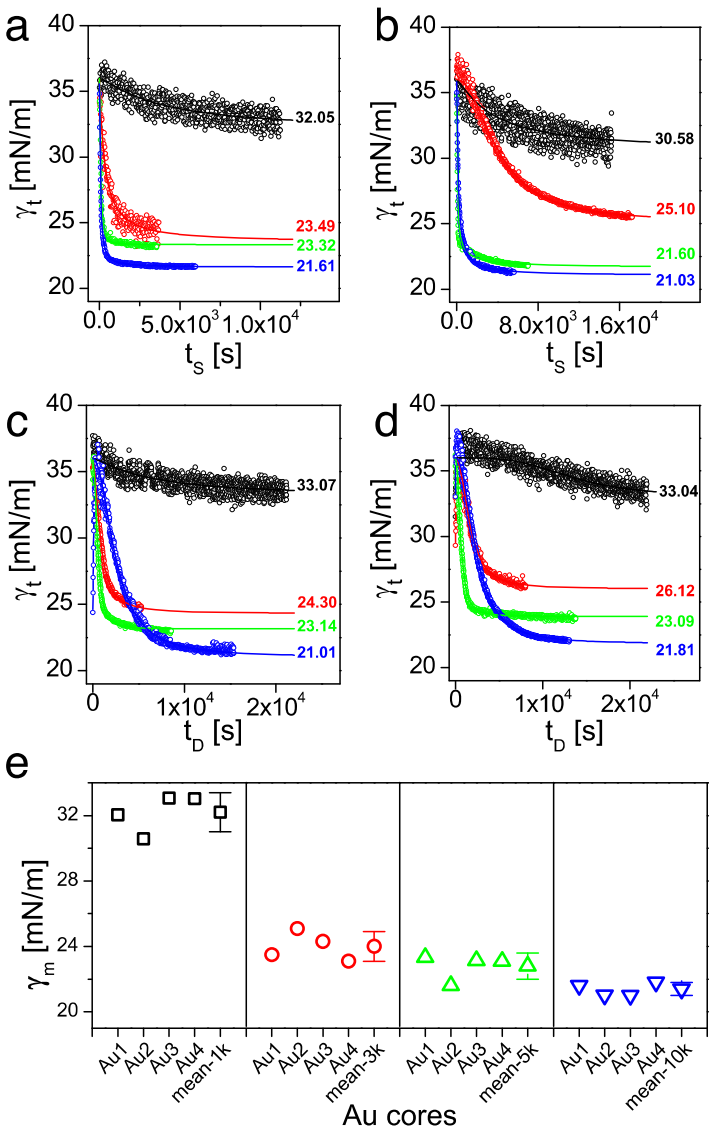

Figure S.V-1. a-d) γ_t versus time (t_D) plots for Au1, Au2, Au3, and Au4, respectively, PEGylated with different PEGs (1 kDa: black, 3 kDa: red, 5 kDa: green, 10 kDa: blue); experimental data and the respective fitting lines are represented by hollow circles and solid lines, respectively . e) Summary of the γ_m values for all the 16 samples and the mean γ_m for each PEG's molecular weight (*i.e.*, mean-1k, -3k, -5k and -10k, for PEGs of 1, 3, 5 and 10 kDa, respectively).

Additionally, Figure S.V-2 shows a heatmap for γ_m, which decreases (i.e., less hydrophilic/more hydrophobic) as R_{PEG}^{TEM} increases.

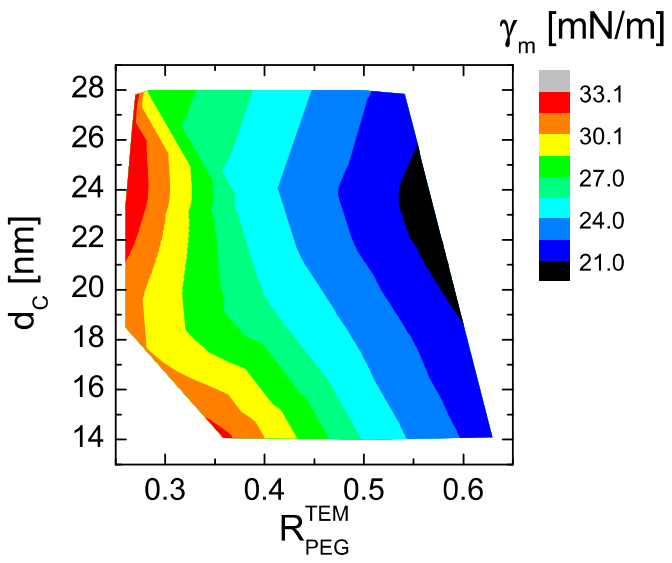

Figure S.V-2. Heatmap for γ_m in a diagram d_C versus R_{PEG}^{TEM}.

VI) AFM measurements on PEGylated NPs: stiffness

Sample patch preparation: diluted samples were dropped on 1x1 cm piece of stainless steel which has smooth surface (roughness *ca.*1nm). Before use, all stainless steel patches were cleaned with aceton and chloroform and then, dried at 180 °C in vacuum. After dropping each sample, the NPs were left to adsorb in the substrate for ca. 20-10 min. Considering that the interaction of water content in PEG can influence the results of stiffness, all the samples were measured in water and in vacuum (water content lower than 2%). For measurements in vacuum, all the samples were dried naturally for 8 hours and then, treated with vacuum for 1 hour prior to AFM measurements. For the AFM measurements in water, samples were immersed and measured immediately.

AFM measurements: Multi-mode IV (Veeco, Santa Barbara, CA) atomic force microscopy was chosen for measurements. Imaging was performed using Tapping Mode (TM) with constant amplitude attenuation. The cantilever approach (Silicon-tip on nitride lever, k = 0.32 N/m, f = 40-75 kHz) was utilized with an initial drive amplitude of 0.499 V (tip oscillation amplitude 1.5 V). By single molecule force spectrometer (SMFS)[6] the indentation behavior of surface terminated with Au NPs-PMA-PEG was reflected, and single force curve against distance of cantilever was recorded at the same time, so that Young's Modulus can be calculated by analysis of the approaching process (see Scheme S.VI-1). A calibration procedure was performed in order to analyze the exact area of the conical tip which was used for all measurements.[7,8]

Each NP was approached *ca.*60 times and more than 15 NPs which are from different areas of substrate were measured. Overall more than 1000 curves for each set of samples were calibrated with NanoScope Analysis 1.5 (Brucker Corporation 2013).

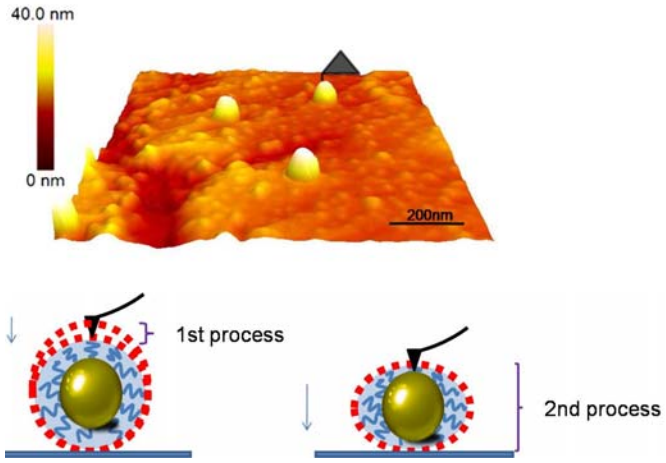

Scheme S.VI-1.

Results and discussion: Trace curves were collected in order to extract nanoindentation Young's modulus (*E*). One have to keep in mind that Young's modulus representing hardness is highly depending on radius of tip, deflection sensitivity, spring constant, tip half angle and Poisson's ratio. Figure S.VI-1 and SVI-5 show the stiffness diagrams for individual NPs (one arbitrary NP for each of the 16 samples) in vacuum (E_V) and in water (E_W), respectively. Figure S.VI-2, VI-3 and VI-4, and VI-6, VI-7 and S.VI-8 summarize the average values calibrated from

all experiment data. From these diagrams/heatmaps, one can see that the Young's modulus depends on the NP's size and the molecular weight of PEG. The Young's modulus increased with increasing core size (for the same molecular weight of PEG). Likewise the Young's modulus increased with increasing molecular weight of PEG for same NP's size. In addition, the Young's modulus in water (E_W) is significantly higher than in vacuum (E_V). Thus the water content in PEG plays important role for hardness of the NPs, which can be explained due to crosslinking of PEG ligands with water molecules.[9] From a statistical point of view, the diameter of NPs in water will be bigger than in vacuum (*cf.* negative staining analysis and DLS hydrodynamic sizes), thus the tip will touch more effective area of NP in water (see Scheme S.VI-2).

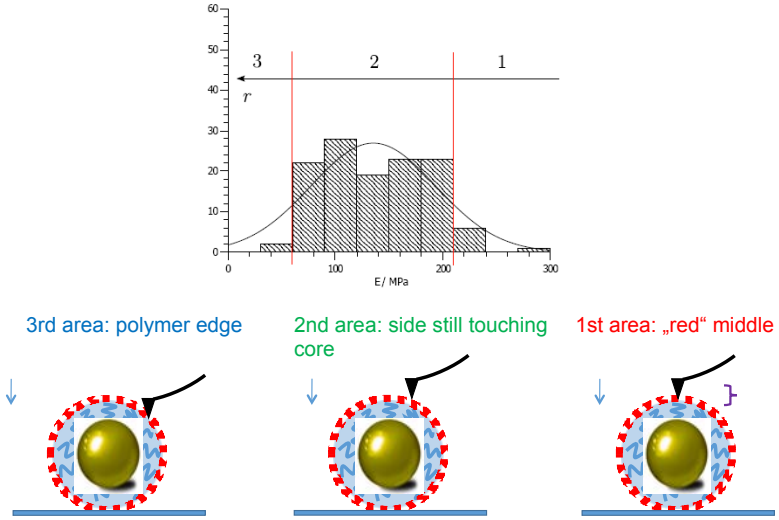

Scheme S.VI-2.

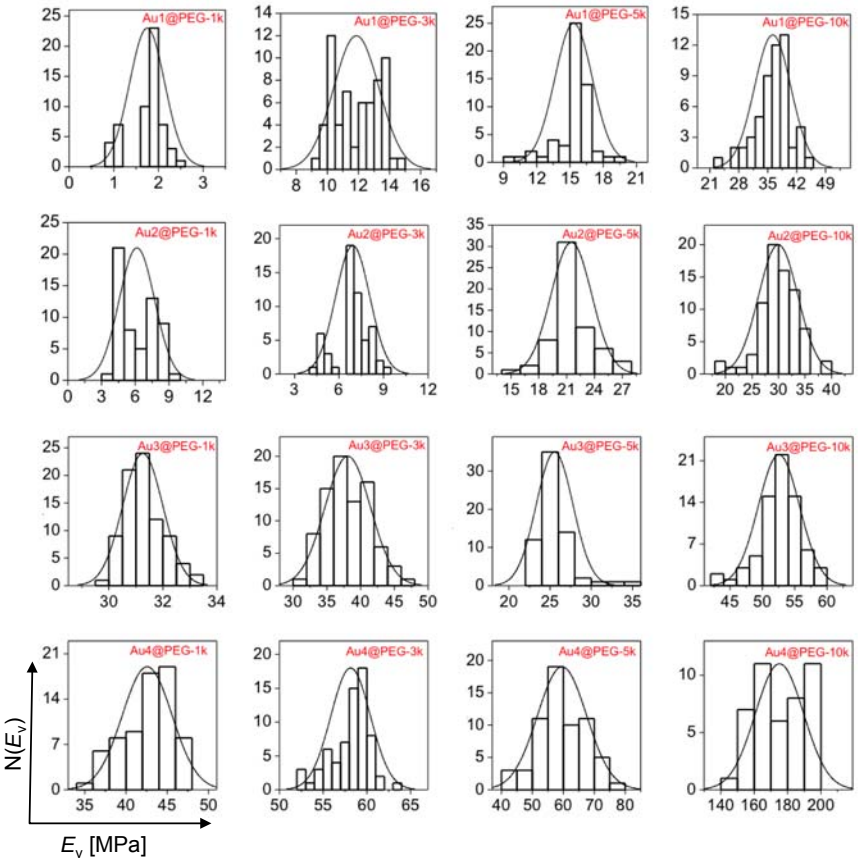

Figure S.VI-1. Stiffness measurements in vacuum (E_V).

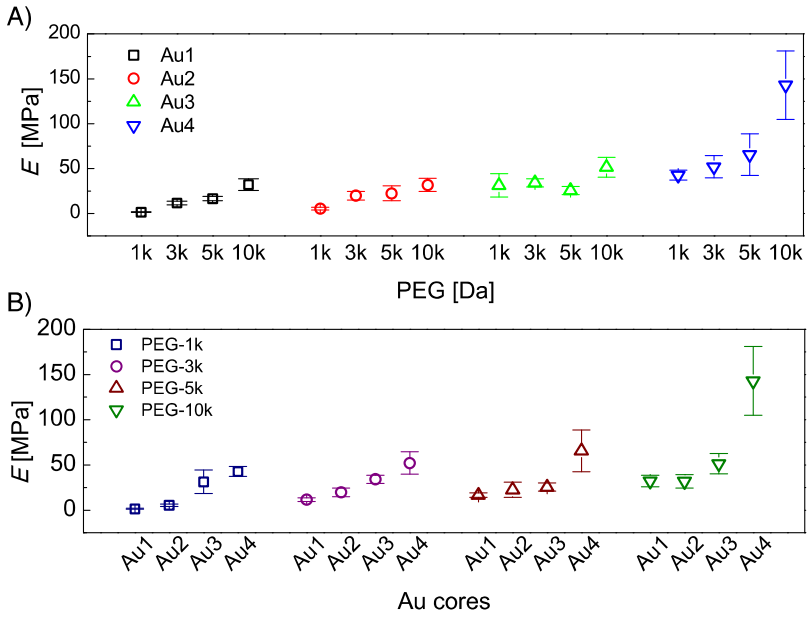

Figure S.VI-2. *E* values in vacuum (E_V). A) PEGylation's dependence for Au1 (black), Au2 (red), Au3 (green) and Au4 (blue); B) Role of core's size for PEG-1k (dark blue), PEG-3k (magenta), PEG-5k (brown) and PEg-10k (olive).

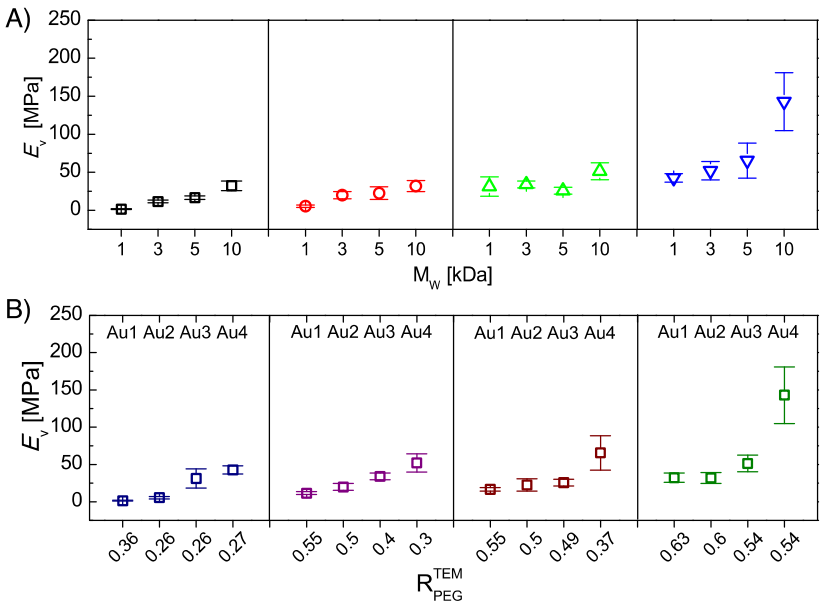

Figure S.VI-3. E values in vacuum (E_V). A) PEGylation's dependence for Au1 (black), Au2 (red), Au3 (green) and Au4 (blue); B) Role of the dimensionless parameter R_{PEG}^{TEM} for PEG-1k (dark blue), PEG-3k (magenta), PEG-5k (brown) and PEG-10k (olive)

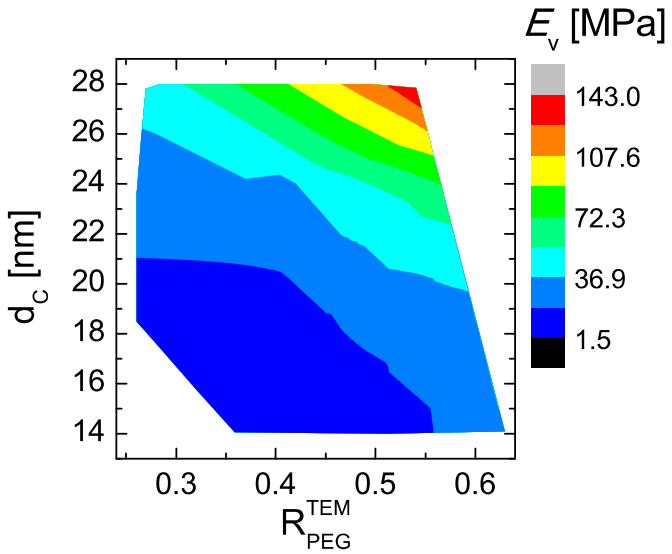

Figure S.VI-4. E_V heatmap in a diagram d_C versus R_{PEG}^{TEM}.

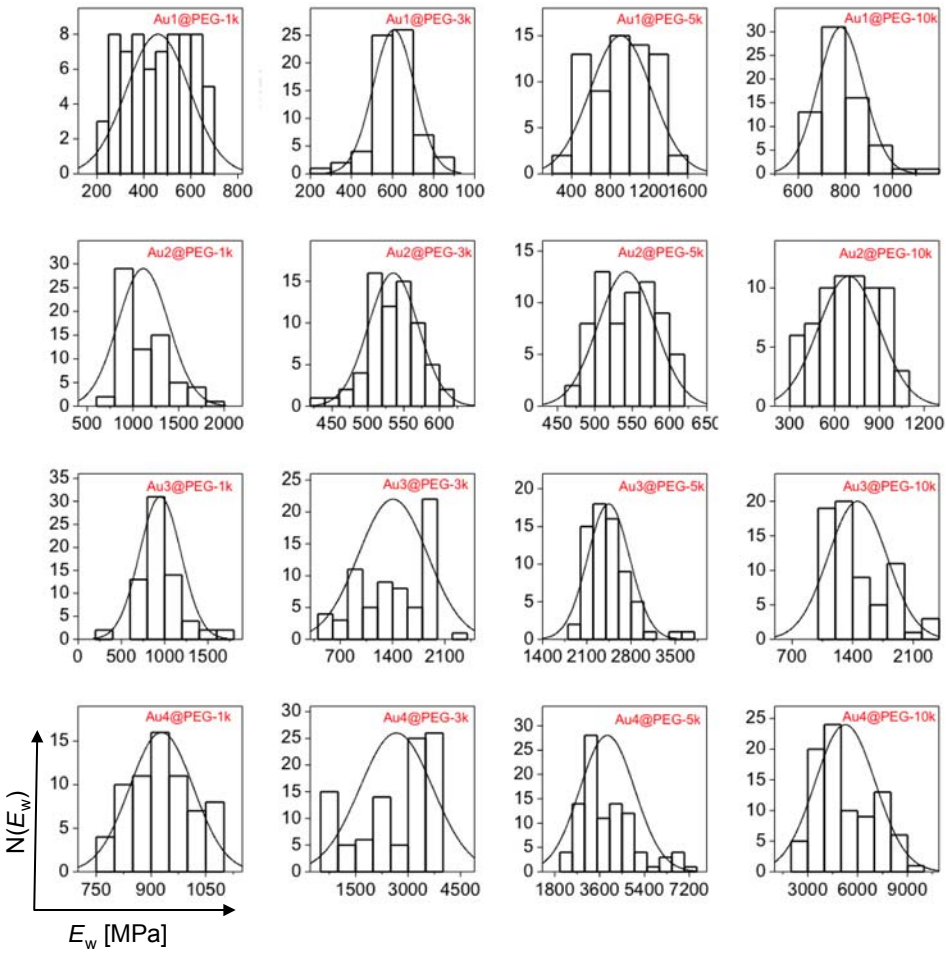

Figure S.VI-5. Stiffness measurements in vacuum (E_W)

Figure S.VI-6. E values in water (E_W). A) PEGylation's dependence for Au1 (black), Au2 (red), Au3 (green) and Au4 (blue); B) Role of core's size for PEG-1k (dark blue), PEG-3k (magenta), PEG-5k (brown) and PEG-10k (olive).

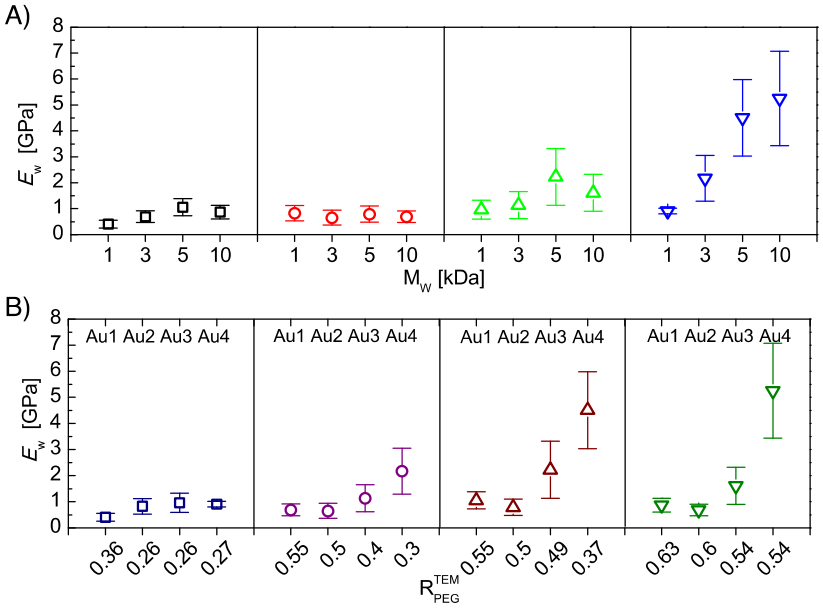

Figure S.VI-7. E values in water (E_W). A) PEGylation's dependence for Au1 (black), Au2 (red), Au3 (green) and Au4 (blue); B) Role of the dimensionless parameter R_{PEG}^{TEM} for PEG-1k (dark blue), PEG-3k (magenta), PEG-5k (brown) and PEG-10k (olive).

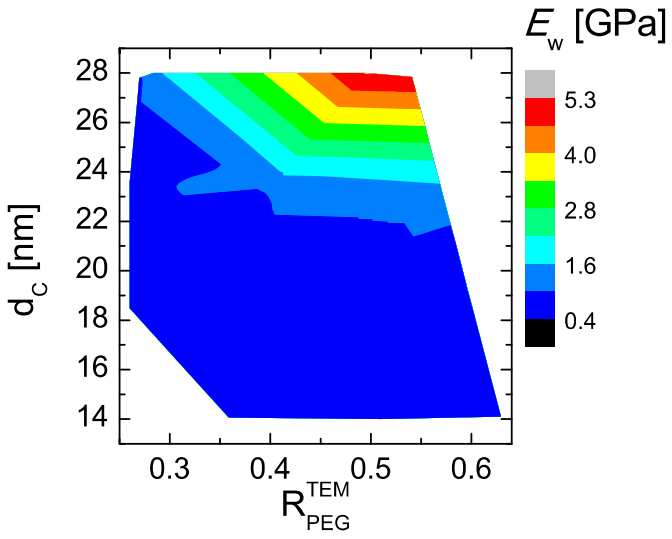

Figure S.VI-8. E_W heatmap in a diagram d_C versus R_{PEG}^{TEM}.

VII) Catalytic properties of PEGylated NPs

Description of the experiment:

The catalytic activity of Au@PEG NPs towards the reduction of methylene blue (MB, blue color) to leucomethylene blue (LMB, colorless), in the presence of an excess of $NaBH_4$ at room temperature (ca. 25 ºC), was followed by UV-vis measurements (Agilent 8453 UV/Vis absorbance spectrometer) in a 1.25 cm plastic cuvette (Sarstedt #67.758.001).

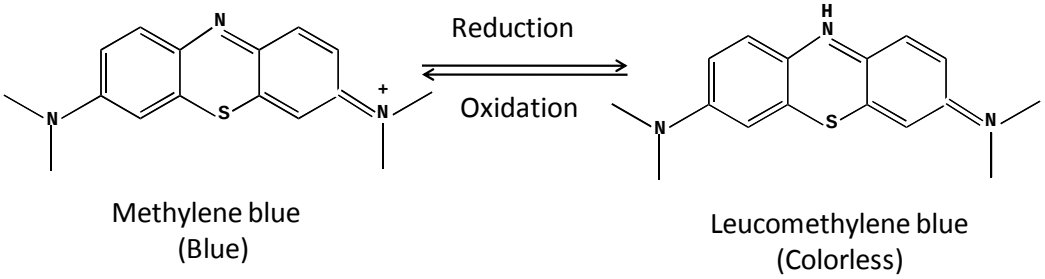

Scheme S.VII-1: Reduction reaction of MB to LMB.

VII.1. Catalysis using the same concentration of the Au@PEG NPs: In a plastic cuvette, 400 µL of MB (9.37×10^{-4} M) was mixed with 10 µL of Au NPs (0.22 nM; 1.3×10^{14} NP's number), then 120 µL of freshly prepared $NaBH_4$ solution ($5.28\cdot10^{-2}$ M, Aldrich #452874) was added immediately. The catalytic properties of the Au@PEG NPs were monitored for the first 90 s of the reaction by collecting UV-Vis spectra (400 - 800 nm) automatically (one spectrum every 3.6 s), *cf.* Figure S.VII-1. The evolution of the absorbance at the maximum (λ_{max} = 664 nm) over time is shown in Figure S.VII-2. Finally, the NP's catalytic properties were calculated by kinetics (*k*, Ln (A/A0)) taking into account the first 30 s at λ_{max} (Table S.II-1). The blank (A_0) was measured with same parameters but using H_2O instead of NPs.

VII.2. Catalysis with same gold amount: In our experiment, given equal number of Au@PEG NPs with different inorganic core (A1 to A4) and different PEGylation (PEG-1k, PEG-3k, PEG-5k and PEG-10k), the mass of gold depends on the diameter of the NPs (Au1-Au4), i.e., 1 nM Au@PEG NPs would be equivalent to 16 mg/L of Au1 (1×10^{-9} mol/L × 6.023×10^{23} NPs/mol × 2.6×10^{-17} g/NP); 32 mg/L of Au2 (1×10^{-9} mol/L × 6.023×10^{23} NPs/mol × 6.4×10^{-17} g/NP); 79 mg/L of Au3 (1×10^{-9} mol/L × 6.023×10^{23} NPs/mol × 1.3×10^{-16} g/NP); and 134 mg/L of Au4 (1×10^{-9} mol/L × 6.023×10^{23} NPs/mol × 2.2×10^{-16} g/NP). In order to prove whether the gold mass plays any role on the catalytic efficiency of NPs, equal gold amounts of Au NPs solution of different concentration was used for the study. Using the same conditions as described above, 10 µL of the Au@PEG NPs (29.4 mg/L, with the four PEG coatings) were used, which is equivalent to 1.96 nM, 0.76 nM, 0.37 nM and 0.22 nM for Au1, Au2, Au3 and Au4, respectively. These values can be also compared in terms of concentration of surface atoms. Given that Au1, Au2, Au3 and Au4 present *ca.* 8900, 16100, 26200 and 37400 surface atoms, respectively, we can express the mass concentration in terms of surface atoms per L as follows: c[mol/L]*N_{AV}*N_{SA} [surface atoms/NP], which gives for Au1, Au2, Au3 and Au4: 1.1×10^{-19}, 7.4×10^{-18}, 5.8×10^{-18} and 4.9×10^{-18}

surface atoms/L, where N_{AV} is the Avogrado's number (6.023×10^{23}). The absorption spectra of the catalytic reactions at equal Au mass and plots of λ_{max} over time are shown in Figure S.VII-3 and Figure S.VII-4, respectively. The catalytic parameters are enlisted in Table S.VII-2.

Results and discussion:

From Figure S.VII-1, Figure S.VII-2 and Table S.VII-1 we can see that under the same concentration of Au@PEG NPs, the size of the inorganic core (i.e., different number of surface atoms) has an impact on their catalytic properties: the bigger the NPs are (more surface atoms), the more efficient catalysts the NPs are. On the other hand, the molecular weight of the PEG used for PEGylation also influences their catalytic properties. Our data show that 5 kDa PEGylated NPs show always the highest catalytic values compared to 1 kDa, 3 kDa and 10 kDa equivalent colloids. From all 16 samples we can see that the best sample in terms of catalytic efficiency is Au4@PEG-5k (k = 33.0 $x10^{-3}$ s^{-1}). This might be due to a more efficient surface accessibility of MB molecules in the case of 5 kDa PEGylation. Possibly 1 kDa and 3 kDa are better packed due to their smaller length, whereas the 10 kDa PEG is long enough to wrap the NPs more efficiently than the 5 kDa PEG.

With the same gold amount (29 mg/L) the catalytic behavior of the 16 samples is indeed significantly marked for the type of PEGylation, *cf.* Figure S.VII-3, Figure S.VII-4 and Table S.VII-2. For each type of core (Au1-Au4), again, PEG-5kDa samples present the fastest kinetic constants compared to the other PEGylations. If we now look at one type of PEGylation with different Au core (i.e., different number of particles: 1.96 nM, 0.76 nM, 0.37 nM and 0.22 nM for Au1, Au2, Au3 and Au4, respectively), the combinations Au2@PEG-5k and Au3@PEG-3k present the highest catalytic rates (k = 66.3 $x10^{-3}$ s^{-1} and 64.7 $x10^{-3}$ s^{-1}, respectively), although they present less concentration of surface atoms than Au1 samples (7.4×10^{-18}/ 5.8×10^{-18} vs 1.1×10^{-19} for Au2/Au3 vs. Au1).

Overall, these measurement confirm that this type of PEGylated AuNPs present fast kinetic constants for the reduction of MB, in the same range of other systems like Ag NPs.[10] However the catalytic reponse is significantly affected by the type of PEGylation. Heatmaps are shown in Figure S.VII-5 and VII-6.

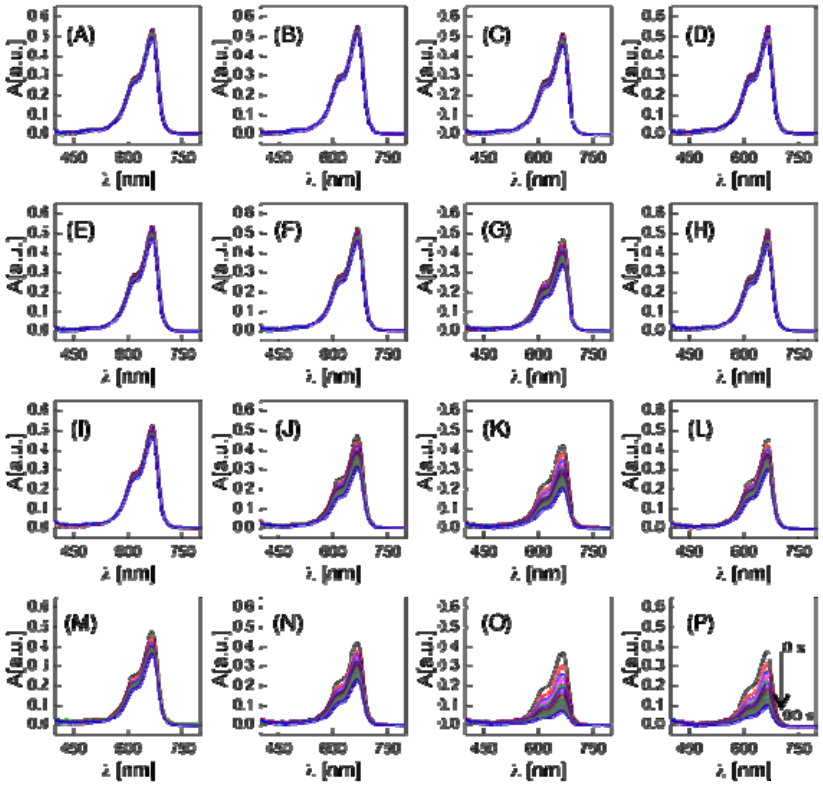

Figure S.VII-1. Absorption spectra collected over 90 s for the reduction of MB to LMB catalyzed by Au@PEG NPs at equal number of particles. (A-D) the spectra of Au1 with different PEGs (1 kDa, 3 kDa, 5 kDa and 10 kDa); (E-H) the spectra of Au2 with 1 kDa, 3 kDa, 5 kDa and 10 kDa; (I-L) the spectra of Au3 with 1 kDa, 3 kDa, 5 kDa and 10 kDa; and (M-P) the spectra of Au4 with 1 kDa, 3 kDa, 5 kDa and 10 kDa. The arrow in panel P shows the evolution to the spectra from 0-90 s.

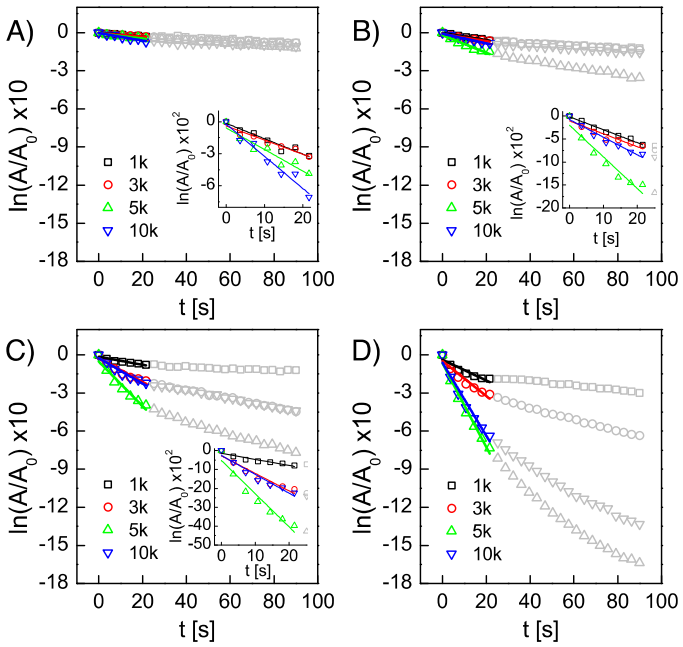

Figure S.VII-2. (A-D) Absorption at λ_{max} (A) vs. time for equal number of NPs, i.e., Au1, Au2, Au3, and Au4, respectively, PEGylated with different PEGs (1 kDa: black; 3 kDa: red; 5 kDa: green; and 10 kDa:

blue). Data considered for the kinetic fitting (first order) are coloured (initial 22 s). Inserts show zoom areas of the fitting regions for selected samples.

Table S.VII-1. Kinetic constant values k [s^{-1}] for the 16 samples (equal molar concentration – 0.22 nM). A first-order catalytic behaviour was considered, i.e., $\ln(A/A_0) = -k \cdot t$, during the initial 22 s of the reaction.

PEG / core	PEG-1k	PEG-3k	PEG-5k	PEG-10k
Au1	1.5 x10^{-3} s^{-1}	3.9 x10^{-3} s^{-1}	5.7 x10^{-3} s^{-1}	2.2 x10^{-3} s^{-1}
Au2	1.5 x10^{-3} s^{-1}	2.8 x10^{-3} s^{-1}	6.8 x10^{-3} s^{-1}	3.8 x10^{-3} s^{-1}
Au3	3.2 x10^{-3} s^{-1}	9.2 x10^{-3} s^{-1}	17.6 x10^{-3} s^{-1}	9.9 x10^{-3} s^{-1}
Au4	8.2 x10^{-3} s^{-1}	13.7 x10^{-3} s^{-1}	33.0 x10^{-3} s^{-1}	28.7 x10^{-3} s^{-1}

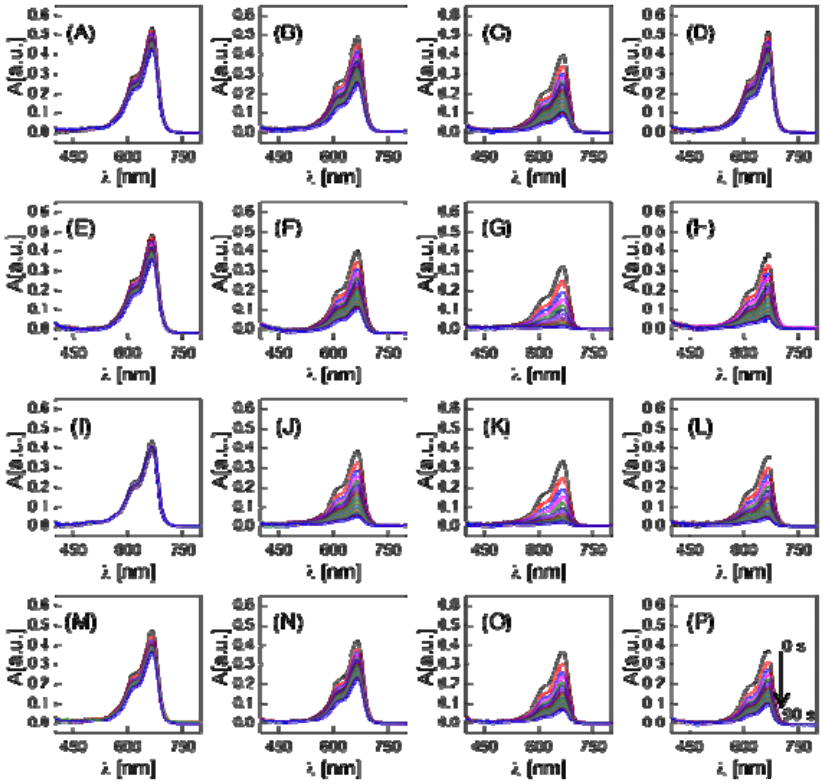

Figure S.VII-3. Absorption spectra A(λ) collected over 90 s for the reduction of MB to LMB catalyzed by Au@PEG NPs at equal mass of gold. (A-D) the spectra of Au1 with different PEGs (1 kDa, 3 kDa, 5 kDa and 10 kDa); (E-H) the spectra of Au2 with 1 kDa, 3 kDa, 5 kDa and 10 kDa; (I-L) the spectra of Au3 with 1 kDa, 3 kDa, 5 kDa and 10 kDa; and (M-P) the spectra of Au4 with 1 kDa, 3 kDa, 5 kDa and 10 kDa. The arrow in panel P shows the evolution to the spectra from 0-90 s.

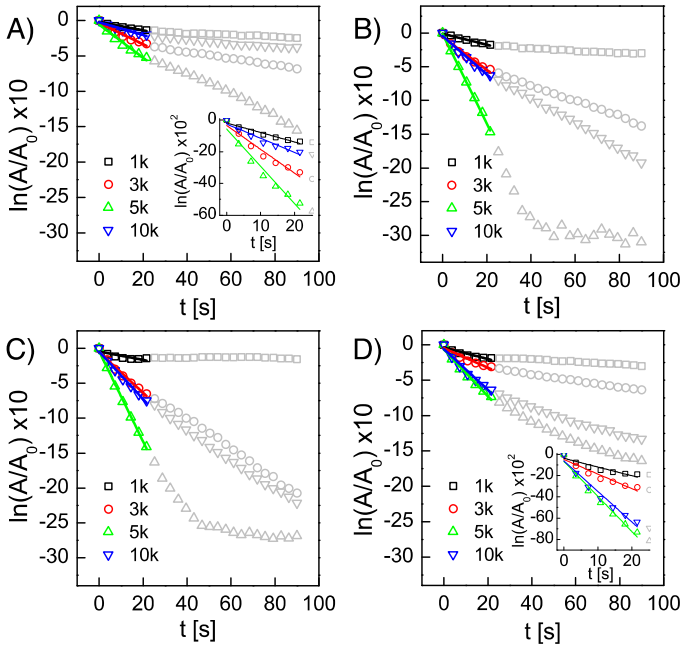

Figure S.VII-4. Absorption (A) at λ_{max} (A) vs. time for equal mass of gold, *i.e.*, Au1, Au2, Au3, and Au4, respectively, PEGylated with different PEGs (1 kDa: black; 3 kDa: red; 5 kDa: green; and 10 kDa: blue). A_0 is the absorption at λ_{max} at time 0 s. Data considered for the kinetic fitting (first order) are coloured (initial 22 s). Inserts show zoom areas of the fitting regions for selected samples.

Table S.VII-2. Summary of the kinetic constant values k [s^{-1}] for the 16 samples (equal Au mass concentration – 29 mg/L). A first-order catalytic behavior was considered, *i.e.*, $\ln(A/A_0) = -k \cdot t$, during the initial 22 s of the reaction

core \ PEG	PEG-1k	PEG-3k	PEG-5k	PEG-10k
Au1	6.0 x10^{-3} s^{-1}	15.0 x10^{-3} s^{-1}	23.4 x10^{-3} s^{-1}	8.9 x10^{-3} s^{-1}
Au2	8.1 x10^{-3} s^{-1}	24.3 x10^{-3} s^{-1}	66.3 x10^{-3} s^{-1}	28.5 x10^{-3} s^{-1}
Au3	6.0 x10^{-3} s^{-1}	29.3 x10^{-3} s^{-1}	64.7 x10^{-3} s^{-1}	34.0 x10^{-3} s^{-1}
Au4	8.2 x10^{-3} s^{-1}	13.7 x10^{-3} s^{-1}	33.0 x10^{-3} s^{-1}	28.7 x10^{-3} s^{-1}

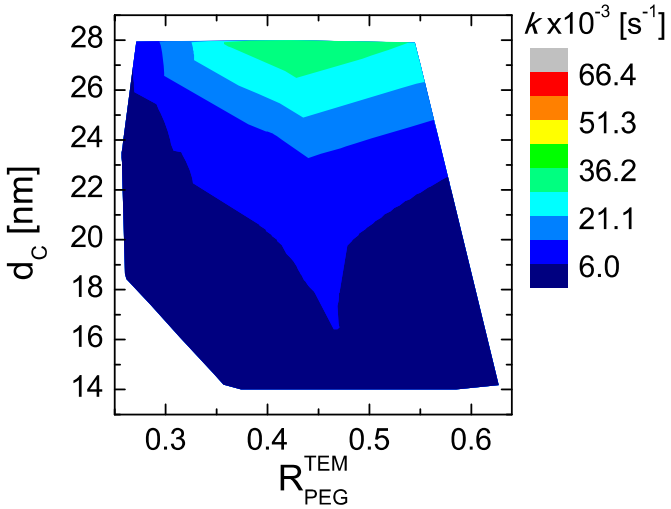

Figure S.VII-5. *k* heatmap for equal number of NPs in a diagram d_C versus R_{PEG}^{TEM}.

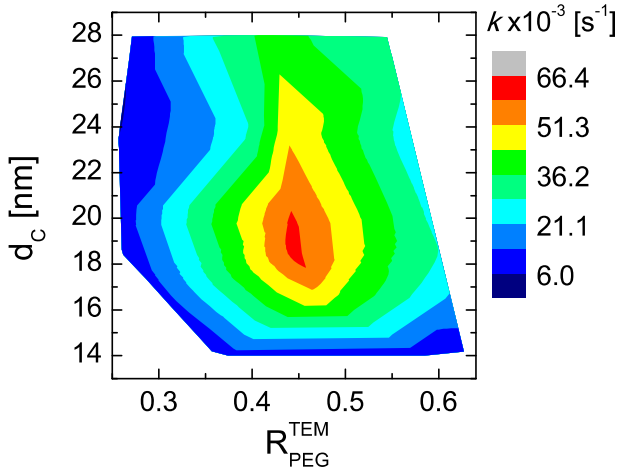

Figure S.VII-6. *k* heatmap for equal mass of gold in a diagram d_C versus R_{PEG}^{TEM}.

VIII) Functionalization of PEGylated NPs

The goal of this section is to derivatize the PEGylated samples previously discussed, *i.e.*, Au1@PEG-10KDa, Au2@PEG-5KDa, Au3@PEG-3KDa, Au4@PEG-1KDa, with a NIR dye (dyomics dy647P1, amino derivative, in the following referred to as Dye) and a quaternary ammonium group (positive in all of the pH range, 2-aminoethyl trimethylammonium chloride hydrochloride, in the following referred to as N+). To do so, we used EDC (1-Ethyl-3-(3-dimethylaminopropyl)carbodiimide) chemistry to covalently bind these molecules to the end terminal carboxylic groups of the PEGs, which are present in all of the samples. NPs were activated in milli-Q water with E_{DC} and sulfo-NHS (N-hydroxysulfosuccinimide) at pH 5, with the following molar ratios (NP:EDC:sulfo-NHS) $1{:}10^6{:}2.5{\cdot}10^6$; after 20 minutes the dye was added with a NP:dye molar ratio of 1:1000. The reaction was then stirred for 1 min and then the quaternary ammonium compound (N+) was added with a NP:N+ molar ratio of $1{:}5{\cdot}10^4$. The reaction was stirred for 5 min, and then the pH was raised to 8 with a concentrated solution of NaOH. The reaction was stirred overnight, and then the NPs were washed by centrifugal precipitation. By this method we prepared Au@PEG-dye-N+; equivalently, we prepared Au@dye in which the N+ was not added.

Figure S.VIII-1 shows a gel with the different samples produced, where one can clearly see the differences in terms of functionalization. The goal of this section is to produce colloids with the same hydrodynamic size but different PEGs and Au core, which also are labeled with a suitable dye for cellular studies, and also with different net surface charge (by using the –N+).

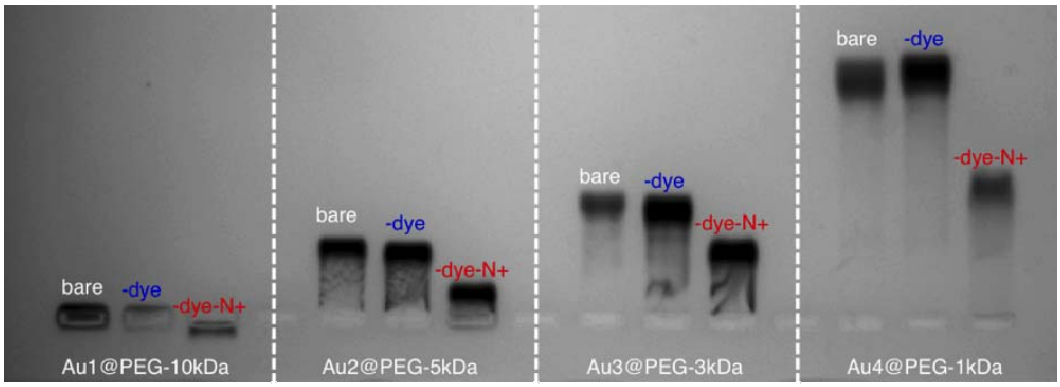

Figure S.VIII-1. Different functionalizations with dye and NR+ of Au NPs.

Indeed the electrophoretical mobilities correlate very well with the ζ-potential of the samples, *cf.* Figure S.VIII-2 and raw data in Table S.VIII-1.

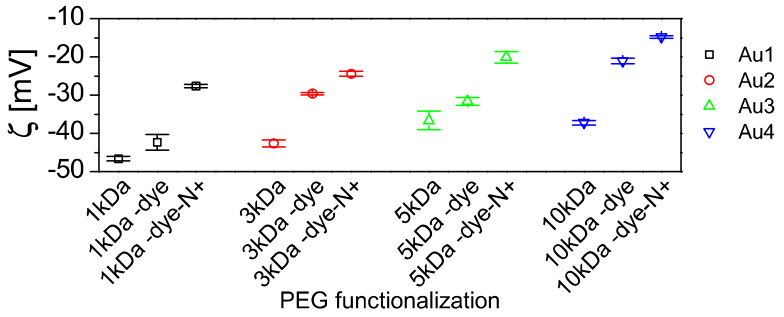

Figure S.VIII-2. ζ-potential values for different functionalization steps with dye and NR+ of Au NPs.

Table S.3.ζ-potential values for each PEGylated core in each step of their functionalization.

Samples	ζ-potential [mV]
Au1@PEG-10kDa	-37.2 ± 0.6
Au1@PEG-10kDa –dye	-21.1 ± 0.7
Au1@PEG-10kDa –dye–N+	-14.8 ± 0.3
Au2@PEG-5kDa	-36.6 ± 2.4
Au2@PEG-5kDa –dye	-31.6 ± 1.0
Au2@PEG-5kDa –dye–N+	-20.1 ± 1.5
Au3@PEG-3kDa	-42.6 ± 1.0
Au3@PEG-3kDa –dye	-29.6 ± 0.3
Au3@PEG-3kDa –dye–N+	-24.4 ± 0.6
Au4@PEG-1kDa	-46.6 ± 0.6
Au4@PEG-1kDa –dye	-42.3 ± 2.0
Au1@PEG-1kDa –dye–N+	-27.6 ± 0.4

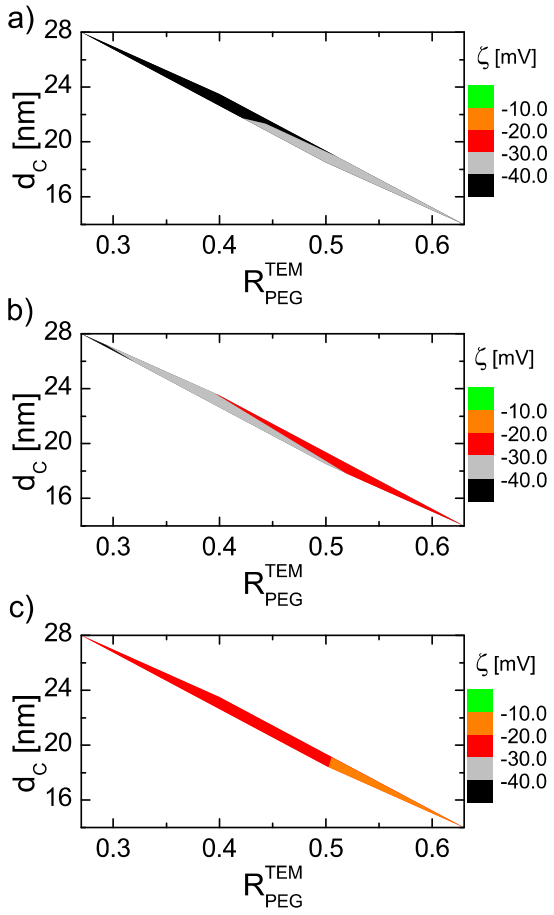

Figure S.VIII-3. Heatmaps for ζ-potential values with a) PEGylated NPs; b)-dye; c)-dye-N+.

9) Cell Studies

Experimental setup: The data shown here are acquired using high-content imaging, where for every condition, several hundreds of images were taken and automated analysis was performed, resulting in minimal 3000 cells per condition that were analyzed. The following parameters related to cell fitness were analyzed (*cf.*, Figure S.IX-1, -2. -3, -4): autophagy (in the following referred to as LC3), cell area (in the following referred to as A), endosome size (in the following referred to as S_E), membrane damage (in the following referred to as MD), mitochondrial health (in the following referred to as MH), reactive oxidative species (in the following referred to as ROS), cell skewness (in the following referred to as SK), viability (in the following referred to as V) and focal adhesion (in the following referred to as FA).

Cell culture: Cell-nanomaterial interaction studies occurred on the following two cell types, being murine C17.2 neural progenitor cells and primary human umbilical vein endothelial cells (HUVECs). The C17.2 cells were cultured in high glucose containing Dulbecco's modified Eagle's medium (DMEM), supplemented with 10% fetal calf serum, 5% horse serum, 1 mM sodium pyruvate, 2mM L-Glutamine and 1% penicillin/streptomycin (Gibco, Invitrogen, Belgium). The cells were passaged every 48 h and split 1/5 in uncoated culture flasks.

HUVECs were purchased from Tebu-Bio (Tebu-Bio, Belgium) The cells were cultured in endothelial basal/growth culture medium (EBM-2/EGM-2, Clonetics, San Diego, CA) with medium changes every 48 h. Cells were passaged when reaching near 80% confluency by lifting the cells with 0.05% trypsin (Gibco) and were plated (1/5) onto tissue-culture flasks coated with collagen.

Cell-nanoparticle interaction studies: For high-content imaging studies, all cell types were seeded at 5000 cells/well in 24 well plates (Nunc, Belgium). Cells were allowed to attach overnight in a humidified atmosphere at 37°C and 5% CO_2, after which the cells were incubated with the gold NPs for 24 h in the full growth medium respective for the cells. For cellular exposure studies, cells were incubated with the NPs at equal mass of gold (62.5, 125 or 250 µg/ml) or equal number of NPs (1.25, 2.5 or 5 nM). Every condition was performed in triplicate, after which the high-content imaging setup was ran using an InCell 2000 High-Content Imaging System (GE Healthcare Life Sciences, Belgium) for a minimum of 3000 cells per well/condition. Data analysis was then performed on the InCell Investigator software (GE Healthcare Life Sciences, Belgium) using in-house developed protocols, using a minimum of 3000 cells/condition, as described elsewhere (Manshian et al, Biomaterials, 2014, 9941-9950). Detailed protocols for the specific steps are outlined in the different sections below.

Cell viability (V) and membrane damage (MD): Following cellular exposure to the Au NPs, the cells were washed twice with phosphate buffered saline (PBS; Gibco, Invitrogen, Belgium) and treated with 2 µM fixable Live-Dead Green dead cell stain (Molecular Probes, Life Technologies Europe, BV, Belgium) in 250 µl/well of PBS (with Ca2+ and Mg2+) and incubated in the dark for 30 min at room temperature. Next, the staining media was aspirated, cells were washed gently with PBS (3x) fixed with 4% paraformaldehyde (PFA) for 15 min at room temperature. The fixative was aspirated and cells were washed three times with PBS. Cells were then counterstained using Hoechst 33342 Nuclear stain (20 µg/ml PBS in 250 µl/well) for 15 min at ambient temperature in the dark. The nuclear counterstain was then removed, cells were

washed three times with PBS and 500 µl of PBS was added to every well, after which the plates were analyzed using the InCell 2000 analyzer (GE Healthcare Life Sciences, Belgium). During acquisition, a minimum of 1000 cells per well were imaged using a 20x objective for the following channels: UV/blue for Hoechst nuclear stain, FITC/FITC for the Live-Dead Green dead cell stain. Data analysis was then performed on the InCell Investigator software (GE Healthcare Life Sciences, Belgium) using in-house developed protocols, using a minimum of 3000 cells/condition. The level of cell viability was calculated as follows: First, cells were segmented based on the Hoechst stain and the perinuclear region was determined by enlarging the nuclear stain 2.5-fold and using the original Hoechst stain images as seed images. For cell viability based on cellular exposure concentrations, cell viability was calculated by determining the number of total cells minus the number of dead cells (dead cells are defined as cells with clear green nuclei, where the intensity is minimally 3-fold above noise level and having an area of minimally 2 µm²). These values were then normalized to control values (100%) to indicate the degree of cell viability.

For membrane damage, the analysis occurred similarly. All green dots in the perinuclear area with a minimum intensity of 3-fold above the noise level and with a size of minimally 0.1 µm² but smaller than 2 µm² were selected. The ratio of this value with the value obtained for control cells was then given to indicate the level of membrane damage.

Oxidative stress (ROS): After labeling the cells, they were washed (3x) with 500 µl PBS/well, after which the cells were incubated with 500 µl full media containing 5 µM CellROX Green (Molecular Probes, Invitrogen, Belgium) for 30 min at 37°C. The staining solution was aspirated, cells were washed with 500 µl PBS/well (3x) and fixed with 4% PFA for 15 min at room temperature. The fixative was removed, cells were washed (3x) with PBS (500 µl/well) after which 500 µl of PBS was added per well and plates were kept at 4°C in a dark container until they were needed for analysis using the InCell 2000 high-content imaging system. For acquisition, the following channels were selected: UV/blue for Hoechst nuclear stain and FITC/FITC for the CellROX Green stain. Data analysis was then performed on the InCell Investigator software (GE Healthcare Life Sciences, Belgium) using in-house developed protocols, using a minimum of 3000 cells/condition. The level of oxidative stress was then calculated as follows: First, cell nuclei were segmented based on the blue channel (Hoechst). As CellROX Green localizes in the nucleus upon oxidation, the intensity of light emitted in the green channel was then determined for every area of the corresponding nuclei. The intensity of every nucleus was then calculated for the green channel and normalized to the intensity level of untreated control cells (100%).

Endosomal size (S_E): After labeling the cells, they were washed (3x) with 500 µl PBS/well, after which the cells were stained in 250 µl PBS (containing Ca2+ and Mg2+) containing 75 nM Lysotracker Red (Molecular Probes, Invitrogen, Belgium) and incubated for 30 min at room temperature. The staining solution was then aspirated, cells were washed with 500 µl PBS/well (3x) and fixed with 4% PFA for 15 min at room temperature. The fixative was removed, cells were washed (3x) with PBS (500 µl/well) after which 500 µl of PBS was added per well and plates were kept at 4°C in a dark container until they were needed for analysis using the InCell 2000 high-content imaging system. For acquisition, the following channels were selected: UV/blue for Hoechst nuclear stain and DsRed/DsRed for the Lysotracker Red stain. Data

analysis was then performed using the InCell Investigator software (GE Healthcare Life Sciences, Belgium) using in-house developed protocols, analyzing a minimum of 3000 cells/condition. The size of the lysosomal network was then calculated as follows: First, cell nuclei were segmented based on the blue channel (Hoechst). Then, the DsRed/DsRed channel was segmented, using the nuclear target channel as seed images. Based on the segmented lysosomal images, the overall area of cellular lysosomes were calculated, for any dot in the lysosomal channel that had an intensity of minimum 3-fold higher than the background noise level. The total area of cellular lysosomes was then normalized to the area of lysosomes in untreated control cells (100%).

Mitochondrial health (MH): After labeling the cells, they were washed (3x) with 500 µl PBS/well, after which the cells were stained in 250 µl PBS (containing Ca2+ and Mg2+) containing 200 nM MitoTracker Red CMXRos (Molecular Probes, Invitrogen, Belgium) and incubated for 30 min at room temperature. The staining solution was then aspirated, cells were washed with 500 µl PBS/well (3x) and fixed with 4% PFA for 15 min at room temperature. The fixative was removed, cells were washed (3x) with PBS (500 µl/well) after which 500 µl of PBS was added per well and plates were kept at 4°C in a dark container until they were needed for analysis using the InCell 2000 high-content imaging system. For acquisition, the following channels were selected: UV/blue for Hoechst nuclear stain and DsRed/DsRed for the MitoTracker Red CMXRos stain. Data analysis was then performed using the InCell Investigator software (GE Healthcare Life Sciences, Belgium) using in-house developed protocols, analyzing a minimum of 3000 cells/condition. The mitochondrial stress and ROS were then calculated as follows: First, cell nuclei were segmented based on the blue channel (Hoechst). Then, the DsRed/DsRed channel was segmented, using the nuclear target channel as seed images. For mitochondrial viability, the level of fluorescence intensity of the segmented mitochondria was determined. The intensity of the mitochondrial signal was then normalized to the intensity level of untreated control cells (100%).

Cell area (A), skewness (SK) and NP uptake: After cellular exposure to the Au NPs, cells were washed (3x) with 500 µl PBS/well and fixed for 15 min at room temperature with 4% PFA. The fixative was then aspirated, cells were washed (3x) with PBS (500 µl/well) after which cells were permeabilised with 250 µl/well of Triton X-100 (1%) for 10 min at room temperature. Cells were then blocked with 10% serum-containing PBS for 30 min at room temperature. Next, cells were stained using 200 µl of staining solution per well first with primary murine anti-α-tubulin antibody for 90 min followed by secondary AF-488-conjugated goat anti-murine antibody for 60 min in the dark at room temperature. The staining solution was aspirated, cells were washed (3x) with PBS (500 µl/well) after which 500 µl fresh PBS was added to each well and the plates were kept at 4°C in a dark container until analyzed using the InCell 2000 high-content imaging system. For acquisition, the following channels were selected: UV/blue for Hoechst nuclear stain and FITC/FITC for the tubulin stain. Data analysis was then performed on the InCell Investigator software (GE Healthcare Life Sciences, Belgium) using in-house developed protocols, using a minimum of 3000 cells/condition. The size of the cells was calculated as follows: First, cell nuclei were segmented based on the blue channel. Cells were then segmented using the FITC channel, where any holes in the cells were filled up and included. Cells on the border of the field of view were excluded from the analysis. The segmentation was based on the blue channel as

seed channel for the nucleus. The total area of every individual cell was then determined. For determination of skewness (*i.e.,* the shape of the cells, being the ratio of cell width over cell length), the same approach was used. After segmentation, the “form factor” was calculated which provides the ratio of the cell width over cell length. This value will always be between 0 (straight line) and 1 (perfect circle). For both parameters, the values obtained were then normalized to the values obtained for untreated control cells (100%).

For NP uptake, a third channel was selected being Cy5/Cy5, which could then be used for visual confirmation of NP uptake. These data were not quantified as ICP-MS was chosen to present a more fair comparison of the level of Au rather than the fluorescence levels.

Autophagy (LC3): After cellular exposure to the Au NPs, cells were washed (3x) with 500 µl PBS/well and fixed for 15 min at room temperature with 4% PFA. The fixative was then aspirated, cells were washed (3x) with PBS (500 µl/well) after which cells were permeabilised with 250 µl/well of Triton X-100 (1%) for 10 min at room temperature. Cells were then blocked with 10% serum-containing PBS (blocking buffer) for 30 min at room temperature. Next, cells were stained using 200 µl of staining solution per well consisting out of primary mouse anti-LC3 antibody (1/400 dilution in blocking buffer; Cell Signalling Technologies, Belgium) and incubated for 90 min in the dark at room temperature. The primary antibody solution was aspirated, cells were washed (3x) with blocking buffer (500 µl/well) after which 200 µl of secondary AF488-conjugated goat anti-mouse IgG antibody (1/250 dilution in blocking buffer; Molecular Probes, Belgium) was added to each well and plates were incubated in the dark for 60 min at room temperature. Following this, the incubation media was aspirated, cells were washed (3x) with PBS (500 µl/well), after which 500 µl fresh PBS was added to each well and the plates were kept at 4°C in a dark container until analyzed using the InCell 2000 high-content imaging system. For acquisition, the following channels were selected: UV/blue for Hoechst nuclear stain and FITC/FITC for the LC3 stain and. Data analysis was then performed on the InCell Investigator software (GE Healthcare Life Sciences, Belgium) using in-house developed protocols, using a minimum of 5000 cells/condition.

The level of autophagy was calculated as follows: First, cell nuclei were segmented based on the blue channel. Using the FITC channel, the cell cytoplasm was then selected, and cells were segmented, where any holes in the cells were filled up and included and any cells on the border of the field of view were excluded from the analysis. The segmentation was based on the blue channel as seed channel for the nucleus. Using the original FITC/FITC channel, any green dots having an intensity of minimum twice that of the noise level and that were localized within the cytoplasm were segmented, where multiple green dots could be localized within a single cell cytoplasm. Then, the cellular intensity of the green channel was measured for every cell, after which this value was normalized to the control value (100%).

Focal adhesions (FA): To analyze the effects on focal adhesion formation, C17.2 and HUVECs were seeded in collagen-coated MatTek glass bottom confocal dishes (MatTek, USA) at 10,000 cells/dish and allowed to attach overnight after which the cells were labelled with the different Au NPs for 24h. Then, cells were fixed (2% PFA for 15 min), permeabilized (1% Triton X-100 for 15 min) and blocked for 30 min in PBS containing 10% goat serum (Gibco, Invitrogen, Belgium) and 2% bovine serum albumin (BSA). Cells were then incubated with primary antibody in blocking solution: anti-vinculin mouse monoclonal (no. ab18058, 1:200; Abcam, Cambridge, UK)

for 2 h at ambient temperature followed by 1 h incubation at ambient temperature with secondary Alexa Fluor 488-conjugated goat anti-mouse antibody (1:250; Molecular Probes, Leiden, Netherlands) and Alexa Fluor 546-conjugated phalloidin (Molecular Probes, Leiden, Netherlands). Subsequently, cells were washed three times with blocking solution prior to being analysed by confocal laser scanning microscopy. To get quantitative data, images were also collected at a 40x magnification by epifluorescence microscopy using an Nikon A1R confocal microscope (Nikon, Belgium). For analysis of focal adhesion areas, confocal images displaying vinculin were background-corrected, thresholded, focal adhesions were identified and the total areas per cell were calculated for 50 cells per condition.

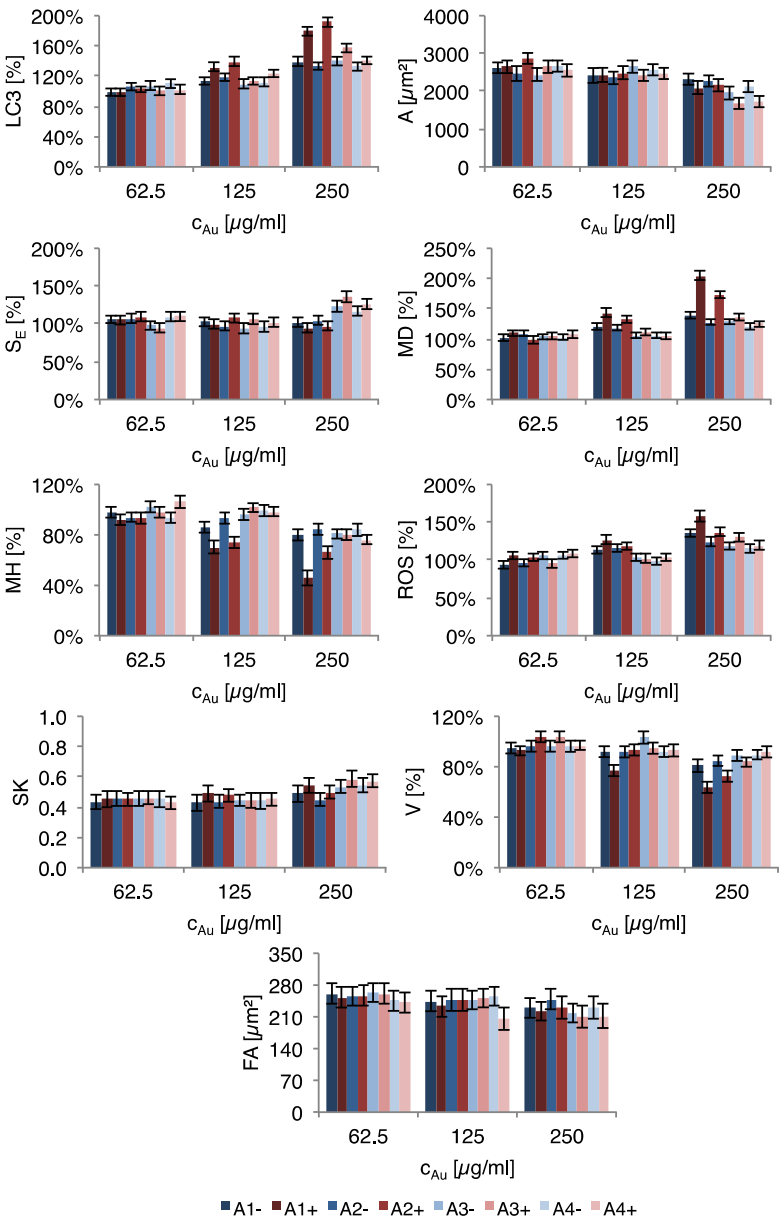

Figure S.IX-1. Overview of the data obtained by high-content imaging and confocal microscopy (focal adhesion size) for C17.2 cells treated with the various Au NPs (*i.e.*, Au1-: Au1@PEG-10kDa–dye; Au1+: Au1@PEG-10kDa–dye–N+, Au2-: Au2@PEG-5kDa–dye; Au2+: Au2@PEG-5kDa–dye–N+, Au3-: Au3@PEG-3kDa–dye; Au3+: Au3@PEG-3kDa–dye–N+, Au4-: Au4@PEG-1kDa–dye; Au4+: Au4@PEG-1kDa–dye–N+) at equal NP numbers (*i.e.*, 1.25, 2.5, 5 nM).

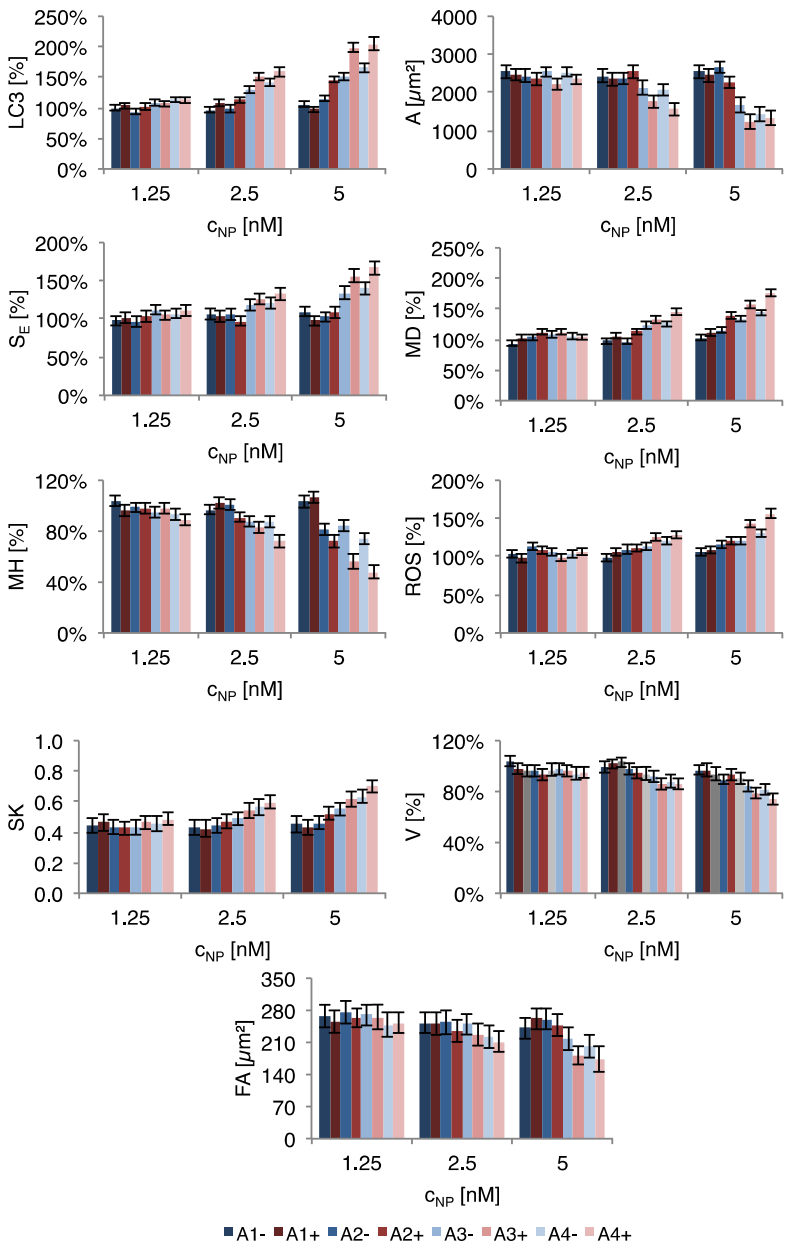

Figure S.IX-2. Overview of the data obtained by high-content imaging and confocal microscopy (focal adhesion size) for C17.2 cells treated with the various Au NPs (*i.e.*, Au1-: Au1@PEG-10kDa–dye; Au1+: Au1@PEG-10kDa–dye–N+, Au2-: Au2@PEG-5kDa–dye; Au2+: Au2@PEG-5kDa–dye–N+, Au3-: Au3@PEG-3kDa–dye; Au3+: Au3@PEG-3kDa–dye–N+, Au4-: Au4@PEG-1kDa–dye; Au4+: Au4@PEG-1kDa–dye–N+) at equal NP mass (*i.e.*, 62.5, 125 and 250 μg/mL).

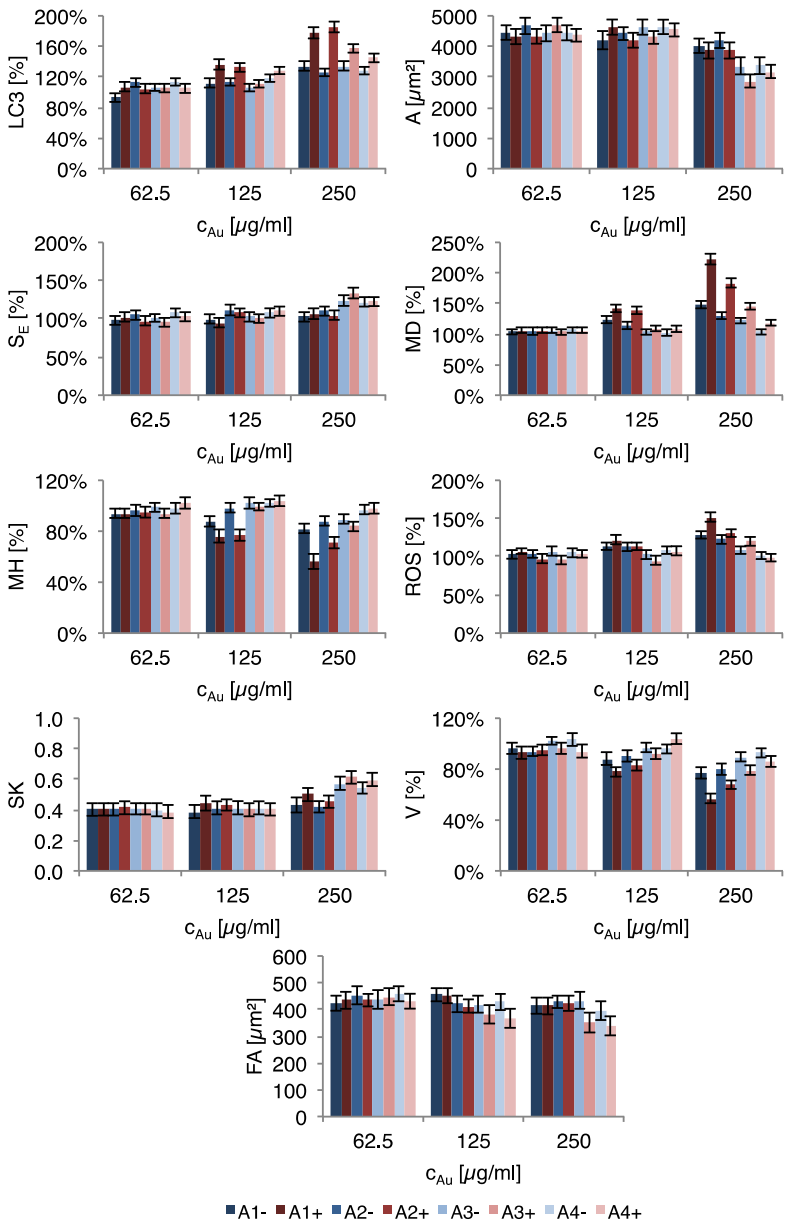

Figure S.IX-3. Overview of the data obtained by high-content imaging and confocal microscopy (focal adhesion size) for HUVEC cells treated with the various Au NPs (*i.e.*, Au1-: Au1@PEG-10kDa–dye; Au1+: Au1@PEG-10kDa–dye–N+, Au2-: Au2@PEG-5kDa–dye; Au2+: Au2@PEG-5kDa–dye–N+, Au3-: Au3@PEG-3kDa–dye; Au3+: Au3@PEG-3kDa–dye–N+, Au4-: Au4@PEG-1kDa–dye; Au4+: Au4@PEG-1kDa–dye–N+) at equal NP numbers (*i.e.*, 1.25, 2.5, 5 nM).

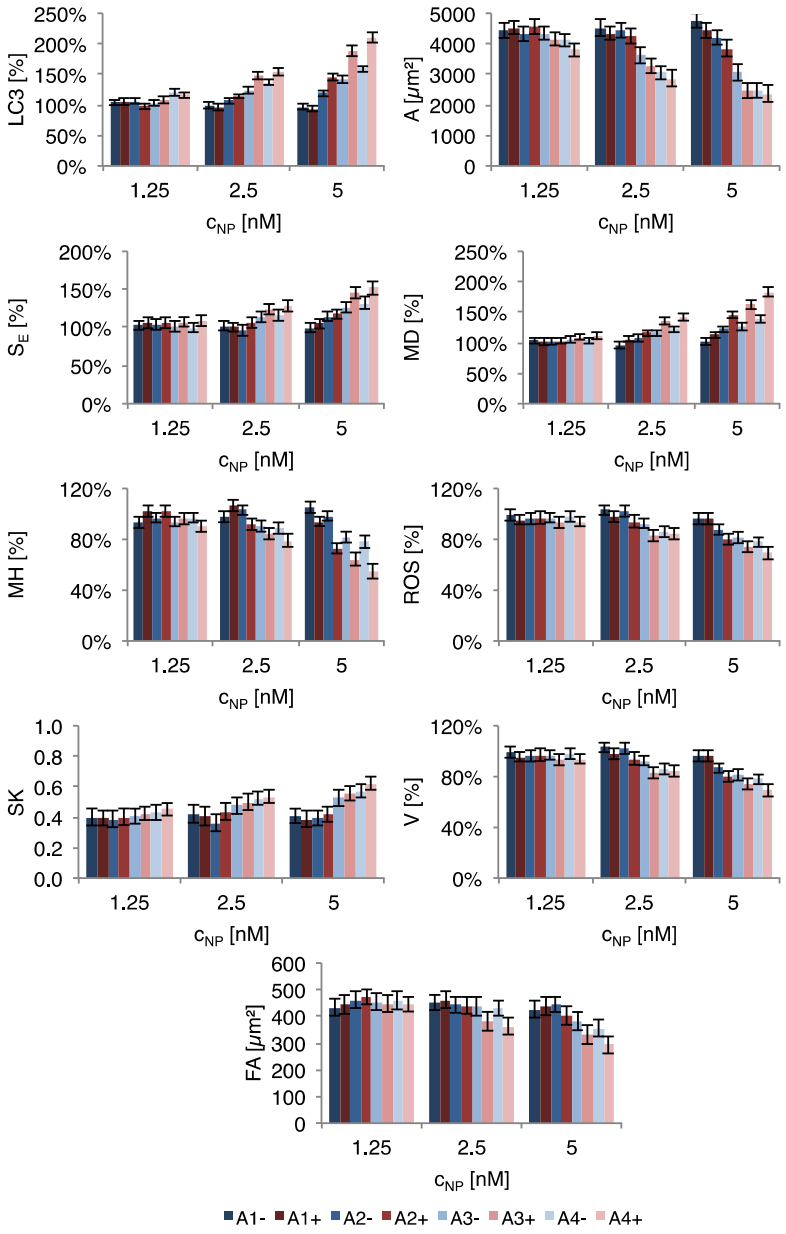

Figure S.IX-4. Overview of the data obtained by high-content imaging and confocal microscopy (focal adhesion size) for HUVEC cells treated with the various Au NPs (*i.e.*, Au1-: Au1@PEG-10kDa–dye; Au1+: Au1@PEG-10kDa–dye–N+, Au2-: Au2@PEG-5kDa–dye; Au2+: Au2@PEG-5kDa–dye–N+, Au3-: Au3@PEG-3kDa–dye; Au3+: Au3@PEG-3kDa–dye–N+, Au4-: Au4@PEG-1kDa–dye; Au4+: Au4@PEG-1kDa–dye–N+) at equal NP mass (*i.e.*, 62.5, 125 and 250 μg/mL).

Figure S.IX-5 shows an overview of the data discussed in the form of heatmaps.

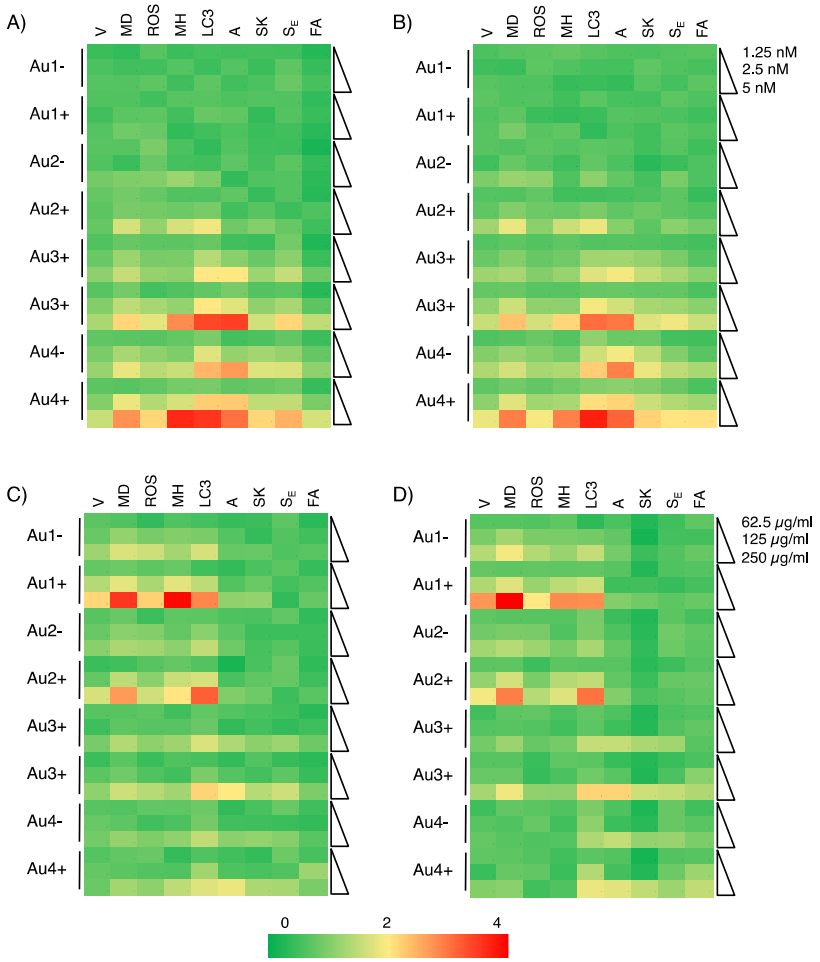

Figure S.IX-5 Overview of the data obtained by high-content imaging and confocal microscopy (focal adhesion size) for HUVEC cells (left) or C17.2 cells (right), treated with the various Au NPs at equal NP numbers (A, B) and equal mass of Au (C, D).

Figure S.IX-6 and IX-7 show heatmaps of more cell affected (in HUVEC cells) parameters when NPs are given at equal number of NPs and mass of gold, respectively.

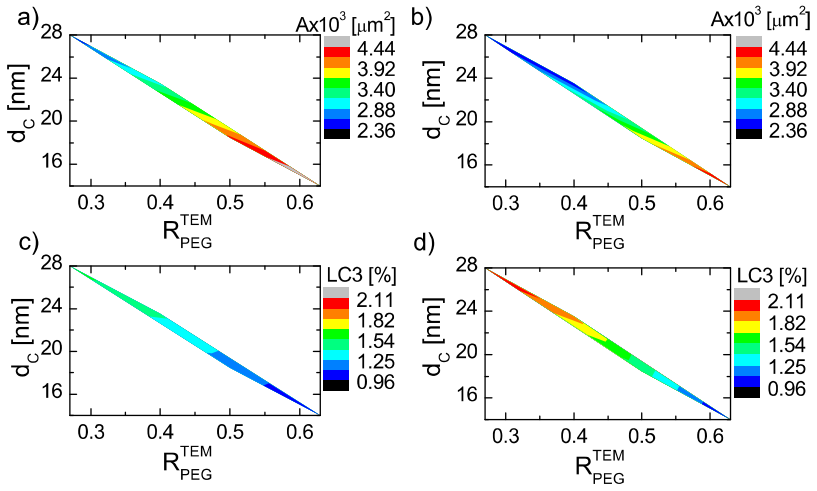

Figure S.IX-6. HUVEC at 5 nM. Cell area (A) & Autophagy (LC3). a, c) Au1-, Au2-, Au3-, Au4-; b, d) Au1+, Au2+, Au3+, Au4+.

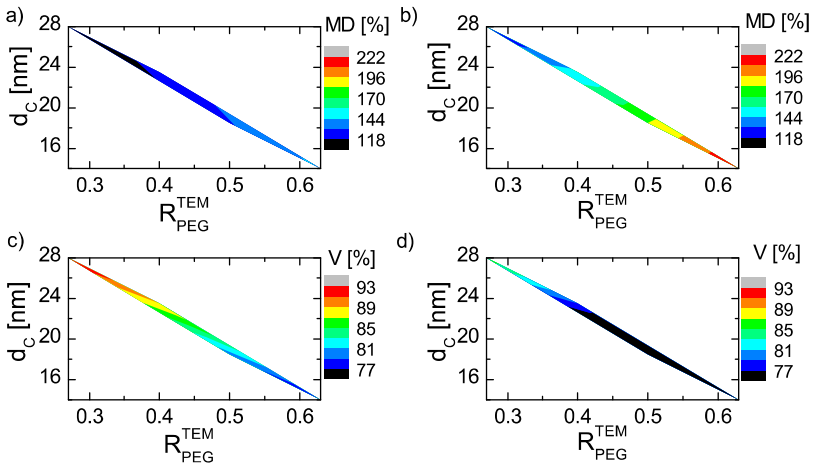

Figure S.IX-7. Contours. HUVEC at 250 μg/mL. Membrane damage (MD) & viability (V). a, c) Au1-, Au2-, Au3-, Au4-; b, d) Au1+, Au2+, Au3+, Au4+.

Figure S.IX-8 and IX-9 show representative images of HUVEC cells incubated with NPS (Figure IX-9: control cells).

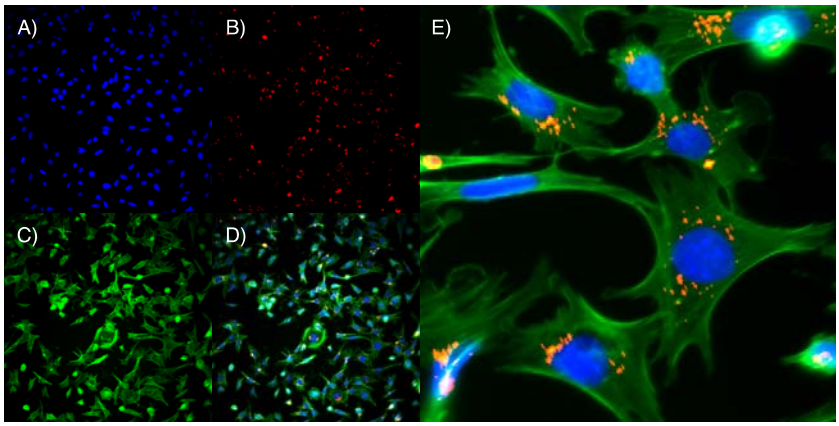

Figure S.IX-8. Representative InCell images of HUVEC cells stained with Au1+ NPs for 24 h at 5 nM. The different channels shown are: A) the cell nuclei counterstained with DAPI (blue), B) Au4+ NPs (red) and C) □-tubulin (green). A merged image of all three channels is displayed in D). E) shows a magnified view of a section of D) displaying a clear perinuclear localization of the NPs.

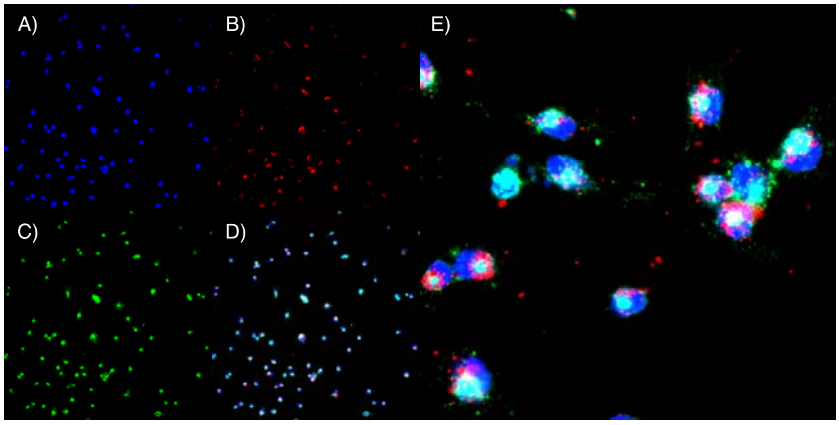

Figure S.IX-9. Representative InCell images of HUVEC cells stained with Au4+ NPs for 24 h at 5 nM. The different channels shown are: A) the cell nuclei counterstained with DAPI (blue), B) Au1+ NPs (red) and C) □-tubulin (green). A merged image of all three channels is displayed in D). E) shows a magnified view of a section of D) displaying a clear perinuclear localization of the NPs

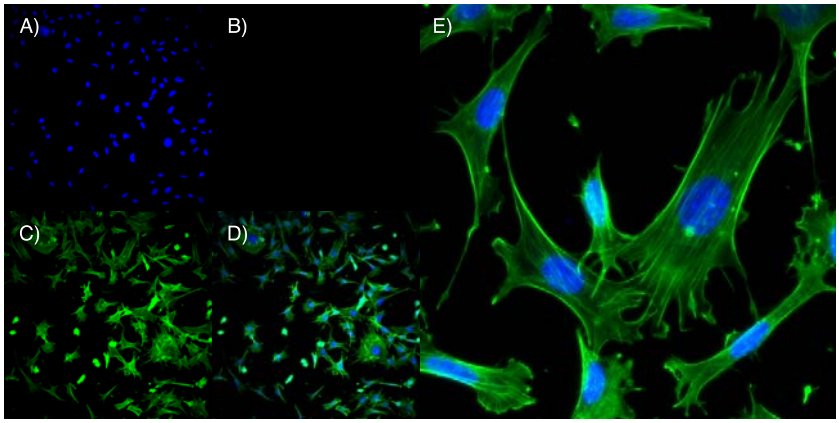

Figure S.XI-10. Representative InCell images of control HUVEC cells. The different channels shown are: A) the cell nuclei counterstained with DAPI (blue), B) lack of any NPs (red) and C) □-tubulin (green). A merged image of all three channels is displayed in D). E) shows a magnified view of a section of D) displaying a stretched morphology of the control cells not exposed to any NPs.

Gene Expression analysis: Gene expression (for a total of 84 genes involved in cytoskeletal signaling and regulation) results for C17.2 cells incubated with 5 nM nanoparticles. What is shown are the genes where significant changes are found in the expression level compared to untreated control cells. The level of upregulation is shown by color-code as indicated above.

The data clearly shows highest levels of upregulation in A4+, A4-, A3+, and A3-, indicating clear alterations in cytoskeletal architecture and regulation for the more internalized NPs, which is in line with the imaging results.

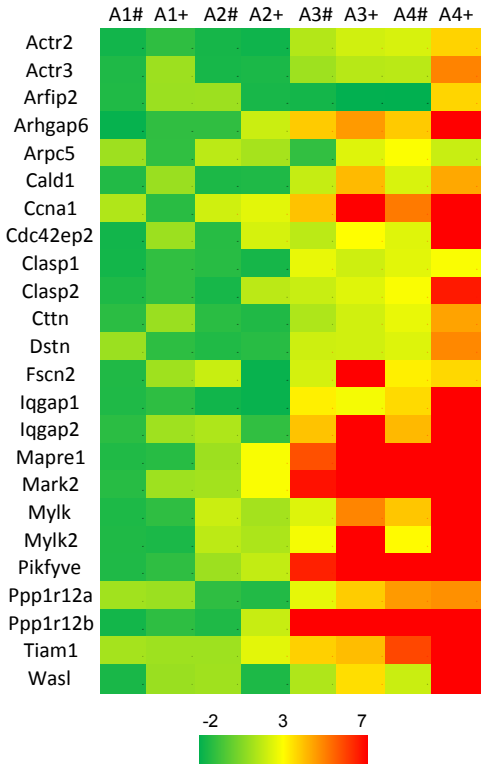

Figure S.IX-11. Heatmap of the genes affected by the NPs. *Actr2*: ARP2 actin-related protein 2 homolog (yeast); *Actr3*: ARP3 actin-related protein 3 homolog (yeast); *Arfip2*: ADP-ribosylation factor interacting protein 2; *Arhgap6*: Rho GTPase activating protein 6; *Arpc5*: Actin related protein 2/3 complex, subunit 5; *Cald1*: Caldesmon 1; *Ccna1*: Cyclin A1; *Cdc42ep2*: CDC42 effector protein (Rho GTPase binding) 2; *Clasp1*: Cyclin A1; *Clasp2*: Cyclin A2; *Cttn*: Cortactin; *Dstn*: Destrin; *Fscn2*: Fascin homolog 2, actin-bundling protein, retinal (Strongylocentrotus purpuratus); *Iqgap1*: IQ motif containing GTPase activating protein 1; *Iqgap2*: IQ motif containing GTPase activating protein 2; *Mapre1*: Microtubule-associated protein, RP/EB family, member 1; *Mark2*: MAP/microtubule affinity-regulating kinase 2; *Mylk*: Myosin, light polypeptide kinase; *Mylk2*: Myosin, light polypeptide kinase 2, skeletal muscle; *Pikfyve*: Phosphoinositide kinase, FYVE finger containing; *Ppp1r12a*: Protein phosphatase 1, regulatory (inhibitor) subunit 12A; *Ppp1r12b*: Protein phosphatase 1, regulatory (inhibitor) subunit 12B; *Tiam1*: T-cell lymphoma invasion and metastasis 1; *Wasl*: Wiskott-Aldrich syndrome-like (human).

ICP-MS uptake studies

In case of cell suspension samples the procedure requires nearly the same procedure as for the NPs. The cells with the internalized Au NPs were digested as described previously with *aqua regia*, but with a difference in volume. 50 µL of sample and 150 µL of *aqua regia* were mixed and then agitated for at least 4 hours. The number of cells was predetermined and afterwards the number of internalized Au NPs per cell could be calculated with the known core radius, the

density, the molar weight of the gold sample and the results determined by the ICP-MS measurements in µg/L of atomic gold content in the digested cells.

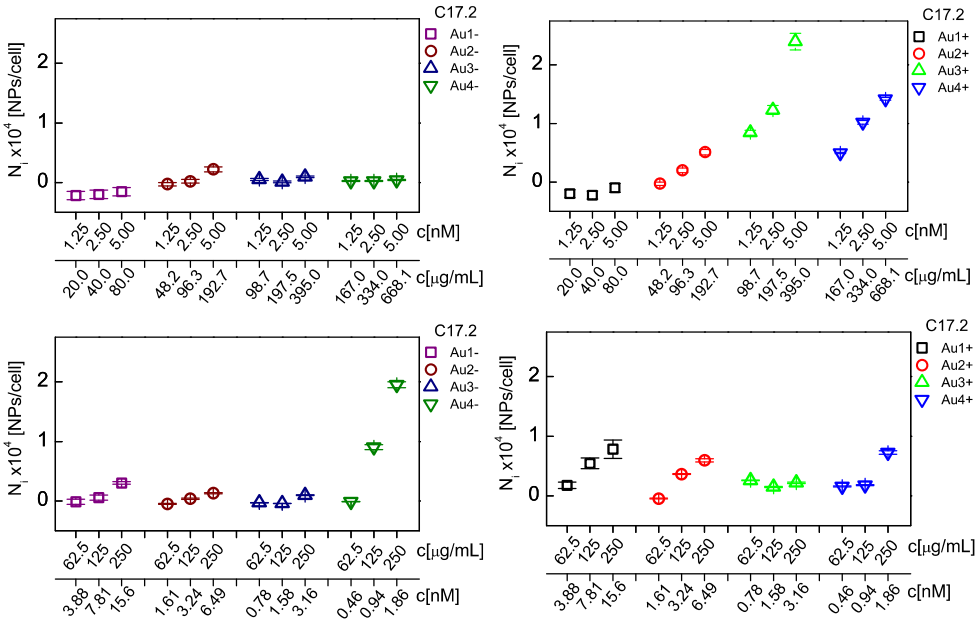

Figure S.IX-12. Overview of NP's internalized (N_i) by C17.2 cells. A) Equal number of Au@PEG NPs; B) Equal number of Au@PEG NPs modified with –Dye and –NR+ (i.e., Au1+, Au2+, Au3+ and Au4+); C) NPs modified with –Dye (i.e., Au1-, Au2-, Au3- and Au4-) at equal mass of gold; D) NPs modified with –Dye and –NR+ (i.e., Au1+, Au2+, Au3+ and Au4+).

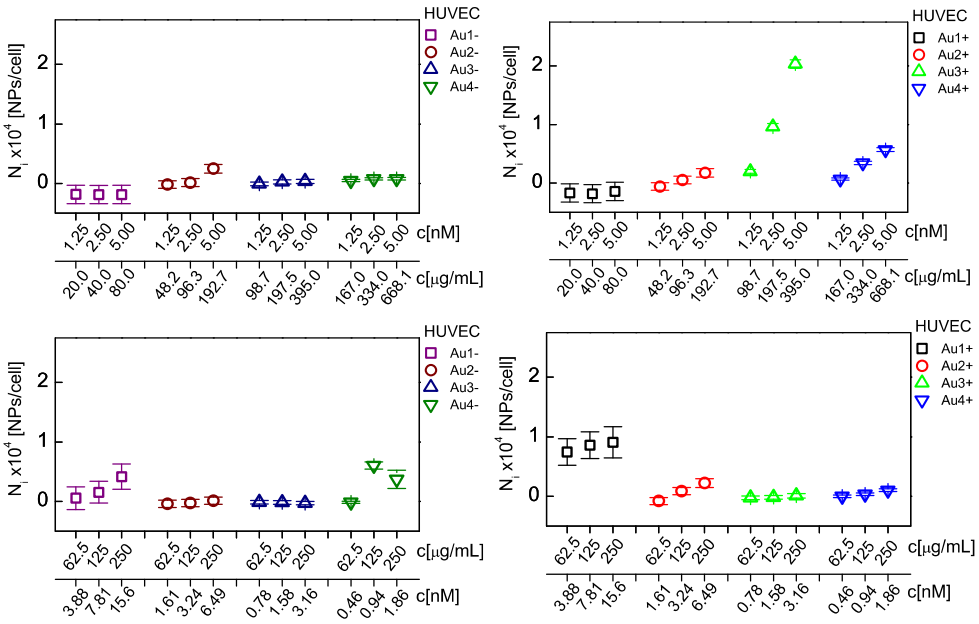

Figure S.IX-13. Overview of NP's internalized (N_i) by HUVEC cells. A) Equal number of Au@PEG NPs; B) Equal number of Au@PEG NPs modified with –Dye and –NR+ (i.e., Au1+, Au2+, Au3+ and Au4+); C)

NPs modified with –Dye (i.e., Au1-, Au2-, Au3- and Au4-) at equal mass of gold; D) NPs modified with –Dye and –NR+ (i.e., Au1+, Au2+, Au3+ and Au4+).

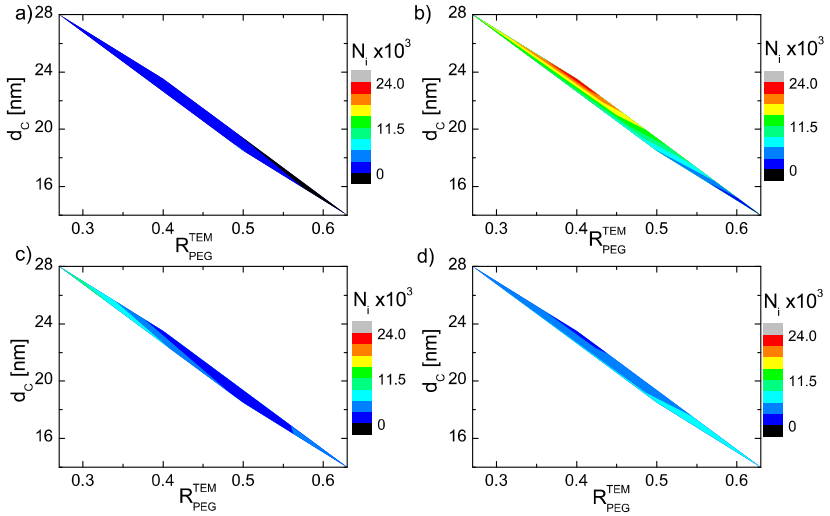

Figure S.IX-14. Internalized NPs per cell (N_i) heatmaps for C17.2 cells. a,b) equal number (5nM) ; c,d) equal mass (250 μg/mL)

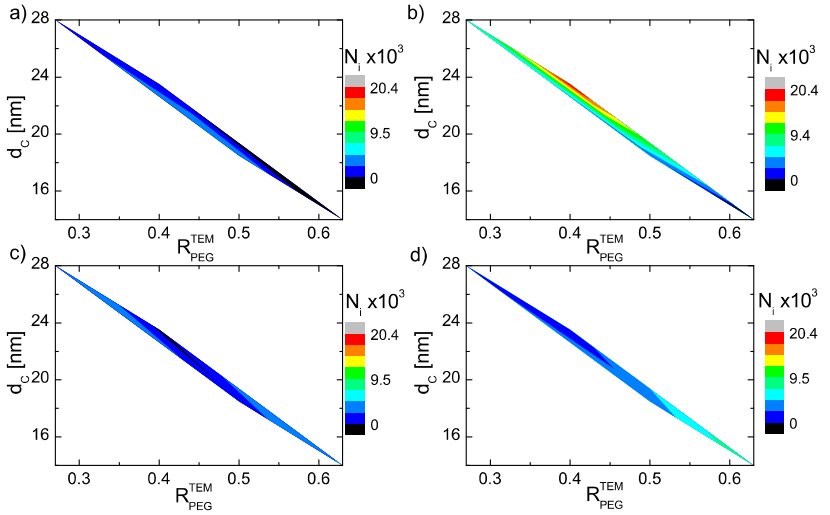

Figure S.IX-15. Internalized NPs per cell (N_i) heatmaps for HUVEC cells. a,b) equal number (5nM) ; c,d) equal mass (250 μg/mL)

10) References

1 Bastus, N. G., Comenge, J. & Puntes, V. Kinetically Controlled Seeded Growth Synthesis of Citrate-Stabilized Gold Nanoparticles of up to 200 nm: Size Focusing versus Ostwald Ripening. *Langmuir* **27**, 11098-11105 (2011).

2 Haiss, W., Thanh, N. T. K., Aveyard, J. & Fernig, D. G. Determination of Size and Concentration of Gold Nanoparticles from UV-Vis Spectra. *Anal. Chem.* **79**, 4215-4221 (2007).

3 Robin Harris, J. in *Electron Microscopy Methods and Protocols* Vol. 117 (Humana Press, 1999).

4 Carpenter, A. *et al.* CellProfiler: image analysis software for identifying and quantifying cell phenotypes. *Genome Biology* **7**, R100 (2006).

5 Xi Yuan, H. & Rosen, M. J. Dynamic surface tension of aqueous surfactant solutions: I. Basic paremeters. *J. Colloid Interface Sci.* **124**, 652-659, doi:http://dx.doi.org/10.1016/0021-9797(88)90203-2 (1988).

6 Ludwig, M. *et al.* AFM, a tool for single-molecule experiments. *Applied Physics A - Materials Science & Processing* **68**, 173-176 (1999).

7 Ni, W. & Cheng, Y.-T. Modeling conical indentation in homogeneous materials and in hard films on soft substrates. *J. Mater. Res.* **20**, 521-528, doi:doi:10.1557/JMR.2005.0071 (2005).

8 Li, X., Gao, H., Murphy, C. J. & Gou, L. Nanoindentation of Cu2O Nanocubes. *Nano Lett.* **4**, 1903-1907, doi:10.1021/nl048941n (2004).

9 Bull, S. J. Nanoindentation of coatings. *J. Phys. D: Appl. Phys.* **38**, R393 (2005).

10 Mignani, A. *et al.* Mild fabrication of silica-silver nanocomposites as active platforms for environmental remediation. *RSC Advances* **5**, 9600-9606, doi:10.1039/C4RA14069A (2015).

Nanomaterials **2015**, *5*, 1297-1316; doi:10.3390/nano5031297

OPEN ACCESS

nanomaterials

ISSN 2079-4991

www.mdpi.com/journal/nanomaterials

Article

Conjugation of Polymer-Coated Gold Nanoparticles with Antibodies—Synthesis and Characterization

Gamze Tan [1,2], Karsten Kantner [2], Qian Zhang [2], Mahmoud G. Soliman [2], Pablo del Pino [3], Wolfgang J. Parak [2,3], Mehmet A. Onur [4], Daniel Valdeperez [2], Joanna Rejman [2,*] and Beatriz Pelaz [2,*]

[1] Faculty of Science and Letters, Department of Biology, Aksaray University, Aksaray 68100,Turkey; E-Mail: gamzetan2003@yahoo.com

[2] Philipp University of Marburg, Marburg 35001, Germany; E-Mails: karsten.kantner@physik.uni-marburg.de (K.K.); qian.zhang@physik.uni-marburg.de (Q.Z.); mahmoud.gamalsoliman@physik.uni-marburg.de (M.G.S.); wolfgang.parak@physik.uni-marburg.de (W.J.P.); daniel.valdepereztoledo@physik.uni-marburg.de (D.V.)

[3] Centro de Investigación Cooperativa Biomagune, San Sebastián 20001, Spain; E-Mail: pdelpino@cicbiomagune.es

[4] Faculty of Science, Department of Biology, Hacettepe University, Ankara 06800, Turkey; E-Mail: mali@hacettepe.edu.tr

* Authors to whom correspondence should be addressed; E-Mails: j_rejman@hotmail.com (J.R.); beatriz.pelazgarcia@physik.uni-marburg.de (B.P.); Tel.: +49-6421-2824161 (J.R. & B.P.); Fax: +49-6421-2824131 (J.R. & B.P.).

Academic Editor: Subramanian Tamil Selvan

Received: 28 June 2015 / Accepted: 30 July 2015 /Published: 7 August 2015

Abstract: The synthesis of polymer-coated gold nanoparticles with high colloidal stability is described, together with appropriate characterization techniques concerning the colloidal properties of the nanoparticles. Antibodies against vascular endothelial growth factor (VEGF) are conjugated to the surface of the nanoparticles. Antibody attachment is probed by different techniques, giving a guideline about the characterization of such conjugates. The effect of the nanoparticles on human adenocarcinoma alveolar basal epithelial cells (A549) and human umbilical vein endothelial cells (HUVECs) is probed in terms of internalization and viability assays.

Keywords: gold nanoparticles; bioconjugation; nanoparticle characterization; toxicity; nanoparticle-cell interaction; cellular uptake; VEGF

1. Introduction

The synthesis in colloidal nanoparticles (NPs) is well advanced [1–6]. Nowadays, a high control concerning material composition, size, shape, *etc.*, is possible [7]. There are also many strategies available to provide water-solubility of these NPs with high colloidal stability [8]. Some correlation of the (nonspecific) interaction of such NPs with cells with their physicochemical properties is possible and some general tendencies are well accepted in literature [9,10]. However, in order to warrant for specific interaction of NPs with cells, their surface has to be modified with ligands targeting cellular receptors. The purpose to bind proteins to the surface of NPs is to provide them a special ligand coat that they interact specifically with cells, *etc.* While there are many reports in literature about the conjugation of NP surfaces with specific ligands, characterization of these NPs is not always sufficient. Bioconjugation in particular may result in unwanted agglomeration, due to crosslinking of NPs. Thus, characterization of the colloidal properties of such conjugates is of high importance. In addition, the ligand density may significantly vary, depending on the used conjugation protocol. In principle, solutions to these hurdles exist, and NPs with a controlled ligand density and controlled ligand orientation can be synthesized [11–13]. However, these synthesis strategies require typically sophisticated protocols, and thus most commonly in literature more simple and less controlled strategies are employed. In the present work, it will be shown that also by simple conjugation strategies, together with appropriate characterization techniques, NP-antibody conjugates can be generated. As, in particular, characterization is crucial in the following, all experimental steps will be presented in the form of a general protocol.

2. Materials and Discussions

2.1. Synthesis of Gold Nanoparticles

Au NPs are standard model systems, which are extensively used in literature to study the interaction of NPs with cells. This is in particular due to the fact that Au is an intrinsically nontoxic material. In the following, a protocol for the synthesis of hydrophilic Au NPs is described according to standard protocols from literature [14–17].

For the synthesis of Au NPs of d_c = 20 nm core diameter, hydrogen tetrachloroaurate (III) hydrate (Alfa Aesar #12325, Ward Hill, MA, USA) and sodium citrate dehydrate 99% (Sigma Aldrich #W302600, St. Louis, MS, USA) were used as chemicals. All chemicals were used without further purification. Ultrapure water with a resistance greater than 18.2 $m\Omega \cdot cm^{-1}$ was used for all experiments. All glassware was cleaned in aqua regia and rinsed with ultrapure water. For the synthesis, a solution containing 150 mL (2.2 mM) trisodium citrate dihydrate ($Na_3C_6H_5O_7 \cdot 2H_2O$) was heated in a 250 mL flask to 100 °C with stirring under reflux. Using a syringe, 1 mL of 25 mM $HAuCl_4 \cdot 3H_2O$ was injected into the flask and stirred at 100 °C. Upon formation of Au NPs, the solution turned deep red. The temperature was then reduced to 90 °C, and the solution was stirred continuously for another

30 min. For further NP growth, then 1 mL sodium citrate (60 mM) and 1 mL of $HAuCl_4$ solution (25 mM) were sequentially injected with a time delay of two minutes between the two injections [17]. After 30 min, the reaction was cooled down to room temperature using an ice bath.

While this protocol virtually always will lead to the formation of Au NPs (as visible by the red color of the solution) the quality of the NPs can vary significantly. Concerning colloidal solutions, the two most important quality indicators are dispersion (*i.e.*, the NPs are individually dispersed and do not agglomerate) and size distribution of the NPs (*i.e.*, the diameter of all NPs should be as similar as possible). Even by using the same synthesis protocol over and over, the quality of the resulting NPs may vary for each batch, which warrants a mandatory quality control.

The size distribution of inorganic NPs, *i.e.*, NPs with a core composed out of an inorganic material such as gold, can be determined with transmission electron microscopy (TEM). Note that organic molecules often do not provide sufficient contrast for being visualized with TEM. For TEM analysis, a diluted drop of Au NPs was dried on a copper grid, and NPs were imaged with TEM. From such images (*cf.* Figure 1), a histogram about the distribution of the core diameter, *i.e.*, the diameter d_c of the inorganic NP core can be obtained. In the present case, the core diameter was determined by analysis of more than 300 NPs, using the free software Image J. From the histogram, the mean diameter of the Au cores was determined to be $d_c = 20.9 \pm 4.3$ nm, *cf.* Figure 1.

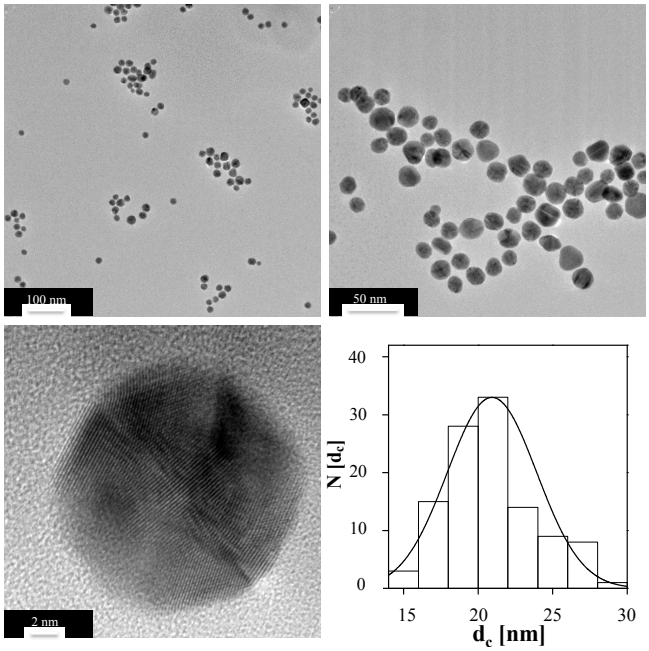

Figure 1. TEM images of the Au NPs at different magnifications (scale bars corresponding to 100 nm, 50 nm and 2 nm), and the corresponding histogram N (d_c) of the core diameter d_c.

The state of dispersion cannot be unequivocally deduced from TEM images, as those are recorded on NPs in dried state. In other words, even well dispersed NPs can form clusters on TEM grids. While the most common method to probe for NP dispersion is measuring the hydrodynamic diameter directly in solution (for example by dynamic light scattering (DLS), as will be described later in more detail), in the case of Au NPs simple analysis can be done by recording UV/Vis absorption spectra. As shown in the absorption spectrum in Figure 2, Au NPs exhibit a peak due to surface plasmon resonance [18].

In case NPs are not well dispersed and start to form agglomerates, this peak is shifted to higher wavelengths and the solution turns from red to blue-black. Agglomeration also leads to scattering at high wavelengths >800 nm. In case of poor size distribution, the plasmon peak broadens.

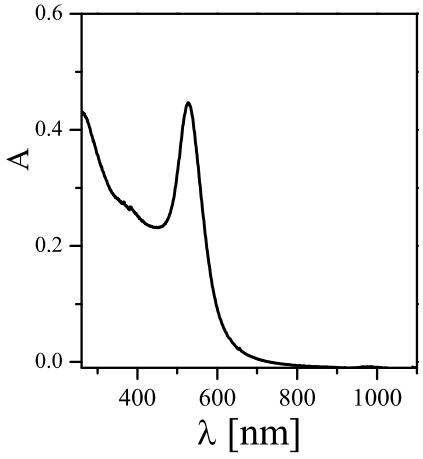

Figure 2. UV/Vis absorption spectrum A (λ) of Au NPs dispersed in water, directly recorded after their synthesis as described in this chapter.

Besides giving an indication about the quality of the NP synthesis, UV/Vis absorption spectra are also helpful for the determination of the concentration of the Au NPs. According to the Lambert-Beer Law, the absorption A of a solution of NPs (with a length of the light path L) is proportional to the NP concentration c_{NP}:

$$A = \varepsilon_{NP} \cdot L \cdot c_{NP} \quad (1)$$

The proportionality factor is the molar extinction coefficient, which is well determined in the case of Au NPs with different sized. In the present case of NPs with a core diameter of $d_c \approx 20$ nm the extinction coefficient at 450 nm is given as ε_{NP} (450nm) = $5.41 \times 10^8 \cdot M^{-1} \cdot cm^{-1}$ [19]. For the present case, 20 µL of Au NP solution directly taken after their synthesis, after dilution 500 µL with water, lead to an absorbance of $A = 0.23$ at 450 nm ($L = 1$ cm). That means that the Au NP concentration was around $c_{NP} \approx 11.1$ nM.

As citric acid capped Au NPs as prepared above are not highly colloidally stable in cell culture media (due to screening of their surface charge by adsorption of counter ions), the NPs were further stabilized by modification with polyethyleneglycol (PEG) [20]. In this work, the as-prepared Au NPs were modified with a heterofunctional PEG chain with a thiol group at one, and a carboxylic group at the other end (molecular mass M_w = 3 kDa, Rapp polymer #133000-4-32, Tuebingen, Germany). 10^5 PEG molecules were added *per* each NP, and the pH was risen to 12 with NaOH (1 M). Alkaline conditions facilitate deprotonation of the thiol terminal, which, in this way, attaches faster to the Au surface [21]. Afterwards, the PEGylated NPs were cleaned by centrifugation in order to remove unbound PEG (three times using 14,000 rpm for 30 min, supernatant containing free PEG is discarded and replaced by fresh buffer).

2.2. Fluorescence Labelling of Proteins

Protein concentrations are often determined by absorption measurements, for example by the Bradford assays, as described later. However, as NPs heavily absorb in the same range of wavelengths

absorption measurements are not well suited for determining protein concentrations in NP-protein conjugates. In contrast, in order to quantify protein conjugation to NPs, it is useful to label proteins with a fluorophore. In this way, protein concentration can be determined by measuring fluorescence emission intensities. In the following, a protocol for conjugation of proteins with fluorescein isothiocyanate (FITC) is given. FITC can be directly linked to the proteins as depicted in Figure 3 [22].

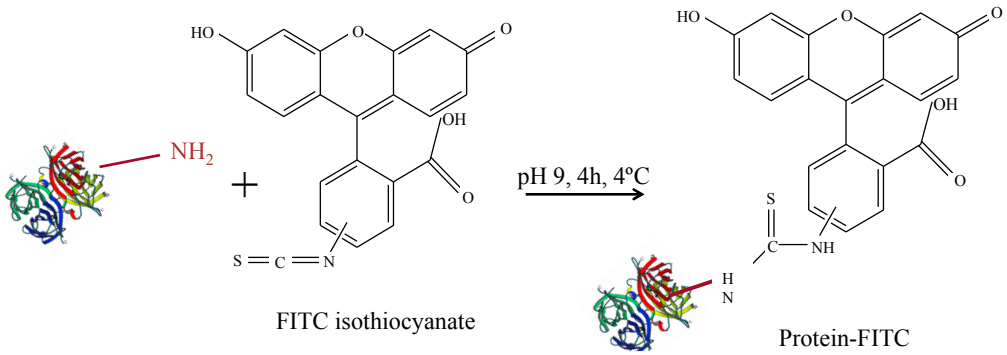

Figure 3. Scheme for FITC-labelling of proteins.

First, a calibration curve based on the Bradford assay [23] (Coomassie Blue, Thermo Scientific #23236, Hampton, NH, USA) to determine protein concentrations was obtained. Under the presence of proteins, a shift in the absorption spectrum of Coomassie Blue occurs and protein concentration is proportional (in a certain range) to the (offset-corrected) absorption A at 595 nm. The calibration curve was done following the fabricant specifications [24]. As protein standards, bovine serum albumin (BSA) was used (Thermo Scientific #23029). Two different calibration curves were recorded, one for high protein concentrations (working range of 100–1500 µg/mL protein concentrations C_P) and a second one for low protein concentrations (working range 1–25 µg/mL protein concentrations C_P). The standard solutions of different protein concentrations C_P were prepared as indicated in the protocol, using 2-(*N*-Morpholino)ethanesulfonicacidhydrate (MES) pH 6.5 as buffer. Following the indication of the guide, in order to get the high concentration curve, 10 µL of NP solution sample were mixed with 300 µL of Coomassie reagent, previously equilibrated at room temperature. To obtain the low concentration curve instead of using 10 µL NP sample and 300 µLCoomassie reagent, 150 µL of sample and 150 µL of reagent were used. After mixing for 30 s and incubating for 10 min for each protein concentration, C_P, the absorption of the protein—Coomassie Blue mix at 595 nm—was recorded with an UV/Vis absorption spectrometer (Agilent 8450 spectrometer, Palo Alto, CA, USA). Single-use plastic cuvettes were used to hold the samples. Samples were prepared by triplicate and measured individually. As an offset, the absorption of Coomassie Blue without protein was subtracted. The offset-corrected absorptions A are plotted *versus* the protein concentrations C_P in Figure 4. A polynomial fit was applied to obtain the final calibration curves.

FITC conjugation was performed using the following protocol. First, the concentration of proteins was determined with the Bradford method as described above. Then, a FITC stock solution was prepared in sodium borate buffer (SBB) at pH = 9, equaling 750 FITC molecules *per* protein. FITC was added to the proteins and the mixture was incubated for at least 4 h at 4 °C. For removal of unbound FITC, the sample was run through a PD 10 or a PD 25 column (depending on the solution volume, GE Healthcare #52-1308-00 and #28-9180-07, respectively, Little Chalfont, UK) and only the

protein containing fraction was collected. After the column purification the protein solution becomes diluted, the protein concentration C_P (of the now FITC-conjugated proteins) was determined again with the Bradford assay. A dilution series of the proteins was obtained and, for each protein concentration, the fluorescence intensity I at 519 nm (the emission wavelength of FITC) was determined. By plotting, the fluorescence intensity *versus* the protein concentration as calibration curve was obtained, *cf.* Figure 5.

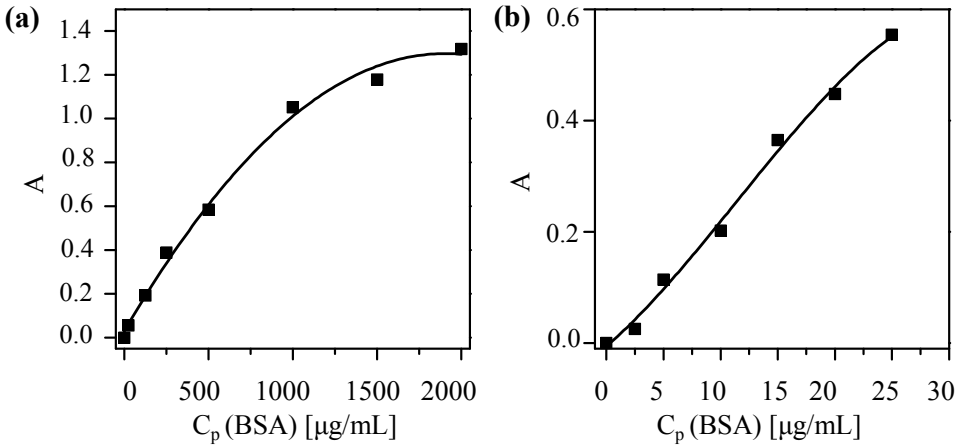

Figure 4. Coomassie assay calibration curves to determine the protein concentration C_P of solutions with (**a**) high concentration and (**b**) low concentrations by measuring the offset-corrected absorption A at 595 nm. The fitting curves are (**a**) $A(C_P) = 0.029 + (0.001\ \text{mL/µg})\cdot C_P - (3 \times 10^{-7}\ \text{mL}^2/\text{µg}^2)\cdot C_P^2$, and (**b**) $A(C_P) = -0.005 + (0.017\ \text{mL/µg})\cdot C_P - (6.789 \times 10^{-4}\ \text{mL}^2/\text{µg}^2)\cdot C_P^2 - (1.97 \times 10^{-5}\ \text{mL}^3/\text{µg}^3)\cdot C_P^3$ and the coefficients of determination (r^2) are equal to 0.994 and 0.989, respectively.

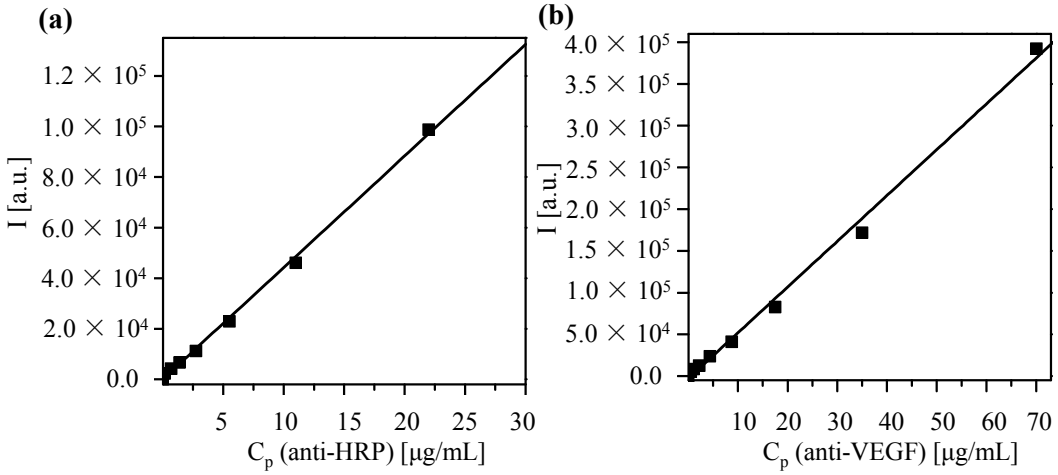

Figure 5. Calibration curve in which the fluorescence intensity I at 519 nm is determined for protein solutions of different concentration C_P. Data are shown for antibodies against (**a**) horseradish peroxidase (HRP) and (**b**) vascular endothelial growth factor (VEGF). A linear fit leads to the following correlation between fluorescence intensity I and concentration C_P: (**a**) $I(\text{C}_\text{P}) = I_0 + (\Delta I/\Delta \text{C}_\text{P})\cdot C_P = -464.28 + (4447.1\ \text{mL/µg})\cdot C_P$; (**b**) $I(C_P) = -3549.4 + (5498.3\ \text{mL/µg})\cdot C_P$. The coefficients of determination (r^2) are equal to 0.998 and 0.995 for HRP and VEGF, respectively.

2.3. Conjugation of NPs with Proteins

Here, an often used strategy based on *N*-(3-Dimethylaminopropyl)-*N*′-ethylcarbodiimide hydrochloride (EDC, Sigma Aldrich) was employed [22]. Note that while EDC chemistry is straightforward for the formation of peptide bonds between amine groups (here present on the protein ligands) and carboxyl groups (here present on the NP surface at the PEG terminal pointing towards solution), it may result in the formation of agglomerates, and thus characterization of the resulting conjugates is required. In addition, amine groups which belong to the functional part of the proteins can be deactivated upon linkage (reaction will occur statistically on the present amine groups of the proteins), and some proteins may lose their biological activity—in the present case, antibodies against HRP (anti-peroxidase, Sigma Aldrich) or against VEGF (anti-VEGF, R&D systems, AB-293-NA) where they are linked to the NPs. As described above, the antibodies were optionally tagged with FITC. In addition to the proteins, 5-(6)-carboxytetramethylrhodaminecadaverine ("TAMRA", Anaspec #81507, Fremont, CA, USA) was also attached as additional fluorophore via its amine group to the NP surface. Third ligand short metoxy-PEG-amine (amine-PE; M_w = 750 kDa, Rap Polymer #12750-2, Tuebingen, Germany) was attached via its amine group to the NP surface, in order to preserve the activity of the antibodies [25] and to prevent nonspecific protein absorption [26,27]. In other words, three different ligands (proteins, TAMRA, PEG) were attached to the PEGylated NPs using EDC chemistry. The ratios were chosen that *per* 1 Au NP 7.5 × 10^6 EDC molecules, 50 antibodies, 10^3 TAMRA molecules, and 2.5 × 10^4 amine-PEG molecules were added for reaction. The reaction scheme is presented in Figure 6.

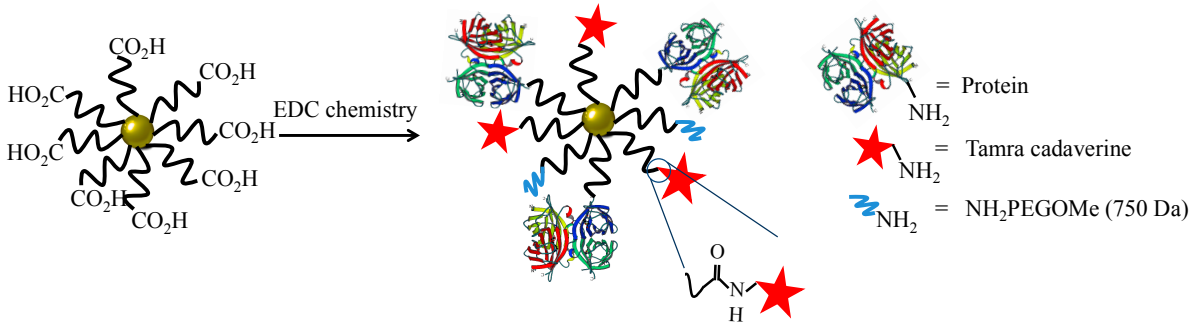

Figure 6. Scheme of the NP modification with antibody, dye and PEG (as passivating agent).

For the reaction 19.23 µL of Au, NPs dispersed in water (corresponding to 4pmol) with concentration c_{NP} = 208 nM were taken, and mixed with 923.5 µL of 4-morpholineethanesulfonic acid (MES, Sigma Aldrich #M8250, 50 mM, pH 6.5) and 57.3 µL of EDC stock solution (100 mg/mL). After 20 min, the sample with a total volume V = 1 mL containing the activated NPs was cleaned from unreacted EDC and the salts, using a pre-packed column PD-10 desalting column (GE healthcare #17-0851-01, Bucks, UK) equilibrated with MES (50 mM, pH 6.5). During this step, the NP volume was roughly diluted twice. In addition, using a high pH such as 8 was tried, with the motivation to take advantage of linking antibodies in an oriented manner [28], but the activation process was not working as well as at pH 6.5, and thus, throughout this work, pH 6.5 was used. The volume of the eluted NP solution was adjusted with MES buffer to 2 mL. Immediately after the NP cleaning, 30 µg of antibodies were added. After incubation for 15 min, 2 µg of TAMRA were added. Finally, after another 15 min of incubation,

75 µg of amine-PEG were added to block the remaining reactive carboxylic groups. The reaction mixture was incubated for another 1 h at room temperature and then incubated at 4 °C overnight. Unbound proteins, dye molecules, and PEG were removed by repetitive centrifugation (14,000 rpm 30 min), until no fluorescence was detected in the supernatant. This required at least five cleaning cycles (pelleting of NPs, discarding of supernatant, resuspending the NP pellet in fresh buffer). In the first washing step, 10 µL of sodium dodecylsulfate (SDS, 10%) was added to remove nonspecifically adsorbed dyes or proteins. Following this protocol, NPs conjugated with anti-HRP or anti-VEGF (with optional FITC label) were synthesized. As a control, the reaction was carried out without adding antibodies, but only TAMRA and PEG, leading to control NPs. In the following, the PEGylated Au NPs before bioconjugation will be referred to as Au-PEG NPs. The NPs after bioconjugation with anti-HRP, anti-VEGF, or without having antibody added will be referred to as Au-PEG-anti-HRP NPs, Au-PEG-anti-VEGF NPs, or Au-PEG-control NPs. In case the antibodies had been labelled with FITC, this is indicated as "*": Au-PEG-anti-HRP* NPs, Au-PEG-anti-VEGF* NPs.

In the vicinity of the Au surface, organic fluorophores may be quenched. Distance dependent measurements have been demonstrated that quenching can occur well up to separation distances of the fluorophores from the Au surface of 10 nm [29]. In the present work, no direct contact of fluorophores with the Au surface is possible due to the layer of 3 kDa PEG. This layer will keep the fluorophores at ≈4 nm distance to the Au surface [30]. In the case of TAMRA, conjugation directly to the PEG terminal pointing towards solution quenching does not impose any problem, as no quantitative fluorescence measurements are performed. The TAMRA merely serves as a label for qualitative fluorescence imaging of NPs that have been internalized by cells and thus quenching does not interfere with experiments. In the case of the FITC-labelled proteins, partial quenching of their fluorescence upon binding to the surface of the PEGylated Au NPs cannot be excluded. However, the proteins will randomly orient on the NP surface. Only in the case that the FITC attached to the protein is oriented towards the NP surface, significant quenching is expected, as in the case FITC attached to the protein is oriented towards solution, away from the NP surface, the distance between FITC and the Au surface is further increased by the size of the protein. Together with the PEG spacer, which is always present, one clearly cannot exclude quenching, though it is not estimated to play a huge role. Due to quenching, there is less fluorescence signal from proteins attached to the NP surface as in comparison to the fluorescence of the free proteins, which have been used for obtaining the calibration curve. In this way, in the procedure described here, the number of proteins attached per NP is underestimated.

2.4. Determination of the Number of Antibodies Bound per NP

The number of antibodies per NP ($R_{P/NP}$) can determined from separately measuring the protein concentration c_P and the NP concentration c_{NP} of NP-antibody conjugates:

$$R_{P/NP} = c_P/c_{NP} \quad (2)$$

The NP concentration can be obtained from the absorption spectra of the conjugates at the wavelengths of the surface plasmon peak, at which the antibodies barely absorb. The protein concentration is determined from fluorescence spectra (*cf.* Figure 7) and the calibration curve shown in Figure 4.

Upon excitation of FITC (at 494 nm), there is also some fluorescence of TAMRA, which however can be clearly distinguished from the FITC fluorescence (*cf.* the green curve in Figure 7). From the FITC fluorescence spectra (*cf.* the green curve in Figure 7), the emission I at 519 nm was determined. Based on the calibration curve given in Figure 5, the protein concentration C_P can be determined as:

$$C_P = (I - I_0)/(\Delta I/\Delta C_P) \quad (3)$$

using the fit parameters I_0 and $\Delta I/\Delta C_P$ from the calibration curve given in Figure 5. The mass concentration C_P of the proteins can be converted in molar concentrations c_P by using the molecular mass M_W of the proteins: $c_P = C_P/M_W$. The results as obtained for the Au-PEG-anti-HRP* and Au-PEG-anti-VEGF* NPs are given in Table 1, based on the data shown in Figures 5 and 7. For each sample, two different dilutions were measured.

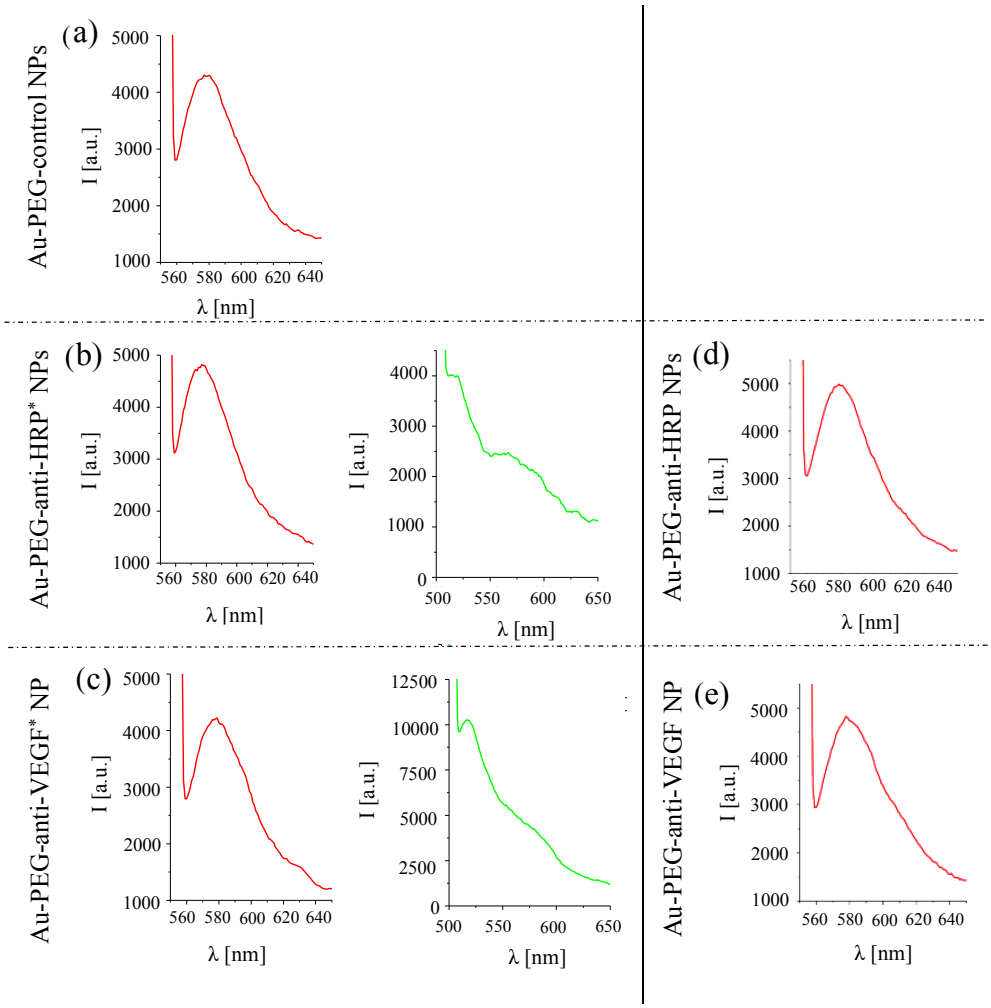

Figure 7. Left side: Fluorescence spectra recorded for (**a**) Au-PEG-control NPs, (**b**) Au-PEG-anti-HRP* NPs, and (**c**) Au-PEG-anti-VEGF* NPs at a NP concentration of c_{NP} = 2 nM. Excitation was performed at 545 nm (TAMRA, drawn in red) or at 494 nm (FITC, drawn in green). Fluorescence spectra were recorded under the same conditions as the spectra recorded for the calibration curve Figure 5. Right side: Fluorescence spectra recorded for (**d**) Au-PEG-anti-HRP NPs, and (**e**) Au-PEG-anti-VEGF NPs for TAMRA excitation (545 nm) at a NP concentration of c_{NP} = 2 nM.

Table 1. Summary of the calculations for the amount of proteins per nanoparticles (NP).

Sample	Au-PEG-anti-HRP* NPs	Au-PEG-anti-HRP* NPs	Au-PEG-anti-VEGF* NPs	Au-PEG-anti-VEGF* NPs
c_{NP} (nM)	2.2	1.5	2.0	0.5
M_W (g/mol)	150,000	150,000	150,000	150,000
$\Delta I/\Delta C_P$ (mL/µg) (*cf.* Figure 5)	4,447.1	4,447.1	5,498.3	5,498.3
$I_0 = I$ (C_P= 0) (a.u.) (*cf.* Figure 5)	−464.28	−464.28	−3,549.4	−3,549.4
I (a.u.) (*cf.* Figure 7)	3,999	2,420	10,212	2,600
C_P (µg/mL)	1.0	0.65	2.5	1.12
c_P (nM)	6.67	4.33	16.67	7.47
$R_P/_{NP}$	2.7	2.4	6.2	6.3

2.5. Physicochemical Characterization of the NP-Antibody Conjugates

As already mentioned, bioconjugation may change the colloidal properties of NPs. Thus, characterization should be also performed with the resulting samples. The UV/Vis absorption spectra shown in Figure 8 indicate that upon bioconjugation, no significant agglomeration occurred, as scattering for wavelengths >800 nm can be neglected.

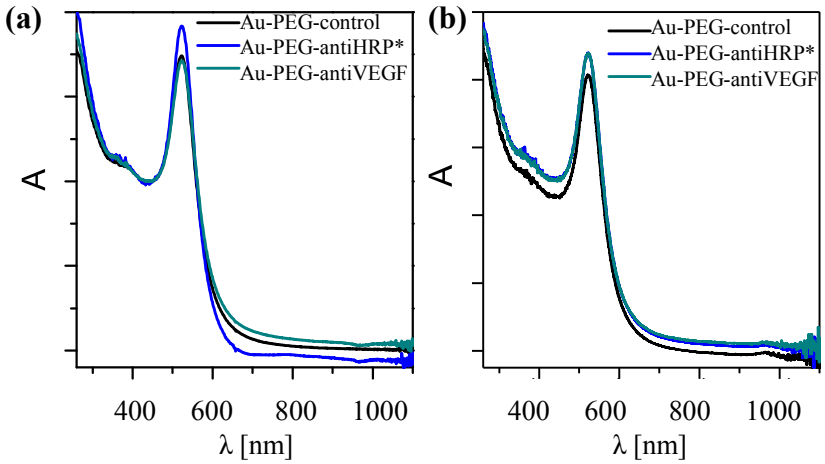

Figure 8. Normalized UV/Vis spectra of the NP-antibody conjugates. (**a**) Au-PEG-control, Au-PEG-anti-HRP*, and Au-PEG-anti-VEGF* NPs; (**b**) Au-PEG-control, Au-PEG-anti-HRP, and Au-PEG-anti-VEGF NPs. Spectra were recorded in a spectrometer Agilent 8453.

While UV/Vis absorption spectra can be a first indication about the presence of bigger agglomerates, it is hard to determine the existence of smaller agglomerates from these data. For this purpose, measurements of the hydrodynamic diameter d_h of the NPs are best suited. One common technique in this direction is dynamic light scattering (DLS; Malvern Zetasizer set-up). However, in the case of small NPs, proteins have similar size to the NPs and thus measurements in cell culture media containing serum are complicated [31]. In Figure 9, DLS measurement for the NP-antibody conjugates are displayed. The hydrodynamic diameters d_h as determined from these data (*cf.* Table 2) demonstrate that any larger agglomerates can be excluded. However, in general, no significant increase in size of the NPs upon antibody attachment could be observed, though the FITC fluorescence clearly proves the presence of the antibodies.

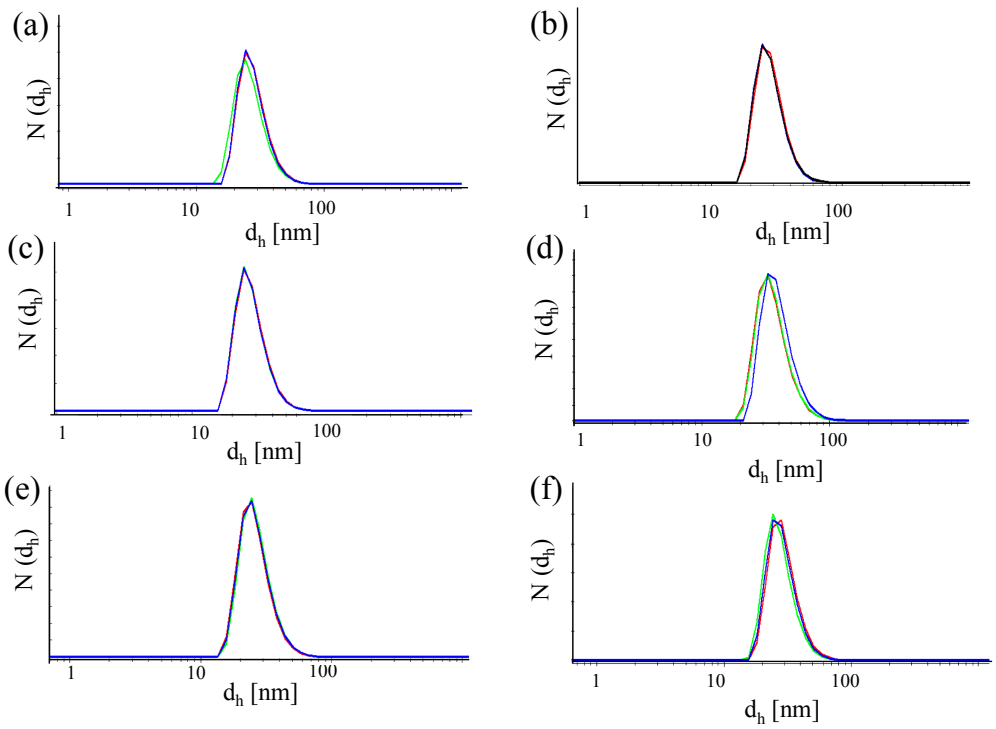

Figure 9. Number distribution N (d_h) of the hydrodynamic diameter recorded or different NPs. (**a**) Au-PEG NPs, (**b**) Au-PEG-control NPs, (**c**) Au-PEG-anti-HRP* NPs, (**d**) Au-PEG-anti-VEGF* NPs, (**e**) Au-PEG-anti-HRP NPs, and (**f**) Au-PEG-anti-VEGF NPs. The concentration of the NP solutions were $c_{NP} \approx 5$ nM, and the measurements were performed in milliQ water. Each sample was measured at least three times and the mean value of the hydrodynamic diameter was determined.

In the same Malvern Zetasizer set-up, the zeta-potential ζ was also determined based on laser Doppler anemometry, *cf.* Figure 10. The data shown in Table 2 show that despite attachment of antibodies, the NPs retained their negative zeta-potential. In the case of conjugation with antibodies without FITC, the NP-antibody conjugates have a less negative zeta potential than the NPs without attached antibodies.

As proteins can also nonspecifically adsorb to the surface of NPs, the conjugation reactions were repeated but without addition of EDC. In this way, all attached proteins are not covalently attached (as due to the lack of EDC, no amide bonds can be formed), but are nonspecifically attached to the NPs. These samples are termed Au-PEG/control, Au-PEG/anti-HRP, and Au-PEG/anti-VEGF NPs. Hydrodynamic diameters and zeta-potentials as determined with these NPs are enlisted in Table 3. There is less reduction of negative zeta potential upon presence of the antibodies. Thus, less antibodies are present per NP and, in this way, attachment of antibodies under the presence of EDC should be mainly of covalent nature.

Table 2. Summary of mean hydrodynamic diameters and zeta-potentials determined in water.

Sample	Au-PEG NPs	Au-PEG-Control NPs	Au-PEG-anti-HRP* NPs	Au-PEG-anti-VEGF* NPs	Au-PEG-anti-HRP NPs	Au-PEG-anti-VEGF NPs
d_h (nm)	27.4 ± 0.4	27.8 ± 0.8	28.0 ± 0.2	38.0 ± 1.9	27.0 ± 0.6	28.9 ± 0.9
ζ (mV)	−32.8 ± 0.6	−20.0 ± 0.9	−18.4 ± 1.6	−24.1± 3.8	−6.3 ± 0.2	−11.8 ± 0.7

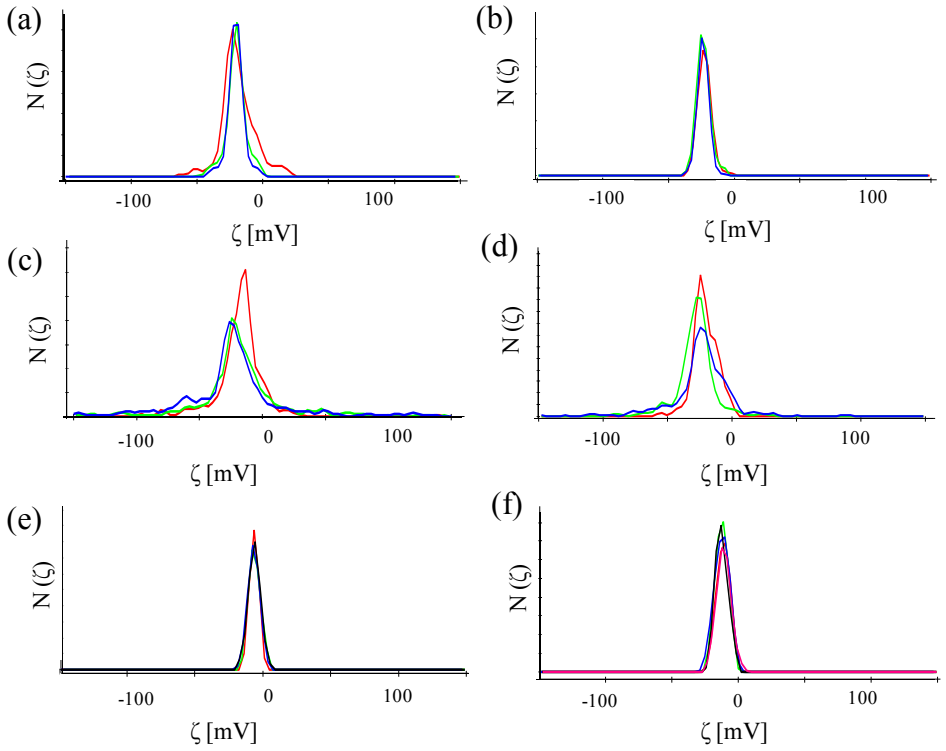

Figure 10. Number distribution N (ζ) of the zeta-potential of (**a**) Au-PEG NPs, (**b**) Au-PEG-control NPs, (**c**) Au-PEG-anti-HRP* NPs, (**d**) Au-PEG-anti-VEGF* NPs, (**e**) Au-PEG-anti-HRP NPs, and (**f**) Au-PEG-anti-VEGF NPs. The concentration of the NP solutions were $c_{NP} \approx 5$ nM, and the measurements were performed in milliQ water. Each sample was measured at least three times and the mean value of the zeta-potential was determined.

Table 3. Summary of mean hydrodynamic diameters and zeta-potentials determined in water.

Sample	Au-PEG NPs	Au PEG-Control NPs	Au-PEG-anti-HRP NPs	Au-PEG-anti-VEGF NPs
d_h (nm)	27.4 ± 0.4	27.4 ± 1.6	26.1 ± 2.1	29.3 ± 1.7
ζ (mV)	−32.8 ± 0. 6	−30.1 ± 1.2	−24.3± 0.9	−31.4± 1.3

2.6. NP Interaction with Cells

NPs can be internalized by cells via endocytosis, as they may trigger toxic effects. In the following, this is investigated for two different cell lines, human adenocarcinoma alveolar basal epithelial cells (A549) and human umbilical vein endothelial cells (HUVECs). A549 cells, purchased from ATCC, were cultured in Dulbecco's Modified Eagle's Medium (DMEM, Sigma Aldrich) supplemented with 10% fetal bovine serum, 2 mM L-glutamine (Sigma Aldrich), and 100 U/mL penicillin/streptomycin (Sigma Aldrich). HUVECs, purchased fromPromoCell, were cultured in Endothelial Cell Basal Medium (ECBM, PromoCell, Heidelberg, Germany) supplemented with 2% fetal calf serum (PromoCell), 0.4% Endothelial Cell Growth Supplement (PromoCell), Epidermal Growth Factor (0.1 ng/mL, PromoCell), Basic Fibroblast Growth Factor (1 ng/mL, PromoCell), heparin (90 µg/mL, PromoCell) and hydrocortisone (1 µg/mL, PromoCell). The cells were grown at 37 °C in a humidified atmosphere containing 5% CO_2.

For uptake experiments, cells were incubated with NPs and after 24 h the amount of incorporated NPs was determined. A549 cells and HUVECs were incubated with Au-PEG NPs of different concentration within medium with or without serum. After 4 h of incubation, the cells were intensively washed and further cultured. Since serum components are known to alter physicochemical characteristics of NPs, we studied their internalization in the presence and absence of serum. Twenty-four hours after adding the NPs, the cells were lysed and the samples were analyzed for their gold content with inductively coupled plasma mass spectrometry (ICP-MS). The protein content of each sample was determined by the Bradford assay (Bio-Rad, Hercules, CA, USA). The results are presented in Figure 11 as ppb of gold per mg of protein.

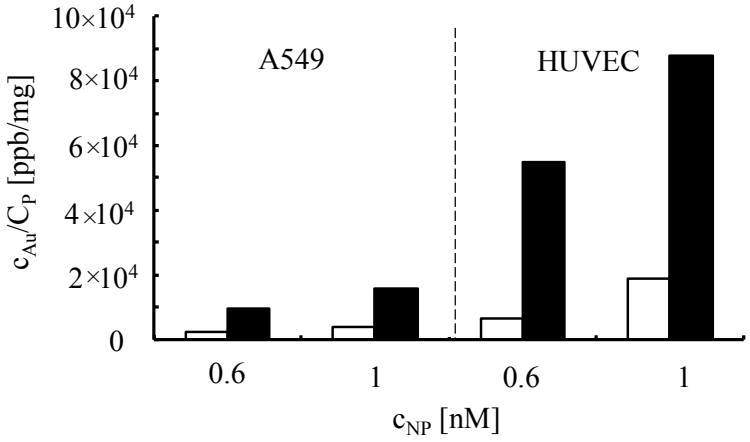

Figure 11. Internalization of Au-PEG NPs by A549 cells and HUVECs. A549 cells and HUVECs were incubated with Au-PEG NPs of c_{NP} = 0.6 nM and c_{NP} = 1 nM concentration cells in medium with (white bars) or without (black bars) serum. Twenty-four hours after adding the particles, the gold concentration c_{Au} and the protein concentration C_P was determined.

For all formulations tested, more NPs were taken up if they were incubated with the cells in the absence of serum, which is consistent with previous findings [31]. We speculate that proteins and other constituents of serum that interact with the NPs change their properties in such a way that they are internalized by an endocytic pathway as it has been previously described [32]. Interestingly, the PEGylated NPs were taken up well by cells. This indicates that coating Au NPs with PEG does not completely preclude their internalization. In addition, NP-antibody conjugates were incorporated by cells, as shown in the fluorescence microscopyimages in Figure 12.

The toxic effect of the NPs to the cells was analyzed with a standard viability assay. Ten thousand cells per well were seeded in 96-well-plates one day before planned experiments. A549 cells and HUVECs were incubated for 4 h with Au-PEG NPs at different concentrations c_{NP} ranging from 0.2 to 1 nM. Subsequently, the cells were intensively washed and further cultured. Cell viability was evaluated 24 h after NPs had been added to the cells by the MTT assay (Roche, Germany) according to the manufacturer's instructions, *cf.* Figure 13. The assay is based on conversion of the tetrazolium dye 3-(4,5-dimethylthiazol-2-yl)-2.5-diphenyltetrazoliumbromide to its insoluble formazan, which is purple in color. Data demonstrate that Au-PEG NPs reduce cellular viability in a concentration-dependent manner.

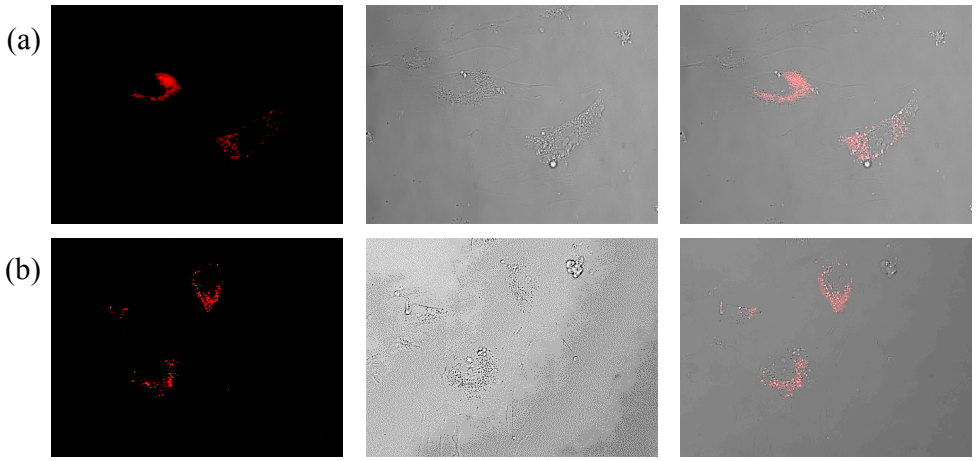

Figure 12. Internalization of functionalized Au NPs by human umbilical vein endothelial cells. HUVECs were exposed to TAMRA-labeled Au NPs functionalized with (**a**) anti-VEGF (Au-PEG-antiVEGF NPs), and (**b**) anti-HRP antibodies (Au-PEG-anti-HRP NPs). The NP-antibody conjugates were removed after 2 h and the cells were intensively washed. The images were taken 1 h later by employing a Zeiss fluorescent microscope. Images show the fluorescence and bright field channel, as the overlay of both channels.

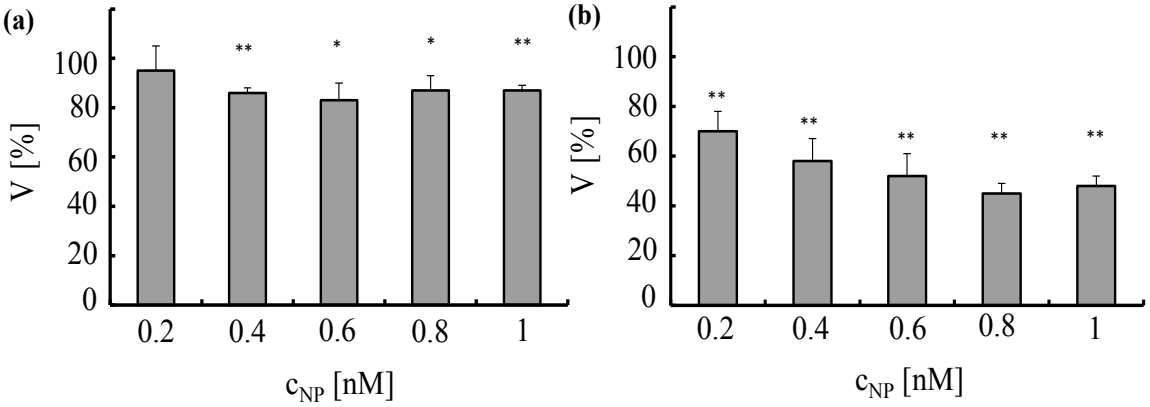

Figure 13. Toxicity induced by Au-PEG NPs in A549 cells (**a**) and HUVECs (**b**)Au-PEG NPs, at concentrations ranging from c_{NP} = 0.2 to 1 nM, were incubated for 4 h with A549 cells or HUVECs in media containing serum. Cell viability (V) was determined 24 h after adding the NPs to the cells. The viability was normalized to 100% for untreated control cells, *$p < 0.01$; **$p < 0.001$(versus control value).

2.7. Effect of Au NPs with Anti-VEGF on VEGF Stimulation of Cells

Under physiological conditions VEGF binds to its receptor (VEGFR) present on the membrane of HUVECs, which initiates cascades of signals that stimulate many processes including angiogenesis [33,34]. VEGF receptors convey information to other signal transduction molecules via autophosphorylation of distinct residues in their structure. If VEGF binds to its receptor, HUVECs proliferate. If one blocks the receptor with an antibody [33,35] or NP [36,37], there is reduced proliferation. Antibody-based therapies relay on a sequestering of VEGF molecules by specific antibodies. In this way, VEGF binding to its receptor is prevented [38].

In a first set of experiments, we tested the response of HUVECs to stimulation with VEGF. To that end, the cells were exposed for 24 or 48 h to VEGF at different concentrations (C_{VEGF} = 2–16 ng/mL). As demonstrated in Figure 14, VEGF stimulated proliferation of HUVECs in a dose-dependent manner. At concentrations ≥ 10 ng/mL the number of cells in culture increased by more than 20% after 24 h and by more than 50% after 48 h. Based on these results, we chose to stimulate HUVECs with VEGF at concentrations of 12 and 16 ng/mL in all subsequent experiments.

Next, in order to verify whether proliferation elicited by VEGF can be neutralized by anti-VEGF antibodies, we pre-incubated HUVECs with the antibody, which was followed by stimulation with VEGF. The results presented in Figure 15 demonstrate that soluble anti-VEGF antibodies inhibit proliferation of endothelial cells induced by VEGF in a dose dependent manner. Note that this is not due to blocking of the VEGF receptor but by binding of anti-VEGF to VEGF, which cancels the biological activity of VEGF.

We next assessed whether a similar effect could be achieved by the anti-VEGF antibodies attached to Au NPs (Au-PEG-anti-VEGF NPs). HUVECs were first incubated with Au-PEG-anti-VEGF NPs for 2 h. This was followed by the stimulation with VEGF for 24 and 48 h. To verify whether the observed effects were specific, in this set of experiments, we also tested Au NPs functionalized with the irrelevant antibody anti-HRP (Au-PEG-anti-HRP NPs).

As demonstrated in Figure 16, Au NPs functionalized with anti-VEGF antibody (Au-PEG-anti-VEGF NPs) exhibited some effect on the proliferation of HUVECs upon stimulation with VEGF over a longer period of time. However, the same trend was observed for NP carrying anti-HRP (Au-PEG-anti-HRP NPs). Therefore, it is likely that the recorded decrease in the number of cells in culture was not caused by a specific interaction of the functionalized Au NPs with VEGF but rather was associated with NP induced toxic effects on cells.

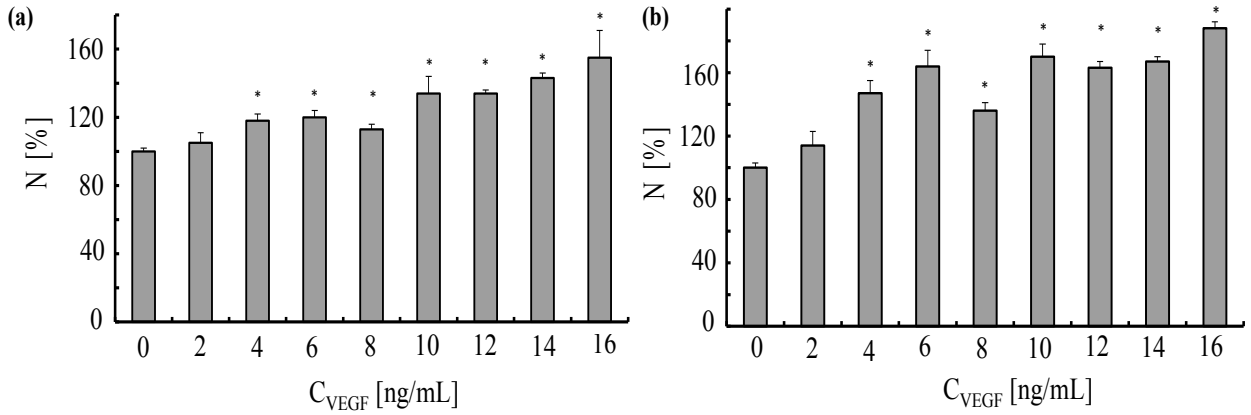

Figure 14. Response of human umbilical vein endothelial cells to vascular endothelial growth factor. The endothelial cells were plated in 96-well plates (5000 cells/well) one day before planned experiments. The cells were exposed for 24 h (**a**) and 48 h (**b**) to different concentrations C_{VEGF} of VEGF. The normalized numbers of cells N in culture were evaluated by performing a proliferation test. Data correspond to the mean value ± standard deviation obtained from n = 4 experiments, *$p < 0.001$ (versus control value, no VEGF).

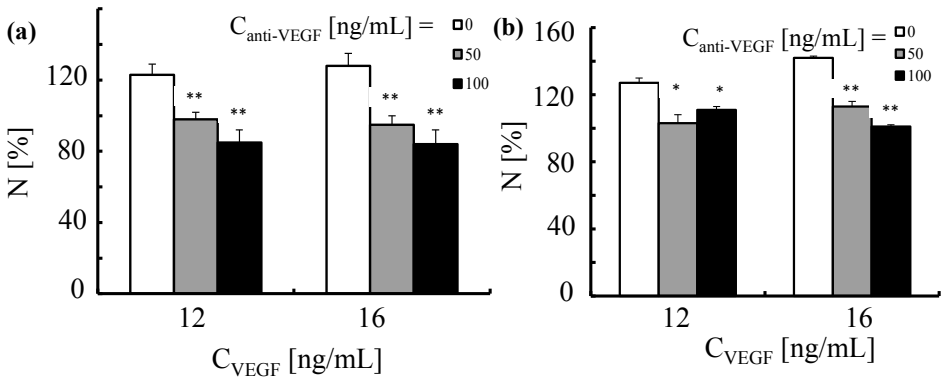

Figure 15. Proliferation of human umbilical vein endothelial cells triggered by VEGF and neutralization induced by anti-VEGF antibody. HUVECs were first exposed for 2 h to anti-VEGF antibody at two concentrations ($C_{\text{anti-VEGF}}$ = 50 and 100 ng/mL). This was followed by the incubation with VEGF (C_{VEGF} = 12 and 16 ng/mL) for (**a**) 24 and (**b**) 48 h. The number of cells was normalized to 100% for untreated control cells. *$p < 0.01$; **$p < 0.001$(*versus* cells treated with VEGF only).

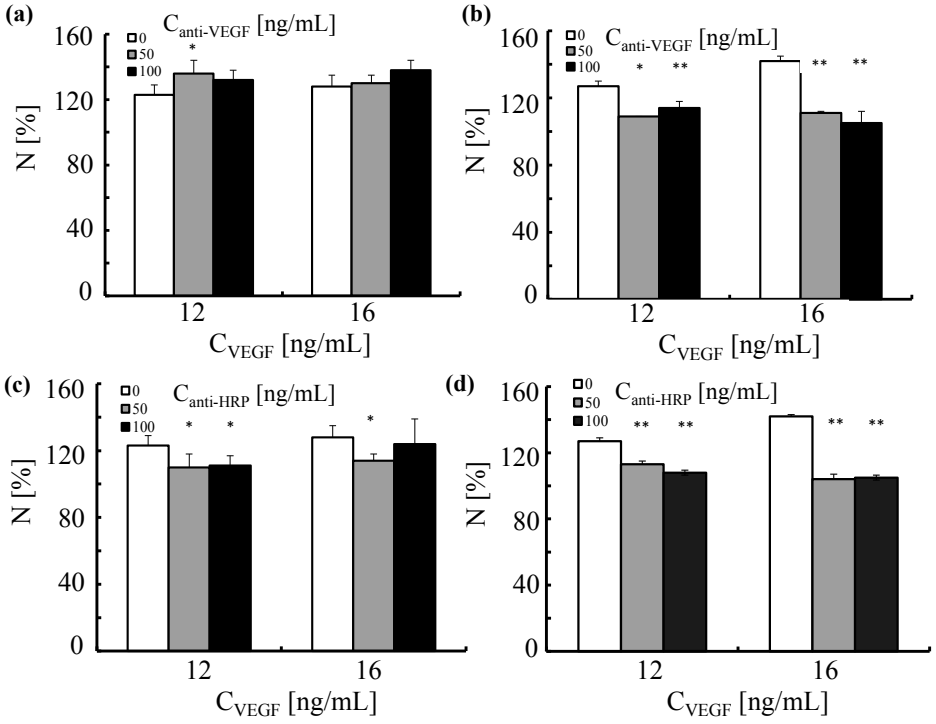

Figure 16. The effect of Au NPs functionalized with anti-VEGF or anti-HRP antibody on the proliferation of human umbilical vein endothelial cells triggered by VEGF. HUVECs were first exposed to Au NPs functionalized with (**a**,**b**) anti-VEGF or (**c**,**d**) anti-HRP antibodies. The NPs were added to the cells to reach concentrations of the antibodies equal to $C_{\text{anti-VEGF}}$ and $C_{\text{anti-HRP}}$ of 50 (grey bars) and 100 ng/L (black bars) (adjusted by the NP concentration by knowing the number $R_{P/NP}$ of antibodies per NP as shown in Table 1). This was followed by the incubation with VEGF (C_{VEGF} = 12 and 16 ng/mL) for (**a**,**c**) 24h and (**b**,**d**) 48 h. The number of cells was normalized to 100% for untreated control cells. *$p < 0.01$; **$p < 0.001$ (*versus* cells treated with VEGF only).

3. Conclusions

A protocol for functionalizing Au NPs with antibodies has been presented, together with characterization procedures, which quantify the number of antibodies per NP. It is demonstrated that biocojungation did not induce agglomeration. While successful bioconjugation could be demonstrated, this does not provide information about the biological activity of the attached antibodies. For this, profound characterization is also required. With the presented data, a biological effect of the NP-antibodies is demonstrated. However, this example demonstrates that such data can be misleading. As the same effect was observed with NP-antibody conjugates with an irrelevant antibody, the effect can't be ascribed to a specific antibody effect but rather to general NP-induced toxicity. This example points out that antibodies can be deactivated, and that controls with irrelevant antibodies are required to demonstrate specific biological activity of NP-antibody conjugates.

Acknowledgements

This work was supported by the German Research Foundation (DFG GRK 1782 to Wolfgang J. Parak) and by the European Commission (grant FutureNanoNeeds to Wolfgang J. Parak). Beatriz Pelaz acknowledges a fellowship from the Alexander von Humboldt Foundation. Gamze Tan thanks TUBITAK for financial support through the 2214A-International Research Fellowship Programme. Qian Zhang is grateful to a Chinese Scholarship Council (CSC) for a fellowship. Mahmoud G. Soliman thanks the Youssef Jameel Foundation for a PhD fellowship.

Author Contributions

Gamze Tan, Daniel Valdeperez, Joanna Rejman and Beatriz Pelaz performed the experiments; Gamze Tan, Mehmet A. Onur, Joanna Rejmanand Beatriz Pelaz analyzed the data. Karsten Kantner, Mahmoud G. Soliman, Daniel Valdeperez, Qian Zhang and Pablo del Pino contributed reagents/materials/analysis tools; Wolfgang J. Parak, Joanna Rejmanand Beatriz Pelaz wrote the paper. Wolfgang J. Parak, Gamze Tan, Mehmet A. Onur, Joanna Rejmanand and Beatriz Pelaz conceived and designed the experiments.

Conflicts of Interest

The authors declare no conflict of interest.

References

1. Gonzalez, E.; Arbiol, J.; Puntes, V.F. Carving at the nanoscale: Sequential galvanic exchange and kirkendall growth at room temperature. *Science* **2011**, *334*, 1377–1380.
2. Ye, X.; Jin, L.; Caglayan, H.; Chen, J.; Xing, G.; Zheng, C.; Doan-Nguyen, V.; Kang, Y.; Engheta, N.; Kagan, C.R.; *et al.* Improved size-tunable synthesis of monodisperse gold nanorods through the use of aromatic additives. *ACS Nano* **2012**, *6*, 2804–2817.

3. Osorio-Cantillo, C.; Santiago-Miranda, A.N.; Perales-Perez, O.; Xin, Y. Size-and phase-controlled synthesis of cobalt nanoparticles for potential biomedical applications. *J. Appl. Phys.* **2012**, *111*, doi:10.1063/1.3676620.
4. Pelaz, B.; del Pino, P. Synthesis applications of gold nanoparticles *Front. Nanosci.* **2012**, *4*, 3–33.
5. Li, N.; Zhao, P.; Astruc, D. Anisotropic gold nanoparticles: Synthesis, properties, applications, and toxicity. *Ang. Chem. Int. Ed. Engl.* **2014**, *53*, 1756–1789.
6. Leung, K.C.F.; Xuan, S.H.; Zhu, X.M.; Wang, D.W.; Chak, C.P.; Lee, S.F.; Ho, W.K.W.; Chung, B.C.T. Gold and iron oxide hybrid nanocomposite materials. *Chem. Soc. Rev.* **2012**, *41*, 1911–1928.
7. Parak, W.J. Complex colloidal assembly. *Science* **2011**, *334*, 1359–1360.
8. Wilhelm, S.; Kaiser, M.; Wuerth, C.; Heiland, J.; Carrillo-Carrion, C.; Muhr, V.; Wolfbeis, O.S.; Parak, W.J.; Resch-Genger, U.; Hirsch, T. Water dispersible upconverting nanoparticles: Effects of surface modification on their luminescence and colloidal stability. *Nanoscale* **2015**, *7*, 1403–1410.
9. Rivera-Gil, P.; Jimenez de Aberasturi, D.; Wulf, V.; Pelaz, B.; del Pino, P.; Zhao, Y.; de la Fuente, J.; Ruiz de Larramendi, I.; Rojo, T.; Liang, X.-J.; *et al.* The challenge to relate the physicochemical properties of colloidal nanoparticles to their cytotoxicity. *Acc. Chem. Res.* **2013**, *46*, 743–749.
10. Nazarenus, M.; Zhang, Q.; Soliman, M.G.; del Pino, P.; Pelaz, B.; Carregal_Romero, S.; Rejman, J.; Rothen-Ruthishauser, B.; Clift, M.J.D.; Zellner, R.; *et al. In vitro* interaction of colloidal nanoparticles with mammalian cells: What have we learned thus far? *Beilstein J. Nanotechnol.* **2014**, *5*, 1477–1490.
11. Itano, M.S.; Neumann, A.K.; Liu, P.; Zhang, F.; Gratton, E.; Parak, W.J.; Thompson, N.L.; Jacobson, K. DC-sign and influenza hemagglutinin dynamics in plasma membrane microdomains are markedly different. *Biophys. J.* **2011**, *100*, 2662–2670.
12. Colombo, M.; Mazzucchelli, S.; Montenegro, J.M.; Galbiati, E.; Corsi, F.; Parak, W.J.; Prosperi, D. Protein oriented ligation on nanoparticles exploiting O6-alkylguanine-DNA transferase (SNAP) genetically encoded fusion. *Small* **2012**, *8*, 1492–1497.
13. Montenegro, J.-M.; Grazu, V.; Sukhanova, A.; Agarwal, S.; Fuente, J.M.D.L.; Nabiev, I.; Greiner, A.; Parak, W.J. Controlled antibody/(bio-) conjugation of inorganic nanoparticles for targeted delivery. *Adv. Drug Deliver. Rev.* **2013**, *65*, 677–688.
14. Turkevich, J.; Stevenson, P.C.; Hillier, J. A study of the nucleation and growth processes in the synthesis of colloidal golde. *J. Discuss. Faraday Soc.* **1951**, 55–75.
15. Ojea-Jimenez, I.; Bastus, N.G.; Puntes, V. Influence of the sequence of the reagents addition in the citrate-mediated synthesis of gold nanoparticles. *J. Phys. Chem. C* **2011**, *115*, 15752–15757.
16. Kimling, J.; Maier, M.; Okenve, B.; Kotaidis, V.; Ballot, H.; Plech, A. Turkevich method for gold nanoparticle synthesis revisited. *J. Phys. Chem. B* **2006**, *110*, 15700–15707.
17. Bastus, N.G.; Comenge, J.; Puntes, V. Kinetically controlled seeded growth synthesis of citrate-stabilized gold nanoparticles of up to 200 nm: Size focusing *versus* ostwald ripening. *Langmuir* **2011**, *27*, 11098–11105.
18. Liz-Marzán, L.M. Nanometals: Formation and color. *Mater. Today* **2004**, *7*, 26–31.

19. Haiss, W.; Thanh, N.T.K.; Aveyard, J.; Fernig, D.G. Determination of size and concentration of gold nanoparticles from UV-Vis spectra. *Anal. Chem.* **2007**, *79*, 4215–4221.
20. Kanaras, A.G.; Kamounah, F.S.; Schaumburg, K.; Kiely, C.J.; Brust, M. Thioalkylated tetraethylene glycol: A new ligand for water soluble monolayer protected gold clusters. *Chem. Commun.* **2002**, *2002*, 2294–2295.
21. Pelaz, B.; Grazu, V.; Ibarra, A.; Magen, C.; del Pino, P.; de la Fuente, J.M. Tailoring the synthesis and heating ability of gold nanoprisms for bioapplications. *Langmuir* **2012**, *28*, 8965–8970.
22. Hermanson, G.T. *Bioconjugate Techniques*; Academic Press: San Diego, CA, USA, 2008.
23. Bradford, M.M. A rapid and sensitive method for the quantitation of microgram quantities of protein utilizing the principle of protein-dye binding. *Anal. Biochem.* **1976**, *72*, 248–254.
24. Thermo Scientific Pierce. Available online: http://www.Piercenet.Com/instructions/2160229.pdf (accessed on 1 April 2015).
25. Dai, Q.; Walkey, C.; Chan, W.C. Polyethylene glycol backfilling mitigates the negative impact of the protein corona on nanoparticle cell targeting. *Angew. Chem. Int. Ed.* **2014**, *53*, 5093–5096.
26. Kingshott, P.; Thissen, H.; Griesser, H.J. Effects of cloud-point grafting, chain length, and density of PEG layers on competitive adsorption of ocular proteins. *Biomaterials* **2002**, *23*, 2043–2056.
27. Xie, J.; Xu, C.; Kohler, N.; Hou, Y.; Sun, S. Controlled pegylation of monodisperse Fe_3O_4 nanoparticles for reduced non-specific uptake by macrophage cells. *Adv. Mater.* **2007**, *19*, 3163–3166.
28. Puertas, S.; Batalla, P.; Moros, M.; Polo, E.; del Pino, P.; Guisan, J.M.; Grazu, V.; de la Fuente, J.M. Taking advantage of unspecific interactions to produce highly active magnetic nanoparticle-antibody conjugates. *ACS Nano* **2011**, *5*, 4521–4528.
29. Dulkeith, E.; Ringler, M.; Klar, T.A.; Feldmann, J.; Muñoz Javier, A.; Parak, W.J. Gold nanoparticles quench fluorescence by phase induced radiative rate suppression. *Nano Lett.* **2005**, *5*, 585–589.
30. Sperling, R.A.; Liedl, T.; Duhr, S.; Kudera, S.; Zanella, M.; Lin, C.-A.J.; Chang, W.H.; Braun, D.; Parak, W.J. Size determination of (bio-) conjugated water-soluble colloidal nanoparticles: A comparison of different techniques. *J. Phys. Chem. C* **2007**, *111*, 11552–11559.
31. Hühn, D.; Kantner, K.; Geidel, C.; Brandholt, S.; de Cock, I.; Soenen, S.J.H.; Rivera Gil, P.; Montenegro, J.-M.; Braeckmans, K.; Müllen, K.; *et al.* Polymer-coated nanoparticles interacting with proteins and cells: Focusing on the sign of the net charge. *ACS Nano* **2013**, *7*, 3253–3263.
32. Lehmann, A.D.; Parak, W.J.; Zhang, F.; Ali, Z.; Röcker, C.; Nienhaus, G.U.; Gehr, P.; Rothen-Rutishauser, B. Fluorescent-magnetic hybrid nanoparticles induce a dose-dependent increase in proinflammatory response in lung cells *in vitro* correlated with intracellular localization. *Small* **2010**, *6*, 753–762.
33. Neufeld, G.; Cohen, T.; Gengrinovitch, S.; Poltorak, Z. Vascular endothelial growth factor (VEGF) and its receptors. *FASEB J.* **1999**, *13*, 9–22.
34. Hanahan, D. Signaling vascular morphogenesis and maintenance. *Science* **1997**, *277*, 48–50.
35. Sullivan, L.A.; Brekken, R.A. The VEGF family in cancer and antibody-based strategies for their inhibition. *mAbs* **2010**, *2*, 165–175.
36. Bhattacharya, R.; Mukherjee, P.; Xiong, Z.; Atala, A.; Soker, S.; Mukhopadhyay, D. Gold nanoparticles inhibit VEGF165-induced proliferation of huvec cells. *Nano Lett.* **2004**, *4*, 2479–2481.

37. Bartczak, D.; Muskens, O.L.; Nitti, S.; Millar, T.M.; Kanaras, A.G. Nanoparticles for inhibition of *in vitro* tumour angiogenesis: Synergistic actions of ligand function and laser irradiation. *Biomater. Sci.* **2015**, *3*, 733–741.
38. Niu, G.Q.; Castro, C.H.; Nguyen, N.; Sullivan, S.M.; Hughes, J.A. *In vitro* cytotoxic activity of cationic paclitaxel nanoparticles on MDR-3T3 cells. *J. Drug Target.* **2010**, *18*, 468–476.

© 2015 by the authors; licensee MDPI, Basel, Switzerland. This article is an open access article distributed under the terms and conditions of the Creative Commons Attribution license (http://creativecommons.org/licenses/by/4.0/).

Comparison of the *in vitro* uptake and toxicity of collagen- and synthetic polymer-coated gold nanoparticles

Oana T. Marisca[1,2], Karsten Kanter[1], Christian Pfeiffer[1], Qian Zhang[1], Beatriz Pelaz[1], Nicolae Leopold[2], Wolfgang J. Parak[1,3], Joanna Rejman[1,4*]

[1]Fachbereich Physik, Philipps Universität Marburg, Marburg, Germany
[2]Facultatea de Fizică, Universitatea Babeş-Bolyai, Cluj-Napoca, Romania
[3]CIC Biomagune, San Sebastian, Spain
[4] Dr. von Hauner Children's Hospital, Ludwig Maximilians University, Munich, Germany
*corresponding author: j_rejman@hotmail.com

Abstract

We studied physico-chemical properties (size, shape, zeta-potential), cellular internalisation and toxicity of gold nanoparticles (NPs) stabilised with the most abundant mammalian protein, collagen. The properties of these gold NPs were compared with the same size gold NPs coated with the synthetic poly(isobutylene-*alt*-maleic anhydride (PMA). Intracellular uptake and cytotoxicity were assessed in two cell lines (cervical carcinoma and lung adenocarcinoma cells) by employing inductive coupled plasma-mass spectrometry (ICP-MS) analysis and a cell viability assay based on 3-(4,5-dimethylthiazol-2-yl)-2,5-diphenyltetrazolium bromide (MTT), respectively. We found that the collagen-coated gold NPs exhibit lower cytotoxicity but higher uptake levels than PMA-coated gold NPs. These results demonstrate that the surface coating of Au NPs plays a decisive role in their biocompatibility.

Introduction

The development of new biocompatible nano-materials is an exponentially growing field of research. For example, the number of potential biomedical applications for gold nanoparticles (Au NPs) has expanded impressively in recent years. A vast part of this research is dedicated to the synthesis of Au NPs which could be employed in various medical fields [1] such as theranostics. They have been proposed as delivery systems to target drugs to diseased cells, tissues and organs and as contrast agents to enhance imaging in time-resolved optical tomography. Moreover, they can be combined with Raman reporters for detection purposes using surface-enhanced Raman scattering, SERS [2,3]. For many of these applications it is essential that the carrier system is biocompatible. The biocompatibility of NPs not only depends on their physicochemical properties associated with the bulk of the NPs, such as size or shape, but also on properties associated with the type of material used for their surface coating, such as Zeta-potential [4]. Although the inertness of gold as such is in general not questioned, the stabilizing coating required to prevent aggregation of Au NPs might induce significant toxicity. As has been demonstrated extensively for other particulate drug systems, such as liposomes, a very important phenomenon governing the fate of Au NPs in living cells as well as in cell culture systems is the adsorption of a protein layer ("corona") on the NP surface. Depending on NP size, shape and charge a variety of different proteins might adsorb and thus determine not only the degree and mode of uptake and toxicity, but also the types of cells involved in the uptake and/or elimination process [5-7].
In this study, we compared two Au NP systems differing in surface coating in terms to their interaction with cells and culture media. One system was coated with a synthetic polymer, dodecylamine-modified poly(isobutylene-*alt*-maleic anhydride (PMA) [8,9], and the other with a protein, collagen. The coated Au NPs were characterized with spectroscopic and microscopic techniques. To assess how the surface coating affects cell-NP interactions, internalization and cytotoxicity tests were performed in two cancer cell lines: cervical carcinoma (HeLa) and lung adenocarcinoma (A549) cells. The uptake of Au NPs was quantitatively evaluated by inductive coupled plasma-mass spectrometry (ICP-MS), and intracellular NP localization was visualized with fluorescence microscopy. Cell viability was probed with the 3-(4,5-dimethylthiazol-2-yl)-2,5-diphenyltetrazolium bromide (MTT) assay [10,11].

2. Materials and methods

2.1 Synthesis of collagen-coated Au NPs

Collagen has both a reducing and a stabilizing role in Au NP formation. A stock solution of gold salt was prepared by dissolving 1 g hydrogen tetrachloraurate (III) hydrate (99.9% metal basis, Alfa Aesar, Germany) in 50 mL ultrapure water. A solution of collagen was prepared by mixing 10 mL ultrapure water with 0.02 g of collagen from bovine Achilles tendon (Sigma-Aldrich, Darmstadt, Germany) in the presence of 500 µL hydrochloric acid 37% (Sigma Aldrich, Darmstadt, Germany). 1.5 mL of collagen solution (0.02 g collagen in 10 mL water) was mixed with 0.5 mL ethanol. Subsequently, 90 mL of ultrapure water were added to the collagen-ethanol solution which was then mixed with 1 mL of gold salt solution. The mixture was heated and stirred until boiling. When it started to boil, the solution was neutralized by quickly adding 2 mL of 1% sodium hydroxide and the heating was turned off. Instantly, the solution turned into a wine-red color and its pH was 7. Sodium hydroxide (Fluka, Netherlands), hydrogen peroxide 10% (AppliChem, Germany), ethanol, sodium chloride (Merck, Darmstadt, Germany) were of analytical grade. All solutions were

prepared in ultrapure water with a resistance higher than 18 MΩ (Direct-Q 3 UV, Millipore). The protocol is given in full detail in the Supporting Information.

2.2 Fluorescence-labelling of collagen-coated Au NPs

Collagen-coated Au NPs were filtered three times and then suspended in bicarbonate buffer pH = 8.6. Their concentration was calculated from the UV-vis absorption spectrum (molar extinction coefficient $\varepsilon = 2.03 \cdot 10^7\ M^{-1}cm^{-1}$) [12]. 1 mg of Dy647 (Dyomics, Germany) was dissolved in 1 mL of bicarbonate buffer pH = 8.6. Then 200 µL collagen Au NPs (2.8 µM) were added to 750 µL dye solution in an Eppendorf tube and allowed to mix for 3 h. The mixture of the dye and the collagen Au NPs was then filtered in 5 steps and the NPs were suspended in water. After sterile filtration again the UV-vis absorption spectrum of labelled collagen Au NPs was recorded. The uptake of collagen Au NPs by HeLa cells was visualized by fluorescence microscopy.

2.3 Synthesis of PMA-coated Au NPs

Hydrogen tetrachloroaurate (III) hydrate (AlfaAesar, Karlsruhe, Germany) sodium borohydride (Sigma, Darmstadt, Germany), and tetraoctylammonium bromide (Sigma, Darmstadt, Germany) were used to synthesise Au NPs (4-5 nm diameter) according to previously published protocols [9,13]. Briefly, an aqueous solution of $HAuCl_4$ was transferred to toluene to form an ionic pair with tetraoctylammonium bromide (TOAB, 4.5 eq), which also acts as a stabilizing agent. In the organic phase sodium borohydride ($NaBH_4$, 10 eq) was added to reduce Au^{3+} to Au^0, leading to the formation of colloidal Au NPs. Ostwald ripening, facilitating formation of a monodisperse suspension, occurred during an overnight incubation. The NPs were washed several times. The hydrophobic Au NPs were transferred into an aqueous solution by coating them with 1-dodecylamine-modified poly(isobutylene-alt-maleic anhydride (PMA, Sigma, Darmstadt, Germany; M_w = 6000 g mol^{-1}) as described previously [8,9,14,15]. For the coating procedure the following parameters referring to previous publications were used: molar extinction coefficient of the Au NPs $\varepsilon = 1.14 \cdot 10^7\ M^{-1}cm^{-1}$, core diameter d_c = 4.4 nm, thickness of surfactant layer l = 1.2 nm, leading to the effective diameter d_{eff} = 6.8 nm, number of added polymer monomer units per effective NP surface area $R_{P/area}$ = 200 nm^{-2}. 75 % of the anhydride rings of the polymer were linked with dodecylamine. Optionally the fluorophore Dy647 was incorporated into the polymer, as described in previous reports [16]. Hereby 1% of the anhydride rings were linked with fluorophore.

2.4 Nanoparticle purification and characterization

Both types of NPs were filtered and then purified by gel electrophoresis (*cf.* Supporting Information Figures S2 and S3). 2% gels were prepared by adding 7 g of agarose in 350 ml of 0.5 x TBE buffer (Tris/Borate/EDTA, pH 8.3) [17]. This mixture was brought to boiling and one-well-gels were prepared. The Au NPs were run in the gels for 60 minutes, with an applied voltage of 10 V/cm. Gel parts containing the NPs were cut out and placed in a dialysis membrane (50 kDa molecular weight cut-off (MWCO), Spectrum Labs) filled with 0.5 x TBE buffer, which was then exposed for 15 min to the same voltage in order to elute the NPs, which were then collected inside the dialysis membrane tubes. The extracted NPs were filtered and concentrated in water *via* ultrafiltration (100 kDa MWCO membranes). Prior to the experiments the NPs were filter-sterilized (0.02 µm) and their concentration was evaluated by UV-vis spectroscopy (molar extinction coefficient ε as given above). UV-vis absorption spectra of the prepared gold colloids were recorded on a Jasco V-630 UV-vis spectrophotometer, by using quartz cuvettes with an optical pathlength of 1 cm (*cf.*

Supporting Information Figure S4). Size and morphology of the Au NPs were determined using transmission electron microscopy (TE , imaging, performed with a JEOL model JEM 1010 microscope. High resolution TEM micrographs of the Au NPs were recorded with a PHILIPS CM 20 microscope operated at 200 kV. The diameters of the inorganic cores d_c of the NPs were calculated from the TEM micrographs using the ImageJ 1.45s software from Wayne Rasband, NIH, USA. The hydrodynamic diameter, d_h , and the zeta potential, ζ, of Au NPs were assessed with a Malvern Zeta-sizer (Malvern Instruments Ltd, Worcestershire, UK), based on dynamic light scattering (DLS) and laser Doppler anemometry (LDA), respectively.

2.5 Cell culture

Cervical carcinoma (HeLa) and adenocarcinoma alveolar basal epithelial (A549) cells were cultured in Dulbecco's Modified Eagle's culture medium (DMEM, Sigma, Darmstadt, Germany) supplemented with 2 mM glutamine (Sigma, Darmstadt, Germany), 10% FBS (fetal bovine serum) and 100 U/mL penicillin/streptomycin (Sigma, Darmstadt, Germany). The cells were grown at 37 °C in a humidified atmosphere containing 5% CO_2. Cells were seeded on 96-well plates at a density 5000 cells/well 24 h before experiments.

2.6 Particle internalization and sample preparation for ICP-MS measurements

A549 and HeLa cells were plated in 96-well plates at a density of 5000 cells/well 24 h prior to the experiments. The cells were incubated with different concentrations of Au NPs for 4 h. Au NPs were incubated with the cells in media with or without serum. The supernatants were collected and stored for further analysis at -20 °C. The cells were cultured for additional 20 h. Then the medium was removed and the cells were lysed with a lysis buffer (Cell Lysis Buffer, Promega, Mannheim, Germany). After 30 min the samples were collected and stored at -20 °C. Prior to ICP-MS measurements, 150 µL of 37% HCl were mixed with 50 µL of 65% HNO_3 and after 5 minutes added to each sample. This was followed by addition of 2.7 mL of 2% HCl. This treatment ensured sample decomposition to near atom size and allowed for more accurate measurements [16].

2.7 Cell Viability

Toxicity induced by gold NPs was evaluated with the MTT assay [11]. The assay is based on the reduction of the tetrazolium salt MTT to formazan by metabolically active cells. The produced formazan can be quantitatively evaluated by UV-vis absorption spectroscopy due to its absorption maximum at 570 nm. Cells were plated in 96-well plates at a density of 5000 cells/well 24 h before experiments. Different concentrations of both types of Au NPs were incubated for 4 h with HeLa or A549 cells in the presence of serum. After removing the medium with the excess NPs, the cells were cultured for additional 20 h. An MTT assay was then performed according to the manufacturer´s instructions (Roche, Germany).

3 Results and discussion

3.1 Synthesis and characterisation of Au NPs

We developed a synthesis procedure for Au NPs in which collagen acts both, as a reducing and as a stabilizing agent. The one step synthesis of protein-coated Au NPs prevents the use of reducing agents and stabilizers of chemical nature. Thus, no surface modification step is required and the synthesized Au NPs are exclusively covered by a protein layer, which in principle could be an advantage in terms of biocompatibility. As shown in Figure 1A the collagen-coated Au NPs synthesized in this work are characterized by the presence of the typical plasmon resonance at 520 nm, which commonly is observed for Au colloids [18][19]. As no surface-enhanced Raman signal for collagen-coated Au NPs was observed (*cf.* the Supporting Information, Figure S1), we assume an adsorption of collagen to Au NPs due to an electrostatic mechanism, similar to that proposed for albumin [20]. The TEM micrographs, shown in Figure 1B demonstrate that the collagen Au NPs display a relatively uniform morphology of approximately spherical shape with a mean diameter of the inorganic Au core of d_c = 7.4 nm, *i.e.* excluding the contribution of the collagen coating to the size, which does not provide contrast in TEM [4].

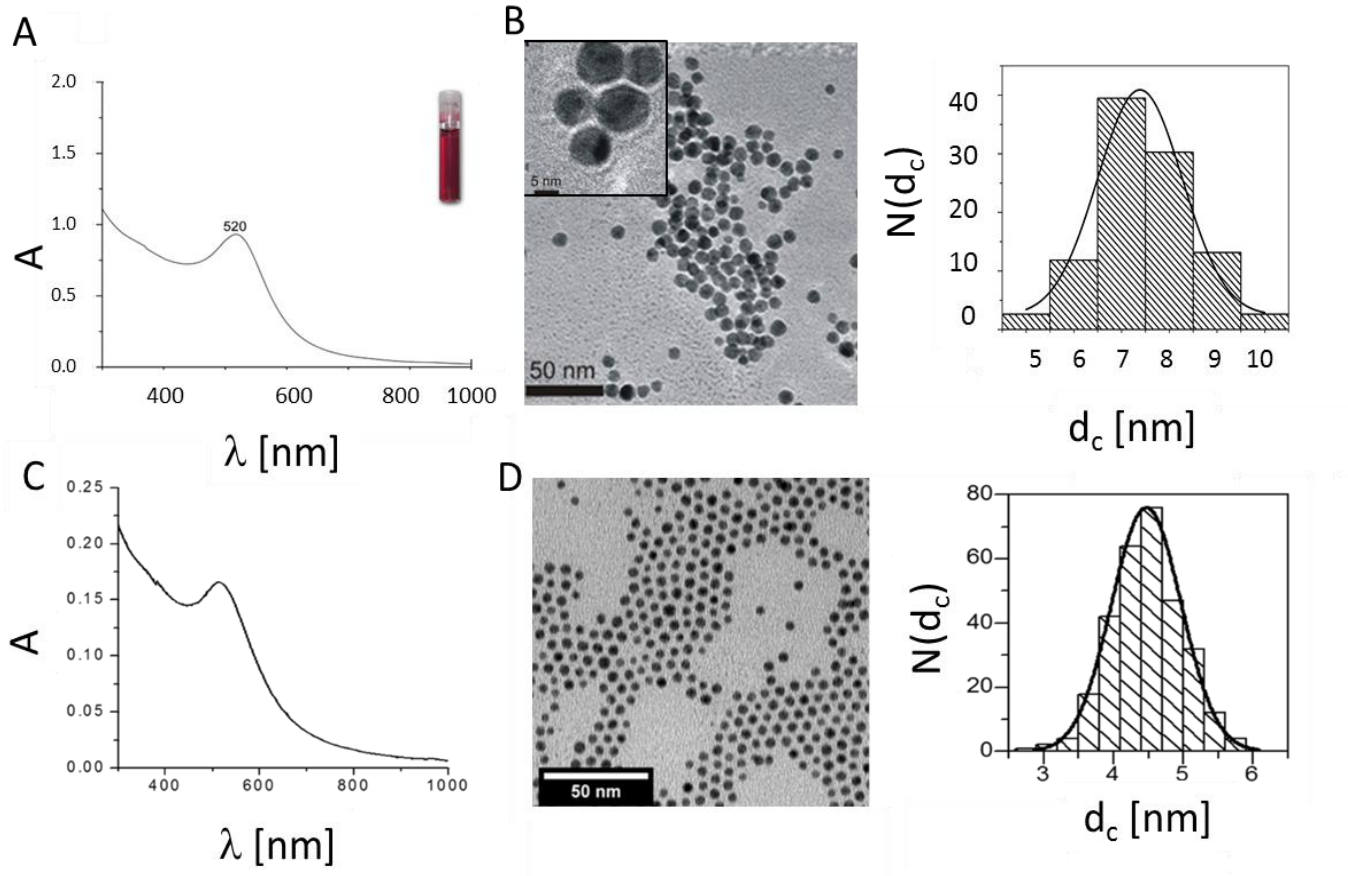

Figure 1. A. UV-vis absorption spectrum A(λ) of collagen coated Au NPs. The inset shows a vial with a solution of the Au NPs in water. B. TEM images and size distribution of collagen-coated Au NPs. The scale bar in the inset corresponds to 5 nm, the scale bar in the main image to 50 nm. From the size distribution N(d_c) of the inorganic cores as seen in the TEM image the mean value ± the standard deviation were determined to be d_c = 7.4 ± 2.4 nm. N corresponds to the number of counted NPs. C. UV-vis absorption spectrum A(λ) of PMA-coated Au NPs. D. TEM images and size distribution N(d_c) of PMA-coated Au NPs. The scale bar corresponds to 50 nm. As result d_c = 4.4 ± 1.1 nm was obtained.

The hydrodynamic diameter obtained by DLS from the number distribution in water and the zeta-potential were $d_h \approx 13.5 \pm 0.5$ nm and $\zeta = -38.0 \pm 2.5$ mV, respectively (the raw data are presented in the Supporting Information Figure S5, the data for dye-modified NPs in Figure S6). As comparison PMA-coated Au NPs, synthesized according to standard procedures [8,9], were used. These had an inorganic core diameter of $d_c = 4.4$ nm, a hydrodynamic diameter $d_h \approx 11.7$ nm and a zeta potential $\zeta = -56.4$ mV in water, respectively. The overall size in water (d_h) as well the zeta-potentials (ζ) are similar for both types of NPs, which suggests similar physico-chemical properties of collagen and PMA Au NPs in water. The high negative zeta potential values indicate a good colloidal stability in water. However, the surface coating of both types of NPs is quite different, one being a protein and the other a synthetic polymer.

The colloidal properties of NPs, however, are strongly dependent on the medium in which they are dispersed. The presence of salt may screen the charge of the NPs and proteins may be adsorbed to the NPs surface [4]. The colloidal properties of the NPs thus should be probed in the medium in which they are administered to cells. Different interaction with cells can be related to changes of colloidal properties in different media [21]. A convenient test involves the detection of changes of the hydrodynamic diameter over time in the respective media. In case the hydrodynamic diameter significantly increases agglomeration of the NPs can be assumed [22]. In Table 1 the time dependence of the hydrodynamic diameter of collagen- and PMA-coated Au NPs upon dispersion in cell medium without and with serum is shown (for the raw data *cf.* the Supporting Information Figure S7). The hydrodynamic diameter of PMA-coated Au NPs was found to be very stable in both types of culture media and it did not change significantly over a period of 4 h. Thus we may assume that the PMA-coated Au NPs are still well dispersed in cell media (*i.e.* supplemented DMEM). Quite differently, collagen-coated Au NPs were stable in medium with serum, but were prone to form aggregates in medium without serum. Similar results were found for bovine serum albumin-coated Au NPs when exposed to comparable media [23,24]. Our data suggest that the collagen is only loosely bound to the surface of the Au NPs. In case of serum-containing media proteins from the medium can adsorb to the NP surface and thus provide colloidal stability.

Table 1. Hydrodynamic diameter d_h of Au NPs dispersed in cell culture medium with or without serum, t = 0 h (*i.e.* before), 2 h, and 4 h after exposure to the medium. The concentration of Au NPs was c(NP) = 100 nM.

		d_h [nm]		
		t_0	t_{2h}	t_{4h}
Collagen-coated Au NPs	+ serum	18.1	18.1	18.1
Collagen-coated Au NPs	- serum	13.5	141.8	220
PMA-coated Au NPs	+ serum	8.7	8.7	8.7
PMA-coated Au NPs	- serum	15.6	15.6	15.6

3.2 Cellular internalization of NPs

We compared the uptake of both types of Au NPs by HeLa and A549 cells. First uptake of NPs was visualized with fluorescence microscopy. For this purpose cells were incubated with Au NPs which were labelled in their collagen or PMA shell with Dy647. In Figure 2 fluorescence microscopy images of cells after 4 h of incubation with the NPs are shown. In these qualitative images it can be seen that the NPs (red fluorescence due to the Dy647) are located in grainy structures around the nucleus (blue fluorescence due to staining with 4',6-diamidino-2-phenylindole (DAPI)), which indicates for both types of NPs uptake *via* endocytosis and final localization in the endolysosomal

compartment. As this is the expected classical pathway for NP internalization no quantitative evaluation and localization studies were performed. Instead NP uptake was quantified *via* ICP-MS.

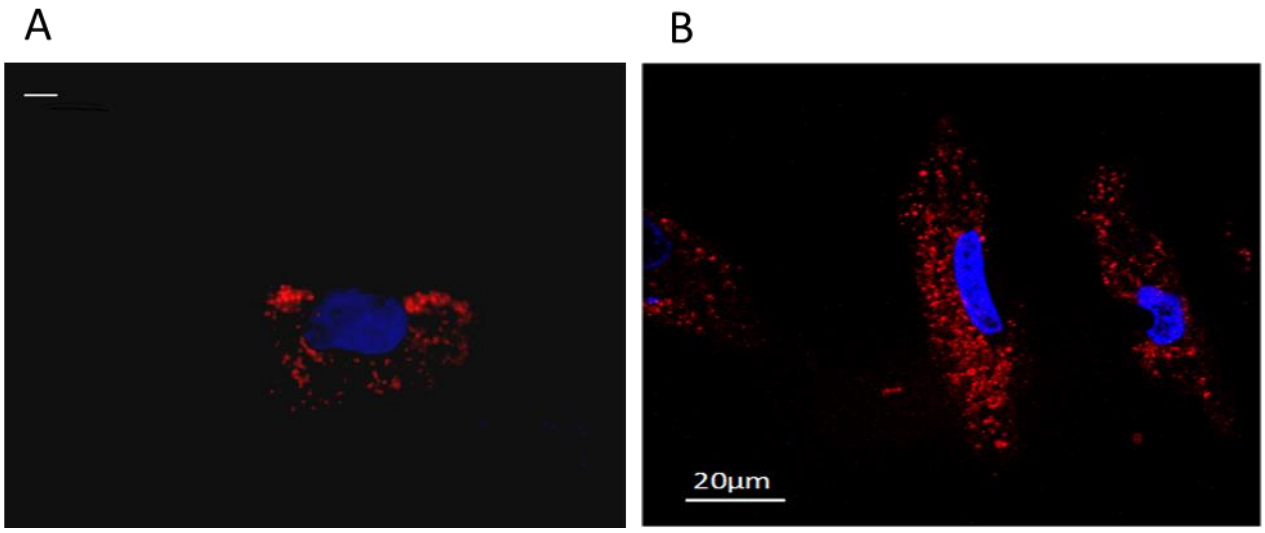

Figure 2. Internalization of Au NPs by HeLa cells. Images of HeLa cells as incubated with fluorescence-labelled Au NPs. A) Collagen-coated Au NPs, the scale bar corresponds to 10 µm. B) PMA-coated Au NPs, the scale bar corresponds to 20 µm. The NPs were labelled with Dy647 and thus appear in read. The nuclei were labelled with DAPI, and thus appear in blue.

For quantitative uptake studies the cells were incubated with the Au NPs in the absence of serum as well as in serum-supplemented media, and NP uptake was quantified as the amount of internalized Au atoms *via* ICP-MS, *cf.* Figure 3. In agreement with previous studies NPs were incorporated by cells to a higher extent in case of serum-absence than in serum-supplemented media[21]. As demonstrated in Figure 3, NPs stabilized with collagen were taken up by both cell lines more efficiently than those stabilized with PMA. In serum-free medium the maximal uptake levels of collagen-coated Au NPs by HeLa and A549 cells measured as number of incorporated Au atoms amounted to 90.000 and 78.000 ppb, respectively. By contrast, maximal uptake levels of PMA-coated Au NPs by HeLa cells and by A549 cells were 1400 ppb and 850 ppb, respectively. In serum-containing medium the maximum levels of incorporated Au were 2500 and 4000 ppb for HeLa and A549 cells, respectively. The maximal uptake levels of PMA-coated Au NPs by both HeLa and A549 cells were 400 ppb, *cf.* Figure 3. Note that cells were incubated with the same concentration of Au NPs. As the collagen-coated Au NPs have a larger inorganic core diameter d_c than the PMS coated NPs, cells were exposed to more Au atoms in the case of collagen-coated Au NPs. One Au NP with core diameter d_c comprises $N_{Au} = (4\pi/3)\cdot(d_c/2)^3\cdot\rho_{Au}/M_{Au}$ Au atoms, using the density of bulk gold ρ_{Au} = 19.32 g/cm^{-3} and the molar mass of one Au atom M_{Au} = 196.96 g/mol [25]. Thus one collagen-coated Au NP in our study represents N_{Au}(collagen NP)/N_{Au}(PMA NP) = (d_c(collagen)/d_c(PMA NP))^3 = (7.4 nm/4.4 nm)^3 ≈ 4.75 times more Au atoms than one PMA-coated NP. Thus, despite the fact that at equal incubation concentrations of collagen- and PMA-coated Au NPs, cells were incubated with a 4.75 times higher concentration of elemental Au in the case of collagen-coated NPs, the difference in internalized elemental Au is much larger in case of collagen-coated NPs. Also in terms of the number of NPs the collagen-coated NPs were internalized to a much higher extent.

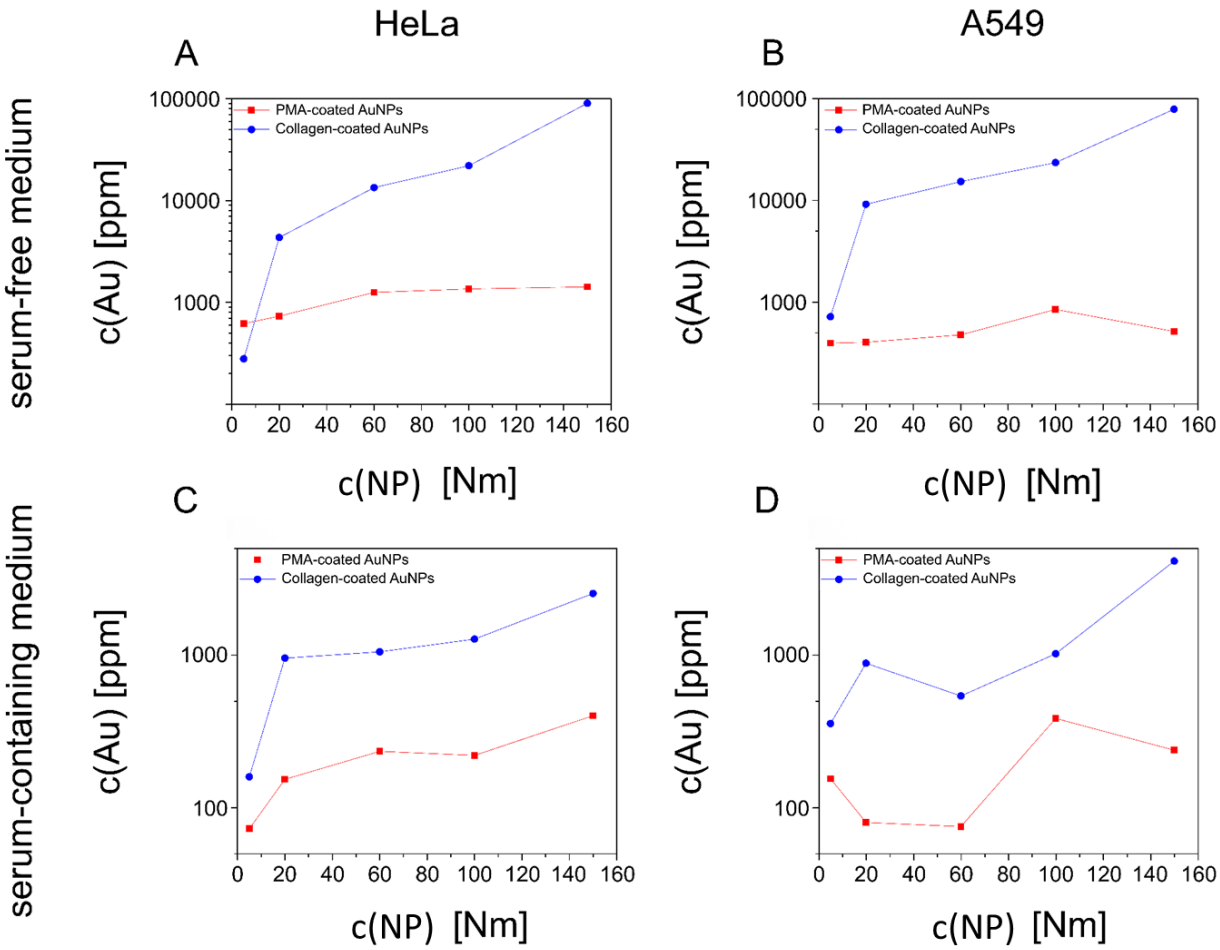

Figure 3. Internalization of Au NPs by cells. Collagen- and PMA-coated Au NPs were added to HeLa (A, C) or A549 (B, D) cells in medium without (A, B) and supplemented (C, D) with serum at different NP concentrations c(NP). After 4 hours of incubation the media with the excess of non-internalized NPs was removed and the cells were thoroughly washed. The cells were cultured for additional 20 h. The medium was then removed and the cells were lysed. The samples were analyzed with ICP-MS and the amount of internalized elemental gold c(Au) was determined. The lines between the individual points are merely intended to guide to the reader.

In the case of serum-free incubation conditions it might be argued that the increase in NP uptake of the collagen- *versus* the PMA-coated NPs was caused by agglomeration of the collagen-coated Au-NPs, causing them to sediment on top of the cells and thus to be incorporated faster. However, increased uptake was also observed under serum-containing conditions, in which the collagen-coated Au NPs did not agglomerate to an appreciable extent. Thus, it appears that collagen *versus* PMA surface coating may have a direct effect on the extent to which NPs are taken up, apart from the effect of agglomeration.

3.3 Cell viability upon incubation with Au NPs

The potential of Au NPs towards future medical applications can be properly evaluated only if possible toxic effects on cells are taken into consideration. Therefore, we assessed the impact of collagen- and PMA-coated Au NPs on the viability of A549 and HeLa cells. The NPs were incubated with the cells in the presence of serum. The cells were exposed to a range of Au NP concentrations between 0.2 nM and 200 nM. As shown in Figure 4 the collagen-coated Au NPs

induced a lower toxic effect than PMA-coated Au NPs, in both cell lines tested. As expected, the most toxic effects were observed at the highest concentration tested (200 nM). Under those conditions, cell viability was reduced to around 80 % for collagen-coated Au NPs and around 60% for PMA-coated Au NPs. Low toxicity of collagen-coated Au NPs is not surprising since collagen is a protein which forms an integral part of biological systems. Similar results were found when testing the cytotoxicity of other protein coated Au NPs, ranging from peptides [26], amino acids [5] to proteins such as albumin [27] [28]. For the direct comparison between collagen- and PMA-coated Au NPs we applied only short exposure times (4 hours). Thus reduction in cell viability occurs only at very high NP concentrations. Data from previous studies show that upon prolonged exposure times toxic effects of PMA-coated Au NPs (and similar NPs) occur already at lower NP concentrations [14,21,29].

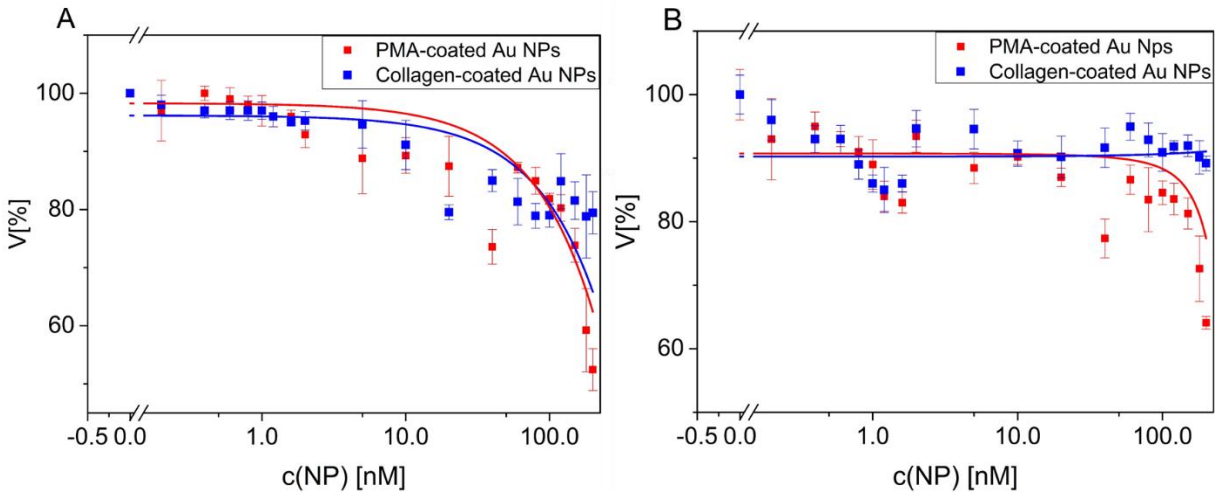

Figure 4. Viability V of HeLa and A549 cells upon incubation with Au NPs. Au NPs were incubated with HeLa (A) and A549 (B) cells for 4 h in medium with serum. Untreated cells were used as a control (100%). Cell viability was assayed 24 h after incubation with an MTT assay. NP concentrations c(NP) between 0.2 nM and 200 nM were tested. The lines between the individual points are merely intended to guide to the reader, they do not correspond to a mathematical fit.

Conclusions

In this work we characterized spherical collagen-coated Au NPs with a mean core diameter of 7 nm. These NPs were obtained by following a straightforward one-step synthesis method. Collagen acted as reducing as well as stabilizing agent. Internalization and toxicity of collagen-coated Au NPs were tested in A549 and HeLa cells. These results were compared with the data obtained for Au NPs in the same size range, but coated with a synthetic polymer (PMA). NPs stabilized with collagen were taken up by both cell lines more efficiently than those stabilized with PMA, both in the presence and absence of serum. Concentration dependent toxicity studies further revealed that at short exposure times collagen-coated Au NPs were less toxic to the cells than PMA-coated Au NPs. Importantly, the collagen-coated NPs, which are internalized to a high degree, exhibit lower toxicity. The results presented here support the notion that the material employed for coating Au NPs play a role in their biocompatibility and the pattern of internalization. In this context naturally occurring macromolecules, such as collagen, may represent a group of interesting stabilizing agents to be used for future biomedical applications.

Acknowledgements

This work was supported by the European Commission (grant FutureNanoneeds to WJP). QZ acknowledges support from the Chinese Scholarship Council (CSC) and BP a fellowship from the Alexander von Humboldt Foundation.

Bibliography

1. Sperling, R.A.; Rivera Gil, P.; Zhang, F.; Zanella, M.; Parak, W.J. Biological applications of gold nanoparticles. *Chemical Society Reviews* **2008**, *37*, 1896-1908.
2. Aroca, R.; Alvarez-Puebla, R.; Pieczonka, N.; Sanchez-Cortez, S.; Garcia-Ramos, J. Surface-enhanced raman scattering on colloidal nanostructures. *Advances in colloid and interface science* **2005**, *116*, 45-61.
3. Leopold, N.; Chiş, V.; Mircescu, N.E.; Marişca, O.T.; Buja, O.M.; Leopold, L.F.; Socaciu, C.; Braicu, C.; Irimie, A.; Berindan-Neagoe, I. One step synthesis of sers active colloidal gold nanoparticles by reduction with polyethylene glycol. *Colloids and Surfaces A: Physicochemical and Engineering Aspects* **2013**, *436*, 133-138.
4. Rivera-Gil, P.; Jimenez De Aberasturi, D.; Wulf, V.; Pelaz, B.; Del Pino, P.; Zhao, Y.; De La Fuente, J.M.; Ruiz De Larramendi, I.; Rojo, T.; Liang, X.-J.*, et al.* The challenge to relate the physicochemical properties of colloidal nanoparticles to their cytotoxicity. *Accounts of chemical research* **2013**, *46*, 743-749.
5. Cai, H.; Yao, P. Gold nanoparticles with different amino acid surfaces: Serum albumin adsorption, intracellular uptake and cytotoxicity. *Colloids and surfaces. B, Biointerfaces* **2014**, *123*, 900-906.
6. Klingberg, H.; B. Oddershede, L.; Loeschner, K.; Larsen, E.H.; Loft, S.; Møller, P. Uptake of gold nanoparticles in primary human endothelial cells. *Toxicol. Res.* **2015**.
7. Pyshnaya, I.A.; Razum, K.V.; Poletaeva, J.E.; Pyshnyi, D.V.; Zenkova, M.A.; Ryabchikova, E.I. Comparison of behaviour in different liquids and in cells of gold nanorods and spherical nanoparticles modified by linear polyethyleneimine and bovine serum albumin. *BioMed research international* **2014**, *2014*, 908175.
8. Lin, C.-A.J.; Sperling, R.A.; Li, J.K.; Yang, T.-Y.; Li, P.-Y.; Zanella, M.; Chang, W.H.; Parak, W.J. Design of an amphiphilic polymer for nanoparticle coating and functionalization. *Small* **2008**, *4*, 334-341.
9. Geidel, C.; Schmachtel, S.; Riedinger, A.; Pfeiffer, C.; Müllen, K.; Klapper, M.; Parak, W.J. A general synthetic approach for obtaining cationic and anionic inorganic nanoparticles via encapsulation in amphiphilic copolymers. *Small* **2011**, *7*, 2929-2934.
10. Berridge, M.V.; Herst, P.M.; Tan, A.S. Tetrazolium dyes as tools in cell biology: New insights into their cellular reduction. *Biotechnology annual review* **2005**, *11*, 127-152.
11. Mosmann, T. Rapid colorimetric assay for cellular growth and survival: Application to proliferation and cytotoxicity assays. *Journal of Immunological Methods* **1983**, *65*, 55-63.
12. Haiss, W.; Thanh, N.T.K.; Aveyard, J.; Fernig, D.G. Determination of size and concentration of gold nanoparticles from uv−vis spectra. *Analytical Chemistry* **2007**, *79*, 4215-4221.
13. Brust, M.; Walker, M.; Bethell, D.; Schiffrin, D.J.; Whyman, R. Synthesis of thiol-derivatised gold nanoparticles in a two-phase liquid-liquid system. *Journal of the Chemical Society, Chemical Communications* **1994**, 801-802.
14. Soliman, M.G.; Pelaz, B.; Parak, W.J.; del Pino, P. Phase transfer and polymer coating methods toward improving the stability of metallic nanoparticles for biological applications. *Chemistry of Materials* **2015**, *27*, 990-997.
15. Tan, G.; Kantner, K.; Zhang, Q.; Soliman, M.G.; Pino, P.d.; Parak, W.J.; Onur, M.A.; Valdepérez, D.; Rejman, J.; Pelaz, B. Conjugation of polymer-coated gold nanoparticles with antibodies - synthesis and characterization *Nanomaterials, submitted*.

16. Kreyling, W.G.; Abdelmonem, A.M.; Ali, Z.; Alves, F.; Geiser, M.; Haberl, N.; Hartmann, R.; Hirn, S.; de Aberasturi, D.J.; Kantner, K.*, et al.* In vivo integrity of polymer-coated gold nanoparticles. *Nat Nano* **2015**, *10*, 619-623.
17. Pellegrino, T.; Sperling, R.A.; Alivisatos, A.P.; Parak, W.J. Gel electrophoresis of gold-DNA nanoconjugates. *Journal of Biomedicine and Biotechnology* **2007**, *2007*, 9.
18. Turkevich, J.; Stevenson, P.C.; Hillier, J. A study of the nucleation and growth processes in the synthesis of colloidal gold. *Discussions of the Faraday Society* **1951**, *11*, 55-75.
19. Nikolai G.Khlebtsov ; A.Dykman, L. Optical properties and biomedical applications of plasmonic nanoparticles. *Journal of Quantitative Spectroscopy & Radiative Transfer* **2010**, *111*, 1–35.
20. Fu, C.; Yang, H.; Wang, M.; Xiong, H.; Yu, S. Serum albumin adsorbed on au nanoparticles: Structural changes over time induced by s-au interaction. *Chemical Communications* **2015**.
21. Hühn, D.; Kantner, K.; Geidel, C.; Brandholt, S.; De Cock, I.; Soenen, S.J.H.; Rivera_Gil, P.; Montenegro, J.-M.; Braeckmans, K.; Müllen, K.*, et al.* Polymer-coated nanoparticles interacting with proteins and cells: Focusing on the sign of the net charge. *ACS Nano* **2013**, *7*, 3253-3263.
22. Caballero-Díaz, E.; Pfeiffer, C.; Kastl, L.; Rivera-Gil, P.; Simonet, B.; Valcárcel, M.; Jiménez-Lamana, J.; Laborda, F.; Parak, W.J. The toxicity of silver nanoparticles depends on their uptake by cells and thus on their surface chemistry. *Particle & Particle Systems Characterization* **2013**, *30*, 1079-1085.
23. Hauck, T.S.; Ghazani, A.A.; Chan, W.C.W. Assessing the effect of surface chemistry on gold nanorod uptake, toxicity, and gene expression in mammalian cells. *Small* **2008**, *4*, 153-159.
24. Brewer, S.H.; Glomm, W.R.; Johnson, M.C.; Knag, M.K.; Franzen, S. Probing bsa binding to citrate-coated gold nanoparticles and surfaces. *Langmuir* **2005**, *21*, 9303-9307.
25. Feliu, N.; Pelaz, B.; Zhang, Q.; Pino, P.d.; Nyström, A.; Parak, W.J. "Nanoparticle dosage - a nontrivial task of utmost importance for quantitative nanotoxicology". *WIREs Nanomedicine & Nanobiotechnology, in revision*.
26. Kumar, A.; Ma, H.; Zhang, X.; Huang, K.; Jin, S.; Liu, J.; Wei, T.; Cao, W.; Zou, G.; Liang, X.J. Gold nanoparticles functionalized with therapeutic and targeted peptides for cancer treatment. *Biomaterials* **2012**, *33*, 1180-1189.
27. Khullar, P.; Singh, V.; Mahal, A.; Dave, P.N.; Thakur, S.; Kaur, G.; Singh, J.; Singh Kamboj, S.; Singh Bakshi, M. Bovine serum albumin bioconjugated gold nanoparticles: Synthesis, hemolysis, and cytotoxicity toward cancer cell lines. *The Journal of Physical Chemistry C* **2012**, *116*, 8834-8843.
28. Choi, S.Y.; Jeong, S.; Jang, S.H.; Park, J.; Park, J.H.; Ock, K.S.; Lee, S.Y.; Joo, S.W. In vitro toxicity of serum protein-adsorbed citrate-reduced gold nanoparticles in human lung adenocarcinoma cells. *Toxicology in vitro : an international journal published in association with BIBRA* **2012**, *26*, 229-237.
29. Soenen, S.J.; Manshian, B.; Montenegro, J.M.; Amin, F.; Meermann, B.; Thiron, T.; Cornelissen, M.; Vanhaecke, F.; Doak, S.; Parak, W.J.*, et al.* Cytotoxic effects of gold nanoparticles: A multiparametric study. *ACS Nano* **2012**, *6*, 5767-5783.

1.09.04. Metal and Metal Oxide Core-shell Nanocomposites

Assembling several inorganic materials into a single nanocomposite, which exhibits the physical and chemical properties of their constituents, represents an innovative and relatively new way to design multifunctional materials.[1-3] Engineered hybrid nanocomposites (including core-shell structures) have been proven to offer novel and frequently unique properties that originate from collective interactions between the constituents. Furthermore, precise hybridization of nanocrystals with on-demand optical, electronic and magnetic properties into hybrid nanocomposites might provide a route to enhanced metamaterials.[4, 5] In literature, a vast variety of nanocomposites have been reported to date[3] including bimetallic nanoparticles,[6, 7] semiconductors materials (as previously described), metals oxides,[8] and mixtures of them.[3, 9] The most general and extended strategy to synthesize these hybrid materials consists of two steps: (i) synthesis of nanoparticles of one material, and (ii) use of the newly prepared NPs as nucleation seeds to deposit the other components (Figure x1)

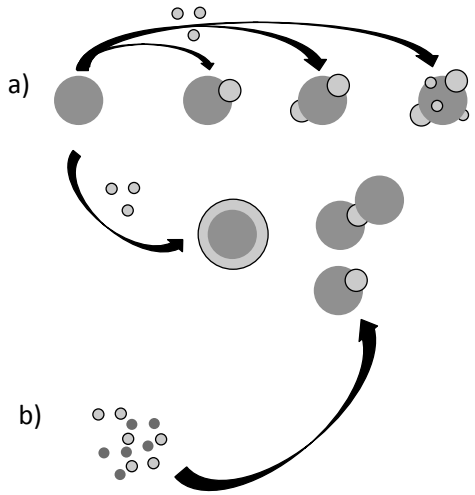

Figure x1. Schemes of different growth mechanisms during the synthesis of hybrid nanoparticles. a) Surface nucleation and growth of a second phase on a seed nanoparticle (material-1). Top: growth of islands (material-2) on “seeds” of material 1; bottom: growth of material 2 from a material 1 seed. b) Simultaneous nucleation and growth of both materials. Adapted from Costi et al.[3]

Given the multiple potential applications of superparamagnetic nanoparticles, nanocomposites carrying the superparamagnetic properties of a ferrite core and the shielding/surface as well as the optical properties of a metallic shell (e.g. gold) add an extra value to the suitability of bare ferrite NPs for bioapplications. In literature, there is a wide variety of composite nanomaterials composed by iron oxide and another inorganic material.[10]

One of the most addressed multicomponent nanomaterials based on iron oxide is based on the core-shell structure containing a core of iron oxide and a thin shell of metallic gold (iron oxide@gold NPs); a myriad of strategies have been described to synthesized this structure, *i.e.* thermal decomposition,[11, 12] reverse micelle method using cetyltrimethylammonium bromide (CTAB) as surfactant,[13, 14] chemical

coprecipitation[15] or growing the gold on the iron oxide by an iterative hydroxylamine seeding.[16]

Even in the absence of external magnetic fields, one of the major challenges in the synthesis and stabilization of magnetic nanomaterials is the prevention of anisotropic magnetic dipolar attraction.[17] Experimentally, providing the magnetic core with an external coating is one of the successful approaches. A shell also provides oxidative stability to the magnetic core which is crucial for the efficient of magnetic materials in applications such as hyperthermia, magnetofection or MRI. Some experimental works have also pointed out that core-shell structures can enhance the capability of these core-shell NPs to heat under AMF.[8, 18]

The use of core-shell structures of magnetic materials have been used to produce ferrites which exhibit specific loss values one order of magnitude higher than the conventional iron oxide nanoparticles.[8] The design of these materials is based on the combination of magnetically hard core with a magnetically soft shell, *cf.* Figure x2.

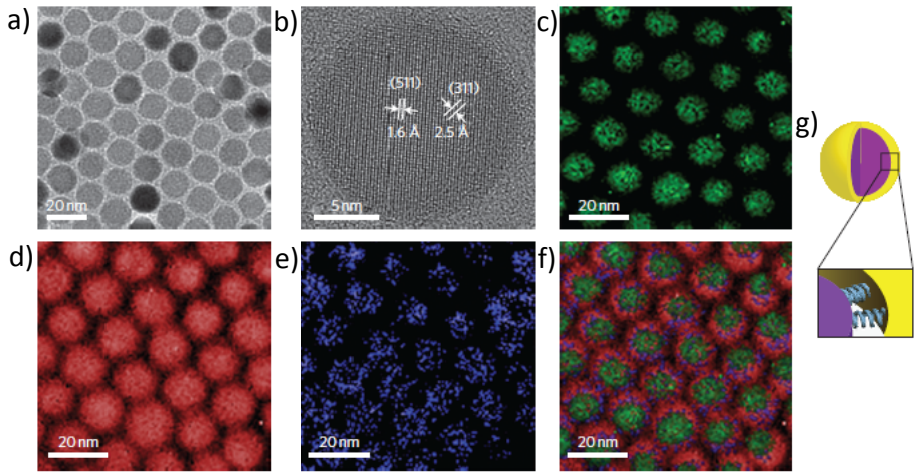

Figure x2. TEM analyses of core–shell nanoparticles a) TEM image b) and high-resolution TEM image of 15 nm $CoFe_2O_4$@$MnFe_2O_4$, c–f) EELS mapped images: c) Co mapped image, d) Fe mapped image, e) Mn mapped image, f) and overlay image of c–e and g) schematic drawing of core–shell nanoparticle with an exchange-coupled magnetism. Adapted from Lee et al. [8]

The generation of bimetallic nanoparticles has been also widely explored aiming to produce materials with new optical properties[19] or to generate highly efficient catalysts.[6] For example Liz-Marzán´s group evaluated the silver growing using gold nanodummbells as templates, *cf.* Figure 3.[20] They evaluated the changes in the optical properties of these nanomaterials. Although many other materials combinations and shapes have been explored.

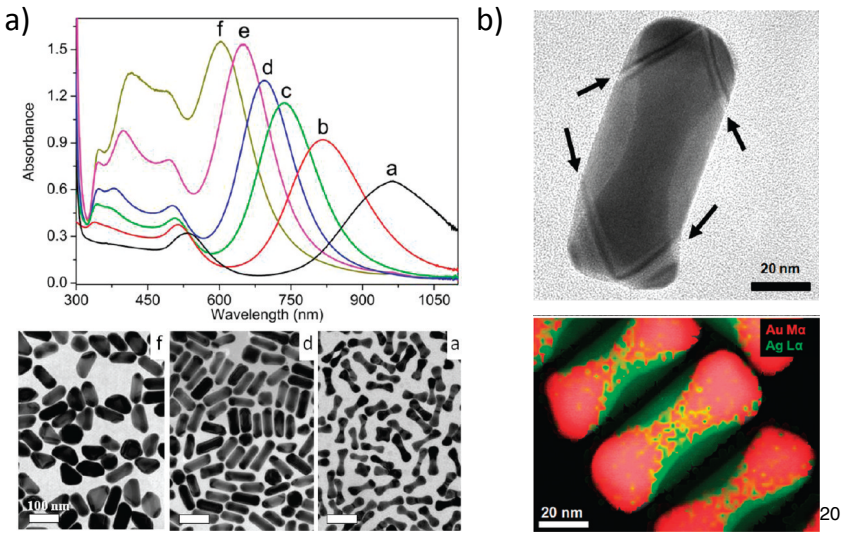

Figure 3. a)UV-visible-NIR extinction spectra of gold dumbbells (a) and bimetallic nanoparticles grown with increasing [Ag^+]/ [Au^0] molar ratios (0.3, 0.7, 1, 1.7, 2.3 from b to f). Lower panel: Representative TEM images corresponding to samples a, d and f (scale bars: 100 nm) b)Upper panel: TEM image showing the core-shell contrast and lower panel: STEM-XEDS elemental map of Au dumbbells@Ag nanoparticles. Adapted from Cardinal et al.

1. Carbone L, Cozzoli PD. Colloidal heterostructured nanocrystals: Synthesis and growth mechanisms.*Nano Today* 2010, 5:449-493.
2. Levin CS, Hofmann C, Ali TA, Kelly AT, Morosan E, Nordlander P, Whitmire KH, Halas NJ. Magnetic-Plasmonic Core-Shell Nanoparticles.*ACS Nano* 2009, 3:1379-1388.
3. Costi R, Saunders AE, Banin U. Colloidal Hybrid Nanostructures: A New Type of Functional Materials.*Angewandte Chemie-International Edition* 2010, 49:4878-4897.
4. Shevchenko EV, Talapin DV, Kotov NA, O'Brien S, Murray CB. Structural diversity in binary nanoparticle superlattices.*Nature* 2006, 439:55-59.
5. Urban JJ, Talapin DV, Shevchenko EV, Kagan CR, Murray CB. Synergism in binary nanocrystal superlattices leads to enhanced p-type conductivity in self-assembled PbTe/Ag2Te thin films.*Nat Mater* 2007, 6:115-121.
6. Sankar M, Dimitratos N, Miedziak PJ, Wells PP, Kiely CJ, Hutchings GJ. Designing bimetallic catalysts for a green and sustainable future.*Chemical Society Reviews* 2012, 41:8099-8139.
7. Cortie MB, McDonagh AM. Synthesis and Optical Properties of Hybrid and Alloy Plasmonic Nanoparticles.*Chemical Reviews* 2011, 111:3713-3735.
8. Lee J-H, Jang J-t, Choi J-s, Moon SH, Noh S-h, Kim J-w, Kim J-G, Kim I-S, Park KI, Cheon J. Exchange-coupled magnetic nanoparticles for efficient heat induction.*Nat Nano* 2011, 6:418-422.
9. Leung KC-F, Xuan S, Zhu X, Wang D, Chak C-P, Lee S-F, Ho WKW, Chung BCT. Gold and iron oxide hybrid nanocomposite materials.*Chemical Society Reviews* 2012.
10. Gupta AK, Gupta M. Synthesis and surface engineering of iron oxide nanoparticles for biomedical applications.*Biomaterials* 2005, 26:3995-4021.
11. Pal S, Morales M, Mukherjee P, Srikanth H. Synthesis and magnetic properties of gold coated iron oxide nanoparticles.*Journal of Applied Physics* 2009, 105:07B504.

12. Wang LY, Luo J, Fan Q, Suzuki M, Suzuki IS, Engelhard MH, Lin YH, Kim N, Wang JQ, Zhong CJ. Monodispersed core-shell Fe3O4@Au nanoparticles.*Journal of Physical Chemistry B* 2005, 109:21593-21601.
13. Carpenter EE, Sangregorio C, O'Connor CJ. Effects of shell thickness on blocking temperature of nanocomposites of metal particles with gold shells.*Ieee Transactions on Magnetics* 1999, 35:3496-3498.
14. Cho SJ, Idrobo JC, Olamit J, Liu K, Browning ND, Kauzlarich SM. Growth mechanisms and oxidation resistance of gold-coated iron nanoparticles.*Chemistry of Materials* 2005, 17:3181-3186.
15. Mikhaylova M, Kim DK, Bobrysheva N, Osmolowsky M, Semenov V, Tsakalakos T, Muhammed M. Superparamagnetism of magnetite nanoparticles: Dependence on surface modification.*Langmuir* 2004, 20:2472-2477.
16. Lyon JL, Fleming DA, Stone MB, Schiffer P, Williams ME. Synthesis of Fe oxide core/Au shell nanoparticles by iterative hydroxylamine seeding.*Nano Letters* 2004, 4:719-723.
17. Kumar C, Mohammad F. Magnetic nanomaterials for hyperthermia-based therapy and controlled drug delivery.*Advanced Drug Delivery Reviews* 2011, 63:789-808.
18. Habib AH, Ondeck CL, Chaudhary P, Bockstaller MR, McHenry ME. Evaluation of iron-cobalt/ferrite core-shell nanoparticles for cancer thermotherapy.*Journal of Applied Physics* 2008, 103.
19. Liz-Marzán LM. Tailoring Surface Plasmons through the Morphology and Assembly of Metal Nanoparticles.*Langmuir* 2006, 22:32-41.
20. Fernanda Cardinal M, Rodríguez-González B, Alvarez-Puebla RA, Pérez-Juste J, Liz-Marzán LM. Modulation of Localized Surface Plasmons and SERS Response in Gold Dumbbells through Silver Coating.*The Journal of Physical Chemistry C* 2010, 114:10417-10423.